

Smart K_d -Concept for Long-term Safety Assessments

Extension towards more
Complex Applications

Carried out by:

The logo for HZDR, consisting of the letters 'H', 'Z', 'D', and 'R' in a bold, blue, sans-serif font. The 'H' has a small orange square above it.The logo for GRS, consisting of the letters 'G', 'R', and 'S' in a stylized, rounded font. The logo is grey.

Smart K_d -Concept for Long-term Safety Assessments

Extension towards more
Complex Applications

Ulrich Noseck (GRS)
Vinzenz Brendler (HZDR-IRE)
Susan Britz (GRS)
Madlen Stockmann (HZDR-IRE)
Julian Fricke (GRS)
Constanze Richter (UIT)
Michael Lampe (G-CSC)
Anne Gehrke (GRS)
Judith Flügge (GRS)

June 2018

Remark:

This R&D report was prepared under funding reference No.s 02 E 11072A and 02 E 11072B by the Federal Ministry of Economics and Energy (BMWi).

The work was conducted by the Gesellschaft für Anlagen- und Reaktorsicherheit (GRS) gGmbH and the Helmholtz-Zentrum Dresden-Rossendorf e.V. (HZDR-IRE).

The authors are responsible for the content of the report.

Keywords:

Distribution Coefficient, Sorption, Surface Complexation, Radionuclide, Transport

Zusammenfassung

Die Langzeitsicherheitsanalyse stellt ein wichtiges Element eines Safety Case für ein tiefes geologisches Endlager für radioaktive Abfälle dar. Nach Definition der OECD/NEA ist sie eine systematische Analyse der Gefährdungen, die mit dem geologischen Endlager zusammenhängen und umfasst die Entwicklung eines Verständnisses, wie und unter welchen Umständen Radionuklide aus einem Endlager freigesetzt werden können, wie wahrscheinlich eine Freisetzung ist und welche radiologischen Konsequenzen das für Mensch und Umwelt hat. Ein wichtiger Bestandteil dieser Abschätzung ist die Simulation von Fluid- und Schadstofftransport durch das Endlagersystem, d.h. durch große Modellgebiete (über mehrere km) und über lange Zeiträume (bis zu 1 Million Jahre). Entscheidend bei der Simulation ist auch eine möglichst realitätsnahe Beschreibung der Schadstoffrückhaltung, die wiederum signifikant durch geochemische Veränderungen beeinflusst wird.

Zur Beschreibung des Einflusses geochemischer Veränderungen auf die Schadstoffrückhaltung wurde im Rahmen des vorangegangenen Vorhabens ESTRAL ein erster Ansatz zur Implementierung des smart K_d -Konzepts in das Transportprogramm r^{3t} (radionuclide, reaction, retardation, and transport /FEI 04/ entwickelt. Der Modellansatz basiert auf mechanistischen Oberflächenkomplexierungsmodellen (SCM), die mit einem „Bottom-Up-Ansatz“ kombiniert werden. In diesem Ansatz wird die Sorption eines Elements an einem Sediment als Summe der Sorption des Elements an jedem einzelnen Mineral beschrieben. Jedes Sediment besteht dabei aus einer definierten Zusammensetzung verschiedener Minerale. In der ersten Entwicklungsstufe wurde ein typisches sedimentäres System, das Steinsalz- und Tonformationen in Norddeutschland überlagert, betrachtet. Dafür wurde der gut untersuchte Referenzstandort Gorleben ausgewählt.

Dieser Ansatz wurde im hier beschriebenen Vorhaben WEIMAR auf verschiedenen Ebenen weiterentwickelt. Ursprünglich wurde das Modellsystem des Referenzstandortes in drei verschiedene hydrogeologische Einheiten unterteilt: einen oberen Grundwasserleiter, einen Grundwassergeringleiter und einen unteren Grundwasserleiter. Nach Auswertung der petrographischen und geologischen Daten sowie in Zusammenarbeit mit der Bundesanstalt für Geowissenschaften und Rohstoffe (BGR) wurde der untere Grundwasserleiter zusätzlich in zwei separate Einheiten unterteilt: die tertiären Elstersande einerseits und die miozänen Braunkohlesande andererseits.

Die Berücksichtigung der geochemischen Einflussgrößen wurde modifiziert und erweitert im Vergleich zum Vorgängervorhaben ESTRAL. In der ersten Entwicklungsstufe wurden der pH-Wert, die Ionenstärke sowie die Konzentrationen von gelöstem anorganischen Kohlenstoff (DIC), Calcium und zehn ausgewählten Radionukliden als Einflussgrößen festgelegt. Im WEIMAR-Vorhaben wurden Aluminium und Sulfat als neue Einflussgrößen implementiert, da sie u.a. als Konkurrenzkat, bzw. Ligand die Sorption der Radionuklide entscheidend beeinflussen können. Basierend auf Ergebnissen von Verifikationsrechnungen wurde zusätzlich die erste Entwicklungsstufe optimiert.

Während der Laufzeit des WEIMAR-Vorhabens wurden das Strömungsprogramm d^3f (distributed density-driven flow) und das Transportprogramm r^{3t} von der bisherigen Plattform UG3 (Unstructured Grids 3) auf die weiterentwickelte Version UG4 übertragen und in diesem Zusammenhang zu einem gemeinsamen Code d^{3f++} zusammengeführt. Entsprechend musste auch das bisher in r^{3t} implementierte Konzept auf den neuen Code d^{3f++} übertragen werden. Erste Verifikationsrechnungen zeigen, dass dies erfolgreich geschehen ist.

Die im Vorhaben ESTRAL entwickelte thermodynamische Datenbank für den erweiterten Debye–Hückel Ansatz (EDH) wurde im Rahmen von WEIMAR wesentlich erweitert und qualifiziert. Einerseits wurden thermodynamische Daten für gelöste Spezies wie Eisen(II,III), Mangan(II,IV), Calcium(II) und Magnesium(II) als mögliche Konkurrenzkat, sowie, Neodym(III) und Europium(III) als relevante Radionuklide/Homologe (für Batch- bzw. Säulenexperimente) in die Datenbank aufgenommen bzw. aktualisiert. Für Europium wurden beispielsweise die Daten aus der neu erstellten, bisher umfangreichsten Projekt-spezifischen Datenbasis (SEM²-Projekt) übernommen. Andererseits wurden auch die Daten für sorbierte Komplexe gründlich überprüft und verbessert. Zur Beschreibung der Systeme mit sehr hohen Ionenstärken, wie sie in weiten Bereichen des unteren Grundwasserleiters auftreten, wurde eine zweite Datenbasis erstellt, die auf dem Pitzer-Ansatz beruht. Dabei konnte Kredit von Ergebnissen des THEREDA-Projekts genommen werden und existierende Daten zu Americium(III), Neodym(III), Uran(IV/VI), Neptunium(V), Thorium(IV), Technetium(IV / VII), Strontium(II) und Cäsium(I) sowie Silicium und Aluminium im hexären System der ozeanischen Salze eingefügt werden. Daten für Selen wurden aus dem VESPA-Vorhaben abgeleitet. Ein umfassender Test der Datenbasis für die Bedingungen des unteren Grundwasserleiters steht noch aus.

Um die Sensitivitäten und Unsicherheiten der berechneten Verteilungskoeffizienten als Folge der Variation der geochemischen Einflussgrößen und auf Basis der deutlich

überarbeiteten thermodynamischen Datenbank zu untersuchen, wurden probabilistische Unsicherheits- und Sensitivitätsanalysen mit dem Softwareprogramm SimLab2 durchgeführt. Da diese Windowsversion seitens des Entwicklers EU Joint Research Center (JRC) nicht mehr weiterentwickelt wird, wurde ein neues Software Paket RepoSUN/SimLab4 exemplarisch für die Sorption von Uran(VI) im unteren Grundwasserleiter genutzt. Für Uran wurden die früheren Ergebnisse generell bestätigt, nämlich dass pH-Wert, Calcium-Konzentration und Konzentration von gelöstem anorganischem Kohlenstoff (DIC) die wichtigsten Einflussgrößen für den K_d -Wert sind. Der Sensitivitätsindex der Radionuklidkonzentration zeigt für Uran wie auch für alle anderen betrachteten Radionuklide eine extrem geringe Sensitivität, was zeigt, dass die Einflussgröße Radionuklidkonzentration die Sorption nicht signifikant beeinflusst. Aus diesem Grund wurde die Radionuklidkonzentration im Vorhaben WEIMAR nicht mehr als geochemische Einflussgröße im Transportcode berücksichtigt.

Mit dem bisherigen Konzept wurden konkrete Anwendungsrechnungen über einen Klimazyklus von 176.500 Jahren durchgeführt. Dabei wurden, ausgehend vom rezenten Zustand, für einen Zeitraum von 150.000 Jahren heutige Klimabedingungen simuliert. Darauf aufbauend wurde eine Meerestransgression für einen Zeitraum von 5.000 Jahren, ein Meeresspiegelhöchststand (Meerwasserüberdeckung) für ebenfalls 5.000 Jahre und eine Regression für einen weiteren Zeitraum von 5.000 Jahren berücksichtigt. Im Rahmen des WEIMAR-Vorhabens wurde nun systematisch überprüft, welche weiteren möglichen Szenarien zur Variation der geochemischen Bedingungen im Deckgebirge eines Salzstocks führen können. Dazu wurden Ergebnisse aus neueren Studien, speziell der geologischen Langzeitprognose der BGR und aus dem FEP-Katalog (Features, Events and Processes), die im Rahmen der VSG-Studie (Vorläufige Sicherheitsanalyse Gorleben) angefertigt wurden, einbezogen. Es zeigte sich, dass im Wesentlichen klimatische Veränderungen von Relevanz sind. Viele FEP haben keinen Bezug zum bzw. nur vernachlässigbare Auswirkungen auf das Deckgebirge und manche FEP können nicht berücksichtigt werden, da geometrische Bedingungen im Modell nicht variierbar sind.

Die methodisch-konzeptionellen Weiterentwicklungen wurden von einem umfangreichen experimentellen Programm begleitet. Es wurden die in den Experimenten eingesetzten Minerale umfangreich charakterisiert, Titrations- sowie Batch-Experimente durchgeführt, der Einfluss von Mikroorganismen auf das Sorptionsverhalten untersucht und der Transport von ausgewählten Kationen in Säulenexperimenten studiert.

Die Charakterisierung der Minerale Quarz, Orthoklas und Muskovit umfasste neben der Ermittlung von spezifischen Oberflächen, die Bestimmung von akzessorischen Mineralbestandteilen und deren Freisetzung unter den in WEIMAR gewählten experimentellen Bedingungen sowie die Charakterisierung der Säure-Base-Eigenschaften der Oberflächen anhand von Titrationsexperimenten. Des Weiteren wurden im Vorhaben Batch-Sorptionsexperimente für Uran(VI), Neptunium(V), Neodym(III), Europium(III), und Nickel(II) an Quarz, Orthoklas und Muskovit unter variierenden pH-Werten, Ionenstärken, Elementkonzentrationen und Volumen/Masse-Verhältnissen durchgeführt. Die Oberflächeneigenschaften und die Batch-Sorptionsexperimente bilden die Grundlage für die Ableitung von Oberflächenkomplexmodellen. Mittels einer auf den Programmen UCODE und PHREEQC basierenden Fitprozedur wurden noch fehlende thermodynamische Datensätze durch Anpassung an die experimentellen Daten erhoben. Soweit möglich wurden diese in die thermodynamische Datenbank des Vorhabens aufgenommen.

Zusätzlich wurden Batch-Sorptionsexperimente mit den Konkurrenzkationen Calcium und Aluminium durchgeführt. Durch Optimierung der Behältermaterialien, der eingesetzten Chemikalien und des Messverfahrens konnte die Analytik von Aluminium im Spurenelementbereich erheblich verbessert werden. Trotzdem konnte aufgrund der hohen Hintergrundbelastung der natürlichen Minerale und relativ geringen Löslichkeiten von Aluminium keine systematische Ableitung von Al-Sorptionsdaten realisiert werden.

Untersuchungen an den verwendeten Mineralen Quarz, Orthoklas und Muskovit zeigten, dass natürlich vorkommende Mikroorganismen in den Mineralen enthalten sind. Bei einem Zeitraum von einigen Wochen bis Monaten, über den die Experimente durchgeführt wurden, können Mikroorganismen wachsen. Um deren Einfluss auf die Sorption abzuschätzen und eine eventuelle Vorbehandlung der Proben zu entwickeln, wurde das Mikrobewachstum und die Auswirkung unterschiedlicher Sterilisationsmethoden Effekte mittels Elektronen- und optischer Spektroskopie sowie Kalorimetrie untersucht. Es konnten keine signifikanten Effekte auf das Sorptionsverhalten in dieser Studie nachgewiesen werden.

Die Säulenexperimente wurden hinsichtlich Aufbau, Material und Füllvorgang optimiert im Vergleich zum vorangegangenen Vorhaben ESTRAL. Es wurden Materialien aus PFA sowie Fritten aus PTFE verwendet, wodurch Wandsorptionseffekte geringgehalten wurden. Durch Aufsättigung der gepackten Säulen unter Vakuumbedingungen konnten Luftschlüsse und die Ausbildung von präferentiellen Fließwegen vermieden werden. Durch diese Vorgehensweise wurden sehr gut reproduzierbare Durchbruchkurven bzw.

Ortsverteilungen erhalten. Die Säulenversuche mit Europium und Nickel an den Mineralen Quarz, Orthoklas und Muskovit zeigen plausible Unterschiede zwischen den drei Mineralen und erwartete Abhängigkeiten vom pH-Wert und der Zusammensetzung der verwendeten Lösung. Die Experimente illustrierten die erhöhte Mobilität von Europium bei niedrigen pH-Werten wie auch bei Anwesenheit des Komplexbildners Sulfat und konkurrierenden Kationen.

Ein zentraler Aspekt des Vorhabens war der Übergang von rein statischen Batch-Sorptionsversuchen zu dynamischen Säulenversuchen. Ein wichtiges Ziel dabei war, die Übertragbarkeit der aus Batchversuchen abgeleiteten Oberflächenkomplexmodelle auf die Beschreibung des reaktiven Stofftransports zu untersuchen. Dieser Schritt wurde zunächst auf reine Minerale und einfache synthetische Stoffgemische beschränkt. Eine Beschreibung des Transports von Europium mit den aus Batchexperimenten abgeleiteten Oberflächenkomplexparametern konnte für ausgewählte geochemische Randbedingungen durch Quarz- und Orthoklassäulen zufriedenstellend dargestellt werden. Allerdings konnten nicht alle Randbedingungen mit den bisher verwendeten Modellen und thermodynamischen Daten adäquat abgebildet werden. Die Voraussetzung für eine bessere Beschreibung ist ein verbessertes Verständnis der beteiligten Prozesse. Um dies zu erreichen, sind weitere Batchexperimente erforderlich. Für Muskovit zeigen die Batchexperimente einen großen Einfluss des Ionenaustausches auf die Sorption. Um dies korrekt beschreiben zu können, müssen zukünftig geeignete Selektivitätskoeffizienten für den Ionenaustausch ermittelt werden.

Eine wesentliche Frage für die reaktive Transportmodellierung ist, in welcher Form die Komplexe des Tracers an der Mineraloberfläche vorliegen. Es wurde eine Methode zur Charakterisierung von Oberflächenkomplexen in Säulensegmenten entwickelt. Dazu wurden die Ortsverteilungen in der Säule durch Einfrieren mit flüssigem Stickstoff fixiert, anschließend Säulensegmente abgetrennt und mittels CLSM (Confocal Laser Scanning Microscopy) und TRLFS (Time Resolved Laser Induced Fluorescence Spectroscopy) analysiert. Mit dieser Methode, die hier exemplarisch auf die Uranmigration an Quarz angewandt wurde, ist es möglich, orts aufgelöst die Eigenschaften der Oberflächenkomplexe zu bestimmen. Die ersten Ergebnisse zeigen abhängig vom pH-Wert die Ausbildung von zwei in der Literatur beschriebenen, unterschiedlichen Uran(VI)-Oberflächenkomplexen.

Zum besseren Verständnis sollte diese Methode auch auf andere in diesem Vorhaben untersuchte Elemente wie z.B. Europium übertragen werden. Generell ist die

Charakterisierung der Struktur der Oberflächenkomplexe ein wichtiger Aspekt bei der Absicherung der verwendeten Oberflächenkomplexmodelle. Hinsichtlich des Konzepts ist zukünftig prioritär die Implementierung von Redoxreaktionen, die in diesem Vorhaben nicht möglich war, anzustreben. In dem Kontext sind auch noch thermodynamische Sorptionsdaten zu redoxsensitiven Elementen wie Technetium bzw. zu reduzierten Formen wie Uran(IV) zu erheben, bzw. in die thermodynamische Datenbasis zu implementieren. Die Datenbasis für hochsalinare Systeme zeigt generell noch Lücken und sollte vervollständigt werden. Abschließend ist eine umfassende Überprüfung des Konzepts des Component Additivity Ansatzes auch an naturnahen Systemen unter Einbeziehung aller relevanten Einflussgrößen eine wichtige, noch offene Fragestellung.

Abstract

A key component of long-term safety assessment for radioactive waste repositories in deep geological formations is the simulation of fluid and contaminant transport through the repository system, i. e. through large model areas over very long time frames. To describe the migration of radionuclides impacted by geochemical changes as realistic as possible a first version of the smart K_d -concept was developed and implemented into the transport program for long-term safety assessment recently. In the frame of the research project WEIMAR which is presented here, this approach was further developed based on methodological / conceptual developments as well as on a comprehensive experimental program.

The approach for implementing geochemical changes and their quantitative impact on radionuclide sorption has been further developed and the geometrical model for flow and transport calculations further refined. This was based on a systematic review of potential scenarios at the reference site, on verification calculations with the geochemically coupled transport code PHAST and on a comprehensive evaluation of the hydrochemical data from the reference site. Moreover, updated probabilistic uncertainty and sensitivity analyses have been performed and the respective software package has been further developed.

The experimental program followed three major tasks. Firstly, the thermodynamic database was substantially enhanced and qualified, in particular surface complexation parameters for uranium(VI), neptunium(V), neodymium(III), europium(III), and nickel(II) on quartz, orthoclase and muscovite were derived or updated. Secondly, effects, which are expected to impact sorption of radionuclides on mineral surfaces like competitive sorption or microbial growth (during the long duration of batch experiments) have been investigated. Thirdly, the question of the chemical structure of surface complexes at the mineral-water interface was addressed: A method was developed to characterize surface complexes and their spatial distribution in column experiments, consisting of sample freezing with liquid nitrogen, subsequent partition of column segments and analysis with CLSM (Confocal Laser Scanning Microscopy) und TRLFS (Time Resolved Laser Induced Fluorescence Spectroscopy).

Finally, a key aspect of the project was the transition of static batch sorption to dynamic column experiments. The description of europium transport using surface complexation parameters derived from batch experiments was satisfactorily for selected geochemical

boundary conditions in quartz and orthoclase filled columns. However, not all geochemical boundary conditions could be adequately described with the applied thermodynamic models and data. Furthermore, effort to comprehensively demonstrate the transfer of the smart K_d -concept to dynamic flow conditions in natural systems is also necessary and will be a focus of upcoming research projects.

Acknowledgement

We want to express our appreciation to colleagues and students who supported this research project:

We are thankful for the scientific work and helpful discussions with Dr. Frank Bok (HZDR-IRE), Dr. Kay Grossmann (HZDR Innovation GmbH), Dr. Norbert Jordan (HZDR-IRE), and Anke Schneider (GRS).

We thankfully acknowledge Prof. Dr. H. Biester, Prof. Dr. W. Durner, Dr. S. Iden, Prof. Dr. A. Schwalb, and Prof. Dr. D. Zachmann for their mentorship of PhD, master, and bachelor students.

We are also grateful to all master and bachelor students as well as trainees. Therefore, many thanks go to Maria Bauditz (trainee), Maria Berger (MSc), Julian Fricke (MSc), Charlotte Glassneck (MSc), Jaqueline Haller-Jans (BSc), Claudia Hinze (trainee), Alexander Schulze (MSc), Lennart Steinbrecher (MSc), and Marc Wendisch (trainee).

We would also like to thank the laboratory staff of HZDR-IRE and GRS gGmbH: This project relied on their sound and trustworthy analyses.

Table of contents

1	Introduction.....	1
2	Evaluation of scenarios.....	5
2.1.1	Cold stage developments	6
2.1.2	Changes in the geomorphology, including overburden and adjoining formations.....	9
2.1.3	Other impacts on the hydrogeological system.....	11
2.2	Implementation of future climatic evolution in model simulations	13
3	Hydrogeochemical concept	17
3.1	Hydrogeological model	17
3.2	Environmental parameters.....	19
3.3	Simplified geochemical model.....	21
3.3.1	Basic terms.....	21
3.3.2	Consideration of Al	24
3.3.3	Reconsideration of Ca	30
4	Geochemical site characterization	35
4.1	Water chemistry.....	35
4.2	Sediments.....	36
5	Mineral properties.....	39
5.1.1	Quartz.....	39
5.1.2	Orthoclase	46
5.1.3	Muscovite	52
6	Thermodynamic databases.....	65
6.1	Speciation in low mineralized water	65
6.1.1	Database for europium	65
6.1.2	Database for manganese.....	68
6.2	Speciation in highly mineralized water	68
6.3	Mineral solubilities	70

6.4	Surface species	71
7	Batch sorption experiments.....	73
7.1	Experimental set-up of Eu, Ni, Cs, Ca and Al batch experiments.....	73
7.2	Experimental set-up of U(VI), Np(V), and Nd(III) batch experiments	74
7.3	Microbial effects on sorption processes	76
7.4	Uranium(VI) batch sorption results.....	76
7.4.1	Sorption of U(VI) onto muscovite	77
7.4.2	Sorption of U(VI) onto orthoclase	78
7.4.3	Influence of ionic strength on U(VI) sorption	80
7.4.4	Influence of Ca on U(VI) sorption as competing cation	81
7.5	Neptunium(V) batch sorption results.....	83
7.5.1	Sorption of Np(V) onto muscovite and orthoclase	83
7.5.2	Influence of ionic strength on Np(V) sorption	86
7.6	Neodymium(III) batch sorption results.....	88
7.6.1	Sorption of Nd(III) onto muscovite and orthoclase.....	88
7.6.2	Influence of ionic strength on Nd(III) sorption.....	89
7.7	Calcium(II) batch sorption results.....	90
7.8	Europium(III) batch sorption results	92
7.8.1	Sorption of Eu(III) onto quartz surfaces.....	92
7.8.2	Sorption of Eu(III) onto orthoclase surfaces	93
7.8.3	Sorption of Eu(III) onto muscovite surfaces.....	94
7.9	Nickel(II) batch sorption results.....	95
7.9.1	Ni(II) sorption onto quartz	96
7.9.2	Ni(II) sorption onto orthoclase	98
7.9.3	Ni(II) sorption onto muscovite	100
7.10	Aluminum(III) batch sorption results.....	102
7.11	Cesium(I) batch sorption results	103
7.11.1	Cs(I) sorption onto muscovite	103
7.11.2	Cs(I) sorption onto orthoclase	105
8	Spectroscopic evidence of surface species	107

8.1	Experimental set-up.....	107
8.2	Spectroscopic results.....	109
9	Column experiments	117
9.1	Experimental set-up.....	117
9.2	Results of europium(III) transport experiments	120
9.2.1	Eu(III) transport experiments with muscovite, orthoclase, and quartz.....	121
9.2.2	Eu(III) transport through a synthetic and natural sediment.....	122
9.3	Results of uranium(VI) transport experiments and U(VI) surface complex identification	123
9.4	Results of nickel(II) transport experiments	126
9.4.1	System Ni(II)-quartz.....	127
9.4.2	System Ni(II)-orthoclase	130
10	Mechanistic sorption modeling	135
10.1	Fitting procedure of surface complexation parameters.....	135
10.2	SCM parameterization	138
10.2.1	System U(VI) with orthoclase and muscovite	138
10.2.2	System Np(V) with orthoclase and muscovite	141
10.2.3	System Nd(III) with orthoclase and muscovite	142
10.2.4	System Eu(III) with quartz, orthoclase, and muscovite.....	144
10.2.5	System Cs(I) with orthoclase	150
10.3	Discussion of SCM results.....	152
11	Europium reactive transport modeling	157
11.1	Data processing of experimental transport measurements	158
11.2	Determination of retardation factors.....	159
11.3	Transport parameter determination with Br breakthrough curves.....	159
11.4	1D reactive transport model set up	161
11.5	Results and discussion of Br and Eu transport simulations	162
11.5.1	Transport parameter determination from Br breakthrough curves.....	163
11.5.2	1D reactive Eu transport simulations.....	166
11.6	Discussion of and conclusion drawn from Eu transport simulations	173

12	Smart K_d-matrices.....	177
12.1	Software packages	177
12.2	Environmental parameters.....	180
12.3	Temperature dependencies	183
12.4	Model input for PHREEQC	184
12.5	Results of smart K_d -matrices and their uncertainty and sensitivity.....	186
12.5.1	Uncertainty analysis and results	186
12.5.2	Sensitivity analysis and results	190
13	Transport modeling and code verification.....	193
13.1	d ^{3f++}	193
13.2	Comparative calculations with code PHAST	193
13.2.1	Comparison of the approaches	194
13.2.2	Model setup	197
13.2.3	Results of d ^{3f++} 1D transport models	199
14	Summary and conclusions	205
15	References	211
	Abbreviations.....	241
	Symbols	246
	List of Figures.....	251
	List of Tables.....	261
A	Digital Appendix	265
A.1	Evaluation of possible Features, Events and Processes (FEPs) and climate scenarios to be considered for Northern Germany.....	265
A.2	Supplementary information on environmental parameters	275
A.3	Geochemical site characterization	291
A.4	Mineral properties	292
A.5	Eu(III), Ni(II), Ca(II), Cs(I), and Al(III) batch sorption experiments	310

A.6	U(VI), Np(V), and Nd(III) batch experiments.....	318
A.7	Microbial effects on sorption processes	321
A.8	Transport experiments with europium and nickel	328
A.9	Pretests of uranium(VI) column experiments	333
A.10	Formal (pseudocode) description of the concept for consideration of chemical changes in d^{3f++}	336

1 Introduction

One natural retardation process to be considered in risk assessment for contaminants in the environment is sorption on mineral surfaces. Realistic geochemical modeling is of high relevance in many application areas such as groundwater protection, environmental remediation, or disposal of hazardous waste. Most often, concepts with constant distribution coefficients (K_d -values) are applied in geochemical modeling with the advantage to be simple and computationally fast, but not reflecting changes in geochemical conditions. However, in long-term safety assessments for nuclear waste repositories in deep formations, geological time scales have to be considered. Possible future climatic changes are expected to alter the boundary conditions, the flow regime and the geochemical environment in the aquifers. The code d^3f++ (distributed density-driven flow) was developed to simulate contaminant transport in large heterogeneous areas over long periods in time, considering hydrogeochemical interactions and radioactive decay.

A preceding project, Realistic Integration of Sorption Processes in Transport Codes for Long-Term Safety Assessments (ESTRAL), introduced a new methodology to use temporally and spatially variant distribution coefficients depending on the geochemical environment. It is an innovative and efficient method, where the smart K_d -concept, a mechanistic approach mainly based on surface complexation modeling and a bottom-up approach of a competitive mineral-specific sorption, is applied (and modified for complex geochemical models) to calculate realistic distribution coefficients for a wide range of environmental parameters. Respective pre-computed multidimensional K_d -matrices can directly be processed by reactive transport codes such as d^3f++ . This strategy has various benefits: (1) rapid computation of K_d -values for large numbers of environmental parameter combinations; (2) variable geochemistry is considered more realistically; (3) efficiency in computing time is ensured, and (4) uncertainty and sensitivity analyses are provided.

As a proof of concept, a well-explored and documented test case was selected. In Germany, the Gorleben salt dome had been investigated as a potential site for a nuclear waste repository. The data sets derived on-site during several decades thus served for a first evaluation of the new approach.

The results of ESTRAL pointed to various shortcomings that initiated a follow-up project – WEIMAR. There, various issues were explicitly addressed: First, a more rigorous evaluation of the filed data from Gorleben should enable an expanded hydrogeochemical

model, considering further processes being competitive to sorption. Here, the Mg^{2+} and Al^{3+} cation as well as the anions sulfate and phosphate deserved special attention. Also, effects induced by gypsum shall be investigated.

A second point was the application of the new methodology on further scenarios of repository developments derived from a comprehensive analysis of features, events and processes (FEP). Preceding simulations indicated that a sea water transgression and the inundation of the area will lead to a decrease of the flow velocities and a horizontal salinity-dependent stratification of the groundwater. Transport simulations using conventional sorption coefficients as well as the newly implemented smart K_d -concept were used to identify the impact of this new handling of sorption processes on the radionuclide distribution in the model area. However, these simulations only considered one possible climatic evolution and only a time frame of 165,000 years. The expected long-term future evolution of the site includes different features, events and processes, including e. g. permafrost conditions. The formation of permafrost in the upper aquifer and an inflow of glacial meltwater into the lower aquifer is expected to cause low salinities and high flow velocities in unfrozen zones. Therefore, literature on possible future climatic evolutions was reviewed, their impact on the geological overburden and adjoining rock evaluated, and their relevance for transport simulations defined. A set of climate transitions was selected and described with regard to their realization in flow and transport models.

An extensive experimental program was drafted to close critical gaps in the thermodynamic databases required for reliable geochemical modeling, eventually leading to realistic K_d -values. The interactions between various radionuclides and quartz, muscovite and orthoclase were put into focus. To cover a broad range of redox states (+I, +II, +III, +V, and +VI), the ions Cs^+ , Ni^{2+} , Eu^{3+} , Nd^{3+} , NpO_2^+ , and UO_2^{2+} were selected, together with Ca^{2+} as the most prominent competing ion that had already been identified in the previous research project ESTRAL. Batch sorption experiments provided the raw data to derive quasi-thermodynamic sorption parameters, covering surface complexation and ion exchange. These experiments were complemented by spectroscopic investigations aiming to offer independent proofs of existence for the chemical species sets to be parameterized. Also, column experiments were performed to check the validity of the batch sorption results, to investigate more complex systems, and to assess the applicability of the component additivity approach.

The newly derived sorption parameters, together with new data published in the external literature could then form a more comprehensive and reliable database to compute smart

K_d -matrices. These matrices were then fed into advanced sensitivity and uncertainty analyses to identify those environmental factors that affect the retardation of radionuclide most under given hydrogeochemical boundary conditions. Sensitivity and uncertainty analyses for the nuclides may also reveal the importance of ternary interaction effects, the non-conservatism of some generic distribution coefficients used so far, and the effects of input parameter correlation. A challenge was posed by the rather high ionic strengths encountered in parts of the lower Gorleben aquifer (with values in a range also expected e. g. for argillaceous rocks in northern Germany). A respective database utilizing the Pitzer or SIT approach to handle activity coefficients in such highly saline brines is certainly required on the long run. Finally, all developments in model and database were transferred into the d^{3f++} code basis, tested and validated by respective computations including other reactive transport codes so far used within the nuclear waste community.

This report addresses the progress achieved during the project WEIMAR, covering the wide area of demands highlighted in the previous paragraphs. It starts with the continued extension and development of modeling concepts, continues with the detailed characterization of the aqueous phase and the sediments on-site, including the major mineral constituents being in the focus of this project. Further chapters tackle the set-up of high-quality databases. Respective critical gaps were closed by a variety of experimental efforts, namely titration and batch sorption experiments, structural investigations to reveal the true speciation, and column experiments to describe transport processes. The report continues with the sophisticated data processing and elucidation of thermodynamic parameters. They are in turn used for state-of-the-art modeling of static systems, reactive transport, and retardation factors utilized in large scale migration codes. Uncertainty and sensitivity analyses are coupled to this modeling approach. Last but not least, a detailed description of code modifications is provided.

Detailed descriptions and additional records are supplied in a digital appendix. The digital appendix is distributed as a CD in the paperback report. It comprises a pdf file with a written, formulated appendix and a directory where supplementary material including Bachelor, Master and PhD theses produced during the project are provided.

2 Evaluation of scenarios

In the previous project ESTRAL /NOS 12b/, the smart K_d -concept was developed and tested for its applicability to realistically model sorption processes in long-term safety assessments. For this purpose, the Gorleben site was chosen as a reference site, because a large hydrogeological and geochemical dataset is available for this site. A possible future climate evolution was deduced from the geological past. Two different climate scenarios were selected: (i) a future constant climate evolution, and the subsequent inundation of the site by sea water as a consequence of global warming and (ii) the development of permafrost conditions. In the course of the ESTRAL project, flow and transport simulations were only conducted for the first scenario. With the advances in the smart K_d -concept, it will be possible to regard further climate scenarios, with the focus on climatic transitions. These may lead to drastic geochemical changes in the overburden of the regarded host rock formation, e. g. melting of inland ice sheets causing the infiltration of large volumes of oxygen-saturated water into the aquifers. Relevant publications concerning the future development of the Gorleben site are the updated geoscientific long-term prognosis for the site /MRU 11/, a FEP catalogue /WOL 12/ and the findings regarding the future climatic evolution /NOS 12a/. These were reviewed in order to derive possible future evolution scenarios for the site, which may lead to spatial and temporal variations of the geochemical environment in the sedimentary overburden. To evaluate their impacts, it was aimed at developing model assumptions and conducting respective model simulations.

In a first step, it was to be assessed, which features, events and processes (FEP) or scenarios may lead to a large-scale (hydro)geochemical alteration of the current conditions of the regarded sedimentary system. These scenarios had to be described with regard to their implementation in groundwater flow and transport models. The aim of the preceding project “Preliminary Safety Analysis Gorleben” (VSG, 2010 – 2013) was to elaborate a preliminary safety analysis for the site with special regard to the long-term safety, to develop a repository concept, and to define the need for further investigations and explorations. The geoscientific site characterization and the long-term prognosis for the development of the site for the future one million years, as part of the project, was the basis for the preliminary safety analysis. The report /MRU 11/ gives a classification of the site developments into probable, less probable and improbable developments. In the WEIMAR project, the focus was on probable future development, which are expected to occur during the next one million years, or to have a permanent effect on current site

conditions. With a focus on the application of the smart K_d -concept in flow and transport models, only those developments were selected, that are expected to have an impact on groundwater flow and radionuclide transport at the Gorleben site.

The FEP catalogue /WOL 12/ is a comprehensive compilation of features, events, and processes, and gives information on site-specific impacts and probability of occurrence. It also classifies the FEP as probable, less probable or improbable. In this review, only the probable and less probable FEP, that are expected to have an impact on the overburden and adjoining rock, are investigated. Some of those were excluded, since they cannot be described with the current code (e. g. two-phase flow or changes in the model geometry) or the current concept of sorption treatment (e. g. colloid formation). 24 FEP remained to be possibly considered within this project. A comprehensive table of all FEP and their evaluation with respect to be possibly regarded or not is given in the digital appendix Section A.1 (Tab. A. 1).

In the following, possible future developments are described based on the findings of both /MRU 11/ and /WOL 12/ with regard to the implementation of future evolutions in model simulations (cf. Sec. 2.2).

2.1.1 Cold stage developments

Probable cold stage developments with an effect on the groundwater regime in Northern Germany include future permafrost growth and decay. Other cold stage developments, such as crustal movement and deformation or earthquakes are not likely to drastically influence the groundwater flow at the Gorleben site. Some additional developments are probable and expected to occur during a cold stage, but their description is highly speculative. An example is the formation of glacial melt water channels, which might substantially change the geometry and structure of the sedimentary layers, however, predicting their evolution and specific development is impossible. The appearance of a near-by inland ice sheet or a complete cover of the site with an inland ice sheet with a maximum ice thickness of 300 m are also probable. Capturing all essential boundary conditions as well as processes in the hydrogeological model would require the set-up of a large, regional geological and hydrogeological model with an extent of more than 100 km /KÖT 07/, implicating an extensive computational effort for the simulations. Additionally, a cover by an inland ice sheet would cause changes in the geological bedding of the formations due to the superimposed load. Changes in the model geometry cannot be regarded with the available code, so a superimposed ice sheet is not considered here.

Therefore, only those cold stage developments are regarded, that can be sufficiently described in the groundwater flow and transport models.

2.1.1.1 Permafrost

Permafrost denotes a thickness of soil, sedimentary deposit or rock of variable depth, that continuously features below-freezing temperatures for a long time /WIL 98/. Its thickness is dependent on climatic conditions, groundwater salinity, geothermal heat flux, the occurrence of surface water bodies, and type of sediments and vegetation. Three types of permafrost are differentiated: continuous, discontinuous and sporadic permafrost, all of them depicted in Fig. 2.1. A transition between these zones may occur either with a de- or increase of the geographic latitude or with an alternating mean annual air temperature (MAAT in Fig. 2.1). Unfrozen zones, so-called taliks, can occur due to the influence of surface water bodies, as well as due to a hydrochemical or hydrothermal influence. Taliks can be open (meaning there is an unfrozen connection between unfrozen deep layers and the surface) or closed (a certain extent at the surface is unfrozen).

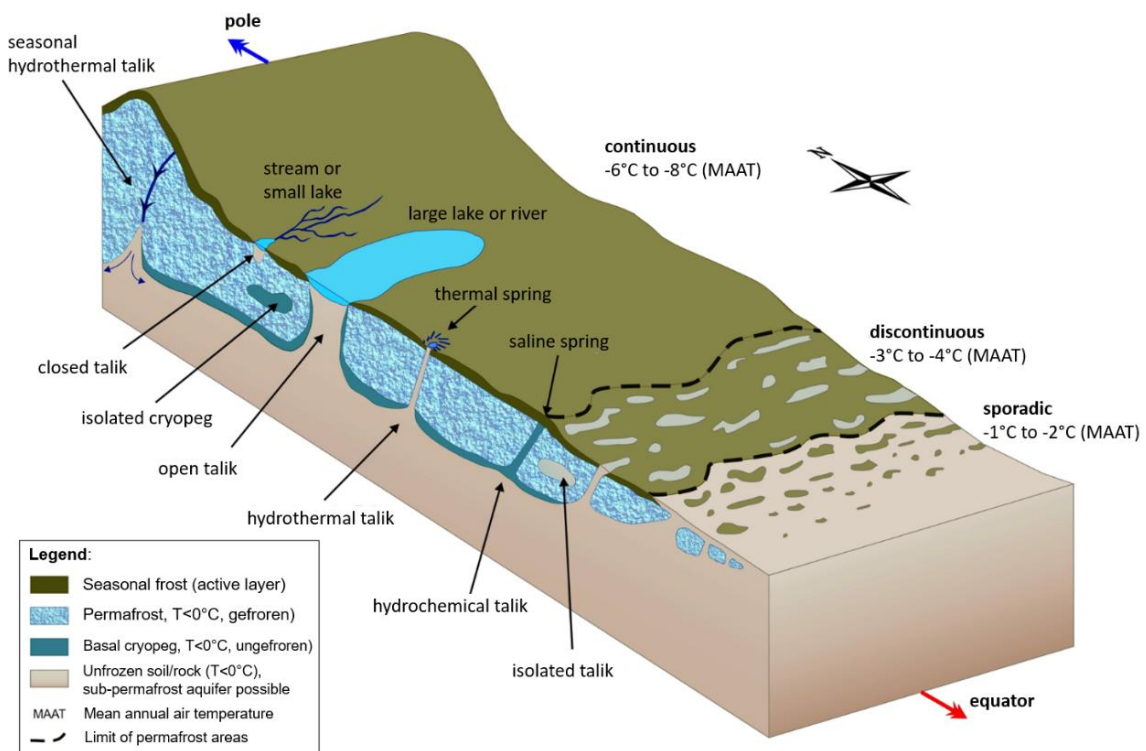


Fig. 2.1 Schematic picture of the different permafrost and talik types (after /MRU 11/, modified from /GAS 00/ and /KAR 79/)

In the geological past, climate states with the formation of permafrost occurred periodically at the Gorleben site with a periodicity of 10,000 a to 30,000 a and a thickness

between 40 m and 140 m /NOS 12a/. According to /MRU 11/, cold stage conditions similar to those during the Weichsel cold stage might occur at ca. 10,000 a after present, leading to permafrost conditions with continuous permafrost at the site from 50,000 a until the maximum of the cold stage. Taking the anthropogenic influence into account, this development might be delayed accordingly. Predicting future climatic evolution of the site is subject to major uncertainty, and predicting quality and quantity of permafrost development and related processes is not possible. Nevertheless, it is highly probable, that permafrost conditions will occur during future cold stages, including the formation of taliks in the areas of the present-day rivers. Permafrost growth and decay was simulated by /DEL 98/ for the Gorleben site and for the past 50,000 a (Fig. 2.2) and the results can be used as a basis for groundwater flow and transport modeling as described in /NOS 12b/. Additional variations of the permafrost climate state could include the development of discontinuous permafrost with larger unfrozen areas, while the frozen percentage of the subsurface remains higher than 50 %. Model simulations with continuous permafrost conditions and only two taliks below the rivers Elbe and Seege /NOS 12b/, /FLÜ 09/ resulted in a drastically reduced groundwater flow through the near-surface aquifer, while the largest part of groundwater flow is concentrated in the lower aquifer and the unfrozen taliks. Considering discontinuous permafrost conditions, the groundwater flow would take place through a larger area of the near-surface formations, leading to lower flow velocities. This effect would be intensified by a lower inflow of melt water into the deeper water-bearing formations with a larger distance to the inland ice sheet.

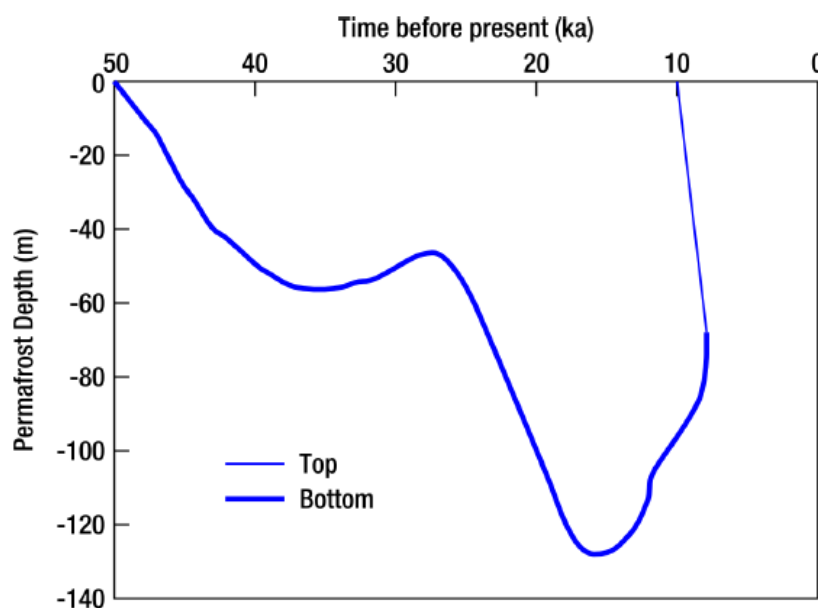


Fig. 2.2 Calculated permafrost depth depending on the surface temperature for the past 50,000 a, modified from /DEL 98/

2.1.2 Changes in the geomorphology, including overburden and adjoining formations

Developments of the geomorphology may be caused by sea level oscillations (trans- and regressions at the site), erosion and sedimentation, diagenesis, fault zones in the overburden and adjoining rock, or triggered by microbial processes. Those of the processes, that would lead to a change in the geometry of the geological formations and thus their representation in a hydrogeological model, had to be neglected here, e. g. erosion and sedimentation or formation of fault zones.

2.1.2.1 Trans- and regression

Sea level oscillations occurred periodically during the geological past. Besides regional tectonic subsidence and epirogenesis, which have an influence on the relative sea level, the oscillations are a result of the Milankovich cycles and thus the global ice volume /IMB 84/. Causes and consequences of a sea level rise for a site in Northern Germany are described in detail in /NOS 12b/ and /FLÜ 09/. A melting of the complete global ice volume would result in a sea level high stand of 65 m at the Gorleben site /ALL 09/, comparable to the sea level during the Holstein warm stage, when the high stand lasted for 5,000 a, followed by a decrease of the global sea level and a local retreat (regression) of the sea at the site. In /NOS 12b/, a sea level rise with a transgression of the North Sea into the Gorleben area (5,000 a) was regarded, including a sea level high stand (5,000 a) and subsequent regression (5,000 a). The consequence of a sea water inundation of the site is a drastic reduction of the groundwater flow velocities. Missing groundwater recharge and lateral inflow lead to a decrease of the advective component of the groundwater flow and the diffusive flux gains influence. As the subsidence at the contact to the salt dome persists and there is a constant sea water salinity at the surface, while the fresh water inflow ceases to exist, the salinity of the groundwater will increase and cause a density-dependent stratification of the groundwater. In this project, it is aimed at regarding several trans- and regressions and the transitions between them during a longer time span. Since a prediction of future trans- and regressions is not possible, potential future climate evolutions for the site have to be deduced from the geological past. Depending on the computational effort, and based on the sea level oscillations during the past 500,000 a (Fig. 2.3), four sea level high stands, including trans- and regression, could be regarded

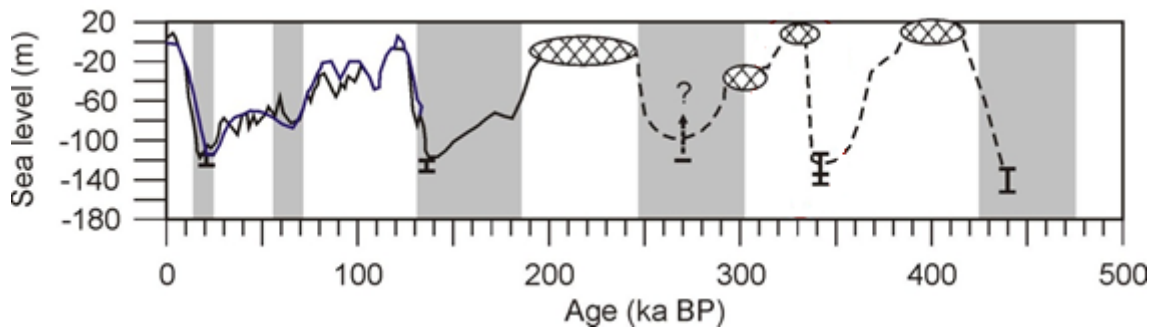


Fig. 2.3 Global sea level record of the past 500,000 a modified from /ROH 98/

Solid lines are based on different climate proxies. The dashed line shows schematic sea-level fluctuations sketched through the control points following the main trends in the oxygen isotope record. Cross-hatched ovals show ranges of interglacial sea-level highstands. Error bars represent ranges of glacial sea-level lowstands according to the model presented in /ROH 98/.

2.1.2.2 Diagenesis

Diagenesis denotes the chemical or physical changes occurring in sediments before consolidation or while in the environment of deposition /WIL 98/. It can be caused by pressure or temperature changes, chemical dissolution or precipitation, leading to the alteration of minerals in sediments or sedimentary rocks /MRU 11/. This again may have an influence on the physical and hydraulic properties of the sediments, i. e. the porosity and permeability. Thus, this will influence the flow regime of the site on the one hand, e. g. due to a reduced permeability and porosity, and on the other hand will have an impact on the geochemical conditions, e. g. due to alteration of minerals or new minerals formation, such as carbonates, sulfates or saline minerals. A sandstone of 35 % porosity will be subject to early diagenetic cementation and a reduction of its porosity to less than 10 %, when it is covered by a sedimentary overburden of ca. 300 m thickness /BAH 98/.

The deeper layers at the regarded site have already been subject to diagenesis, thus diagenetic alteration of sediments or sedimentary rocks would only affect the upper layers. In a hydrogeological model, the changes induced by diagenesis could only be taken into account by adapting the hydraulic parameters, but without explicitly modeling the geometry changes originating from an additional sedimentary overburden, i. e. compaction or relocation of the sedimentary layers (geometry changes are not possible to be modelled, see above). This procedure is not straightforward thus diagenetic processes and their impacts will therefore be neglected in the hydrogeological models.

2.1.3 Other impacts on the hydrogeological system

Besides the geological and climatically induced processes, other probable future developments, e. g. triggered by microbial activity, will have an impact on the geological and hydrogeological system.

2.1.3.1 Microbial processes

The living conditions of microorganisms are manifold, and their habitats are characterized by a large range of conditions, including e. g. temperature, composition of solution and rock matrix, water availability and oxygen saturation. Even in saliniferous formations, microbial activity is possible and has to be considered /ALE 14/.

Microbial processes in the sedimentary overburden are part of the cycles of matter. Microbial depletion or rock forming processes may change the mineralogical composition of a formation. Like in the geological past, a microbial colonization of the sediments is to be expected, although the alteration of the rocks through mineral alteration is not expected to be significant.

However, a crucial impact of microbial processes is to be expected on the geochemical conditions in the groundwater. Especially the anaerobic nitrate and sulfate reduction is of importance in the sedimentary overburden at the respective site /KLI 07/. Nitrate reduction is mostly a consequence of the anthropogenic input of nitrate from agriculture in the uppermost few meters of the sediments, while sulfate reduction is based on the dissolution of sulfate minerals in the sediments, e. g. gypsum in the cap rock of the salt dome. It is expected that the microbial sulfate reduction will persist in the future with the present dependency of the reducing processes on the depth and the content of total dissolved solids (TDS) in the groundwater. In groundwater with TDS of 0.1 – 10 g l⁻¹ sulfate reduction is connected to the oxidation of organic carbon and release of CO₂. In presence of carbonate and calcite, CO₂ is altered to hydrogen carbonate in groundwater with TDS of 0.5 – 10 g l⁻¹. Even in higher depths and under saline conditions with TDS of up to 200 g l⁻¹, anaerobic sulfate reduction is possible due to the presence of organic matter from Tertiary and Quarternary lignite sediments.

Consequently, for a further development of the smart K_d-concept, at least the effect of sulfate reduction as part of the hydrogeochemical concept should be considered. However, the critical evaluation of the redox measurements at the reference site showed that

these data are not suitable for the development of a simplified conceptual model for redox processes to be implemented in our approach. Therefore, this task was shifted towards a future project investigating a site with more sound and available redox data.

2.1.3.2 Future developments of the salt formation

Salt tectonics, in a narrower sense diapirism, is a possible future development, that will have an influence on the shape and the position of the saline formation. The diapir stadium of the salt formation has already been reached today, and it is expected, that the uplift tendency will further weaken during the future one million years. Causes for an increased uplift could be a change in compressive stress or in additional surcharge. An increase of compressive stress in the geological underground is not to be expected in this tectonically inactive area, and also an additional deposition of several 100 m sediment thickness is unlikely to be built up. A short-term rise of the uplift rate of the salt formation could be initiated by a long-lasting cover by a thick ice sheet. However, this would be restricted to a few 10,000 years due to the distance of the location from a potential center of glaciation in Scandinavia, thus the influence on the current uplift rate can be neglected.

On the other hand, the subsidence of saline evaporites at the contact to groundwater bearing sedimentary units could lead to the reduction of the thickness of the saline formation. The subsidence rate is also not constant and influenced by several factors, such as the uplift rate of the salt formation or the groundwater salinity and its flow velocity. In the past, the subsidence rate at the Gorleben salt formation varied between 0.0015 and 0.43 mm a⁻¹ (Kötter /MRU 11/ expects a subsidence of 50 m to 100 m to be possible in the future one million years).

As stated above, the model geometry for the groundwater flow and transport simulations must not be subject to changes. Therefore, neither uplift or subsidence may be regarded in model simulations as explicit processes. Only the contact of the aquifer to the salt formation and the dissolution of salt minerals are implemented in the model set-up in form of a steady source of soluble salt.

2.2 Implementation of future climatic evolution in model simulations

To perform groundwater flow and transport simulations employing the smart K_d -concept in comparison to the use of conventional K_d -values, a possible future climatic evolution for the reference site had to be derived and implemented in a hydrogeological model.

The hydrogeological model, which consists of three hydrogeological units, namely the upper aquifer (UAF), the aquitard (AT) and the lower aquifer (LAF), is based on /KLI 02a/ (Fig. 2.4) and described in detail in /FLÜ 09/ and /NOS 12b/. The main structural elements, such as two hydraulic windows, a rim syncline adjacent to the salt formation, and the contact to the saline formation in the lower aquifer, are implemented in the model (Fig. 2.5). Based on model simulations for the present state /NOS 12b/, a future climatic evolution is to be modelled.

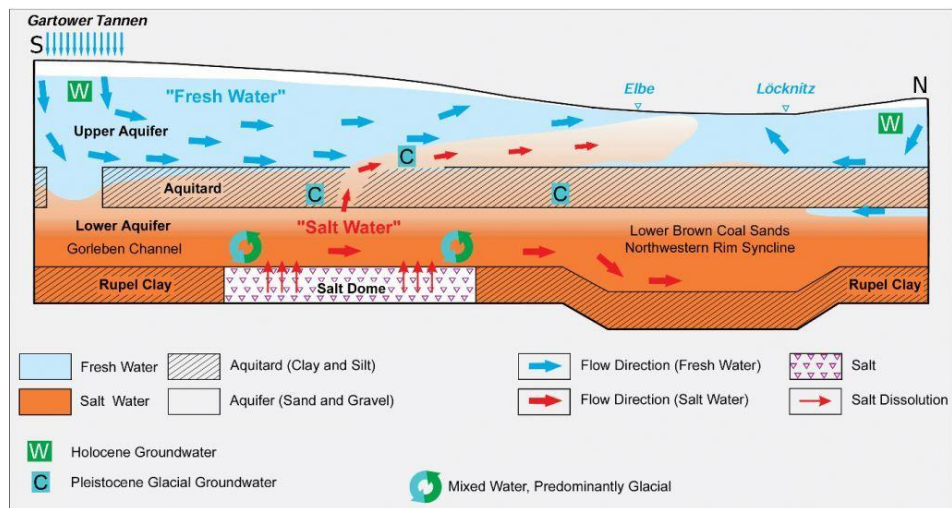


Fig. 2.4 Schematic cross section of the hydrogeological system at the reference site Gorleben (modified from /KLI 02a/)

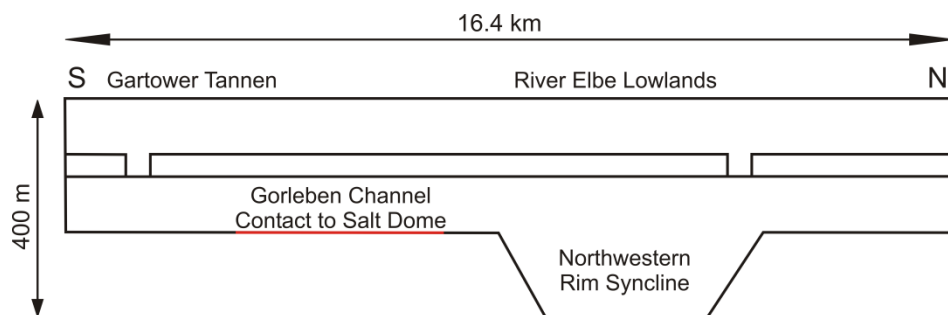


Fig. 2.5 Geometry of the groundwater flow and transport model, vertical exaggeration: factor 10

/NOS 12a/ gives a comprehensive review on the expected future climatic evolution for two sites in Sweden /NÄS 10/ and Finland /CED 04/ and derives a possible scenario for Northern Germany. Therefore, a future evolution as presented in Tab. 2.1 is possible for the Gorleben site in Northern Germany. Followed by 5,000 years of temperate, terrestrial climate, a sea level rise is assumed for 5,000 years with a subsequent sea level high stand of 50 m for 5,000 years and another 5,000 years of sea level regression until reaching the present sea level. After a following 30,000 years of temperate, terrestrial conditions, a periglacial cycle is assumed with a varying distance of the inland ice sheet and therefore an alternating permafrost thickness. The evolution during the subsequent 120,000 years is derived from the climatic evolution of the Weichselian cold stage and characterized during the first 87,000 years by a variation between temperate, terrestrial and periglacial conditions with a permafrost thickness of 50 m (larger distance to the ice sheet) and 100 m (near-by ice sheet). A longer uninterrupted period of periglacial conditions (33,000 years), again with a varying permafrost thickness of up to 150 m, represents another extensive period of glaciation. The climatic cycle is completed by a period of 5,000 years of temperate, terrestrial climate. The transitions between the different climatic conditions can be regarded as a stepwise, abrupt change of the boundary conditions or as transient changeovers (Fig. 2.6).

Tab. 2.1 Assumed climate evolution during the future 240,000 years /NOS 12b/

Time after present	Climate state
0 – 5,000 years	temperate, terrestrial
5,000 – 10,000 years	temperate, coastal: sea water rise
10,000 – 15,000 years	temperate, aquatic: marine transgression
15,000 – 20,000 years	temperate, coastal: lowering of sea level
20,000 – 50,000 years	temperate, terrestrial
50,000 – 55,000 years	periglacial, near-glacier conditions: permafrost 50 m
55,000 – 70,000 years	periglacial, near-glacier conditions: permafrost 100m
70,000 – 75,000 years	periglacial, far-glacier conditions: permafrost 50 m
75,000 – 85,000 years	periglacial, far-glacier conditions: no permafrost
85,000 – 90,000 years	periglacial, near-glacier conditions: permafrost 100m
90,000 – 110,000 years	periglacial, near-glacier conditions: permafrost 150 m

110,000 – 115,000 years	periglacial, near-glacier conditions: permafrost 100 m
115,000 – 130,000 years	temperate, terrestrial
130,000 – 140,000 years	periglacial, far-glacier conditions: permafrost 50 m
140,000 – 150,000 years	temperate, terrestrial
150,000 – 160,000 years	periglacial, near-glacier conditions: permafrost 100 m
160,000 – 178,000 years	temperate, terrestrial
178,000 – 185,000 years	periglacial, near-glacier conditions: permafrost 100 m
185,000 – 202,000 years	temperate, terrestrial
202,000 – 220,000 years	periglacial, far-glacier conditions: permafrost 50 m
220,000 – 230,000 years	periglacial, near-glacier conditions: permafrost 150 m
230,000 – 235,000 years	periglacial, near-glacier conditions: permafrost 50 m
235,000 – 240,000 years	temperate, terrestrial

The different climate states can be realized in the model by a variation of the boundary conditions. The boundary conditions for the present state as described in /FLÜ 09/ are also valid for future temperate, terrestrial climate states. The center of the model surface features a hydrostatic pressure, while the Northern and the Southern part of the surface are characterized by groundwater recharge. There is a lateral inflow of groundwater into the lower aquifer from the North. At the contact of the lower aquifer to the salt formation, a constant salt concentration is defined. All other model boundaries are closed to flow and transport.

For the assumed climate states and transitions, a detailed description on their implementation in the models and the definition of respective boundary conditions are given in /NOS 12a/ and /NOS 12b/. Here, only a brief summary is given.

For the time of a trans- and regression of the sea and a sea level high stand, it is assumed that the lateral inflow from the North will vanish. At the surface, the groundwater recharge and hydrostatic pressure boundary conditions are also not valid anymore. Depending on the sea level, a pressure boundary condition is defined at the model surface. The salt concentration defined for the model surface equals sea water salinity.

During permafrost conditions, part of the sedimentary units will be frozen. Frozen areas are represented in the model with a drastic reduction of the permeability. With 50 m of permafrost thickness, the upper half of the upper aquifer will be frozen, while with a thickness of 100 m the entire thickness of the upper aquifer will be affected. With a maximum thickness of 150 m, the aquitard will be frozen as well. Taliks are expected to occur under the thermal influence of the rivers Elbe and Seege. Both are assumed to be open taliks (cf. Fig. 2.1). The lateral inflow from the North will persist during times of permafrost. The inflowing water volume is dependent on the distance of the ice sheet and proportional to the permafrost thickness. At the model surface, a hydrostatic pressure is defined.

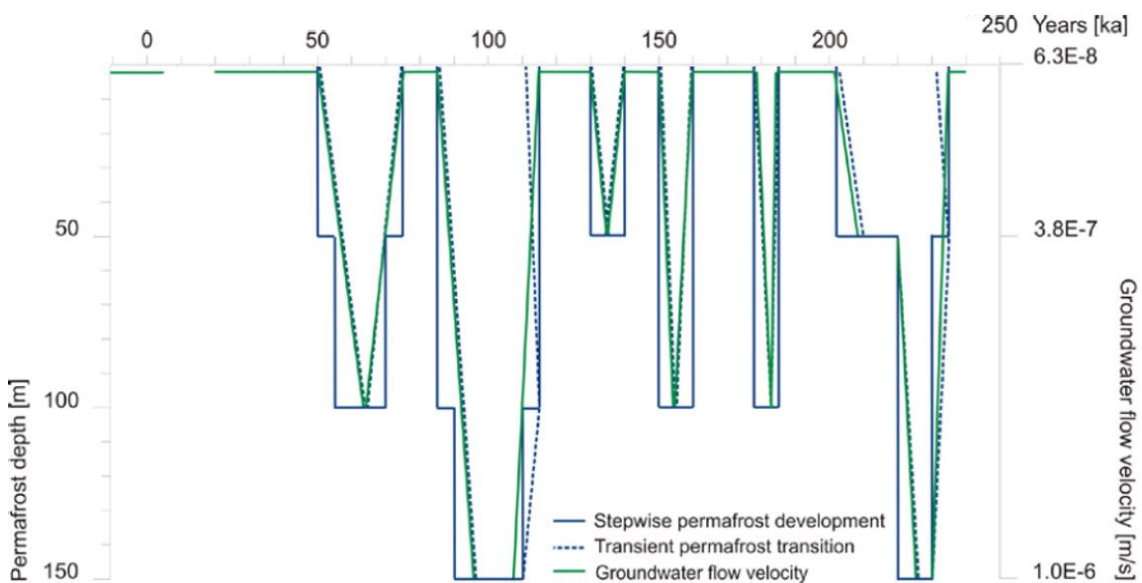


Fig. 2.6 Development of permafrost thickness and groundwater flow velocity (lateral inflow) for an assumed climatic cycle of 240,000 a (after /NOS 12b/)

Transport simulations should be set up with the purpose to achieve of a wide distribution of the pollutants in all hydrogeological units of the model. The aim is to analyze the impact of the climate transitions and climate states on the transport as well as to define the differences in employing the smart K_d -concept and conventional K_d -values. At this stage of concept development, it is not aimed at modeling a realistic radionuclide source. Thus, the location, magnitude and duration of a source of radionuclides (and an inter tracer) will be chosen based on the findings of the flow simulations.

3 Hydrogeochemical concept

One objective of the project was to update and further develop the concept to describe changing geochemical conditions and their impact on sorption currently implemented in d^{3f++}. This concept was developed within the ESTRAL project and is denoted in the following as ESTRAL concept. The further development concerned the structure of the hydrogeological model as well as the consideration of additional processes, components and environmental parameters. In addition, during the project phase the flow and transport codes d^{3f} and r^{3t} have been updated and coupled into one code d^{3f++}. Therefore, the concept had to be appropriately updated in the new code d^{3f++}. This approach has been applied still on the radionuclide transport in the sedimentary overburden of a repository site in a salt formation.

3.1 Hydrogeological model

The hydrogeological model, which is divided into three hydrogeological units, namely the upper aquifer (UAF), the aquitard (AT) and the lower aquifer (LAF), is described in detail in /NOS 12a/. Based on further discussions, it became clear that the tertiary sediments (Miocene brown coal sands) are of tropical origin and contain a higher fraction of quartz compared to the Elsterian sands but no feldspar and calcite. Both types of sediments are the components of the lower aquifer. Accordingly, it was decided to divide the lower aquifer into two different hydrogeological units. The boundary between the Miocene and the Elsterian sands is located at the southern rim of the north-western rim syncline (see Fig. 3.1).

In Fig. 3.2 the location of the Miocene brown coal sands, denoted as LAF2 and the Elsterian sands, denoted as LAF1 in the schematic two-dimensional model is shown. For a further simplification the occurrence of the brown coal sands in the southern part of the model is neglected (Fig. 3.2, bottom).

As a consequence, the specification of the lithological distribution was updated based on the discussions mentioned above. The updated mineral content for each hydrogeological unit is listed in Tab. 4.2 (cf. Sec. 4.2). The typical groundwater composition for each hydrogeological unit is discussed in Section 4.1 and the initial data used in the model are compiled in Tab. 4.1.

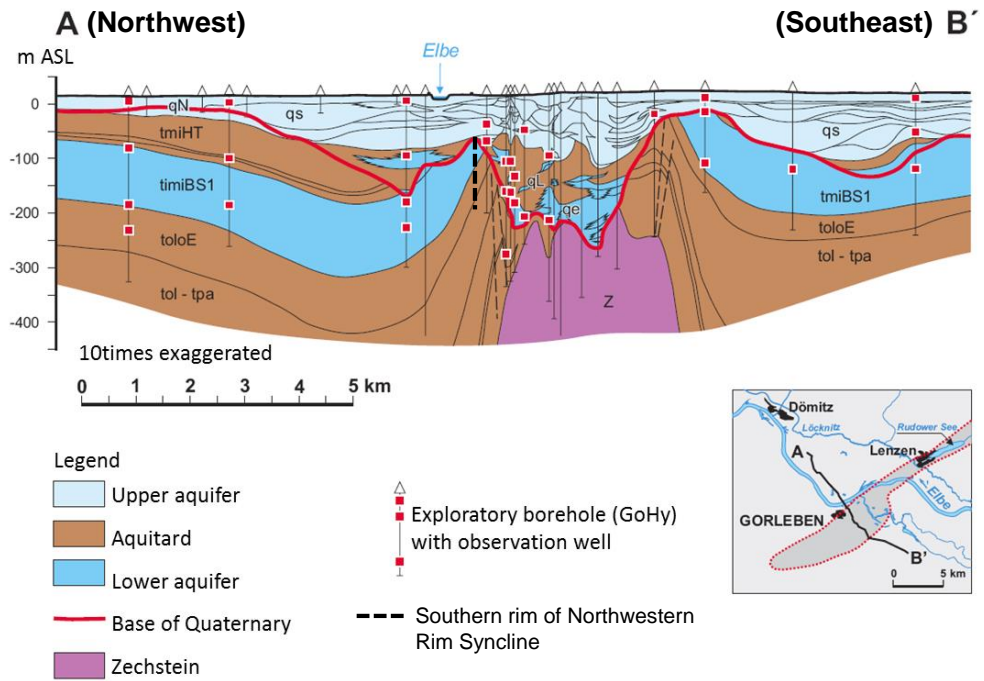


Fig. 3.1 Aquifer subdivision in the overburden of Gorleben salt dome after /KLI 07/

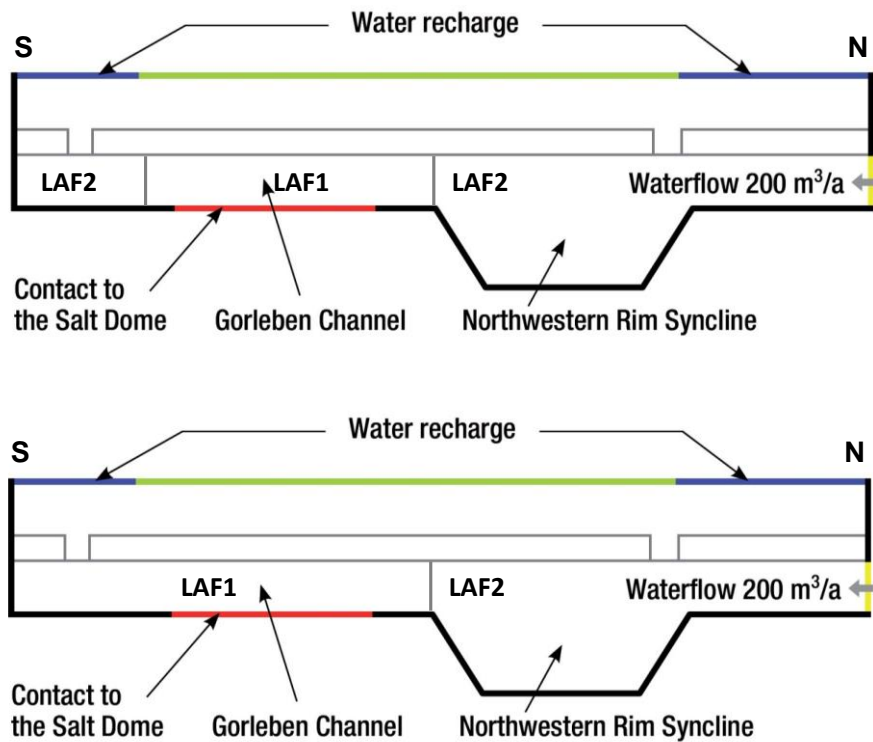


Fig. 3.2 2D cross section for the new model geometry with a subdivision of the lower aquifer into two different hydrogeological units

Top: Model geometry according to the occurrence of Miocene brown coal sands (LAF2);
 Bottom: Final model geometry with simplification at the southern rim.

3.2 Environmental parameters

In the ESTRAL concept the parameters pH, ionic strength, concentration of dissolved inorganic carbon (DIC), Ca and the considered radionuclides were in the first step identified and selected as environmental parameters affecting the sorption coefficients of the radionuclides. During the further development the relevance of the existing environmental parameters was checked and additional components and processes to be considered as environmental parameters were discussed.

Additional environmental parameters can be correlated to components and to processes. For the components two main groups can be distinguished:

- cations acting as competitive ions for the sorption sites and
- ligands, typically anions, forming complexes with the radionuclides in solution and therewith usually decreasing their sorption.

Beside the components, additional processes or effects might impact the geochemical conditions. Therefore, it needs to be evaluated, in which way these processes / effects might influence the chemical conditions, and it needs to be decided, whether they have to be considered in the model. Key potential processes or effects, which are not yet satisfyingly implemented, are redox processes, high ionic strength and ion exchange.

A basis for an evaluation is the existence of sound site data. Therefore, a detailed analysis of existing geochemical data from groundwater wells measured during the hydrogeological investigation program at Gorleben site, was performed with respect to the effects and processes mentioned above. Details of the evaluation are described in the digital appendix.

One consequence of the analysis of the existing environmental parameters was the negligence of the radionuclide concentration, since all sensitivity analysis showed them to be not relevant compared to pH and concentrations of Ca and DIC. Further the assumptions are still valid that radionuclides do not affect each other and do not impact the geochemical conditions. In accordance with that numerical problems identified by verification calculations could be solved (cf. Sec. 13).

With respect to the competing cations the analysis showed that the concentrations of several potential competing cations as for example the trivalent lanthanides occur in only

very low concentration ranges, where it is not expected that they will act as competitive cations. As a consequence, Mn will be regarded as a potential competing cation with respect to sorption. Mn may occur in nature in the oxidation states +II, +III and +IV. As the redox state in the Gorleben groundwater samples is not well established, it was decided to focus on +II to reflect the most reducing conditions.

As a further ligand being relevant under the conditions at the site sulfate was identified. Main sources for calcium and sulfate are the sulfate-bearing minerals in the cap rock of the salt dome. Updated thermodynamic calculations based on Pitzer interaction coefficients show that at high ionic strengths above app. 4 mol/l for a halite brine anhydrite is the concentration determining mineral. A Ca and SO₄ concentration of 0.0375 mol/l in equilibrium with anhydrite in saturated NaCl brine was calculated, which will be used as boundary condition in the transport calculations for both components. For the sulfate anion transport without sorption will be implemented in the conceptual model. Sulfate will become an additional environmental parameter.

Two alternative approaches are available for speciation calculations of radionuclides in high saline solutions. The SIT (Specific Ion Interaction Theory, see /GRE 13/) model is less complex and a database in PHREEQC format is available, mostly building on the respective data collection from the OECD/NEA TDB, see /LEM 13/ for the most recent version. However, the data quality is quite heterogeneous and high effort is necessary for a systematic evaluation of all data needed. Therefore, during the WEIMAR project data for the more complex Pitzer model /PIT 91/ were derived with less effort from the THEREDA project. A limitation here is that not all ion-ion interaction coefficients are available so far. Therefore, it is decided to continue the concept development using the Pitzer model but to keep the SIT model as an alternative.

With respect to redox conditions results of redox pair analyses amongst others NO₂/NO₃⁻, Fe(II)/Fe(III) and S²⁻ / SO₄²⁻ as well as measurements of the redox potential and oxygen content have been evaluated. This analysis showed a very inconsistent picture. In consequence, the critical evaluation of the redox measurements at Gorleben site in /KLI 94/ is supported by this detailed analysis of the field data. In the most recent discussion with experts from the BGR it was agreed, that these data are not suitable for the development of a simplified conceptual model for redox processes to be implemented in our approach. It is rather necessary to investigate a site with more sound and available redox data, which should be done in a future project.

3.3 Simplified geochemical model

One focus of the work concerned the implementation of additional environmental parameters. The components Al and SO₄ have been selected as additional environmental parameters (digi. App. Sec. A.2). It has also been decided that the radionuclide concentrations are no more regarded as environmental parameters.

In conclusion the environmental factors in the new concept are ionic strength, pH, [Ca], [DIC], [Al] und [SO₄]. The concentration of SO₄ is determined by initial and boundary conditions and its transport is assumed to be not retarded. The treatment of all other environmental factors is described in the following.

3.3.1 Basic terms

In the following activities are always denoted in curly brackets and concentrations in square brackets. Both are connected by the activity coefficient γ as for example

$$\{A^{\beta+}\} = [A^{\beta+}] \gamma_{A^{\beta+}} . \quad \text{Eq. 3.1}$$

Further, all concentrations are denoted in mol/m³, but the thermodynamic constants are related to mol/l. Accordingly the concentrations, and activities are divided by 10³ in all (thermodynamic) calculation steps.

The activity coefficients depend on the ionic strength IS , which is defined as

$$I = 0.5 \sum_i \frac{[i]}{10^3} z_i^2 \quad \text{Eq. 3.2}$$

with the concentration of the dissolved ions $[i]$ in [mol m⁻³] and their corresponding charges z_i .

In the existing concept the ionic strength is calculated from the relative concentration of sodium chloride as follows. The concentration for the saturated NaCl solution $c_{sat,NaCl}$ is calculated via the mass fraction, density and molar weight of NaCl as

$$c_{sat,NaCl} = m_{NaCl} \cdot \rho_{NaCl} / M_{NaCl} = 5428.78 \text{ [mol m}^{-3}\text{]}$$

with the mass fraction $m_{NaCl} = 0.265$ /D'A 67/ and the density $\rho_{NaCl} = 1197.2 \text{ kg m}^{-3}$ of saturated NaCl solution at 20°C and the molar weight $M_{NaCl} = 0.05844 \text{ kg mol}^{-1}$. The sodium chloride concentration is then calculated as $c_{NaCl} = c_{rel,NaCl} \cdot c_{sat,NaCl}$.

In a simplified approach for the ionic strength it was then assumed that the ions Na, K, Mg and SO₄ are distributed as in seawater, i. e. their concentrations are derived from the Cl concentration by scaling factors as follows

$$IS = 0.5([Cl] + [Na^+] + [K^+] + 4 \cdot [Mg^{2+}] + 4 \cdot [SO_4^{2-}]) / 10^3 = [Cl] \cdot 0.5(1 + 0.859 + 0.017 + 4 \cdot 0.097 + 4 \cdot 0.053) / 10^3 \quad \text{Eq. 3.3}$$

resulting in

$$IS = 1.24 \cdot [Cl] / 10^3. \quad \text{Eq. 3.4}$$

This approach was not fully consistent, since it did not include the contributions of Ca, DIC and Ca, which are now all considered as environmental parameters. Therefore, it is proposed to calculate the contributions for Cl, Na, K and Mg assuming the distribution in seawater by

$$IS^* = 0.5([Cl] + [Na^+] + [K^+] + 4 \cdot [Mg^{2+}]) / 10^3 = [Cl] \cdot 0.5(1 + 0.859 + 4 \cdot 0.097 + 4 \cdot 0.053) / 10^3 \quad \text{Eq. 3.5}$$

resulting in

$$IS^* = 1.13 \cdot [Cl] / 10^3. \quad \text{Eq. 3.6}$$

In order to calculate the final ionic strength, the concentrations of Ca, SO₄ and DIC (assumed as HCO₃⁻) have to be added in the following way:

$$IS = IS^* + 2 ([Ca^{2+}] + [SO_4^{2-}] + 0.25[DIC]) / 10^3. \quad \text{Eq. 3.7}$$

The activity coefficients are derived from the Specific Ion Interaction Theory (SIT) /CIA 80/. For the relevant ions the single activity coefficients are formulated according to SIT:

$$\begin{aligned}
\log \gamma_{AlOH^{2+}} &= -4D + \varepsilon_{AlOH,Cl} \cdot [Cl^-]/10^3 \quad \text{with } \varepsilon_{AlOH,Cl} = 0.09 \\
\log \gamma_{Al(OH)_2^+} &= -D + \varepsilon_{Al(OH)_2,Cl} \cdot [Cl^-]/10^3 \quad \text{with } \varepsilon_{Al(OH)_2,Cl} = -0.27 \\
\log \gamma_{Al(OH)_3} &= 0 \\
\log \gamma_{Al(OH)_4^-} &= -D + \varepsilon_{Al(OH)_4,Cl} \cdot [Cl^-]/10^3 \quad \text{with } \varepsilon_{Al(OH)_4,Cl} = -0.07 \\
\log \gamma_{Al^{3+}} &= -9D + \varepsilon_{Al,Cl} \cdot [Cl^-]/10^3 \quad \text{with } \varepsilon_{Al,Cl} = 0.33 \\
\log \gamma_{OH^-} &= -D \\
\log \gamma_{H^+} &= -D + \varepsilon_{H,Cl} \cdot [Cl^-]/10^3 \quad \text{with } \varepsilon_{H,Cl} = 0.12
\end{aligned} \tag{Eq. 3.8}$$

with an extended Debye-Hückel-Term $D = \frac{0.5114\sqrt{IS}}{1+1.5\sqrt{IS}}$ and the interaction coefficients

ε_i . The data are taken from /RAN 09/.

Since the pH-value is a function of the ionic strength I , the activity correction need to be performed by $pH = -\log([H^+]_{kor} \gamma_{H^+})$.¹

After a transport step of protons and hydroxyl ions the pH-values is calculated from their concentrations as

$$pH^T = [H^+]^{kor} \gamma_{H^+} \tag{Eq. 3.9}$$

with

$$[H^+]/10^3 - x = [H^+]^{kor}, \tag{Eq. 3.10}$$

$$x = \frac{[H^+]^T/10^3 + [OH^-]^T/10^3}{2} - \sqrt{\left(\frac{[H^+]^T/10^3 + [OH^-]^T/10^3}{2}\right)^2 - [H^+]^T[OH^-]^T/10^6 + \frac{K_W}{\gamma_{H^+}\gamma_{OH^-}}} \tag{Eq. 3.11}$$

and the ionic product of water $K_W = 10^{-14} \text{ mol}^2 \text{ L}^{-2}$.

¹ Correctly. the activity coefficient for H^+ is derived by

$$\log \gamma_{H^+} = -z^2 D + \sum \varepsilon_{H^+,k} [k]/10^3$$

with the concentration of the most relevant anions (Cl^- , HCO_3^- ; SO_4^{2-}) $[k]$, and the SIT interaction coefficients ε_i . For H^+ only the interaction coefficient $\varepsilon_{H^+,Cl} = 0.12$ is available. The interaction coefficients of other monovalent cations Na^+ and Li^+ with the relevant anions $\varepsilon_{Na^+,HCO_3^-} = 0.0$ and $\varepsilon_{Li^+,SO_4^{2-}} = -0.03$ show that these interactions are low. Considering typical SO_4 concentrations this contribution is always below 1 % of the interaction of H^+ with Cl^- . Then it is

$$\log \gamma_{H^+} = -D + 0.12[Cl^-]/10^3$$

3.3.2 Consideration of Al

Besides Ca as major cation in natural waters, Al was identified as additional environmental parameter affecting the sorption coefficients of the radionuclides and will be considered in transport simulations. In natural waters Al occurs in lower concentrations than Ca. However, Al might be important as well as a competitive cation for sorption sites on minerals. After the transport step the concentration of Al in solution is determined by the mineral generic Gibbsite. The concentration determining mineral for Al is likely not a feldspar. But it is also not expected that the Al concentration can be described by the thermodynamic data for pure gibbsite. Therefore, it is recommended to consider a mixed mineral denoted in the following as „generic gibbsite” or $\text{Al}(\text{OH})_3$ /KLI 14/. In the concept it is assumed that generic gibbsite will be always available.

3.3.2.1 Solubility of generic gibbsite

We follow the approach to determine the solubility constant ($\log K_{SPG}$) for such a generic “gibbsite” from the available groundwater datasets of the Gorleben sediments. Therefore, an optimization procedure using PHREEQC coupled with the parameter estimation code UCODE has been applied.

All datasets containing Al data have been used and appropriately implemented into the PHREEQC /PAR 13/ input file. Nearly all data stem from the lower aquifer (LAF). By variation of the $\log K_{SP}$ -value (solubility product) for gibbsite a best fit to the field data was done manually. The fit was performed with the EDH (cf. Sec. 6.2) and with the Pitzer database (cf. Sec. 6.1.2) yielding values of $\log K_{sp} = 10.35$ (EDH) and $\log K_{sp} = 9.82$ (Pitzer), respectively. The values for crystalline gibbsite ($\log K_{sp} = 7.76$) und amorphous gibbsite ($\log K_{sp} = 9.67$) indicate that the values derived for the generic gibbsite are plausible. In Fig. 3.3 the experimental and modelled data are shown as a function of pH. Noticeable are high Al concentrations at high ionic strength calculated with the Pitzer database, which is illustrated in Fig. 3.4.

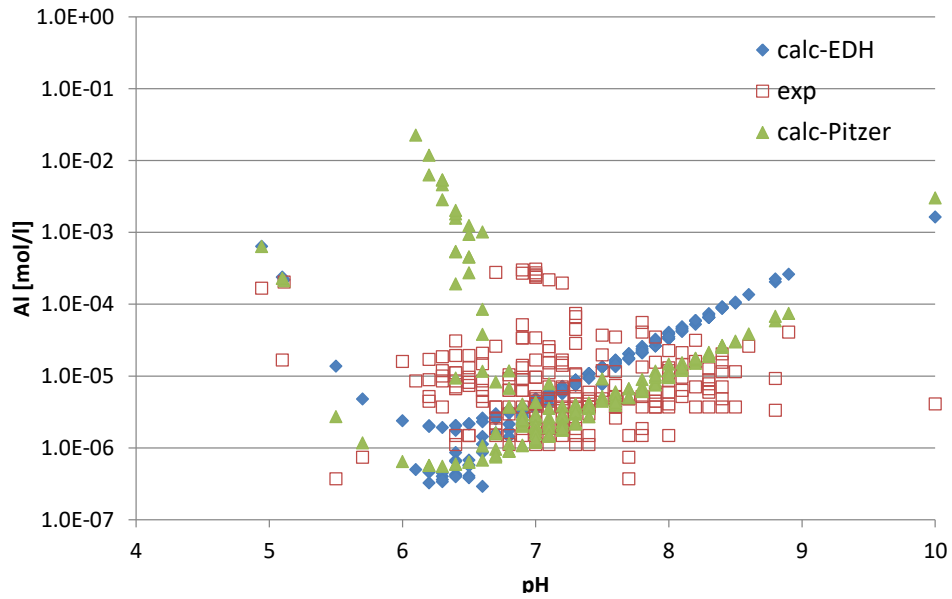


Fig. 3.3 Al concentrations: Field data and data calculated with WEIMAR_PIT.dat and WEIMAR_EDH.dat, respectively, in equilibrium with generic gibbsite as function of pH value

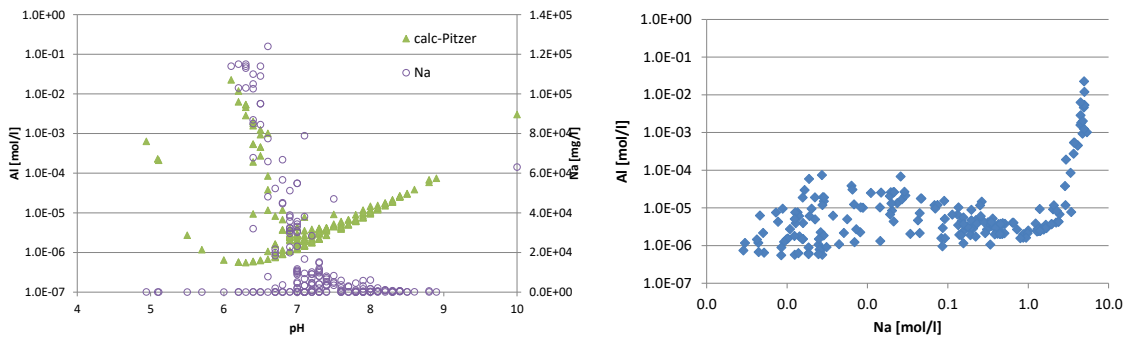


Fig. 3.4 Al concentration in logarithmic scale calculated with WEIMAR_PIT.dat in equilibrium with gibbsite and measured Na-concentrations of the corresponding Gorleben field data as a function of pH value (left) and Al concentration as a function of Na concentration (right)

The equations describing Al concentration in our model are explained in the following. In the digital appendix Section A.10 a pseudocode script of the whole concept is compiled.

The concentrations of protons, Ca, DIC, Al and SO₄ resulting from the transport step are denoted as initial concentrations and marked as $[X]^T$. The concentration of SO₄ will not be changed by chemical reactions. The new concept is based on the ESTRAL-concept /NOS 12a/. In the new concept the assumption that calcite will be always available in all hydrogeological units is no more valid. Therefore, the amount of calcite needs to be

balanced in each element for each time step and for each element an initial amount of calcite has to be given.

As described in /NOS 12a/ in the first step the saturation index for calcite needs to be calculated to determine whether the solution is over- or undersaturated with respect to calcite. These two cases will be distinguished in the following.

3.3.2.2 Calcite oversaturation

In this case the approach is the same as in the ESTRAL-concept, i. e. the pH value, the concentration of Ca and DIC are determined by precipitation of calcite and Al does not influence the chemical conditions. In addition, the total concentration of Al needs to be calculated. This concentration is determined by the pH value and the solubility of generic gibbsite (gG) as follows

$$[Al_{tot}] = 10^{(\log K_{SP,G} + 9D - 3pH)} + 10^{(\log K_{SP,G} + \log K_{AlOH2+} + 4D - 2pH)} + 10^{(\log K_{SP,G} + \log K_{Al(OH)2+} + D - pH)} + 10^{(\log K_{SP,G} + \log K_{Al(OH)3})} + 10^{(\log K_{SP,G} + \log K_{Al(OH)4-} + D + pH)} \quad \text{Eq. 3.12}$$

The solubility product for generic gibbsite and the stability constants of the complexes are listed in Tab. 3.1. The parameter D is calculated from the ionic strength as described in Chapter 3.3.1 by the following equation

$$D = \frac{0.5114\sqrt{IS}}{1 + 1.5\sqrt{IS}}. \quad \text{Eq. 3.13}$$

Tab. 3.1 Solubility products and stability constants of relevant complexes for Al

Chemical formula	Parameter	Value
Al(OH) ₃ "gen. Gibbsite"	log K _{SP,gG}	10.35
AlOH ²⁺	log K _{AlOH2+}	-4.9573
Al(OH) ₂ ⁺	log K _{Al(OH)2+}	-10.5943
Al(OH) ₃	log K _{Al(OH)3}	-16.4328
Al(OH) ₃ ⁻	log K _{Al(OH)4-}	-22.8797

The calculated concentrations for Al_{tot}, protons, hydroxide ions, Ca and DIC are used in the next transport step.

3.3.2.3 Calcite undersaturation

Under these conditions two different cases need to be distinguished.

A) It is enough calcite available for dissolution to reach equilibrium: In this case the approach is similar to the ESTRAL-concept. Again, pH value and the concentration of Ca and DIC are determined by dissolution of calcite as in the ESTRAL-concept. The concentration of Al is then calculated by formula Eq. 3.12 as described in Section 3.3.2.2.

B) Calcite is no more or not in sufficient amount available for dissolution to reach equilibrium: In this case it is assumed that the pH-value is determined by the mineral generic gibbsite which is always available in the system, as mentioned above. The concentration of Ca and DIC will not be influenced by dissolution or precipitation of generic gibbsite and the resulting pH change. If some (but not sufficient) calcite was available in the system, it will become completely dissolved and the respective amounts for Ca and DIC will be added to their concentrations in solution. The system calcite, Ca and DIC will not impact the pH value.

After the transport step for each time step and space the saturation index of generic gibbsite (SI_{gG}) is calculated using the initial values from the transport step pH^T and $[Al]^T$. and to be evaluated, whether gibbsite dissolves ($SI_{gG} < 0$) or precipitates ($SI_{gG} > 0$):

$$SI = \frac{\{Al^{3+}\}/10^3}{(\{H^+\}/10^3)^3 K_{SP,gG}} \quad \text{Eq. 3.14}$$

with

$$\{Al^{3+}\}/10^3 = [Al_{tot}]/10^3 / (1/\gamma_{Al^{3+}} + K_{Al(OH)_2} / (\gamma_{Al(OH)_2} \cdot \{H^+\}/10^3) + K_{Al(OH)_2+} / (\gamma_{Al(OH)_2+} \cdot (\{H^+\}/10^3)^2) + K_{Al(OH)_3} / (\gamma_{Al(OH)_3} \cdot (\{H^+\}/10^3)^3) + K_{Al(OH)_4} / (\gamma_{Al(OH)_4} \cdot (\{H^+\}/10^3)^4)) \quad \text{Eq. 3.15}$$

The values for the solubility product and stability constants for the relevant complexes are listed in Tab. 3.1. For $SI_{gG} < 1$ the concentration $[Al]$ will be increased and for $SI_{gG} > 1$ it will be decreased accordingly. The procedure for determination of the chemical equilibrium is carried out in two nested iteration loops. In the outer loop $[Al]$ will be varied as long as the equilibrium is reached ($SI_{gG} = 1$). In the inner iteration loop a consistent pH-value and the corresponding SI_{gG} for generic gibbsite are calculated.

Inner iteration: During the dissolution and precipitation of gibbsite three hydroxide ions are released or withdrawn to the solution. However, it has to be considered that in dependence of the pH-value a different average number of OH ions is bound to Al-species in solution. Therefore, primarily the average number of OH groups ($N_{OH,0}$) bound to Al at the initial pH value is calculated. The pH dependence of $N_{OH,0}$ within the interesting pH range between 6.0 and 8.0 is fitted by a sigmoid function with the following form

$$f(x) = \frac{a}{b + ce^{-d(x-f)}} + t, \quad \text{Eq. 3.16}$$

which is illustrated in Fig. 3.5. The fitted parameters are listed in Tab. 3.2.

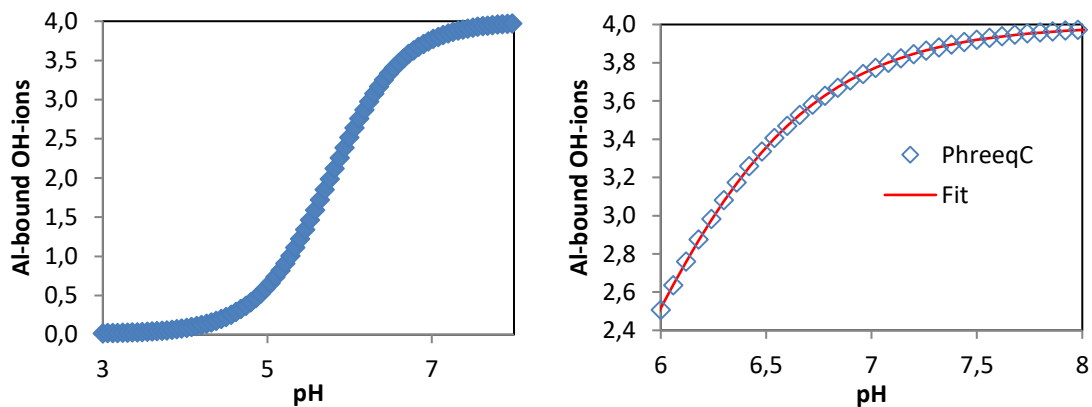


Fig. 3.5 Number of Al-bound hydroxyl ions as function of pH, calculated by PHREEQC (left) and fitted by a sigmoid function (right)

Tab. 3.2 Fitted set of parameters for the sigmoid function

Parameter	Value
a	3.97949
b	0.99836
c	3.14996
d	2.25661
f	5.25813
t	0.01171

From Eq. 3.16 and Tab. 3.2 the average number of OH groups $N_{OH,0}$, which are withdrawn or added to the solution by precipitation or dissolution of generic gibbsite at the initial pH, respectively, can be deduced. For all further pH values calculated within the inner loop the average number of OH groups N_{OH} will be determined. The difference between $N_{OH,0}$ and N_{OH} yields the number of OH groups, which are released or consumed

by change in Al speciation as function of the pH value compared to the initial pH value. The change of the concentration of free OH groups can be calculated from $N_{OH,0}$, N_{OH} and the change in concentration of $\Delta[Al]$:

$$\Delta[OH_{Al}] = \Delta[Al_{tot}] (N_{OH,0} - N_{OH}) - \Delta[Al_{tot}] (3 - N_{OH,0}), \quad \text{Eq. 3.17}$$

with

$$\Delta[Al_{tot}] = [Al_{tot,0}] - [Al_{tot}], \quad \text{Eq. 3.18}$$

which leads to a change in pH value considering the correction of $[H^+]$ and $[OH^-]$ due to the autoprotolysis of water.

$$x = \frac{[H^+]/10^3 + [OH^-]/10^3 + \Delta[OH_{Al}]/10^3}{2} - \sqrt{\left(\frac{[H^+]/10^3 + [OH^-]/10^3 + \Delta[OH_{Al}]/10^3}{2} \right)^2 - [H^+][OH^-] + \Delta[OH_{Al}]/10^6 + \frac{K_w}{\gamma_H \gamma_{OH^-}}} \quad \text{Eq. 3.19}$$

The corrected concentrations of protons $[H^+]^{korr}$ and hydroxyl ions $[OH^-]^{korr}$ can be derived from its initial concentrations by

$$[H^+]/10^3 - x = [H^+]^{korr} \quad \text{and} \quad [OH^-]/10^3 + \Delta[OH_{Al}]/10^3 - x = [OH^-]^{korr} \quad \text{Eq. 3.20}$$

pH_{korr} is then

$$pH_{korr} = -\log([H^+]^{korr} \gamma_{H^+}) \quad \text{Eq. 3.21}$$

The aim of the inner iteration is a variation of the pH value until it is identical to pH_{korr} (abort criterion: $\Delta pH < 0.001$). In each iteration step of the inner loop the current pH value and the corrected pH value are compared and from that an upper (pH_{high}) and lower (pH_{low}) pH value derived. In the first iteration step pH and pH_{korr} are compared; pH_{low} is set to the lower and pH_{high} the higher value of both. In the following steps

$pH_{low}(l)$: If $pH < pH_{korr} = pH_{low}(l-1)$ (from last iteration step), else MAX (pH ; $pH_{low}(l-1)$)

$pH_{high}(l)$: If $pH > pH_{korr} = pH_{high}(l-1)$, else MIN (pH_{korr} ; $pH_{high}(l-1)$)

Outer iteration: In dependence of the initial saturation index [aI] will be increased or decreased, respectively, until SI_{gG} changes its algebraic sign. Then [Al] will be optimized by nested intervals as long as $SI = 1$ (abort criterion $(SI_{gG}-1) < 0.0001$). From the final pH value and γ_{H^+} the final concentration of protons is determined:

$$[H^+] = 10^{-\log(pH_{final}/\gamma_{H^+})} 10^3 \quad \text{Eq. 3.22}$$

The values calculated for $[Ca]$, $[DIC]$, $[Al_{tot}]$, $[OH]$ and $[H^+]$ are then used by the transport code d^{3f++} for the next transport step.

3.3.3 Reconsideration of Ca

Verification calculations of the ESTRAL concept showed that for systems near equilibrium conditions fairly good results were achieved (cf. Sec. 13.2). However, with a less equilibrated solution discrepancies in the environmental parameters between d^{3f++} calculation results and those calculated with the coupled code PHAST occur causing for some radionuclides significant deviations in distribution coefficients. The reasons for this are certain simplifying assumptions in the concept for the treatment of calcite, see /NOS 12a/. Therefore, based on the experiences of the implementation of Al and generic gibbsite into the system a revision and modification of the concept for treatment of Ca / calcite was done.

The new concept now considers dissolution and precipitation of calcite in a similar way and consists of an inner and outer loop. After the transport step for each time step and space point the saturation index of calcite (SI_{Cc}) is calculated using the initial values from the transport step pH^T , $[DIC]^T$ and $[Ca]^T$. This indicates whether calcite dissolves ($SI_{Cc} < 0$) or precipitates ($SI_{Cc} > 0$):

$$SI_{Cc} = \log IAP_{CC} - \log K_{SP,Cc} \quad \text{Eq. 3.23}$$

With

$$IAP_{CC} = \{CO_3^{2-}\}\{Ca^{2+}\} = \frac{\gamma_{CO_3}[DIC]}{1 + \frac{K_{CO_3}}{\gamma_{HCO_3}} \gamma_{CO_3} e^{-pH} + K_{HCO_3} \gamma_{CO_3} (e^{-pH})^2} \gamma_{Ca}[Ca^{2+}] \quad \text{Eq. 3.24}$$

The values for the solubility product and stability constants for the relevant complexes are listed in Tab. 3.3. For $SI_{Cc} < 0$ the concentration $[DIC]$ (and accordingly $[Ca]$) will be increased, whereas for $SI_{Cc} > 0$ it will be decreased. The procedure for determination of the chemical equilibrium is carried out in two nested iteration loops. In the outer loop $\Delta[DIC]$ will be varied as long as the equilibrium is reached ($SI_{Cc} = 0$). In the inner iteration loop a consistent pH-value and the corresponding SI_{Cc} for calcite are calculated.

Tab. 3.3 Solubility products and stability constants of relevant complexes for Ca

Chemical formula	Parameter	Value
CaCO ₃ (calcite)	$\log K_{SP, Cc}$	-8.481
CO ₃ ²⁻	$\log K_{CO32-}$	10.329
HCO ₃ ⁻	$\log K_{HCO3}$	16.6808

Inner iteration: The inner iteration always starts with pH^T . As a consequence of the calcite dissolution or precipitation the carbonate equilibrium is changed and protons are released to or withdrawn from the solution. It needs to be considered that in dependence of the pH-value a different average number of protons is bound to carbonate in solution. Therefore, primarily the average number of protons ($N_{H,0}$) bound to carbonate at the initial pH value is calculated. The pH dependence of $N_{H,0}$ within the interesting pH range is fitted by a step function with the following form

$$f(x) = -\frac{a}{a+be^{-c(pH-d)}} - \frac{a}{a+ge^{-h(pH-i)}} + j \quad \text{Eq. 3.25}$$

which is illustrated in Fig. 3.6. The fitted parameters are listed in Tab. 3.4.

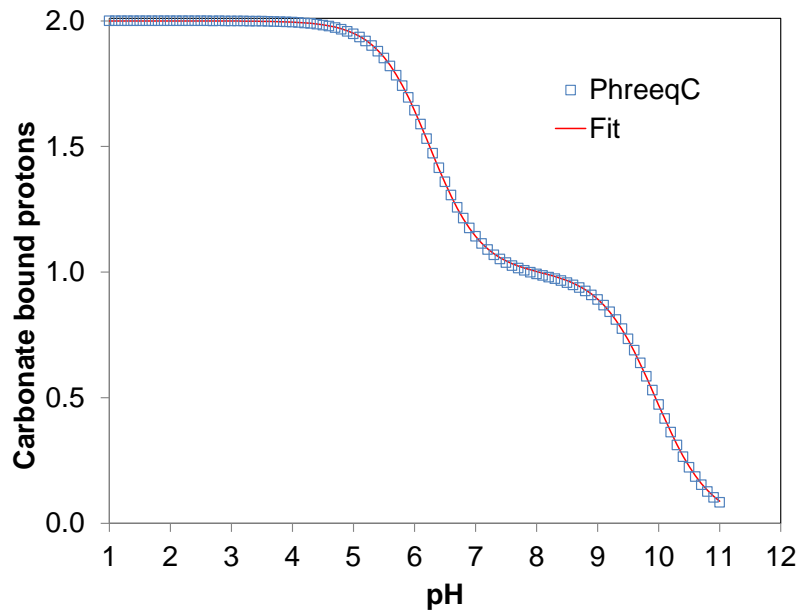


Fig. 3.6 Number of carbonate-bound protons as function of pH, calculated by PHREEQC and fitted by a step function

Tab. 3.4 Fitted set of parameters for the step function

Parameter	Value	Parameter	Value
<i>a</i>	3.0	<i>g</i>	1.0747
<i>b</i>	1.98433	<i>h</i>	2.22078
<i>c</i>	2.37406	<i>i</i>	10.4078
<i>d</i>	-6.42219	<i>j</i>	2.0

From these results the average number of protons $N_{H,0}$, which are withdrawn or added to the solution by precipitation or dissolution of calcite at the initial pH, respectively. Then within the inner loop the average number of protons N_H will be determined. The difference between $N_{H,0}$ and N_H yields the number of protons, which are released or consumed by change in carbonate speciation as function of the pH value compared to the initial pH value. The change of the concentration of carbonate-bound protons in solution can be calculated from $N_{H,0}$, N_H and the change in concentration of $\Delta[DIC]$:

$$\Delta[HCO_3] = \Delta[DIC] N_{H,0} \quad \text{Eq. 3.26}$$

with

$$\Delta[DIC] = [DIC]^T - [DIC] \quad \text{Eq. 3.27}$$

in the first inner iteration step and

$$\Delta[HCO_3] = \Delta[DIC] N_{H,0} - [DIC] N_H \quad \text{Eq. 3.28}$$

in all other iteration steps.

This, eventually leads to a change in pH value considering the correction of $[H^+]$ and $[OH^-]$ due to the autoprotolysis of water.

$$x = \frac{[H^+]/10^3 + [OH^-]/10^3 + \Delta[HCO_3]/10^3}{2} - \sqrt{\left(\frac{[H^+]/10^3 + [OH^-]/10^3 + \Delta[HCO_3]/10^3}{2}\right)^2 - \frac{[OH^-]([H^+] + \Delta[HCO_3])}{10^6} + \frac{K_w}{\gamma_{H^+}\gamma_{OH^-}}} \quad \text{Eq. 3.29}$$

The corrected concentrations of protons $[H^+]^{korr}$ and hydroxyl ions $[OH^-]^{korr}$ can be derived from its initial concentrations by

$$[H^+]^{korr} = [H^+]/10^3 + \Delta[HCO_3]/10^3 - x \quad \text{and} \quad [OH^-]^{korr} = [OH^-]/10^3 - x \quad \text{Eq. 3.30}$$

pH_{korr} is then

$$pH_{korr} = -\log([H^+]^{korr} \gamma_{H^+}) \quad \text{Eq. 3.31}$$

Applying pH_{korr} an updated carbonate concentration is calculated by

$$[CO_3^{2-}] = \frac{[DIC]}{1 + \frac{K_{CO_3}}{\gamma_{HCO_3}} \gamma_{CO_3} e^{-pH} + K_{HCO_3} \gamma_{CO_3} (e^{-pH})^2} \quad \text{Eq. 3.32}$$

Finally, with the updated concentration of $[CO_3^{2-}]$ and $[Ca^{2+}]$ a new value of SI_{Cc} is calculated.

The aim of the inner iteration is a variation of the pH value until it is in equilibrium with the changed amount of carbonate in solution (abort criterion: $f_{abs}(\text{delta } pH) < 0.001$), with $\text{delta } pH = pH - pH_{korr}$. In each iteration step of the inner loop the current pH value and the corrected pH value are compared and from that an upper (pH_{high}) and lower (pH_{low}) pH value is derived. In the first iteration step pH and pH_{korr} are compared; pH_{low} is set to the lower and pH_{high} to the higher value of both. In the following steps

$pH_{low}(I)$: If $pH > pH_{korr} = pH_{low}(I-1)$ (from last iteration step), else $MAX(pH; pH_{low}(I-1))$

$pH_{high}(I)$: If $pH > pH_{korr} = pH$, else $MIN(pH_{korr}; pH_{high}(I-1))$

The pH-value for the next inner iteration step is calculate as $0.5(pH_{low} + pH_{high})$.

Outer iteration: In dependence of the saturation index $[DIC]$ will be increased or decreased until SI_{Cc} changes its algebraic sign. Then $[DIC]$ will be optimized by nested intervals as long as $SI_{Cc} = 0$ (abort criterion $f_{abs}(SI_{Cc}) < 0.0001$). From the final pH value and γ_{H^+} the final concentration of protons is determined:

$$[H^+] = 10^{-\log(pH_{final}/\gamma_{H^+})} 10^3 \quad \text{Eq. 3.33}$$

The values calculated for $[Ca]$, $[DIC]$, $[OH]$ and $[H^+]$ are then used by the transport code d³f++ for the next transport step. A pseudocode script of the concept is listed in the digital appendix Section A.10.2.

4 Geochemical site characterization

As a reference site the sedimentary overburden at the Gorleben site as described in /NOS 12a/ was chosen for smart K_d transport simulations since comprehensive dataset on its geology and hydrogeology are available (e. g. /KLI 02a/, /KLI 04/). In the following sections, the hydrological (Sec. 4.1) and sedimentological system (Sec. 4.2) of the Gorleben overburden are described in detail.

4.1 Water chemistry

The hydraulic system is divided into an upper aquifer (UAF) with freshwater conditions, an intercalated aquitard (AT) and a lower aquifer (LAF) with saline groundwater /KLI 02b/. New selection criteria have been applied as described in detail in the digital appendix Section A.3. Depending on the stratigraphic classification the LAF is divided into two units as described in Sections 3.1 and 4.2.

Chemical data for the different groundwater types are taken from the well-documented HYGOR-BGR database /KLI 04/ and are given in Tab. 4.1. For identifying significant outliers in the groundwater data outlier tests have been applied. In the literature, numerous outlier tests are described and are more or less well-suited depending on the type and size of the dataset. For datasets with sample sizes < 30 the Dean-Dixon-Test /DIX 50/, /DIX 51/ is recommended and therefore used for UAF and AT. However, for datasets with more than 30 samples (as in the case of LAF1 and LAF2) the David-Hartley-Pearson Test /DAV 54/ was used. As a result, only one groundwater measuring points (GWM 352) was identified as significant outlier for AT and consequently not considered in further calculations.

Tab. 4.1 Chemical data for the different groundwater types of the Gorleben overburden (concentrations in mol L⁻¹)

	UAF	AT	LAF1	LAF2
No. of GWM	14	15	82	73
Outliers	0	1	0	0
pH	7.3	7.9	6.9	7.1
K	3.1E-05	1.5E-04	1.4E-02	6.0E-03
Na	3.8E-04	6.9E-03	2.3E+00	9.5E-01
Mg	1.1E-04	3.3E-04	2.8E-02	1.3E-02
Ca	9.2E-04	3.6E-04	2.8E-02	1.7E-02
Fe	2.2E-05	1.0E-05	1.4E-04	7.1E-05
Mn	3.5E-06	2.1E-06	2.7E-05	2.0E-05
Al	1.9E-06	3.3E-06	1.9E-06	5.7E-06
Cl	3.4E-04	4.8E-03	2.5E+00	1.2E+00
SO4	2.7E-04	1.9E-05	3.0E-02	1.1E-02
HCO3	1.6E-03	3.7E-03	3.7E-03	4.4E-03
PO4	5.5E-06	1.8E-05	1.6E-04	7.1E-06
SiO2	3.8E-03	3.3E-04	2.3E-04	2.1E-04
TDS^a	7.1E-03	2.2E-02	5.2E+00	2.4E+00
IS_calc^b	3.8E-03	9.2E-03	2.6E+00	1.2E+00

^aTDS = Total Dissolved Solids (original in mg L⁻¹, converted in mol L⁻¹ with factor 35E-06)

^b Calculated ionic strength (IS) from main cation and anions

4.2 Sediments

The sediments of the three hydrogeological units UAF, AT and LAF differ in term of their origin and mineralogical composition. The UAF consists of quaternary sands from the Weichselian and Saalian cold stages. The AT is represented by the Lauenburger Clay Complex and the Hamburg Clay. The LAF is divided into two hydrogeological units (Sec. 3.1, Fig. 3.1), whereby the LAF1 consists mainly of Elsterian sands above the salt dome which were deposited during the Elsterian glacial (sands of the Elsterian meltwater channels) and contain feldspar and calcite, similar to the Weichselian and Saalian sands of the UAF. The LAF2 consists mainly of Tertiary Lower Brown Coal Sands (Miocene lignite sands) in the North-Western rim syncline and in the south of the model area, which are of tropical origin, i. e. they do have a higher content of quartz and do not contain any feldspar or calcite. This will have a significant impact for the geochemical conditions and to some extent also on the sorption properties.

To define representative mineral compositions of the different sedimentary units of the Gorleben overburden the weight-percentage of relevant minerals were estimated based on sediment analyses carried out from /GRI 82 – 94/, /KAN 92/, /ZIR 03/.

The assumed mineral composition of the hydrogeological units of the Gorleben overburden is given in Tab. 4.2.

Tab. 4.2 Mean mineral composition of the four sedimentary units UAF, AT and LAF1/LAF2 of the Gorleben overburden (in wt%)

Mineral	UAF	AT	LAF1	LAF2
	Saalian and Weichselian meltwater sands	Lauenburg Clay Complex	Elsterian Sands	Miocene Lower Brown Coal Sands
Quartz	85	25	85	95
Feldspar*	10	5	10	n.r.
Muscovite	0.5	3	0.5	0.5
Gibbsite	0.5	n.r.	0.5	0.5
Goethite	0.5	2	0.5	0.5
Calcite	2	10	2	n.r.
Kaolinite	1.5	15	1.5	3.5
Illite	n.r.	40	n.r.	n.r.

* applicable for Albite, Anorthite, Orthoclase and Microcline

n.r. mineral phases not quantitatively relevant in the sedimentary unit

t mineral phases only relevant for transport processes

5 Mineral properties

This section is based on /BRI 18/ and /RIC 15/ and describes mineral as well as material properties such as the surface site density (SSD), the specific surface area (SSA), mineral composition and surface impurities, surface charge properties, and grain size distribution of quartz (Sec. 5.1.1), orthoclase (Sec. 5.1.2), and muscovite (Sec. 5.1.3) used for laboratory experiments. Information concerning the experimental set-ups and applied methods are provided in Appendices A.4.2 – A.4.7. All experiments in this study were conducted with identical mineral phases to guarantee comparability of collected data. Information on techniques, equipment, and supporting institutions are provided in the digital appendix (digi. App. Sec. A.4).

To comprehensively describe surface charge properties precise definitions points of zero charge (reference pH values) are a prerequisite. Sections 5.1.3.3, 5.1.2.2, and 5.1.1.3 depict acid-base characteristics of quartz, orthoclase, and muscovite which are based on the determination and interrelations of reference pH values for each mineral. According definitions of e. g. pH_{mass} (pH of the end point of mass titration), pH_{IEP} (pH of the isoelectric point), pH_{cip} (pH of the common intersection point), etc. are provided in detail in digital appendix Section A.4.6. Where necessary experimental data had to be processed which is outlined in the digital appendix Section A.4.7.

5.1.1 Quartz

Schlingmeyer Quarzsand GmbH & Co KG (Schwülper, Germany) provided the quartz sample (supplier specification: G20EAS extra). According to the supplier the quartz mineral is composed of 99.7 wt% SiO_2 which was confirmed by HF digestion analyses of this study (digi. App. Tab. A. 2). Further components relate to Al_2O_3 (0.2 wt%), K_2O (0.05 wt%), CaO (0.05 wt%), Fe_2O_3 (0.04 wt%), and TiO_2 (0.01 wt%). The Eu background concentration equaled 0.03 mg kg^{-1} solid which was deemed negligible. The quartz sediment was deposited about 70 million years ago (Late Cretaceous fluvialite deposit), mined in the Northern Plane of Germany (Uhry, Germany) without addition of chemical agents, and was washed with local groundwater after extraction according to the supplier. Due to the non-invasive mining process the quartz sample was used without further purification or preconditioning treatment as a natural sediment. The XRD and SEM/EDX analyses confirmed information provided by the supplier that the sample was free of humic substances and soluble salt contaminations. The quartz sediment appeared with rounded edges due to fluvial transport and without any further detectable

impurities or organic components. The cumulative mass-median diameter was $d_{50} = 350 \mu\text{m}$ (medium sand). The particle size fraction (*PSF*) covered 150 – 800 μm and BET analysis yielded a $SSA_{BET} = 0.06 \text{ m}^2 \text{ g}^{-1} \pm 10\%$ (RSD, (Tab. 5.1)). The Tab. 5.1 summarizes BET measurements of pristine quartz samples. Recommended overall sample area of at least 1 m^2 /MAC 11/, /SIM 99/) for SSA_{BET} determinations was not met in any of the measurements (Tab. 5.1). Therefore, SSA_{BET} of the quartz mineral might have been influenced by errors $> 9.5\%$ RSD and should be used with care.

5.1.1.1 Leaching experiment of quartz for Fe, Al, and amorphous silica

To choose an appropriate quartz mineral for the planned lab experiments two Uhry quartz minerals were analyzed via extraction experiments for Fe and Al. Iron and aluminum hydroxides at the surface highly influence sorption behavior of mineral surfaces and may therefore bias experimental data. It was the aim to find a natural quartz mineral as pure as possible. According to the retailer G20 EAS extra is supposed to be the purer quartz mineral compared to G20 EA – both derived from Uhry site, Lower Saxony, Germany (Schlingmeier Quarzsand GmbH & Co. KG). Experimental set-up is briefly described in the digital appendix Section A.4.4.

As expected, higher Al and Fe concentrations were observed for the quartz sample G20 EA compared to G20 EAS (Fig. 5.1 and Fig. 5.2). At this point and based on acid leaching results the quartz mineral G20 EAS extra was favored for experiments of the present research study. For a detailed characterization of the quartz mineral (G20 EAS extra) HF digestions provide the mineral composition and accessory impurities (digi. App. Tab. A. 2).

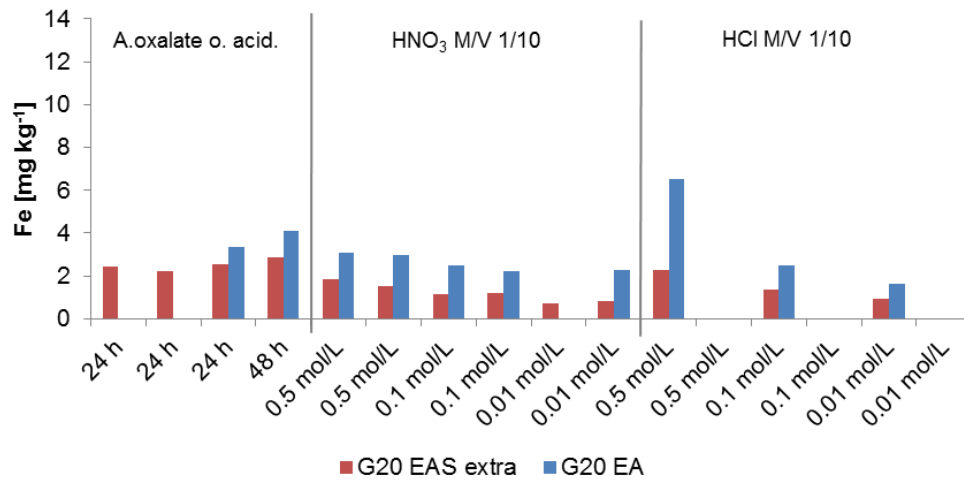


Fig. 5.1 Results of Fe acid leaching and extraction experiments using the quartz minerals G20 EAS extra and G20 EA

In case of missing results samples were not analyzed. A. oxalate o. acid = ammonium oxalate oxalic acid, M/V – solid-liquid ratio [g ml⁻¹].

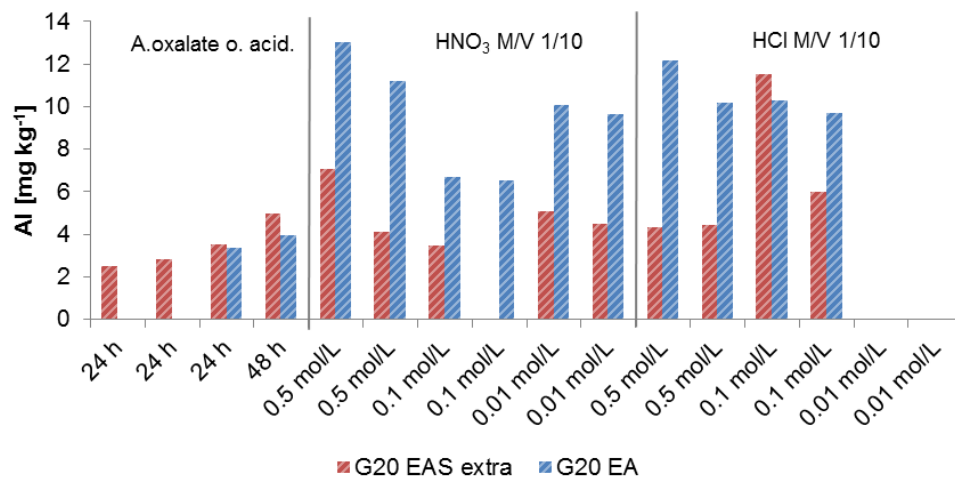


Fig. 5.2 Results of Al acid leaching and extraction experiments using the quartz minerals G20 EAS extra and G20 EA

In case of missing results samples were not analyzed. A. oxalate o. acid = ammonium oxalate oxalic acid, M/V solid-liquid ratio [g ml⁻¹].

Beside Fe and Al components varying concentrations of amorphous silicon dioxide (amorphous SiO₂ = diatomaceous earth = fossilized remains of diatoms) also influence the sorption behavior of crystalline SiO₂. Amorphous SiO₂ and crystalline SiO₂ have the same chemical compositions, but a different number of binding sites. Amorphous SiO₂ offers a higher amount of sorption site and may therefore influence surface complexation behavior of quartz minerals. The minerals G20 EA and G20 EAS extra are mined in

Northern Germany (Lower Saxony), where some diatomaceous earth deposits exist. Again, the experimental set-up is summarized in the digital appendix Section A.4.4.

Results show similar amorphous silicon dioxide concentrations for both quartz minerals (Fig. 5.3) which is expected since both minerals originate from the same site. To conclude, the quartz mineral G20 EAS extra was used to determine surface complexation parameters (SCPs) and to examine transport behavior of the trivalent lanthanide Eu (Sec. 8). The mineral is further referred to as quartz.

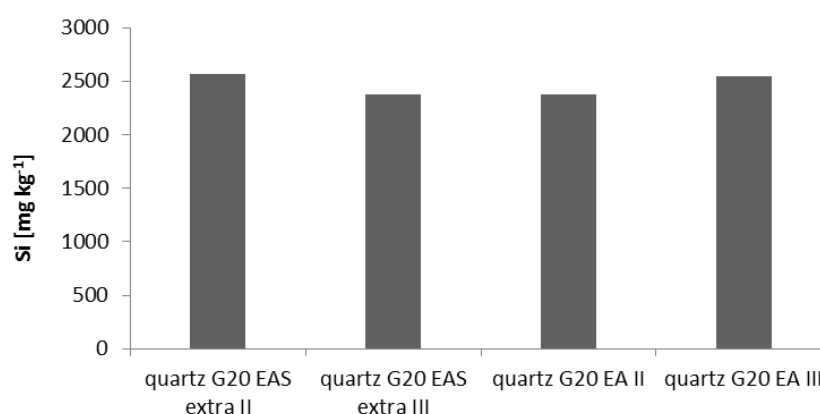


Fig. 5.3 Analysis of quartz for amorphous SiO₂

No significant differences are observed. Twofold measurements are undertaken: quartz G20 EAS extra II, III, and quartz G20 EA II, III.

5.1.1.2 Release of Al from orthoclase, muscovite, and quartz equilibrated with 0.01 mol L⁻¹ NaClO₄

The release of Al from orthoclase, muscovite, and quartz in 0.01 mol L⁻¹ NaClO₄ solution was investigated

- to identify appropriate geochemical boundary conditions (e. g. initial Al concentrations, M/V) for batch sorption experiments (Sec. 7) and
- to consider the released Al for calculation of % sorbed fraction values from experimental raw data (ICP-MS measurements [$\mu\text{g L}^{-1}$]).

The release of Al was determined in equilibrated suspensions after pH adjustment was achieved. This was realized within 30 d. Samples were taken between pH 5 and 8 for orthoclase, muscovite, and quartz (Fig. 5.4). For quartz additional data were taken below pH 5 and above pH 8. The highest released Al concentrations were attained at pH 5 for muscovite with $5 \cdot 10^{-6}$ mol L⁻¹ (data at pH 8 were not available), at pH 8 for orthoclase

with $2 \cdot 10^{-5} \text{ mol L}^{-1}$ and at pH 4.3 for quartz with $1.9 \cdot 10^{-4} \text{ mol L}^{-1}$. The lowest release was between pH 5 and pH 8 matching the trend of Al solubility limit, which was calculated with PHREEQC (Fig. 5.4, red line). The oversaturation of Al (data points above red line) regarding e. g. 200 g L⁻¹ quartz data between pH 3 to 4.5 could be due to kinetic effects of precipitation processes. Because of high Al concentrations released from the minerals, the limit of quantification (LOC) of $\sim 3 \cdot 10^{-8} \text{ mol L}^{-1}$ Al and the relative low solubility of Al, batch sorption experiments with orthoclase, muscovite, and quartz were not feasible. To minimize released Al concentrations, purified quartz sand from MERCK was used instead. Concerning orthoclase and muscovite a purification is not possible since Al is a constituent in the crystal structure of these minerals. The “MERCK quartz” was preconditioned by the vendor: washed with hydrochloric acid and calcined at 900 °C. Since 40 % of the particles were between 0.2 to 0.8 mm, the MERCK quartz was comparable to the quartz used in this study. Released Al concentrations between pH 3 to 4.5 were more than one order of magnitude lower. Therefore, the MERCK quartz samples were subsequently used for batch sorption experiments (Sec. 7.10) to gain insight into Al sorption affinity to natural quartz. Nevertheless, no data could be collected between pH 5 to 8 because of the relative low solubility of Al and LOC as mentioned before.

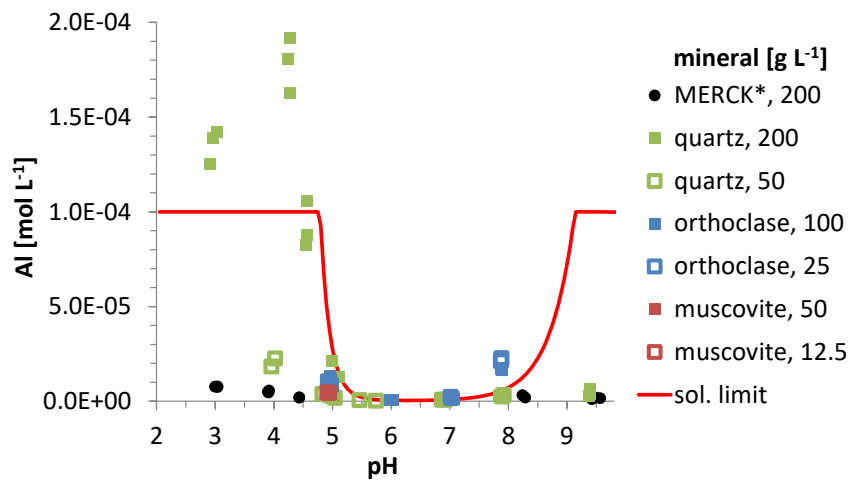


Fig. 5.4 Al released from quartz, orthoclase and muscovite equilibrated with $0.01 \text{ mol L}^{-1} \text{ NaClO}_4$ solution

Batch sample solutions were analyzed after the systems were in equilibrium, after adjustment of constant pH. At pH 6 and 7 Al concentrations of muscovite samples and several quartz samples were lower than the limit of quantification = $3.3 \cdot 10^{-8} \text{ mol L}^{-1}$ Al. At pH 8 no data was collected for muscovite. MERCK* = purified natural quartz from MERCK. Sol. limit = solubility limit of Al calculated with PHREEQC.

5.1.1.3 Quartz surface charge properties

Fig. 5.5 depicts mass (A) and electrolyte (B) titration data of quartz. Titration results must be assessed with caution since surface impurities of the natural quartz mineral potentially bias experimental raw data. Interestingly, depending on the initial pH condition (pH_{ini}), mass titration results approached two different end points (pH_{mass} , Fig. 5.5 A):

- Experiments initiated at pH_{ini} 3.0 did not show any change with increasing solid content. This implied an ideal, pristine (hydr)oxide silica surface (free of relevant basic or acidic impurities); $pH_{mass} = 2.9$ and agreed well with cited silica pH_{ppzc} (e. g. /POL 10/).
- In contrast, measurements that were started at $pH_{ini} = 4.5$ converged towards $pH_{mass} = 6.5$ which contradicted the former observation.

Results supported the assumption that two "types" of silica surface functional groups might exist which behave differently depending on surrounding pH conditions. One "type" of sites behaved pH independent whereas as a second "type" of sites evolved pH depend properties. This observation could be related to findings of /LÜT 96/ who observed Cd sorption processes in unexpectedly low pH ranges at silica solid-solution interfaces. /LÜT 96/ had to assume that besides Si-OH groups the examined surface was partially composed of cation exchange sites due to small amounts of Na-impurities. Interestingly, similar findings were made in the present study: Quartz also showed minor surface impurities (digi. App. Tab. A. 2) and Eu sorption processes were also observed at $pH < 4$ (Sec. 7.8). These unexpected results highlight that assumingly well-studied surfaces like silica surfaces still bear unknowns that have yet to be uncovered.

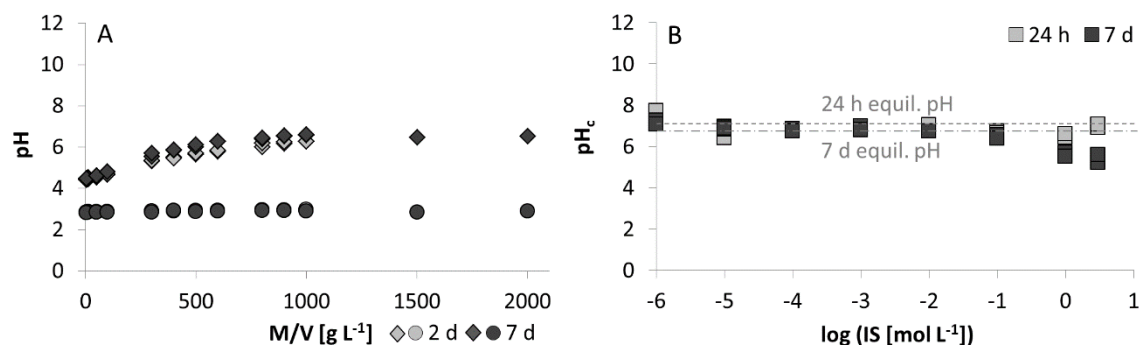


Fig. 5.5 Experimental mass (A) and electrolyte (B) titration data of quartz after 24 h, 2 d, and 7 d

Experiments were carried out in doublets. A: Discontinuous mass titration: Circles – $pH_{ini} = 3.0$, diamonds – $pH_{ini} = 4.5$. B: Discontinuous electrolyte titration: $M/V = 1200 \text{ g L}^{-1}$,

dashed line illustrates reference sample (suspension without addition of NaClO_4) after 7 h, dotted-dashed line represents reference after 7 d equilibration time. pH_c stands for pH values that were corrected for electrolyte influences after /HAG 14/, /BRI 18/, IS – ionic strength [$\log(IS \text{ mol L}^{-1})$], M/V – mass volume ratio [g L^{-1}].

Fig. 5.5 B presents discontinuous electrolyte titration results using equilibration times of 24 h and 7 d ($M/V = 1200 \text{ g L}^{-1}$, increasing NaClO_4 concentrations). Horizontal lines in Fig. 5.5 B depict pH measurements of reference samples after 24 h and 7 d; reference samples were suspensions with $M/V = 1200 \text{ g L}^{-1}$ in $10^{-5} \text{ mol L}^{-1} \text{ NaClO}_4$. The pH decrease of the reference samples after 7 d (≈ 0.3 pH units) were attributed to pH-measurement uncertainties (0.16 pH units after /DIN 07/, /BRI 18/) and potential CO_2 influence during equilibration time. Electrolyte titration results after 7 d indicated that rising IS concentrations ($> 0.1 \text{ mol L}^{-1} \text{ NaClO}_4$) caused decreasing endpoints; hence, $\text{pH}_{\text{mass}} \neq \text{pH}_{\text{pzse}} \neq \text{pH}_{\text{ppzc}}$ could be assumed. For pristine oxide surfaces and symmetric counterion associations the pH should be independent of IS and $\text{pH} = \text{pH}_{\text{pzse}} = \text{pH}_{\text{ppzc}}$ (e. g. /PRE 98/, /LÜT 12/). To conclude, data indicated asymmetric counterion associations after 7 d that effected pH conditions at $IS > 0.1 \text{ mol L}^{-1}$. This observation might be specific for NaClO_4 and should be verified for other electrolytes.

Mass titration experiments offer a reliable means to determine a mineral's pH_{ppzc} if surface contaminations and mineral dissolution do not occur /POL 10/. If both cannot be excluded (as in the present study) /POL 10/ suggest that potentiometric titrations are more suitable to define a mineral's reference pH, e. g. pH_{nphc} or pH_{cip} . The pH_{nphc} for natural minerals or the pH_{pznpc} for pristine surfaces are determined via potentiometric titrations and ideally coincidence with the pH_{cip} . As potentiometric titration data was collected with only one IS ($10 \text{ mmol L}^{-1} \text{ NaClO}_4$ electrolyte concentration), a potential pH dependence of pH_{nphc} could not be verified. Due to the lack of data a literature data set had to be used: /BOL 57/ collected surface charge measurements from amorphous silica at different IS s (Fig. 5.6) and as Fig. 5.6 shows, data from /BOL 57/ agreed well with titration data collected in this study. Data from /BOL 57/ exhibited a pH_{pznpc} below 4.0 (Fig. 5.6) and since both data sets agreed well /BOL 57/ pH_{pznpc} was assumed to offer a good estimate of the quartz reference pH of this study. Whether the quartz surface of this study exhibited truly pristine mineral surface characteristics or whether the mineral surface charge development was influenced by potential impurities could not explicitly be verified.

For the subsequent surface charge modeling study data from /BOL 57/, 10 mM NaCl was used as a more comprehensive data set compared to data collected in this study

(Fig. 5.6). This approach was reasonable since both potentiometric data sets at 10 mM electrolyte concentration matched well and exhibited similar reference pH values: pH_{ppzc} /BOL 57/, pH_{nphc} respectively (this study).

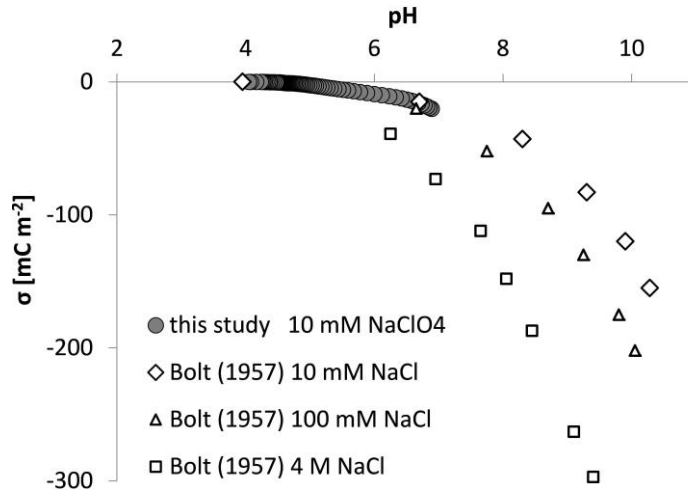


Fig. 5.6 Continuous potentiometric acid-base titration of quartz (solid symbols) in comparison to titration data of a silica sol at different electrolyte concentrations published by /BOL 57/ (open characters)

Measurements of this study were determined in 10 mM NaClO_4 , /BOL 57/ used increasing concentrations of NaCl . σ corresponds to the surface charge density [mC m^{-2}].

5.1.2 Orthoclase

The orthoclase (supplier specification: Kali Norflot 600) was obtained from Sibelco Deutschland GmbH, Ransbach-Baumbach, Germany. According to the supplier the orthoclase was mined in a pegmatite host rock formation, ground to a particle fraction of approximately $600 \mu\text{m}$, and composed of 18.8 wt% Al_2O_3 , 10.5 wt% K_2O , and 3.6 wt% Na_2O . Thus, orthoclase was the predominant component of this sample (K-feldspar). The oxides Fe_2O_3 (0.1 wt%) and CaO (0.8 wt%) represent minor components (digi. App. Tab. A. 2). The composition was confirmed by HF digestion of this study (digi. App. Tab. A. 2). The Eu background concentration equaled 0.4 mg kg^{-1} solid representing insignificant potential for artefacts in the planned experiments. Leaching of Ca from orthoclase is illustrated in Section 5.1.3.2, information on Al release from orthoclase in equilibrated suspensions is provided in Section 5.1.1.2.

Compared to the ideal structural formula of orthoclase (KAlSi_3O_8) a deficit of K_2O (4 wt%) and an excess of approximately 2 wt% SiO_2 was detected via HF analysis (digi. App. Tab. A. 2). The difference in K_2O was balanced by Na_2O (5.12 wt%) which indicates

minor admixtures of albite. Albite was confirmed by EDX-analysis (Fig. 5.7) and XRD (Fig. 5.8). The excess SiO₂ was probably due to minor quartz admixtures, consistent with XRD and EDX analysis (Fig. 5.7, Fig. 5.8). The XRD measurements revealed microcline (66 wt%, semi-quantitative analysis, Rietveld method), albite (31 wt%), and quartz (3 wt%). Microcline is the low-T modification of K-feldspar and common for pegmatite occurrences. The chemical composition is identical to orthoclase, whereas the crystalline order differs (triclinic vs. monoclinic). Results of XRD and EDX analysis fully support findings of HF digestion measurements. In the following, the mineral Kali Norflot 600 is referred to as orthoclase or feldspar.

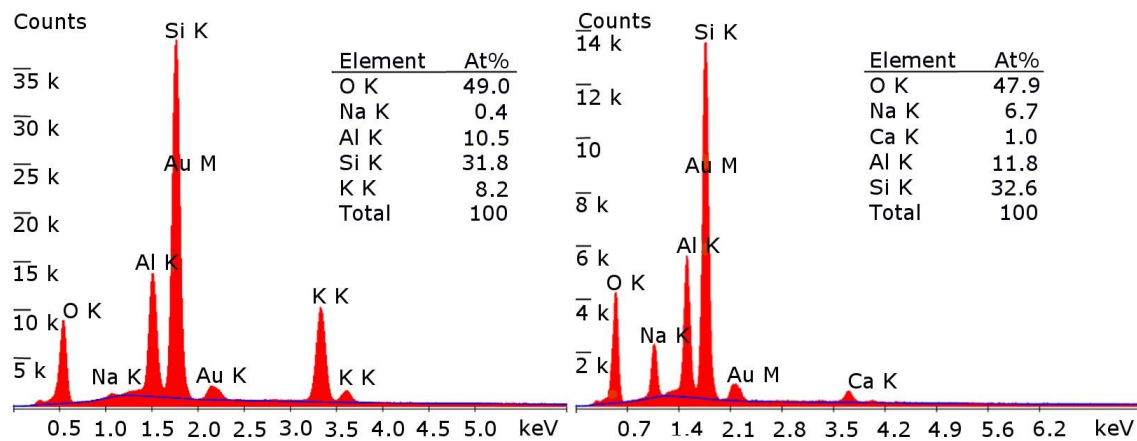


Fig. 5.7 EDX analyses (area scan) of orthoclase, PSF 30 μm – 400 μm

Left: Identified orthoclase particle (KAlSi₃O₈). Right: Albite grain (NaAlSi₃O₈). The inserts illustrate element distributions [At%] of individual mineral components. Blue line – background noise; K, L, M – excitation energy of incident X-ray energy (shells of Bohr's model).

For the scheduled experiments the orthoclase sample as obtained from the supplier was milled. The sample size of 30 – 400 μm was used for titration and transport (Sec. 9.1) experiments. The milled, geochemically untreated orthoclase is referred to as pristine mineral phase. Conducted SEM analyses showed typically cleaved orthoclase grains /BRI 18/. The BET analysis yielded $SSA_{BET} = 0.19 \text{ m}^2 \text{ g}^{-1} \pm 3\%$ (RSD, Tab. 5.1) for the particle size fraction 30 – 400 μm. The SSA_{BET} after /BRU 38/ followed expectations: The larger the particle size fraction, the smaller SSA_{BET} . Orthoclase samples from titration experiments and mineral preconditioning for column experiments (digi. App. Sec. A.8.1) exhibited minor effects on the SSA (Tab. 5.1). However, since the examined sample size for BET measurements was well below recommendations made by e. g. /MAC 11/ and /SIM 99/ ($\geq 1 \text{ m}^2$ recommended overall sample area, Tab. 5.1) influences from mineral

preconditioning or experimental set-up could not explicitly be identified (Tab. 5.1). Accordingly, limitations regarding further utilization of SSA_{BET} of orthoclase have to be considered.

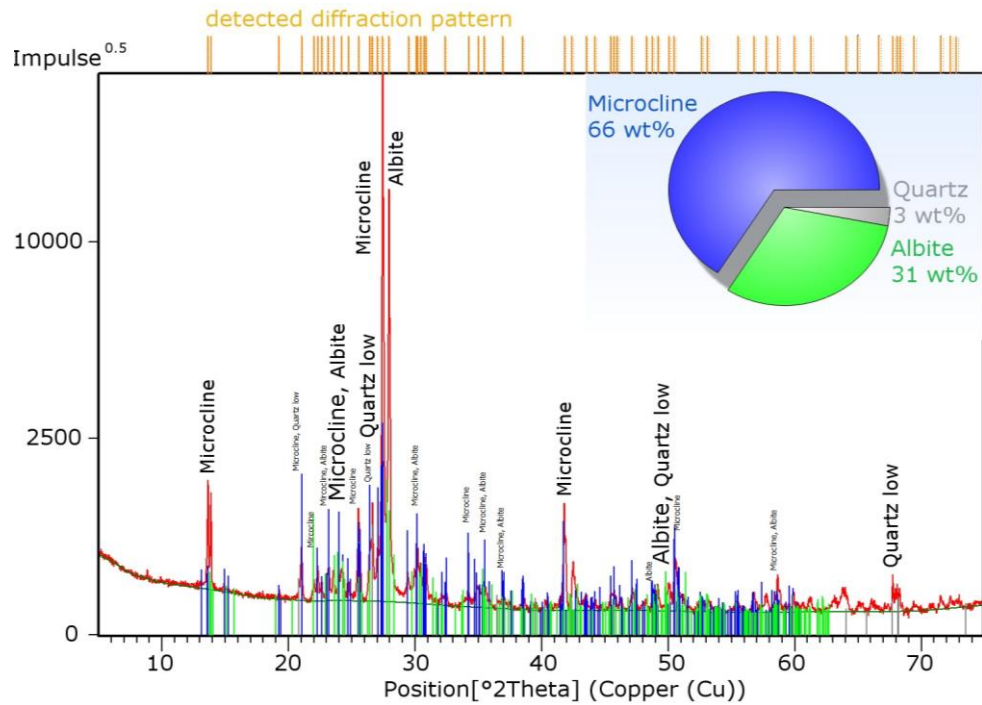


Fig. 5.8 XRD analysis of orthoclase, PSF 63 μm – 400 μm

Application of ICSD (2009) database. Identified mineral phases: albite (green), microcline (blue), and quartz (grey). Blue, green, grey vertical lines represent ICSD diffraction patterns, orange/red collected XRD reflection angles of orthoclase. Quartz low refers to α -quartz. The insert illustrates calculated wt% of mineral components using the Rietveld method.

5.1.2.1 Comparison of batch and flow-through leaching experiments of orthoclase

Leaching experiments offered information about the dissolution behavior of the minerals and about potential free competing ions in solution that may influencing the geo-chemical conditions of the experiments. To investigate the leaching of orthoclase batch and flow-through experiments were performed to see the difference of the dissolution behavior under static (batch) and in presence of fresh solution under dynamic conditions (flow-through). Both processes can be observed in nature. The experimental set-up and the leached elements with their corresponding concentrations are given in the digital appendix Section A.4.2.

Fig. 5.9 shows the dissolution of the main elements from orthoclase as well as uranium over time in batch and flow-through experiment. These results indicated that even after three months the dissolution has not reached yet a steady state.

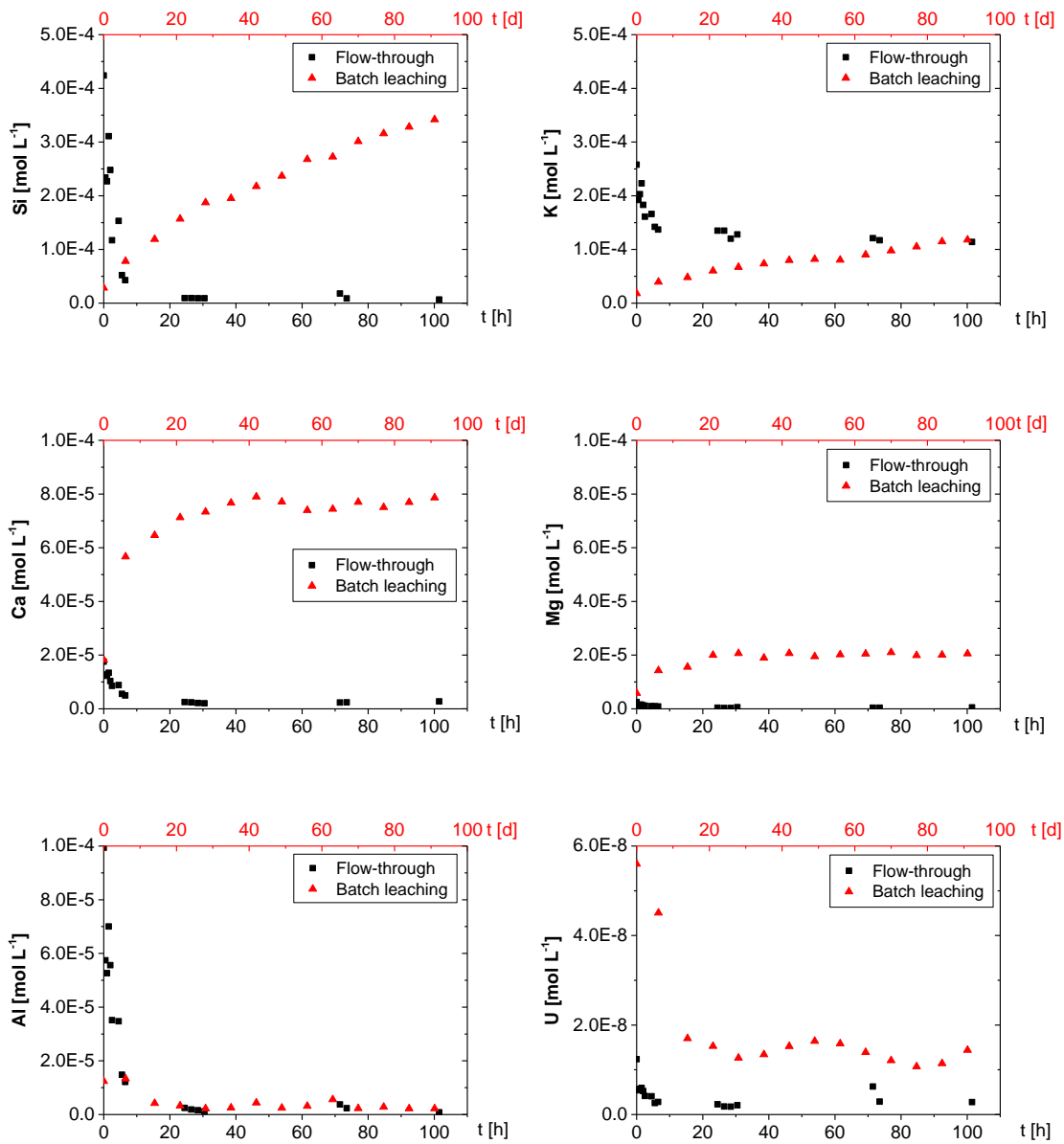


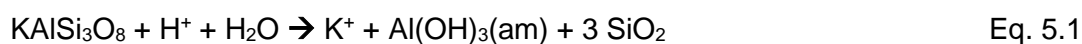
Fig. 5.9 Dissolution of main elements and uranium from orthoclase obtained in batch leaching experiments (shown as red triangles) and in flow-through leaching experiments (shown as black squares)

The results indicated that the main elements Si, Al and K were dissolved from the mineral as major constituents of the crystal structure of orthoclase (ideal structural formula KAISi_3O_8), whereby Al has a low solubility. Beside them Ca and Mg were found to represent minor fractions. The small concentration of U in the mineral was considered for the

selection of the uranium concentrations in the experiments. Furthermore, the concentrations of representative lanthanides (Eu, Gd, Nd, and Dy) were below the detection limit so that no effect onto the sorption processes during the experiment was expected. These results correspond well with HF digestion analysis which gave the main composition of orthoclase (digi. App. Tab. A. 2).

The analyzed elemental concentrations from the leaching experiments as well as the pH adjustments were used to decide which proposed dissolution scheme of orthoclase and muscovite (cf. Sec. 5.1.3) most probably happened. There, however, the results from the flow-through experiments were not considered as they are heavily dominated by kinetic effects. In the batch leaching experiment, the dissolved elements accumulate until a saturation limit is reached. In the flow-through experiment fresh background electrolyte has the contact with the mineral the whole time. In fact, there is no accumulation and the amount of the elements is lower. The respective dissolution reactions for the conditions applied in this study, i. e., a pH range from 3 to 10, ambient atmosphere, and temperature have been discussed in detail in /RIC 15/.

The following dissolution reaction was proposed for orthoclase:



5.1.2.2 Orthoclase surface charge properties

Fig. 5.10 depicts measurements of mass (A) and electrolyte (B) titration experiments of orthoclase. For orthoclase, mass titration experiments were carried out with two pH_{ini} values ($\text{pH}_{\text{ini}} = 2.9$ and $\text{pH}_{\text{ini}} = 4.7$) which did not converge towards the same endpoint (pH_{mass}) within 7 d (Fig. 5.10 A) as would be expected for a mineral surface with negligible impurities (e. g. /POL 10/) After 7 months, pH measurements indicated an equilibrium $\text{pH} = 8.3$ (data not displayed here) that was either due to mineral dissolution, potential secondary phase precipitation, and/or governed by surface impurities. All equilibrium pH values determined either after 5 h, 7 d, or 7 months exceeded the pH_{IEP} which equalled 3.5. Hence, mass titration experiments supported the assumption of basic impurities at the orthoclase surface.

Zeta-potential measurements yielded negative electrokinetic potentials at pH conditions $> \text{pH}_{\text{IEP}}$ ($\text{pH}_{\text{IEP}} = 3.5$, digi. App. Fig. A. 21). The pH_{IEP} was in fair agreement with IEP values observed by /STI 95/ who report $\text{pH}_{\text{IEP}} = 1.5 - 6.1$ depending on the degree of K^+

vs. H^+ exchange on the surface. The more K^+ is exchanged for H^+ the higher pH_{IEP} . Calculated pH_{IEP} from ideally composed feldspar minerals result in a reference pH of 3.0 – 3.1 /STI 95/. On this basis, the zeta-potentials would suggest K^+ vs. H^+ exchange at the present orthoclase surface.

Fig. 5.10 B shows orthoclase electrolyte titration results. The dotted and dash-dotted horizontal lines depict the equilibrium pH of reference samples (reference suspensions: M/V 400 g L^{-1} , $10^{-5}\text{ mol L}^{-1}$ $NaClO_4$). The pH of references changed by 0.4 pH units over the first 7 d (Fig. 5.10 B) and by 0.9 pH units over 8 months (data not displayed here). The shift in pH might be caused by Na^+ vs. H^+ exchange processes and/or be due to potential atmospheric CO_2 influence. /STI 95/ reported pH shifts of approximately 0.5 pH units after 500 d of adularia feldspar in different electrolyte solutions which they related to surface ageing processes. Considering data collected after 5 h where mineral ageing processes are not yet relevant and excluding the possibility of a CO_2 influence during 5 h equilibration time measurements indicated asymmetric counterion associations which affected pH conditions at $IS > 1\text{ mol L}^{-1}$.

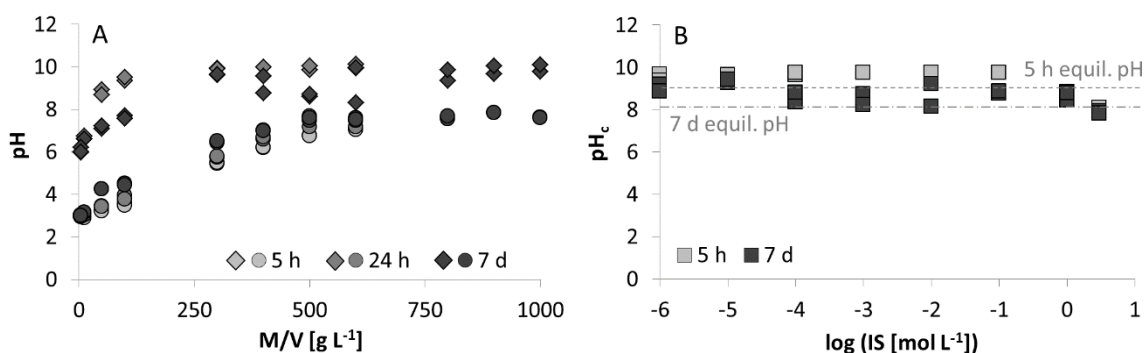


Fig. 5.10 Mass (A) and electrolyte (B) titration measurements of orthoclase after 5 h, 24 h, and 7 d

Experiments were conducted in duplicate. A: Discontinuous mass titration: Circles – $pH_{ini} = 2.9$, diamonds – $pH_{ini} = 4.7$. B: Discontinuous electrolyte titration: $M/V = 400\text{ g L}^{-1}$, dashed line – reference sample (without addition of $NaClO_4$) after 24 h, dotted-dashed line – reference after 7 equilibration time. pH_c – pH corrected for electrolyte influences after /HAG 14/, /BRI 18/. IS – ionic strength [$\log(IS\text{ mol L}^{-1})$].

Since $pH_{mass} \neq pH_{IEP}$, a pH_{ppzc} did not exist for orthoclase. Hence, potentiometric titration measurements returned relative surface charge data that needed to be transformed into absolute values (digi. App. Sec. A.4.7). Two different approaches were followed to determine absolute surface charges from the raw data which is illustrated in the digital appendix Section A.4.7. Fig. 5.11 depicts relative data in relation to the shifted processed, absolute data. Titration measurements appeared to approach a threshold at $pH > 7.6$

(Fig. 5.11). This threshold could be caused by fully deprotonated surface functional groups (Si-O⁻ and Al-O⁻). In the absence of better information and following /BRI 18/ a rough estimate of the SSD equaled 1.9 sites nm⁻² with $\sigma_{\text{sat}} = 0.3 \text{ C m}^{-2}$. Detailed information is provided by /BRI 18/.

/BRI 18/ provides a comparison of potentiometric measurements found in literature with data of this study. Large differences in feldspar mineral titration data was observed including a variety of published reference pH values (pH_{pzc} , pH_{pznpc} , pH_{pzse}) which illustrates the complexity of mineral titration experiments and the difficulty to correctly interpret experimental data.

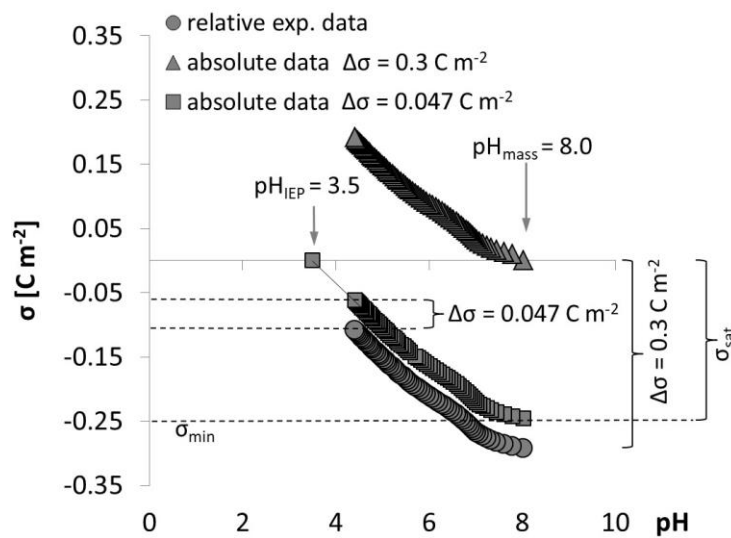


Fig. 5.11 Continuous potentiometric acid-base titration measurements of orthoclase

Circles – relative surface charge, squares – absolute data using $\Delta\sigma = 0.047 \text{ C m}^{-2}$, triangles – absolute data using $\Delta\sigma = 0.3 \text{ C m}^{-2}$. σ_{sat} – surface charge density [C m^{-2}] of fully deprotonated surfaces, σ_{min} – minimum value of absolute surface charge density.

5.1.3 Muscovite

The muscovite (supplier specification: mica WG) was obtained from Normag GmbH (Bad Homburg, Germany) as a fine powder. The mineral originated from China. Information regarding detailed provenience, mining, or potential preconditioning was not available. Mining conditions are covered by a trade secret. However, mineral analysis provided by Normag GmbH correspond well with HF digestion analysis of this study. Major constituents were Al₂O₃ (28.4 wt%), K₂O (9.4 wt%), Fe₂O₃ (4.9 wt%), and TiO₂ (0.65 wt%). Na₂O, CaO, and MgO were found to represent minor fractions, in sum below 3 wt%. In comparison to the ideal composition of muscovite (KAl₃Si₃O₁₀(OH)₂) the composition of the

muscovite mineral deduced from HF digestion analysis (digi. App. Tab. A. 2) showed reduced Al concentrations which were balanced with Fe and Mg concentrations. Deficits in K_2O were offset by Na_2O (1.0 wt%). Background concentration of Eu corresponded to 0.98 mg kg^{-1} which refers to the Eu concentration of the pristine, untreated mineral. Eu background concentration were considered insignificant regarding artefacts in batch and column experiments. Tab. A. 2 in the digital appendix presents an overview of the untreated muscovite components derived from HF digestion in comparison to the ideal structural formula and supplier data. In the following, the mineral is referred to by mica or muscovite.

Particle size fraction of the muscovite varied between $20 \mu\text{m} - 400 \mu\text{m}$. According to the cumulative distribution sum of particle sizes 50 % of the sieved mineral was smaller than $153 \mu\text{m}$ (d_{50}), 20 % exceeded the mean diameter of $225 \mu\text{m}$. Only 0.2 wt% mica grains ranged below $4.5 \mu\text{m}$. Using separation by sedimentation only $< 1 \text{ wt\%}$ clay fraction ($< 2 \mu\text{m}$) in the preliminary sieved powder mica was found. In this fraction about 10 wt% montmorillonite was detected.

For some experiments preconditioning of muscovite had to be performed (digi. App. Sec. A.8.1) that potentially altered crystal characteristics and surfaces. Alteration affects most efficiently the clay fraction, especially, the montmorillonite portion. Therefore, the clay fraction is most suitable to detect such changes via XRD. Comparative XRD analyses were performed. In the following, "preconditioning" refers to sample preparation with $0.05 \text{ g L}^{-1} \text{ NaClO}_4$, diethylenglycol preparation denotes sample treatment for XRD analyses. The effect of glycolation is briefly summarized in the digital appendix Section A.4.3.

Generally, preconditioning did not affect mineral lattice structure. The preconditioned muscovite exhibited no higher interlayer swelling potential and no lattice structure alteration; no differences in Bragg angles were observed. Occurrence of montmorillonite was suggested by a slight inconsistency at $6.2^\circ [2\theta]$. Only treatment with diethylenglycol triggered lattice structure spreading of the clay fraction of the pristine and preconditioned samples which were caused by small fractions of montmorillonite. Detailed information is provided by /BRI 18/.

Fig. 5.12 shows SEM images of preconditioned (right) and pristine (left) muscovite samples ($20 \mu\text{m} - 400 \mu\text{m}$). Typical muscovite characteristics such as the prominent and highly perfect $\{001\}$ cleavage, the flaky, thin mineral sheets, and 60° angles are shown in both samples. No differences due to preconditioning could be detected. Both samples

showed isolated Fe-oxide (FeOX) and Zr impurities. The insert of Fig. 5.12 highlights a typical FeOX impurity. Via EDX muscovite atomic weight ratio ([At%] ratio) of K:Al:Si 1:2:3 was corroborated; some Fe and Mg impurities were identified. Results back up conclusions drawn from muscovite HF digestion and XRD analyses.

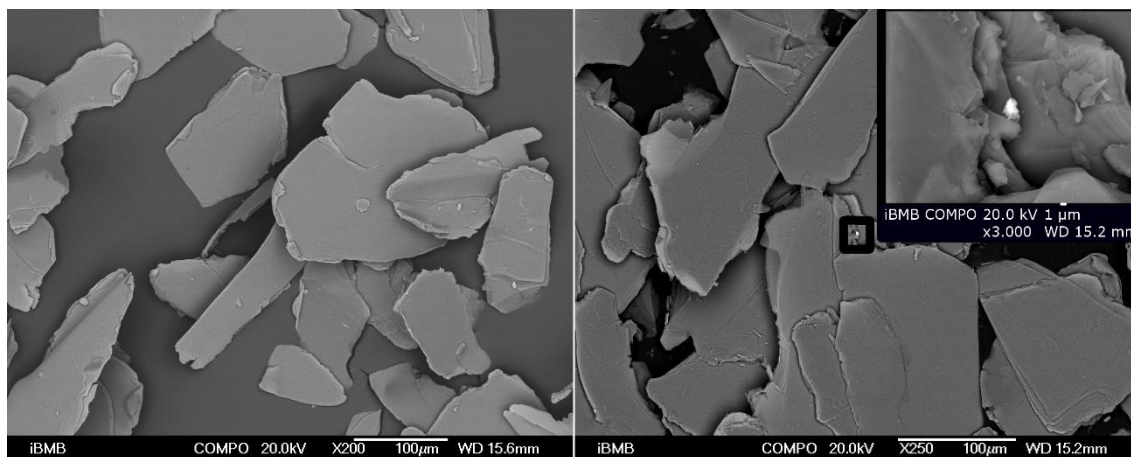


Fig. 5.12 SEM analysis of preconditioned (right) and pristine (left) muscovite, particle size fraction 20 – 400 μm

The insert illustrates FeOX of the preconditioned muscovite sample. FeOX and Zr impurities were occasionally found on pristine and preconditioned muscovite surfaces with no detectable preference of either sample. WD – working distance, x – magnification factor. COMPO – back-scattering measurement mode, sensitive to atomic number and sample density.

The SSA was determined via BET /BRU 38/ As discussed /BRI 18/ correct and reliable determination of the SSA is particularly challenging. Measurements after /BRU 38/ of pristine and preconditioned samples were conducted. Tab. 5.1 presents an overview of BET measuring conditions and SSA_{BET} . The SSA_{BET} values of the muscovite samples showed the influence of particle size and preconditioning procedures (Tab. 5.1): SSA_{BET} decreased with increasing particle size. Preconditioning of muscovite samples for column experiments (digi. App. Sec. A.8.1) did not show significant influences on the muscovite surface (Tab. 5.1), whereas samples taken from titration experiments indicated an increase of the SSA by factor two. Since linearity of the BET isotherm had always been fulfilled in the relative pressure range of 0.05 – 0.2 p/p_0 the presence of micropores could be excluded /ROU 07/.

The Tab. 5.1 summarizes SSA_{BET} data relevant for surface complexation and reactive transport modeling. Generally, the BET method yielded reproducible results. In repetitive measurements of identical samples, the relative standard deviation (*RSD*) ranged between 0.4 – 7.7 % agreeing well with error ranges reported by /EVE 74/. BET analysis of

different muscovite sample aliquots that experienced identical preconditioning procedures and identical measuring conditions revealed larger *RSDs* between 6.7 –11 %. Comparable error estimations have been reported in literature (e. g. /DAV 90/, /CAS 92/, /MAC 11/) Since the robustness of SSA_{BET} is highly dependent on sample preparation, measurement environment, and data evaluation utilization of SSA_{BET} in thermodynamic sorption models (TSMs) must be assessed with care.

Due to their structure phyllosilicates like muscovite are especially prone to exchange of interlayer cations against cations of the surrounding solution. The potential cation exchange capacity (CEC_{pot} [cmol(+) kg⁻¹]) was determined following DIN ISO 13536:1997-04 (1997) which describes the CEC_{pot} at pH 8.1 in a buffered BaCl₂-solution. However, it should be kept in mind that applying DIN ISO 13536:1997-04 (1997) to muscovite is subject to bias. The CEC determination may be blurred by excessive Ba incorporation during Ba treatment by exchange of Ba²⁺ vs. K⁺ (mineral: Öllacherite). The CEC_{pot} equaled 41.5 cmol(+) kg⁻¹ solid according to DIN ISO 13536:1997-04 (1997). This value was inconsistent with individually determined cations and, therefore, considered to be an artefact value. The cation Na⁺ contributed 0.1 cmol(+) kg⁻¹ solid, K⁺ 1.99 cmol(+) kg⁻¹, Ca²⁺ and Mg²⁺ yielded 1.8 cmol(+) kg⁻¹ and 1.4 cmol(+) kg⁻¹, respectively. In sum Na⁺, K⁺, Mg²⁺, and Ca²⁺ contributions to CEC_{pot} equaled 5.3 cmol(+) kg⁻¹ which was used as the CEC of muscovite (CEC_{WG}). As is shown in Tab. 5.2 CEC_{WG} lied well within the range of CEC values reported in literature.

Tab. 5.1 Summary of multipoint BET analyses of muscovite (mica), orthoclase (ortho), and quartz

Multipoint analysis (> 10 data points) after /BRU 38/ between 0.05 – 0.2 p/p₀ (relative pressure) was evaluated. No information of vacuum conditions can be supplied. Outgassing was achieved over 100 min at 373 K. Uncertainties are indicated by relative standard deviations (*RSDs*). [1] adsorber gas, [2] correlation coefficient (CC) of BET isotherm /BRU 38/, [3] measurement of identical sample, – no data available, *d*₅₀ mass-median diameter, *d*₈₀ 80 % quantile of cumulative particle size distribution. SSA relates to specific surface area, *SSA*_{BET} to the SSA after /BRU 38/, *PSF* to particle size fraction. Appl. indicates preconditioning procedure and/or subsequent application to column, batch, or mineral titration experiments. Pristine indicates samples without preconditioning treatment. Preconditioning procedures are described in digital appendix Section A.8.1. * indicates a single measurement without replicates: 5 point BET analysis, outgassing temperature 423.15 K over 2 h, 0.05 – 0.3 p/p₀ was evaluated, device: Quantachrome Autosorb Automated Gas Sorption System, Autosorb for Windows®, Version 1.19.

Sample	<i>PSF</i> [μm]	Appl.	<i>d</i> ₅₀ [μm]	<i>d</i> ₈₀ [μm]	BET measuring condition	Replicates	<i>SSA</i> _{BET} [m ² g ⁻¹]	Overall sample area [m ²]
mica	20 – 400	pristine	153	225	0.85 g solid ≠ < 0.01 g, N ₂ ^[1] , CC > 0.99 ^[2]	3	0.66 ≠ 0.01	0.56 ≠ < 0.01 ^[3]
	20 – 400	column	-	-	2.41 g solid ≠ 0.2 g, N ^[1] , CC > 0.99 ^[2]	5	0.68 ≠ 0.03	1.3 ≠ 0.1
	> 200	pristine	361	527	0.34 g solid ≠ < 0.01 g, N ₂ ^[1] , CC > 0.99 ^[2]	3	0.46 ≠ 0.05	0.16 ≠ < 0.01 ^[3]
ortho	30 – 400	pristine	171	242	3.10 g solid ≠ < 0.01 g, Kr ^[1] , CC > 0.99 ^[2]	3	0.19 ≠ 0.01	0.60 ≠ < 0.01 ^[3]
	30 – 400	column	-	-	1.84 g solid ≠ < 0.01 g, Kr ^[1] , CC > 0.99 ^[2]	3	0.15 ≠ 0.01	0.28 ≠ < 0.01 ^[3]
	< 120	pristine	-	-	-	7	0.99 ≠ 0.2	-
	< 63*	titration	-	-	1.14 g solid, N ₂ ^[1] , CC > 0.99 ^[2]	-	4.3	4.9
	> 200	pristine	377	552	2.83 g solid ≠ < 0.01 g, Kr ^[1] , CC > 0.99 ^[2]	3	0.05 ≠ 0.01	0.14 ≠ < 0.01 ^[3]
quartz	150 – 800	pristine	349	512	4.01 g solid ≠ < 0.01 g, Kr ^[1] , CC > 0.99 ^[2]	4	0.06 ≠ 0.01	0.26 ≠ < 0.01 ^[3]
	150 – 800	pristine	349	512	6.27 g solid ≠ 1.0 g, Kr ^[1] , CC > 0.99 ^[2]	12	0.08 ≠ 0.01	0.47 ≠ 0.09

Tab. 5.2 Cation exchange capacities ($CECs$ [$\text{cmol}(+) \text{kg}^{-1}$]) of muscovite and illite

^[1] CEC yielded from non-linear regression (detailed information provide /OSM 98/ and /OSM 99/). CEC_{WG} denotes the CEC of muscovite calculated from exchangeable cations Na^+ , K^+ , Ca^{2+} , and Mg^{2+} (cf. Sec. 5.1.1) phlogopite structural formula $\text{NaMg}_3\text{Si}_3\text{AlO}_{10}(\text{OH})_2$.

Mineral	CEC [$\text{cmol}(+) \text{kg}^{-1}$]	Reference
Illite/mica	20-50	/KUN 88/
Illite	10-40	/BER 06/
Illite	20-50	/APP 05/
Na-illite	14.6	/SHA 87/
Na-illite	12.7	/POI 99b/
Ca-illite	17.7	/SHA 87/
Phlogopite (Mg-mica)	5 – 10	/CHO 09/
K-muscovite ^[1]	10	/OSM 98/
Li-muscovite ^[1]	45	/OSM 99/
Muscovite	≤ 5	/BER 06/
Muscovite	4.01	/PAN 17/
Muscovite (CEC_{WG})	5.3	this study

5.1.3.1 Comparison of batch and flow-through leaching experiments of muscovite

To investigate the leaching of muscovite batch and flow-through experiments were performed to see the difference of the dissolution behavior under static (batch) and in presence of fresh solution under dynamic conditions (flow-through). Both processes can be observed in nature. The experimental set-up and the leached elements with their corresponding concentrations are given in the digital appendix Section A.4.2.

Fig. 5.13 shows the dissolution of the main elements from muscovite as well as uranium over time in batch and flow-through experiment. These results indicated that even after three months the dissolution has not reached yet a steady state.

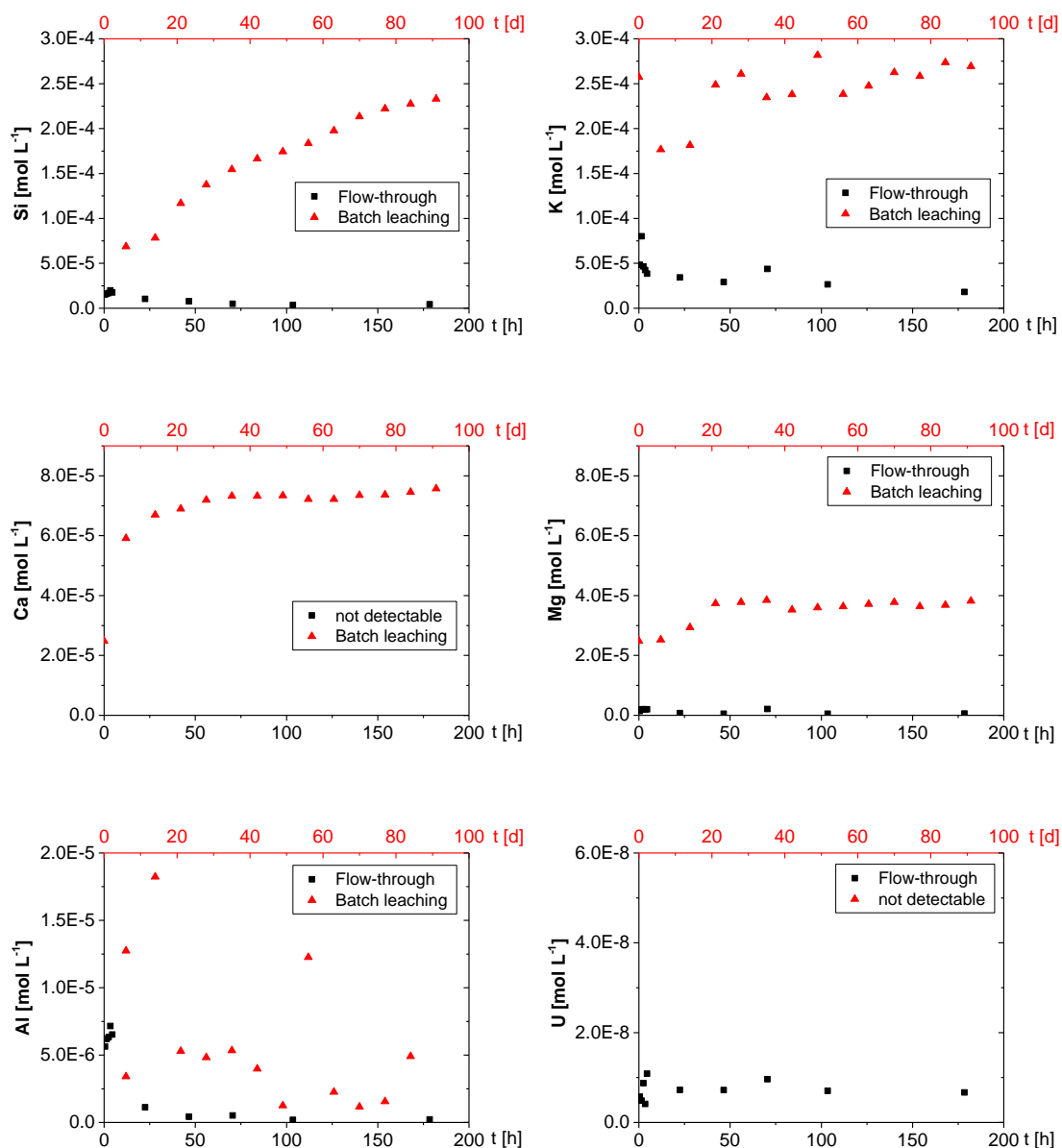


Fig. 5.13 Dissolution of main elements and uranium from muscovite obtained in batch leaching experiments (shown as red triangles) and in flow-through leaching experiments (shown as black squares)

The results indicated that the main elements Al, K, and Si were dissolved from the mineral as major constituents of the crystal structure of muscovite (ideal structural formula: $\text{KAl}_3\text{Si}_3\text{O}_{10}(\text{OH})_2$). Beside them Ca and Mg were found to represent minor fractions. Furthermore, the concentrations of the elements that were used for the sorption experiments at HZDR and GRS, e. g. U, Ni, and representative lanthanides (Eu, Gd, Nd, and Dy), were insignificant and have no effect onto the sorption processes during the experiments. These results correspond well with HF digestion analysis (digi. App. Tab. A. 2).

For muscovite, the molar ratio of K:Al:Si obtained after the batch dissolution experiment (cf. Sec. 5.1.2) was 269:4.91:233, which equals 1:0.02:0.87. Moreover, the pH increased by 1.8 pH unit during the equilibration time. An indication that the solution had reached equilibrium in contact with amorphous quartz and gibbsite phases was given by geochemical speciation calculations based on the leachate analyses. Thus, the following dissolution reaction for muscovite best describes this:



5.1.3.2 Release of Ni from orthoclase, muscovite and quartz equilibrated with 0.01 mol L⁻¹ NaClO₄

Information about released Ni concentrations was of great importance

- to define the initial Ni concentrations for batch sorption experiments (Sec. 7.9) and
- for the calculation of % sorbed fraction values from batch sorption raw data (ICP-MS measurements [$\mu\text{g L}^{-1}$]).

The samples were the same as in batch Ni sorption experiments (Sec. 7.9). The release of Ni was determined in equilibrated suspensions after pH adjustment was achieved and before Ni was added. Samples were taken after 48 d. Results show pH and M/V dependencies (Fig. 5.14): the lower the pH and the higher the M/V, the higher the released Ni concentration from all minerals. Above pH 6 concentrations of all samples were lower than the limit of quantification (LOQ = $4.6 \cdot 10^{-9}$ mol L⁻¹ Ni). At pH 5 leached Ni concentrations mainly ranged between 10^{-8} to $4.6 \cdot 10^{-8}$ mol L⁻¹ Ni for all minerals, hence, $5 \cdot 10^{-7}$ mol L⁻¹ was selected as the lowest initial Ni concentration for batch sorption experiments (Sec. 7.1).

mol L⁻¹ Ca was chosen as the lowest initial concentration for the batch sorption experiments (Sec. 7.7).

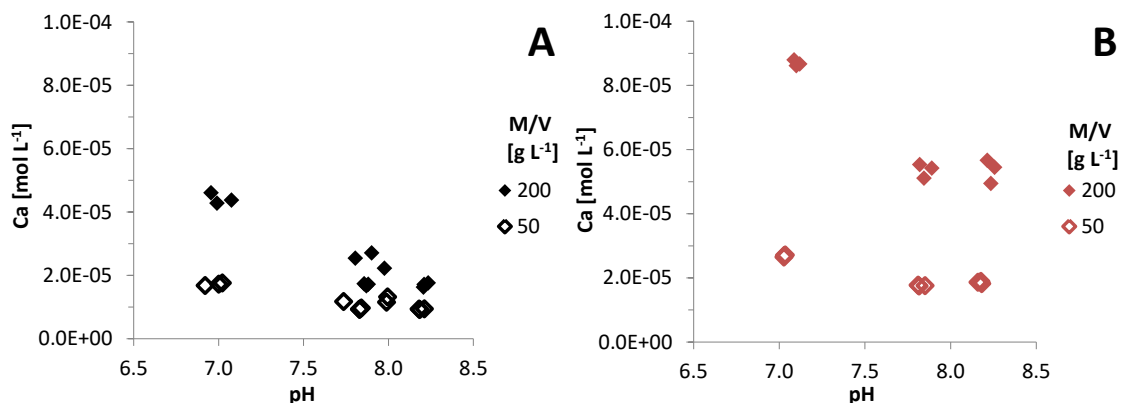


Fig. 5.15 Ca released from orthoclase (A) and muscovite (B), equilibrated with 0.01 mol L⁻¹ NaClO₄

Batch sample solutions were analyzed after the systems were in equilibrium, after adjustment of constant pH.

5.1.3.4 Muscovite surface charge properties

The determination and characterization of surface charge properties is based on /BRI 18/. Methods are outlined in detail in the digital appendix Section A.4.5, relevant theoretical background is given in Section A.4.6 (digital appendix).

In Fig. 5.16 results of discontinuous mass (A) and electrolyte (B) titration of muscovite are illustrated. Similar to orthoclase mass titration (Fig. 5.10) no instantaneous pH_{mass} was obtained (Fig. 5.16 A). After 7 d measurements returned pH_{mass} ≈ 7.9 which was independent of pH_{ini} (Fig. 5.16 A). However, this pH might had been influenced by mineral dissolution or secondary phase precipitation that occurred during the equilibration time of 7 d. As expected, zeta-potential measurements resulted in a low IEP (pH_{IEP} = 2.4) for the muscovite (digi. App. Sec. A.4.5). An increase of pH_{mass} in relation to pH_{IEP} implied that basic impurities were situated at the muscovite surface. Zeta-potential exhibited permanent negative surface charge above pH_{IEP} which was attributed to isomorphous substitution which is typical for mica minerals. Comparing orthoclase and muscovite zeta-potential measurements showed expected results: Due to isomorphous substitution the electrokinetic potential of muscovite was smaller compared to orthoclase (data provided in /BRI 18/).

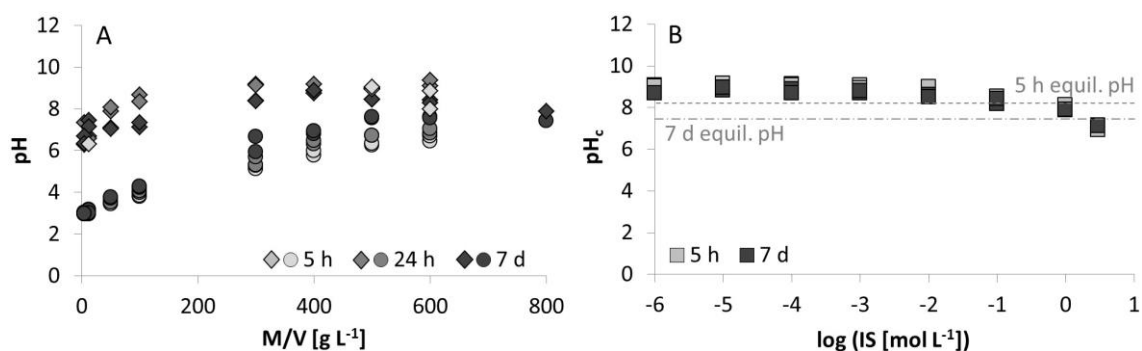


Fig. 5.16 Experimental mass (A) and electrolyte (B) titration results of muscovite after 5 h, 24 h, and 7 d

(A) Discontinuous mass titration: Circles – $\text{pH}_{\text{ini}} = 2.9$, diamonds – $\text{pH}_{\text{ini}} = 4.7$. (B) Discontinuous electrolyte titration: $M/V = 400 \text{ g L}^{-1}$, dashed line – reference after 5 h (without addition of NaClO_4), dotted-dashed line – reference after 7 d, $\text{pH}_c - \text{pH}$ corrected for electrolyte influences after /HAG 14/ (digi. App. Sec. A.4.8) IS – ionic strength [$\log(IS \text{ mol L}^{-1})$].

Fig. 5.16 B depicts electrolyte titration results of muscovite. The equilibrium pH of reference samples after 5 h and 7 d are displayed. For reference samples a $M/V = 400 \text{ g L}^{-1}$, $10^{-5} \text{ mol L}^{-1} \text{ NaClO}_4$ were prepared; experimental conditions were equal to mass titration samples. The pH difference of reference samples measured after 5 h and 7 d amounts to 0.8 pH units. This pH difference might be related to cation exchange processes of the mica mineral: H^+ bound in mica mineral interlayers can exchange with K^+ or Na^+ in the suspension /PAS 81/. Furthermore, decreasing pH values as a function of IS were observed: At $IS > 10 \text{ mM NaClO}_4$ electrolyte concentration asymmetric counterion associations affected the pH of electrolyte titration samples; no difference between 5 h and 7 d equilibration time was observed.

As a first conclusion, muscovite mass and electrolyte titration experiments indicated basic impurities at the surface and asymmetric counterion association affinities which became relevant at $IS > 10 \text{ mM NaClO}_4$. Since $\text{pH}_{\text{mass}} \neq \text{pH}_{\text{IEP}}$ potentiometric titration yielded relative data (Fig. 5.16). As for orthoclase data processing, mica titration measurements could be related to two different reference pH values (pH_{IEP} , pH_{mass}) to transform relative data to absolute values:

- Relative data was scaled to $\text{pH}_{\text{IEP}} = 2.4$ with $\Delta\sigma = 5 \text{ mC m}^{-2}$, and
- potentiometric titration data (raw data) was shifted to fit pH_{mass} with $\Delta\sigma = 51 \text{ mC m}^{-2}$ which would be interpreted to represent the surface charge of edge sites (Al-OH and Si-OH functional groups).

More detailed information is provided in the digital appendix (digi. App. Sec. A.4.7) and in /BRI 18/.

A comparison between potentiometric titration measurements of /ZOR 00/, /BAE 97/, /AVE 98/, and this study is provided in /BRI 18/. Generally, considerable scatter of titration measurements can be observed. Especially at high and low pH values extreme surface charge density values (σ) were observed where mineral dissolution, surface precipitation, as well as cation exchange reactions interfere.

6 Thermodynamic databases

In general, the data can be divided into three groups: (i) thermodynamic data for the aqueous element species, (ii) thermodynamic data for solid mineral phases, and (iii) thermodynamic sorption data for the representative sorbates (pair of element and mineral). Dependent on the salinity of the different groundwater types of the Gorleben overburden (Sec. 4.1) two databases are required:

- I. The WEIMAR_EDH.dat database for groundwater solutions with ionic strength lower than 0.5 mol L^{-1} as in the case of the UAF and AT. It utilizes the Davies approach /DAV 62/ to represent ion-ion interactions.
- II. The WEIMAR_PIT.dat database for high saline solutions as in the case of both LAF units using the Pitzer formalism. Here, we could take advantage of the current activities within the THEREDA project (www.thereda.de) /MOO 15/, where already up-to-date data releases for selected radionuclides are available.

In the following sections we will give a detailed description of the compilation of the relevant data for aqueous species, mineral solubilities and surface species.

6.1 Speciation in low mineralized water

WEIMAR_EDH.dat: The basis for the Extended Debye–Hückel (EDH) based database is the PSI/Nagra Chemical Thermodynamic Database (TDB) 12/07 formatted for PHREEQC /THO 14/ which contains the most important thermodynamic data for aqueous species for repository-relevant elements compiled in the OECD/NEA Thermochemical Databases (NEA TDB). Data which are not included or which have to be updated were either intensively reviewed in the framework of several projects (e. g. SEM² project for Eu³⁺) and explained in the following sections or were taken from international databases or original literature (e. g. for Nd³⁺ from LLNL database). All added thermodynamic data are clearly commented in the WEIMAR_EDH.dat (digital appendix: WEIMAR_EDH_20171130_GRS-500.dat).

6.1.1 Database for europium

The element europium is relevant for the geochemical modeling due to its use as chemical analogue for several trivalent actinides. Moreover, the isotope Eu-155 with a lifetime of 4.76 years is part of the nuclear waste inventory being a fission product – although to

a small amount only. Finally, all thermodynamic data generated for Eu will also have a large impact on rare earth element mining, processing and recycling – a technology field with increasing importance. Several reviews and systematic studies focusing on the aqueous chemistry are available /CUR 00/, /RAR 87/, /LUO 07/, /MIL 92/, /SPA 95/ and /WOO 90/. Complexation constants were determined using different techniques, e. g. solvent extraction, potentiometry, ion exchange, and spectroscopies (fluorescence, UV-vis). However, the different experimental conditions (ionic strength, temperature, lanthanide concentration, pH range, etc.), methods, and techniques applied hamper both consistency and accuracy of the derived Eu aqueous complexation constants. However, the WEIMAR project could take advantage of efforts from a parallel BMBF-funded project, SEM². There, a quality-assured thermodynamic database for Eu was developed. An extensive data survey of more than 290 publications provided a large pool of data records for aqueous Eu complexes listed in Tab. 6.1. Many published Eu data sets had to be discarded due to the inadequate description of experimental conditions, use of pH buffers that acted as additional ligands, missing details for extrapolation to infinite dilution or postulation of fictitious species. Some papers presented no original data but rather analogue values from other REE or compilations from secondary references.

Tab. 6.1 Summary of the aqueous inorganic Eu complexation data records

System	Total number of considered data sets	Selected data set for Eu database
Eu-hydroxide	101	53
Eu-fluoride	124	51
Eu-chloride	201	67
Eu-nitrate	154	91

The remaining selected experimental data were processed adapting the OECD-NEA method to determine the $\log K$ value for standard conditions /LEM 13/: First, consistency checks had to select those data records that could be grouped based on identical species sets. Then the $\log K$ values for the species formation reaction were plotted as a function of IS using equation (Eq. 6.1) to obtain $\log K^\circ$ values and SIT interaction parameter ε .

$$\log K^\circ = \log K - \Delta z_i^2 D + \Delta \varepsilon m_x - n \log a_{H_2O} \quad \text{Eq. 6.1}$$

Here, z_i is the charge of species i , m_x is the ionic strength express in molality units, D is the Debye-Hückel term, $\Delta \varepsilon$ is the difference of all ion-ion-interaction coefficients, n the stoichiometric coefficient of water in the formation reaction (may be zero) and a_{H_2O} is the

water activity. As an example, the $\log K^\circ$ fit for the formation reaction of the 1:1 fluoro complex is given in Fig. 6.1.

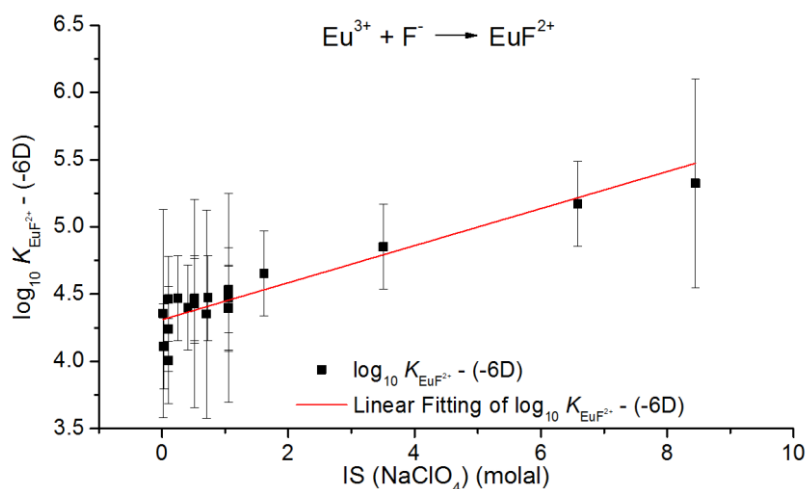


Fig. 6.1 Linear fitting of the $\log K$ values for the formation reaction of the EuF^{2+} complex as a function of ionic strength

So far, the data selection and processing methodology as described above resulted in a comprehensive and reliable thermodynamic database for Eu aqueous hydroxide, fluoride, chloride, nitrate, carbonates and sulfates.

For Eu(III) solid phases solubility limits were adapted to measurements carried out with amorphous lanthanide/actinide hydroxides and -carbonates. In the absence of original experimental data, solubility measurements from amorphous Am(III), Cm(III), and Nd(III) solids as analogues were considered. Adaptations were necessary to prevent an underestimation of potential precipitation reactions during column and batch experiments: For $Eu(OH)_3(am)$ and $Eu(CO_3)(OH)(am)$ mean values of Eu(III), Am(III), Cm(III) solubility constants from /SPA 95/, /LEM 13/, and /RAR 87/ were included; the solubility constant of $Eu_2(CO_3)_3 \cdot 3H_2O(am)$ was taken from /RAR 87/. The following adaptations were used in the database (errors indicate the single standard deviation of considered literature data):

- $Eu(OH)_3 + 3H^+ = Eu^{3+} + 3H_2O$ $\log K = 17.56 \pm 2.6$
- $Eu_2(CO_3)_3 \cdot 3H_2O + 3H^+ = 2Eu^{3+} + 3HCO_3^- + 3H_2O$ $\log K = -5.94$
- $Eu(CO_3)(OH) + 2H^+ = Eu^{3+} + HCO_3^- + H_2O$ $\log K = 3.14 \pm 0.9$

6.1.2 Database for manganese

As explained earlier (Sec. 3.2), manganese turned out to be the only cation present in sufficient amounts to be able to affect radionuclide speciation besides the already considered element Fe and Ca. Thus, efforts were started to provide an appropriate database for this element. Ligands considered are oxide/hydroxide, carbonate, chloride, sulfate, phosphate and silicate. The species selection followed the one realized in the PSI/Nagra TDB 12/07 (i. e. implicitly following the Extended Debye-Hückel model from Davies), also using their recommendations for thermodynamic data. Due to the expected anoxic conditions, only species containing Mn^{2+} were considered, however including also those with mixed Mn valency. This set of species and parameters (containing 10 mineral phases and 8 aqueous complexes with relevance to this project) was extended towards some other Mn minerals regularly found in natural environments: Rancieit ($Ca, Mn^{II})(Mn^{IV}_{3.5}O_8) \cdot 3H_2O$) and Feitknechtit (β - $MnOOH$). Respective data were taken from the LLNL database (llnl.dat 85 2005-02-02) and ANDRA Database (Thermo-Chimie_PHREEQC_eDH_v9b0.dat). With respect to the aqueous speciation, recently published /BRO 16/ stability constants for three aqueous $Mn^{II}(OH)_x^{2-x}$ complexes (2:x:4) were also added. The same source provided solubility constants for Manganosite (MnO) and Bixbyite (Mn_2O_3).

6.2 Speciation in highly mineralized water

To provide a proper description of contaminant transport also for higher saline solutions (as found in the lower aquifer adjacent to the salt dome), the chemical model has to account for ion-ion interactions. Activity and concentration (here consistently expressed on the molality scale, i. e. $mol\ kg^{-1}$ water or m in short) of any dissolved species differ from each other as soon as the ionic strength I_m in solution exceeds a very low threshold. Thus activity coefficients must be introduced. For very dilute systems ($I_m < 10^{-3} m$), Debye and Hückel developed a theory /DEB 23/. Later many (mostly empirical) extensions were proposed, with the Davies equation /DAV 38/, /DAV 62/ being the most popular one. But still an upper application limit of 0.5 m hampers its use for truly saline solutions. Here, more elaborate models come into play, the most prominent ones being the Pitzer (PIT) virial coefficient method /PIT 91/ and the Brønstedt–Guggenheim–Scatchard approach /BRØ 22/, /GUG 35/, /SCA 36/. The latter has been further developed into the so-called specific ion interaction theory (SIT). For details see discussion and further references in e. g. /GRE 13/.

The SIT approach was adopted for the use in the OECD/NEA Thermochemical Data Base (NEA TDB). The reason for choosing the SIT was the linear formulation of the model and the possibility to estimate ion interaction coefficients from various correlation laws. Moreover, because of its simplicity in comparison to e. g. the Pitzer virial method it promises a large potential for many real-world applications. The main purpose of the SIT within the NEA TDB is the extrapolation of equilibrium and formation constants to zero ionic strength. The SIT coefficients published by the NEA (regularly updated with every new volume issued) are mainly based on works by /CIA 80/. However, the use of the SIT model had been hindered by a lack of implementation in commonly used geochemical speciation codes so far. Only recently, it was introduced into the PHREEQC program /PAR 13/, accompanied by an appropriate database being an extension of the NEA compilation. Nevertheless, this database is still limited in scope – and also in quality due to excessive use of extrapolations and analogies, sometimes in a multi-step way. Thus, it is strongly advised to critical evaluate SIT coefficients before any serious application.

WEIMAR_PIT.dat. Considering the said above, it seemed to be more realistic to create a reliable – though limited in scope – Pitzer-based database than a SIT-based one. Namely, the WEIMAR project could take advantage of the current activities within the THEREDA project (www.thereda.de) /MOO 15/, that provides quality assured Pitzer-based solubility data for the matrix elements (the hexary system of oceanic salts including carbonates and phosphates), the concrete materials (cement phases with Al and Si) as well as radionuclides and fission products (Am(III), Nd(III), U(IV/VI), Np(V), Th(IV), Tc(IV & VII), Sr(II) and Cs(I)). The provided data for the hexary salt system and the cement phases is valid in the temperature range from 0 to 100 °C, whereas radionuclide and fission product data is valid for 25 °C only. These data sets are state-of-the-art for the concerned elements and have been subject of intensive testing by the THEREDA team.

Selenium data were transferred from the aforementioned VESPA project /BIS 16/ as well as from /HAG 12/. The two selenium data sets are not fully consistent in terms of Ca-phases and HSeO_3^- species; and neither they are with the recent OECD/NEA-TDB data collection /OLI 05/. However, they are the best that can be obtained currently. Hence, for the considered oxidation state the selenate data of the data set /BIS 16/ are sufficient to describe the selenate solubility.

For the redox relevant element Mn, there is no consistent and complete Pitzer data set available yet in literature. For the Mn(+II) subsystem at 25 °C, a Pitzer data set was

obtained by /PIT 74/. Before including such data, that describe a reduced subsystem only, consistency tests have to be performed.

For Eu there is no Pitzer data set for the description of both the Eu aqueous speciation and the mineral solubility in saline solutions available.

6.3 Mineral solubilities

Solubility constants for mineral phases which are relevant for the site-specific sediments or which can precipitate in the model system in the context of a nuclear waste repository were extensively reviewed. Data which are not included in the TDB were implemented as described in /NOS 12b/ and/or were updated and clearly commented as described in the following. As for the aqueous systems, the different levels of salinity encountered in the application case “Gorleben Cap Rock” calls for two separate TDB versions.

The most important thermodynamic data for solid phases which are relevant in the context of a nuclear waste repository are compiled in the OECD/NEA Thermochemical Database (NEA Update TDB) which is mostly included in the PSI/Nagra TDB 12/07 (as basis for the WEIMAR.dat database). An extensive review has been done for solid uranium phases take advantage of the current activities within the THEREDA project (www.thereda.de) /MOO 15/, where already up-to-date data releases for solid U(IV/VI) phases were available. Ligands considered were oxide/hydroxide, silicate, carbonate, sulfate and phosphate. However, data without relevance for our model system were not considered, e. g. high pressure-temperature phases like $\text{Na}_2\text{UO}_4(\text{cr})$, $\text{CaUO}_4(\text{cr})$, $\text{K}_2\text{UO}_4(\text{cr})$, $\text{MgUO}_4(\text{cr})$ or data for complexes with fluoride, bromide, etc. Uranium phases which are not included in the PSI/Nagra TDB 12/07 were implemented manually and clearly commented in the database.

To clarify the solubility behavior of orthoclase and muscovite an extensive literature study has been done as discussed in detail in /RIC 15/, and also published in /RIC 16/. In case of orthoclase, however, no original experimental solubility constants were accessible. Thus, microcline, the triclinic form of K-feldspar, was used as an analogue. It is chemically very similar to orthoclase (the monoclinic version of K-feldspar), and thus its values can be used as approximation for orthoclase /HOC 96/. Namely, the solubility of orthoclase with $\log K_{\text{sp}} -0.12$ was taken from /STE 00/. Log K_{sp} calculations based on Gibbs free energies of formation confirm that the value is in the expected dimension. For muscovite, only calculations based on formation data are possible. Averaging the respective

solubility constants yields a $\log K_{sp} = 14.15 \pm 0.74$ (the error representing 2σ). In Tab. 6.2 the resulting $\log K_{sp}$ values for orthoclase and muscovite are summarized.

Tab. 6.2 Solubility constants for orthoclase and muscovite

Mineral	Formula	IAP	Log K_{sp}
Orthoclase	$KAlSi_3O_8$	$\{K^+\}\{Al^{3+}\}\{H_4SiO_4^0\}^3\{H^+\}^{-4}$	-0.12
Muscovite	$KAl_3Si_3O_{10}(OH)_2$	$\{K^+\}\{Al^{3+}\}^3\{H^4SiO_4^0\}^3\{H^+\}^{-10}$	14.15

6.4 Surface species

Required thermodynamic data for surface species for relevant element-mineral-pairs were taken from the thermodynamic sorption data base RES³T /BRE 03/, which is available under www.hzdr.de/res3t. Evaluation criteria and the selection process is well-described in /NOS 12b/. For some of the elements thermodynamic sorption data from chemical analogues (e. g. for trivalent actinides the REE) were used to fill critical data gaps. Additionally, appropriate batch- and column experiments (Sec. 7 and Sec. 9) were performed to derive SCPs as described in Section 10.

The following Tab. 6.3 gives an overview of available SCM data in RES³T relevant for the project. Thereby the different colored sections identify the number of available SCM data in RES³T. The batch experiments performed at GRS and HZDR are marked with asterisk.

Tab. 6.3 Number of available SCM data in RES³T (Query date: 02/2018)

Elements / Minerals		Quartz	Feldspar	Mica	Fe(III)-minerals	Al-minerals	Kaolinite	3-layer-clay minerals
RN (& analogues)	Cs ⁺ , (Rb ⁺ , K ⁺)	24	1 **	**	33	7	2	5
	Ra ²⁺ , (Sr ²⁺ , Ba ²⁺)	10	**	**	57		7	9
	Ni ²⁺	9 **	**	**	20	1	5	32
	Am ³⁺ , Cm ³⁺ , (REE)	25 **	**	**	110		9	37
	Th ⁴⁺ (Pu ⁴⁺ , Np ⁴⁺ , U ⁴⁺)	14			68	14	4	42
	NpO ₂ ⁺	3	*	6 *	25	11	2	11
	UO ₂ ²⁺	94	5 *	10 *	343	11	18	84
	SeO ₄ ²⁻	n.r.	n.r.	n.r.	20	1		
Matrix components	Ca ²⁺	15	*	*	40	1	4	16
	Mg ²⁺	19			15			
	Al ³⁺	10 **	**	**	3		2	9
	Fe ³⁺	2			3			
	CO ₃ ²⁻	18	1 ^g	1 ^g	201 ^g		1	25
	Si(OH) ₄	2			22	3		9
	SO ₄ ²⁻	1			41	7	2	

Classification: no SCM data 1 - 9 SCM data > 10 SCM data

Batch experiments: * HZDR ** GRS

() Chemical analogues

n.r.: not relevant for sorption

All reaction constants were converted to infinite dilution ($IS=0 \text{ mol L}^{-1}$) using the Davies equation /DAV 62/. Because the reported reaction constants are related to different site densities, it was necessary to convert the values to a reference state to enable comparison and averaging. Here, the procedure according to /KUL 02/ was followed, based on a reference surface site density of $2.31 \text{ sites nm}^{-2}$. This value of course was then also used for all subsequent predictive modeling. The protolysis constants (pK-values), stability constants (log K -values) and reaction equations for surface and exchange reactions are given in the databases.

7 Batch sorption experiments

To investigate the sorption of repository-relevant radionuclides onto quartz, orthoclase, and muscovite, batch sorption experiments as well as TRLFS and ATR FT-IR measurements (Sec. 8), and column experiments (Sec. 9) were performed. With the resulting experimental data, SCP such as stability constants for relevant surface complexes were derived (Sec. 10), which are necessary for geochemical modeling (Sec. 12). Section 5 provides the mineral characterization of quartz, orthoclase and muscovite including information about the supplier, pretreatment, sieving, leachate analyses, characterization of physical properties such as grain size distribution, point-of-zero-charge or specific surface area.

All batch experiments were carried out with the same pristine quartz, orthoclase, and muscovite samples (Sec. 5). For Eu batch experiments Norflot Kali MF 6.400 was used which was identical to Norflot Kali 600 but previously grinded by the supplier to a particle size $< 120 \mu\text{m}$. Hence, both orthoclase samples had identical geochemical compositions and only differed in their particle size distribution. A summary of tools, equipment, techniques, and involved institutions are provided in the digital appendix Section A.5.1.

7.1 Experimental set-up of Eu, Ni, Cs, Ca and Al batch experiments

Europium batch experiments with orthoclase and muscovite were performed previous to this research project. Detailed information of the experimental set-up provide /NOS 12a/ and /BRI 11/. Quartz batch experiments were carried out during the course of the WEIMAR project /FRI 14/; the experimental set-up followed /NOS 12a/ and /BRI 11/ to ensure comparability.

Pristine muscovite and orthoclase samples were sieved for sorption experiments: 20 – 400 μm were separated for muscovite, 30 – 400 μm for orthoclase; the particle size of quartz was 150 – 800 μm (Tab. 5.1). Quartz was not sieved and used as provided by the supplier. For orthoclase Eu batch experiments the particle size equaled $\leq 120 \mu\text{m}$. For Eu sorption experiments none of the solids underwent preconditioning procedures, otherwise preconditioned orthoclase and muscovite was used as described in Section A.8.1 in the digital appendix.

Batch experiments were prepared under laboratory conditions and ambient atmosphere. Low density polypropylene (LDPE) wide mouth bottles were used. The experimental set-up is described in Tab. 7.1. The NaClO₄ solution was considered an inert background electrolyte which does not interfere with solution or surface complexation speciation reactions. NaSO₄ was used in Ni batch experiments as a ligand. The initial pH values (pH_{ini}) ranged between 3.5 – 9 which were adjusted over several weeks via the addition of NaOH, HCl, and HClO₄ (1 – 100 mmol L⁻¹). The pH was measured in the supernatant of suspensions. Samples were shaken head first overnight. As pH_{ini} remained constant the respective element was added to the suspensions. The initial concentrations ranged between 10⁻³ and 10⁻⁸ mol L⁻¹. Experiments were prepared in triplets or in duplicate. Following /BRA 05a/ and /ADE 94/ an equilibration time of 24 h was allowed for Eu batch experiments. For batch experiments with Ni, Ca, and Cs element and mineral-specific equilibration times were determined (Sec. 5.1.3.2, 5.1.3.3, digi. App. Sec. A.5.7 and /STE 17/): 3, 7 and 14 d were necessary for Ni with quartz, orthoclase and muscovite, respectively. In terms of Ca with orthoclase and muscovite 7 d were needed. For Cs with orthoclase and muscovite 3 d were sufficient, for Al batch experiments 7 d were used. After equilibration was reached samples were centrifuged and filtered with 0.02 µm or 0.2 µm filters. To prevent sorption processes on container walls centrifuged and filtered samples were immediately acidified. ICP-MS analyses yielded element concentrations of the supernatant solutions.

Tab. 7.1 Geochemical boundary conditions of batch sorption experiments with Eu, Ni, Cs, Ca, Al and quartz, orthoclase, muscovite

	Eu	Ni	Cs	Ca	Al
Quartz [g L⁻¹]	50, 12.5	200, 50	-	-	200 (MERCK quartz)
Orthoclase [g L⁻¹]		100, 25	50, 12.5	200, 50	-
Muscovite [g L⁻¹]		50, 12.5	50, 12.5	200, 50	-
pH	3.5-9	5-8	4-9	5-8	3-9
C₀ [mol L⁻¹]	10 ⁻⁸ -10 ⁻⁵	5·10 ⁻⁷ -10 ⁻⁵	10 ⁻⁸ -10 ⁻⁵	2·10 ⁻⁴ - 1.6·10 ⁻³	2·10 ⁻⁵ -10 ⁻⁴

7.2 Experimental set-up of U(VI), Np(V), and Nd(III) batch experiments

Batch experiments of U(VI), Np(V), and Nd(III) sorption onto orthoclase and muscovite were performed with varying pH and different experimental boundary conditions under

ambient atmosphere and room temperature. The aqueous speciation of these three elements is given in the digital appendix Section A.6.1. All batch experiments have been carried out as triplicates in $0.01 \text{ mol L}^{-1} \text{ NaClO}_4$ (for considering ionic strength effects 1 mol L^{-1}) in the pH range from 5 to 8 for uranium, 5 to 12 for neptunium, and 4 to 9 for neodymium.

The pH conditioning of the mineral suspensions was a process that can potentially last up to three months. Suitable solid-to-liquid ratios (M/V) of $1/20$ and $1/80 \text{ g mL}^{-1}$ and sorption time (one week) were chosen from preliminary experiments as described in detail in /RIC 15/. After achieving stable pH values ($\text{pH} \pm 0.1$) for the M/Vs during a conditioning stage, the elements U(VI), Np(V), or Nd(III) were added to get a final concentration in solution of $10^{-5} \text{ mol L}^{-1}$ and $10^{-6} \text{ mol L}^{-1}$. However, for Np(V) only one concentration of $10^{-6} \text{ mol L}^{-1}$ was used. After a sorption time of one week, the suspension was centrifuged (1 h at $6800\times g$ – Avanti J-20XP, Beckman Coulter), and the supernatant analyzed with ICP-MS for U(VI) and Nd(III) or LSC for Np(V). To be sure that no precipitation in Nd(III) solution takes place, the scattered light intensity was used to see precipitations (digi. App. Sec. A.6.2). After all sorption experiments the centrifuge tubes were leached with $1 \text{ mol L}^{-1} \text{ HNO}_3$ to remobilize the metal that originally was sorbed onto the wall.

To investigate the influence of microorganisms present in the investigated minerals (orthoclase, muscovite, quartz), batch experiments were performed with various growth-inhibiting conditions (sterile/non-sterile, with/without light, work in a laminar flow box, and sodium azide as inhibitor). The experiments were performed analog to the sorption experiments. The samples had a M/V of $1/20 \text{ g mL}^{-1}$ in $0.01 \text{ mol L}^{-1} \text{ NaClO}_4$, the pH was 7 and $10^{-6} \text{ mol L}^{-1}$ was the final U(VI) concentration in the solutions. The samples were centrifuged at $2800\times g$ (Megafuge 1.0, Heraeus) for one hour and analyzed by ICP-MS. A detailed description of these microbiological experiments is provided in Section A.7 in the digital appendix.

To investigate the influence of the ionic strength on the sorption of U(VI), Np(V) and Nd(III), batch experiments in $1 \text{ mol L}^{-1} \text{ NaClO}_4$ were performed (for Nd(III) only for M/V $1/20 \text{ g mL}^{-1}$ and $10^{-5} \text{ mol L}^{-1}$).

Furthermore, the influence of calcium (Ca^{2+}) as competing cation on the sorption of U(VI) was investigated. Batch samples from pH 5 to 8 at an M/V of $1/20 \text{ g mL}^{-1}$ were prepared. After stabilization of the pH, $1.5 \cdot 10^{-3} \text{ mol L}^{-1} \text{ Ca}$ was added and sorbed for one week. Subsequently, $10^{-6} \text{ mol L}^{-1} \text{ U(VI)}$ was added and sorbed for an additional week, then the

samples were centrifuged and the supernatant was analyzed by ICP-MS for U(VI) and by AAS for Ca. Auxiliary experiments with only Ca were performed to determine the amount of Ca that can sorb on the minerals.

7.3 Microbial effects on sorption processes

The investigation of the influence of microorganisms indicated that natural microorganisms were present in the minerals orthoclase, muscovite, and quartz. The results showed that each mineral contained different kinds of microorganisms representing the different origin of the minerals. A detailed description is given in the digital appendix Section A.7 and a detailed look on the species of microbes can be found in /RIC 15/. However, there are no microbes contained in the minerals that originate from human skin (e. g. hand surfaces) but some soil microbes are present. Thus, the microbes are not in the samples because of the work in the lab, they are rather bound to the pristine minerals from the area where they were mined and processed. During this study it was shown that no verifiable effect on the sorption behavior onto orthoclase, muscovite, and quartz occurs. The observed sorption is mainly attributed to the surface of the mineral, and not to the microorganisms themselves. Thus, the results of batch experiments were used to predict sorption processes at mineral surfaces.

7.4 Uranium(VI) batch sorption results

Uranium batch experiments were performed with orthoclase and muscovite based on the experimental set-up described in Sec. 7.2. Detailed information can be found in /RIC 15/ and /RIC 16/. Important for the retention and mobilization of uranium is the understanding of the speciation (digi. App. Sec. A.6.1).

At acidic conditions the uranyl ion dominates the speciation and with increasing pH various hydroxide species become more dominant. From pH 6 on carbonate species are the main species. This also is coupled with a change in the average charge of the aqueous species, moving from +2 to -4. This in turn directly implies changes in the electrostatic contributions to any surface binding reactions, of course to be discussed in combination to the shift on pzc (point-of-zero-charge) for the mineral surface due to increasing pH.

7.4.1 Sorption of U(VI) onto muscovite

The results for both M/V are shown in Fig. 7.1.

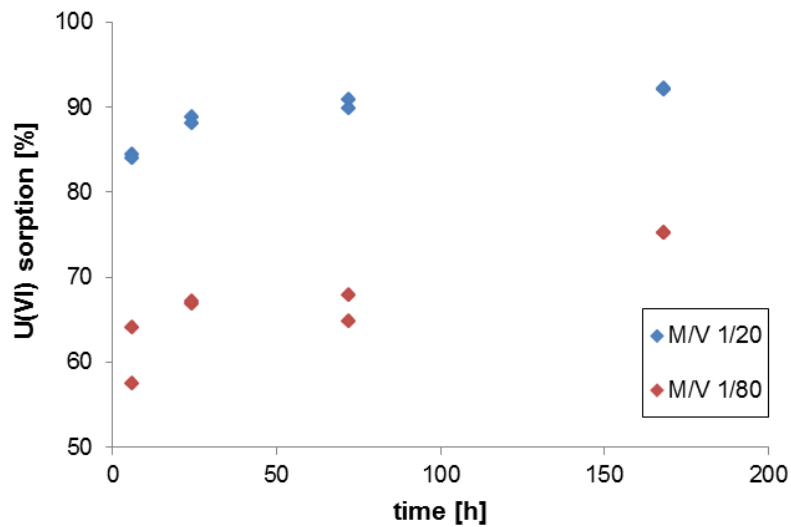


Fig. 7.1 Sorption kinetics of U(VI) in $0.01 \text{ mol L}^{-1} \text{ NaClO}_4$ onto muscovite

The uranium sorption onto muscovite shows still an increase for both investigated M/V after three days. After one week no significant increase is detectable as well for the M/V of 1/20 as for the ratio of 1/80. Because of this all further sorption experiments of U(VI) onto muscovite were done with a sorption time of one week (7 days).

The results for the sorption at a uranium concentration of $10^{-6} \text{ mol L}^{-1}$ are shown in Fig. 7.2 and for the concentration of $10^{-5} \text{ mol L}^{-1}$ in Fig. 7.3.

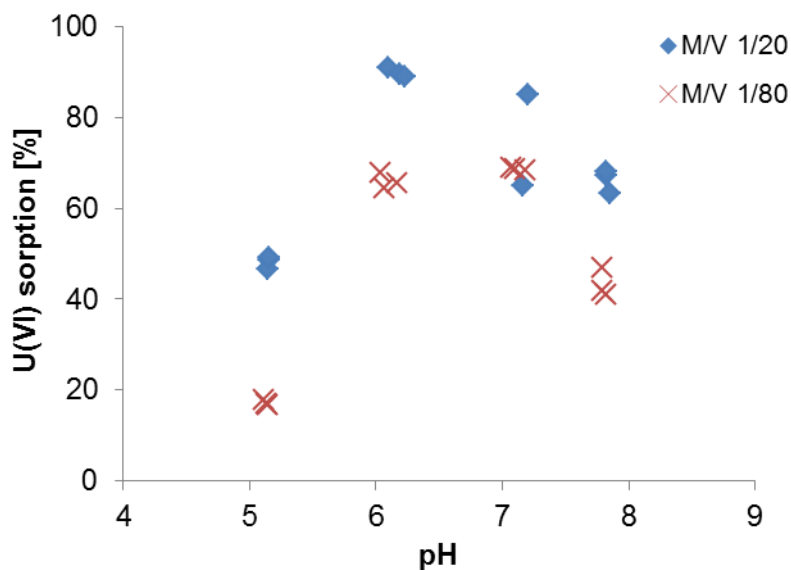


Fig. 7.2 Sorption of $10^{-6} \text{ mol L}^{-1}$ U(VI) in $0.01 \text{ mol L}^{-1} \text{ NaClO}_4$ onto muscovite

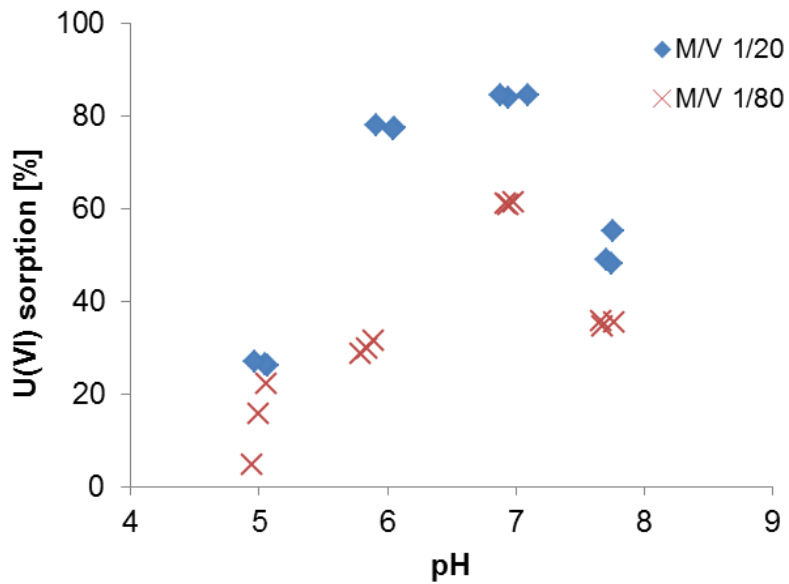


Fig. 7.3 Sorption of 10^{-5} mol L $^{-1}$ U(VI) in 0.01 mol L $^{-1}$ NaClO $_4$ onto muscovite

The sorption of uranium onto muscovite shows for all conditions an maximum at a pH-value of 7. Only for a U(VI) concentration of 10^{-6} mol L $^{-1}$ combined with a M/V of 1/20 highest sorption occurs already at pH 6. With a higher amount of solid in the suspension the sorption is higher, because of more free binding places at the mineral. At lower uranium concentrations (10^{-6} mol L $^{-1}$) the uranium sorption is generally higher. This is because of the lower amount of required sorption places.

7.4.2 Sorption of U(VI) onto orthoclase

The experiment to determine the sorption kinetic of uranium onto orthoclase was done in analogy to muscovite (Sec. 7.4.1). Fig. 7.4 shows the results of the U(VI) sorption kinetic experiment onto orthoclase.

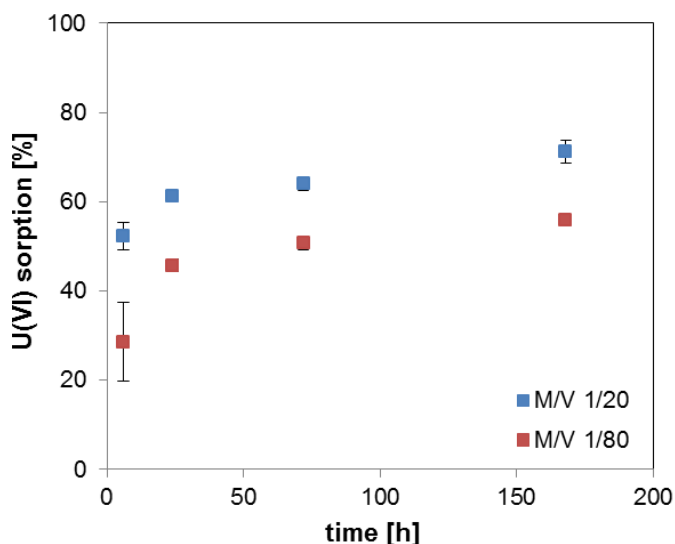


Fig. 7.4 Sorption kinetics of U(VI) in 0.01 mol L⁻¹ NaClO₄ onto orthoclase

The uranium sorption onto orthoclase increases with increasing sorption time for both investigated M/Vs. After one week the sorption is the highest for both M/Vs. For further sorption experiments of U(VI) onto orthoclase a sorption time of one week (7 days) will be used because it shows the highest sorption in this experiment. A longer sorption may result to higher sorption results but it will also increase the required time of the experiments a lot.

The results for the sorption at uranium concentration of 10⁻⁶ mol L⁻¹ and 10⁻⁵ mol L⁻¹ are shown in (Fig. 7.5 and Fig. 7.6), respectively.

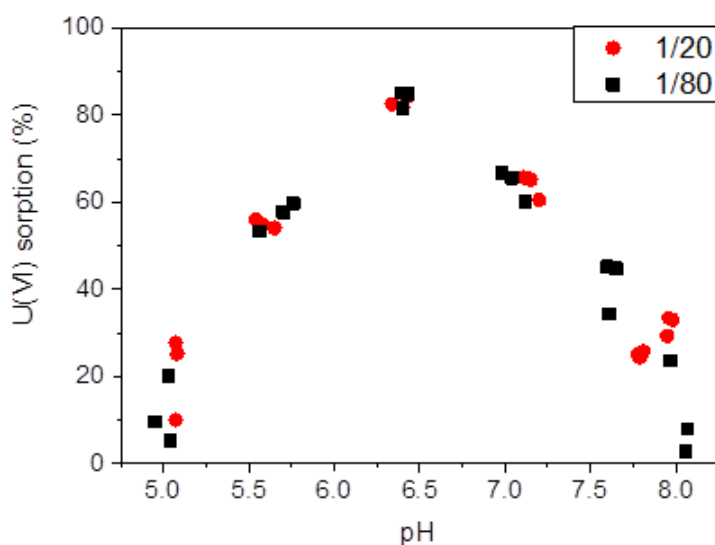


Fig. 7.5 Sorption of 10⁻⁶ mol L⁻¹ U(VI) in 0.01 mol L⁻¹ NaClO₄ onto orthoclase

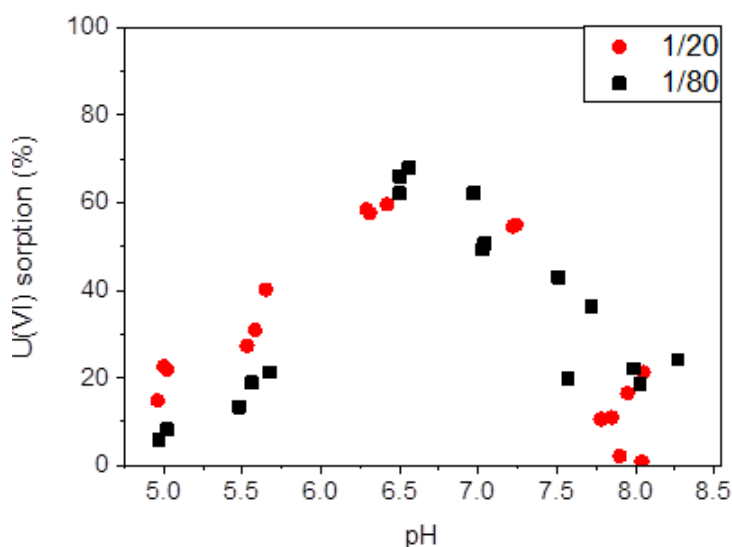


Fig. 7.6 Sorption of 10^{-5} mol L $^{-1}$ U(VI) in 0.01 mol L $^{-1}$ NaClO $_4$ onto orthoclase

The sorption of U(VI) onto orthoclase exhibits a behavior similar to muscovite. For all M/Vs and all concentrations the maximum is at a pH value of 7. Compared to muscovite the sorption onto orthoclase is in general a bit lower. The maximum sorption for muscovite at a uranium concentration of 10^{-6} mol L $^{-1}$ at pH 6 reaches around 90 % and for orthoclase at the same conditions only around 70 %.

7.4.3 Influence of ionic strength on U(VI) sorption

Due to shifts of the pH at high ionic strength, a pH correction (Δ pH) for the experiments in 1 mol L $^{-1}$ NaClO $_4$ was necessary according to the following equation where IS stands for the ionic strength /PET 11/:

$$\Delta\text{pH} = 0.0046 IS^2 + 0.27 IS - 0.0152 \quad \text{Eq. 7.1}$$

The influence of the ionic strength on the sorption of U(VI) onto muscovite is shown in Fig. 7.7. A shift of the sorption curve can be observed thus indicating that the sorption takes place predominantly as an outer-sphere complex.

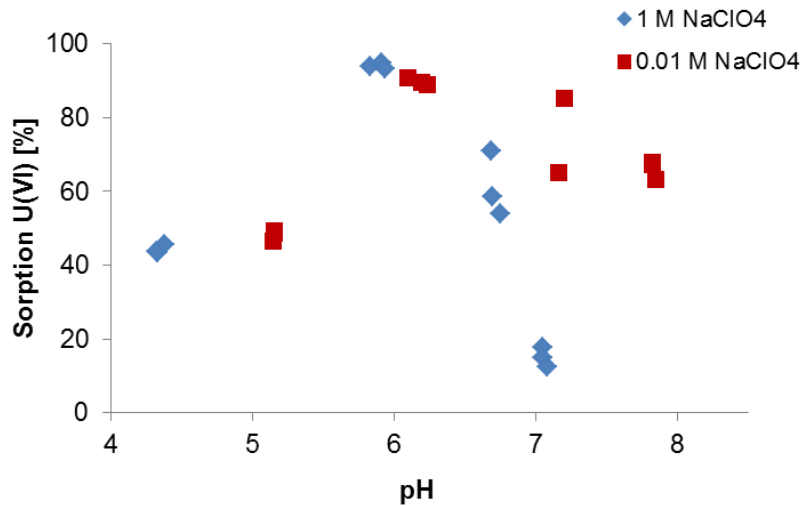


Fig. 7.7 Sorption of 10^{-6} mol L⁻¹ U(VI) in 1 mol L⁻¹ NaClO₄ onto muscovite

For orthoclase Fig. 7.8 illustrates the influence of the ionic strength on the sorption of 10^{-6} mol L⁻¹ U(VI). Similar to the case of muscovite a shift of the sorption curve is indicating that the sorption takes mostly place as an outer-sphere complex.

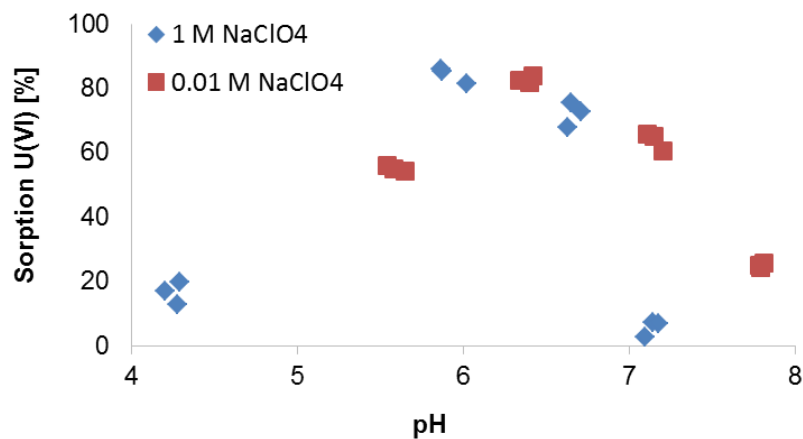


Fig. 7.8 Sorption of 10^{-6} mol L⁻¹ U(VI) in 1 mol L⁻¹ NaClO₄ onto orthoclase

7.4.4 Influence of Ca on U(VI) sorption as competing cation

The sorption of metal cations such as U(VI) is affected by various factors, such as competition for sorption sites on the mineral surface with other cations or the formation of ternary complexes in aqueous solution (which in some cases may sorb themselves). One of the most prominent actors is the Ca²⁺ cation. It is ubiquitous in natural waters as well as in clay pore waters and may also be leached from backfill materials. Calcium can form ternary complexes with U(VI) and carbonate. Thus, its presence will change U(VI) retardation in a way difficult to predict. Accordingly, respective sorption experiments were

performed to allow for a better characterization and parameterization of these competition processes in the quaternary system U(VI)-mineral-Ca-CO₂, having a higher practical relevance than many simple laboratory systems.

To understand the uranium behavior in presence and absence of calcium, its speciation was calculated with PHREEQC as given in the digital appendix Section A.6.1 (Fig. A. 31). The results showed that the influence of Ca is important at higher pH values and differ significantly from the one without Ca. It indicates that the Ca₂(UO₂(CO₃)₃) complex /BER 96/, /BER 01/ is dominant at pH 8. This neutral complex is expected to not sorb on the mineral surface. /JOS 11/ found that in presence of this complex the sorption decreases and more calcium remains in solution. In addition, Ca itself can also sorb on the surface and thus reduce the binding sites available for U(VI). At lower pH values this complex is not formed and thus the sorption of U(VI) is not influenced.

The comparison of the sorption of U(VI) onto muscovite with and without Ca is shown in Fig. 7.9. Obviously, the influence of Ca is relevant only at pH 8 (and above).

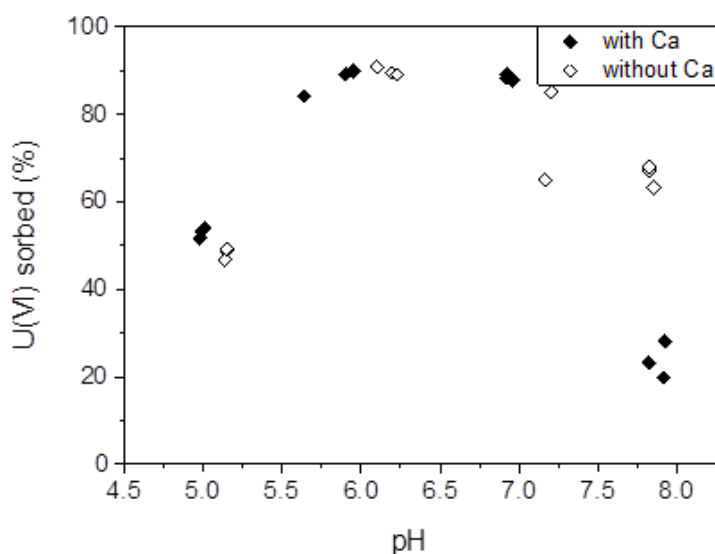


Fig. 7.9 Sorption of 10^{-6} mol L⁻¹ U(VI) onto muscovite with $1.5 \cdot 10^{-3}$ mol L⁻¹ Ca as competing cation

The sorption of U(VI) onto orthoclase in presence and absence of Ca is shown in Fig. 7.10. As for muscovite the effect of Ca is only relevant at pH 8 and higher.

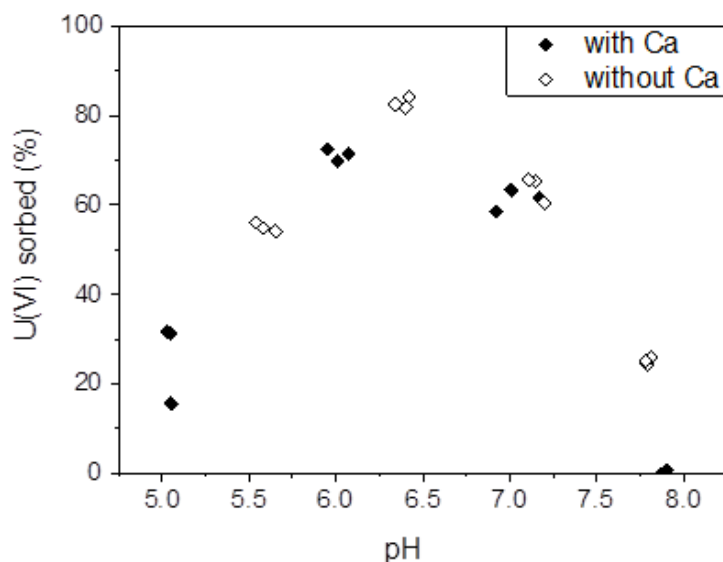


Fig. 7.10 Sorption of 10^{-6} mol L $^{-1}$ U(VI) onto orthoclase with $1.5 \cdot 10^{-3}$ mol L $^{-1}$ Ca as competing cation

7.5 Neptunium(V) batch sorption results

To extend sorption experiments to pentavalent actinides, Np(V) sorption onto orthoclase and muscovite was studied. Detailed information can be found in /RIC 15/. Experimental boundary conditions were chosen according to the ones selected for U(VI) to get comparable results (Sec. 7.2). The aqueous speciation of Np(V) is given in Section A.6.1 in the digital appendix. In general, neptunium speciation is much less complex and is dominated by the neptunyl(V) ion until pH 7. At higher pH values, neptunium-carbonate complexes are dominant and only one hydroxide complex that occurs with a low abundance. Due to the stability of pentavalent neptunium under oxidic conditions, neptunium is generally the most soluble and mobile actinide, and thus of great concern at waste storage sites /MAH 13/.

7.5.1 Sorption of Np(V) onto muscovite and orthoclase

The pH dependent sorption of Np(V) onto both orthoclase and muscovite yields an increasing sorption percentage with rising pH (see Fig. 7.11 and Fig. 7.12). A comparison of M/V 1/20 and 1/80 g mL $^{-1}$ shows no difference in the sorbed amount. These sorption curves do not reflect the typical sorption curves observed in presence of carbonate in studies performed by /SCH 10b/, /TAC 10/, /FRÖ 11/, /TUR 98/, /WU 09/, onto kaolinite, montmorillonite, gibbsite, and Opalinus clay, respectively. The effect that Np(V) shows a lesser sorption than U(VI) is also observed in this study. Only at high pH values (≥ 10)

an unusual effect is observed, where sorption tends to increase rapidly. Thus, the first slow increase of sorption from pH 7 to 10 is most likely due to the formation of neptunium surface complexes similar to those found in the previously mentioned studies.

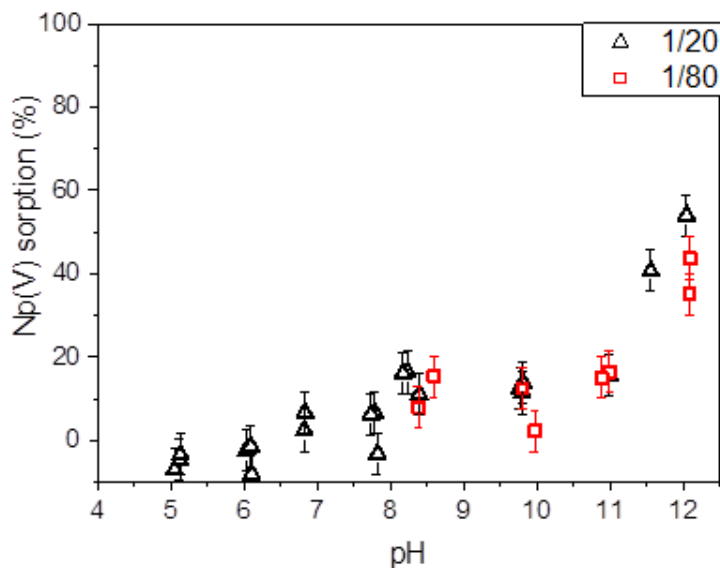


Fig. 7.11 Sorption of 10^{-6} mol L⁻¹ Np(V) onto orthoclase at varying M/V

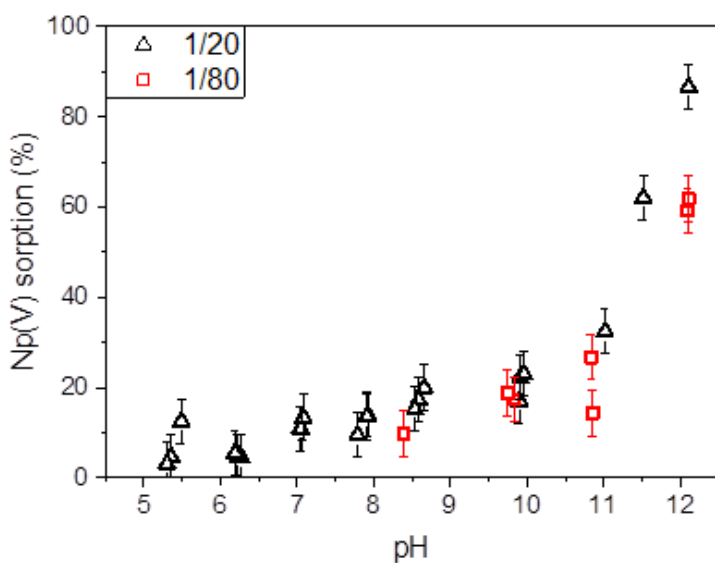


Fig. 7.12 Sorption of 10^{-6} mol L⁻¹ Np(V) onto muscovite at varying M/V

The observed increase at high pH values cannot be explained in detail based on available sorption data, but a few assumptions can be made. The absence of Np in the supernatant might not be only due to sorption, but also due to the formation of a Np-precipitate, vial wall sorption or the formation of Np(V) colloids.

At the higher pH values where the increase in sorption occurs, the decrease of Np in solution was observed; negatively charged neptunium-carbonate complexes dominate the aquatic Np speciation under these conditions (see Fig. 7.13). The surface of both investigated minerals is negatively charged, thus the formation of a neptunium surface complex is not expected. Additionally, vial wall sorption cannot be excluded. Negatively charged complexes are dominating in this system from pH 8 onwards, much before the steep increase in sorption starting at pH 11 meaning that negatively charged species would already be present. Therefore, it must be considered that wall sorption could contribute to this increase of sorption, although not significantly enough to account for the entirety.

The formation of colloids was tested by using scattered light intensity measurements. Due to the fact that before phase separation, besides colloids (if they exist), small mineral particles also exist in the solution, which can interfere with the scattered light intensity, and therefore do not necessarily indicate that colloids are present. Whereas after phase separation, colloids and mineral particles will be in the solid phase, and thus cannot be distinguished. For this reason, samples at pH 6 and 12 with only 10^{-6} mol L⁻¹ Np in 0.01 mol L⁻¹ NaClO₄ were tested for colloids. These samples showed no sign of an increase in the light scattering, and thus no formation of a precipitate could be observed. The presence of neptunium colloids in other aluminosilicate suspensions, such as kaolinite and montmorillonite /TUR 98/, /SCH 10a/, has not been reported. In these studies, the Np(V) concentration has been comparable to the concentration used in the present work, thus a reason for colloid formation in the investigated orthoclase and muscovite suspensions is difficult to explain.

As a last option a Np precipitate was considered. /ATW 10/ mentioned the potential precipitation of Np(V) hydroxides. This could be the case in this work, but Np-carbonates dominate at the higher pH values where the effect was observed. /NAK 91/ observed in some blank tests a decrease of neptunium in solution at pH values ≥ 11 , and referred it as precipitation because the Np solubility (concentration: $6 \cdot 10^{-6}$ mol L⁻¹) was exceeded at these pH values. Regardless, the precipitate form was not identified. A closer look to the pH-Eh diagram of neptunium (Fig. 7.13) showed that with increasing pH and a slight shift of Eh to lower values the formation of Np(IV) might be possible. Furthermore, a reduction of Np(V) to Np(IV) can be forced by some soluble compounds of the mineral, e. g., iron. This reduction process was described in /GOG 06/ with the following reaction:



The measurement of the redox potential of $10^{-6} \text{ mol L}^{-1}$ Np samples at pH 6 and 12 indicated a shift of the Eh from 0.3 V to approximately 0 V. Thus, Np at higher pH values samples tend to be reduced. It is not clear which process triggers the reduction at higher pH values in the investigated systems, but it might be due to some of the minor mineral components like iron. From these results, the formation of a Np precipitate like $NpO_2(\text{am})$, as shown in Fig. 7.13, can be assumed, or the reduction of Np(V) to Np(IV) followed by sorption of Np(IV), which is generally stronger than sorption of Np(V). Further studies are required to resolve these questions.

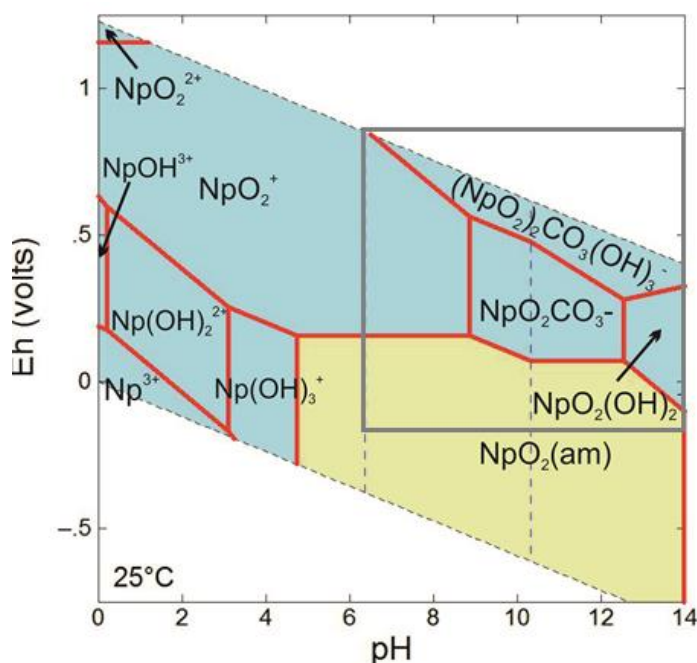


Fig. 7.13 pH-Eh diagram of $10^{-6} \text{ mol L}^{-1}$ Np in 0.01 mol L^{-1} NaClO_4 , under ambient atmosphere. The grey square represents the area of interest for the performed experiments

7.5.2 Influence of ionic strength on Np(V) sorption

To investigate the effect of the ionic strength on the Np(V) sorption, batch experiments in 1 mol L^{-1} NaClO_4 (M/V of $1/20 \text{ g mL}^{-1}$ and $10^{-6} \text{ mol L}^{-1}$ Np(V)) were performed in the pH range relevant for neptunium surface complex formation (pH 7 to 10). This was described before and illustrated in comparison to the results of 0.01 mol L^{-1} NaClO_4 (see Fig. 7.14 and Fig. 7.15). In these figures, pH values for 1 mol L^{-1} NaClO_4 were corrected

as described in Section 7.4.3. A shift of the sorption curve at higher ionic strength is not observed indicating inner-sphere sorption of neptunium. Additionally, because the amount of sorption is quite low, a definitive identification of the sorption complex is quite difficult, thus the formation of an outer-sphere surface complex cannot be excluded. Np(V) sorption onto other minerals as described in /MAH 13/ was also found to be dominated by inner-sphere sorption and consistent with this work.

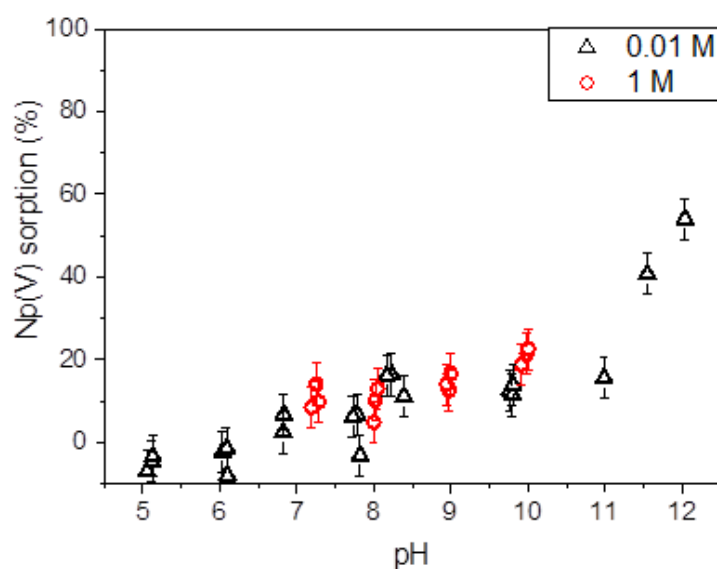


Fig. 7.14 Sorption of 10^{-6} mol L⁻¹ Np(V) under ambient atmosphere onto orthoclase in 0.01 mol L⁻¹ and 1 mol L⁻¹ NaClO₄

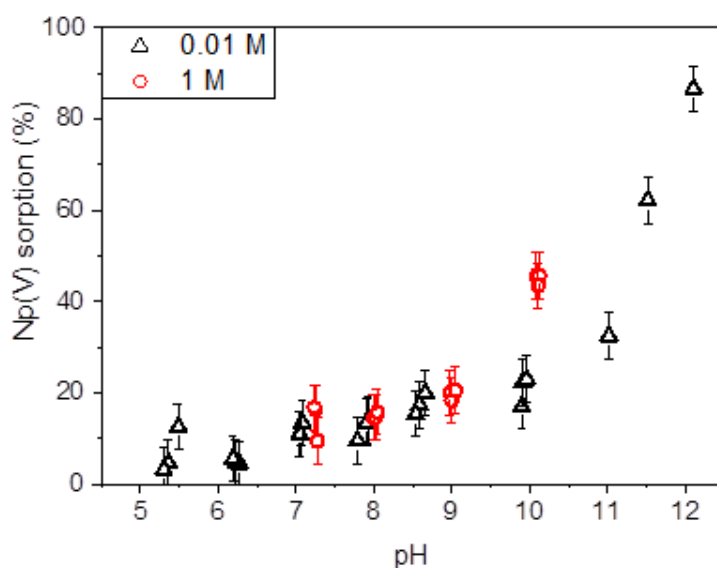


Fig. 7.15 Sorption of 10^{-6} mol L⁻¹ Np(V) under ambient atmosphere onto muscovite in 0.01 mol L⁻¹ and 1 mol L⁻¹ NaClO₄

7.6 Neodymium(III) batch sorption results

Batch sorption experiments with Nd(III) as chemical analogue for trivalent actinides were performed onto orthoclase and muscovite. Detailed information can be found in /RIC 15/. Main parameters were chosen according to the ones selected for U(VI) and Np(V) to get comparable results (Sec. 7.2).

The aqueous speciation of neodymium as well as the saturation indices of Nd(III) phases were calculated with PHREEQC and shown in the digital appendix Section A.6.1, Fig. A. 33 and Fig. A. 34. The speciation of Nd under acidic conditions is dominated by the Nd^{3+} ion. With increasing pH, several hydroxides and oxides become relevant followed by a carbonate complex at high pH values. In general, lanthanides are forming insoluble hydroxides and carbonates that precipitate at neutral pH unless complexing agents are present. Consequently, NdOHCO_3 may precipitate at pH values above 6.4 and $\text{Nd}_2(\text{CO}_3)_3$ at pH values above 6.7. The occurrence of a crystalline $\text{Nd}(\text{OH})_3$ phase certainly can be neglected. To identify precipitations, the scattered light intensity was measured (digi. App. Sec. A.6.2). As a result, it was shown that for concentrations of $10^{-5} \text{ mol L}^{-1}$ Nd there was no significant increase due to a precipitation at all pH values, at $10^{-4} \text{ mol L}^{-1}$ Nd the scattered light increased at pH 7 and higher. Therefore, the sorption experiments were performed in lower concentrations and the stock solution was prepared at acidic pH values to avoid a precipitation of Nd phases such as $\text{Nd}(\text{OH})_3(\text{am})$, $\text{Nd}_2(\text{CO}_3)_3$, or NdCO_3OH .

7.6.1 Sorption of Nd(III) onto muscovite and orthoclase

Nd(III) sorption onto orthoclase and muscovite was quantitative, depending on the conditions used, i. e., from neutral pH onwards. The formation of neodymium surface species was favoured at pH values where the positively charged neodymium hydroxide and carbonate species start to dominate aqueous Nd speciation. In general, the observed results were in good agreement with the observed sorption edges of Nd(III) and Ln(III).

As expected, with the decrease of the M/V from 1/20 to 1/80 g mL^{-1} there was only a slight reduction of sorption at the lowest investigated pH values due to the shortage of available binding sites on the mineral surfaces. At higher pH values maximum sorption (all the neodymium binds onto the mineral surfaces) was attained under all investigated conditions (see Fig. 7.16 and Fig. 7.17). As expected, increasing Nd(III) concentration shifted the sorption edges to higher pH values. In general, Nd(III) sorption was stronger

onto muscovite than on orthoclase. Thus, for orthoclase complete sorption was reached around pH 7 (10^{-5} mol L⁻¹ Nd(III)), whereas on muscovite it was reached already at pH 6.

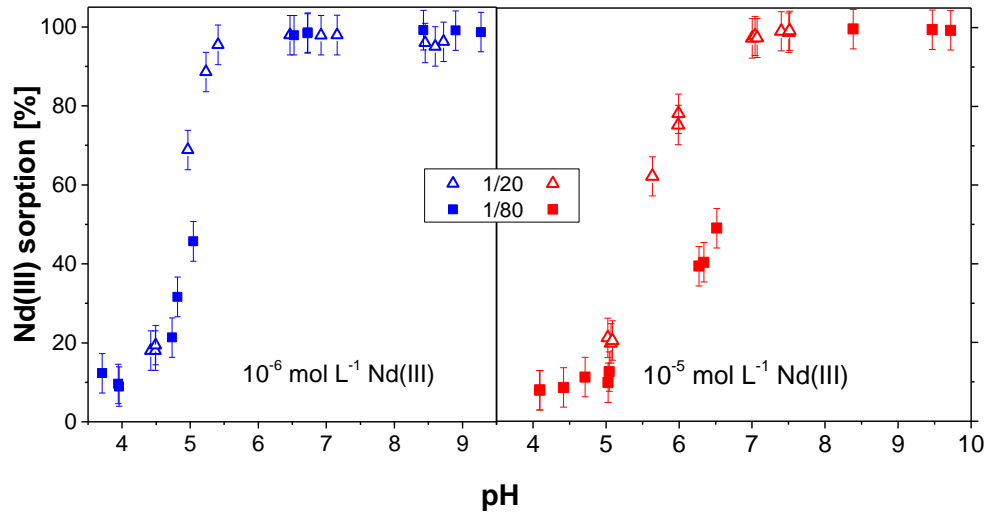


Fig. 7.16 Sorption onto orthoclase at 10^{-6} mol L⁻¹ Nd(III) (left) and 10^{-5} mol L⁻¹ Nd(III) (right) at M/V of 1/20 g mL⁻¹ and 1/80 g mL⁻¹

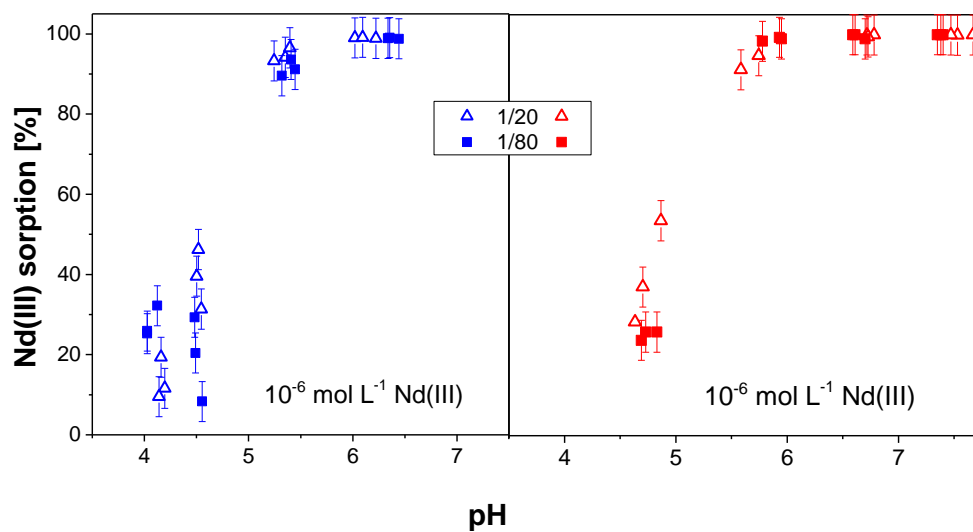


Fig. 7.17 Sorption onto muscovite at 10^{-6} mol L⁻¹ Nd(III) (left) and 10^{-5} mol L⁻¹ Nd(III) (right) at M/V of 1/20 g mL⁻¹ and 1/80 g mL⁻¹

7.6.2 Influence of ionic strength on Nd(III) sorption

To investigate the influence of the ionic strength on the sorption of Nd(III) onto orthoclase and muscovite, batch experiments in 1 mol L⁻¹ NaClO₄ (M/V of 1/20 g mL⁻¹ and 10^{-5} mol L⁻¹ Nd(III)) were performed. The results were compared to those of 0.01 mol L⁻¹

NaClO₄ (see Fig. 7.18). In this figure, pH values for 1 mol L⁻¹ NaClO₄ were corrected as described in /RIC 15/. A shift of the sorption curve at higher ionic strength to higher pH values, meaning a decrease of sorption at higher ionic strength, can be observed as was also shown by /GLA 00/. This indicates an influence of the sorption by electrostatic forces allowing Nd(III) to adsorb to orthoclase and muscovite via the formation of outer-sphere complexes /DAV 98/. In contrast, /AJA 98/ found the adsorption of Nd on kaolinite independent of ionic strength and assumed inner-sphere surface complexation mechanisms.

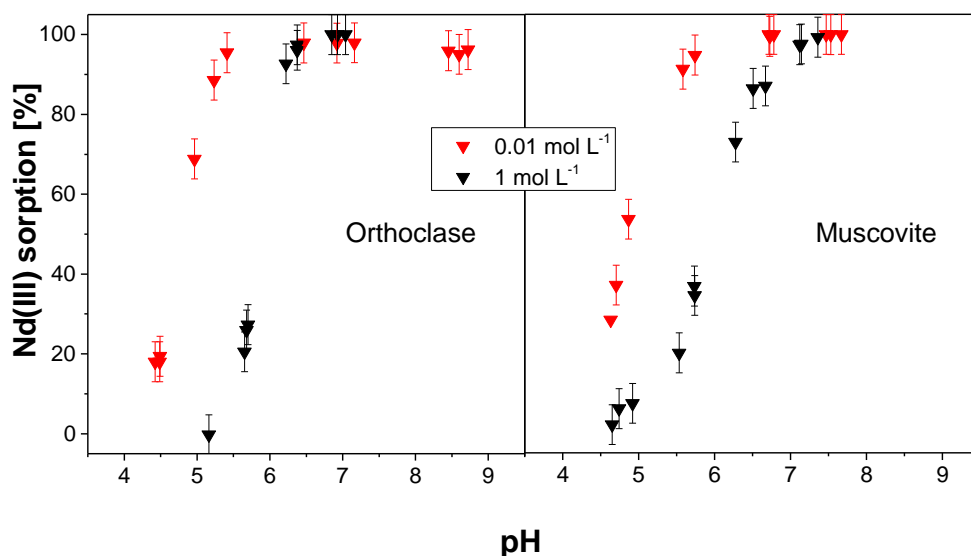


Fig. 7.18 Sorption onto orthoclase (left) and muscovite (right) at two different ionic strengths, M/V 1/20 g mL⁻¹ and 10⁻⁵ mol L⁻¹ Nd(III)

7.7 Calcium(II) batch sorption results

Calcium is both a major component of most natural waters and a sorbing agent reacting with most mineral surfaces. Though its affinity to these surfaces is weaker than that of many transition metals, lanthanides or actinides, its abundance is often much larger. Thus, calcium may be a significant competitor for heavy metal sorption in natural systems. Moreover, it can form binary and ternary aqueous complexes with contaminants such as uranium, rendering the effects on sorption even more complicated. The influence of Ca to U sorption with orthoclase and muscovite was considered in Section 7.4.3.

In this section Ca batch sorption experiments were carried out with orthoclase and muscovite in 0.01 mol L⁻¹ NaClO₄ background solutions and between pH 5-8. Kinetic sorption results indicate that sorption equilibrium is reached within 7 d with orthoclase and muscovite (Fig. A. 30). Sorbed fractions of Ca are below 40 % over the whole range of chosen

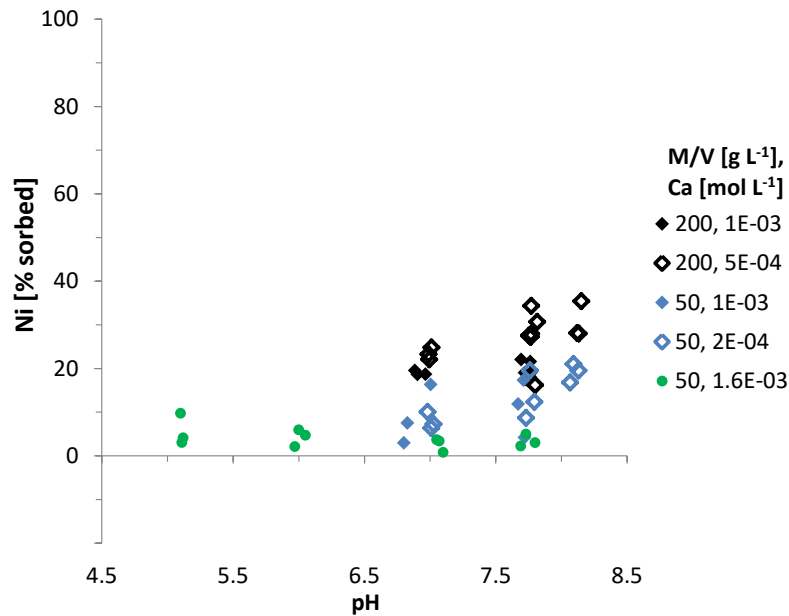


Fig. 7.20 Results of Ca batch sorption experiments with muscovite

0.01 M NaClO₄ background solution.

7.8 Europium(III) batch sorption results

This section is based on /BRI 18/, for supplementary detailed information see /BRI 18/. Batch experiments with orthoclase and muscovite were carried out during the research project ESTRAL /NOS 12b/. For reasons of comparability and completeness and since data was processed anew during the WEIMAR research project, sorption results of Eu on orthoclase and muscovite surfaces are again briefly illustrated in this section. In addition, new data of Eu batch experiments with quartz are depicted and discussed. Error bars in Fig. 7.21 – Fig. 7.23 represent double standard deviations of the Eu equilibrium concentration in the supernatant (C_{equil}) as described in the digital appendix Section A.5.4, error bars of pH measurements depict conservative error estimations as described in /DIN 07/ (also cf. /BRI 18/).

7.8.1 Sorption of Eu(III) onto quartz surfaces

Fig. 7.21 depicts experimental batch data of quartz. Generally, measurements followed expectations: The larger the initial Eu concentration (Eu C_0), the less Eu was immobilized. The uptake of Eu was also positively correlated with the pH and the M/V. For 12.5 g L⁻¹ maximum immobilization rates reached 82 %Eu(III) immobilized, for 50 g L⁻¹ a maximum of 94 %Eu(III) immobilized was observed. Relatively high Eu immobilization was found at pH < 5 which agreed with results of /LÜT 96/. A comparison of quartz batch

data of this study with literature (e. g. /KIT 99/, /STU 08a/) showed that collected data matched literature data well provided that similar geochemical boundary conditions were compared (digi. App. Fig. A. 24).

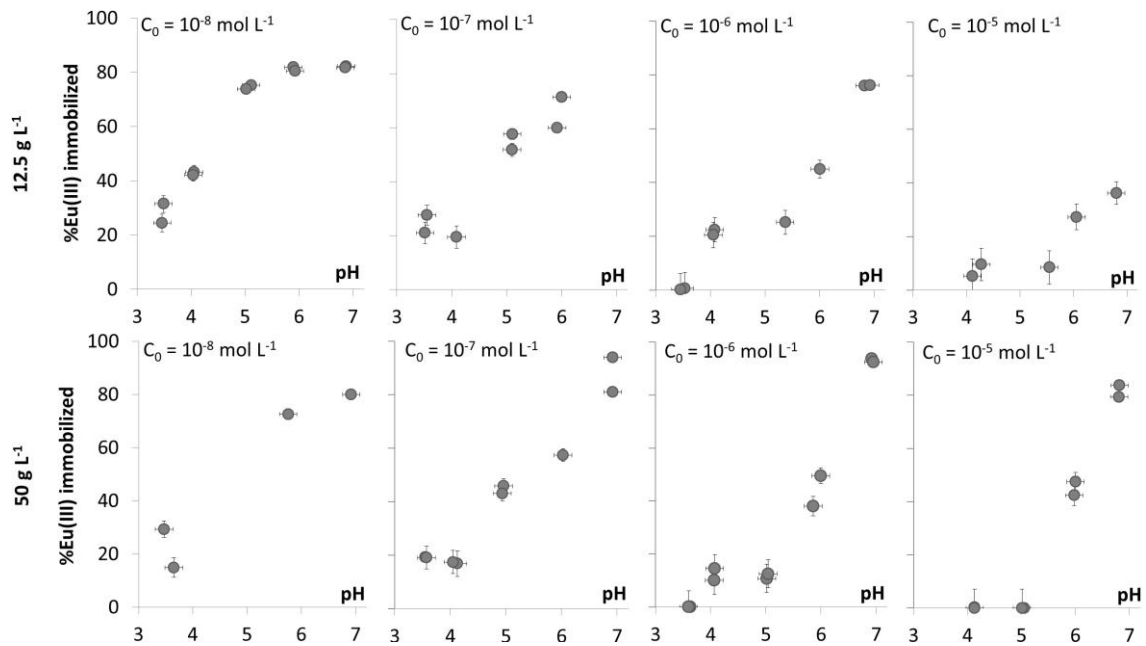


Fig. 7.21 Results of Eu batch experiments with quartz in 10 mM NaClO₄ background electrolyte

Laboratory conditions ($p\text{CO}_2 = 10^{-3.4}$ bar, $T = 296.0 \text{ K} \pm 2 \text{ K}$), C_0 – initial Eu concentration.
Top: $M/V = 12.5 \text{ g L}^{-1}$, bottom: $M/V = 50 \text{ g L}^{-1}$.

7.8.2 Sorption of Eu(III) onto orthoclase surfaces

Measurements of orthoclase batch experiments are shown in Fig. 7.22. Generally, results followed expectations: Immobilization of Eu [%] was positively correlated with increasing pH and M/V . Smaller initial Eu concentrations (Eu C_0) returned larger relative Eu uptake in comparison to high C_0 (cf. Fig. 7.23). Unfortunately, during experimental set-up sorption affinities/immobilization rates of Eu were underestimated for the considered geochemical systems. Hence, much data described almost 100 % Eu immobilization, only high Eu C_0 delivered a sorption edge as intended (Fig. 7.23). In future, for this system smaller M/V s should be used to receive a more comprehensive picture of sorption affinities of the trivalent lanthanide.

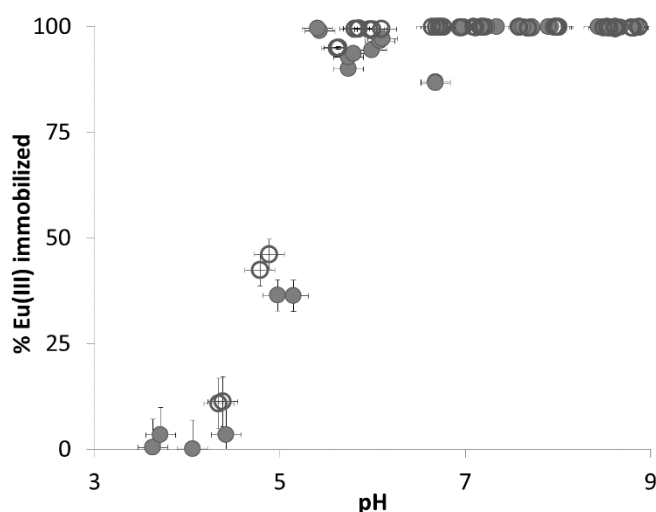


Fig. 7.22 Results of Eu batch experiments with orthoclase (10 mM NaClO₄ background electrolyte)

Laboratory conditions: pCO₂ 10^{-3.4} bar, T = 296.0 K ± 2 K. Data comprise two M/Vs (12.5 g L⁻¹ (solid circles)) and 50 g L⁻¹ (open circles)), four Eu C₀ with 10⁻⁵ – 10⁻⁸ mol L⁻¹ as a function of pH (cf. /NOS 12b/).

7.8.3 Sorption of Eu(III) onto muscovite surfaces

Fig. 7.23 shows muscovite batch data in comparison to quartz and orthoclase measurements. Muscovite batch experiments were performed under identical conditions as for quartz and orthoclase. Due to the high adsorption capacity of muscovite only the experiments with the low M/V and high Eu concentrations yielded sorption edges. The higher M/V and low Eu concentrations resulted in 100 % Eu immobilization. Sorption edges were substantiated for:

- M/V = 12.5 g L⁻¹, C₀ = 10⁻⁶ mol L⁻¹
- M/V = 12.5 g L⁻¹, C₀ = 10⁻⁵ mol L⁻¹
- M/V = 50 g L⁻¹, C₀ = 10⁻⁵ mol L⁻¹

These experimental results are shown in Fig. 7.23 and evidently corroborate the findings of quartz and orthoclase experiments: Quartz returned lowest, and muscovite yielded highest relative Eu immobilization rates (Fig. 7.23). As expected, Eu immobilization [%] was positively correlated with rising pH and M/Vs. Lowest Eu uptake equaled 24 %Eu(III) immobilized at pH 3.2 for muscovite; smaller values were not collected. That the lowest measured Eu uptake equaled approx. one fourth of C₀ even at low pH was attributed to cation exchange processes which agreed well with findings from /PAN 17/.

However, for future experiments smaller M/V s and/or smaller $\text{Eu } C_0$ are recommended to collect more data in the range of the sorption edge; hence, geochemical boundary conditions should consider different sorption capacities of quartz, muscovite, and orthoclase.

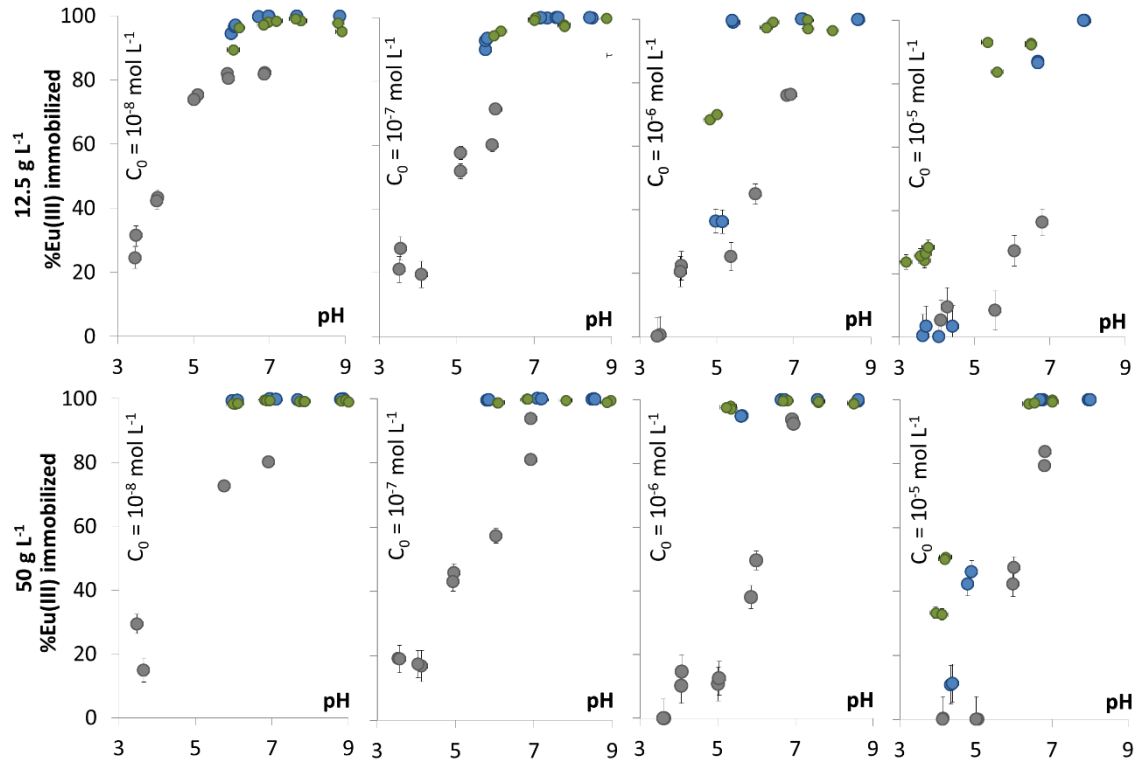


Fig. 7.23 Results of Eu batch experiments with orthoclase (blue), quartz (grey), and muscovite (green) (10 mM NaClO_4 background electrolyte)

Laboratory conditions: $p\text{CO}_2$ $10^{-3.4}$ bar, $T = 296.0 \text{ K} \pm 2 \text{ K}$. C_0 – initial Eu concentration.

7.9 Nickel(II) batch sorption results

To investigate sorption characteristics of Ni under varying geochemical conditions batch experiments were conducted. Geochemical conditions were chosen which are likely to be present in the aquifer system at the Gorleben site following /NOS 12b/. Error bars in Fig. 7.24 – Fig. 7.32 represent the double standard deviation of the Ni measurement uncertainty of the ICP-MS which was calculated by $10^{-7} \text{ mol L}^{-1}$ Ni long term precision measurements of the ICP-MS (Sec. A.5.4).

Collected sorption data will be used for determination of surface complexation constants with the geochemical speciation code PHREEQC /PAR 99/ in combination with the

parameter estimation code UCODE /POE 08/. Determination of surface complexation constants was not performed in this study but will be realized in a continuing PhD thesis.

7.9.1 Ni(II) sorption onto quartz

Generally, results show expected sorption correlations concerning sorbed fractions of Ni and pH, initial Ni concentration (C_0), M/V and ionic strength (Fig. 7.24 to Fig. 7.26): The higher the pH and the lower the initial Ni concentration, the more sorption occurs. A higher M/V results in higher sorbed fractions. Moreover, a higher ionic strength results in lower sorbed fractions. This indicates a weak bonding of Ni on quartz and thus may indicate the formation of outer-sphere complexes.

However, referring to the batch experiments applying quartz and Ni in 0.01 and 0.2 mol L⁻¹ NaClO₄ background solution there are some negative values at pH 5 and 6 (Fig. 7.25, Fig. 7.26). This could be caused by a higher release of Ni from quartz than determined in Section 5.1.3.2.

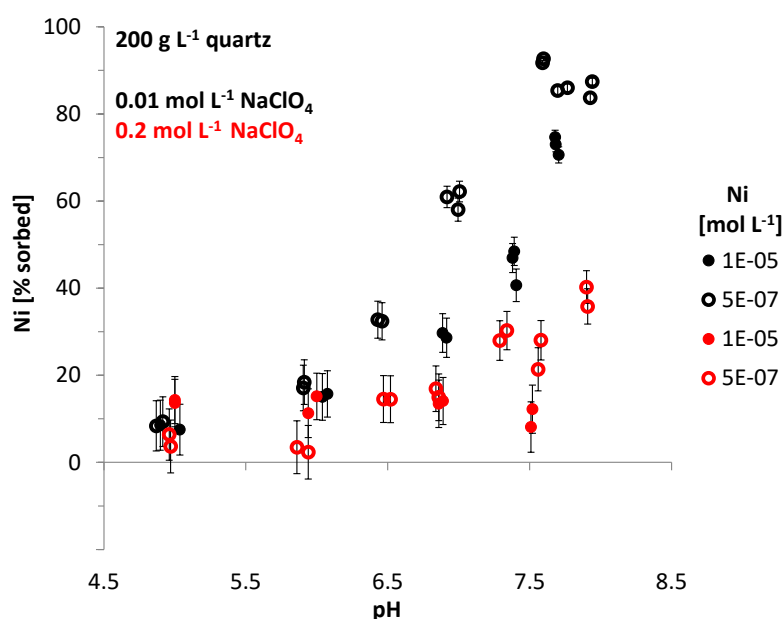


Fig. 7.24 Results of Ni batch sorption experiments with 200 g L⁻¹ quartz in 0.01 and 0.2 mol L⁻¹ NaClO₄ solutions

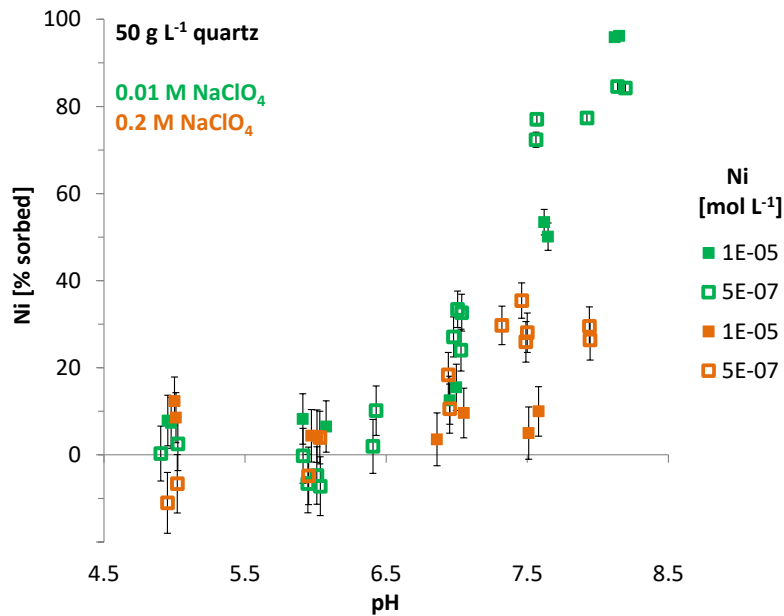


Fig. 7.25 Results of Ni batch sorption experiments with 50 g L⁻¹ quartz in 0.01 and 0.2 mol L⁻¹ NaClO₄ solutions

Further batch experiments were conducted to investigate the impact of SO₄²⁻ as a ligand. To retain the same ionic strength compared to 0.2 mol L⁻¹ NaClO₄ a 0.066 mol L⁻¹ Na₂SO₄ background solution was applied. Sulfate shows no significant effect to sorbed fractions (Fig. 7.26). This was not expected since speciation calculations reveal NiSO₄ as the main aquatic species with nearly 56 % between pH 5-8 (digi. App. Fig. A. 26 B) which probably would not have the identical sorption behavior as Ni²⁺. In contrast, in 0.2 mol L⁻¹ NaClO₄ solution the main species is Ni²⁺ with up to 100 % between pH 5-8 (Fig. A. 26 A).

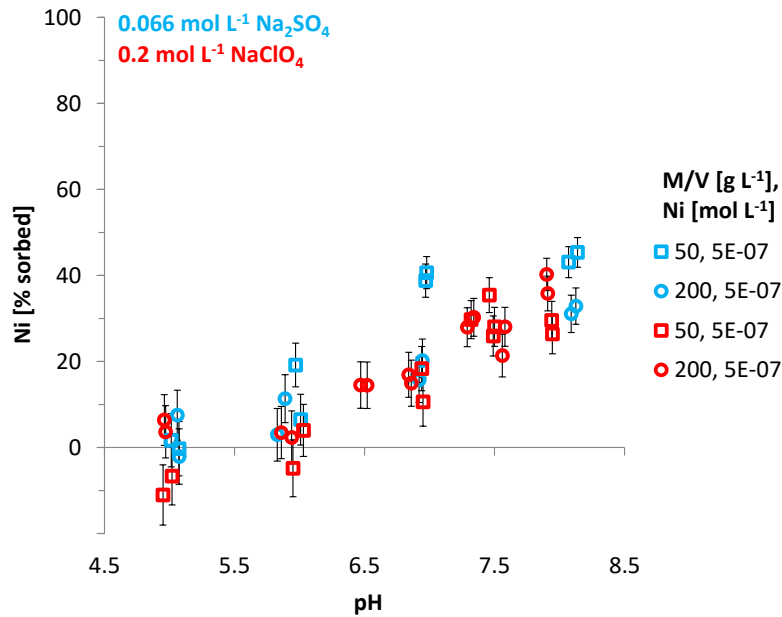


Fig. 7.26 Comparison of Ni batch sorption results with quartz in 0.066 mol L⁻¹ Na₂SO₄ and 0.2 mol L⁻¹ NaClO₄ solutions

7.9.2 Ni(II) sorption onto orthoclase

Sorption data show expected correlations like in the batch system with quartz (Sec. 7.9.1) regarding sorbed fractions of Ni and pH, C₀, M/V and ionic strength which are illustrated in Fig. 7.27 to Fig. 7.29: The higher the pH and the lower the initial Ni concentration, the more sorption occurs. Furthermore, a higher M/V results in higher sorbed fractions, a higher ionic strength results in lower sorbed fractions. As in the case of quartz sorption experiments this could indicate a weak bonding of Ni on orthoclase too and thus may imply the formation of outer-sphere complexes.

Additional batch experiments were carried out to investigate the impact of SO₄²⁻ as a ligand. A 0.066 mol L⁻¹ Na₂SO₄ background solution was applied to retain the same ionic strength compared to 0.2 mol L⁻¹ NaClO₄. As in the case of quartz sorption experiments (Fig. 7.26) sulfate has no significant effect to sorbed fractions on orthoclase as well (Fig. 7.29).

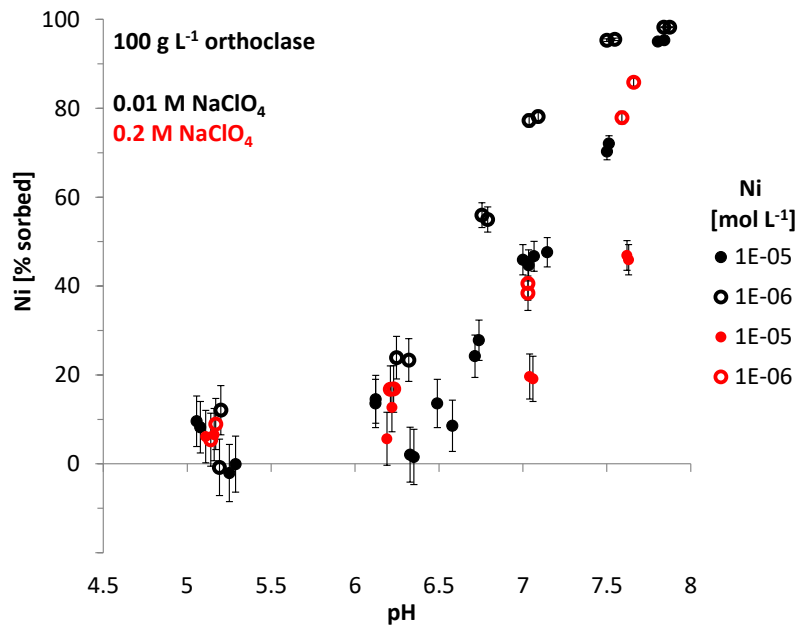


Fig. 7.27 Results of batch sorption experiments with Ni and 100 g L⁻¹ orthoclase in 0.01 and 0.2 mol L⁻¹ NaClO₄ solution

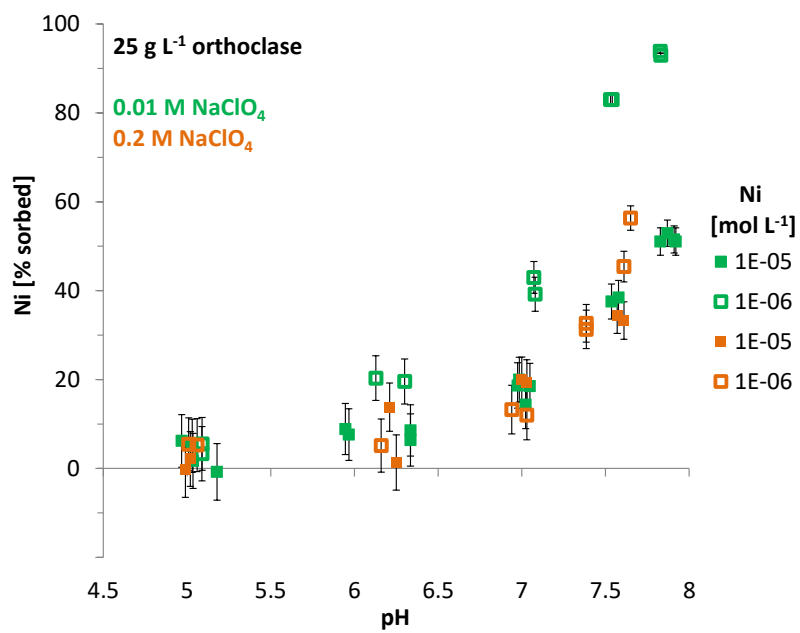


Fig. 7.28 Results of Ni batch sorption experiments with 25 g L⁻¹ orthoclase in 0.01 and 0.2 mol L⁻¹ NaClO₄ solutions

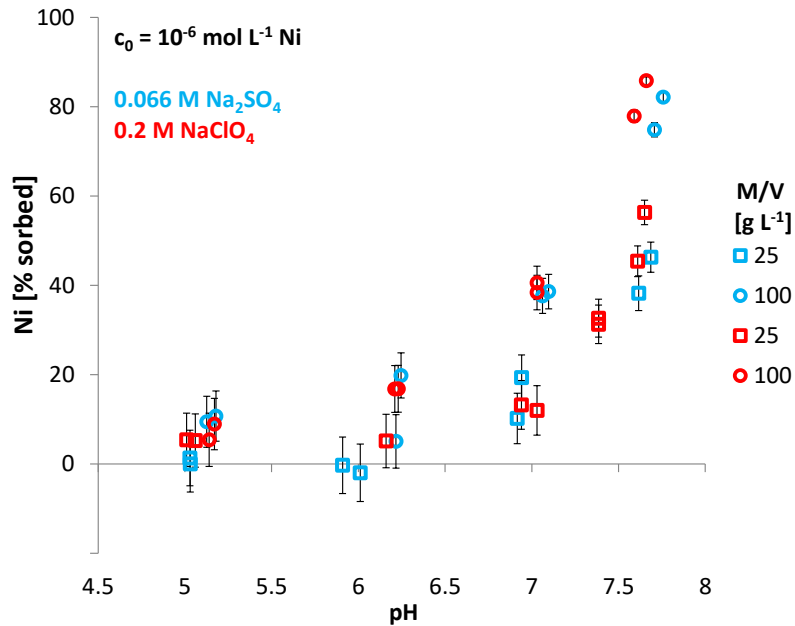


Fig. 7.29 Comparison of Ni batch sorption results with orthoclase in 0.066 mol L^{-1} Na_2SO_4 and 0.2 mol L^{-1} NaClO_4 solutions

7.9.3 Ni(II) sorption onto muscovite

In general, expected sorption correlations were observed concerning sorbed fractions of Ni and pH, C_0 , M/V and ionic strength which are depicted in Fig. 7.30 to Fig. 7.32. Correlations are comparable to the batch sorption results with quartz (Sec. 7.9.1) and orthoclase (Sec. 7.9.2): The higher the pH and the lower the initial Ni concentration, the higher the sorbed fractions. Moreover, a lower M/V and higher ionic strength results in lower sorbed fractions. As in the case of quartz and orthoclase sorption experiments the ionic strength dependency could indicate a weak bonding of Ni on muscovite too and thus may point to the formation of outer-sphere complexes.

More batch experiments were conducted to investigate the impact of SO_4^{2-} as a ligand. Here, a 0.033 mol L^{-1} Na_2SO_4 background solution was applied to retain the same ionic strength as in the 0.1 mol L^{-1} NaClO_4 solution. Like in the case of quartz and orthoclase sorption experiments (Fig. 7.26 and Fig. 7.29, respectively) sulfate has no significant effect to sorbed fractions on muscovite (Fig. 7.32).

Ni sorption data with quartz, orthoclase and muscovite cannot be compared directly since at least the M/V is different. But it is obvious that the sorption affinity of Ni towards muscovite is much higher compared to orthoclase and quartz when regarding sorption edges. For example, regarding the initial concentration of $10^{-5} \text{ mol L}^{-1}$ Ni and 50 g L^{-1} muscovite

(Fig. 7.30) the sorption edge ranges between pH 5 and 7. On the contrary, the sorption edge of 100 g L⁻¹ orthoclase (Fig. 7.27) and 200 g L⁻¹ quartz (Fig. 7.24) ranges between pH 6 and 8. The difference between orthoclase and quartz is not that obvious compared to muscovite. However, the affinity of Ni towards orthoclase is higher than towards quartz.

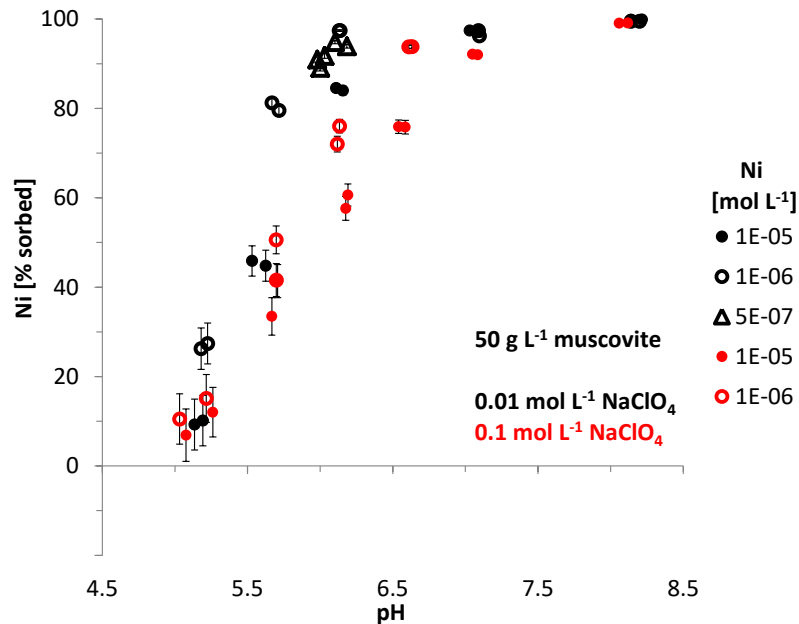


Fig. 7.30 Results of Ni batch sorption experiments with 50 g L⁻¹ muscovite in 0.01 and 0.1 mol L⁻¹ NaClO₄ solutions

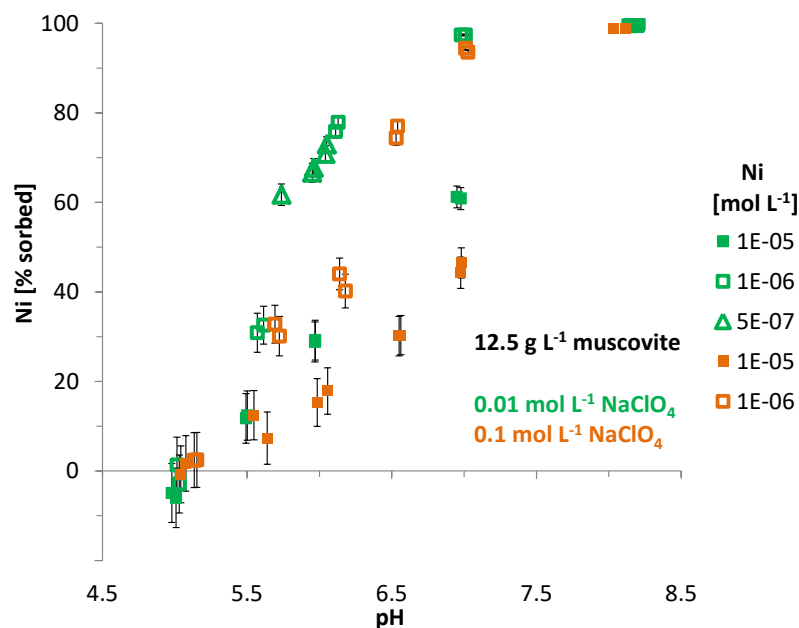


Fig. 7.31 Results of Ni batch sorption experiments with 12.5 g L⁻¹ muscovite in 0.01 and 0.1 mol L⁻¹ NaClO₄ solutions

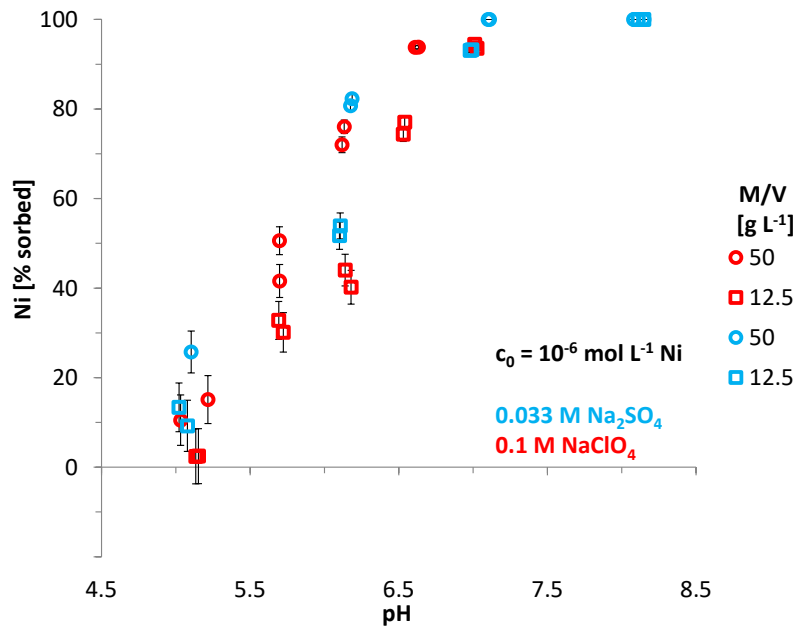


Fig. 7.32 Comparison of Ni batch sorption results with orthoclase in 0.033 mol L⁻¹ Na₂SO₄ and 0.1 mol L⁻¹ NaClO₄ solutions

7.10 Aluminum(III) batch sorption results

In natural waters Al occurs in lower concentrations than major cations like Ca. However, Al might be important as well as a competitive cation for sorption sites on minerals. Therefore, it was intended to investigate the sorption affinity of Al with quartz, muscovite and orthoclase. Because of high Al concentrations released from the minerals (Sec. 5.1.1.2), the limit of quantification (LOC) of $\sim 3 \cdot 10^{-8}$ mol L⁻¹ Al and the relative low solubility of Al, batch sorption experiments with natural orthoclase, muscovite, and quartz were not feasible. Preconditioned MERCK quartz was used instead as elucidated in Section 5.1.1.2. Nevertheless, no data could be collected between pH 5 to 8 because of the relative low solubility of Al and LOC as mentioned before.

Al sorption on MERCK quartz increased sharply above pH 4 regarding $C_0 = 2 \cdot 10^{-5}$ mol L⁻¹ Al (Fig. 7.33). Since there was a data gap between pH 5 to 8, two trends of sorbed fractions could be imaginable: (a) sorption maximum between pH 5 to 8 and subsequent decrease or (b) continuous increase of sorbed fractions and plateau at pH 8. Considering the aquatic speciation of Al (Fig. A. 25) trend (a) seems more likely because the charge of Al species decreases with increasing pH and in turn these species tend to have a lower affinity towards negative charged oxide surfaces. For example, above pH 8 more than 98 % of solved Al would be present as Al(OH)₄⁻ (Fig. A. 25).

Since batch sorption experiments with natural orthoclase, muscovite, and quartz were not feasible, determination of surface complexation constants could not be performed in this study. Even with highly purified MERCK quartz just a small range of geochemical conditions could be investigated. More data (especially between pH 5 to 8) would be needed to determine SCPs.

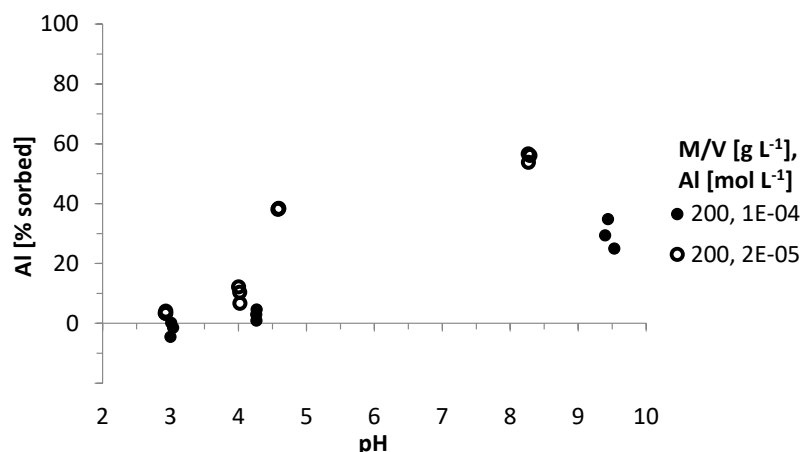


Fig. 7.33 Results of Al batch sorption experiments with 200 g L⁻¹ MERCK quartz in 0.01 mol L⁻¹ NaClO₄ solutions

Merck quartz = purified quartz sand from MERCK which was preconditioned by the vendor: washed with hydrochloric acid and calcined at 900 °C.

7.11 Cesium(I) batch sorption results

Cs batch sorption experiments with orthoclase and muscovite were conducted during the research project ESTRAL /NOS 12a/. However, orthoclase results did not meet any expectations and indicated errors in the experimental execution. For this reason, orthoclase and muscovite experiments were carried out anew during the master thesis /STE 17/ in this study. Additional experiments with muscovite were performed to substantiate the previous findings.

7.11.1 Cs(I) sorption onto muscovite

Results revealed expected sorption correlations concerning sorbed fractions of Cs, C₀, and M/V which are depicted in Fig. 7.34 and Fig. 7.35: The higher the M/V and the lower the initial Ni concentration, the more sorption occurs. No dependency on pH was observed for initial concentrations below 10⁻⁵ mol L⁻¹ Cs. This indicated that cation exchange is the dominant sorption mechanism /POI 99/. Cs sorption onto mica minerals

and in general phyllosilicates is mostly described by cation exchange processes e. g. see /SAW 70/, /SAW 72/, /POI 99b/, and /CHO 09/.

Results scattered regarding $C_0 = 10^{-7}$ and 10^{-8} mol L⁻¹ Cs and significant differences in sorbed fractions were not observed (Fig. 7.34 and Fig. 7.35). New collected data from this study were in good agreement with sorption data from /NOS 12a/ except for $C_0 = 10^{-8}$ mol L⁻¹ Cs. No explanation could be found for the gap in sorbed fractions between both data sets.

Surface complexation modeling was not performed in this study since selectivity coefficients were lacking for modeling of cation exchange processes. This is intended to be realized in a following project.

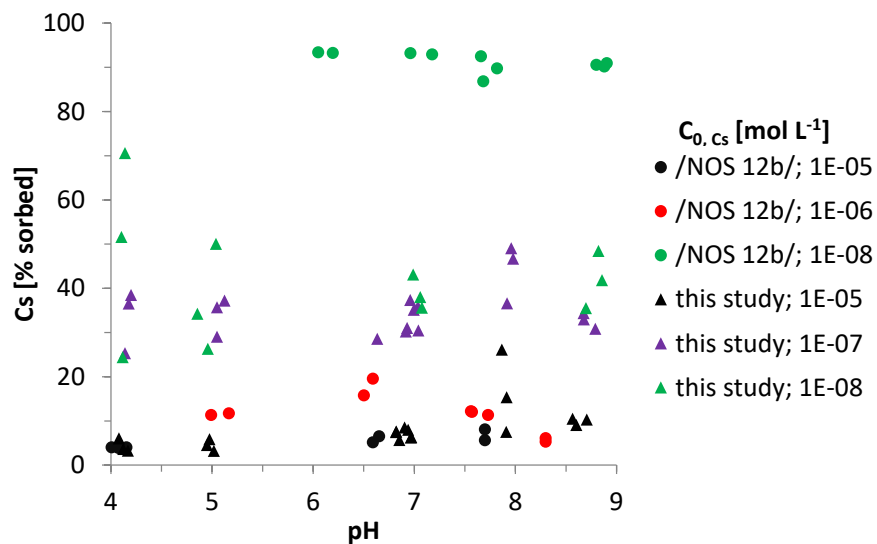


Fig. 7.34 Results of Cs batch sorption experiments with 50 g L⁻¹ muscovite in 0.01 mol L⁻¹ NaClO₄

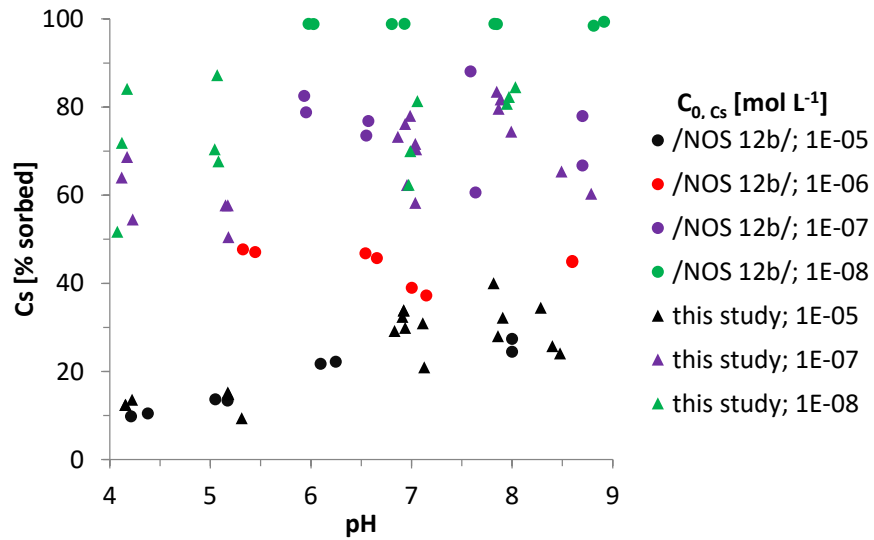


Fig. 7.35 Results of Cs batch sorption experiments with 50 g L⁻¹ muscovite in 0.01 mol L⁻¹ NaClO₄

7.11.2 Cs(I) sorption onto orthoclase

All batch sorption experiments yielded a consistent dataset concerning sorption tendencies as a function of pH, C_0 , and M/V: An increasing pH, lower C_0 , and higher M/V results in higher sorbed fractions (cf. Fig. 10.12). Detailed information are provided in /STE 17/. Results are shown in combination with mechanistic sorption modeling results in Section 10.2.5.

8 Spectroscopic evidence of surface species

For a detailed characterization of sorption processes the surface structures were studied on a molecular level. A major goal of the experimental part of this project was to gain more confidence in the surface species actually relevant for sorption processes onto muscovite and orthoclase. Therefore, different spectroscopic techniques were used combining Time-resolved laser-induced fluorescence spectroscopy (TRLFS) with Attenuated total reflection Fourier transform-infrared (ATR FT-IR) spectroscopy. Detailed information of these spectroscopic measurements are given in /RIC 15/.

TRLFS is a useful method to identify different complexes through small spectral changes induced by different ligand environments that can be distinguished at very low concentrations. It is very selective, sensitive, and dynamic and it allows for the analysis of luminescent elements represented in the case of actinides and lanthanides by U, Pa, Cm, Am, Eu, Dy, Tb, Sm, and Gd /MOU 01/.

The ATR FT-IR spectroscopy is a good tool to study solid/liquid interfacial phenomena *in situ* /HIN 01/. Thus, no altering of the sample is required resulting in more natural conditions. In addition, sorption processes on mineral surfaces can be studied in detail with ATR FT-IR /MÜL 13/ and /LEF 04/.

8.1 Experimental set-up

TRLFS was applied in case of uranium, which has excellent fluorescence properties. For this investigation, batch samples of the minerals with a grain size $< 63 \mu\text{m}$ and a M/V of 1/20 were prepared and pH values from 4 to 9 in 0.5 step size were adjusted. When the pH was stable, U(VI) was added to obtain a concentration of $10^{-5} \text{ mol L}^{-1}$. For each experiment two kinds of TRLFS samples were prepared. The first one is the supernatant, where the U(VI) species in solution could be investigated. The second is the mineral suspension. Therefore, the supernatant was separated from the mineral and the mineral was washed twice with 3 ml of deionized water (Milli-Q water with a resistivity of $18.2 \text{ M}\Omega \text{ cm}^{-1}$). The TRLFS-samples were filled into quartz glass tubes of 4 cm length and $4.35 \pm 0.2 \text{ mm}$ in diameter (outer one) and a wall thickness of $1 \pm 0.2 \text{ mm}$ (Quarzglasrohr Ilmasil PN, QSIL GmbH, Ilmenau, Germany) and were attached to a specifically designed sample holder, in principle a plastic rod as adapter for the sample. The samples were measured at room temperature as well as at cryogenic conditions (153 K), because

carbonate complexes can only be detected at low temperatures as described in /STE 11/. A gate width for luminescence detection of 0.5 ms was set. With a delay generator time-resolved spectra were recorded by measuring 31 spectra at delay times between 0.5 and 1319.4 μ s. The delay time setting was based on the formula: $0.1+x^4/700$ to create larger step sizes for the tailing of the time-resolved spectra, i. e. when the changes are smaller. At each delay time, the spectrum consists of an average of 50 measurements.

For investigating the influence of Ca^{2+} on the sorption of U(VI) one of the batch samples (orthoclase $<63 \mu\text{m}$ with $1.5 \cdot 10^{-3} \text{ mol L}^{-1}$ Ca and $10^{-5} \text{ mol L}^{-1}$ U(VI) at pH 4 to 9) were used in the same way as the samples described above. For characterization of the $\text{Ca}_2\text{UO}_2(\text{CO}_3)_3$ complex, measurements at cryogenic conditions were also performed as outlined above. Baseline corrected TRLFS data were stacked to a 3D data cube and deconvoluted with Parallel Factor Analysis (PARAFAC) from the N-way toolbox for Matlab /AND 00/. Recent applications providing more details on how PARAFAC can be utilized for spectroscopy are given in /DRO 15/ and /SAI 10/.

For complementary molecular information of U(VI) and Np(V) species on orthoclase and muscovite surfaces, ATR FT-IR spectroscopy was applied. Infrared spectra were measured from 1800 to 800 cm^{-1} on a Bruker Vertex 80/v vacuum spectrometer equipped with a Mercury cadmium telluride (MCT) detector at a spectral resolution of 4 cm^{-1} . Spectra were averaged over 256 scans. A horizontal diamond crystal with nine internal reflections (DURA SamplIR II, Smiths Inc.) was used. For the performance of *in situ* sorption experiments, a thin mineral film prepared directly on the surface of the ATR diamond crystal as stationary phase is required. Aliquots of $5 \mu\text{L}$ of 2.5 g L^{-1} suspensions of orthoclase and muscovite, respectively, were pipetted on the crystal and subsequently dried with a gentle stream of N_2 . This procedure was repeated for an average mass density per area of 0.08 mg cm^{-2} . The mineral film was conditioned by flushing with the blank solution (0.01 mol L^{-1} NaCl) for 60 min using a flow cell ($V = 200 \mu\text{L}$) at a rate of $100 \mu\text{L min}^{-1}$. Subsequently, the sorption reactions were induced by rinsing the mineral film with the U(VI) or Np(V) solution (0.01 mol L^{-1} NaCl) for 90 min. Finally, the loaded mineral phase was flushed again with the blank solution (30 min) to gain more information on the reversibility of the sorbed species.

8.2 Spectroscopic results

TRLFS:

Results of the TRLFS measurements at 274 K for orthoclase and muscovite indicated that samples with muscovite showed no signal for U(VI), and thus are not mentioned in the following. This most probably is due to a high iron content in the sample (4.47 wt% compared to 0.07 wt% in orthoclase) responsible for quenching /TAH 93/. Quenching of the U(VI) luminescence by carbonate /BAL 78/ restrains the observation of the luminescence spectra for $(\text{UO}_2)_2\text{CO}_3(\text{OH})_3^-$, $\text{UO}_2(\text{CO}_3)_2^{2-}$, and $\text{UO}_2(\text{CO}_3)_3^{4-}$ at room temperature, while only $\text{Ca}_2\text{UO}_2(\text{CO}_3)_3$ is still detectable /BER 96/. Thus, the solutions without Ca^{2+} , showed no U(VI) luminescence signals at higher pH values where the carbonate complexes are present. However, in presence of Ca^{2+} a luminescence signal could be observed that indicates the formation of $\text{Ca}_2\text{UO}_2(\text{CO}_3)_3$. In Fig. 8.1 its deconvoluted steady state emission spectrum in the presence of Ca^{2+} is shown. Six emission bands were identified at 464, 483, 503, 525, 550, and 577 nm, which are in very good agreement with the literature values for the $\text{Ca}_2\text{UO}_2(\text{CO}_3)_3(\text{aq})$ complex /KRA 12/, /SCH 14a/. The respective luminescence lifetime calculation indicated the presence of a single species with a lifetime of 80.3 ± 3.0 ns. This lifetime is longer compared to the ones of 39.5 ± 4 ns and 43 ± 12 ns by /SCH 14a/ and /BER 01/, but this is in accordance to the fact that these measurements were performed at 298 K. Thus, the measurement of the U(VI) speciation with TRLFS confirmed the speciation calculated with PhreeqC (digi. App. Sec. A.6, Fig. A. 31).

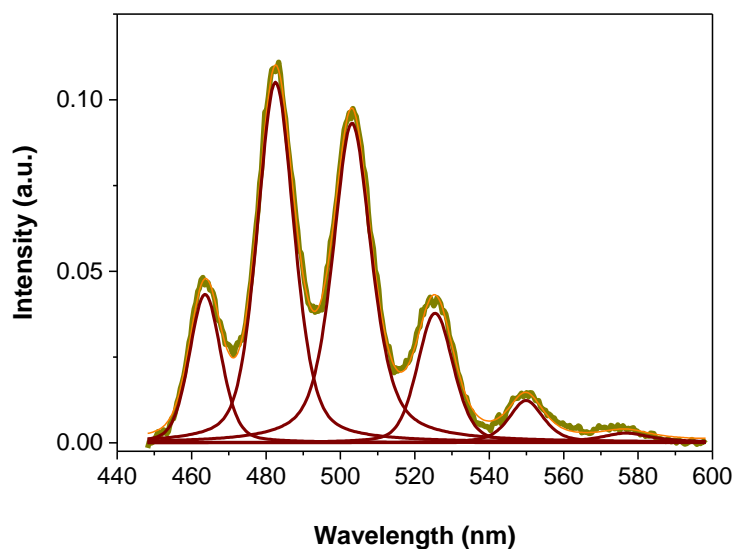


Fig. 8.1 Luminescence spectrum of aqueous U(VI) deconvoluted by PARAFAC analysis. ($[\text{U(VI)}] = 10^{-5} \text{ mol L}^{-1}$, $[\text{Ca}^{2+}] = 1.5 \cdot 10^{-3} \text{ mol L}^{-1}$, $[\text{NaClO}_4] = 0.01 \text{ mol L}^{-1}$, $T = 274 \text{ K}$)

Furthermore, with TRLSFS measurements at cryogenic temperatures ($-120^{\circ}\text{C} = 153\text{ K}$) the surface speciation of U(VI) on orthoclase and muscovite in the absence and presence of Ca^{2+} was identified. This lower temperature allowed for the detection of carbonate species as shown before. The obtained TRLSFS data were analyzed with Parallel factor analysis. For the sorption of U(VI) onto orthoclase in absence of Ca^{2+} , two species (A, B) were determined, whereas in presence of Ca^{2+} again two species (C, D) were observed. Fig. 8.2 shows the normalized intensity profiles of these species.

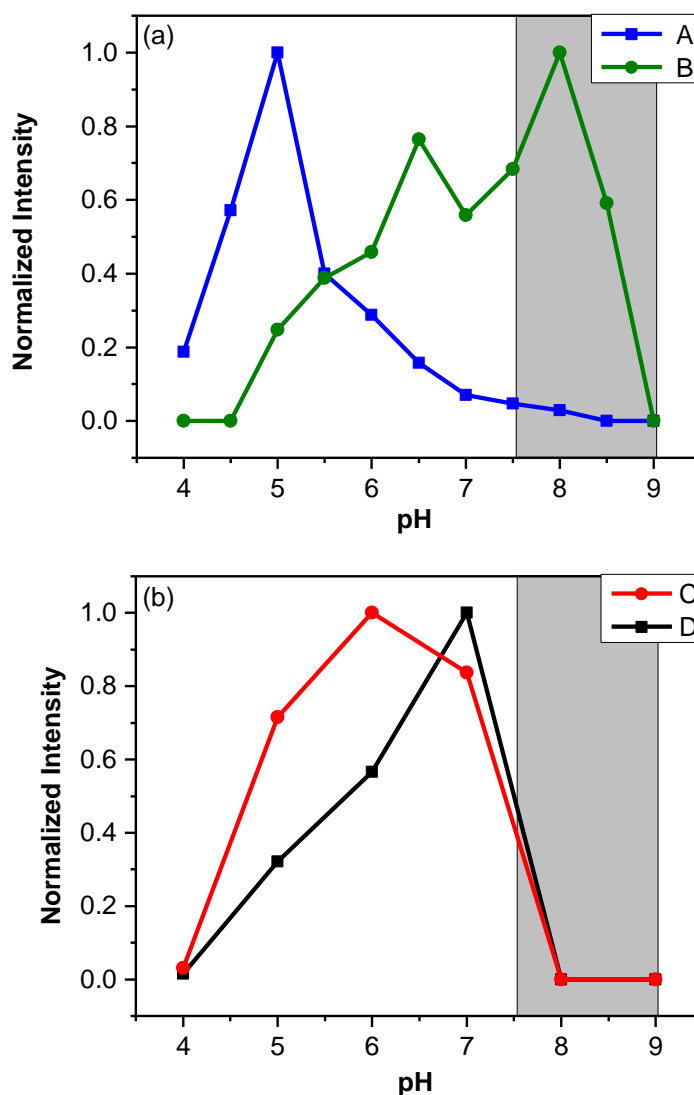


Fig. 8.2 Normalized intensity profiles of $10^{-5} \text{ mol L}^{-1}$ U(VI) sorbed onto orthoclase in $0.01 \text{ mol L}^{-1} \text{ NaClO}_4$ in the absence of Ca^{2+} referred to the amount of sorbed uranium (a) and in presence of $1.5 \cdot 10^{-3} \text{ mol L}^{-1} \text{ Ca}^{2+}$ (b). The capital letters in the plots indicate the species determined with PARAFAC and the grey region represents the area with most differences

In the acidic pH region, species A was the most prominent one, although at pH 7 it was undetectable. Species B dominates the alkaline pH range starting at pH 6. The results of the TRLFS measurements of U(VI) sorbed on orthoclase in presence of Ca^{2+} showed again a species that is dominant at lower pH values (C) and one that is more common over the whole pH range (D).

Experimentally obtained spectroscopic fingerprints, i. e., major peak maxima and luminescence lifetimes τ , were compared to previously published values and summarized in Tab. 8.1. There, the three mineral groups aluminosilicates, SiO_2 polymorphs, and Al-(hydr)oxides were considered. For aluminosilicates, direct spectroscopic results are published for uranyl ion sorption on montmorillonite /CHI 94/, /KOW 04/, albite /WAL 05/, or muscovite /ARN 06/. With respect to interactions of uranyl ions with silanol surface groups, there are a few papers related to respective TRLFS investigations on SiO_2 samples /GLI 98/, /GAB 01/, /BRE 05/. Various publications provide detailed spectroscopic information about UO_2^{2+} bound onto aluminol groups /BAU 05/, /WAN 05b/, /CHA 06/, /FRO 06/. However, the fluorescence parameters derived from these works differ significantly or are not sparsely given at all.

The most prominent Ca-induced effect in the U(VI) surface speciation on orthoclase was the absence of species B when Ca^{2+} is present in the system (grey area in Fig. 8.2). Species A and C, both occurring at lower pH values, had comparable positions of their emission bands indicating them to be the same surface complex. The peak positions indicated a $\equiv\text{SiO}_2\text{UO}_2\text{O}$ surface complex being in accordance with the results for SiO_2 . The same complex was also found to be dominating the sorption of U(VI) onto pure albite (Walter et al. 2005). Species D, occurring in presence of Ca^{2+} , is comparable to the $\equiv\text{SiO}_2\text{UO}_2\text{OH}^-$ surface complex described by /ILT 12/. Thus, the binding of U(VI) onto orthoclase tends to be through the SiO_2 sites of this mineral. Comparison of the peak position with aqueous U(VI)-carbonate species /WAN 04/ leads to the assumption that the species B is a U(VI)-carbonate surface complex, like $\equiv\text{SiO}_2\text{UO}_2\text{OHCO}_3^{3-}$ postulated by /GAB 01/ or $\equiv\text{XO UO}_2\text{CO}_3^-$ by /DAV 01/ onto quartz. The absence of species B when Ca^{2+} is present in the system is due to the formation of $\text{Ca}_2\text{UO}_2(\text{CO}_3)_3(\text{aq})$ in the solution that traps almost all the uranium preventing any significant formation of a U(VI)-carbonate surface species. This is also the reason for the drop of sorption at pH 8 observed in the batch experiments when Ca^{2+} is present.

Tab. 8.1 Luminescence decay lifetimes τ and main emission bands (peak maxima positions, rounded to full nm) for the species obtained from a series of TRLFS data of U(VI) sorbed on orthoclase compared to literature values

Surface species	Emission bands (nm)	τ (μ s)	T (K)	PARAFAC species or reference
$\equiv\text{SiO}_2\text{UO}_2^0$	490; 511; 535; 561	352 ± 4.2	153	A
$\equiv\text{SiO}_2\text{UO}_2\text{OHCO}_3^{3-}$	479; 500; 521; 544; 570	644 ± 6.6	153	B
$\equiv\text{SiO}_2\text{UO}_2^0$	494; 515; 538; 565	304.5 ± 2.6	153	C
$\equiv\text{SiO}_2\text{UO}_2\text{OH}^-$	481; 502; 523; 546; 573	334.7 ± 3.1	153	D
$\equiv\text{SiO}_2\text{UO}_2^0$	494 – 496; 514 – 516	-	4	/ILT 12/
	-	170 ± 25	RT	/GAB 01/
UO_2^{2+} on SiO_2	-	180 ± 20		/DRO 07/
$\equiv\text{SiO}_2\text{UO}_2\text{OH}^-$	501 – 503; 522 – 526	-	4	/ILT 12/
	-	360 ± 50	RT	/GAB 01/
$(\text{UO}_2)_x(\text{OH})_y^{(2x-y)+}$ on SiO_2	506; 528	400 ± 30	RT	/DRO 07/
UO_2^{2+} on Kaolinite	487; 501; 520; 542; 567	42.5 ± 3.3		/KRE 07/
$(\text{UO}_2)_x(\text{OH})_y^{(2x-y)+}$ on $\text{Al}(\text{OH})_3$	480; 497; 519; 542; 564; 586	5.6 ± 1.6	RT	/BAU 05/
UO_2^{2+} on $\text{Al}(\text{OH})_3$	499; 519	106 – 141 233 – 247	RT	/FRO 06/
Aquatic species				
$(\text{UO}_2)_2(\text{OH})_3\text{CO}_3^-$	523; 542.3; 561.3	144	4	/WAN 04/
$\text{UO}_2(\text{CO}_3)_3^{4-}$	480; 499; 520; 542; 566	883	6	/WAN 04/
	481; 500; 521; 544	887	153	/GÖT 11/
	480; 499; 520; 543; 566	820.4 ± 11.8	153	/STE 11/

In situ ATR FT-IR:

As a very useful tool for the investigation of reactions of heavy metals at the mineral-water interface ATR FT-IR spectroscopy was applied in this work /LEF 04/. The sensitivity of the UO_2 antisymmetric stretching mode ν_3 , which occurs at 961 cm^{-1} for the fully hydrated UO_2^{2+} , to changes in the coordination environment of the cation has previously been shown on different mineral oxide surfaces /MÜL 12/, /MÜL 13/, /SCH 14a/. For

evaluation of the U(VI) sorption process on orthoclase and muscovite, information on the distribution of the metal ion species in solution and on the surface is required. The ATR FT-IR spectrum of an aqueous 20 $\mu\text{mol L}^{-1}$ U(VI) solution in 0.1 mol L^{-1} NaCl at pH 5.5 showed the ν_3 mode of the U(VI) moiety 923 cm^{-1} (Fig. 8.4, green trace) /MÜL 08/. This spectrum of U(VI) hydrolysis serves as a reference for the evaluation of the surface complex. In general, coordination of aqueous UO_2^{2+} ions on surfaces reduces the force constants of the O=U=O bonds. Thus, a displacement of water molecules from the first shell lowers the frequency of the ν_3 (UO_2) stretching mode and the extent of this shift correlates with the type of surface bonding and coordination. Chemical bonding, namely the formation of inner-sphere sorption complexes results in a considerable red-shift of $\nu_3(\text{UO}_2)$. In contrast, physical interaction, i. e., outer-sphere complexation, reveals only very small $\nu_3(\text{UO}_2)$ shifts because of the remaining intact first hydration sphere /LEF 04/.

The time-resolved infrared spectra obtained during conditioning, sorption, and flushing steps of *in situ* U(VI) sorption experiments onto orthoclase (A) and muscovite (B) are illustrated in Fig. 8.3. The spectra of the conditioning (red traces) indicated stable stationary phases of orthoclase (A) and muscovite (B) due to no significant bands, which is indispensable for the detection of sorbed species during the following sorption process. The ATR FT-IR difference spectra calculated between the conditioning and at several time steps after induction of U(VI) sorption are shown as black traces. Absorption bands with maxima at 982 and 917 cm^{-1} can be observed. The intensities of these bands increased with time of sorption because of U(VI) accumulation on the mineral surfaces. The forming U(VI) surface structures seem to be very similar for both minerals. Compared to the aqueous solution reference spectrum (Fig. 8.4, green trace) a very small shift of the ν_3 mode of the U(VI) moiety by 6 cm^{-1} due to U(VI) sorption occurs. The sorption process seems to be confirmed by the band at 982 cm^{-1} , this band is absent in the spectrum of the aqueous solution and can be assigned to surface modes that undergo significant alterations during the sorption reactions. After sorption, the U(VI) loaded mineral films were flushed again with blank solution. The obtained difference spectrum (blue trace) shows negative bands at equal frequencies to those observed during the sorption stage. This represents desorbed uranium complexes released from the orthoclase and muscovite film by the flushing. It indicated that the sorbed U(VI) species is only weakly bound to the surface and can be easily released. This is in accordance with previous observations of outer-sphere sorption complexes /JOR 11/, /MÜL 12/.

As consequence of the only small shift of the ν_3 mode of the U(VI) surface structures, similar complex structures in solution and at the interface, i. e., the formation of outer-sphere complexes, can be assumed as prior also shown by the influence of the ionic strength (Sec. 7.4.3).

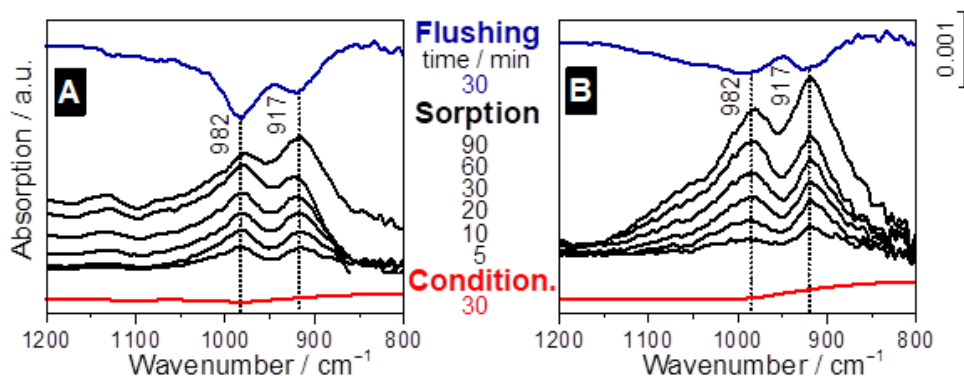


Fig. 8.3 *In situ* time-resolved ATR FT-IR spectra of U(VI) sorption on orthoclase (A) and muscovite (B) ($20 \mu\text{mol L}^{-1}$ U(VI), 0.01 mol L^{-1} NaCl, pH 6, air, 0.08 mg cm^{-2}). The spectra of the conditioning, sorption, and flushing processes are recorded at different times as given (from bottom to top). For more details, the reader is referred to the text. Indicated values are in cm^{-1}

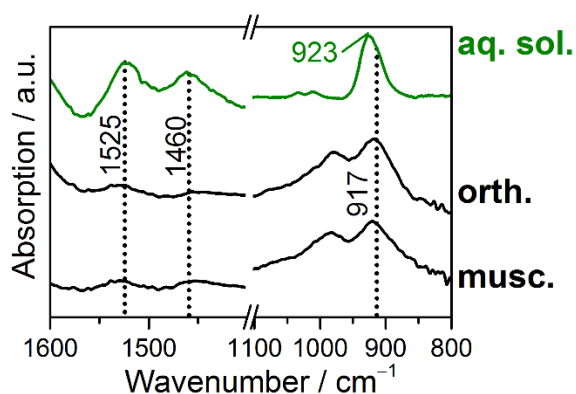


Fig. 8.4 Comparison of ATR FT-IR spectra of U(VI) aqueous solution ($20 \mu\text{mol L}^{-1}$ U(VI), 0.1 mol L^{-1} NaCl, pH 5.6) and U(VI) surface complex on orthoclase and muscovite ($20 \mu\text{mol L}^{-1}$ U(VI), 0.01 mol L^{-1} NaCl, pH 6)

The assignment of ν_3 peak positions is in accordance with the findings from a previous study of U(VI) sorption onto anatase (TiO_2) where two different U(VI) surface species could be identified: one inner-sphere complex with ν_3 at 895 cm^{-1} occurring at low coverage and one outer-sphere complex with ν_3 at 917 cm^{-1} dominating the U(VI) speciation

at high surface coverage [MÜL 12]. At higher frequencies, the slight appearance of intrinsic bands at 1525 and 1460 cm^{-1} may provide further evidence of the presence of the hydroxide complex from solution that can physically interact with the surface.

Neptunium has also been studied by ATR FT-IR to get a closer look on the surface. ATR FT-IR spectra were recorded at different pH values (6 and 9.6). Due to the low loading of the mineral film with Np(V) spectra were recorded wherefrom no information to the bonding mechanism would be possible to discern. Thus, this method was not useful for the investigation of the sorption of neptunium onto orthoclase and muscovite under the investigated conditions.

9 Column experiments

Column experiments were carried out with pure muscovite, orthoclase, quartz mineral phases as introduced in Section 5 and a natural Sediment. Only for Eu column experiments a synthetic sediment composed of 10 wt% muscovite, 10 wt% orthoclase, 80 wt% quartz and a natural sediment were used. The mineral distribution of the synthetic sediment was based on /NOS 12b/ and represented a simplified composition of the sediment found at the Gorleben site in Northern Germany. The natural sediment was obtained from flush drillings at the Gorleben site carried out between 1979 and 1998. Grain sizes and SSA_{BET} of mineral samples are reported in Tab. 5.1. In the following section, the experimental set-up of column experiments and collected results are described in detail. Section 11.1 offers information on data processing of experimental transport measurements, Section A.8.1 in the digital appendix provides information on preconditioning of mineral samples for column experiments. The digital appendix Section A.5.4 supplies further information on equipment, techniques, chemicals, and supplementary data, respectively.

9.1 Experimental set-up

A new column design was developed (Fig. 9.1, cf. /BRI 18/) where all components could be easily screwed together. Great attention was paid to recovery rates: Columns, column tubing, and tube connectors were composed of perfluoroalkoxy alkane polymers (PFA); pump tubing was composed of Fluran®; frits were made of sintered polytetrafluoroethylene (PTFE) with a mean pore diameter of 10 μm . Sealing rings framed each frit and were also composed of PTFE (Fig. 9.1, cf. /BRI 18/). The materials PFA and PTFE are highly inert towards almost all chemicals with only some exceptions and were therefore used to prevent potential sorption on containing walls.

Columns were homogeneously dry-packed with preconditioned muscovite or orthoclase samples, and untreated quartz and natural sediment samples. Homogeneity was reached with a stepwise packing procedure: Within five steps equal amounts of solid were tightly compacted in each column (122.5 mm in length, 41 mm in diameter) to ensure uniform bulk densities and homogeneous hydrodynamic properties. After packing, columns were filled with degassed background electrolyte under vacuum conditions. Vacuum conditions reduced the possibility of air intrusions in the columns during flooding and prevented the formation of preferential flow paths.

Geochemical equilibrium with background electrolytes (NaClO_4 , Na_2SO_4 , and/or an artificial groundwater; Tab. 9.1 – Tab. 9.3, and cf. digi. App. Tab. A. 8) was achieved during the first days to weeks of the column experiment before the pulse solution was added. An equilibrated column system was characterized by $\text{pH}_{\text{equil}} \approx \text{pH}_{\text{ini}}$ (effluent pH = influent pH) and by a steady effluent composition (ICP-MS, ICP-OES analyses). The term background electrolyte (BE) describes the influent; pH adjustment of the influent took place via the addition of appropriate amounts of HNO_3 , NaOH , and HClO_4 ; for Ni column experiments for $\text{pH}_{\text{ini}} > 7$ NaHCO_3 salt was used, otherwise no buffer was used. Background electrolytes were kept in lightproof containers and were renewed approximately every two to four days to prevent major algae growth. After equilibrium was reached in the columns a pulse input of Eu or Ni and NaBr took place (pulse/peak solution). The NaBr served as an ideal, conservative tracer to characterize hydraulic transport parameters of each experiment. For each experiment ≈ 1.5 pore volumes (PVs [V/V_0]) of pulse solution (PS) were injected into the columns. The PS contained $10^{-5} \text{ mol L}^{-1}$ Eu or Ni and $10^{-5} \text{ mol L}^{-1}$ NaBr in the respective BE for each transport experiment.

A constant flow rate of $\approx 0.3 \text{ cm}^3 \text{ min}^{-1}$ (steady state flow conditions) was ensured during the experiments via a peristaltic pump from the bottom of each column through the system (Fig. 9.1). The initial pH (pH_{ini}) of background electrolytes was also kept constant with pH_{ini} ranging between 3.5 and 7.4. The flow rates were gravimetrically verified and the pH was measured periodically. The flow rate was slow enough to reach equilibrium between the electrolyte and the mineral surface and resulted in feasible experimental time frames ranging between 1.1 and 37 d (Tab. 9.1 – Tab. 9.3). The effluent was sampled every 13 minutes and used for pH measurements as well as ICP-MS analysis for Eu, Ni, and Br. Experimental set-up was realized under ambient conditions (Fig. 9.1).

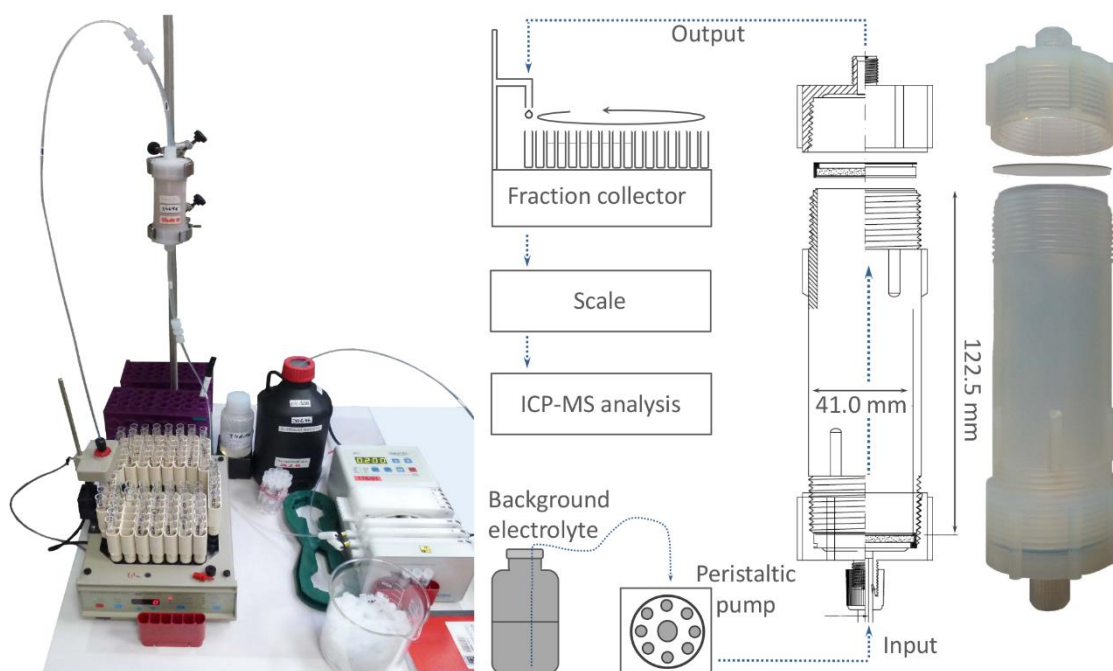


Fig. 9.1 Experimental set-up of column experiments

Background electrolyte stored in lightproof containers, column, tubing, tube connectors made from PFA, frits and sealing rings composed of PTFE. Frits and sealing rings were situated at both ends of the column.

Column experiments returned Eu, Ni spatial distributions (SDs) and/or Eu, Ni, Br breakthrough curves (BTCs). The BTCs were collected in the effluent of each column with a time increment of 13 minutes (fraction collector). For SDs the body of each column was separated into 24 equally spaced samples. Mineral samples were dried at 378 K overnight and were subsequently suspended in 5 % and 2 % HNO_3 to remobilize sorbed Eu and Ni from the mineral surfaces, respectively. Suspensions were filtered with 0.2 μm syringe filters and analyzed via ICP-MS for Eu and Ni.

After each experiment the empty column system (columns, frits, tubing) was leached with 5 % and 2 % HNO_3 to remobilize potentially sorbed Eu or Ni from containing walls. Samples were analyzed via ICP-MS for residual Eu and Ni. Recovery rates were calculated for each column experiment and represented the sum of Eu, Ni from BTCs and/or SDs and leached column systems. Eu background concentration of the minerals was negligible (Sec. 5) and not included in recovery rate calculations. Raw data of Ni SDs were corrected for the Ni background concentrations of the minerals and included in recovery rate calculations.

9.2 Results of europium(III) transport experiments

A large amount of column experiments were conducted during this study (Tab. 9.1), hence, easy handling of columns and experimental set-up was of decisive interest. Tab. 9.1 shows the experimental matrix of Eu column experiments with boundary conditions. Varying geochemical conditions were used to characterize Eu transport:

- The NaClO_4 solution was applied as an inert background electrolyte to show sorption behavior of Eu without the influence of the background electrolyte.
- Sulfate (SO_4^{2-}) is a constituent of the natural groundwater at the Gorleben study site /NOS 12a/, /KLI 02b/; hence, the Na_2SO_4 background electrolyte represented the influence of sulfate ligands on Eu solution speciation and surface complexation.
- The artificial groundwater was used as a background electrolyte to simulate geochemical conditions as close to nature as possible and showed the influence of SO_4^{2-} as well as competing cations on surface complexation and solution speciation. A detailed composition of the artificial groundwater is provided in the digital appendix Tab. A. 8.

Typical pH values of the Gorleben groundwater range between pH 6 – 8 /KLI 02b/. Considering batch results (Sec. 7.8) Eu had been completely immobilized at $\text{pH} \geq 7$ regarding all systems (Fig. 7.23). Hence, to design a feasible experimental set-up for transport experiments with manageable experimental time frames pH_{ini} had to be reduced compared to natural pH conditions. Therefore, taking batch results into account $\text{pH}_{\text{ini}} = 3.5$ and $\text{pH}_{\text{ini}} = 5.5$ were used for column experiments.

Tab. 9.1 Summary of quartz (Q), orthoclase (FS), muscovite (mica), synthetic sediment (SynSed), and natural sediment (NatSed) column experiments including geochemical conditions

Flow rates equaled 0.3 ml min^{-1} , except for [1] where flow rates were reduced to $\approx 0.1 \text{ ml min}^{-1}$. All experiments were carried out in duplicate, except for [2] which represent single experiments, 1.5 PVs of the peak solution were used for the pulse input of Eu, $\text{Br} = 10^{-5} \text{ mol L}^{-1}$. Tab. A. 8 in the digital appendix provides the composition of the artificial groundwater. The synthetic sediment was composed of 80 % quartz, and 10 % orthoclase and muscovite, respectively. The initial pH of the influent (background electrolyte) is

symbolized by pH_{ini}, ID stands for the identification/name of the column experiment, exp. time frame for the experimental time frame [d].

Solid	ID	pH _{ini}	Exp. time frame [d]	Background electrolyte
Quartz	Q-i	3.5	12	10 mmol L ⁻¹ NaClO ₄
	Q-ii	5.6	11	10 mmol L ⁻¹ NaClO ₄
	Q-iii	5.6	12	5 mmol L ⁻¹ Na ₂ SO ₄
	Q-iv	5.5	12	50 mmol L ⁻¹ Na ₂ SO ₄
	Q-v	5.5	12	art. groundwater
	Q-v	5.5	37[1]	5 mmol L ⁻¹ Na ₂ SO ₄
Orthoclase	FS-i	3.6	18	10 mmol L ⁻¹ NaClO ₄
	FS-ii	3.5	8	50 mmol L ⁻¹ Na ₂ SO ₄
	FS-iii	5.5	10	50 mmol L ⁻¹ Na ₂ SO ₄
Mica	mica-i	3.6	14 ^[2]	10 mmol L ⁻¹ NaClO ₄
	mica-ii	3.6	22	50 mmol L ⁻¹ Na ₂ SO ₄
	mica-iii	5.5	23 ^[2]	50 mmol L ⁻¹ Na ₂ SO ₄
	mica-iv	5.5	23 ^[2]	art. groundwater
Synthetic sediment	SynSed	3.5	18	0.01 mol L ⁻¹ NaClO ₄
Natural sediment	NatSed	3.5	18	0.01 mol L ⁻¹ NaClO ₄

9.2.1 Eu(III) transport experiments with muscovite, orthoclase, and quartz

All column results revealed a consistent and sound picture of Eu migration which matched sorption tendencies observed with batch experiments well: For quartz Eu showed lowest retardation compared to orthoclase and muscovite; the retention in the synthetic sediment column was mainly governed by the mica mineral. Interrelations between Eu surface complexation and the pH could be observed; sulfate solution complexation reactions with Eu resulted in expected enhanced migration of the trivalent lanthanide; and cations in the artificial groundwater (e. g. Ca²⁺, Mg²⁺, Al³⁺, etc.) posed competition on Eu surface complexation which also limited Eu retardation and triggered faster transport processes. Details are provided in /BRI 18/. A compilation of experimental data is shown in Section 11 in combination with results of reactive transport models.

Exemplarily, Fig. 3.1 shows Eu transport through muscovite, orthoclase, and quartz under the influence of 50 mmol L⁻¹ Na₂SO₄. As expected, Eu traveled fastest through the

quartz column; the highest retardation was measured for Eu transport through muscovite.

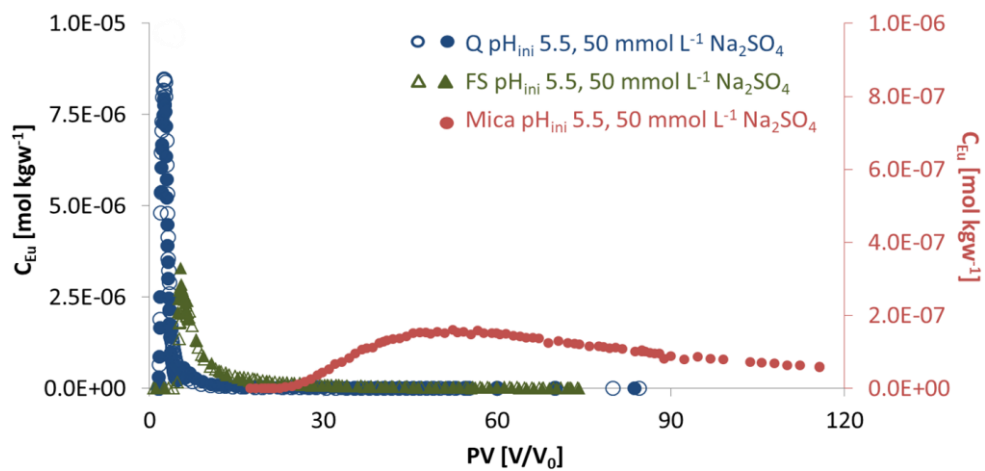


Fig. 9.2 Eu transport through quartz (Q-iv, blue), orthoclase (FS-iii, green), and muscovite (mica-iii, red) with $50 \text{ mmol L}^{-1} \text{ Na}_2\text{SO}_4$ background electrolyte, $\text{pH}_{ini} = 5.5$

Feldspar and quartz column experiments carried out in doublets (solid and empty characters). See /BRI 18/ for detailed information. C_{Eu} – Eu concentration (aq), PV – pore volume.

9.2.2 Eu(III) transport through a synthetic and natural sediment

Fig. 9.3 compares Eu transport through quartz, orthoclase, the synthetic sediment and the natural sediment. Experiments were carried out under identical geochemical conditions. It is shown that highest retardation was observed for the natural sediment. Europium sorption tendencies also returned higher affinities towards the natural sediment compared to the synthetic one which could be due to organic influences or different mineral and/or grain size distribution in terms of the natural sediment. A comparison of column experiment mica-i and the natural sediment (data not displayed here) revealed that Eu was highest retarded in the muscovite column where the entire element concentration was immobilized in the first cm of the column, with a maximum peak concentration of $1.7 \cdot 10^{-4} \text{ mol solid}^{-1}$ after 14 d experimental time frame.

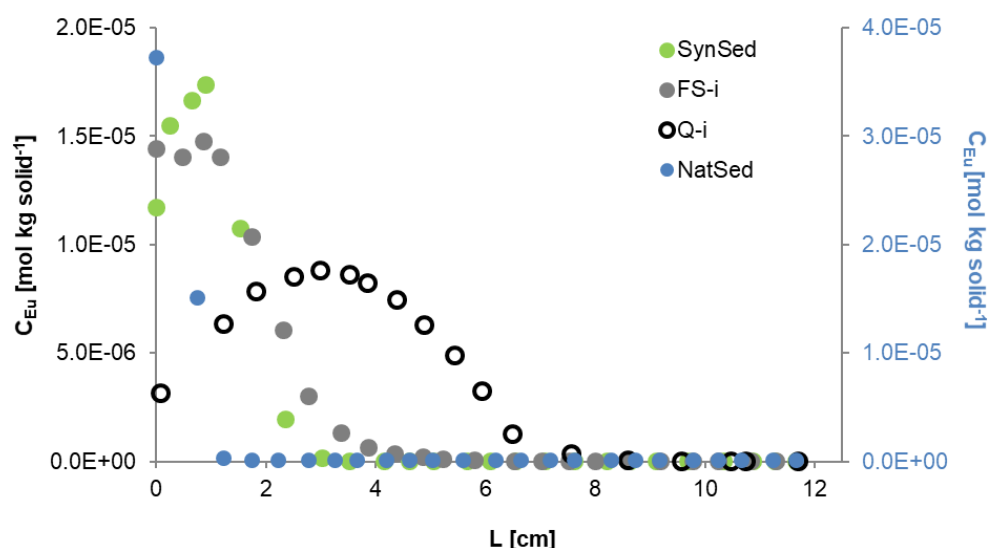


Fig. 9.3 Eu transport through a synthetic sediment (SynSed, green) and natural sediment (NatSed, blue) with $10 \text{ mmol L}^{-1} \text{ NaClO}_4$, $\text{pH} \approx 3.5$

For comparison reasons SDs of orthoclase (FS-i) and quartz (Q-i) are illustrated (cf. Tab. 9.1). C_{Eu} – Eu concentration (aq), L [cm] – column length, L = 0 cm column inlet, L = 12.25 cm column outlet.

9.3 Results of uranium(VI) transport experiments and U(VI) surface complex identification

It was the aim to develop a method to identify Eu surface complexes on different mineral surface or e. g. sediments. Therefore, a combination of column experiments, TRLFS (time resolved laser induced fluorescence) and CLSM (confocal laser scanning microscopy) measurements was used to collect data to identify surface complexes under varying geochemical conditions. The method was qualified with transport experiments of U(VI) through quartz columns. Uranium(VI) was used since surface complexation reactions on quartz have been thoroughly evaluated with spectroscopic means in the past.

9.3.1.1 In-situ surface complex identification

The experimental procedure involves classic column experiments (Sec. 9.1) to collect transport data of U(VI) under defined geochemical conditions. It was the aim to collect spatial distributions (SDs) of U(VI) in the quartz columns. Once, the experiments were stopped (before U(VI) was detected in the effluent of the column), SDs were fixed (conserved) with liquid nitrogen in the columns. The solidified columns were separated into equally spaced slices of 0.5 – 1 cm widths. The samples were analyzed via TRLFS and CLSM to identify U(VI) surface complexes. Fig. 9.4 offers a schematic overview of the

developed method. In future this method is supposed to be adapted for Eu(III) surface complexation analyses.

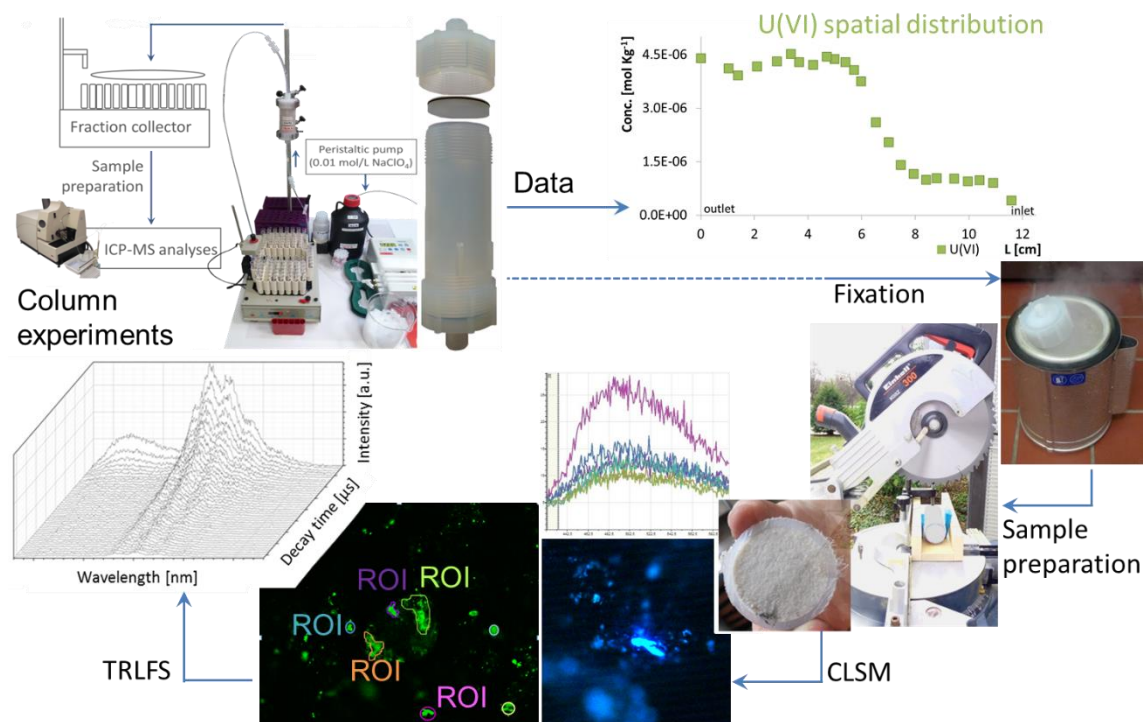


Fig. 9.4 Schematic overview of the developed method: Steps to be followed to identify U(VI) surface complexes via CLSM and TRLFS measurements

CLSM – confocal laser scanning microscopy, TRLFS – time resolved laser induced fluorescence, ROI – regions of interest

More detailed information regarding experimental set-up of column experiments is given in Section 9.1. The development of the method, analysis, and results are described in detail in /SCH 14b/.

9.3.1.2 Identification of U(VI) surface complexes

The identification of U(VI) surface complexes was subdivided in two parts. First, preliminary trials were performed to get first impressions of the experimental system (digi. App. Sec. A.9). Then, main laboratory experiments were carried out to identify U(VI) surface complexes and to, hence, qualify the developed method (Sec. 9.3.1.1).

Main column experiments were carried out as described in Sections 9.1 and 9.3.1.1 (Fig. 9.1 and Fig. 9.4). Fig. 9.5 illustrates U(VI) SD in the quartz column. According to this experiment, the highest U(VI) concentrations were expected within 0 – 6 cm (0 cm outlet,

12 cm inlet of the column). Shaded rectangles indicate samples that were analyzed via CLSM and TRLFS (Fig. 9.5).

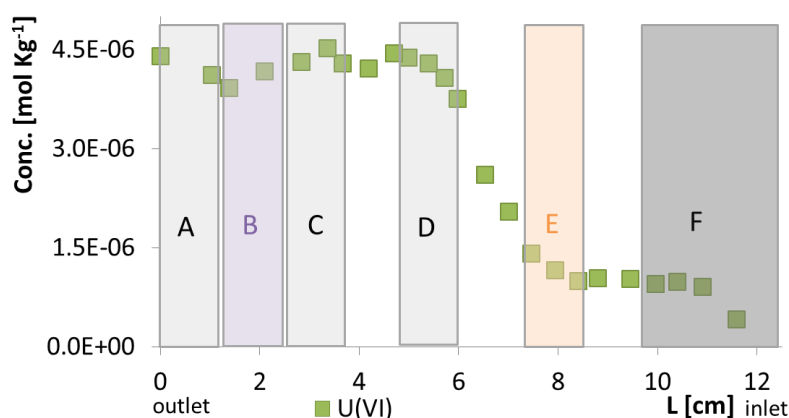


Fig. 9.5 U(VI) spatial distribution on quartz (G20 EAS extra), shaded rectangles indicate sample position for CLSM, TRLFS analysis

Experiment U(VI) on quartz was stopped after 24 h ($\text{pH}_{\text{ini}} 4.9$, 10 mmol NaClO_4), 36.2 % of the injected U(VI) has left the column after 24 h, recovery rate U(VI) 99.8 %. 0 cm, slice A stands for the outlet of the column where fractions are collected. 12 cm, slice F stands for the inlet of the column

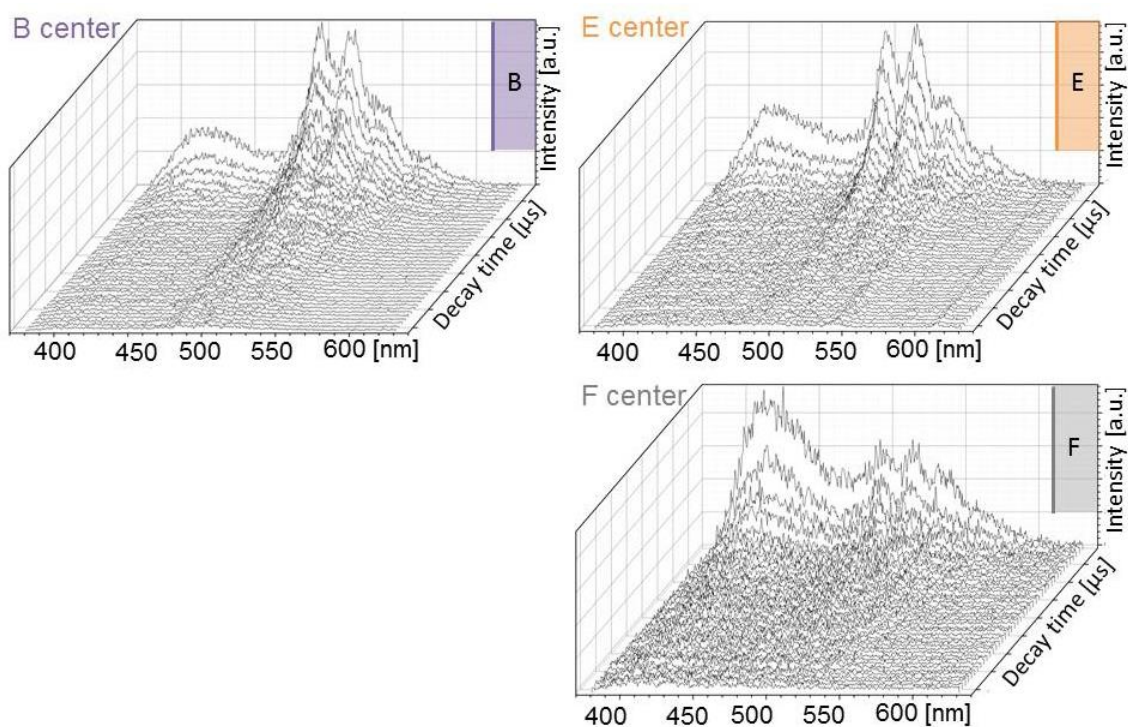


Fig. 9.6 TRLFS spectra of the top side of quartz column samples B, E, F (Fig. 9.5), measurements carried out in the center of each sample, inlet of the column sample F, outlet sample A. Geochemical conditions of column experiments: $\text{pH}_{\text{ini}} 4.9$, 10 mmol NaClO_4 , ambient conditions

Typical U(VI) surface complex peaks are found between 490 and 550 nm ($\equiv\text{SiO}_2\text{UO}_2^0$). Peak between 400 and 480 nm was an interfering signal and may originate from organic matter or abrasion of PFA column walls, increasing noise with decreasing U(VI) concentration in the column (Fig. 9.5)

Analysis with CLSM clearly showed that U(IV) surface complexes could be evidenced in the samples (data not shown here, cf. /SCH 14b/). Further refinement of CLSM measurements would be necessary to be able to make clear statements about the location of the surface complex and whether the measured fluorescence originates from surface complexes or e. g. precipitates.

Fig. 9.6 summarizes major findings of TRLFS analysis: Spectra show that the higher the sorbed U(VI) fraction, the better and clearer the collected signals. Furthermore, fluorescence spectra and measurements of decay times clearly identify two surface complexes: $\equiv\text{SiO}_2\text{UO}_2^0$ and $\equiv\text{SiO}_2\text{UO}_2\text{OH}^-$. Both complexes are strongly pH dependent /GAB 01/. Due to U(VI) surface complexation a small pH shift occurred in the column, which resulted in the formation of these two complexes on the mineral's surface. Hence, measurements clearly proved that via CLSM and TRLFS measurements it was possible to identify U(VI) surface complexes. Moreover, changes in geochemical conditions cause changes regarding the formation of U(VI) surface complexes which was also depicted with the newly developed method.

To make similar statements concerning Eu(III) surface complexes the introduced method needs adaptation to the trivalent lanthanide.

9.4 Results of nickel(II) transport experiments

Selected geochemical conditions in Ni column experiments were based on batch experiments (Sec. 7.9). In all experiments a $0.01 \text{ mol L}^{-1} \text{ NaClO}_4$ background solution was injected. The NaClO_4 solution was applied as an inert background electrolyte to show sorption behavior of Ni without the influence of the background electrolyte. For studying the transport behavior of Ni in quartz columns pH 5.0 and pH 7.3 were chosen since batch experiments (Sec. 7.9.1) showed huge differences in sorption affinity between these pH values. Concerning orthoclase columns pH 5.8 and pH 7.4 were used for same reasons (cf. Sec. 7.9.2). All column experiments were conducted in duplicate.

9.4.1 System Ni(II)-quartz

As intended, the Br⁻ breakthrough curves of all experiments (Fig. 9.7, Fig. 9.8) show the typical characteristics of a tracer: a sharp increase in Br⁻ concentration after 1 PV, a plateau lasting additional 1.5 PV (volume of pulse solution) and afterwards a sharp decrease in concentration. In both cases pH 5.0 and pH 7.3 the results are reproducible. An overview about the experimental attributes including some soil physics of each quartz column is listed in Tab. 9.2.

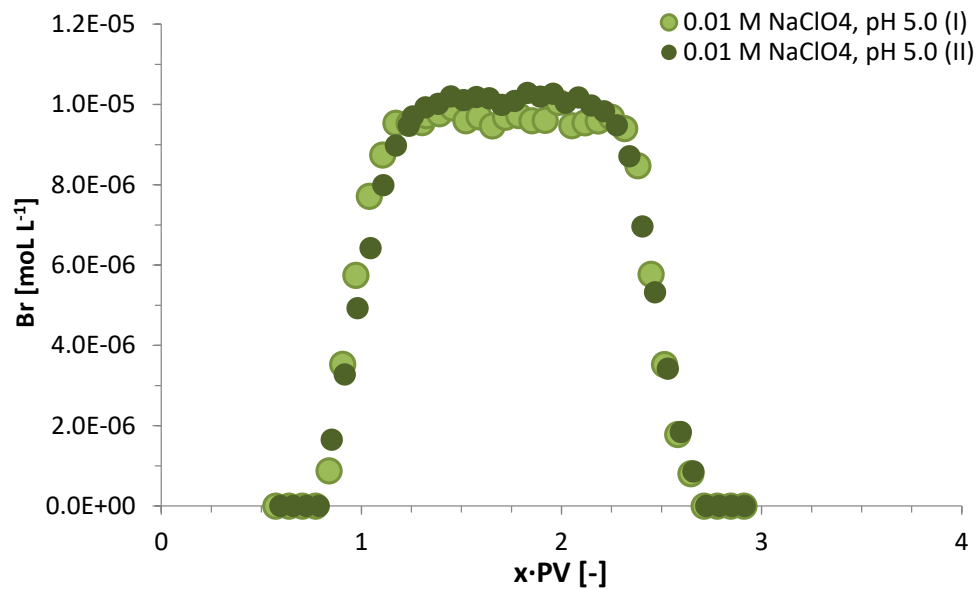


Fig. 9.7 Br⁻ tracer breakthrough curves of quartz columns: pH 5.0, 0.01 mol L⁻¹ NaClO₄

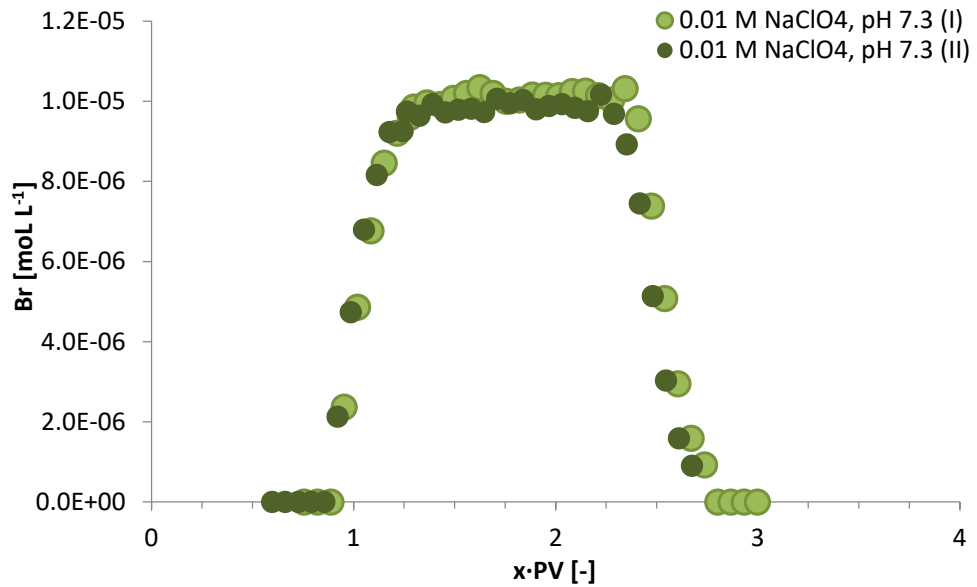


Fig. 9.8 Br tracer breakthrough curves of quartz columns: pH 7.3, 0.01 mol L⁻¹ NaClO₄

Retardation results of Ni (Fig. 9.9, Fig. 9.10) are plausible and reproducible as well. As expected, at pH 5.0 the retardation of Ni is very low compared to pH 7.3. At pH 5.0 Ni starts to be released after approx. 2.5 PV. In contrast Ni is still retarded in the column at pH 7.3 after ~ 20 PV flowed through the column. The results conform to the batch data (Fig. 7.26).

Tab. 9.2 Overview of experimental details concerning quartz columns with Ni

Column number/replicate	(I)	(II)	(I)	(II)
Background solution	0.01 mol L ⁻¹ NaClO ₄			
pH	5.0		7.3	
Duration [d]	4.0	4.0	2.9	2.9
Recovery rate [%]: Ni, Br	113, 95	95, 100	96, 95	98,92
PV [ml]	59.3	58.9	58.9	59.0
Bulk density [g cm ⁻³]	1.68	1.68	1.69	1.68
Flow velocity tracer [ml min ⁻¹]	0.303	0.289	0.297	0.290
Flow velocity overall [ml min ⁻¹]	0.302	0.289	0.295	0.289
SD (overall) [ml min ⁻¹]	0.003	0.009	0.008	0.007
Total applied·PV [-]	29.2	28.1	20.7	20.3

In case of the pH 5.0 columns a short decrease of pH was observed at the same time as the concentration of Ni rise in the collected fractions (Fig. 9.9). This was observed due to sorption of Ni onto quartz. In case of the columns at pH 7.3 the pH remained stable over the whole time (not shown here).

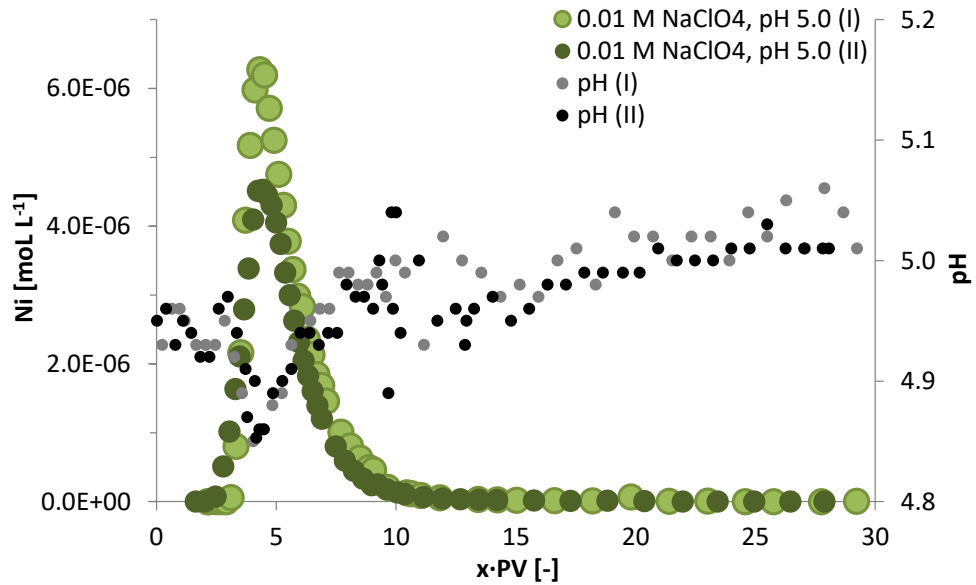


Fig. 9.9 Ni breakthrough curve of quartz columns: pH 5.0, 0.01 mol L⁻¹ NaClO₄

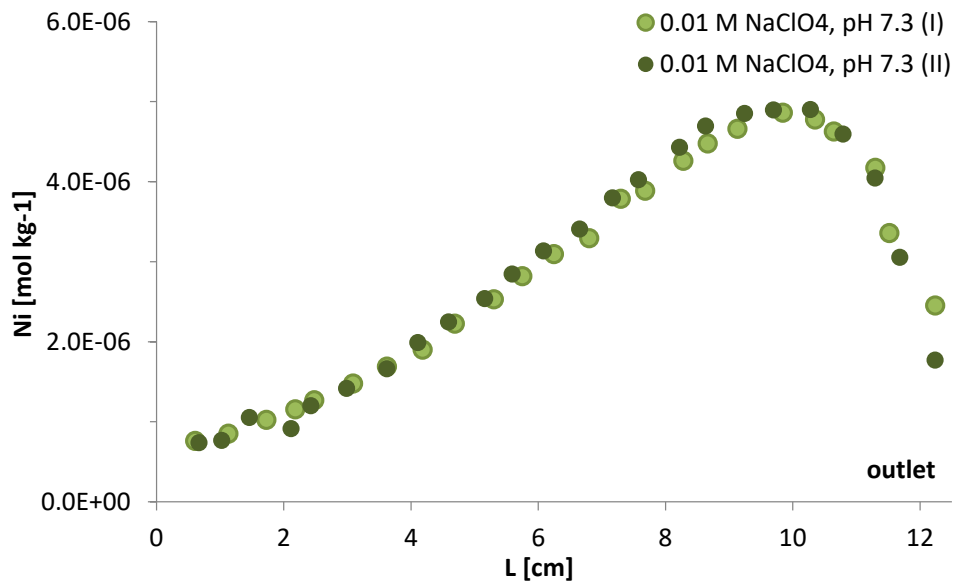


Fig. 9.10 Ni spatial distribution of quartz columns: pH 7.3, 0.01 mol L⁻¹ NaClO₄

Abscissa labeling: 12.25 cm stands for the outlet of the column where fractions are collected (Fig. 9.1). 0 cm stands for the inlet of the column. Experiments were stopped after approx. 20 PV flowed through the column.

9.4.2 System Ni(II)-orthoclase

Br⁻ breakthrough curves of all experiments (Fig. 9.11, Fig. 9.12) show again the typical characteristics of a tracer: a sharp increase in Br⁻ concentration after 1 PV, a plateau lasting additional 1.5 PV and afterwards a sharp decrease in concentration. In both cases at pH 5.8 and pH 7.4 the results are reproducible. Applied geochemical conditions and soil physics of all column experiments are summarized in Tab. 9.3. Recovery rates of Ni are not as precise as in case of Br because of raw data correction. Correction was necessary since Ni was released by orthoclase while treatment with 2 % HNO₃ for 24 h to perform spatial distributions (Sec. 9.1).

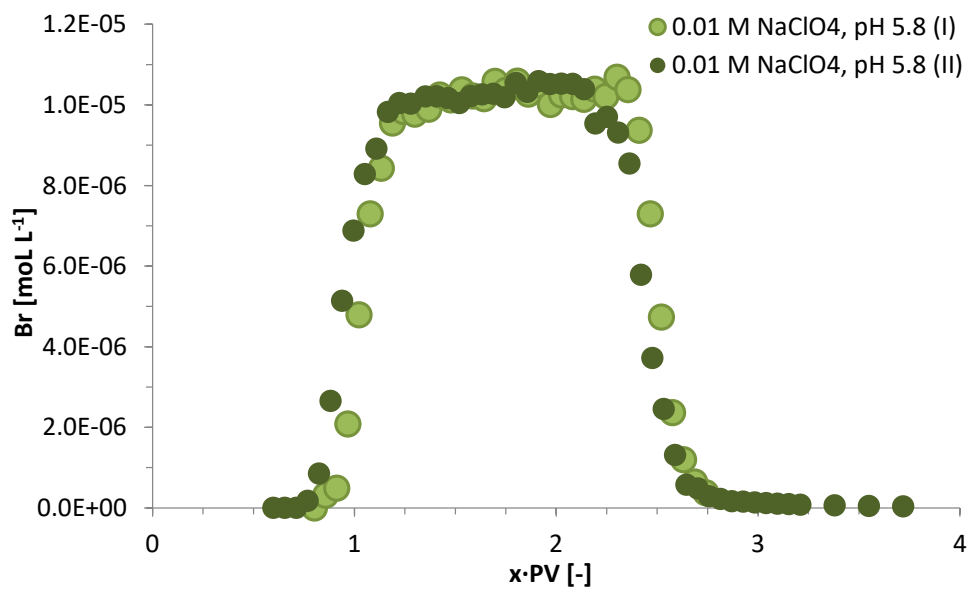


Fig. 9.11 Br⁻ tracer breakthrough curves of orthoclase columns: pH 5.8, 0.01 mol L⁻¹ NaClO₄.

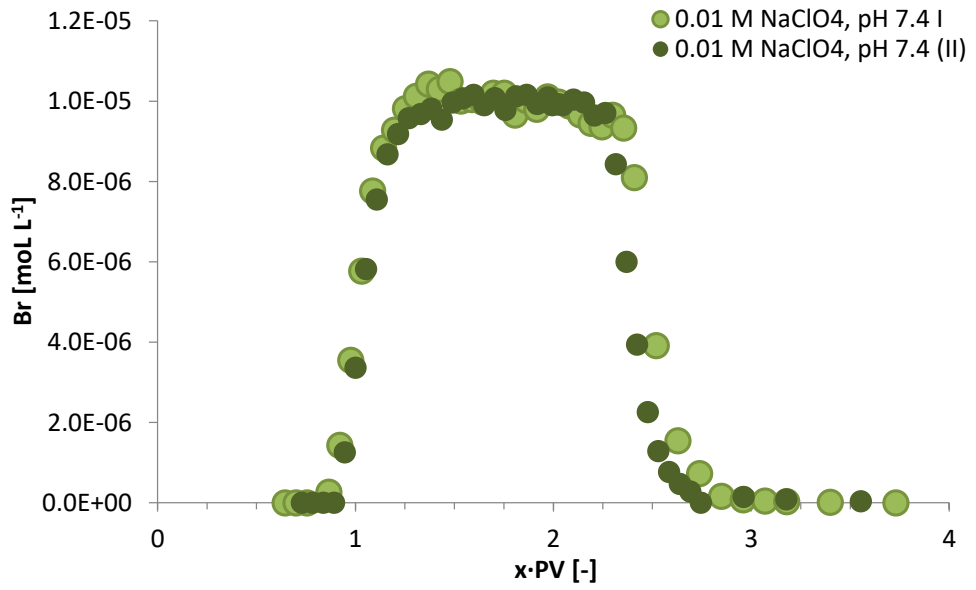


Fig. 9.12 Br⁻ tracer breakthrough curves of orthoclase columns: pH 7.4, 0.01 mol L⁻¹ NaClO₄

Retardation results of Ni (Fig. 9.13, Fig. 9.14) are plausible and reproducible as well. At pH 5.8 and pH 7.4 experiments were stopped after ~ 6 and 23 PVs were flown through the columns, respectively (Tab. 9.3). Taking this into account the retardation of Ni at pH 7.4 is approx. 8 times higher than at pH 5.8. Under both geochemical conditions pH values were stable over the whole experimental time (data not shown here).

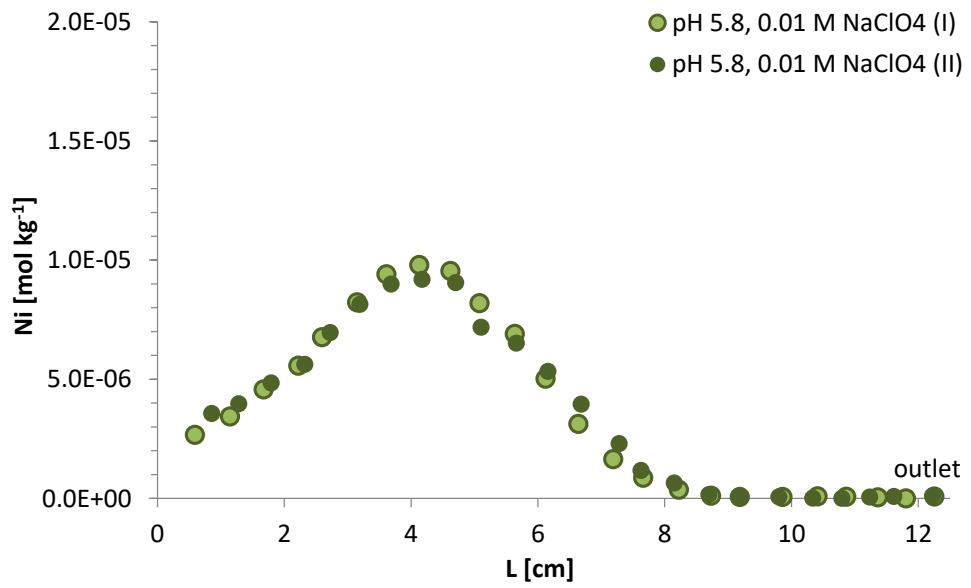


Fig. 9.13 Ni spatial distribution of orthoclase columns: pH 5.8, 0.01 mol L⁻¹ NaClO₄

Abscissa labeling: 12.25 cm stands for the outlet of the column where fractions are collected (Fig. 9.1). 0 cm stands for the inlet of the column. Experiments were stopped after approx. 6 PV flowed through the column.

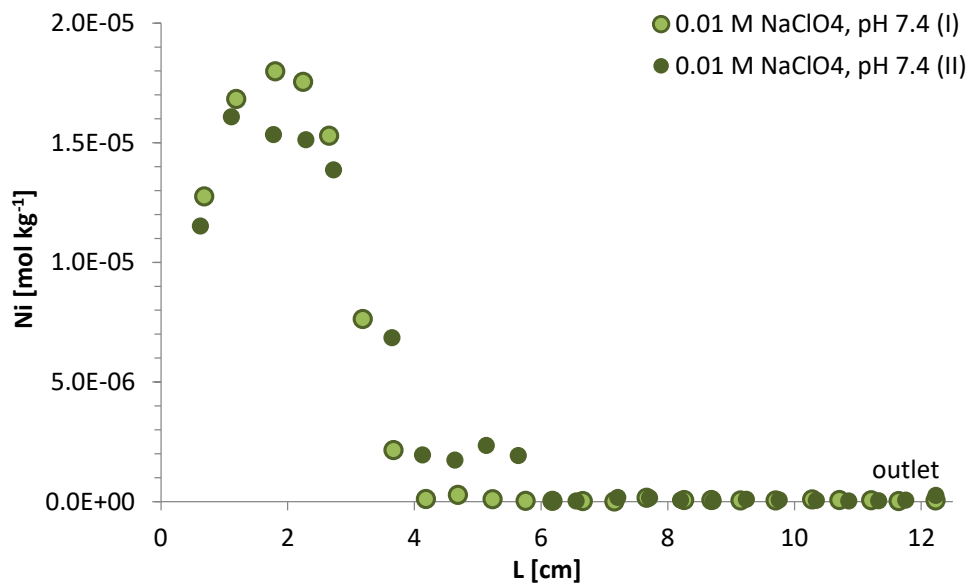


Fig. 9.14 Ni spatial distribution of orthoclase columns: pH 7.4, 0.01 mol L⁻¹ NaClO₄

Abscissa labeling: 12.25 cm stands for the outlet of the column where fractions are collected (Fig. 9.1). 0 cm stands for the inlet of the column. Experiments were stopped after approx. 23 PV flowed through the column.

Tab. 9.3 Overview of experimental details concerning orthoclase columns with Ni

Column number/replicate	(I)	(II)	(I)	(II)
Background solution	0.01 mol L ⁻¹ NaClO ₄			
pH	5.8		7.4	
Duration [d]	1.1	1.1	3.9	3.9
Recovery rate [%]: Ni, Br	83, 102	82, 100	91, 100	99, 93
PV [ml]	72.5	72.5	72.5	72.6
Bulk density [g cm ⁻³]	1.47	1.47	1.47	1.47
Flow velocity tracer [ml min ⁻¹]	0.308	0.316	0.308	0.301
Flow velocity overall [ml min ⁻¹]	0.307	0.315	0.305	0.300
SD (overall) [ml min ⁻¹]	0.002	0.002	0.003	0.003
Total applied x·PV [-]	6.2	6.4	23.6	23.0

10 Mechanistic sorption modeling

In this section the application of thermodynamic sorption models to describe results of batch and column sorption experiments is presented. The determination of mineral- and element-specific parameters – so-called surface complexation parameters – is main focus of this section. Surface complexation parameters (SCPs) comprise protolysis constants ($\log K_{\text{prot}}$), the SSD, the capacitance of the BSM (C_1), the co- and counterion association coefficients ($\log K_{\text{Na}}$ and $\log K_{\text{ClO}_4}$) for the BSM, the SSA, and the surface complexation constant. These parameters are derived from absolute surface charge data (surface charge models /BRI 18/) and batch data (surface complexation models, SCMs). The development of reactive transport models (RTMs, Sec. 11) and the application of SCPs to RTMs (Sec. 11) were also major scopes to describe sorption and transport tendencies of relevant RNs within this study. Therefore, the geochemical speciation code PHREEQC (Version 3.1.2 – 8538, /PAR 13/) was used in combination with the universal parameter estimation code UCODE (Version 2005, /POE 08/).

10.1 Fitting procedure of surface complexation parameters

Briefly, PHREEQC allows solution speciation calculations, determination of saturation indices and ion speciation and/or distributions in aqueous phases, in solid solutions, and in pure phases, as well as calculations of element distribution speciation for exchange sites and surface sites, and 1D reactive transport simulations. Equilibrium and nonequilibrium calculations are possible with PHREEQC /PAR 13/. The Debye-Hückel and Davies expression may be used to account for electrostatic interactions of ions in dilute aqueous solutions. The Debye-Hückel and Davies approaches account for varying thermodynamic ion activities α_i and activity coefficients γ_i (index i symbolizes specific ions) both depending on ionic strength (I_S) and e. g. ion charge (z) /PAR 13/. For SCP determination and RTMs, the Davies equation was used to calculate γ for charged solution species. The Debye-Hückel equation was applied for uncharged species with Debye-Hückel parameters a , $b = 0$. The ion exchange can be described by means of the Gaines-Thomas, the Gapon, or the Vanselow convention in PHREEQC. Here, the activity of an exchange species α_{EX} was set to its equivalent fraction (Gaines-Thomas convention) /PAR 13/. For surface complexation calculations PHREEQC uses the generalized two-layer model after /DZO 90/ (DDLm) and a nonEDLM following /DAV 90/. The CD-MUSIC model option (charge distribution multi-site complexation) (e. g. /HIE 89a/, /HIE 89b/)

provides the implementation of more complex SCMs such as the basic Stern model (BSM) or triple layer model (TLM), and three plane models (TPM) /PAR 13/.

Fig. 10.1 depicts the coupling of PHREEQC with UCODE for SCP determination. UCODE is based on the minimization of the least squares objective function applying a so-called modified Gauss-Newton optimization /HIL 98/, where "modified" refers to the combination of the Gauss-Newton optimization with the Levenberg-Marquardt algorithm that enables more robust fitting procedures. UCODE was applied as a shell to optimize SCPs. The parameter estimation code extracts PHREEQC results and compares extracted values with observations. If predefined UCODE conversion criteria are not met, UCODE supplies PHREEQC with new parameter values according to the modified Gauss-Newton optimization. The fitting procedure continues until user-defined UCODE convergence criteria are fulfilled.

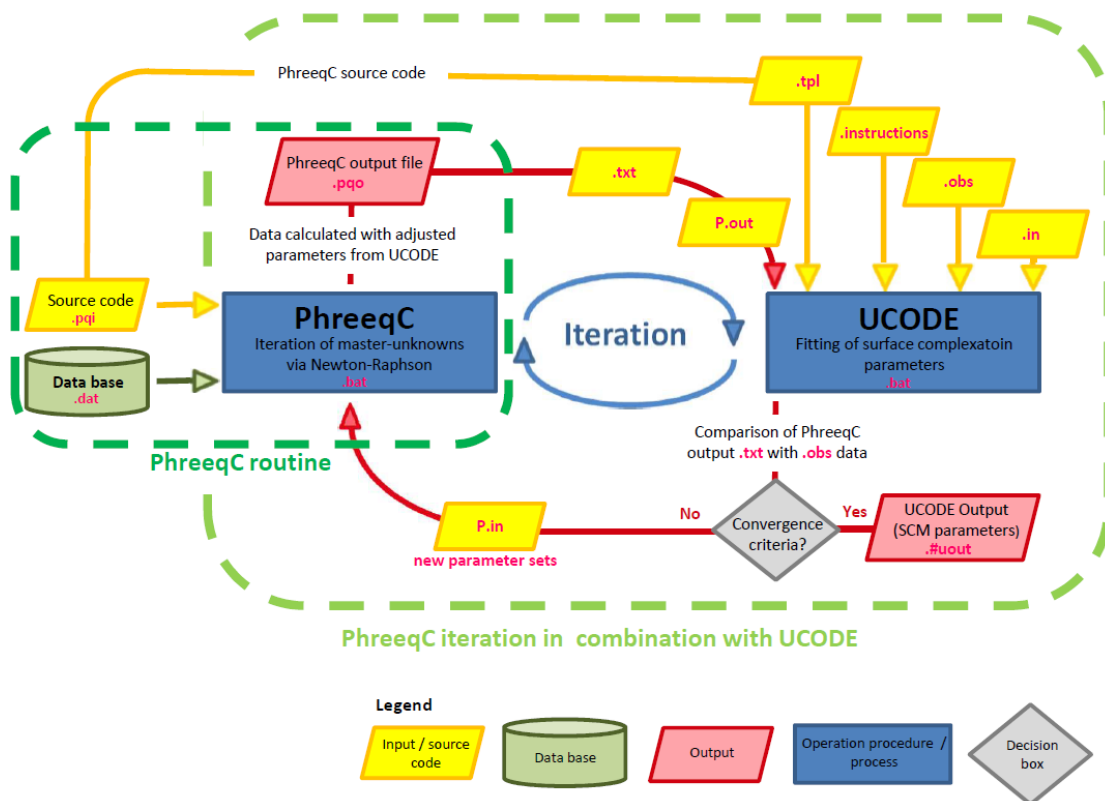


Fig. 10.1 Flowchart of PHREEQC application in combination with UCODE for parameter estimation (after /BRI 18/ and /NOS 12b/).

Data files: .dat – database, .pqj – PHREEQC input file, .pqr – PHREEQC output file, P.out – PHREEQC output file in UCODE routine, .tpl – template file for UCODE routine, .instructions – UCODE instruction file to extract fitted data from UCODE selected output file (.txt), .obs – observations for UCODE routine, .in – input file UCODE, P.in – PHREEQC input file, #uout – UCODE output file, .bat – PHREEQC and UCODE batch files.

This study applied common statistical means (goodness of fit (gof)) to judge whether a fit was satisfying or whether the fitting processes had to be rerun /HIL 98/: The 95 % confidence intervals of the parameter distribution (*CI*), the least squares objective function value (*LSOF*), the mean error (*ME*), the standard errors (*SEs*), the correlation matrix for adjustable parameters, as well as the parameter standard deviation (*psd*) were taken into account /BRI 18/. No prior information was supplied for UCODE iteration procedures, no weighing of experimental data was included.

Generally, identical fit criteria were used for all fitting procedures to guarantee comparability of model output: Adjustable parameters were not constrained, parameter estimation converged as maximum fractional change of parameter values between iteration runs fell below 0.001 /POE 08/. Parameter estimation also successfully completed if the fractional decline of the sum of squared weighted residuals was below 0.001 over three parameter estimation runs /POE 08/. A maximum of 200 iterations was allowed before UCODE stopped without finding a (local) minimum of the least squares objective function. The maximum change of a parameter value between two iteration runs equaled $\leq 10\%$ of the initial parameter value. Gauss-Newton settings and Marquardt parameters were left at default settings /POE 08/. A PHREEQC model run generated simulation values with respect to observations (forward) and UCODE determined the gof as well as sensitivities which were obtained by central difference perturbation. Relative perturbation amplitude equaled 1 % of the final parameter value.

Whenever possible a function file was used, i. e. the calculation of adjustable parameters was linked to a second fitting parameter. This procedure was applied to reduce the number of parameters and to minimize parameter correlation.

The term fitting approach corresponds to the application of PHREEQC in combination with UCODE. A satisfying fitting approach yielded a calibrated model. Here calibration describes a TSM that yields optimized, valid, and reliable SCPs (based on gof) and that can therefore be used to simulate surface charge development, surface complexation, and the reactive transport where experimental data is lacking. Simulation or model run refer to a single PHREEQC calculation with SCPs from e. g. experimental data, literature, or calibrated models; for simulations no SCP optimization is necessary. The SCP sets derived in this study represent standard conditions: $I_S = 0 \text{ mol L}^{-1}$, activity coefficient of surface species equaling unity, while equilibrium conditions were assumed for each system.

Detailed information on the development of the different Eu TSMs, model constraints and limitations, data processing and approaches to find first estimates for e. g. the SSD and the conditional cation exchange coefficients ($\log K_c$) is provided in /BRI 18/, /RIC 15/, and /STE 17/.

10.2 SCM parameterization

In the following section, the results of the estimation of U(VI), Np(V), Nd(III), Eu(III), and Cs(I) SCPs via inverse modeling is presented. Parameters were derived for the pure mineral phases orthoclase, muscovite, and quartz (Sec. 5). For surface complexation modeling the DDLM, BSM, and a noEDLM were used whereas SCPs of all RNs were derived using the DDLM and only Eu SCPs were also estimated with the BSM and the noEDLM (in addition to the DDLM). Detailed information on model set up, initial parameter values for inverse modeling, model limitations, and a short summary of all model approaches are provided in /BRI 18/ and /RIC 15/.

10.2.1 System U(VI) with orthoclase and muscovite

According to the spectroscopic results of the TRLFS measurements (Sec. 8), several surface species were indicated. In the absence of Ca^{2+} , the two uranyl surface complexes $\equiv\text{XO-UO}_2^+$ and $\equiv\text{XO-UO}_2\text{CO}_3^-$ were formed, whereas the presence of Ca^{2+} leads to the formation of $\equiv\text{XO-UO}_2^+$ and $\equiv\text{XO-UO}_2\text{OH}$ surface complexes as the formation of the aqueous $\text{Ca}_2\text{UO}_2(\text{CO}_3)_3(\text{aq})$ complex reduces the free UO_2^{2+} concentration in solution. In addition, ATR FT-IR spectroscopy confirmed an outer-sphere surface species in the absence of Ca^{2+} . These experimental results were used for the assessment of surface complexation parameters to improve the basis for a mechanistic modeling of the sorption processes of U(VI) onto orthoclase and muscovite including the influence of Ca^{2+} . Detailed information is provided in /RIC 15/ and published in a peer-reviewed journal /RIC 16/. For the sorption onto orthoclase, a $\log K_{\equiv\text{XO-UO}_2^+}$ of 1.69 and a $\log K_{\equiv\text{XO-UO}_2\text{CO}_3^-}$ of 8.96 were determined, whereas $\log K_{\equiv\text{XO-UO}_2^+}$ of 0.41 and $\log K_{\equiv\text{XO-UO}_2\text{CO}_3^-}$ of 8.71 best described the sorption onto muscovite in the absence of Ca^{2+} . Both surface complexes described the experimental data quite well as shown in Fig. 10.2 and Fig. 10.3 (dashed lines). However, there are some differences except for the series with the highest U(VI) concentration (10^{-5} mol L^{-1}) and lowest M/V ($1/80$ g mL^{-1}) for orthoclase, and to a lesser extent, also for muscovite.

The fitted log K for the most fundamental U(VI) surface complex $\equiv\text{XO-UO}_2^+$ (1.69 for orthoclase and 0.41 for muscovite) are generally in good agreement with published values, e. g. log K 1.67 for albite /ARN 00/ and log K -0.5 for muscovite /ARN 01/. Concerning uranium-carbonate surface complexes, a comparison with values for feldspar and mica is not possible, because there are no comparable values, but the fitted log K values for orthoclase and muscovite (8.99 and 8.71) are close to those published for quartz with log K 10.18 /DAV 01/ and kaolinite with log K 10.85 /JUN 99/.

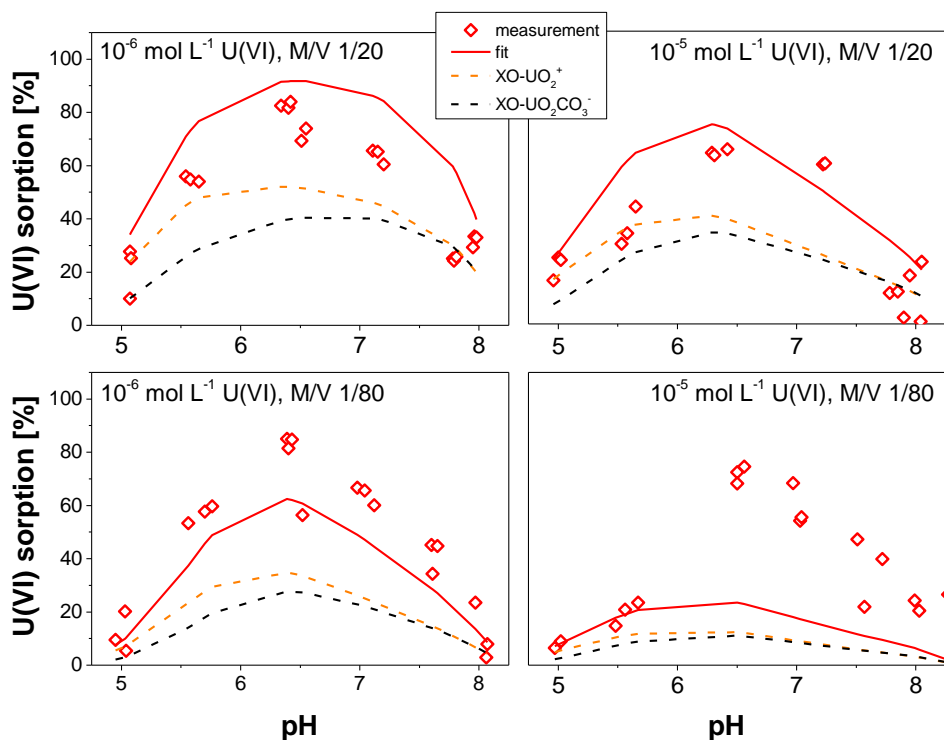


Fig. 10.2 Fitted surface speciation for the U(VI) sorption onto orthoclase ($10^{-5} \text{ mol L}^{-1}$ and $10^{-6} \text{ mol L}^{-1}$ U(VI), M/V 1/20 and 1/80 g mL^{-1})

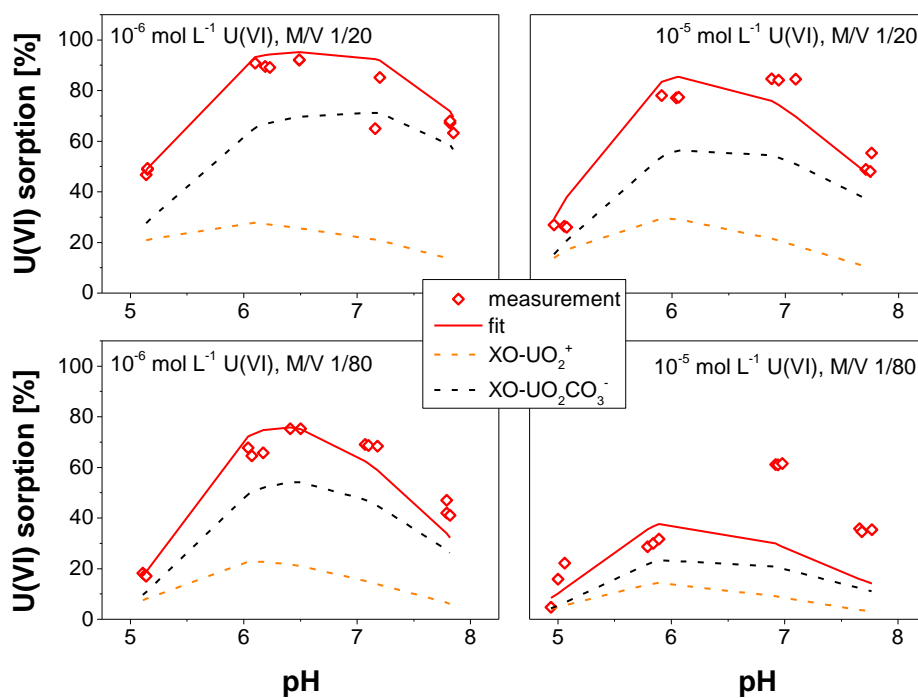


Fig. 10.3 Fitted surface speciation for the U(VI) sorption onto muscovite ($10^{-5} \text{ mol L}^{-1}$ and $10^{-6} \text{ mol L}^{-1}$ U(VI), M/V 1/20 and 1/80 g mL^{-1})

To get a better understanding of the aquatic and surface speciation of the U(VI) sorption onto orthoclase and muscovite, the obtained log K -values were used to model the speciation with PHREEQC. Results are shown in Fig. 10.4 and illustrate that surface species dominate the total speciation at circumneutral pH values in the presence of the investigated minerals.

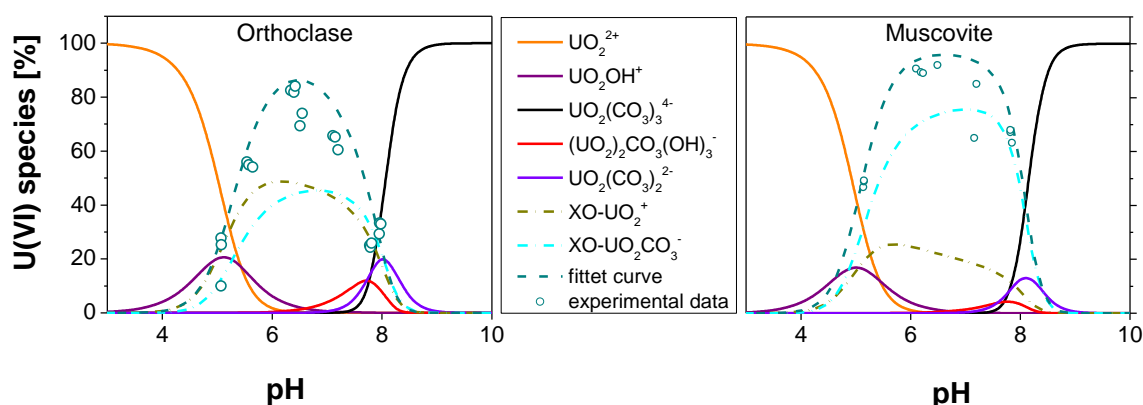


Fig. 10.4 Aquatic and surface speciation of $10^{-6} \text{ mol L}^{-1}$ U(VI) in 0.01 mol L^{-1} NaClO_4 , under ambient air onto orthoclase (left) and muscovite (right)

Furthermore, the predictive modeling for the experiments with Ca^{2+} is shown in Fig. 10.5 using the log K -values obtained in this work as described above. For orthoclase the sorption is overpredicted. This is in accordance with the spectroscopic results, where the

uranium-carbonate complex was not observed in presence of Ca^{2+} . Consequently, this complex leads to an overestimation of the experimental data. In contrast, the predictive modeling of muscovite is in very good agreement with the experimental data.

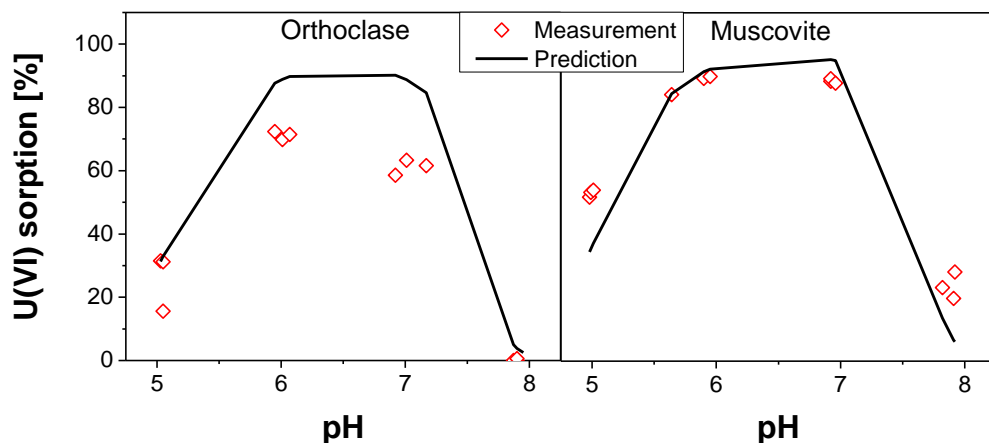


Fig. 10.5 Prediction of sorption of U(VI) in presence of Ca^{2+} for orthoclase (left) and muscovite (right) using the log K values obtained in this work

10.2.2 System Np(V) with orthoclase and muscovite

Based on the spectroscopic measurements (Sec. 8) no information to the bonding mechanism of Np(V) was possible. Therefore, the surface species $\equiv\text{XO-NpO}_2$ as described in literature /WAN 01b/ was used to fit the experimental data. This surface complex describes the experimental data quite well as shown in Fig. 10.6 (dashed lines). The obtained log K -values (orthoclase: -3.92 and muscovite: -4.58) are in good agreement to literature data for other aluminosilicates like log K -4.04 for kaolinite, log K -3.62 for gibbsite, and log K -4.15 for biotite, all obtained by /WAN 01b/. Because of the weak sorption, a fit with more species does not improve the prediction.

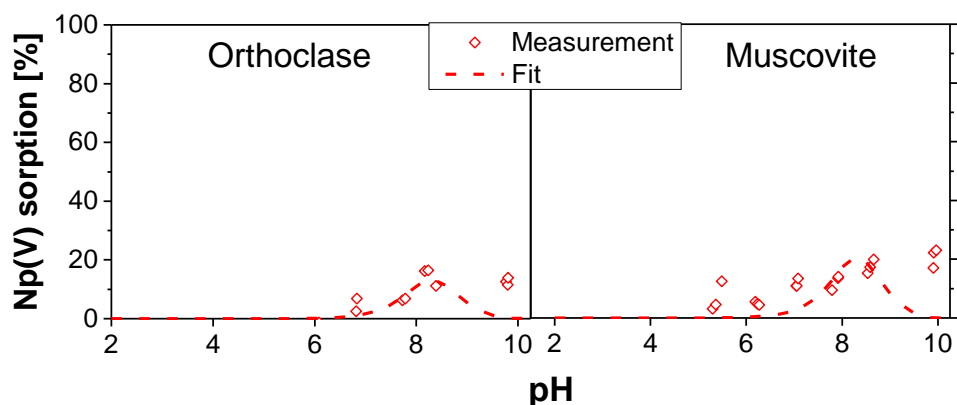


Fig. 10.6 Fitted surface speciation with $\equiv\text{XO-NpO}_2$ surface complex for Np(V) onto orthoclase (left) and muscovite (right) (10^{-6} mol L $^{-1}$ Np(V), 0.01 mol L $^{-1}$ NaClO $_4$, M/V 1/20)

10.2.3 System Nd(III) with orthoclase and muscovite

According to literature two surface species $\equiv\text{XO-Nd}^{2+}$ and $\equiv\text{XO-NdCO}_3$, were used to fit the experimental data. The fitted sorption curves of Nd(III) onto orthoclase and muscovite are shown in Fig. 10.7 and Fig. 10.8 (dashed lines). The fitted log K (4.85 for $\equiv\text{XO-Nd}^{2+}$ / 9.46 for $\equiv\text{XO-NdCO}_3$ (orthoclase) and 3.77 for $\equiv\text{XO-Nd}^{2+}$ / 10.10 for $\equiv\text{XO-NdCO}_3$, (muscovite)) are in general in good agreement with published values of comparable systems. Due to a lack of SCM data of neodymium and other Ln(III) onto feldspar and mica, studies of Ln(III) and An(III) onto quartz and clay minerals were chosen for comparison. For example, /KIT 99/ gave log K values of 4.55 and 5.07 for $\equiv\text{SiO-Eu}^{2+}$ and $\equiv\text{SiO-Am}^{2+}$ onto quartz, which are in good agreement to the calculated values for orthoclase. /BRA 05b/ calculated log K values of 3.1 both for $\equiv\text{XO-Eu}^{2+}$ and $\equiv\text{XO-Cm}^{2+}$ onto illite, which are close to the obtained value for muscovite. Less data is available for carbonates. /FER 08/ calculated a log K of 8.3 for $\equiv\text{XO-EuCO}_3$ onto montmorillonite, but nevertheless this value is in the same range as the values obtained for $\equiv\text{XO-NdCO}_3$ onto orthoclase and muscovite.

For muscovite both surface complexes of Nd(III) describe the experimental data quite well (Fig. 10.8).

Obviously, the SCM results for orthoclase (Fig. 10.7) with 10^{-5} mol L $^{-1}$ U(VI) and a M/V of 1/80 g mL $^{-1}$ show a discrepancy between the fit and the observed experimental data. However, solid Nd(III) phases may precipitate at higher pH values and have to consider in the fitting procedure.

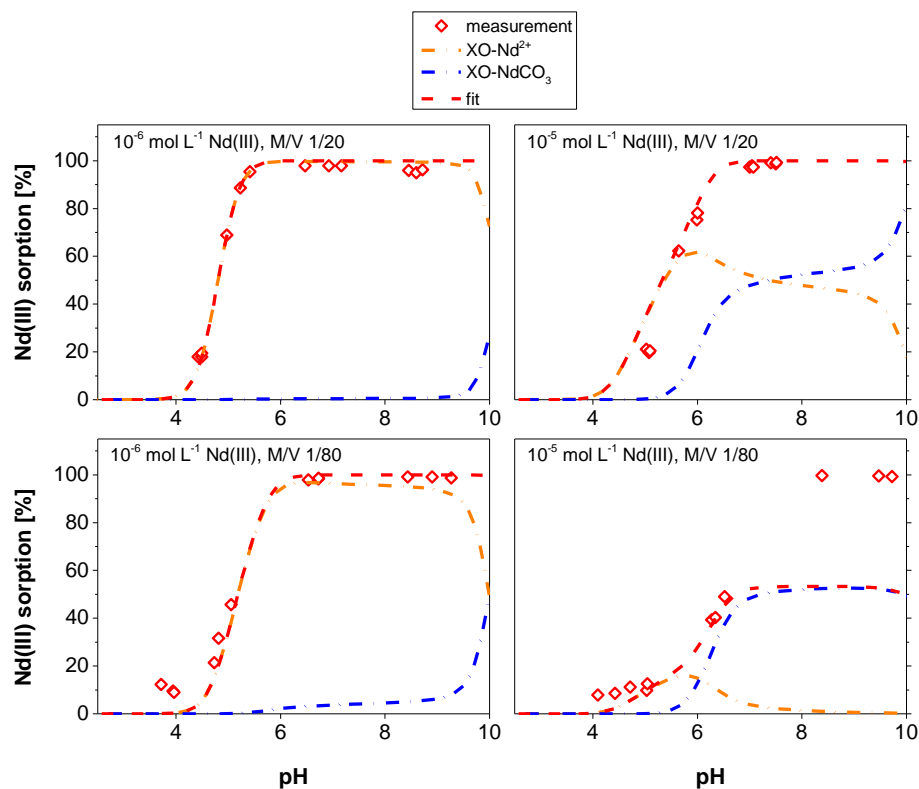


Fig. 10.7 Fitted surface speciation for the Nd(III) sorption onto orthoclase (10⁻⁵ mol L⁻¹ and 10⁻⁶ mol L⁻¹ Nd(III), M/V 1/20 and 1/80 g mL⁻¹)

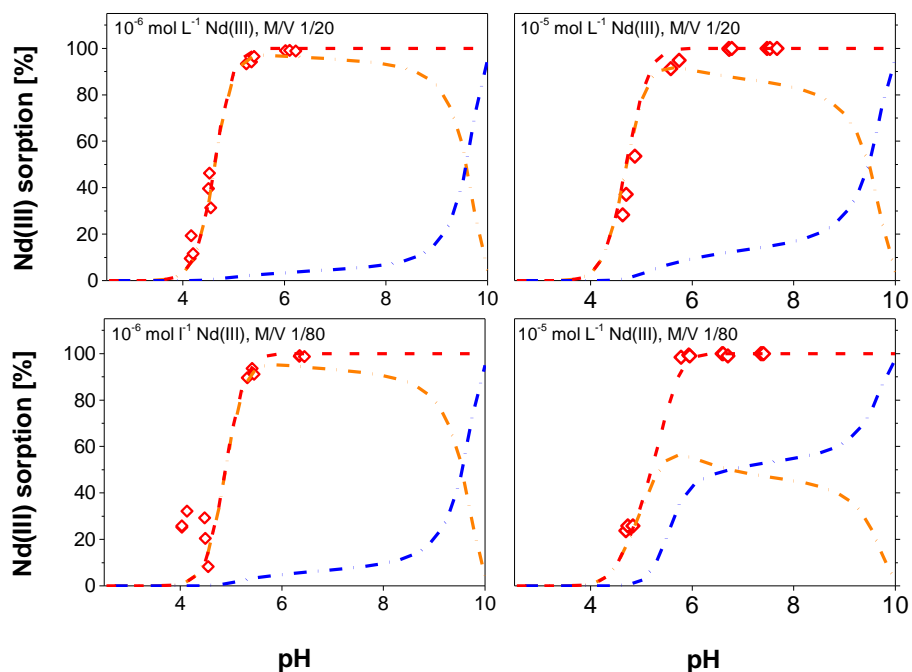


Fig. 10.8 Fitted surface speciation for the Nd(III) sorption onto muscovite (10⁻⁵ mol L⁻¹ and 10⁻⁶ mol L⁻¹ Nd(III), M/V 1/20 and 1/80 g mL⁻¹). Legend given in Fig. 10.7

10.2.4 System Eu(III) with quartz, orthoclase, and muscovite

Since Eu(III) is a chemical homologue of Cm(III) and Am(III), studies involving Cm(III) and Am(III) were included to gather information of Eu surface complexation and speciation reactions. Unfortunately, no clear spectroscopic evidence exists on the nature of Eu surface complexes on quartz, orthoclase, or muscovite surfaces. Aquo ions of Eu^{3+} and Cm^{3+} are solvated by 8 – 9 surrounding water molecules (e. g. /STU 06/, /STU 08b/, /KUM 12/). During inner-sphere surface complexation processes water molecules are released and Eu sorbes to the surface in a monodentate, bi- or multidentate manner /GEC 13/. So far, the structure of Eu surface complexes has not been clearly determined but evidently strongly depends on the mineral surface structure and pH /KUM 12/, as well as IS, temperature, competing cations, complexing ligands, etc. /GEC 13/.

The structure of surface complexes depends on element-specific sorption affinities to sorb as mono-, bi-, multidentate, or e. g. ternary surface complexes and on geochemical system properties. Additionally, the nature of surface sites has still not been fully understood either and might also have significant influence as /BAR 96/ postulate. They consider differently coordinated surface hydroxyl coordinations (SHCs) on hematite and goethite (singly-, doubly-, triply surface hydroxyl coordinations) and suggest that these different surface sites may have influence on the nature of surface complexes and on complexation constants. Considering different SHCs would increase the number of SSDs which could substantiate the occurrence multidentate surface complex formations as proposed by e. g. /FER 16/. Spectroscopic studies by /FER 16/ and modeling studies of /POL 13/ postulate bi-, tri-, and tetradentate surface complexes of trivalent lanthanides on different mineral surfaces. However, the present study aimed to develop SCMs as simple as possible while still describing experimental data as good as possible. In the absence of clear spectroscopic evidence, literature data and gof of inverse optimization procedures decided whether mono-, multidentate, or ternary surface complexes represented final Eu surface complexation constants ($\log K_{\text{Eu}}$). However, it should already be pointed out here, that presumingly straightforward models can describe measurements well but might not reflect natural, realistic conditions. Detailed information is provided in /BRI 18/.

Surface complexation constants of Eu ($\log K_{\text{Eu}}$) for orthoclase and quartz were determined with the BSM, the DDLM, and a non-electrostatic model (nonEDLM). Europium SCMs were based on surface charge models of the respective mineral phase as described in detail in /BRI 18/. With surface charge models the following SCPs were

determined: $\log K_{\text{prot}}$, SSD, C_1 and $\log K_{\text{Na}}$, $\log K_{\text{ClO}_4^-}$ for BSMs. With SCMs as discussed in this section $\log K_{\text{Eu}}$ was estimated via inverse modeling (PHREEQC, UCODE, Sec. 10.1). Information on initial parameter values for fitting procedures, a discussion of conditional cation exchange coefficients for muscovite, a description of the determination of the SSD, as well as the application of the Pauling bond valence rules for the BSM is provided in /BRI 18/.

Mineral-specific SCPs (SCP set) are identified via a unique ID (identification): SCP stands for surface complexation parameter, the following letter defines the respective mineral (Q – quartz, M – muscovite, FS – feldspar/orthoclase), Roman numbers relate to a surface charge model as discussed in /BRI 18/, and the suffix e. g. mono, bi, tri, etc. defines the kind of considered Eu surface complex(s). Exemplarily, the parameter set *SCP Q I mono* defines surface complexation parameters for quartz that are based on the first quartz surface charge model (here DDLM) and assumes a monodentate Eu surface complex. The various surface charge models, data, and $\log K$ values are compiled and discussed in detail in /BRI 18/.

10.2.4.1 Quartz

1-pK DDLM

Fitted data of a monodentate (dashed grey line), bidentate (dash-dotted grey line), a hydrolyzed monodentate (solid grey line), and a hydrolyzed bidentate (dashed black line), as well as a combination of a mono- and bidentate (solid black line) Eu surface complexes are presented in comparison to experimental data (Fig. 10.9). The latter model approach of a mono- and bidentate surface complex (*SCP Q I mono+bi*, solid black line in Fig. 10.9) assumed a simultaneous formation of both Eu surface complexes at the mineral-water interface. Optimized $\log K_{\text{Eu}}$ s mostly overestimated experimental data on average (Fig. 10.9) which was indicated by mainly negative *MEs* (data not provided here, see /BRI 18/). The *MEs* ranged between -1.3 %Eu(III) immobilized for the SCM assuming a bidentate (*SCP Q I bi*) and +8.4 %Eu(III) immobilized for the SCM simulating a monodentate Eu surface complex (*SCP Q I mono*). To the authors knowledge, no spectroscopic evidence exists for ternary Eu-hydroxo complexes on quartz surfaces. Smallest *MEs*, *SEs*, and adequate *psds* were obtained with a bidentate Eu surface complex (*SCP Q I bi*) and a combination of bi- and monodentate complexes (*SCP Q I mono+bi*). Both parameter sets were used for reactive transport simulations (Sec. 11).

For high initial Eu concentrations ($C_0 = 10^{-5} \text{ mol L}^{-1}$) fitted results show the influence of precipitating Eu-carbonates ($\text{Eu}(\text{CO}_3)(\text{OH})\cdot 0.5\text{H}_2\text{O}(\text{cr})$, $\text{Eu}(\text{CO}_3)(\text{OH})(\text{cr})$, and $\text{Eu}_2(\text{CO}_3)_3\cdot 3\text{H}_2\text{O}(\text{s})$) which is evident by the discontinuous progression of the fits at pH 6.6 (Fig. 10.9). Precipitation reactions resulted in an overestimation of immobilized Eu [%] for $C_0 = 10^{-5} \text{ mol L}^{-1}$, $\text{SLR} = 12.5 \text{ g L}^{-1}$. For $\text{SLR} = 50 \text{ g L}^{-1}$ precipitation reactions were necessary to increase Eu immobilization compared to approaches where precipitation was not considered. Excluding precipitation of Eu phases returned an underestimation of measurements for both SLRs (results not shown here). Concluding, the 1-pK DDLM supports the assumption that for high Eu C_0 and elevated pH values precipitation of Eu carbonates occurred (Fig. 10.9) which was substantiated by batch sorption measurements.

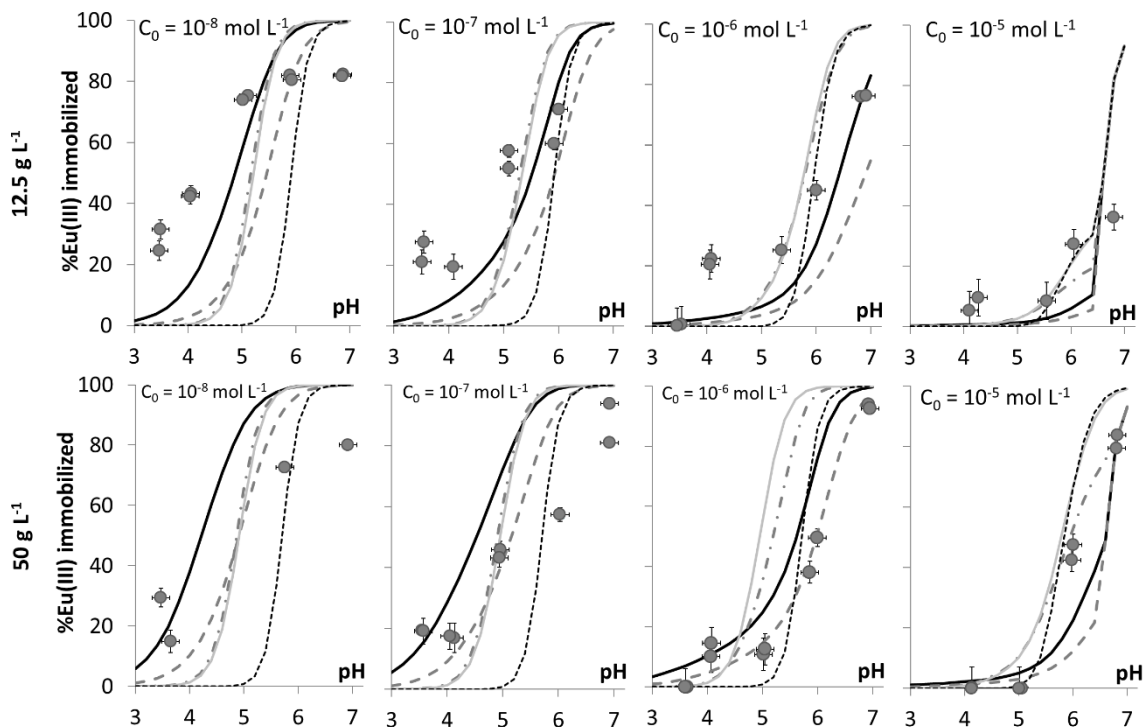


Fig. 10.9 1-pK DDLM results: Model was calibrated with experimental quartz batch data [%Eu(III) immobilized] (10 mM NaClO_4 background electrolyte, laboratory conditions: $p\text{CO}_2$ 10–3.4 bar, $T = 296.0 \text{ K} \pm 2 \text{ K}$)

C_0 – initial Eu concentration, grey solid circles – quartz batch data, monodentate Eu surface complex (dashed grey line), bidentate complex (dash-dotted grey line), hydrolyzed monodentate complex (solid grey line), hydrolyzed bidentate complex (dashed black line), combination of mono- and bidentate complexes (solid black line).

noEDLM

Results of noEDLM approaches are shown in Fig. 10.10. A comparison between noEDLM results and electrostatic models (DDLm, BSM) revealed that the noEDLMs did not reproduce experimental data equally well: For noEDLMs *MEs* ranged between -4.3 – +6.7 %Eu(III) immobilized for *SCP* $Q_{noEDLM}mono+bi$ and *SCP* $Q_{noEDLM}bi$, respectively (data not provided here, see /BRI 18/). Furthermore, fitting procedures using *SCP* sets *SCP* $Q_{noEDLM}mono+bi$ and *SCP* $Q_{noEDLM}bi$ returned large parameter *CIs* of $\log K_{EuS}$ between 1.3 – 2.3 $\log K$ units. Similar to DDLms precipitation reactions occurred and overestimated Eu immobilization at $pH \geq 6.5$ ($SLR = 12.5 \text{ g L}^{-1}$, $Eu C_0 = 10^{-5} \text{ mol L}^{-1}$, Fig. 10.10). Due to the smaller amount of surface sites for $SLR = 12.5 \text{ g L}^{-1}$ in comparison to the larger *SLR* more Eu remained in solution and was therefore prone for precipitation reactions. However, before precipitation reactions abruptly increased Eu immobilization, model results levelled off at 54 % immobilized Eu for *SCP* $Q_{noEDLM}mono$ and *mono+bi*. This was due to saturation of surface sites and formation of $EuSiO(OH)_2^{+3}$ solution species.

Comparing fitted results of *SCP* $Q_{noEDLM}mono$ and *SCP* $Q_{noEDLM}mono+bi$ returned similar results since $\log K_{Eu}$ for the bidentate surface complex ($\log K_{bi}$) turned out to be negligible for optimization procedures (Fig. 10.10). Consequently, a combination of mono- and bidentate surface complexes and hence increasing the number of adjustable parameters was not justified considering *gof* where similar *SEs* and *LSOF* values were returned for *SCP* $Q_{noEDLM}mono$ and *mono+bi*. Thus, *SCP* $Q_{noEDLM}mono+bi$ was excluded from Eu reactive transport simulations (Sec. 11).

To conclude, considering *gof* of *SCP* $Q_{noEDLM}mono$ revealed that a monodentate Eu surface complex reproduced Eu surface complexation on silica surfaces adequately which was in accordance with /WAN 01a/ and /KIT 99/. Since *SCP* $Q_{noEDLM}bi$ and *SCP* $Q_{noEDLM}mono+bi$ resulted in large parameter *CIs*, *LSOF* values, and *MEs* compared to *SCP* $Q_{noEDLM}mono$, only *SCP* $Q_{noEDLM}mono$ was used for noEDLM reactive transport models (Sec. 11).

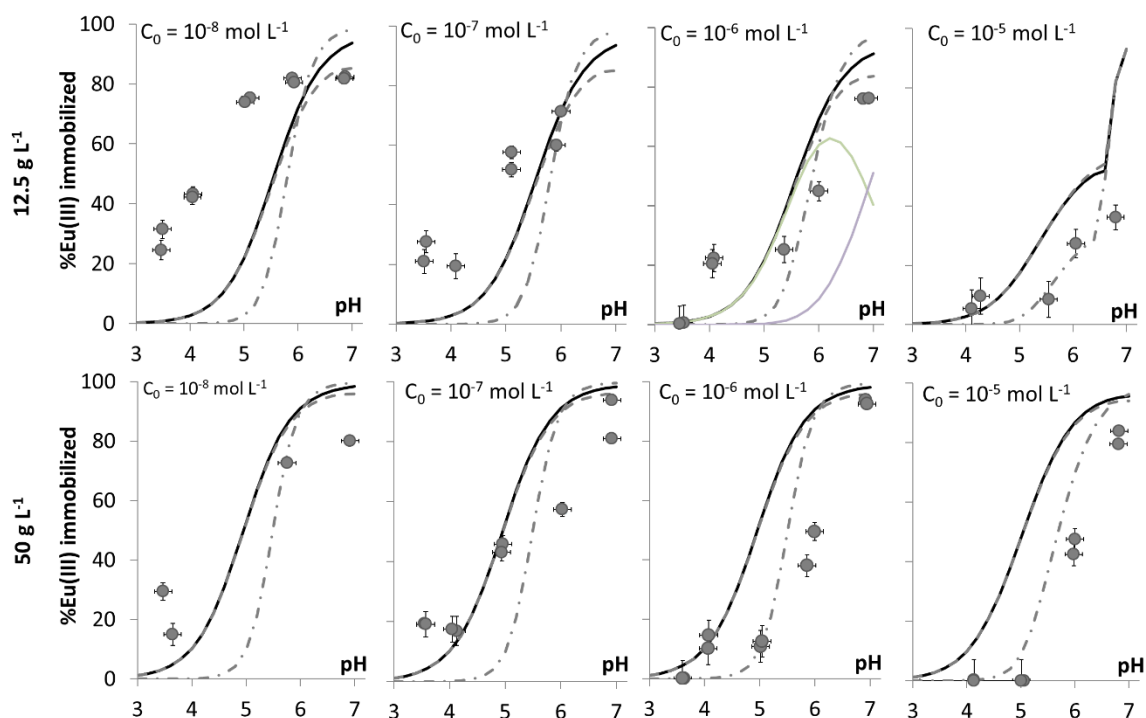


Fig. 10.10 Results of Eu batch experiments with quartz and fitted noEDLM results (10 mM NaClO₄ background electrolyte, laboratory conditions: pCO₂ 10^{-3.4} bar, T = 296.0 K ± 2 K)

Contribution of monodentate Eu surface complexes (dashed grey line), bidentate complex (dash-dotted grey line), mono- + bidentate surface complex (solid black line).

1-pK BSM

For 1-pK BSMs monodentate, bidentate, a combination of mono- and bidentate surface complexes, as well as a hydrolyzed Eu surface species were used (Fig. 10.11). The *MEs* ranged between -2.2 %Eu(III) immobilized and -1.0 %Eu(III) immobilized, for *SCP Q II bi* and *SCP Q II H₂O_{mono}*, respectively. Precipitation of Eu carbonates became evident for pH ≥ 6.5 for Eu C₀ = 10⁻⁵ mol L⁻¹ as it had already been observed for DDLMs and noEDLMs. The BSM returned better fitting results compared to noEDLMs and partially also compared to DDLMs which was indicated by smaller *SEs*, *MEs*, and *LSOF* values as well as smaller parameter *C*s and *psds*. Exact values for *gof* are provided in /BRI 18/. However, all optimized BSM log*K*_{EuS} overestimated experimental data on average (negative *MEs*). Considering *gof*, it was not possible to clearly identify a BSM approach that fitted measurements best since only small differences in *gof* could be observed. For example: *SCP Q II bi* yielded *ME* = -1.0 %Eu(III) immobilized which corresponded to the optimum of *ME* = 0 best; however, considering the *psd*, *SE*, and the *LSOF* *SCP Q II mono* resulted in slightly smaller values. Since two fitting parameters did not result in a

significantly better fitting result of experimental data an increase of adjustable parameters was not justified, either. Furthermore, *SCP Q II mono+bi* resulted in a relatively large parameter Cl of $\log K_{bi}$ in comparison to *SCP Q II mono* and *SCP Q II bi*. Therefore, *SCP Q II mono* and *SCP Q II bi* were used for Eu transport models.

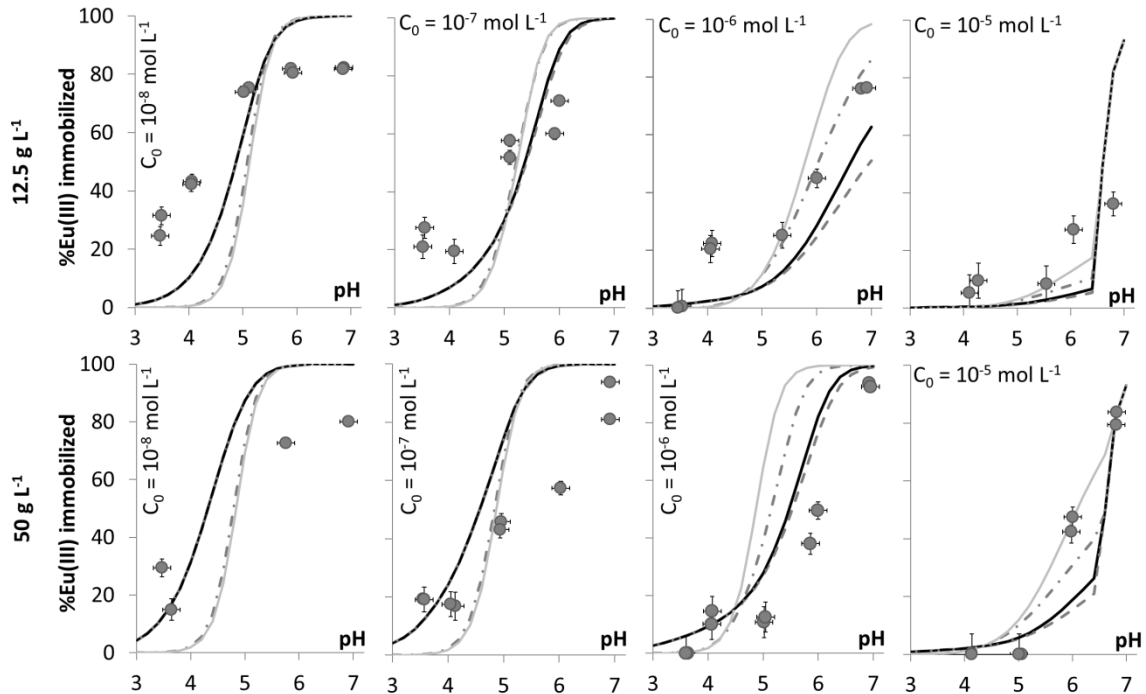


Fig. 10.11 Experimental batch data of quartz with Eu and 1-pK BSM results using mono-, bi-, and mono- combined with bidentate surface complexes (10 mM NaClO_4 background electrolyte, laboratory conditions: $p\text{CO}_2$ $10^{-3.4}$ bar, $T = 296.0 \text{ K} \pm 2 \text{ K}$)

C_0 – initial Eu concentration, solid circles – quartz Eu batch data. Contribution of monodentate Eu surface complex (dashed grey line), bidentate Eu surface complex (dash-dotted grey – line), mono- + bidentate surface complex (solid black line), hydrolyzed monodentate surface complex – solid grey line.

10.2.4.2 Orthoclase

Experimental data was adequately represented by DDLMs and noEDLMs considering gof of fitting approaches /BRI 18/. Due to very similar gof of electrostatic model approaches and noEDLMs no explicit preference could be identified; however, it was evident that *SCP FS_{noEDLM}mono* overestimated Eu batch data in comparison to all remaining model approaches. Nevertheless, gof and $psds$ ranged within the same order of magnitudes for noEDLMs compared to DDLMs and BSMs. BSM results supported the assumption that multidentate surface complexes or hydrolyzed Eu species accounted for Eu surface complexation which agrees with modeling studies of e. g. /FER 16/, /POL 13/,

and /STU 06/. Based on this finding tri-, tetradenate, and the hydrolyzed monodentate surface species were considered in Eu transport studies for BSMs in addition to all final DDLM and noEDLM SCP sets (Sec. 11). Detailed information, data, and parameter sets are provided in /BRI 18/.

10.2.4.3 Muscovite

For muscovite a noEDLM, the BSM, and the DDLM were used for $\log K_{Eu}$ estimations. Exchange processes of Na⁺, K⁺, H⁺, and Eu were considered by means of half reactions; conditional cation exchange selectivity coefficients of /POI 99a/ and /BRA 05b/ were used /BRI 18/. Following literature studies different Eu surface complexes were included /TER 06/, /LEE 13/, /KUM 13/, /FER 16/: monodentate, bidentate, and multi-dentate surface complexes, as well as hydrolyzed mono- and bidentate, and a combination of monodentate and hydrolyzed monodentate surface complexes. However, none of the electrostatic models or nonEDLMs yielded valid model results: All optimizations resulted in convergence problems of PHREEQC. No $\log K_{Eu}$ could be determined for the muscovite surface. Non-convergence was based on the application of $\log K_c Na/H$, $\log K_c Na/K$ /POI 99a/ and $\log K_c Na/Eu$ from /BRA 05b/ (with $\log K_c Na/Na = 0$) which caused mass law equations to not converge during optimization procedures. Hence, mass balances of all relevant elements failed. This finding showed that $\log K_c s$ did not represent the considered geochemical system correctly since $\log K_c s$ are highly system-dependent and cannot be easily transferred from literature. The selectivity of cations towards mineral surfaces is apart from lattice characteristics and geochemical surrounding also dependent on the hydration enthalpy of the index and exchanging cations. Generally speaking, $\log K_c Na/Eu$ seemed to be too large by orders of magnitudes to be adequate for muscovite Eu SCMs.

In the absence of $\log K_{Eu}$ and adequate $\log K_c s$ for muscovite, reactive transport models could not be developed based on the present study (Sec. 11) and simulation of Eu transport in muscovite environments must be postponed to future research projects.

10.2.5 System Cs(I) with orthoclase

This section is based on the master thesis /STE 17/ accomplished during this study. According to /BRI 18/ three different surface charge models were used to describe the acid-base properties of orthoclase surfaces. The DDLM combined with the 1-pK approach

and the following monodentate Cs surface complex was applied to describe sorbed Cs fractions on orthoclase.



A summary of the fixed parameters SSA, SSD, log K_s, the fitted final log K_{Cs} of the monodentate Cs surface complex, and goodness of fit values are listed in Tab. 10.1. Model A, B, C describe the three different surface charge models mentioned above combined with the final surface complexation model used in /STE 17/.

Tab. 10.1 Summary of final SCPs and goodness-of-fit values of calibrated SCMs for orthoclase and Cs

Model A, B, and C based on three different surface charge models for orthoclase referring to /BRI 18/. The DDLM were combined with the 1-pK-approach. Log K_{Cs} relate to the monodentate Cs surface complex. SSA, SSD, log K_s were fixed, log K_{Cs} was fitted. RMSE = root mean square error.

Cal. Model Parameter	Model A	Model B	Model C
SSA [m ² g ⁻¹]	0.2		
SSD [sites nm ⁻²]	3.8	5.9	3.8
LogK _s	3.5	3.5	8
LogK _{Cs}	-2.60±0.11	-3.05±0.12	-3.85±0.21
ME [%]	5.8	6.8	12.0
RMSE [%]	15.6	17.5	23.6

Model C obviously showed the poorest fit (Fig. 10.12): sorbed fraction underestimation up to pH 8, overestimation above pH 8. Results of model A and B revealed a better fit compared to model C. However, both models still underestimate sorbed fractions from pH 4 to pH 6 in most cases. There were just little differences between model calibration A and B. Model A showed the best fit with lowest ME and RMSE (also cf. Tab. 10.1). Further information is provided in /STE 17/.

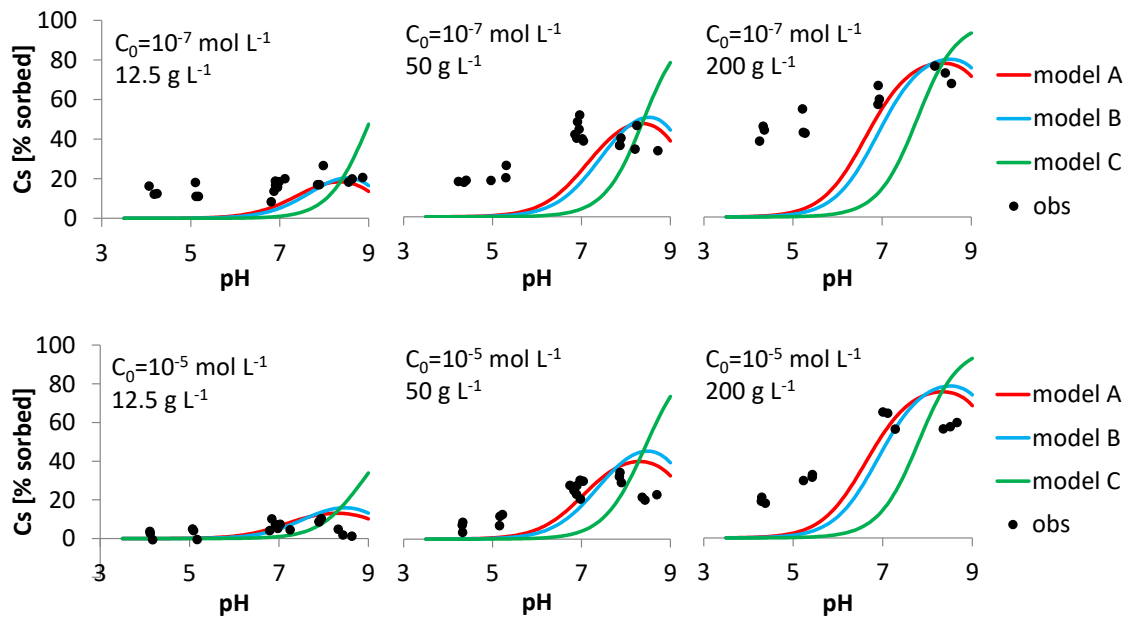


Fig. 10.12 Calibrated surface complexation models for orthoclase and Cs

0.01 mol L⁻¹ NaClO₄ was used as background solution. Model A, B, C refer to SCPs listed in Tab. 10.1. Obs stands for observation results of batch sorption experiments (Section 7.11.2).

10.3 Discussion of SCM results

In general, the results of the fitted surface complexation constants for the sorption of U(VI), Np(V), and Nd(III) onto orthoclase and muscovite are in good agreement to literature data of similar systems as described in /RIC 15/. SCM data for U(VI) are already published in a peer-reviewed journal /RIC 16/. However, the SCM results for 10⁻⁵ mol L⁻¹ U(VI) and Nd(III) at a M/V of 1/80 g mL⁻¹ onto orthoclase and to a lesser extend for U(VI) also on muscovite showed a discrepancy between the fit and the observed experimental data. For Nd(III) this can be due to the fact that solid phases may precipitate at higher pH values, which have to be considered in the fitting procedure. Otherwise, several SCM parameters like the protolysis constants, the specific surface area (SSA) and surface site density (SSD) implemented in the model can affect the results. The SSA is a measured value based on the used mineral, and thus cannot be changed, whereas the used SSD is taken from literature data and might deviate in the investigated systems. A closer look to the available surface sites per metal-cation (Me) calculated with the parameters used for the surface complexation modeling as given in Tab. 10.2 indicated that at these conditions (10⁻⁵ mol L⁻¹, M/V of 1/80 g mL⁻¹) only half of the amount of metal-cation (U(VI) or Nd(III)) has the possibility to directly sorb to the mineral surface of orthoclase. Thus, for future work a precise characterization of the SSD and protolysis constant that can be

derived by titration experiments should be performed to check the effects of these parameters on the quality of fit.

Tab. 10.2 Calculated number of sites at the used parameters of the surface complexation modeling (* U(VI) / Nd(III))

Mineral	SSA (m ² g ⁻¹)	SSD (sites nm ⁻²)	M/V (g mL ⁻¹)	No. of sites per metal ion	
				10 ⁻⁶ mol L ⁻¹ Me*	10 ⁻⁵ mol L ⁻¹ Me*
Orthoclase	0.083	3.1	1/20	21.4	2.1
	0.083	3.1	1/80	5.3	0.5
Muscovite	0.66	2.61	1/20	143.0	14.3
	0.66	2.61	1/80	35.8	3.6

An additional reason for the difference between experiment and fit can be due to undetected surface precipitation of Nd(III). Furthermore, for uranium the formation of oligomeric uranium species is possible even if such species are not spectroscopically identified in this system. The obtained final data sets including the specific surface site parameter and the optimized formation constants logK are provided in Tab. 10.3.

Tab. 10.3 Experimentally determined surface complexation parameters for U(VI), Np(V), and Nd(III) sorption onto orthoclase and muscovite. This work* refers to peer-reviewed values published in /RIC 16/

	Orthoclase	Reference	Muscovite	Reference
SSA [m ² g ⁻¹]	0.083	This work	0.66	This work
SSD [sites nm ⁻²]	3.1	/ARN 00/	2.61	/ARN 01/
pK ₁	6.47	/ARN 00/	6.01	/ARN 01/
pK ₂	-7.85	/ARN 00/	-7.86	/ARN 01/
logK ≡XO-UO ₂ ⁺	1.69 ± 0.58	This work*	0.41 ± 0.31	This work*
logK ≡XO-UO ₂ CO ₃ ⁻	8.96 ± 0.62	This work*	8.71 ± 0.12	This work*
logK ≡XO-NpO ₂	-3.92 ± 0.03	This work	-4.58 ± 0.03	This work
logK ≡XO-Nd ²⁺	4.85 ± 0.01	This work	3.77 ± 0.01	This work
logK ≡XO-NdCO ₃	9.46 ± 0.02	This work	10.10 ± 0.03	This work

The surface complexation model calibration for the system with Cs and orthoclase resulted in a satisfying fit using the monodentate surface complex $\equiv XO - Cs^{+0.5}$ (Sec. 10.2.5). However, it seems that additional Cs sorption processes are needed to describe Cs sorption onto orthoclase especially below pH 7. Since cations like Na^+ , K^+ , Ca^{2+} , and Al^{3+} existed in background solution (cf. Sec. 5.1.2.1), the implementation of competitive sorption processes could improve model calibration as well. The obtained final model data set of this study is provided in Tab. 10.1.

/BRI 18/ compares published data and final SCPs of quartz SCMs (DDLm, BSM, noEDLM) of this study with literature values – where available. So far, not many SCMs of Eu on quartz or amorphous silica have been reported in literature that used similar model approaches. It could be shown that for the DDLm $\log K_{Eu}$ agreed well with literature; for noEDLM approaches no comparable study was available. For the BSM a comparison of results was also rather challenging, for example: The BSM approach of /KIT 99/ used a substantially different capacity C_1 resulting in major differences of surface complexation constants and co-/ counterion association coefficients. Detailed information on model comparison is provided in /BRI 18/.

Generally, Eu sorption edges on quartz were adequately represented with SCMs. The application of a bidentate (*SCP Q I bi*) and a combination of a mono- and bidentate surface complex (*SCP Q I mono+bi*) for SCM calibration represented experimental data satisfactorily for the DDLm which was evidenced by gof of model approaches; for the noEDLM a monodentate Eu surface complex (*SCP Q noEDLM mono*) yielded adequate fitting results. The model approaches *SCP Q II mono* and *bi* returned fits as close to measurements as possible for the BSM. A comparison of gof between electrostatic models and noEDLMs revealed that electrostatic models fitted experimental data more realistic whereas the optimized $\log K_{mono}$ of *SCP Q I* could be substantiated with literature data. However, mono- as well as bidentate surface complexes have been evidenced via TRLFS measurements or modeling studies for Eu or chemical homologues on silica surfaces which substantiates the chosen model approaches of the present work at the current state of knowledge (e. g. /STU 08b/, /KUM 12/).

The DDLm, BSM, and noEDLM were used to optimize orthoclase $\log K_{Eu}$. All SCMs fitted experimental data equally well; hence, no preference of a certain electrostatic models or $\log K_{Eu}$ value could be identified with SCMs. Detailed information may be obtained from /BRI 18/.

For muscovite, neither the application of the DDLM, nor the BSM, or noEDLM converged since mass balances of all relevant elements failed. All SCMs showed major convergence problems of PHREEQC due to the implementation of cation exchange processes. Cation exchange processes could not be described realistically with $\log K_c$ s from literature. To identify whether non-convergence was truly based on erroneous $\log K_c$ s, cation exchange reactions were excluded from electrostatic models and noEDLMs for testing purposes: As a result, all SCMs without exchange processes converged for all postulated Eu surface complexation reactions. However, as expected optimized $\log K_{Eu}$ highly underestimated Eu uptake [%Eu(III) immobilized] at low pH (data not shown here). Under the aspect that muscovite is a cation exchanger, SCMs without cation exchange were not further considered even though models converged. In future, $\log K_c$ s for muscovite should be determined to correctly evaluate batch data. This finding supports the following statement /PAR 99/: "...ion-exchange modeling requires data on material from the study site for appropriate model application." which also agrees well with findings from /VOE 00/ who postulated that the reliable definition of the CEC at relevant geochemical conditions is a "... key prerequisite for accurate transport modeling."

11 Europium reactive transport modeling

Europium SCPs for orthoclase and quartz as presented in the previous section (Sec. 10) are prerequisites for RTMs which are the main focus of this section. In the present study, RTMs were used to simulate Eu transport processes based on mechanistic surface charge models /BRI 18/ and SCMs (Sec. 10) under consideration of inner and outer sphere surface complexation as well as aqueous speciation calculations (PHREEQC). Hence, each SCM that yielded reasonable fitting results of batch experiments (Sec. 10.2.4) formed the basis for respective RTMs. Since it was not possible to adequately describe the cation exchange for muscovite under the given geochemical conditions (Sec. 10.2.4.3), RTMs could only be developed for mineral systems without the influence of cation exchange processes. The simulation and assessment of Eu migration through muscovite columns and systems with the synthetic as well as natural minerals should to be subject to upcoming research projects.

Numerous studies have dealt with the estimation of SCPs from e. g. batch experiments (cf. RES3T, www.hzdr.de/res3t, /BRE 03/) of which some included the examination of the surface charge development of quartz, orthoclase, or muscovite surfaces in detail (e. g. /HIE 89a/, /ARN 99/, /MAS 04/); however, only few focused on surface complexation of trivalent lanthanides or actinides on these surfaces (e. g. /WAN 01b/, /STU 06/, /HOU 76/); and even less studies have drawn conclusions between SCPs derived from titration as well as Eu batch experiments and the performance of RTMs. Regardless whether mechanistic (surface charge model, SCM, RTM) or empirical approaches (linear distribution coefficient K_d , retardation factor R_f) are considered SCPs or K_d -values derived from titration and/or batch experiments sometimes do not represent retardation during transport processes adequately. Discrepancies between surface complexation constants and K_d -values of batch and column experiments have been tried to be explained with the following arguments /HAN 14/, /RUS 10/, /CUR 01/, /POR 00/, /MAR 98/:

- Desorbed antecedent species might be transported out of a column system during transport experiments while in batch experiments these species remain in solution and continue to compete for sorption sites affecting exchange and sorption equilibria in the systems.
- Substantially different SLRs may cause differences in batch and column experiment K_d -values which is referred to as the "solids effect" in literature.

- It is also discussed that batch experiments reflect true equilibrium conditions while column experiments might not be in local equilibrium but influenced by kinetics of sorption or desorption processes during transport processes.
- The loss of particles, variations in flow rates, and the presence of immobile water during column experiments are also assumed to influence sorption coefficients and surface complexation constants determined with transport experiments.
- Mixing differences and differences in solid-particle spacing have also been reported to explain the discrepancy in sorption coefficients between both methods.
- The organic content of a sample has likewise been discussed to influence local equilibrium conditions: With increasing organic matter an increase of sorption nonequilibrium during transport experiments has been observed.

However, the true reason or the actual mechanism causing the differences have not yet been resolved /POR 00/. To further complicate matters, K_d -values do not reflect a uniform sorption tendency with respect to the experimental set-up, meaning that sorption coefficients have been reported to be stronger, weaker, and sometimes equal between batch and column experiments (e. g. /HAN 14/). To illustrate the ongoing discussion dealing with the difference between K_d -values and surface complexation constants from batch and transport experiments a brief overview of some relevant literature is provided in /BRI 18/.

11.1 Data processing of experimental transport measurements

Breakthrough curves of Br and Eu were corrected for the volume of the tubing and frits which is referred to as dead volume. This volume is crucial to determine the correct temporal position as well as PVs of BTCs and was determined gravimetrically in this study.

The volume of the tubing and tube connections was measured for each column experiment individually; the dead volume of the frits which comprised the pore volume of the frits and the space in front of the frits in the caps for both ends of the column was measured for selected columns. Since all column systems were identical the dead volume of the frits was assumed to be similar for all transport experiments. Hence, a mean dead volume of the frits was used for all column experiments.

11.2 Determination of retardation factors

The retardation factor R_f [-] as well as the linear distribution coefficient K_d assume linear sorption isotherms (Henry isotherm) that do not consider kinetic effects, diffusion and dispersion processes, local nonequilibrium conditions, or e. g. interrelations of geochemical processes and changing geochemical conditions that may occur during transport experiments and under natural conditions. Exclusively linear sorption processes would result in symmetrical SDs and BTCs that can be evaluated and assessed with the R_f and the linear K_d -approaches. Under the assumption of a linear sorption isotherm (K_d approach, Henry isotherm) and hence, an instantaneously equilibrated system the R_f [-] is related to the linear K_d [$\text{cm}^3 \text{g}^{-1}$] as follows

$$R_f = 1 + \frac{\rho_b K_d}{\theta} \quad \text{Eq. 11.1}$$

where ρ_b relates to the bulk density [g cm^3] and θ to the water content which was assumed to be equal to the porosity [-] of the column. The R_f describes the position of a BTC or a SD of a potential pollutant in relation to the BTC of an ideal tracer (e. g. Br^-). In this study, R_f values were calculated from experimental data and reactive transport simulations (no fitting); K_d -values were calculated from experiments and simulations considering the above equation (Sec. 11.1). Even though R_f as well as the K_d -approaches are only applicable to linear sorption processes without biasing influences (kinetics, high dispersion, diffusion, etc.), in this study R_f and K_d -values were used as a measure to compare simulated with experimental results of all column experiments. Hence, for asymmetrical BTCs and/or SDs the R_f and K_d describe the first Eu peak concentration; hence, calculated K_d and R_f values should only be considered rough estimates keeping in mind that Eu transport processes did not follow linear properties for most experiments (Sec. 11.5).

11.3 Transport parameter determination with Br breakthrough curves

The CXTFIT code /TOR 98/ is part of the free software package STANMOD (STudio of ANalytical MODels, Version 2.0, /SIM 99/ and comprises three different transport models: the conventional, deterministic, 1D equilibrium advection dispersion equation (ADE), a chemical and physical nonequilibrium transport model, and a stochastic stream tube model. The former was used in this study to optimize solute transport parameters (conventional 1D ADE) which were fitted using a nonlinear LSOF method /SIM 99/.

Under the assumption of homogeneous media, steady flow, equilibrium conditions, and linear sorption properties Eq. 11.2 was used to simulate 1D transport problems of Br breakthrough in this study /TOR 98/

$$R_f \frac{\delta C_r}{\delta t} = -v \frac{\delta C_r}{\delta x} + D \frac{\delta^2 C_r}{\delta x^2} \quad \text{Eq. 11.2}$$

considering Eq. 11.2 for BTCs

$$C_f = C_r - \frac{1}{Pe} \frac{\delta C_r}{\delta x} \quad \text{Eq. 11.3}$$

where R_f [-] corresponds to the retardation factor Eq. 11.2 C_r refers to the volume averaged or resident concentration of the liquid phase [mol L^{-1}], C_f to the flux-averaged concentration [mg L^{-1}], D is the dispersion coefficient [$\text{cm}^2 \text{h}^{-1}$], v [cm h^{-1}] relates to the pore water velocity (also water flow velocity), and Pe to the Péclet number. In Equation Eq. 11.3 t relates to the time [h], x to the location [cm], and C to the concentration [mg L^{-1}]. Detailed information provides /TOR 98/.

Breakthrough curves of the ideal NaBr tracer that were corrected for the dead volume of the tubing and frits (Sec. 11.1) were used as calibration data sets to determine solute transport parameters with CXTFIT for each column experiment. For transport parameter optimization procedures Br concentrations were used as a function of time [h] as flux-averaged concentration [mg L^{-1}], fitted transport parameters were not constrained, and the total Br mass was included whereas the solute mass was known and kept constant throughout the fitting procedures. The ideal Br tracer was injected as a pulse input over ≈ 1.5 PVs (boundary value problem: pulse input, solute mass is known as kept constant). No initial concentration was allowed in the system (initial value problem: zero initial concentration $C_r(t_0) = 0$).

The D [$\text{m}^2 \text{h}^{-1}$] served as an adjustable parameter. Where necessary, the application time t [h] was also optimized (cf. Sec. **Fehler! Verweisquelle konnte nicht gefunden werden.**); v [cm h^{-1}] was used as a control since it was a measured parameter. Fitted dispersion coefficients D were converted to dispersivities (dispersion length) λ [m] ($\lambda = D/v$) for each experiment and used in PHREEQC transport simulations as a fixed solute transport parameter.

11.4 1D reactive transport model set up

PHREEQC combines 1D flow and transport processes with geochemical speciation calculations and offers four different transport models, whereas the 1D advection-dispersion reaction equation (ADRE, Eq. 11.4) was used in this study. Under the assumption that v and D are equal for all solute species, Equation 4.45 was used for transport simulations of Eu /PAR 99/.

$$\frac{\delta C_{sol}}{\delta t} = -v \frac{\delta C_{sol}}{\delta x} + D \frac{\delta^2 C_{sol}}{\delta x^2} - \frac{\partial C_{imm}}{\partial t} \quad \text{Eq. 11.4}$$

C_{sol} [mol L⁻¹] is the total element concentration in solution, $\frac{\partial C_{imm}}{\partial t}$ [mol L⁻¹ s⁻¹] is the change of the immobilized concentration over time [s] where C_{imm} stands for the immobilized concentration [mol L⁻¹], x is the location [m] /PAR 99/. Transport simulations with PHREEQC were based on explicit finite differences that were calculated forward in time. Each column was discretized into 180 cells with a length of 0.07 cm ($Pe_{grid} < 2$ with Pe_{grid} representing the grid Péclet number to prevent numerical dispersion). Dispersion was simulated central in space (mean velocities in the middle of each spacial decrement), whereas advection was calculated upwind (upstream velocities). All columns were defined with two flux boundary conditions (Cauchy boundary condition) at each end (Eq. 11.5) /PAR 13/

$$C_{sol}(x_{end}, t) = C_0 + \frac{D}{v} \cdot \frac{\partial C_{sol}(x_{end}, t)}{\partial x} \quad \text{Eq. 11.5}$$

where t is the time [s], x_{end} [m] the last cell of the column; x stands for the location [m], C_0 relates to the initial Eu concentration [mol L⁻¹] of the pulse solution (with the simplifying assumption 1 kgw = 1 L).

PHREEQC simulated the reactive transport of Eu for homogeneous porous columns using equilibrium-controlled surface and solution speciation reactions for each timestep, transport parameter λ was derived from CXTFIT optimizations of the dispersion coefficient D ($\lambda = D/v$). RTMs were based on surface charge /BRI 18/ and SCMs (Sec. 10.2.4); limitations and challenges as discussed in /BRI 18/ also applied for Eu RTMs. The summarized final SCP sets estimated with SCMs (Sec. 10.2.4, /BRI 18/) were used as fixed parameter values for transport simulations; no fitting or optimization of parameters was

performed. Surface complexation and co- and counterion association coefficient reactions were used. Further information is provided in /BRI 18/.

Advection was the main transport process for solutes due to high pore water velocity $v \approx 3.2 \pm 0.7 \text{ cm h}^{-1}$ (mean value over all transport experiments \pm standard deviation), dispersivities on the mm scale (small dispersion influence), and large Péclet numbers; diffusion was expected to be negligible (estimated diffusion coefficient $10^{-10} \text{ m}^2 \text{ s}^{-1}$). Transport processes were only considered in the mobile, liquid phase – no colloidal transport was considered. The digital appendix provides PHREEQC RTMs.

The reactive transport was simulated in two steps: First, the transport of the pulse solution was simulated as it was shifted through the column; the second step initiated the transport of the background electrolyte pushing the Eu and Br peak injection further down the column. All columns were equally discretized in 180 cells to guarantee comparability. Since $\text{pH}_{\text{ini}} \approx 3.5$ and ≈ 5.5 no precipitation reactions were considered since first Eu precipitates occur at $\text{pH} \approx 6.4$ /BRI 18/; the influence of CO_2 was also excluded due to low pH_{ini} and to reduce simulation times.

/DAV 05b/ offered the basis to judge whether a reactive transport simulation was satisfying or not: They stated that an error of model predictions in comparison to experimental data ranging between $0.5 - 1 \log K_d$ units ($|\Delta \log K_d|$) evidenced system understanding. /DAV 05b/ found that in most cases sorption trends and the magnitude of experimental data was satisfactorily represented over a range of experimental conditions if discrepancies between simulations and experiments stayed within or below the given K_d error range. To compare experimental transport data with PHREEQC simulations the K_d and R_f were calculated from measurements and predictions (cf. Sec. 11.2). For RTM evaluation smallest $|\Delta \log K_d|$ values were preferred over larger ones in this study.

11.5 Results and discussion of Br and Eu transport simulations

Transport simulations of this section are based on experimental results of Eu transport experiments through homogeneous porous media that have already been introduced in Section 9.2 as well as SCMs (Sec. 10.2.4) and surface charge models /BRI 18/. /BRI 18/ presents supplementary information and data on reactive transport simulations, Tab. 9.1 offers an overview of the experimental matrix of column experiments; Tab. 11.1 summarizes recovery rates, transport parameters, R_f (Eq. 11.2) and K_d -values from measurements and predictions (cf. Sec. 11.2).

Column experiments yielded Br BTCs and Eu SDs or Eu BTCs depending on the geochemical conditions. Since all ideal tracer BTCs followed expectations without exception, Br BTCs of quartz column experiments are exemplarily depicted (Sec. **Fehler! Verweisquelle konnte nicht gefunden werden.**) whereas tracer BTCs of orthoclase, muscovite, and the synthetic sediment can be found in /BRI 18/.

11.5.1 Transport parameter determination from Br breakthrough curves

Parameter optimizations with CXTFIT transport models yielded adequately fitted transport parameters for all column experiments which was characterized by mean squared errors (*MSEs*) on the ppm (parts per million) scale (cf. Tab. 11.1). Therefore, fitting results of two Br BTCs (Q-iii, Q-vi: 5 mmol L⁻¹ Na₂SO₄, pH_{ini} ≈ 5.5, Tab. 9.1) are exemplarily illustrated and discussed in the following section. A summary of all fitted transport parameters including gof provides Tab. 11.1; CXTFIT models and fitting results of remaining column experiments may be obtained from the digital appendix.

Transport parameter optimization of column experiment Q-iii with CXTFIT returned a very small dispersion coefficient ($D = 0.23 \text{ cm}^2 \text{ h}^{-1}$) and hence a small dispersivity $\lambda = 0.06 \text{ cm}$ which ranged on the mm scale indicating that the column was homogeneously packed without preferential pathways. Potential influences of dead end pores or dispersion processes (including diffusion) played therefore also only minor roles during transport experiments. The large Péclet number of ≈ 250 (Tab. 11.1) indicated that transport processes in the column were strongly dominated by advection.

For Q-iii fitting procedures with CXTFIT, the dispersion coefficient D [cm² h⁻¹], the pore water velocity v [cm h⁻¹] and the application time of the pulse solution t [h] served as adjustable parameters. Optimizations returned a time difference of 0.3 h between the fitted application time $t = 5.3 \text{ h}$ and the experimental application time $t = 5.0 \text{ h}$ (initial value) which was attributed to an erroneously determined dead volume (Sec. 11.1); the fitted v returned $3.68 \pm 0.08 \text{ cm h}^{-1}$ which agreed well with measurements where $v = 3.61 \pm 0.11 \text{ cm h}^{-1}$. Since the flow rate was precisely measured the pore water velocity v was assumed to be accurate which was substantiated with the CXTFIT optimization procedure. The time difference between measured and fitted application time of the pulse solution t was attributed to the stepwise packing procedure (Sec. 9.1): It was assumed that due to the compaction of the mineral in the columns the space in front of the frits was individually reduced for each experiment. Hence, the application of an identical dead volume of the frits for each column experiment (Sec. 11.1) turned out to be

unfavorable and resulted in biased corrections of BTCs. For future column experiments the dead volume of the frits should be individually determined for each experiment to exclude this potential error source.

Using D and v (without t) as adjustable parameters for fitting approaches of erroneously corrected Br BTCs resulted in substantial discrepancies between measured and fitted water flow velocities (Δv) which can be explained with the following example: The smaller the pore volume of a column V_0 (e. g. underestimation of the dead volume), the faster the water flow velocity is required to transport the same volume/amount of e. g. pulse solution through the column in an identical application time t . Hence, differences in optimized and experimental v indicate dead pore space, air intrusions in the column, or incorrectly determined dead volume (Sec. 11.1). As each column was saturated under vacuum conditions (Sec. 9.1) the columns were fully saturated, and it could be assumed that e. g. air intrusions did not occur. Furthermore, Br BTCs did not show pronounced tailings which was substantiated with small dispersivities λ and indicated an erroneously defined dead volume. Hence, the application time t [h] was included in optimization procedures which resulted in differences between optimized and measured application times t for columns with erroneous dead volume (up to 0.3 h). Using three fitting parameters (D , v , t) was only applied for quartz column experiments and revealed a consistent picture of Br BTCs where Δv equaled only 2 % on average. However, as v was calculated from the measured flow rate, for orthoclase and muscovite only D and if necessary t were used as fitting parameters. Since the discrepancies between fitted and measured application time t could be comprehensively explained the approach to include t as an adjustable parameter was justified for this study.

Since the shape of tracer BTCs and the dispersivity λ should be independent of the pore water velocity v for ideal tracers and homogeneous columns, column experiment Q-iii was repeated with the identical geochemical boundary conditions but with v reduced by factor 2.7 (Q-vi). It was also the aim to verify whether the shape of the SD of was influenced by dispersion and/or diffusion influences or rather by concentration dependent surface complexation /BRI 18/. As illustrated in Fig. 11.1 A the shape of the Br BTCs did not change with reduced v and CXTFIT results of Q-vi indicated that λ did not differ with decreasing v either (Fig. 11.1 B). Using D as a fix parameter that was reduced by factor 2.7 ($D = 0.06 \text{ cm}^2 \text{ h}^{-1}$) in relation to the optimized D of column Q-iii ($D = 0.17 \text{ cm}^2 \text{ h}^{-1}$) resulted in an acceptable fit (Tab. 11.1, Fig. 11.1 B) and substantiated the assumption that the dispersivity λ was independent from the pore water velocity v .

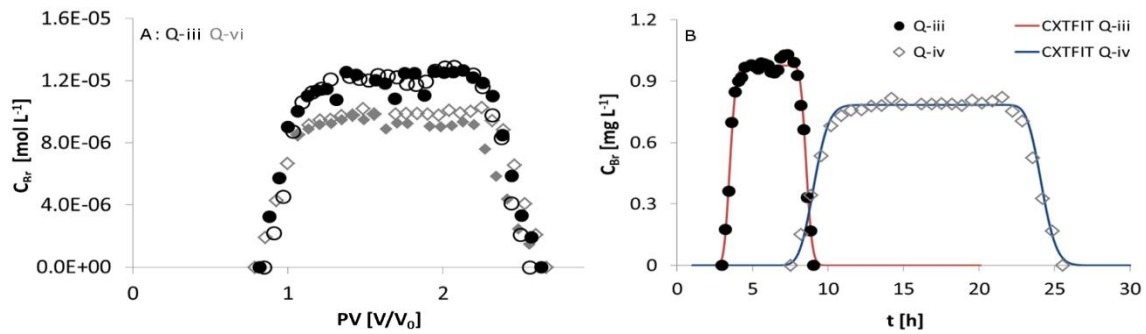


Fig. 11.1 A: Experimental Br BTCs (black, grey symbols) of Q-iii and Q-vi. B: Experimental and fitted BTCs of Q-iii (red line = fit with $q = 84 \text{ cm d}^{-1}$) and Q-iv (blue line = fit with $q = 32 \text{ cm d}^{-1}$)

Reduced Br C_0 of Q-vi due to new pulse solution preparation. The time lag of both BTCs resulted from reduced pore water velocities by factor 2.7 for Q-vi. Tab. 11.1 provides further information including optimized transport parameters. t [h] – considered experimental time frame, q – Darcy velocity [cm d^{-1}].

All Eu transport experiments resulted in similar ideal Br tracer BTCs /BRI 18/; hence, the following conclusions drawn from column Q-iii and Q-vi were assumed to be applicable to all column experiments:

- The columns were homogeneously packed, advective transport dominated the system.
- The occurrence of stagnant zones, dead end pores, or preferential path ways could be excluded due to dispersivities λ on the mm scale.
- The dead volume carried incalculable errors for many column experiments which resulted in application time differences between fitted and measured values.
- The dispersivity λ was independent of v substantiating the fact that columns were homogeneously packed without preferential path ways and negligible diffusion and/or dispersion processes.

To conclude, based on Br tracer BTCs asymmetrical shapes of Eu BTCs or SDs as well as differences in K_d -values between batch and column experiments could not be attributed to high dispersivities or diffusion from stagnant zones, inhomogeneously packed columns, or local nonequilibrium. Hence, concentration dependent surface complexation and/or interrelation between surface complexation reactions and solution composition (e. g. interaction of pH and surface complexation) presumably governed Eu migration under the given geochemical conditions. Both latter effects had already been observed

during batch (concentration dependence) and column experiments (interrelation between Eu transport and pH) /BRI 18/.

11.5.2 1D reactive Eu transport simulations

Experimental results of batch and column experiments revealed large differences in K_d -values which covered over three orders of magnitude for orthoclase and up to two orders of magnitude for quartz and muscovite /BRI 18/. Hence, it was refrained from using batch experiments to predict Eu transport with an empirical approach such as the linear K_d due to the large discrepancies that occurred between batch and column experiments. Furthermore, it could be assumed that transport experiments which revealed spatial and temporal pH variations due to Eu surface complexation could not be represented by the empirical K_d -approach either since geochemical interactions and hence, potentially variable sorption affinities over the experimental time frame of the column experiments cannot be represented with the linear (constant) K_d -approach. Consequently, this study focused on mechanistic reactive transport model simulations.

11.5.2.1 Transport simulations of quartz column experiments pH_{ini} 3.5 (Q-i)

Reactive transport simulations of Q-i resulted in BTCs regardless of the SCM assumed surface complex, whereas measurements returned a SD for Eu retardation (quartz, 10 mmol L⁻¹ NaClO₄, pH_{ini} 3.5). The mean calculated R_f -value over all simulation approaches equalled 2 ± 1 (\pm standard deviation) showing that predicted Eu migration was retarded only by factor two on average in comparison to the ideal Br tracer (R_f from column experiment Q-I = 380, cf. Tab. 11.1). Differences between predictions and experimental data expressed in $|\Delta \log K_d|$ (Sec. 11.4) exceeded at least 2 for all simulations (Tab. 11.2) representing unsatisfying predictions /DAV 05b/ (cf. Sec. 11.4). The following reasons were identified for insufficient RTM performance: All SCMs underestimated Eu immobilization during batch experiments at low pH values /BRI 18/ which consequently resulted in an underestimation of predicted Eu transport through quartz columns at low pH. Furthermore, pH_{ini} 3.5 of column experiments represented the lower pH range covered by batch experiments where only very few data was available for SCM calibrations. Hence, extrapolation of SCPs to geochemical conditions that were not profoundly substantiated by batch data failed.

Tab. 11.1 Summary of transport parameters of quartz (Q-i – Q-vi), orthoclase (O-i – O-iii), muscovite (mica-i – mica-iv), and synthetic sediment (SynSed-i, SynSed-ii) column experiments

Errors of the measured pore water velocity v given as the single standard deviation [cm h^{-1}]. R_f , K_d calculated from measurements. Parameter uncertainties of CXTFIT optimizations represent 95 % CI. Dispersivity was used in PHREEQC simulations as a fixed transport parameter and was calculated with D from CXTFIT fits. For PHREEQC $Pe_{\text{grid}} < 2$ to prevent numerical dispersion. – indicates that the parameter was not used for CXTFIT optimization. PV – pore volume, art. GW – artificial groundwater, $C_{Eu,Br}$ – Eu, Br concentration (aq), PS – pulse solution, BE+PS – background electrolyte + pulse solution in $PV[V/V_0]$, Δv – difference between fitted (CXTFIT) and measured v .

			Quartz						Orthoclase			Muscovite				Syn. Sed.	
			Q-i	Q-ii	Q-iii	Q-iv	Q-v	Q-vi	FS-i	FS-ii	FS-iii	mica-i	mica-ii	mica-iii	mica-iv	SynSed-i	SynSed-ii
Measurements																	
Background electrolyte (BE)		[mmol L ⁻¹]	NaClO ₄	NaClO ₄	Na ₂ SO ₄	Na ₂ SO ₄	art. GW	Na ₂ SO ₄	NaClO ₄	Na ₂ SO ₄	Na ₂ SO ₄	NaClO ₄	Na ₂ SO ₄	Na ₂ SO ₄	art. GW	NaClO ₄	art. GW
			10	10	5	50	App. Tab. A.7.2	5	10	50	50	10	5	50	App. Tab. A.7.2	10	App. Tab. A.7.2
pH _{ini}		[-]	3.5	5.6	5.6	5.5	5.5	5.5	3.6	3.5	5.5	3.6	3.6	5.5	5.5	3.5	5.5
Pulse solution	C_{Eu}	[mol L ⁻¹]	1.07E-05	1.05E-05	1.03E-05	9.5E-06	9.2E-06	1.00E-05	1.00E-05	1.00E-05	1.09E-05	1.00E-05	9.9E-06	9.6E-06	9.8E-06	1.01E-05	9.93E-06
	C_{Br}	[mol L ⁻¹]	7.5E-06	8.97E-06	1.2E-05	1.02E-05	8.8E-06	7.5E-06	9.09E-06	1.06E-05	9.8E-06	1.0E-05	1.02E-05	8.5E-06	7.5E-06	8.7E-06	1.0425E-05
BE+PS	PV	[V/V ₀]	81	75	80	85	80	94	136	60	75	42	100	116	123	122	250
Application time PS	t	h	5.2	5.0	5.3	5.0	5.3	15.0	4.7	4.6	4.7	8.3	7.8	7.2	7.2	4.6	5.1
Pore water velocity	v	[cm h ⁻¹]	3.61	3.63	3.47	3.64	3.42	1.309	3.59	3.94	3.92	1.53	2.34	2.600	2.55	3.43	3.58
		±	0.11	0.11	0.04	0.101	0.05	0.04	0.07	0.06	0.08	0.07	0.04	0.03	0.13	0.06	0.06
Darcy velocity	q	[cm h ⁻¹]	1.38	1.39	1.32	1.39	1.31	0.499	1.33	1.36	1.35	0.924	1.35	1.49	1.47	1.31	1.37
Bulk density	ρ_b	[g cm ⁻³]	1.64	1.64	1.64	1.64	1.64	1.64	1.63	1.64	1.64	1.13	1.19	1.19	1.19	1.64	1.64
Total pore space	V_0	[cm ³]	61.7	61.7	61.7	61.7	61.7	55.97	55.9	55.7	96.2	92.9	92.9	92.9	92.9	61.8	61.9
Total porosity	Φ	[cm ³ cm ⁻³]	0.382	0.382	0.382	0.382	0.382	0.381	0.371	0.346	0.345	0.604	0.574	0.575	0.575	0.381	0.382
Recovery rate Eu		[%]	97	96	90	100	105	100	95	95	103	101	101	67	96	94	105
Recovery rate Br		[%]	102	98	100	95	94	96	102	102	100	98	101	98	97	98	100
Retardation factor	R_f	[-]	380	920	190	1.8	16	210	1700	2.6	4.8	2600	1200	52	390	1800	120
Distribution coefficient	K_d	[m ³ kg ⁻¹]	8.8E-02	2.1E-01	4.5E-02	1.8E-04	3.4E-03	5.0E-02	3.9E-01	3.4E-04	7.9E-04	1.39	5.7E-01	2.4E-02	1.9E-01	4.1E-01	2.8E+01
		[L kg ⁻¹]	88	210	45	0.18	3.4	49.7	390	0.34	0.79	1400	570	24	190	410	410
CXTFIT																	
Dispersion coefficient	D	[cm ² h ⁻¹]	0.23	0.13	0.17	0.28	0.095	0.060	0.502	0.296	0.297	0.054	0.201	0.28	0.16	0.35	0.11
		±	0.097	0.05	0.08	0.19	0.09	-	0.29	0.30	0.17	0.026	0.06	0.09	0.05	0.13	0.04
Péclet number	Pe	[-]	190	346	249	162	440	267	88	163	162	350	143	116	195	120	409
Pore water velocity	v	[cm h ⁻¹]	3.68	3.60	3.50	3.83	3.59	1.35	-	-	-	-	-	-	-	-	3.50
		±	0.08	0.04	0.07	0.11	0.11	0.03	-	-	-	-	-	-	-	-	0.035
Difference b/t fitted and measured v	Δv	[cm h ⁻¹]	0.067	-0.030	0.032	0.18	0.17	0.039	-	-	-	-	-	-	-	-	-0.084
		h	5.1	-	5.0	-	4.7	14.9	4.5	4.9	4.8	-	-	-	-	-	-
Application time PS	t	±	0.095	-	0.098	-	0.14	0.29	0.13	0.17	0.087	-	-	-	-	-	-
Coefficient of determination	R^2	[-]	0.991	0.993	0.991	0.978	0.972	0.988	0.984	0.964	0.991	0.985	0.994	0.993	0.994	0.994	0.996
Mean square error	MSE	mg L ⁻¹	3.7E-04	3.6E-04	1.1E-03	1.7E-03	1.6E-03	8.7E-04	1.3E-03	4.6E-03	1.0E-03	1.5E-03	6.1E-04	5.5E-04	3.4E-04	4.7E-04	5.2E-04
Optimized parameters			v, D, t	v, D	v, D, t	v, D	v, D, t	v, t	D, t	D, t	D, t	D, t	D	D	D	D	v, D
PHREEQC																	
Dispersivity	λ	[cm]	0.06	0.04	0.05	0.07	0.03	-	0.1	0.08	0.08	-	-	-	-	-	-
Grid Péclet number	Pe_{grid}	[-]	1.1	1.9	1.4	0.9	2.6	-	0.5	0.9	0.9	-	-	-	-	-	-

11.5.2.2 Transport simulations of quartz column experiments $\text{pH}_{\text{ini}} \approx 5.5$ (Q-ii – Q-v)

Tab. 11.2 compares K_d -values from measurements and reactive transport simulations of quartz column experiments Q-I – Q-v (cf. Tab. 9.1); green values represent an acceptable discrepancy ($|\Delta\log K_d|$) between experiments and predictions below $0.5 \log K_d$, orange values ranged within $0.5 - 1.0 \log K_d$, and red values exceed $1.0 \log K_d$ /DAV 05b/. According to /DAV 05b/ predictions where $|\Delta\log K_d| \leq 1$ between measurements and simulations applies demonstrate profound system understanding. Discrepancies that exceed $1 \log K_d$ unit represent insufficient predictions of measurements. In Tab. 11.2, negative $\Delta\log K_d$ s indicate stronger retention of simulated Eu transport in comparison to K_d -values from measurements, positive values represent less retardation with respect to experimental data (Sec. 9.2).

Tab. 11.2 Summary of K_d -values calculated from experimental data and reactive transport simulations of quartz column experiments (Q-i – Q-v)

Differences between K_d -values from measurements and predictions are provided as $\Delta\log K_d$. A transport simulation proves system understanding if $|\Delta\log K_d| \leq 1$ /DAV 05b/: $|\Delta\log K_d| > 1$, $0.5 \leq |\Delta\log K_d| \leq 1$, $|\Delta\log K_d| < 0.5$. For details on SCMs cf. Section 10 and /BRI 18/. * PHREEQC convergence problems after 50 PVs. K_d [L kg^{-1}] – calculated distribution coefficient (cf. Sec. 11.2).

	Q-i		Q-ii		Q-iii		Q-iv		Q-v	
	K_d	$\Delta\log K_d$								
Experimental K_d	88		214		45		0.18		4.4	
DDLm bi	0.041	3.3	200	0.028	18	0.39	7.7	-1.6	34	-0.89
DDLm mono+bi	0.17	2.7	58	0.57	5.6	0.90	2.8	-1.2	8.2	-0.27
noEDL mono	0.76	2.1	188	0.06	9.7	0.66	1.9	-1.0	55	-1.09
BSM mono	0.14	2.8	48	0.65	7.0	0.80	3.09	-1.2	21	-0.67
BSM bi	0.047	3.3	119	0.25	20.1	0.35	2.9	-1.2	43	-0.99

Column experiment Q-ii ($10 \text{ mmol L}^{-1} \text{ NaClO}_4$, pH 5.6) was satisfactorily predicted with all SCP sets (Tab. 11.2); best results were obtained with *SCP Q I bi* for Q-ii (DDLm, bidentate surface complex, /BRI 18/). The shape of the SD, the maximum peak concentration, as well as the pH development were accurately predicted with *SCP Q I bi* for

Q-ii (Fig. 11.2, also /BRI 18/); all RTMs described the initial drop in pH due to surface complexation which returned to pH_{ini} during the course of the simulations. The noEDLM also yielded a satisfying simulation; however, the prediction did not reflect the shape of the SD nor the maximum satisfyingly (Fig. 11.2, Q-ii).

Transport experiment Q-iii ($5 \text{ mmol L}^{-1} \text{ Na}_2\text{SO}_4$, pH 5.6) was also adequately simulated with all SCMs; here, best results with the smallest $|\log K_d|$ values yielded *SCP Q I bi* (DDLm, bidentate surface complex) and *SCP II bi* (BSM, bidentate surface complex). Only RTMs using bidentate surface complexes yielded SDs where the position of the maximum Eu concentration was predicted in the column, all other approaches resulted in BTCs within the experimental time frame of 80 PVs /BRI 18/. For *SCP II bi* the maximum Eu concentrations as well as the shape of the SD were adequately predicted (steeper front compared to a shallower back of the SDs); however, the spatial position was accelerated in comparison to measurements. Hence, RTMs underestimated Eu immobilization which was the case for all simulation approaches (Fig. 11.2 Q-iii, /BRI 18/). Each RTM predicted an initial pH decrease for Q-iii that could not be substantiated with pH measurements (Fig. 11.2 Q-iii). However, the discrepancy faded after 5 PVs and the simulations returned to $\text{pH}_{\text{ini}} = 5.6$ (Fig. 11.2 Q-iii).

Quartz transport experiments carried out with $50 \text{ mmol L}^{-1} \text{ Na}_2\text{SO}_4$, $\text{pH}_{\text{ini}} = 5.5$ (Q-iv) could not be satisfyingly predicted with RTMs; neither the shape, nor the maximum peak concentration were adequately predicted which was evidenced by $\log K_d > 1$ (Tab. 11.2, Fig. 11.2 Q-iv). Furthermore, the RTM that was based on *SCP Q II bi* revealed convergence problems after 50 PVs had passed the column and returned major surface charge imbalances as well as non-converging mass balances for Na^+ , sulfate, and the IS which implied that the RTM was ill-defined. Whether the non-convergence was exclusively caused by the surface charge model and e. g. lacking co- and counterion association coefficients (for details cd. /BRI 18/) could not be profoundly reasoned based on the current state of data and knowledge. However, as a complete breakthrough of Eu was predicted within 50 PVs results are nevertheless displayed in Fig. 11.2 Q-iv. Interestingly, the pH developments of Q-iv predicted with different RTMs partly followed observations: An initial decrease caused by surface complexation reactions was followed by an increase of pH that exceeded pH_{ini} (Fig. 11.2 Q-iv). However, the increase of predicted pH conditions beyond pH_{ini} was delayed in comparison to measured values for all model approaches.

A comparison of predicted immobilization tendencies of Eu under sulfate influence (Q-iii: 0.005 mmol Na₂SO₄ and Q-iv: 0.05 mmol Na₂SO₄) showed that for Q-iii transport processes were overestimated and hence, retardation was underestimated. For predictions of Q-iv on the other hand, migration of Eu was underestimated and therefore immobilization of the trivalent actinide was overestimated. Even though both systems experienced Eu-sulfate speciation in solution, sorption tendencies that were predicted with the same RTMs showed contradictory developments in relation to measurements for Q-iii and Q-iv. This once more indicates that RTMs were ill-defined and that Eu transport under sulfate influence has not yet been understood. Experimental batch data of Eu with a sulfate background electrolyte is necessary to compare immobilization processes of Eu during batch and column experiments offering a first means to assess RTMs and helping to better define surface reactions with sulfate electrolytes.

For reactive transport simulations of column experiment Q-v (artificial groundwater, pH_{ini} 5.5) all but the nonEDLM predicted Eu transport under the influence of the artificial groundwater reasonably well with $|\log K_d|$ ranging between 0.27 and 0.99 for the electrostatic models (cf. Tab. 11.2, Fig. 11.2 Q-v). Generally, Eu transport was underestimated (negative $\log K_d$ -values) which mostly resulted in SDs within the experimental frame of 80 PVs /BRI 18/ instead of BTCs as had been observed during transport experiments. Only *SCP Q I mono+bi* (DDLm, combination of mono and bidentate surface complex) yielded a BTC but still overestimated Eu retardation indicated by a shifted occurrence in PV [V/V₀] of the Eu peak concentration; however, the shape of the BTC which was characterized by a steep front and long tailing was adequately simulated. Competing cations (Ca²⁺, Al³⁺, Mg²⁺, Na⁺) that were contained in the artificial groundwater posed competition for sorption sites on Eu surface complexation which decreased Eu retardation and accelerated Eu migration. To consider the competition of all competing cations on Eu sorption processes more data would be necessary for the different mechanistic model approaches. The predicted pH development of Q-v (Fig. 11.2 Q-v) did not follow experimental data: The initial pH increase that had been observed during column experiments could not be verified or described with RTM simulations. To fully explain the reproducible experimental pH development further research is necessary. The complexity of the influence of the artificial groundwater on Eu migration has not yet been fully uncovered and hence, RTMs could only reflect the system based on the current state of knowledge.

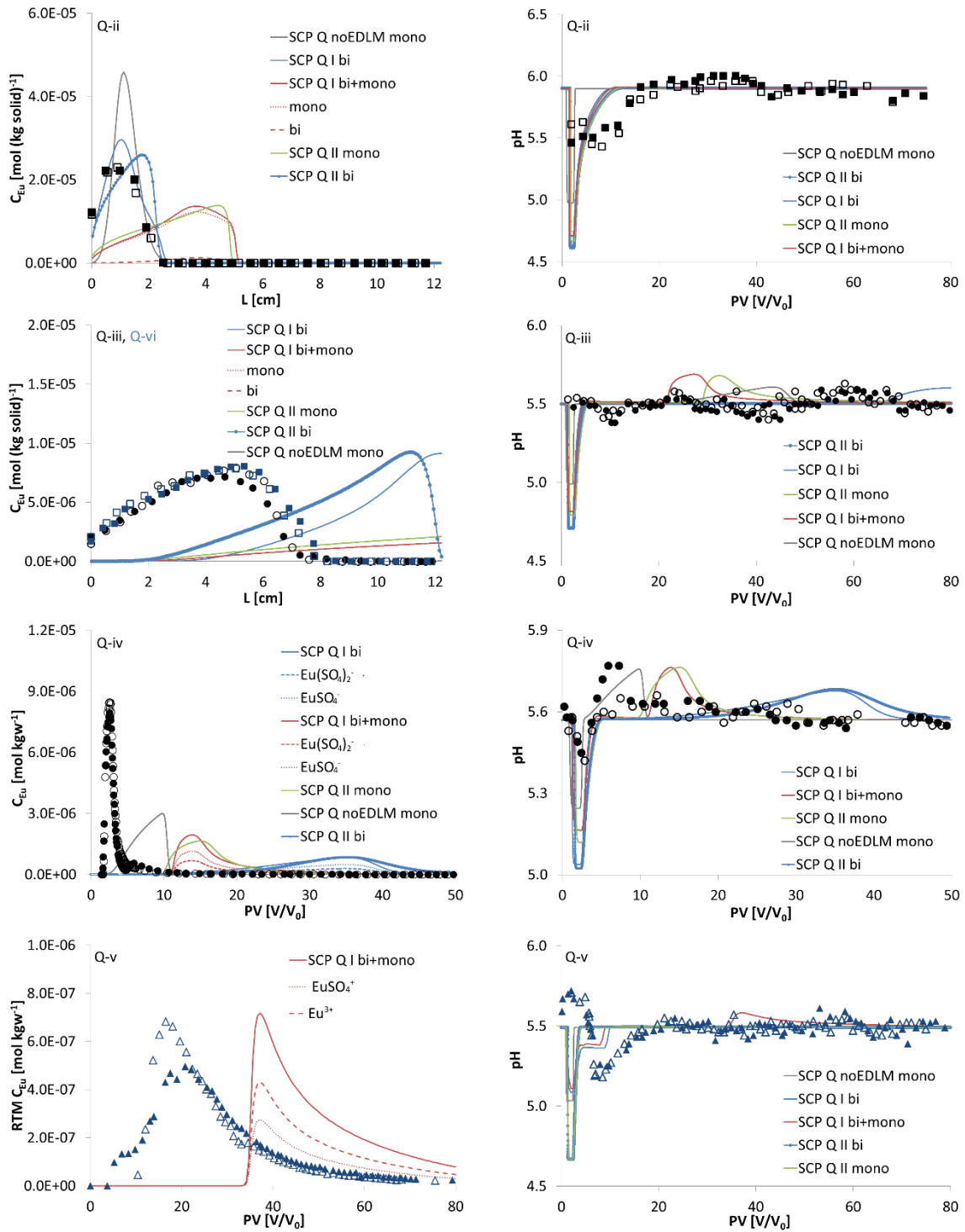


Fig. 11.2 Reactive transport simulations of Eu through quartz columns, $\text{pH}_{\text{ini}} \approx 5.5$ (Q-ii – Q-v)

Simulated SDs relate to the following PV (cf. Tab. 11.1): Q-ii $t = 75$ PV, Q-iii $t = 80$ PV. Reactive transport models (RTMs) – colored solid lines. For details cf. Tab. 9.1 and Tab. 11.1.

Considering the performance of RTMs for Q-i – Q-v it was not possible to explicitly identify an Eu surface complex or electrostatic model that described Eu transport processes

through homogeneous quartz columns adequately for all geochemical conditions (Fig. 11.2). However, considering that smaller $|\log K_d|$ are preferred over larger ones, from Tab. 11.2 it was concluded that the DDLM and the BSM predicted Eu transport equally well; the noEDLM simulated Q-ii and Q-iii adequately but showed discrepancies for Q-v compared to the EMs. Based on these results it was not unambiguously possible to prefer electrostatic models over the noEDLM. Since the combination of a monodentate and bidentate surface complex (*SCP Q I mono+bi*) did not yield more precise results for the DDLM and keeping in mind that it was the scope to develop as simple as possible RTMs the application of a bidentate Eu surface complex was preferred over a combination of surface complexes (Tab. 11.2). At this state of knowledge and in the absence of spectroscopic data as well as batch experiments under sulfate influence or artificial groundwater, a bidentate Eu surface complex seemed to describe Eu transport processes over the different geochemical conditions best for electrostatic model approaches (Tab. 11.2). To substantiate the assumption of a bidentate Eu surface complex spectroscopic data and additional batch experiments are needed for identical geochemical conditions. So far, results are only substantiated by TRLFS studies carried out by /STU 08b/ who found evidence of a tridentate Cm complex on a quartz surface.

To conclude, SCPs derived from batch experiments resulted in sufficient Eu transport simulations ($|\log K_d| \leq 1$) for all column systems except for $\text{pH}_{\text{ini}} = 3.5$ and high ligand concentrations using electrostatic models (DDLM, BSM). To address the influence of sulfate, competing cations, and low pH conditions on Eu surface complexation in detail further research is necessary to better assess and describe Eu surface complexation during transport experiments. A better definition of the system would result in a more realistic formulation of RTMs that then return more reliable predictions and increased system understanding.

11.5.2.3 Transport simulations of orthoclase column experiments

As for quartz, Eu transport experiments with $\text{pH}_{\text{ini}} = 3.5$ could not be adequately simulated with any RTM and regardless of the background electrolyte. Transport experiment FS-iii was adequately predicted with the DDLM and BSM approaches. However, a preferable RTM and hence a SCP set from batch experiments could not be identified that predicted Eu transport through orthoclase columns best. Influences of different surface charge models on RTM simulations could not be clearly observed either /BRI 18/. However, a comparison of transport simulations using electrostatic and noEDLMs showed that all noEDLMs resulted in inadequate predictions with $|\Delta \log K_d| > 1$. Consequently, the

consideration of the surface charge development of orthoclase seemed to enhance RTM performance even though one specific preferable surface charge model could not be presented. Once again, more research is needed to undoubtedly describe the surface charge development of mineral and sediment surfaces under different geochemical influences (especially sulfate) and to uncover the reasons for large discrepancies between batch and column experiments.

More detailed information and illustration of the simulated results of Eu transport through orthoclase columns is provided in /BRI 18/.

11.6 Discussion of and conclusion drawn from Eu transport simulations

In this study, Eu surface complexation constants ($\log K_{EuS}$) were derived from batch experiments and used in RTMs (DDLm, BSM, noEDLM). Generally, RTMs and the simulation of Eu transport under different geochemical conditions was a synthesis of surface charge and surface complexation models and it was assumed that surface complexation constants from batch experiments were transferable to column experiments. It was the scope to develop straightforward models with the smallest number of parameters possible that still accurately described the reactive transport and retardation of Eu over a range of experimental conditions ($|\Delta \log K_d| < 1$, /DAV 05b/). Thus, it was not the aim to predict Eu migration in detail but to capture main features and tendencies with SCPs from batch experiments. However, to predict Eu transport and retardation processes as close to measurements as possible Eu sorption during batch experiments should yield similar K_d -values in relation to column experiments under comparable geochemical conditions. In this study batch experiments revealed up to three orders of magnitude lower distribution coefficients /BRI 18/ which resulted in evident differences between experimental Eu transport data and predictions.

From reactive transport simulations of quartz column experiments the following conclusions were drawn:

- Eu transport at $\text{pH}_{\text{ini}} \approx 3.5$ could not be accurately represented with any RTM.
- At $\text{pH}_{\text{ini}} \approx 5.5$ ($10 \text{ mmol L}^{-1} \text{ NaClO}_4$ and $5 \text{ mmol L}^{-1} \text{ Na}_2\text{SO}_4$ background electrolyte) most RTMs resulted in adequate predictions ($|\Delta \log K_d| < 1$).
- Eu migration under the influence of $50 \text{ mmol L}^{-1} \text{ Na}_2\text{SO}_4$ could not be sufficiently described ($|\Delta \log K_d| > 1$).

- The implementation of a competing surface complexation reaction of Al^{3+} resulted in reasonably well representations of Eu transport processes in artificial groundwater for most model approaches /BRI 18/.
- Bidentate surface complexes seemed to describe Eu transport best for the DDLMs and BSMs regarding the different geochemical conditions.
- Spectroscopic evidence under similar geochemical conditions would be needed to further substantiate the latter finding.
- Batch experiments that include the complexing effect of a sulfate ligand would offer valuable information of Eu surface complexation and would offer a good means to more realistically set-up RTMs which has to be considered for future research projects.

Orthoclase RTM predictions revealed the following:

- Transport experiments at $\text{pH}_{\text{ini}} \approx 3.5$ could not be accurately predicted with any RTM, regardless of the background electrolyte ($|\Delta \log K_d| > 1$).
- Reactive transport simulations based on the DDLM *SCP FS VII* yielded adequate predictions for column experiments with $\text{pH}_{\text{ini}} 5.5$ and $50 \text{ mmol L}^{-1} \text{ Na}_2\text{SO}_4$ background electrolyte ($|\Delta \log K_d| < 1$).
- The RTMs that were based on basic Stern SCM *SCP FS V* and *VI* resulted in less adequate simulations compared to DDLM approaches which was probably mainly attributed to the lack of co- and counterion association coefficients for Na_2SO_4 /BRI 18/.
- Predictions with noEDLM approaches were not able to satisfyingly simulate any column experiment ($|\Delta \log K_d| > 1$).
- No preferable orthoclase SCP set or RTM could be identified that predicted migration processes of the trivalent lanthanide best.
- Whether Eu retardation in orthoclase columns would be adequately simulated under inert background electrolyte conditions or low ligand concentrations at $\text{pH}_{\text{ini}} \approx 5.5$ as it was the case for quartz, should be verified in future research projects with new sets of transport experiments.

The reasons for the insufficient simulations of $\text{pH}_{\text{ini}} 3.5$ for orthoclase and quartz transport experiments could be found in the absence of sufficient data since experimental conditions of column experiments exceeded experimental conditions of batch experiments at the lower pH range. Furthermore, transport results revealed that even though retardation tendencies during Eu column experiments agreed well with observations from batch experiments, K_d -values differed by orders of magnitude between both experimental set-ups considering comparable geochemical conditions. The gof of SCMs also had influence on RTM simulations: Quartz and orthoclase batch experiments were underestimated with SCMs at low pH values; thus, RTM predictions at low pH conditions also underestimated Eu retardation resulting in a faster predicted migration of Eu in comparison to measurements. It should also be mentioned that RTMs combine all simplifications, limitations, as well as parameter uncertainties of surface charge and SCMs; thus, even though the transferability of $\log K_{\text{Eu}}$ from batch to column experiments was challenging for some geochemical conditions in this study results did not necessarily indicate that the approach is generally not applicable. Transport simulations of this study rather highlighted that the acid-base behavior of ubiquitously present minerals is still not yet fully understood, that surface complexation constants for competing surface complexation reactions of the different electrostatic models are lacking, that no data for the exact definition of Na_2SO_4 co- and counterion association coefficients on the examined mineral phases is available, that no adequate spectroscopic evidence could be found in literature to more precisely back up proposed surface complexes, and that fundamental batch experimental data describing Eu immobilization under the influence of sulfate is also not available and lacking. All the latter result of simplified RTMs can only offer first impressions of Eu transport under the chosen geochemical conditions. Findings call for a more sophisticated and accurate experimental determination as well as definition of surface complexation constants and emphasize the need for more research to

- clearly identify lanthanide surface complexes for relevant geochemical conditions and mineral phases,
- improve the understanding of the solid-solution interface,
- further support the development of thermodynamic databases,
- and finally, to improve the performance of RTMs.

From this study it was concluded that parametrization of SCMs should be performed with measurements that cover a broad range of experimental conditions relevant for transport processes. However, to assess the applicability of surface complexation constants from

batch to transport processes, for selected geochemical conditions batch experiments should be accompanied by column experiments whenever possible.

12 Smart K_d -matrices

In the ESTRAL project we developed an approach, where the smart K_d -concept was applied for complex geochemical models /NOS 12b/. Moving to the smart K_d -concept allows accounting for environmental parameters varying in time and space, depending on the geochemical conditions of the investigated system. Moreover, this concept generates predictive values perfectly applicable within the conventional paradigm of distribution coefficients. Aim was to merge a description of sorption as realistic as possible with high computational speed in reactive transport calculations.

In general, the sorption of radionuclides onto mineral surfaces was described by smart K_d -values based on surface complexation modeling (SCM) for a wide range of environmental parameters (Sec. 3.2). For the geochemical calculations of smart K_d -values within this project, two separate thermodynamic databases containing thermodynamic data for the representative elements and minerals were created and explained in Section 6. The calculation of the smart K_d -matrices and the used programs and their capabilities are described in the following.

To describe the sorption of radionuclides as a function of important environmental parameters, the smart K_d -values were pre-calculated using special computer programs and saved as multidimensional smart K_d -matrices to be accessed during reactive transport simulations. The fundamental strategy for calculating smart K_d -values is described in /NOS 12b/. To reduce the calculation time of such a complex system, we had successfully run a further calculation variant via a high-speed cluster computer (Linux system). There were no differences in the results between the standard windows system and the Linux system, but the calculation time is 6 times faster. The used programs and their capabilities are described in the following section.

12.1 Software packages

PHREEQC /PAR 13/: For modeling the complete speciation patterns of contaminants including their sorption onto mineral phases the geochemical speciation code PHREEQC was used. This code was selected for several reasons: I) PHREEQC can be downloaded as freeware (available at http://www.brr.cr.usgs.gov/projects/GWC_coupled/phreeqc, used version 3.3.7) and is therefore used by a large community, the code has an active development; there is open access to its source code and an exhaustive manual. II) The

program can be run from a batch file to be launched directly from other external codes (here: UCODE). III) In PHREEQC a variety of different SCM types for modeling surface complexation processes is implemented: DDLM (Diffuse Double Layer model) /DZO 90/, nonEDLM (Non-electrostatic model) /DAV 90/, /BAE 95/, /BRA 99/, /KUR 51/, and CD-MUSIC (Charge Distribution Multi-Site Complexation model (e. g. /HIE 89a/, /HIE 89b/). IV) Several databases are available in PHREEQC format to be used as basis for an own project-specific database.

UCODE /POE 14/: This computer program was used as data processor / Interface. The main input file of UCODE controls the iteration process: It tells which models to execute, which parameters to substitute, and how to extract the PHREEQC-computed values. There is also a chance to modify input parameters by some simple arithmetic and logic. Here the variation of the geochemical parameters (E_i) and the assemblage of smart K_d -matrices were performed. UCODE can also be downloaded as freeware (available at <http://igwmc.mines.edu/freeware/ucode>, used version UCODE_2014, 1.004).

SimLab: For Sensitivity and Uncertainty Analysis (SA/UA) of the calculated smart K_d -values a third code SimLab was coupled to PHREEQC and UCODE. Via SA the main influence parameter for the retardation of radionuclides was identified. The windows version SimLab2 (as described in /NOS 12b/) was already used here. However, this version is no longer supported by the developer EU Joint Research Center (JRC) in Ispra / Italy. Therefore, a comparable calculation of the (first for UAF system) had been successfully done with a new software package RepoSUN/SimLab4 /BEC 16/, which is developed at the GRS Braunschweig, using the SimLab4 library developed by JRC Ispra.

The coupling of these three computer codes provides various benefits: (1) The most important thing is that we can calculate the distribution coefficient for a large number of environmental parameters. (2) Consequently, the geochemistry is describing more realistically under changing geochemical conditions. (3) The resulting smart K_d -matrices can be exploited for SA/UA, whereby SimLab provides in contrast to UCODE also methods for Global Sensitivity Analysis. (4) The data transfer between the different codes and the structured storage of the results can be organized in an automatic manner. (5) And not least this offline coupling is more efficient in computing time than a direct coupling with transport programs.

In the following section the coupling procedure is described in detail and is illustrated by a general computation schema (Fig. 12.1). Thereby the different colored sections identify the individual computer programs.

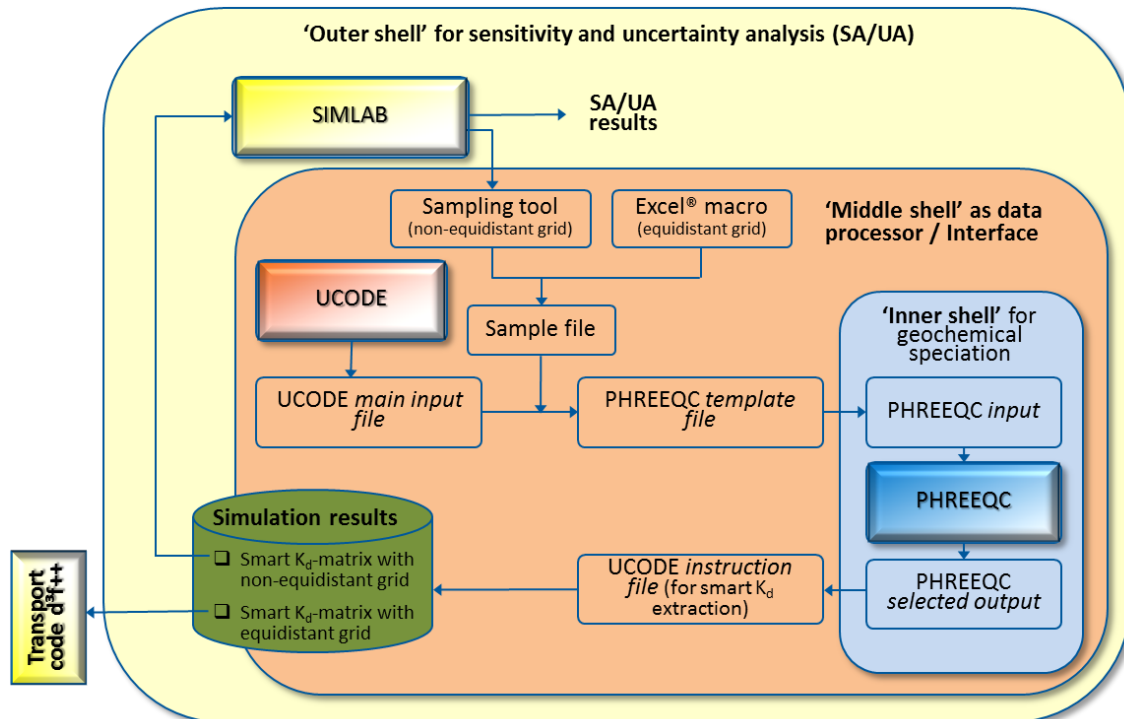


Fig. 12.1 Flowchart of the coupled codes PHREEQC, UCODE and SIMLAB for calculating smart K_d -values and their sensitivity and uncertainty analysis.

There are some rules that must be obeyed: First of all, a sample file including sets of model input parameters (varied in the range between minimum and maximum value of the respective field data) must be created. For implementing the smart K_d -matrices in the transport codes d^3f++ , the grid must be rather simple for being readable for the code. Thus, an equidistant sample grid was easily generated via a Microsoft EXCEL® macro, just taking the minimum and maximum value for each input parameter and dividing this range by the number of steps (variations per parameter). In order to investigate the sensitivity and uncertainty of the calculated smart K_d -values the software SimLab has as the outermost shell a code providing an input parameter variation tool to vary all parameters simultaneously and according to their error distribution functions and mutual correlations. Consequently, a non-equidistant grid of smart K_d -values was created allowing for SA/UA.

In a second step (middle shell), the program UCODE takes each parameter vector from the sample file line by line (enlarged by all constant parameters), convert it into a valid (i. e. correctly formatted and complete) input file for the speciation code PHREEQC and

pass it on to such a code. The innermost shell then computes a geochemical speciation with associated species distributed between mobile and immobile phases, adapting a respective template (a description of the PHREEQC input file is given in the Section 12.4). After each simulation run, the middle shell UCODE takes the output (resulting smart K_d -values) from the PHREEQC selected output and adds these values to a separate text file with all the simulation results. Then the next parameter combination, as taken from the sample file, is implemented from UCODE in the PHREEQC input file and the resulted K_d -values are also saved in the results file. This is done until all parameter combinations in the sample file are processed. All calculated smart K_d -values (there might be more than one covering a variety of elements simultaneously) are then linked to the respective input parameter as a large matrix (by a separate program, e. g., PASTE.EXE, a freeware port of the respective Linux command to Windows) in one single text file. The outer shell finally performs a statistical analysis to obtain ranking tables.

The total number of variation steps directly scales the size of the resulting smart K_d -matrix. The use of an equidistant grid has the advantage of requiring only very simple (and consequently very fast) interpolation algorithms inside the transport code d^{3f++}. However, this does not take into account that each environmental parameter is subject to a specific distribution function, which usually is not the uniform distribution. Therefore, a non-equidistant grid is necessary for being more realistic. The associated nearest-neighbor search in such multidimensional matrices (required for the interpolation) is described in /MCN 01/ and should be implemented in d^{3f++} in the future.

12.2 Environmental parameters

The concept developed in the previous ESTRAL project should be extended in the WEIMAR project to consider further important processes such as redox reactions and ion exchange as well as further relevant competing cations (e. g. Al, Fe, Mg) and complexing ligands (e. g. PO_4^{3-} , SO_4^{2-}) (cf. Sec. 3.2). In ESTRAL we considered the pH, dissolved inorganic carbon (DIC), ionic strength (salt concentration, IS), Ca^{2+} and the radionuclide concentration [RN] as first important environmental parameters. Now, the competing cation Al^{3+} and the complexing ligand SO_4^{2-} were considered additionally. Results from ESTRAL /NOS 12b/ identified that the total [RN]-concentration did not affect the sorption significantly. Consequently, this parameter was now set as fix in the model input using the maximum concentrations as given in /NOS 12b/ (estimated from far field calculations /KEE 05/). Furthermore, the consideration of ion exchange processes had been implemented in the current concept. However, for describing such a complex

natural system the cation exchange capacity as well as selectivity coefficients for e. g. muscovite have to be evaluated. Unfortunately, the consideration of redox reactions was not possible due to the lack of existing data for the selected reference site Gorleben. Therefore, an alternate model site with well-documented redox data is necessary, but still not possible to consider any more in this project. Finally, the application of the concept on highly mineralized solutions (as occurring in the lower aquifer at Gorleben site) using the Pitzer formalism should be realized. Unfortunately, not all necessary Pitzer data were available for our complex natural system or are under discussion at that time.

In the actual work following parameters were considered:

- E₁: pH
- E₂: Dissolved inorganic carbon (DIC)
- E₃: Ionic strength (IS)
- E₄: Total concentration of calcium [Ca]
- E₅: Total concentration of aluminum [Al]
- E₆: Total concentration of sulfate [SO₄²⁻]

For most of these parameters the chemical groundwater data as described in Section 4.1 (based on HYGOR-BGR database /KLI 04/) were used to derive lower and upper limits for the parameter variation. Thereby, the minimum and maximum values were calculated from the mean plus / minus threefold standard deviation. Recommended minimum and maximum concentrations for E₁ – E₆ are given for each hydrogeological unit in Tab. 12.1.

Tab. 12.1 Recommended minimum and maximum values of environmental parameters (concentrations in mol L⁻¹)

Environmental parameter ^a	UAF		AT		LAF1		LAF2		Distribution
	Min	Max	Min	Max	Min	Max	Min	Max	
E ₁ : pH	6.4	8.2	6.7	9.1	5.1	8.6	5.5	8.6	Uniform
E ₂ : DIC	4.1E-04	5.3E-03	1.0E-03	1.2E-02	4.5E-04	2.2E-02	1.3E-03	1.2E-02	log-Uniform
E ₃ : IS	9.4E-04	1.7E-02	4.6E-04	7.5E-02	1.2E-02	2.0E+01	3.0E-03	2.0E+01	log-Uniform
E ₄ : [Ca]	2.2E-04	3.1E-03	1.0E-05	4.2E-03	3.5E-04	1.0E+00	1.1E-04	8.2E-01	log-Uniform
E ₅ : [Al]	7.7E-07	4.3E-06	2.3E-08	1.7E-04	3.8E-07	4.7E-05	3.8E-07	4.7E-05	log-Uniform
E ₆ : [SO ₄ ²⁻]	1.1E-05	3.6E-03	1.2E-07	6.2E-04	3.5E-05	5.4E+00	8.1E-06	1.4E+00	log-Uniform

^a based on field data /KLI 04/

Obviously, there are more complexing and competing ions than considered as environmental parameters; the most important amongst them being silicate. The concentration of the ion SiO_3^{2-} was primarily determined by equilibria with solubility limiting mineral phase quartz, and considered as secondary environmental parameters. Organic material, which is ubiquitous in the sediment and might impact the sorption of RN, is not considered at this stage to keep the model system simple. Nevertheless, a source of dissolved inorganic carbon (DIC), e. g. due to metabolic activities of sedimentary organic material, is included in the transport code d^{3f++}.

12.3 Temperature dependencies

A further working step was to check the temperature dependency in our PHREEQC calculations for the climatic scenario “permafrost”. For our model area Gorleben we assumed a constant temperature field of 14 °C as a mean value between the natural 8°C at the surface and 20 °C in 400 m depth. /KAP 61/, /LEG 04/. Therefore, the expected reaction enthalpies ΔRH for relevant mineral phases have been retrieved and used to predict the temperature effect on $\log K$ by means of the van’t Hoff approximation, but the observed changes in the solubility always lie within the error limits. Furthermore, for modeling the radionuclide transport with permafrost conditions, temperatures of 5 °C were expected. The influence of such a temperature dependency was checked in the PHREEQC calculations. It has been shown that there was no significant effect for the calculated K_d -values for 14 °C and 5 °C (Tab. 12.2).

Tab. 12.2 Comparison of K_d -values (in $\text{m}^3 \text{kg}^{-1}$) for temperature 14 °C and 5 °C

Radionuclide	K_d -value for 14 °C	K_d -value for 5 °C
Cs	5.32e+00	4.68e+00
Sr	2.33e-07	1.81e-07
Ni	1.12e-02	9.28e-03
Am	3.49e+00	2.97e+00
Th	1.47e+00	1.43e+00
Np(V)	4.28e-04	3.92e-04
U(VI)	1.74e-03	2.41e-03
Se(VI)	1.13e-03	1.41e-03

12.4 Model input for PHREEQC

In PHREEQC all site-specific conditions including composition of groundwater solution (Sec. 4.1), equilibrium phases (quartz), surface complexation parameters (Tab. 12.3) and exchange parameters were defined for calculating the smart K_d -values for each hydrogeological unit as described in detail in /NOS 12b/. In general, we used the DDLM /DZO 90/ for modeling surface complexation reactions. Ion exchange processes, which might occur in the aquitard (higher clay content) and at the interface to the upper aquifer, were now considered in the extended concept. Thereby, the most important minerals for ion exchange are phyllosilicates, mainly muscovite and illite. The total number of their exchange sites was calculated from the total cation exchange capacity (CEC) of the sediment given in /GRI 82 - 94/ less the amount of 'surface charge' of relevant exchangeable phases /APP 16/. However, for describing such a complex natural system the cation exchange capacity as well as selectivity coefficients for e. g. muscovite have to be evaluated.

Recommended SCPs including SSAs and protolysis constants (pK-values) for site-specific minerals are given in Tab. 12.3. All reaction equations and constants for ion exchange and surface complexation are given in the WEIMAR_EDH_20171130_GRS-500.dat database (cf. digital appendix); the full bibliographic details are cited in RES³T. The structure of the PHREEQC input file (as basis for the template file for the UCODE routine for smart K_d -calculations) is exemplarily provided in the digital appendix for the UAF.

Tab. 12.3 Recommended surface complexation parameters for site-specific minerals at the Gorleben overburden

	Quartz	Orthoclase	Muscovite	Gibbsite	Goethite	Kaolinite	Illite
SSA [m ² g ⁻¹]	0.06 ± 0.006 ^a	0.19 ± 0.006 ^a	0.66 ± 0.01 ^a	32 ^b	60 ^c	11.33 ± 0.06 ^a	57 ^d
SSD [sites nm ⁻²]	2.31	2.31	2.31	2.31	2.31	2.31	2.31
pK ₁ ^e	-	6.36	6.01	7.53	7.13	8.33	5.12
pK ₂ ^e	7.20	7.64	7.65	9.87	9.60	9.09	7.71

^a Mean of threefold BET measurements at HZDR (reported uncertainties represent 95 % confidence limit ($\pm 2\sigma$)).

^b Recommended SSA for gibbsite published in /KAR 10/.

^c Recommended SSA for goethite published in /MAT 06/.

^d Mean SSA published in /JER 06/ and /WAR 90/.

^e References are given in the WEIMAR.dat database and their full bibliographic details are cited in RES³T.

12.5 Results of smart K_d -matrices and their uncertainty and sensitivity

To investigate the sensitivity and uncertainty of the calculated smart K_d -values under variation of the influencing parameters and to analyze their individual influences, a probabilistic uncertainty and sensitivity analysis (UA/SA) was performed with the software program SimLab2. Additionally, UA/SA were done with a new software package RepoSUN/SimLab4 /BEC 16/ exemplary for the sorption of U(VI) in the upper aquifer (UAF) at the Gorleben site /STO 17/.

For the varying parameters uncertainty intervals were defined as indicated in Tab. 12.1. Log-uniform distributions were assumed for all parameters, except from the pH value, which was assumed to be uniformly distributed. The results, i. e. the K_d -values, were analyzed in the following way:

- As the output distribution covers several orders of magnitude, a log-transformation was performed on the output data. This was then used for all further calculations.
- A histogram of the model output visualizes the distribution.
- Some statistical measures were calculated to characterize the distribution (minimum, maximum, mean, standard deviation).
- The sensitivity indices were calculated for each of the input parameters.

12.5.1 Uncertainty analysis and results

The statistical characteristics (mean, minimum, maximum and standard deviation 2σ), which characterize the distribution of the log K_d -values for Cs, Ra, Ni, Am, Th, Np, U and Se in UAF and AT (LAF under discussion) are given in Tab. 12.4.

In the following we will compare exemplary the results for U(VI) in UAF to previous results from the ESTRAL project /NOS 12b/ as well as to results from the additional UA/SA using new software package RepoSUN/SimLab4. The statistical measures characterizing the distribution of the log K_d -values for U(VI) in UAF are given in Tab. 12.5.

Tab. 12.4 Mean smart K_d -values for UAF, and AT (LAF under discussion) and their minimum, maximum and standard deviation 2σ (K_d in $\text{m}^3 \text{kg}^{-1}$, logarithmic)

	Mean	Min	Max	SD (2σ)
UAF				
log K_d (Cs)	-1.2	-2.4	-0.7	1.2
log K_d (Ra)	-0.3	-1.0	0.3	0.5
log K_d (Ni)	-1.6	-3.4	-0.4	1.6
log K_d (Am)	-0.6	-1.7	1.0	1.1
log K_d (Th)	0.6	-0.6	1.6	1.0
log K_d (Np)	-2.4	-2.9	-2.2	0.3
log K_d (U)	-1.7	-4.2	-0.4	1.7
log K_d (Se)	-5.4	-12.2	-3.2	3.4
AT				
log K_d (Cs)	-0.3	-1.4	0.2	1.0
log K_d (Ra)	0.1	-1.2	1.6	1.7
log K_d (Ni)	-0.7	-2.4	0.6	1.2
log K_d (Am)	3.3	1.7	3.8	0.9
log K_d (Th)	1.1	-1.7	2.4	1.7
log K_d (Np)	-0.9	-1.9	-0.4	0.5
log K_d (U)	-2.4	-5.3	0.1	2.1
log K_d (Se)	-8.0	-10.8	-5.5	2.1

Tab. 12.5 Statistical characteristics of the distribution of the log K_d -values for U(VI) in the upper aquifer (K_d in $\text{m}^3 \text{kg}^{-1}$, logarithmic)

	SimLab2	RepoSUN/Sim-Lab4	ESTRAL
Mean	-1.7	-1.3	-3.0
Maximum	-0.4	0.6	0.9
Minimum	-4.2	-4.0	-7.0
Standard Deviation	1.7	1.8	1.9

A suitable tool for the description of the calculated smart K_d -values and their resulting total variance is the frequency distribution function. In Fig. 12.2 the histograms of the smart K_d -values for uranium(VI) is presented. Here, and in all following discussion, the smart K_d -values are presented in logarithmic form to account for their spreading over several orders of magnitude. The distribution is bell-shaped and slightly left skewed. In general, the log K_d (U(VI)) range over 5 orders of magnitude.

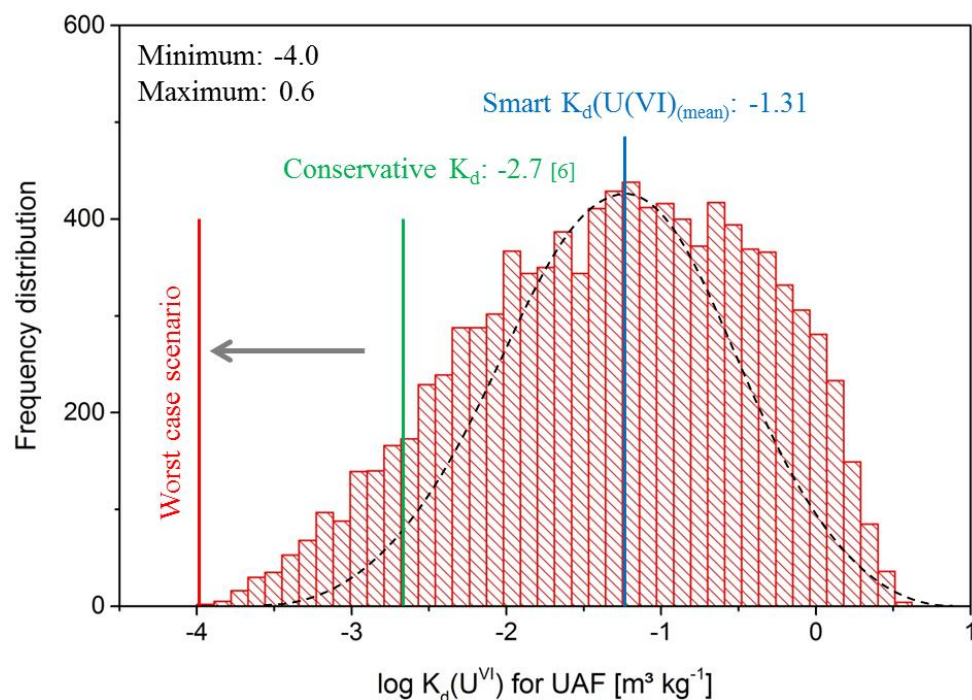


Fig. 12.2 Histogram of 10,000 pre-calculated smart K_d -values for U(VI) sorption in the upper aquifer based on Random sampling (K_d in $\text{m}^3 \text{kg}^{-1}$, logarithmic scale).

We could demonstrate that constant K_d -values (here for U(VI) $\log K_d$ of -2.7 /SUT 98/, green line in Fig. 12.2) used so far in transport modeling with r^{3t} are too crude an assumption. It is obvious that using only a mean K_d -value (blue line in Fig. 12.2) would not be suitable, and the distribution is not even a Gaussian. Both observations strongly support that the full range of the calculated K_d -values must be taken into consideration for reactive transport calculations. The U(VI) distribution coefficients rather range over several orders of magnitude. For considering worst-case scenarios much smaller K_d -values (red line in Fig. 12.2) have to be used than in conventional conservatism concepts followed so far.

Comparing to the results from the ESTRAL project the frequency distribution of the $\log K_d$ -values for U(VI) looked rather flat and extending over 8 orders of magnitude. The "worst case scenario" K_d is about three orders of magnitude lower than it is presented now in Fig. 12.2. These differences are primarily originating from an updated thermodynamic database, due both to a steadily on-going literature review as well as own experimental work to derive surface complexation parameters for those systems where hardly any such parameters were available. A prominent example is the lack of parameters for

the sorption on mica and feldspars, see /RIC 16/. The reduced parameter range (due to a more rigorous screening of the original Gorleben field data) had only a minor effect.

Comparing the smart K_d -values for UAF and AT (Fig. 12.3 and Fig. 12.4; shown as blue bars) to results from published experimental investigations with comparable sandy (for UAF) or clayey substrates (for AT) is very encouraging: /ZAV 04/ published $\log K_d$ -values for U(VI) between -6.1 and -1.2 for sandy Frenchman flat sediment, and /BRA 08/ derived a $\log K_d$ of -1.2 from sorption experiments with U(VI) onto natural sandy sediment (all K_d in [$\text{m}^3 \text{kg}^{-1}$]), which compares well with our calculated mean smart K_d -value of -1.3. /VIL 11/ published values for the sorption of selected radionuclides on bentonite samples reported from the Nuclear Waste Management Organization (NWMO) Canada, which also compare well with our smart K_d -values for the AT.

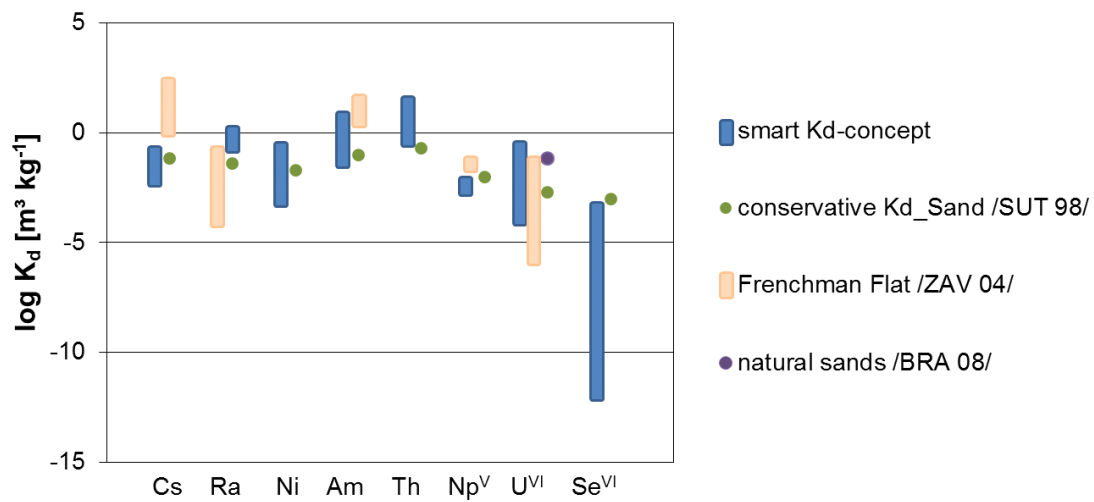


Fig. 12.3 Smart K_d -values for UAF compared to respective published values

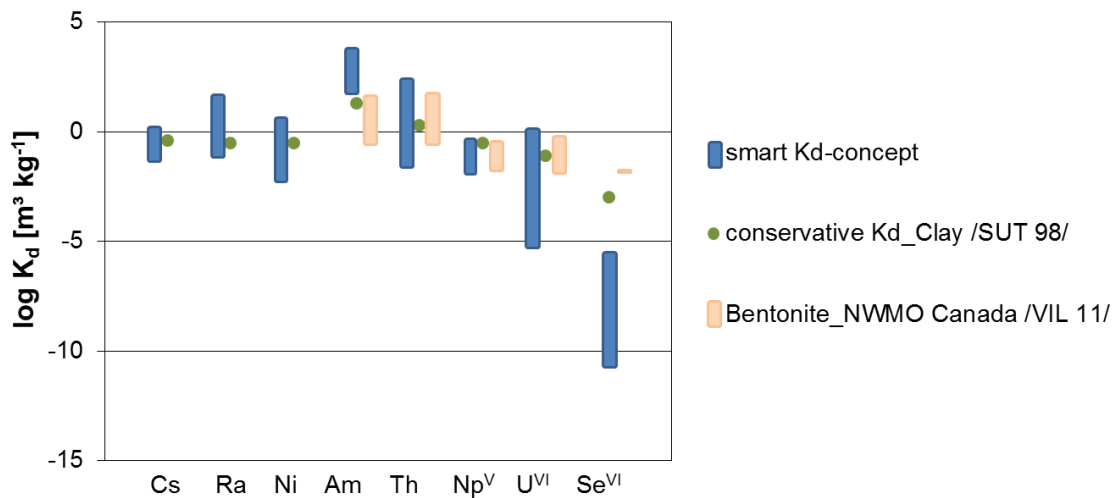


Fig. 12.4 Smart K_d -values for AT compared to respective published values

12.5.2 Sensitivity analysis and results

For visualization, the smart K_d -values were plotted as a function of different environmental parameters. In Fig. 12.5 the three-dimensional plot for the most sensitive parameter pH, DIC, and Ca is given from the pre-calculated five-dimensional smart K_d -matrix for U(VI).

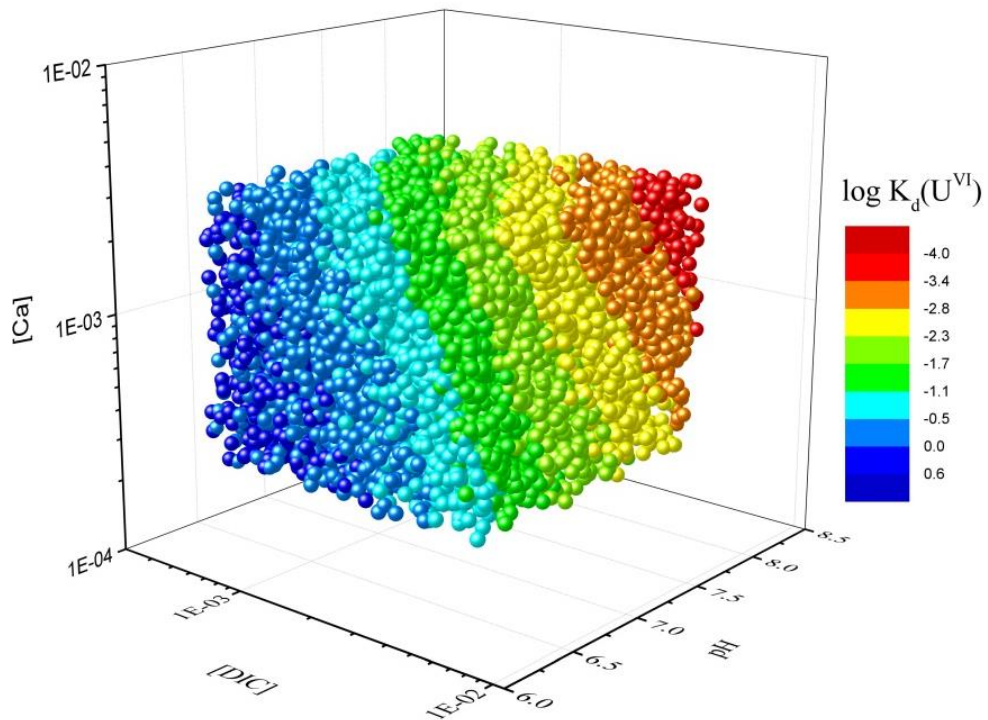


Fig. 12.5 3-D subsets from 5-D smart K_d -matrix for U(VI) sorption in the UAF as a function of pH, [DIC], and [Ca] (K_d in $\text{m}^3 \text{kg}^{-1}$)

It is obvious that mainly the pH and the DIC influences the sorption of U(VI), the smart K_d become lower with increasing pH, which can be explain with the sorption maximum of U(VI) in the near neutral pH range (at nearly pH 6.5). Due to the Ca and DIC concentration in groundwater, calcite dissolves and causes an increase of DIC, pH and Ca in the UAF and abets the formation of relatively stable aqueous uranium complexes like $\text{Ca}_2\text{CO}_3(\text{UO}_2)_3$. Consequently, with increasing Ca and DIC more uranium is bound in such aqueous complexes and not available for sorption processes.

As an important result of the SA we obtained importance indicators (also called sensitivity indices). It enables to identify the most sensitive parameters, with the highest ranked factor. The ranking list of sensitivity indices first order for the UAF and AT are presented in Tab. 12.6 and exemplarily for the sorption of U(VI) in UAF in Tab. 12.7 with additionally

total sensitivity indices. The difference between the total sensitivity index and the first-order sensitivity index is an indicator for the level of interaction of the respective parameter. A difference of zero would mean that a parameter does not contribute to the output variance via interactions, but solely via the main effect (first-order sensitivity index). So for the sorption of U(VI) in the UAF the most important parameters show little interaction. They contribute mostly direct to the model output variance.

Tab. 12.6 Sensitivity indices first order for log K_d -values for radionuclides in UAF and AT calculated with eFAST (25 000 parameter samples)

E_i	Cs	Ra	Ni	Am	Th	Np	U	Se
UAF								
pH	<0.001	0.959	0.992	0.641	0.689	0.928	0.461	0.423
DIC	0.011	0.008	<0.001	0.306	0.285	0.003	0.425	0.082
IS	0.768	0.002	0.001	<0.001	<0.001	<0.001	<0.001	0.003
[Ca]	0.044	0.001	<0.001	<0.001	0.003	0.0	0.084	<0.001
[Al]	<0.001	<0.001	<0.001	0.001	0.007	0.009	0.002	<0.001
[S]	0.044	0.010	0.003	0.022	0.001	0.022	<0.001	0.005
AT								
pH	<0.001	0.966	0.772	0.814	0.649	0.489	0.365	0.317
DIC	0.004	0.022	0.002	0.122	0.204	0.095	0.324	0.025
IS	<0.001	<0.001	<0.001	<0.001	<0.001	<0.001	<0.001	<0.001
[Ca]	0.005	<0.001	<0.001	<0.001	<0.001	0.001	0.210	<0.001
[Al]	<0.001	<0.001	<0.001	<0.001	<0.001	<0.001	<0.001	<0.001
[S]	<0.001	<0.001	<0.001	<0.001	<0.001	<0.001	<0.001	<0.001

Tab. 12.7 Sensitivity indices for log K_d -values for U(VI) in UAF calculated with eFAST (25 000 parameter samples) using SimLab2

E_i	$S_{1,i}$	$S_{T,i}$	$S_{T,i} - S_{1,i}$	Rank
pH	0.461	0.485	0.024	1
DIC	0.425	0.445	0.020	2
Ca	0.084	0.097	0.013	3
Al	0.002	0.003	0.001	4
IS	0.0002	0.001	0.001	5
S	0.00004	0.001	0.001	6

In general, indices ranked highest are the most sensitive parameters. It is obvious that pH mainly influences the sorption of radionuclides, followed by [DIC], and [Ca].

Comparing these results with the results of ESTRAL project /NOS 12b/ it already shows that there also the pH mainly influences the sorption of radionuclides, followed by [Ca], and [DIC]. The fact that the radionuclides themselves have very low sensitivity indices identified that the total [RN]-concentration does not affect the sorption significantly. Consequently, the parameter RN was now set as fix in the model input using the maximum concentrations as given in /NOS 12b/ (estimated from far field calculations /KEE 05/).

13 Transport modeling and code verification

To test the new chemical concept implemented in d^{3f++} described in Section 3.3 verification calculations with the reactive transport code PHAST have been performed. The objective of these calculations was to identify any shortcomings due to introduced model simplifications or any bugs in code implementation. The calculations have been restricted to well defined 2D test cases, which facilitated the comparison of geochemical parameters calculated by d^{3f++} and PHAST, respectively, and therewith the identification of any shortcomings in the d^{3f++} code.

13.1 d^{3f++}

The original flow code d^{3f} and the transport code r^{3t} were applications of the software platform UG and had been developed more than a decade ago /FEI 99/, /FEI 04/. The platform UG had recently been advanced to a substantially revised version UG4. In this context the codes d^{3f} and r^{3t} were transferred from the UG3 platform to this new code platform and were combined to one joint code denoted as d^{3f++} /SCH 16/. During this process adaptations for the ESTRL concept, which was already implemented in the r^{3t} code on the UG3 platform, needed to be performed.

First code verification tests of r^{3t} on the UG3 platform with the geochemically coupled transport code PHAST identified that the law of mass conservation was not precisely fulfilled due to numerical problems in the description of the equilibrium of the environmental factors and the dependence of the K_d -values from those. This problem was then solved by the transfer of the codes to the UG4 platform using available approaches for correct treatment of the interdependencies of the K_d -values from the environmental factors. In addition, it was decided to no more consider the dependency of the K_d -value from the radionuclide concentration itself, since it was shown in all sensitivity analyses that they are not relevant compared to pH and concentrations of Ca and DIC (digi. App. Sec. A.2).

13.2 Comparative calculations with code PHAST

The original smart K_d -concept was implemented in the code r^{3t} (radionuclides, reaction, retardation, and transport, /FEI 04/) during the project ESTRAL /NOS 12a/. This code enabled to simulate the transport and retention of radionuclides based on the

precomputed flow field and salt distributions provided by the code d^{3f} (distributed, density driven flow, /FEI 99/). Both codes were based on the simulation toolbox UG3 (unstructured grids, /BAS 94/, /BAS 97/), a software framework for the numerical solution of coupled systems of partial differential equations. All simulations presented in /NOS 12a/ were performed with r^{3t} and d^{3f} .

With the transfer to the renewed code version UG4, d^{3f} and r^{3t} were united to one coupled code d^{3f++} /SCH 16/ which comprises the smart K_d -concept. The comparative calculations with PHAST /PAR 10/ and d^{3f++} presented here were performed in order to evaluate the ESTRAL smart- K_d concept and to qualify its implementation in the code d^{3f++} .

The calculations were conducted step wise: First, a tracer transport was simulated with consideration of the processes advection, diffusion and dispersion. Second, the transport of radionuclides that underlie the process of sorption – depending on the actual geochemical conditions – was simulated.

Fairly similar results were expected for the flow and tracer calculations. Small differences could arise due to the different discretization and the different formulation and implementation of the flow and transport equations in the two codes. Larger differences were expected for the transport of the radionuclides as the smart K_d -concept in d^{3f++} constitutes a simplification of the full geochemical model used in PHAST. However, it is anticipated that the agreement is good enough to justify this simplification.

13.2.1 Comparison of the approaches

There are several differences in the philosophy and handling of d^{3f++} /SCH 16/ and PHAST /PAR 10/ so that it is useful to compare the approaches in a first step.

PHAST contains the geochemical model PHREEQC which is used to calculate geochemical reactions /PAR 99/. The reactions and thermodynamic properties of the aqueous and solid chemical species that shall be considered are stored in the thermodynamic database file. The database file used in the calculations presented here was developed during the ESTRAL project /NOS 12a/.

In each time step, three operations are performed in PHAST sequentially (Fig. 13.1). First, the flow equation is solved for the potentiometric head values and the interstitial velocities are derived from the heads. Second, the transport of each component is

calculated receiving the total aqueous concentrations per cell. And third, the equilibrium and kinetic reaction equations are solved which yields molalities and activities of the aqueous species, surface species, saturation indices of minerals, etc. for every cell. In the test case presented here, the third time step comprises the simultaneous equilibration of the solution with calcite and the given reactive surface. K_d -values are calculated based on a Basic program and saved in an output file.

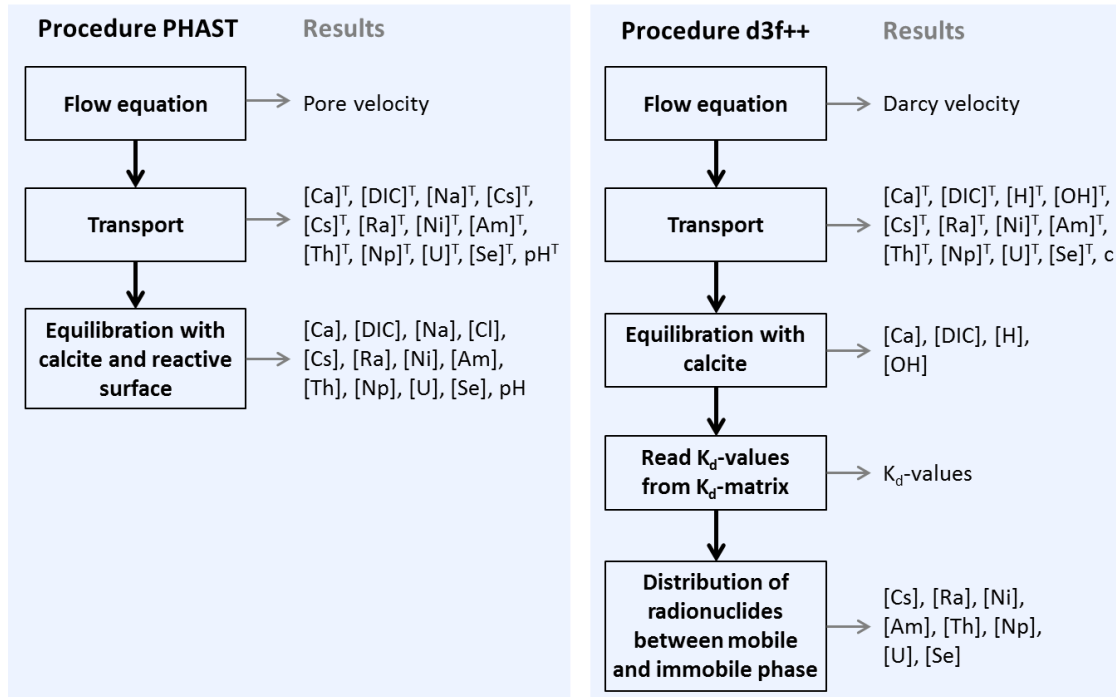


Fig. 13.1 Comparison of the procedures in PHAST and d^{3f++}
The superscript “T” stands for temporal

In d^{3f++}, a reduced set of chemical components is considered to keep the model simple and to reduce the computational effort. It is assumed that it is sufficient to simulate the transport of Ca²⁺, DIC, H⁺, OH⁻, and NaCl to describe the processes that are most important for the sorption of the radionuclides. In each time step, the flow equation is solved for the pressure and the Darcy velocities are derived (Fig. 13.1). Next, the transport of each aqueous component is simulated. These first two steps agree on the whole with the procedure in PHAST but the third step differs strongly. According to the ESTRAL smart- K_d concept /NOS 12a/, the equilibration of the solution with calcite and the equilibration of the solution with the mineral surface are split into two separate processes. The first process is performed during runtime of d^{3f++} but the latter is brought implicitly into the simulation with the K_d -values.

In each time step, the equilibration with calcite is performed as an iterative process in d^{3f++} based on simplifying assumptions e. g. concerning the computation of the pH-value. This process yields the equilibrium concentrations of Ca and DIC as well as the equilibrium pH. The ionic strength, however, is directly derived from the relative concentration of sodium chloride which may change in space and time due to advection, diffusion and dispersion.

Tab. 13.1 Surface composition for UAF used for smart K_d -calculations

Mineral phase/group	Reference binding sites [sites/nm ²]	Specific surface area [m ² /g]	Solid mass [g/kgw]
Quartz	2.31	0.007	9010
Feldspar		0.21	1060
Mica		1.72	53
Fe(III)-oxides/-hydroxides		0.26	53
Al-hydroxides		0.11	53
2-layer-clay minerals		0.07	159

The equilibrium concentrations of Ca, DIC, the equilibrium pH and the ionic strength are used to identify the suitable distribution coefficients (K_d) from the smart K_d -matrix or rather to interpolate between the K_d -values of the most similar combinations of parameters within the matrix. The smart K_d -matrix contains distribution coefficients that were obtained during equilibrium calculations with PHREEQC /PAR 99/ (in combination with UCODE /POE 08/) for numerous combinations of parameters ([Ca], [DIC], pH, and ionic strength) with the surface characterized in Tab. 13.1 (see Fig. 13.2). A near-seawater solution was determined for each set of parameters by adding Na, Cl, K, S, and Mg ions as well as several radionuclides: Cs, Ra, Ni, Am, Th, Np, U, Se. This solution was balanced with the reactive surface and the resulting K_d -values for the radionuclides were saved in the matrix. Thus, the K_d -values in the matrix incorporate the equilibrium with the reactive surface.

In the simulations with d^{3f++}, the smart K_d -values obtained from the matrix are used to distribute the radionuclide between the mobile and the immobile phase within each time step.

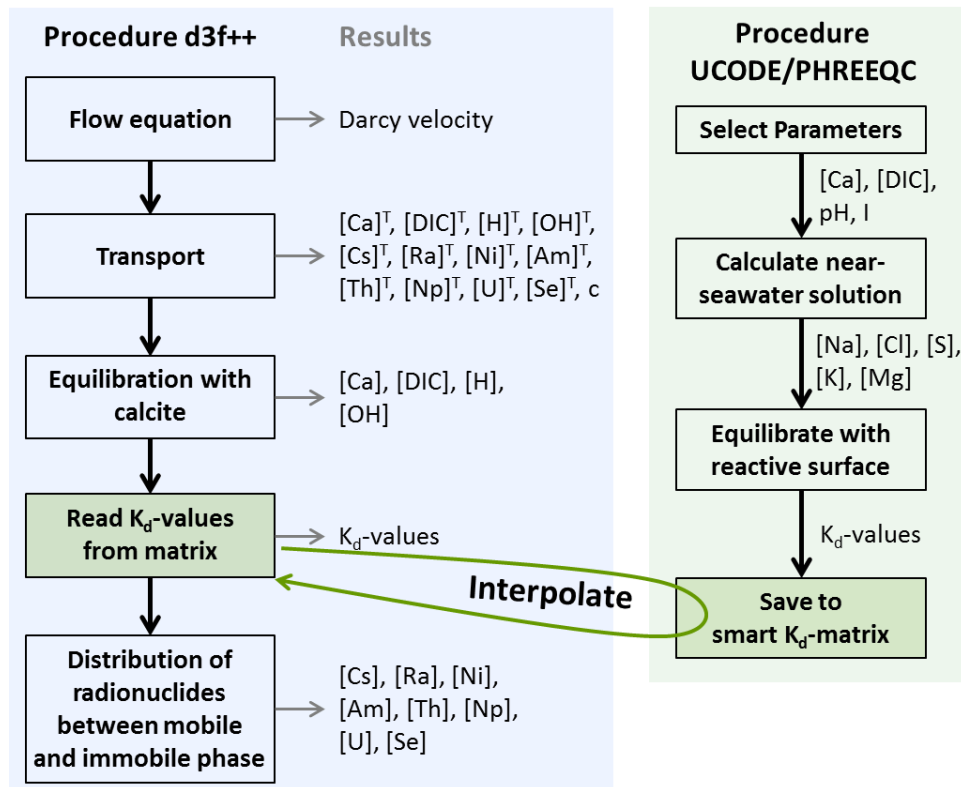


Fig. 13.2 Schema of the workflow in d^3f++ and the generation of the K_d -matrix

13.2.2 Model setup

The model domain consists of a horizontal box of 20 m times 3 m with an inflow zone located at the left side between 1 m and 2 m (Fig. 13.3). The inflow is constant in its strength but its chemical composition changes in time. The right side of the model is open to flow and transport. The upper and lower model boundaries as well as parts of the left boundary are impermeable to flow and diffusive/dispersive flux.

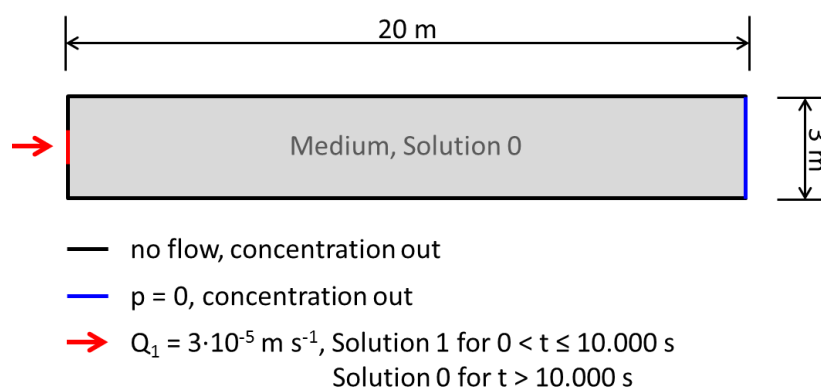


Fig. 13.3 Model domain with boundary conditions

The model domain contains a homogeneous medium that owns the reactive surface defined in Chapter 13.2.1 (Tab. 13.1). It is assumed that calcite is present in the entire model domain and may be dissolved or precipitate from the solution at any time. The hydraulic parameters of the medium are set to typical values for aquifers (Tab. 13.2).

Tab. 13.2 Hydraulic parameters

Parameter	Unit	Value
Permeability κ	m^2	$1.019368 \cdot 10^{-11}$
Porosity ρ	-	0.2
Molecular Diffusion Coefficient D_m	m^2s^{-1}	$1.0 \cdot 10^{-9}$
Longitudinal / Horizontal / Vertical Dispersivity $D_L / D_H / D_V$	m	0.2
Specific Storage S_s	m^{-1}	0
Tortuosity T	-	1
Density ρ	kg m^{-3}	$1.0 \cdot 10^3$
Viscosity μ	$\text{kg m}^{-1} \text{s}^{-1}$	$1.0 \cdot 10^{-3}$

Initially, the model domain is filled with Solution 0 (cf. Tab. 13.3) which contains sodium, chloride, calcium, and inorganic carbon.

Tab. 13.3 Composition of Solution 0 and 1

Parameter	Unit	Solution 0	Solution 1
pH	[-]	7.0	7.0
Ionic strength	$[\text{mol L}^{-1}]$	0.08104	0.08104
Na	$[\text{mol m}^{-3}]$	1.0	1.0
Cl	$[\text{mol m}^{-3}]$	60.0	60.0
Ca	$[\text{mol m}^{-3}]$	25.02	25.02
DIC	$[\text{mol m}^{-3}]$	1.0	1.0
Cs	$[\text{mol m}^{-3}]$		$1.0 \cdot 10^{-5}$
Ra	$[\text{mol m}^{-3}]$		$1.0 \cdot 10^{-5}$
Ni	$[\text{mol m}^{-3}]$		$1.0 \cdot 10^{-5}$
Am	$[\text{mol m}^{-3}]$		$1.0 \cdot 10^{-7}$
Th	$[\text{mol m}^{-3}]$		$1.0 \cdot 10^{-7}$
Np	$[\text{mol m}^{-3}]$		$1.0 \cdot 10^{-5}$
U	$[\text{mol m}^{-3}]$		$1.0 \cdot 10^{-5}$
Se	$[\text{mol m}^{-3}]$		$1.0 \cdot 10^{-5}$

The initial solution composition may change within the first time step because of the instantaneous equilibration with calcite (d^{3f++}) or with calcite and the reactive surface (PHAST). During the first 10,000 s, Solution 1 enters the model domain. This solution has the same chemical composition as Solution 0 but additionally contains several radionuclides as listed in Tab. 13.3. After that, Solution 0 flows into the model domain again until the end of the simulation.

13.2.3 Results of d^{3f++} 1D transport models

Initially, tracer transport simulations were performed to compare the two models without the influence of sorption. The results after 100,000 s simulation time show a very good agreement (Fig. 13.4). The curves of both simulations lie nearly perfectly one upon another. This implies that not only the transport but also the flow models in PHAST and d^{3f++} agree quite well.

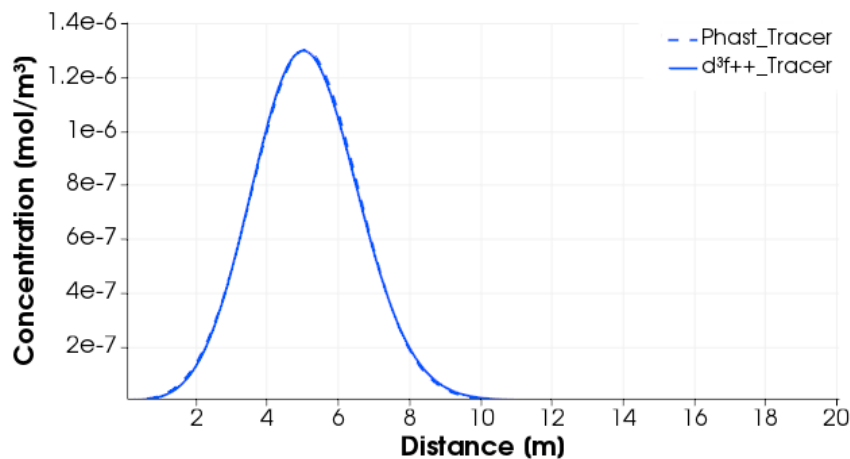


Fig. 13.4 Spatial distribution of the tracer after 100,000 s simulation time

In contrast to the tracer, the radionuclides underlie the effect of sorption. This effect is influenced by many factors. Due to the simplifications made in the ESTRAL smart K_d -concept, only DIC, Ca, ionic strength, and pH are considered here for the comparison of the codes. Their spatial distributions after 100,000 s simulation time show a fundamental difference between the models in d^{3f++} and PHAST (Fig. 13.5): PHAST computes values for DIC, CA, IS, and pH that vary over the length of the model area whereas their values from d^{3f++} are constant in space, thus also in time.

The reason for this difference lies in the meaning of the solution in d^{3f++} and PHAST. In d^{3f++} , the solution in the model area is only determined by the instantaneous

equilibration with calcite. The treatment of the reactive surface comes with the K_d -values. In PHAST, however, the composition of the solution is influenced by the equilibration both with calcite and with the reactive surface. The reactive surface influences the solution until all sites are occupied. Then, the values for DIC, Ca, IS, and pH are determined only by the equilibrium with calcite. Thus, these values should be compared to the results from d^{3f++} .

The values for DIC, Ca, IS, and pH computed with PHAST after saturation of the surface match quite well the results from d^{3f++} (see Tab. 13.4). The divergence is very low i. e. it is smaller than 2 % for all four parameters. Larger differences between the results of the two codes arise for the K_d -values which describe the sorption of the nuclides for the actual geochemical conditions. The K_d -values from d^{3f++} and PHAST diverge by 2 to 8 % for all radionuclides except for Uranium for which the divergence amounts to 68 %.

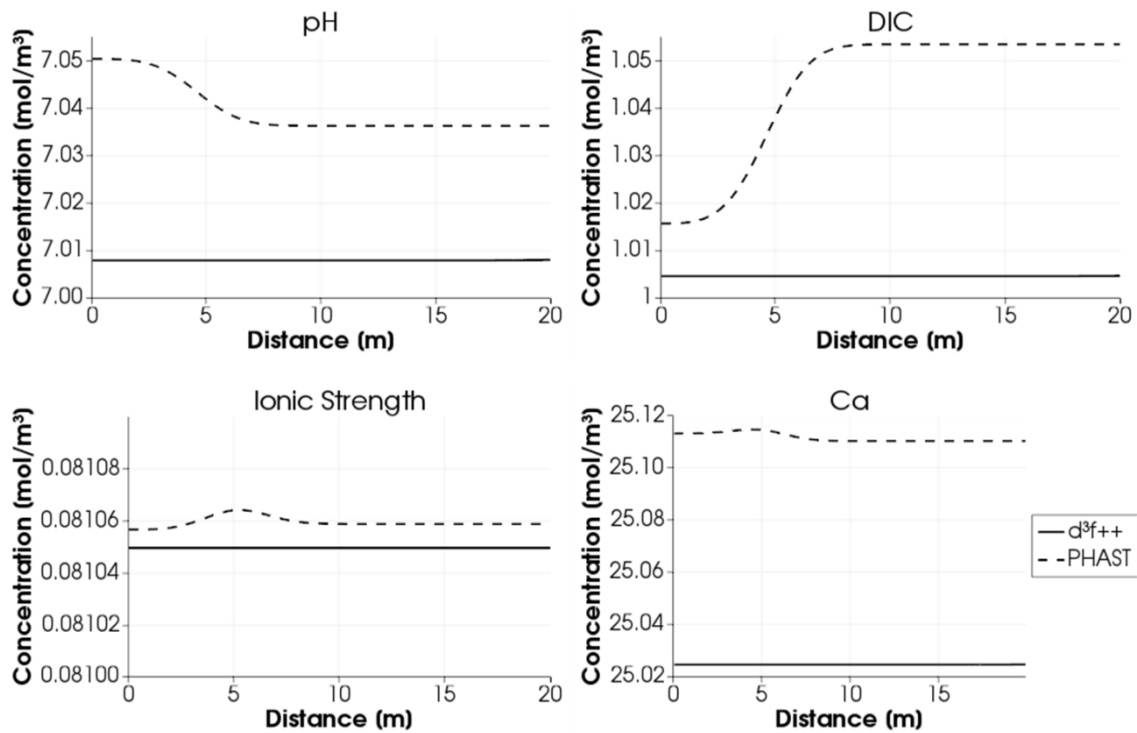


Fig. 13.5 Spatial distributions of DIC, Ca, IS, and pH after 100,000 s

Tab. 13.4 Values in equilibrium for PHAST and d^{3f++} after 500.000 s

	PHAST	d^{3f++}	Divergence [%]
pH [-]	7.05	7.01	0.6
IS [mol L ⁻¹]	0.08106	0.08105	0.01
Ca [mol m ⁻³]	25.11	25.02	0.4
DIC [mol m ⁻³]	1.02	1.0	2.0
K _d Cs [m ³ kg ⁻¹]	1.4	1.37	2.1
K _d Ra [m ³ kg ⁻¹]	0.045	0.042	6.7
K _d Ni [m ³ kg ⁻¹]	0.00067	0.00069	3.0
K _d Am [m ³ kg ⁻¹]	1.00	1.08	8.0
K _d Th [m ³ kg ⁻¹]	3.32	3.45	3.6
K _d Np [m ³ kg ⁻¹]	0.00015	0.00014	6.7
K _d U [m ³ kg ⁻¹]	0.00022	0.00037	68.2
K _d Se [m ³ kg ⁻¹]	0.0036	0.0037	2.8

The spatial distributions after 500,000 s (Fig. 13.6) reflect the effect of the K_d -values which result in a different retardation for each radionuclide. The substance with the weakest sorption is Np whose peak lies at a distance of 11 m from the inflow (in comparison: the peak of the tracer would lie at 25 m). The order of the other radionuclides by ascending strength of the sorption is: U, Ni, Se, Ra, Cs, Am, and Th. No peak can be distinguished for Am, Cs, and Th. Their sorption is so high that the main mass of the nuclides accumulates within the first cells of the model.

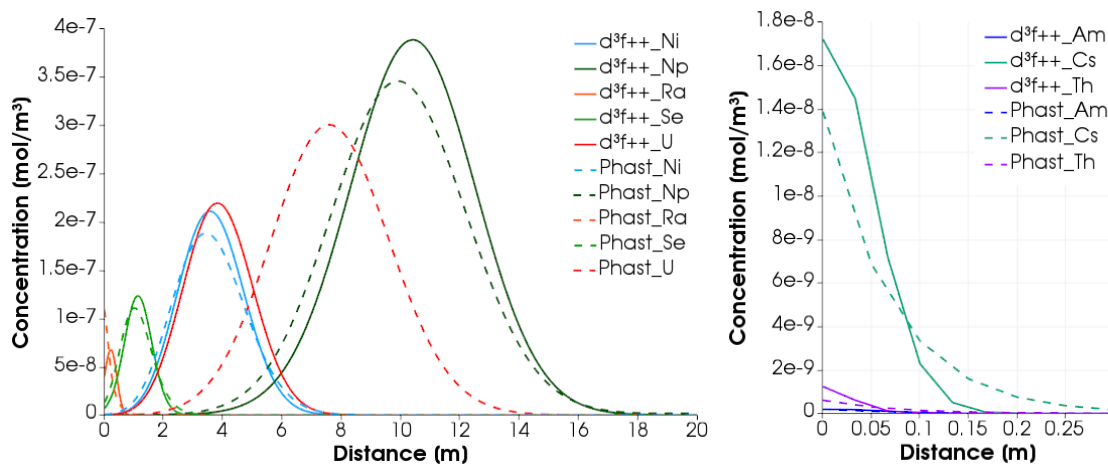


Fig. 13.6 Spatial distribution of the radionuclides after 500,000 s model time

For most of the radionuclides, the results of d^{3f++} and PHAST agree quite well. In most cases the position of the peak matches reasonably well but its height differs slightly (e. g.

for Se and Ni). The position of the peak for Np differs about 0.5 m and the concentration in the peak for PHAST lies about 10 % under the value for d^{3f} . This, however seems to be acceptable.

As expected from the differences in the K_d -values, the curves of Uranium differ strongly. This radionuclide is transported in PHAST nearly twice as fast as in d^{3f++} and also its concentration in the peak is about 30 % higher. Tests showed that the procedure used for the generation of the smart K_d -matrix yields (with the parameter setting taken from the transport simulation) values that were very similar to the results from PHAST. This suggests that the multidimensional interpolation between the data points in the smart K_d -matrix produces in some cases large errors. This applies particularly, where a K_d -value shows a strongly non-linear dependence on a parameter and where only few data points are used to describe this.

A new smart K_d -matrix was generated based on these findings. It was assumed that an increase of data points for the pH from eight to twelve would ameliorate the simulation results for Uranium. Moreover, the range of the data points for pH, DIC, IS, and Ca were narrowed to bring the data points closer to each other.

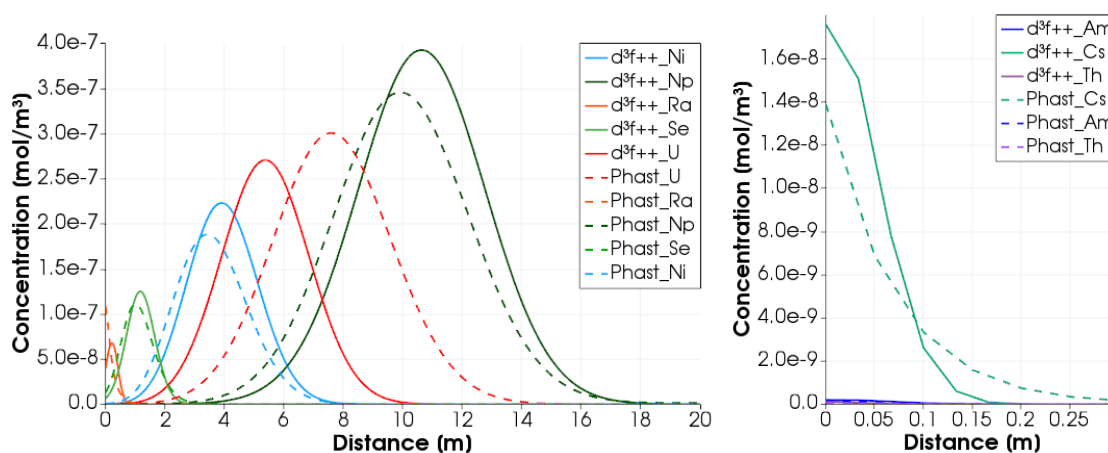


Fig. 13.7 Spatial distribution of the radionuclides after 500,000 s model time calculated with the new smart K_d -matrix

As expected, the curves of Uranium from d^{3f++} and PHAST moved closer together with the new smart K_d -matrix (Fig. 13.7) although curves for Ni agree slightly less than before. Analyses showed that Ca has the biggest influence on the distribution coefficient of Uranium for the given geochemical conditions besides the pH (Fig. 13.8). Thus, a new smart K_d -matrix with more data points for Ca should yield even better results.

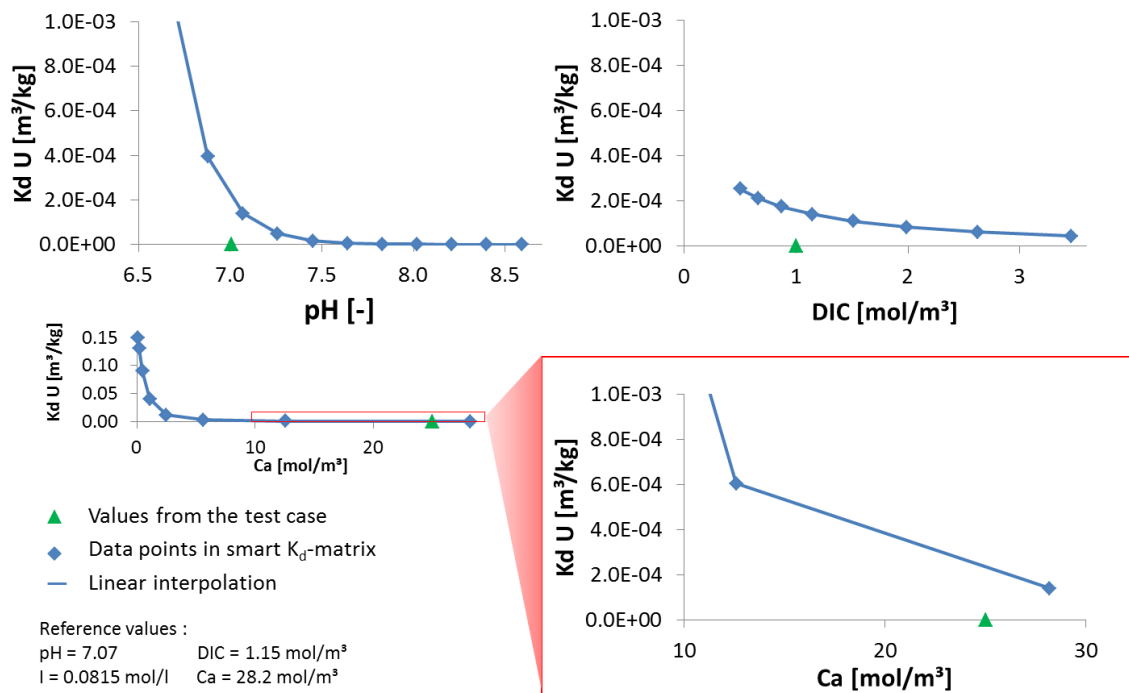


Fig. 13.8 K_d -values for Uranium as functions of pH, DIC, and Ca

The solution used in the test case presented here is already almost in equilibrium with calcite before it enters the model area. Thus, the changes in the solution composition calculated by d^{3f++} are very low. Originally, it was planned to perform calculations with a second solution which is less balanced in advance. It showed, however, that d^{3f++} was not able to bring the solution into a correct equilibrium with calcite. The reasons for this were certain simplifying assumptions in the equilibrium process. A revision and modification of the ESTRAL smart K_d -concept yielded much better results for the pure equilibrium calculations. The resulting concept is presented in Chapter 3.3.3 but it was not possible to implement it into d^{3f++} within this project.

Further work should comprise comparative calculations with an unbalanced solution once the modified ESTRAL smart K_d -concept is implemented. Furthermore, also the simplifications introduced with the new WEIMAR smart K_d -concept presented in Chapter 0 should be tested and further comparative calculations with PHAST and d^{3f++} should be performed.

14 Summary and conclusions

One important element of a safety case for a repository for radioactive waste in deep geological formations is the long-term safety assessment. OECD/NEA defined it as a systematic analysis of the hazards associated with geological disposal facility and the ability of the site and designs to provide the safety functions and meet technical requirements. The task involves developing an understanding of how, and under what circumstances, radionuclides might be released from a repository, how likely such releases are, and what would be the consequences of such releases to humans and the environment. A key component of this assessment is the simulation of fluid and contaminant transport through the repository system, i. e. through large model areas over very long time frames. The aim is a realistic as possible description of the contaminant retardation, which is in turn influenced by chemical changes.

To describe the impact of geochemical changes on the contaminant retardation within the preceding project ESTRAL a first approach for implementation of the smart- K_d concept into the transport code r^{3t} (radionuclide, reaction, retardation, and transport /FEI 04/) was developed. This modeling approach is based on mechanistic surface complexation models (SCM), which are combined with a bottom-up approach, i. e. sorption for each element on a particular geological unit (a mixture of a defined composition of minerals) is described as the sum of the sorption of the element on every single mineral fraction. In the first stage of development a typical sedimentary system overlying rock salt and clay formations in Northern Germany was considered. Therefore, the well and detailed investigated reference site at Gorleben was selected.

Within the WEIMAR project described here, this approach was further developed on different levels. Originally, the model system had been divided into three different hydrogeological units: an upper aquifer, an aquitard and a lower aquifer. After detailed evaluation of petrographic and geological data and in co-operation with the responsible organisation Bundesanstalt für Geowissenschaften und Rohstoffe (BGR) the lower aquifer has been divided into two separate hydrogeological units: the Miocene lignite sands and the Elsterian sands.

The consideration of environmental parameters has been modified and extended compared to the preceding project ESTRAL. In the first stage of development the pH value, ionic strength, and the concentration of dissolved organic carbon (DIC), Ca and the radionuclide concentrations of the regarded ten radionuclides. In the WEIMAR project Al

and SO_4 have been implemented as new environmental parameters, since they may strongly influence as competing cation or ligand the sorption of radionuclides. Based on results from verification calculations the first stage of development has been optimized.

During the term of the WEIMAR project the flow code d3f (distributed density-driven flow) and the transport code r³t were transferred from the UG3 (Unstructured Grids 3) platform to the newly developed code platform UG4 and were combined to one joint code denoted as d³f++. Accordingly, the hitherto in r³t implemented concept needed to be transferred to the new code d³f++. First verification calculations show that this was successfully done.

The thermodynamic database for the extended Debye Hückel (EDH) approach developed within the ESTRAL project has been substantially enhanced and qualified within the WEIMAR project. On the one hand thermodynamic data for dissolved species like iron(II,III) manganese(II,IV), calcium(II) and magnesium(II) as potential competing cations as well as Neodymium(III) and Europium(III) as relevant radionuclides/homologues (for batch and column experiments) have been included or updated in the database. For example, data for europium have been adopted from the newly developed most complete project-specific database. On the other hand data for sorbed complexes have been thoroughly checked and improved. For the description of systems with very high ionic strengths, as they occur in large parts of the lower aquifer, a second database, resting upon the Pitzer approach, has been created. Thereby, results from the THEREDA project could be considered, particularly existing data for neodymium(III), uranium(IV/VI), neptunium(V), thorium(IV), technetium(IV/VII), strontium(II), cesium(I) as well as silica und aluminum for the hexary system of oceanic salts have been included. Data for selenium have been derived from the VESPA project. An extensive test of the database for the conditions of the lower aquifer is future task.

To investigate the uncertainty and sensitivity of the calculated distribution coefficients due to the variation of the environmental parameters and on the basis of the significantly improved database probabilistic uncertainty and sensitivity analyses have been performed with the software SimLab2. In addition, the newly developed software package RepoSUN/SimLab4 has exemplarily been applied on the sorption of uranium(VI) in the upper aquifer. For uranium previous results have been generally confirmed, namely the most relevant environmental parameters for the K_d -value, pH, Ca and DIC concentration have been confirmed. The sensitivity indices for the radionuclide concentrations show for uranium and all other radionuclides very low sensitivity, indicating that the

environmental parameter radionuclide concentration does not significantly influence sorption. For this reason, the radionuclide concentration is no more considered as an environmental parameter in the new concept.

The current concept had been applied to concrete transport calculations for a climate cycle of 176 500 years. A constant climate over a period of 161 500 years followed by a 10 000 year long permafrost period and 5 000 years transgression was considered. In the frame of the WEIMAR project it has been systematically been proved, whether further additional probable scenarios might cause changes in the geochemical conditions of the overburden at the Gorleben salt dome. For that purpose, recent studies, especially the geological long-term prognosis and the FEP catalogue for the preliminary safety analyses Gorleben (VSG) have been evaluated. It turned out that mainly climatic changes are of relevance. Many FEP only have low reference to or insignificant impact on the overburden. Few other FEP could not be considered, since it is not possible to transiently vary geometrical conditions.

The methodological / conceptual developments have been accompanied by a comprehensive experimental program. The minerals used in the experiments have been extensively characterized, titration and batch sorption experiments were performed, the influence of microorganisms on the sorption behavior was studied and the transport of selected cations in column experiments has been investigated.

The characterization of the minerals quartz, orthoclase, and muscovite comprised the determination of specific surface areas, accessory minerals and release of elements under the applied experimental conditions as well as the characterization of acid-base properties of the surfaces by titration experiments. Moreover, batch sorption experiments with uranium(VI), neptunium(V), neodymium(III), europium(III), and nickel(II) on quartz, orthoclase and muscovite under varying pH, ionic strengths, element concentrations and solid/liquid ratios have been performed. Using a fitting procedure based on the programs UCODE and PHREEQC and the data from the batch sorption experiments together with the information about the surface properties missing data for the surface complexation models have been derived and fed into the WEIMAR thermodynamic database.

Furthermore, batch experiments with competing cations calcium and aluminum have been performed. By optimization of container materials, applied chemicals and the measuring procedure the analytics of aluminum in the trace element concentration range could be significantly improved. Despite that no systematic determination of surface

complexation data for aluminum was possible due to the relatively low solubility of aluminum in the neutral pH range and its quite high background contents in the natural minerals.

Microbial investigations on the minerals quartz, orthoclase and muscovite showed that microorganisms occur in the minerals, which can grow over the experimental time frame of several weeks to months. In order to estimate their influence on the sorption and to develop a suitable pre-treatment method for the samples the microbial growth and the effect of different sterilization methods have been studied by electron and optical spectroscopy and calorimetry. No significant effects on the sorption behavior could be identified in this study. Consideration of slightly longer time spans, necessary for the growth of biofilms, might be reasonable.

Column experiments have been optimized with respect to the set-up, the material and the filling procedure. Mainly PFA and for the frits PTFE material was used to keep sorption on the container walls low. By water saturation of the mineral-filled columns under vacuum conditions air inclusions and resultant preferential pathways could be avoided. By this procedure highly reproducible breakthrough curves and spatial distributions have been obtained. The column experiments with europium and nickel on the minerals quartz, orthoclase and muscovite show plausible differences between the three minerals and expected dependencies from the pH value and the composition of the applied solution. The experiments illustrate an increased mobility of europium and nickel at low pH values as and in presence of the complexing agent sulfate and competing cations.

One key aspect of the project was the transition of pure static batch sorption to dynamic column experiments. It was an important objective to investigate the transferability of surface complexation parameters derived from batch experiments to the description of the reactive particle transport. This step has been initially restricted on pure minerals and simple synthetic mineral mixtures. The description of the europium transport using surface complexation parameters derived from batch experiments was satisfactorily for selected geochemical boundary conditions in quartz and orthoclase filled columns. However, not all boundary conditions could adequately be described with the applied thermodynamic models and data. Prerequisite for a better description is a better understanding of the involved processes, which can only be derived by additional batch experiments. The results of the batch experiments with muscovite indicate that ion exchange plays an important role in cation retardation. In order to correctly describe this process, selectivity coefficients for the ion exchange need to be derived in the future.

One key question for reactive transport simulation is, what is the chemical form of the tracer complexes at the mineral surface. A method has been developed to characterize surface complexes in column experiments. For this purpose, spatial distributions in the column have been fixed by freezing with liquid nitrogen, subsequent partition of column segments and analysis with CLSM (Confocal Laser Scanning Microscopy) und TRIFS (Time Resolved Laser Induced Fluorescence Spectroscopy). With this method, which has been exemplarily been applied to the migration of uranium through quartz columns, it became feasible to space-resolved determine the properties of surface complexes. First results show in dependence of the different pH values in different parts of the column the occurrence of two different uranium(VI) surface complexes, which were described in literature.

To get a better understanding of the effects in column experiments this method should be transferred to other elements studied in the project like europium or nickel. Generally, the characterization of the structure of surface complexes is an important aspect for confirmation of the applied surface complexation models. With respect to the smart-Kd concept and the transport of key environmental parameters the implementation of redox reactions, which was not possible within the WEIMAR project, envisaged in future. In this context thermodynamic sorption data for redox-sensitive elements like technetium or for reduced forms like uranium(IV) have to be determined and implemented into the thermodynamic database. The database for high saline systems generally show gaps yet and need to be complemented. Finally, a comprehensive review of the concept of the component additivity approach for natural systems including all relevant environmental parameters is an important open issue.

15 **References**

- /ADE 94/ Adeleye, S., Clay, P., Oladipo, M.: Sorption of caesium, strontium and europium ions on clay minerals. *Journal of Materials Sciences*, 29:954–958, ISSN 0022-2461, eISSN 1573-4803, 1994.
- /AJA 98/ Aja, S.: The Sorption of the rare Earth Element, Nd, onto Laolinite at 25 C. *Clays and Clay Minerals*, 46(1):103–109, ISSN 0009-8604, 1998.
- /ALA 06/ Alakomi, H.-L., Saarela, M., Gorbushina, A. A., Krumbein, W. E., McCullagh, C., Robertson, P., Rodenacker, K.: Control of biofilm growth through photodynamic treatments combined with chemical inhibitors: in vitro evaluation methods. In *Heritage, Weathering and Conservation (HWC-2006)*, pages 713–717, London. Taylor & Francis Ltd., January 2006.
- /ALE 14/ Alexander, W. R., McKinley, I., Kawamura, H., Pescatore, C., Luik, A. V., Nelson, R., Janeczek, J., Verhoef, E., Neeft, E., Bracke, G., Fischer-Appelt, K., Noseck, U., Wolf, J., Steininger, W., Rempe, N. T., Debois, G., Li, S., Strozyk, F., Abe, S., van Gent, H., Schmatz, J., Kukla, P. A., Urai, J. L., Dulinski, M., Rózanski, K., Brudnik, K., Kolonko, P., Tadych, J., Sadler, M., Schléder, Z., Schönherr, J., Hammer, J., Merineit, J., Behlau, J., Mingerzahn, G., Kühnlenz, T., Schramm, M., Zulauf, G., Zulauf, J., Minkley, W., Knauth, M., Reuning, L., Becker, S., Crotofino, F., Metz, V., Rosenberg, Y. O., Böttle, M., Ganor, J., Meleshyn, A.: Natural Analogues for Safety Cases of Repositories in Rock Salt. *Salt Club Workshop Proceedings. NEA/RWM, R(2013)10*, March 2014.
- /ALL 09/ Allison, L., Alley, R. B., Fricker, H. A., Thomas, R. H., Warner, R. C.: Ice sheet mass balance and sea level. *Antarctic Science*, 21:413–426, 2009.
- /AND 00/ Andersson, C. A., Bro, R.: The N-way Toolbox for MATLAB. *Chemometrics and Intelligent Laboratory Systems*, 52:1–4, 2000.

- /APP 05/ Appelo, C., Postma, D.: Geochemistry, groundwater and pollution. CRC Press, Amsterdam, ISBN 978-0-415-36428-7, 2005.
- /APP 16/ Appelo, T.: Bilateral statement from Tony Appelo during PHREEQC Modeling Course in Dresden (22.-26.08.2016). In PHREEQC Modeling Course, August 2016.
- /ARN 99/ Arnold, T., Zorn, T., Bernhard, G., Nitsche, H.: Applying the DDLM to model the sorption of uranium onto quartz and muscovite. Technical Report FZR-285, 1999.
- /ARN 00/ Arnold, T., Zorn, T., Bernhard, G., Nitsche, H.: Modeling the sorption of uranium(VI) onto albite feldspar. Annual report 1999, 2000.
- /ARN 01/ Arnold, T., Zorn, T., Zänker, H., Bernhard, G., Nitsche, H.: Sorption behavior of U(VI) on phyllite: experiments and modeling. Journal of Contaminant Hydrology, 47:219–231, ISSN 0169-7722, 2001.
- /ARN 06/ Arnold, T., Utsunomiya, S., Geipel, G., Ewing, R., Baumann, N., Brendler, V.: Adsorbed U(VI) Surface Species on Muscovite Identified by Laser Fluorescence Spectroscopy and Transmission Electron Microscopy. Environmental Science and Technology, 40:4646–4652, ISSN 0013-936X, 2006.
- /ATW 10/ Atwood, D. A., ed.: Radionuclides in the Environment. John Wiley & Sons, Chichester, West Sussex, ISBN 978-0-470-71434-8, June 2010.
- /AVE 98/ Avena, M. J., Pauli, C. P. D.: Proton adsorption and electrokinetics of an Argentinean montmorillonite. Journal of Colloid and Interface Science, 202(1):195–204, ISSN 0021-9797, June 1998.
- /BAE 95/ Baeyens, B., Bradbury, M.: A quantitative mechanistic description of Ni, Zn and Ca sorption on Na-Montmorillonite. Part II: Sorption measurements. PSI-Report, 95-11(2), ISSN 1019-0643, 1995.

- /BAE 97/ Baeyens, B., Bradbury, M. H.: A mechanistic description of Ni and Zn sorption on Na-montmorillonite Part I: Titration and sorption measurements. *Journal of Contaminant Hydrology*, 27(3-4):199–222, ISSN 0169-7722, 1997.
- /BAH 98/ Bahlburg, H., Breitzkreuz, C.: *Grundlagen der Geologie*. Enke Verlag, Stuttgart, ISBN 3-432-29761-0, 1998.
- /BAL 78/ Balzani, V., Bolletta, F., Gandolfi, M. T., Maestri, M.: Bimolecular electron transfer reactions of the excited states of transition metal complexes. In *Organic Chemistry and Theory. Topics in Current Chemistry*, volume 75, pages 1–64. Springer, Berlin, Heidelberg, ISBN 978-3-540-08834-9, eISBN 978-3-540-35821-3, 1978.
- /BAR 96/ Barrón, V., Torrent, J.: Surface Hydroxyl Configuration of Various Crystal Faces of Hematite and Goethite. *Journal of Colloid and Interface Science*, 177(2):407–410, ISSN 0021-9797, February 1996.
- /BAS 94/ Bastian, P., Wittum, G.: Robustness and adaptivity: The UG concept. In Hemker, P., Wesseling, P., eds: *Multigrid Methods IV. proceedings of the fourth european multigrid conference*, 1994.
- /BAS 97/ Bastian, P., Birken, K., Johannsen, K., Lang, S., Neuß, N., Rentz-Reichert, H., Wieners, C.: UG A flexible software tool for solving partial differential equations. *Computing and Visualization in Science*, 1(1):27–40, 1997.
- /BAU 89/ Baumann, J.: *Geochemische Auswertung ausgewählter Wasseranalysen aus dem hydrogeologischen Untersuchungsprogramm Gorleben*. Technical report, February 1989.
- /BAU 05/ Baumann, N., Brendler, V., Arnold, T., Geipel, G., Bernhard, G.: Uranyl sorption onto gibbsite studied by time-resolved laser-induced fluorescence spectroscopy (TRLFS). *Journal of Colloid and Interface Science*, 290(2):318–324, ISSN 0021-9797, October 2005.

- /BEC 16/ Becker, D.-A.: RepoSTAR – Ein Codepaket zur Steuerung und Auswertung statistischer Rechenläufe mit dem Programmpaket RepoTREND. Technical Report GRS-411, Braunschweig, Förderkennzeichen 02E10367 (BMW), ISBN 978-3-944161-93-8, May 2016.
- /BER 96/ Bernhard, G., Geipel, G., Brendler, V., Nitsche, H.: Speciation of uranium in seepage waters from a mine tailing pile studied by time-resolved laser-induced fluorescence spectroscopy (TRLFS). *Radiochimica Acta*, 74:87–91, ISSN 0033-8230, March 1996.
- /BER 01/ Bernhard, G., Geipel, G., Reich, T., Brendler, V., Amayri, S., Nitsche, H.: Uranyl(VI) carbonate complex formation: Validation of the $\text{Ca}_2\text{UO}_2(\text{CO}_3)_3(\text{aq.})$ species. *Radiochimica Acta*, 89:511–518, ISSN 0033-8230, March 2001.
- /BER 06/ Bergaya, F., Lagaly, G., Vayer, M.: Cation and Anion Exchange. In *Handbook of Clay Science*, volume 1, pages 979–1001. Elsevier Ltd., 2006.
- /BIS 16/ Bischofer, B., Hagemann, S., Altmaier, M., Bosbach, D., Bracke, G., Brendler, V., Curtius, H., Finck, N., Franzen, C., Gaona, X., Geckeis, H., Heberling, F., Herm, M., Kindlein, J., Marsac, R., Metz, V., Muñoz, A. G., Rozov, K., Schäfer, T., Scharge, T., Totskiy, Y., Wiedemann, M., Yalcintas, E.: VESPA Behaviour of Long-Lived Fission and Activation Products in the Nearfield of a Nuclear Waste Repository and the Possibilities of their Retention. Project report, Gesellschaft für Anlagen- und Reaktorsicherheit (GRS) gGmbH, ISBN 978-3-944161-55-6, June 2016.
- /BOL 57/ Bolt, G. H.: Determination of the Charge Density of Silica Sols. *The Journal of Physical Chemistry*, 61(9):1166–1169, ISSN 0022-3654, eISSN 1541-5740, September 1957.
- /BRA 13/ Bragg, W. H., Bragg, W. L.: The reflection of X-rays by crystals. *Proceedings of the Royal Society of London, Series A: mathematical, physical, and engineering sciences*, 88(605):428–438, ISSN 0370-1662, 1913.

- /BRA 99/ Bradbury, M. H., Baeyens, B.: Modelling the sorption of Zn and Ni on Ca-montmorillonite. *Geochimica et Cosmochimica Acta*, 63(3/4):325–336, ISSN 0016-7037, 1999.
- /BRA 05a/ Bradbury, M., Baeyens, B.: Experimental measurements and modeling of sorption competition on montmorillonite. *Geochimica et Cosmochimica Acta*, 69(17):4187–4197, ISSN 0016-7037, 2005.
- /BRA 05b/ Bradbury, M., Baeyens, B., Geckeis, H., Rabung, T.: Sorption of Eu(III)/Cm(III) on Ca-montmorillonite and Na-illite. Part 2: Surface complexation modelling. *Geochimica et Cosmochimica Acta*, 69(23):5403–5412, ISSN 00167037, 2005.
- /BRA 08/ Brasser, T., Scherschel, C., Brendler, V., Richter, A., Nebelung, C., Verhoff, M., Klinger, C., Reichelt, C.: ISDA - Ein Integriertes Sorptions-Datenbanksystem. Project report, ISBN 978-3-939355-23-6, October 2008.
- /BRE 03/ Brendler, V., Vahle, A., Arnold, T., Bernhard, G., Fanghänel, T.: RES3T: Rossendorf expert system for surface and sorption thermodynamics. *Journal of Contaminant Hydrology*, 61:281–291, ISSN 0169-7722, March 2003.
- /BRE 05/ Brendler, V., Baumann, N., Arnold, T., Geipel, G.: Uranium(VI) surface speciation on quartz. Forschungszentrum Rossendorf, Institute of Radiochemistry, 2005.
- /BRI 11/ Britz, S.: Sorption studies of Eu^{3+} on muscovite and orthoclase. Diploma thesis, 2011.
- /BRI 18/ Britz, S.: Europium sorption experiments with muscovite, orthoclase, and quartz: Modeling of surface complexation and reactive transport. Dissertation zur Erlangung des Grades einer Doktorin der Naturwissenschaften (Dr. rer. nat.), 10.24355/dbbs.084-201806051207-0, 2018.

- /BRØ 22/ Brønsted, J.: Studies on solubility IV. The principle of the specific interaction of ions. *Journal of the American Chemical Society*, 44(5):877–898, ISSN 0002-7863, eISSN 1520-5126, May 1922.
- /BRO 16/ Brown, P. L., Ekberg, C.: *Hydrolysis of Metal Ions*, Vol. 2. Wiley - VCH, Weinheim, ISBN 978-3-527-33010-2, 2016.
- /BRU 38/ Brunauer, S., Emmett, P., Teller, E.: Adsorption of gases in multimolecular layers. *Journal of the American Chemical Society*, 60:309–319, ISSN 0002-7863, eISSN 1520-5126, 1938.
- /CAS 92/ Cases, J., Berend, I., Besson, G., Uriot, J., Thomas, F.: Mechanism of adsorption and desorption of water vapor by homoionic montmorillonite: I. The sodium exchanged form. *Langmuir*, 8:2730–2739, ISSN 0743-7463, 1992.
- /CED 04/ Cedercreutz, J.: *Future Climate Scenarios for Olkiluoto with Emphasis on Permafrost*. Olkiluoto, Finland, POSIVA 2004-06, ISBN 951-652-132-0, 2004.
- /CHA 06/ Chang, H.-S., Korshin, G. V., Wang, Z., Zachara, J. M.: Adsorption of uranyl on gibbsite: A time-resolved laser-induced fluorescence spectroscopy study. *Environmental Science and Technology*, 40:1244–1249, ISSN 0013-936X, 2006.
- /CHI 94/ Chisholm-Brause, C., Conradson, S., Buscher, C., Eller, P., Morris, D.: Speciation of uranyl sorbed at multiple binding sites on montmorillonite. *Geochimica et Cosmochimica Acta*, 58:3625–3631, ISSN 0016-7037, 1994.
- /CHO 09/ Cho, Y., Komarneni, S.: Cation exchange equilibria of cesium and strontium with K-depleted biotite and muscovite. *Applied Clay Science*, 44(1-2):15–20, ISSN 01691317, 2009.
- /CIA 80/ Ciavatta, L.: The specific interaction theory in evaluating ionic equilibria. *Annali di Chimica*, 70:551–567, ISSN 0003-4592, 1980.

- /CUR 00/ Curti, E.: Nagra/PSI Thermochemical Database Update: Selection of Data for Europium. Project Report Internal PSI Report TM-44-00-04, Paul Scherrer Institute, Villigen, Switzerland, 2000.
- /CUR 01/ Curtis, G. P., Davis, J. A., Kohler, M., Kent, D. B.: Reactive transport modeling of uranium(VI) migration through quartz porous media under variable chemical conditions. In Davis, J., ed.: Surface complexation modeling of uranium(VI). Adsorption on natural mineral assemblages, pages 181–191. U.S. Geological Survey, 2001.
- /D'A 67/ D'Ans, J.: Makroskopische physikalisch-chemische Eigenschaften, volume 1 of Taschenbuch für Chemiker und Physiker. Springer, Berlin, 1967.
- /DAV 38/ Davies, C. W.: The extent of dissociation of salts in water. Part VIII. An equation for the mean ionic activity coefficient of an electrolyte in water, and a revision of the dissociation constants of some sulfates. Journal of the Chemical Society (Resumed), pages 2093–2098, ISSN 0368-1769, 1938.
- /DAV 54/ David, H., Hartley, H., Pearson, E.: The distribution of the ratio, in a single normal sample, of range to standard deviation. Biometrika, 41(3/4):482–493, ISSN 0006-3444, eISSN 1464-3510, December 1954.
- /DAV 62/ Davies, C.: Ion Association. Butterworths, Washington D.C., USA, 1962.
- /DAV 90/ Davis, J. A., Kent, D. B.: Surface complexation modeling in aqueous geochemistry. In Hochella, M., White, A., eds: Mineral-water Interface Geochemistry, volume 23 of Mineralogical Society of America Reviews in Mineralogy, pages 177–258. Mineralogical Society of America, Washington, DC, 1990.
- /DAV 98/ Davis, J., Coston, J., Kent, D., Fuller, C.: Application of the Surface Complexation Concept to Complex Mineral Assemblages. Environ. Sci. Technol., 32:2820–2828, 1998.

- /DAV 01/ Davis, J. A., Kohler, M., Payne, T. E., Bargar, R., Reitmeyer, R., Waite, T. D., McBeath, M., Coston, J. A., Lumpkin, G., Joye, J. L., Fenton, B., Curtis, G. P., Kent, D. B.: Surface complexation modeling of uranium(VI). Adsorption and natural mineral assemblages. U.S. Geological Survey, Washington, DC 20555-0001, ISBN 9780160616839, 2001.
- /DAV 05a/ Davis, J. A., Ochs, M., Olin, M., Payne, T. E., Tweed, C. J.: Interpretation and prediction of radionuclide sorption onto substrates relevant for radioactive waste disposal using thermodynamic sorption models. Technical report, OECD NEA, 2005.
- /DAV 05b/ Davis, J. A., Ochs, M., Olin, M., Payne, T., Tweed, C.: NEA Sorption Project Phase 2: Interpretation and Prediction of Radionuclide Sorption onto Substrates Relevant for Radioactive Waste Disposal Using Thermodynamic Sorption Models. Technical Report OECD No. 2005, ISBN 92-64-01206-0, 2005.
- /DEB 23/ Debye, P., Hückel, E.: Zur Theorie der Elektrolyte. I. Gefrierpunktserniedrigung und verwandte Erscheinungen. Physikalische Zeitschrift, 24:185–206, 1923.
- /DEL 98/ Delisle, G.: Numerical simulation of permafrost growth and decay. Journal of Quaternary Science, 13:325–333, 1998.
- /DIN 07/ DIN Deutsches Institut für Normung e. V.: Norm DIN EN 1992-1-1 : pH-Messung von wässrigen Lösungen mit pH-Messketten mit pH-Glaselektroden und Abschätzung der Messunsicherheit, 2007.
- /DIX 50/ Dixon, W.: Analysis of extreme values. Annals of mathematical statistics, 21:488–506, ISSN 0003-4851, 1950.
- /DIX 51/ Dixon, W.: Ratios involving extreme values: Annals of Mathematical Statistics. The Annals of Mathematical Statistics, 22(1):68–78, March 1951.
- /DRO 07/ Drot, R., Roques, J., Simoni, É.: Molecular approach of the uranyl/mineral interfacial phenomena. Comptes Rendus Chimie, 10(10-11):1078–1091, ISSN 1631-0748, October 2007.

- /DRO 15/ Drobot, B., Steudtner, R., Raff, J., Geipel, G., Brendler, V., Tsumishima, S.: Combining luminescence spectroscopy, parallel factor analysis and quantum chemistry to reveal metal speciation: a case study of uranyl(VI) hydrolysis. *Chemical Science*, 6:964–972, 2015.
- /DZO 90/ Dzombak, D. A., Morel, F. M.: *Surface complexation modeling*. John Wiley & Sons, Inc., 1990.
- /EVE 74/ Everett, D. H., Parfitt, G. D., Sing, K. S. W., Wilson, R.: The SCI/IUPAC/NPL project on surface area standards. *Journal of Applied Chemistry and Biotechnology*, 24:199–219, ISSN 1935-0554, 1974.
- /FEI 99/ Fein, E., Schneider, A.: d^{3f} Ein Programmpaket zur Modellierung von Dichteströmungen. Project Report GRS-139, Gesellschaft für Anlagen- und Reaktorsicherheit (GRS) mbH, BMWi-FKZ 02C04650, ISBN 3-923875-97-5, 1999.
- /FEI 04/ Fein, E.: Software Package r3t. Model for Transport and Retention in Porous Media. Project Report GRS-192, Gesellschaft für Anlagen- und Reaktorsicherheit (GRS) mbH, Braunschweig, BMWi-FKZ 02E9148/2, 2004.
- /FER 08/ Fernandes, M. M., Baeyens, B., Bradbury, M.: The influence of carbonate complexation on lanthanide/actinide sorption on montmorillonite. *Radiochimica Acta*, 96:691–697, ISSN 0033-8230, 2008.
- /FER 16/ Fernandes, M. M., Scheinost, A., Baeyens, B.: Sorption of trivalent lanthanides and actinides onto montmorillonite: Macroscopic, thermodynamic and structural evidence for ternary hydroxo and carbonato surface complexes on multiple sorption sites. *Water Research*, 99:74–82, ISSN 0043-1354, August 2016.
- /FLÜ 09/ Flügge, J.: *Radionuclide Transport in the Overburden of a Salt Dome The Impact of Extreme Climate States*. Dr. rer. nat., ISBN 978-3-86853-109-1, 2009.

- /FRI 14/ Fricke, J.: Sorption von Europium an Quarz - Batchversuche und geochemische Modellierung. Technische Universität Braunschweig, Master thesis, thesis available at GRS, Theodor-Heuss-Str. 4, 38122 Braunschweig, Germany, 2015.
- /FRO 06/ Froideval, A., Nero, M. D., Gaillard, C., Barillon, R., Rossini, I., Hazemann, J.: Uranyl sorption species at low coverage on Al-hydroxide: TRLFS and XAFS studies. *Geochimica et Cosmochimica Acta*, 70:5270–5284, ISSN 0016-7037, 2006.
- /FRÖ 11/ Fröhlich, D., Amayri, S., Drebert, J., Reich, T.: Sorption of neptunium(V) on Opalinus Clay under aerobic/anaerobic conditions. *Radiochimica Acta*, 99(2):71–77, ISSN 0033-8230, 2011.
- /GAB 01/ Gabriel, U., Charlet, L., Schläpfer, C., Vial, J., Brachmann, A., Geipel, G.: Uranyl Surface Speciation on Silica Particles Studied by Time-Resolved Laser-Induced Fluorescence Spectroscopy. *Journal of Colloid and Interface Science*, 239(2):358–368, ISSN 00219797, 2001.
- /GAS 00/ Gascoyne, M.: A review of published literature on the effects of permafrost on the hydrogeochemistry of bedrock. Project report, Swedish Nuclear Fuel and Waste Management Co (SKB), Stockholm, R-01-56, 2000.
- /GEC 13/ Geckeis, H., Lützenkirchen, J., Polly, R., Rabung, T., Schmidt, M.: Mineral-water interface reactions of actinides. *Chemical Reviews*, 113(2):1016–1062, ISSN 0009-2665, 2013.
- /GLA 00/ Gladysz-Plaska, A., Pietryka, K., Majdan, M.: Affinity of neodymium and samarium toward AD10N zeolite. *ACH-Models in Chemistry*, 137:775–787, 2000.
- /GLI 98/ Glinka, Y. D., Jaroniec, C., Jaroniec, M.: Studies of surface properties of disperse silica and alumina by luminescence measurements and nitrogen adsorption. *Journal of Colloid and Interface Science*, 201:210–219, ISSN 0021-9797, 1998.

- /GOG 06/ Gogolev, A., Zakharova, E., Rodygina, N., Fedoseev, A., Shilov, V.: Reduction of Neptunium(V) and Uranium(VI) with Iron(II) in Bicarbonate Solutions. *Radiochemistry*, 48:249–253, ISSN 1066-3622, May 2006.
- /GÖT 11/ Götz, C., Geipel, G., Bernhard, G.: The influence of the temperature on the carbonate complexation of uranium(VI): a spectroscopic study. *Journal of Radioanalytical and Nuclear Chemistry*, 287(3):961–969, ISSN 0236-5731, eISSN 1588-2780, March 2011.
- /GRE 13/ Grenthe, I., Mompean, F., Spahiu, K., Wanner, H.: TDB-2 Guidelines for the extrapolation to zero ionic strength. OECD Nuclear Energy Agency, Issy-les-Moulineaux (France), June 2013.
- /GRI 82 – 94/ Grimm, W.-D.: Sedimentpetrographische Untersuchungen an Proben aus dem Raum Gorleben 1982-1994. Project report, München, 1994.
- /GRO 07/ Großmann, K., Arnold, T., Krawczyk-Bärsch, E., Diessner, S., Wobus, A., Bernhard, G., Krawietz, R.: Identification of Fluorescent U(V) and U(VI) Microparticles in a Multispecies Biofilm by Confocal Laser Scanning Microscopy and Fluorescence Spectroscopy. *Environmental Science & Technology*, 41(18):6498–6504, ISSN 0013-936X, eISSN 1520-5851, September 2007.
- /GUG 35/ Guggenheim, E.: The specific thermodynamic properties of aqueous solutions of strong electrolytes. *The London, Edinburgh, and Dublin Philosophical Magazine and Journal of Science*, 19(127):588–643, ISSN 1941-5982, March 1935.
- /HAG 12/ Hagemann, S., Moog, H. C., Herbert, H.-J.: Rückhaltung und thermodynamische Modellierung von Iod und Selen in hochsalinaren Lösungen. *GRS-Bericht*, 245:167, 2012.
- /HAG 14/ Hagemann, S., Bischofer, B., Scharge, T.: Entwicklung von Methoden und Modellen zur Bestimmung des Redoxpotentials salinärer Lösungen. *GRS-Bericht*, 260, 2014.

- /HAL 15/ Haller-Jans, J.: Sorption von Nickel an LDPE und PFA sowie Muskovit, Orthoklas und Quarz unter verschiedenen geochemischen Bedingungen. Technische Universität Braunschweig, Bachelor thesis, available at GRS, Theodor-Heuss-Str. 4, 38122 Braunschweig, Germany, October 2015.
- /HAN 14/ Hanna, K., Martin, S., Quilès, F., Boily, J.-F.: Sorption of Phthalic Acid at Goethite Surfaces under Flow-Through Conditions. *Langmuir*, 30(23):6800–6807, ISSN 0743-7463, eISSN 1520-5827, June 2014.
- /HIE 89a/ Hiemstra, T., de Wit, J. C. M., von Riemsdijk, W. H.: Multisite proton adsorption modeling at the solid / solution interface of (hydr)oxides: A new approach. II. Application to various important (hydr)oxides. *Journal of Colloid and Interface Science*, 133(1):105–117, ISSN 0021-9797, January 1989.
- /HIE 89b/ Hiemstra, T., van Riemsdijk, W., Bolt, G.: Multisite proton adsorption modeling at the solid/solution interface of (hydr)oxides: A new approach. I. Model description and evaluation of intrinsic reaction constants. *Journal of Colloid and Interface Science*, 133(1):91–104, ISSN 0021-9797, November 1989.
- /HIL 98/ Hill, M. C.: *Methods and Guidelines for Effective Model Calibration*. Technical report, U.S. Geological Survey, Denver, CO, USA, 1998.
- /HIN 01/ Hind, A. R., Bhargava, S. K., McKinnon, A.: At the solid/liquid interface: FTIR/ATR the tool of choice. *Advances in Colloid and Interface Science*, 93(1-3):91–114, ISSN 0001-8686, October 2001.
- /HOC 96/ Hochleitner, R.: *GU-Naturführer Mineralien und Kristalle: Mineralien nach Strichfarben bestimmen*. Gräfe und Unzer, München, 1996.
- /HOU 76/ Hougardy, J., Stone, W., Fripiat, J.: NMR-study of adsorbed water. I. Molecular orientation and protonic motions in the two-layer hydrate of a Na-vermiculite. *The Journal of Chemical Physics*, 64:3840–?, 1976.

- /ILT 12/ Ilton, E. S., Wang, Z., Boily, J.-F., Qafoku, O., Rosso, K. M., Smith, S. C.: The Effect of pH and Time on the Extractability and Speciation of Uranium(VI) Sorbed to SiO₂. *Environ. Sci. Technol.*, 46:6604–6611, 2012.
- /IMB 84/ Imbrie, J., Hays, J. D., Martinson, D. G., McIntyre, A., Mix, A. C., Morley, J. J., Pisias, N. G., Prell, W. L., Shackleton, N.: The Orbital Theory of Pleistocene Climate: Support from a Revised Chronology of the Marine $\delta^{18}\text{O}$ Record. In Berger, A. L., Imbrie, J., Hays, J., Kukla, G., Saltzman, B., eds: *Milankovitch and Climate. Part 1*. Dordrecht (D. Reidel Publishing Company), 1984.
- /JER 06/ Jerez, J., Flury, M.: Humic acid-, ferrihydrite-, and aluminosilicate-coated sands for column transport experiments. *Coll. Surf. A.*, 273:90–96, 2006.
- /JOR 11/ Jordan, N., Foerstendorf, H., Weiß, S., Heim, K., Schild, D., Brendler, V.: Sorption of selenium(VI) onto anatase: Macroscopic and microscopic characterization. *Geochimica et Cosmochimica Acta*, 75(6):1519–1530, ISSN 0016-7037, March 2011.
- /JOS 11/ Joseph, C., Schmeide, K., Sachs, S., Brendler, V., Geipel, G., Bernhard, G.: Sorption of uranium(VI) onto Opalinus Clay in the absence and presence of humic acid in Opalinus Clay pore water. *Chemical Geology*, 284(3-4):240–250, ISSN 00092541, 2011.
- /JUN 99/ Jung, J., Hyun, S., Lee, J., Cho, Y., Hahn, P.: Adsorption of UO₂²⁺ on natural composite materials. *Journal of Radioanalytical and Nuclear Chemistry*, 242(2):405–412, ISSN 0236-5731, 1999.
- /KAN 92/ Kantor, W., Krone, F., Nitsch, M.: Ergebnisse zur Bestimmung der Porengrößenverteilung und begleitender physikalisch-chemischer sowie mineralogischer Untersuchungen in Lockergesteinen an Proben aus den Schächten I und II. Technical Report BGR-Fachbericht A9G41111000, 1992.
- /KAP 61/ Kappelmeier, O.: Geothermik. In *Lehrbuch der Angewandten Geologie*, volume 1, pages 863–889. Enke, Stuttgart, 1961.

- /KAR 79/ Karte, J.: Räumliche Abgrenzung und regionale Differenzierung des Periglaziärs, volume 35 of Bochumer geographische Arbeiten. Geographisches Institut der Ruhr-Universität Bochum, Bochum, 1979.
- /KAR 10/ Karamalidis, A. K., Dzombak, D. A.: Surface complexation modeling: gibbsite. John Wiley & Sons, Hoboken, 2010.
- /KEE 05/ Keesmann, S., Noseck, U., Buhmann, D., Fein, E., Schneider, A.: Modellrechnungen zur Langzeitsicherheit von Endlagern für abgebrannte Brennelemente in Salz- und Granitformationen. Technical Report GRS-206, Braunschweig, ISBN 3-931995-73-9, July 2005.
- /KIT 99/ Kitamura, A., Fujiwara, K., Yamamoto, T., Nishikawa, S., Moriyama, H.: Analysis of Adsorption behavior of cations onto quartz surface by electrical double-layer model. Journal of Nuclear Science and Technology, 36(12):1167–1175, ISSN 0022-3131, eISSN 1881-1248, December 1999.
- /KLI 94/ Klinge, H.: Zusammenfassende Bearbeitung der chemischen und isotopegeochemischen Zusammensetzung der Grundwässer im Deckgebirge des Salzstocks Gorleben und seiner Randsenken Projektgebiet Gorleben Süd. Project report, Hannover, June 1994.
- /KLI 02a/ Klinge, H., Köthe, A., Ludwig, R.-R., Zwirner, R.: Geologie und Hydrogeologie des Deckgebirges über dem Salzstock Gorleben. Zeitschrift für Angewandte Geowissenschaften, (2):7–15, 2002.
- /KLI 02b/ Klinge, H., Köthe, A., Ludwig, R.-R., Zwirner, R.: Geologie und Hydrologie des Deckgebirges über dem Salzstock Gorleben. Zeitschrift für Angewandte Geowissenschaften, February 2002.
- /KLI 04/ Klinge, H., Baharian-Shiraz, A.: Projekt Gorleben, Dokumentation hydrogeologischer Basisdaten. Project report, Bundesanstalt für Geowissenschaften und Rohstoffe, Hannover, 2004.

- /KLI 07/ Klinge, H., Boehme, J., Grissmann, C., Houben, G., Ludwig, R. R., Rübél, A., Schelkers, K., Schildknecht, F., Suckow, A.: Standortbeschreibung Gorleben, Teil 1: Die Hydrogeologie des Deckgebirges des Salzstocks Gorleben. E. Schweizerbart'sche Verlagsbuchhandlung oHG, ISBN 978-3-510-95962-4, 2007.
- /KLI 14/ Klinge, H., Houben, G.: Internes Memo zur Besprechung bei BGR (Klinge, Houben), February 2014.
- /KÖT 07/ Köthe, A., Hoffmann, N., Krull, P., Zirngarst, M., Zwirner, R.: Standortbeschreibung Gorleben, Teil 2: Die Geologie des Deck- und Nebengebirges des Salzstocks Gorleben. Geologisches Jahrbuch, Reihe C. Schweizerbart'sche, E., C 72, ISBN 978-3510959631, 2007.
- /KOW 04/ Kowal-Fouchard, A., Drot, R., Simoni, E., Ehrhardt, J. J.: Use of Spectroscopic Techniques for Uranium(VI)/Montmorillonite Interaction Modeling. *Environmental Science & Technology*, 38(5):1399–1407, ISSN 0013-936X, eISSN 1520-5851, March 2004.
- /KRA 11/ Krawczyk-Bärsch, E., Lünsdorf, H., Arnold, T., Brendler, V., Eisbein, E., Jenk, U., Zimmermann, U.: The influence of biofilms on the migration of uranium in acid mine drainage (AMD) waters. *Science of The Total Environment*, 409(16):3059–3065, ISSN 0048-9697, July 2011.
- /KRA 12/ Krawczyk-Bärsch, E., Lünsdorf, H., Pedersen, K., Arnold, T., Bok, F., Steudtner, R., Lehtinen, A., Brendler, V.: Immobilization of uranium in biofilm microorganisms exposed to groundwater seeps over granitic rock tunnel walls in Olkiluoto, Finland. *Geochimica et Cosmochimica Acta*, 96:94–104, ISSN 0016-7037, November 2012.
- /KRE 07/ Krepelová, A.: Influence of Humic Acid on the Sorption of Uranium(VI) and Americium(III) onto Kaolinite. Dissertation zur erlangung des akademischen grades doctor rerum naturalium (dr. rer. nat.), 2007.
- /KUL 02/ Kulik, D. A.: Sorption modelling by Gibbs energy minimisation: Towards a uniform thermodynamic database for surface complexes of radionuclides. *Radiochimica Acta*, 90:815–832, ISSN 0033-8230, 2002.

- /KUM 12/ Kumar, S., Kar, A. S., Tomar, B. S., Bhattacharyya, D.: X-ray absorption fine structure spectroscopy study of Eu(III) sorption products onto amorphous silica and γ -alumina: Effect of pH and substrate. *Polyhedron*, 33(1):33–40, ISSN 0277-5387, February 2012.
- /KUM 13/ Kumar, S., Pente, A., Bajpai, R., Kaushik, C., Tomar, B.: Americium sorption on smectite-rich natural clay from granitic ground water. *Applied Geochemistry*, 35:28–34, ISSN 0883-2927, August 2013.
- /KUN 88/ Kuntze, H., Roeschmann, G., Schwerdtfeger, G.: *Bodenkunde*. Verlag Eugen Ulmer Stuttgart, 1988.
- /KUR 51/ Kurbatov, M., Wood, G. B., Kurbatov, J.: Isothermal adsorption of cobalt from dilute solutions. *J. Phys. Chem.*, 55(7):1170–1182, July 1951.
- /KUR 82/ Kurek, E., Czaban, J., Bollag, J.-M.: Sorption of Cadmium by Microorganisms in Competition with Other Soil Constituents. *Applied and Environmental Microbiology*, 43(5):1011–1015, ISSN 0099-2240, May 1982.
- /LEE 13/ Lee, S. S., Schmidt, M., Laanait, N., Sturchio, N. C., Fenter, P.: Investigation of Structure, Adsorption Free Energy, and Overcharging Behavior of Trivalent Yttrium Adsorbed at the Muscovite (001)Water Interface. *The Journal of Physical Chemistry*, 117(45):23738–23749, ISSN 0022-3654, eISSN 1932-7455, November 2013.
- /LEF 04/ Lefèvre, G.: In situ Fourier-transform infrared spectroscopy studies of inorganic ions adsorption on metal oxides and hydroxides. *Advances in Colloid and Interface Science*, 107(2-3):109–123, ISSN 0001-8686, March 2004.
- /LEG 04/ Legarth, B., Tischner, T., Huenges, E.: Stimulating for productivity: Hydraulic Proppant Fracturing Treatments in Rotliegend Sandstones. In Wolfgramm, M., Huenges, E., eds: *Sandsteine im In-situ-Geothermielabor Groß-Schönebeck: Reservoircharakterisierung, Stimulation, Hydraulik und Nutzungskonzepte*. GeoForschungsZentrum Potsdam in der Helmholtz-Gemeinschaft, Potsdam, April 2004.

- /LEM 13/ Lemire, R., Berner, U., Musikas, C.: Chemical Thermodynamics of iron Part I. Nuclear Energy Agency, pages 1082–, 2013.
- /LUO 07/ Luo, Y.-R., Byrne, R. H.: The influence of ionic strength of yttrium and rare earth element complexation by fluoride ions in NaClO₄, NaNO₃ and NaCl solution at 25°C. *Journal of Solution Chemistry*, 36:673–689, ISSN 0095-9782, eISSN 1572-8927, 2007.
- /LÜT 96/ Lützenkirchen, J., Behra, P.: On the Surface Precipitation Model for Cation Sorption at the (Hydr)oxide Water Interface. *Aquatic Geochemistry*, 1:375–397, ISSN 1380-6165, 1996.
- /LÜT 12/ Lützenkirchen, J., Preocanin, T., Kovacevic, D., Tomišić, V., Lövgren, L., Kallay, N.: Potentiometric Titrations as a Tool for Surface Charge Determination. *Croatica Chemica Acta - izd. tromjesečno Hrvatsko kemijsko društvo*, 85:391–417, ISSN 0011-1643, eISSN 1334-417X, 2012.
- /MAC 11/ Macht, F., Eusterhues, K., Pronk, G. J., Totsche, K. U.: Specific surface area of clay minerals: Comparison between atomic force microscopy measurements and bulk-gas (N₂) and -liquid (EGME) adsorption methods. *Applied Clay Science*, 53(1):20–26, ISSN 01691317, 2011.
- /MAH 13/ Maher, K., Bargar, J. R., Jr., G. E. B.: Environmental Speciation of Actinides. *Inorganic Chemistry*, 52(7):3510–3532, 2013.
- /MAR 98/ Maraqa, M. A., Zhao, X., Wallace, R. B., Voice, T. C.: Retardation Coefficients of Nonionic Organic Compounds Determined by Batch and Column Techniques. *Soil Science Society of America Journal*, 62(1):142–152, eISSN 0361-5995, 1998.
- /MAS 04/ Maslova, M. V., Gerasimova, L. G., Forsling, W.: Surface Properties of Cleaved Mica. *Colloid Journal*, 66(3):322–328, ISSN 1061-933X, May 2004.

- /MAT 06/ Mathur, S., Dzombak, D.: Surface complexation modeling: Goethite. In Lützenkirchen, J., ed.: Surface Complexation Modelling, Volume 11, 1st Edition, volume 11, pages 443–468. Academic Press, ISBN 9780123725721, eISBN 9780080467788, September 2006.
- /MCN 01/ McNames, J.: A Fast Nearest Neighbor Algorithm Based on a Principle Axis Search Tree. IEEE Transactions on Pattern Analysis and Machine Intelligence, 23:964–976, September 2001.
- /MIL 92/ Millero, F.: Stability constants for the formation of rare earth inorganic complexes as a function of ionic strength. Geochimica et Cosmochimica Acta, 56:3123–3132, ISSN 0016-7037, 1992.
- /MOO 15/ Moog, H. C., Bok, F., Marquardt, C., Brendler, V.: Disposal of Nuclear Waste in Host Rock formations featuring high-saline solutions: Implementation of a Thermodynamic Reference Database (THEREDA). Applied Geochemistry, 55:72–84, ISSN 0883-2927, April 2015.
- /MOU 01/ Moulin, V., Moulin, C.: Radionuclide speciation in the environment: a review. Radiochimica Acta, 89(11-12), ISSN 0033-8230, eISSN 2193-3405, January 2001.
- /MRU 11/ Mrugalla, S.: Geowissenschaftliche Langzeitprognose. Bericht zum Arbeitspaket 2. Vorläufige Sicherheitsanalyse für den Standort Gorleben. Technical Report GRS-275, Köln, ISBN 978-3-939355-51-9, July 2011.
- /MÜL 08/ Müller, K., Brendler, V., Foerstendorf, H.: Aqueous Uranium(VI) Hydrolysis Species Characterized by Attenuated Total Reflection Fourier-Transform Infrared Spectroscopy. Inorganic Chemistry, 47(21):10127–10134, ISSN 0020-1669, eISSN 1520-510X, November 2008.
- /MÜL 12/ Müller, K., Foerstendorf, H., Meusel, T., Brendler, V., Lefèvre, G., Comarmond, M. J., Payne, T. E.: Sorption of U(VI) at the TiO₂water interface: An in situ vibrational spectroscopic study. Geochimica et Cosmochimica Acta, 76:191–205, ISSN 0016-7037, January 2012.

- /MÜL 13/ Müller, K., Foerstendorf, H., Brendler, V., Rossberg, A., Stolze, K., Gröschel, A.: The surface reactions of U(VI) on γ -Al₂O₃ In situ spectroscopic evaluation of the transition from sorption complexation to surface precipitation. *Chemical Geology*, 357:75–84, ISSN 0009-2541, October 2013.
- /NAK 91/ Nakayama, S., Sakamoto, Y.: Sorption of Neptunium on Naturally-Occurring Iron-Containing Minerals. *Radiochimica Acta*, 52-53:153–157, ISSN 0033-8230, 1991.
- /NÄS 10/ Näslund, J. O., Bogren, J., Gustavson, G., Moberg, Alexandersson, H., Jansson, P., Whitehouse, P., Hartikainen, J., Olvmo, M., Lokrantz, H., Sohlenius, G., Helmens, K., Kjellström, E., Brandefelt, J., Standberg, G., Centre, R., Brydsten, L., Engqvist, A., Lindborg, T., Birgersson, M.: Climate and climate-related issues for the safety assessment SR-Site. Technical report, Swedish Nuclear Fuel and Waste Management Co (SKB), Stockholm, TR-10.49, 2010.
- /NEW 14/ Newsome, L., Morris, K., Lloyd, J. R.: The biogeochemistry and bioremediation of uranium and other priority radionuclides. *Chemical Geology*, 363:164–184, ISSN 0009-2541, January 2014.
- /NOS 12a/ Noseck, U., Becker, D.-A., Brassler, T., Fahrenholz, C., Flügge, J., Herbert, H.-J., Ionescu, A., Kröhn, K.-P., Kull, H., Meleshyn, A., Mönig, J., Röhlig, K.-J., Rübél, A., Rothfuchs, T., Wolf, J.: Scientific Basis for a Safety Case of Deep Geological Repositories. Project Report GRS - 298, Braunschweig, BMWi-FKZ 02E10719, ISBN 978-3-939355-77-9, November 2012.
- /NOS 12b/ Noseck, U., Brendler, V., Flügge, J., Stockmann, M., Britz, S., Lampe, M., Schikora, J., Schneider, A.: Realistic integration of sorption processes in transport codes for long-term safety assessments. Project Report GRS-297, Gesellschaft für Anlagen- und Reaktorsicherheit (mbH), Braunschweig, BMWi-FKZ 02E10548, ISBN 978-3-939355-76-2, September 2012.

- /OLI 05/ Olin, A., Noläng, B., Osadchii, E.: Chemical thermodynamics of selenium. Elsevier B.V., Amsterdam, 2005.
- /OSM 98/ Osman, M. A., Caseri, W. R., Suter, U. W.: H⁺/Li⁺ and H⁺/K⁺ Exchange on Delaminated Muscovite Mica. *Journal of Colloid and Interface Science*, 198:157–163, ISSN 0021-9797, 1998.
- /OSM 99/ Osman, M. A., Moor, C., Caseri, W. R., Suter, U. W.: Alkali Metals Ion Exchange on Muscovite Mica. *Journal of Colloid and Interface Science*, 209:232–239, ISSN 0021-9797, 1999.
- /PAN 17/ Pan, D., Fan, F., Wang, Y., Li, P., Hu, P., Fan, Q., Wu, W.: Retention of Eu(III) in muscovite environment: Batch and spectroscopic studies. *Chemical Engineering Journal*, 330:559–565, ISSN 1385-8947, December 2017.
- /PAR 99/ Parkhurst, D. L., Appelo, C.: User's Guide to Phreeqc (Version2) A Computer Program for Speciation, Batch Reaction, one-dimensional Transport, and inverse geochemical Calculations. Denver, CO, USA, 1999.
- /PAR 10/ Parkhurst, D. L., Kipp, K. L., Charlton, S. R.: PHAST Version 2: A Program for Simulating Groundwater Flow, Solute Transport, and Multi-component Geochemical Reactions. Technical report, 2010.
- /PAR 13/ Parkhurst, D. L., Appelo, C.: Description of input and examples for PHREEQC version 3: A computer program for speciation, batch-reaction, one-dimensional transport, and inverse geochemical calculations. In U.S. Geological Survey Techniques and Methods, book 6, volume A43 of Modeling Techniques. U.S. Geological Survey, Denver, Colorado, January 2013.
- /PAS 81/ Pashley, R.: DLVO and Hydration Forces between Mica Surfaces in Li⁺, Na⁺, K⁺ and Cs⁺ Electrolyte Solutions: A Correlation of Double-Layer and Hydration Forces with Surface Cation Exchange Properties. *Journal of Colloid and Interface Science*, 83(2), ISSN 0021-9797, October 1981.

- /PET 11/ Petrov, V., Gaona, X., Fellhauer, D., Dardenne, K., Kalmykov, S., Altmaier, M.: Contribution to Migration Conference. In Migration Conference, 2011.
- /PIT 74/ Pitzer, K., Mayorga, G.: Thermodynamics of electrolytes. III. Activity and osmotic coefficients for 2-2 electrolytes. *Journal of Solution Chemistry*, 3(7):539–546, ISSN 0095-9782, eISSN 1572-8927, 1974.
- /PIT 91/ Pitzer, K.: Activity coefficients in electrolyte solutions. 2nd ed. CRC Press, Boca Raton, 1991.
- /POE 08/ Poeter, E. P., Hill, M. C., Banta, E. R., Mehl, S., Christensen, S.: UCODE_2005 and Six Other Computer Codes for Universal Sensitivity Analysis, Calibration, and Uncertainty Evaluation, 2008.
- /POE 14/ Poeter, E. P., Hill, M. C., Lu, D., Tiedeman, C. R., Mehl, S.: UCODE_2014, with New Capabilities to Define Parameters Unique to Predictions, Calculate Weights using Simulated Values, Estimate Parameters with SVD, Evaluate Uncertainty with MCMC, and More, 2014.
- /POI 99a/ Poinssot, C., Baeyens, B., Bradbury, M.: Experimental Studies of Cs, Sr, Ni, and Eu sorption on Na-illite and the modelling of Cs sorption. PSI-Report, 99(06), ISSN 1019-0643, 1999.
- /POI 99b/ Poinssot, C., Baeyens, B., Bradbury, M. H.: Experimental and modelling studies of caesium sorption on illite. *Geochimica et Cosmochimica Acta*, 63(19/20):3217–3227, ISSN 0016-7037, 1999.
- /POL 10/ Polly, R., Schimmelpfennig, B., Rabung, T., Flörsheimer, M., Klenze, R., Geckeis, H.: Quantum chemical study of inner-sphere complexes of trivalent lanthanide and actinide ions on the corundum (0001) surface. *Radiochimica Acta*, 98(9-11):627–634, ISSN 0033-8230, November 2010.

- /POL 13/ Polly, R., Schimmelpfennig, B., Flörsheimer, M., Rabung, T., Kupcik, T., Klenze, R., Geckeis, H.: Quantum chemical study of inner-sphere complexes of trivalent lanthanide and actinide ions on the corundum (110) surface. *Radiochimica Acta*, 101(9):561–570, ISSN 0033-8230, eISSN 2193-3405, September 2013.
- /POR 00/ Porro, I., Newman, M. E., Dunnivant, F. M.: Comparison of Batch and Column Methods for Determining Strontium Distribution Coefficients for Unsaturated Transport in Basalt. *Environmental Science & Technology*, 34(9):1679–1686, ISSN 0013-936X, eISSN 1520-5851, May 2000.
- /PRE 98/ Preocanin, T., Kallay, N.: Application of Mass Titration? to Determination of Surface Charge of Metal Oxides. *Croatica Chemica Acta - izd. tromjesečno Hrvatsko kemijsko društvo*, 71(4):1117–1125, ISSN 0011-1643, eISSN 1334-417X, 1998.
- /PRE 06/ Preocanin, T., Kallay, N.: Point of zero charge and surface charge density of TiO₂ in aqueous electrolyte solution as obtained by potentiometric mass titration. *Croatica Chemica Acta izd. tromjesečno Hrvatsko kemijsko društvo*, 79(1):95–106, ISSN 0011-1643, eISSN 1334-417X, 2006.
- /PRI 01/ Prikryl, J. D., Jain, A., Turner, D. R., Pabalan, R. T.: Uranium VI sorption behavior on silicate mineral mixtures. *Journal of Contaminant Hydrology*, 47(2-4):241–253, ISSN 0169-7722, February 2001.
- /RAN 09/ Randall, M., Fuger, J., Grenthe, I., Neck, V., Rai, D.: Chemical Thermodynamics Series Volume 11, Chemical Thermodynamics of Thorium. Technical report, OECD Nuclear Energy Agency, Issy-Les-Moulineaux (France), 2009.
- /RAR 87/ Rard, J. A.: Update of the europium data base. Project report, Lawrence Livermore National Laboratory, 1987.
- /RIC 15/ Richter, C.: Sorption of environmentally relevant radionuclides (U(VI), Np(V)) and lanthanides (Nd(III)) on feldspar and mica. Dissertation zur Erlangung des akademischen Grades Doctor rerum naturalium, 2015.

- /RIC 16/ Richter, C., Müller, K., Drobot, B., Steudtner, R., Großmann, K., Stockmann, M., Brendler, V.: Macroscopic and spectroscopic characterization of uranium(VI) sorption onto orthoclase and muscovite and the influence of competing Ca²⁺. *Geochimica et Cosmochimica Acta*, 189:143–157, ISSN 0016-7037, September 2016.
- /ROH 98/ Rohling, E. J., Fenton, M., Jorisson, F. J., Bertrand, P., Ganssen, G., Caulet, J. P.: Magnitudes of sea-level lowstands of the past 500,000 years. *Nature*, 394:162–165, ISSN 0028-0836, 1998.
- /ROU 07/ Rouquerol, J., Llewellyn, P., Rouquerol, F.: Is the BET equation applicable to microporous adsorbents? *Studies in Surface Science and Catalysis*, 160:49–56, 2007.
- /RUS 10/ Rusch, B., Hanna, K., Humbert, B.: Sorption and Transport of Salicylate in a Porous Heterogeneous Medium of Silica Quartz and Goethite. *Environmental Science & Technology*, 44(7):2447–2453, ISSN 0013-936X, eISSN 1520-5851, April 2010.
- /SAI 10/ Saito, T., Sao, H., Ishida, K., Aoyagi, N., Kimura, T., Nagasaki, S., Tanaka, S.: Application of Parallel Factor Analysis for Time-Resolved Laser Fluorescence Spectroscopy: Implication for Metal Speciation Study. *Environmental Science and Technology*, 44:5055–5060, ISSN 0013-936X, 2010.
- /SAW 70/ Sawhney, B.: Potassium and Cesium Ion selectivity in relation to clay Mineral structure. *Clays and Clay Minerals*, 18(1):47–52, ISSN 0009-8604, 1970.
- /SAW 72/ Sawhney, B.: Selective Sorption and Fixation of cations by clay Minerals: A review. *Clays and Clay Minerals*, 20:93–100, ISSN 0009-8604, 1972.
- /SCA 36/ Scatchard, G.: Concentrated solutions of strong electrolytes. *Chemical Reviews*, 19(3):309–327, ISSN 0009-2665, December 1936.

- /SCH 67/ Schwabe, K.: Azidität konzentrierter Elektrolytlösungen. *Electrochimica Acta*, 12:67–93, ISSN 0013-4686, 1967.
- /SCH 10a/ Scheffer, F., Schachtschabel, P., Blume, H.-P., Brümmer, G., Horn, R., Kandeler, E., Kögel-Knabner, I., Kretzschmar, R., Stahr, K., Wilke, B.-M.: *Lehrbuch der Bodenkunde*, 16. Auflage. Spektrum Akademischer Verlag, Heidelberg, 2010.
- /SCH 10b/ Schmeide, K., Bernhard, G.: Sorption of Np(V) and Np(IV) onto kaolinite: Effects of pH, ionic strength, carbonate and humic acid. *Applied Geochemistry*, 25(8):1238–1247, ISSN 08832927, 2010.
- /SCH 14a/ Schmeide, K., Gürtler, S., Müller, K., Steudtner, R., Joseph, C., Bok, F., Brendler, V.: Interaction of U(VI) with Äspö diorite: A batch and in situ ATR FT-IR sorption study. *Applied Geochemistry*, 49:116–125, ISSN 0883-2927, October 2014.
- /SCH 14b/ Schulze, A.: Spatial distribution of uranium(VI) surface complexes in quartz columns. Technische Universität Braunschweig, Master thesis, available at GRS, Theodor-Heuss-Str. 4, 38122 Braunschweig, Germany, 2014.
- /SCH 16/ Schneider, A.: Modelling of Data Uncertainties on Hybrid Computers. Technical Report GRS - 392, Braunschweig, BMWi-FKZ 02E11062A, ISBN 978-3-944161-73-0, June 2016.
- /SHA 87/ Shainberg, I., Alperovitch, N., Keren, R.: Charge density and Na-K-Ca exchange on smectites. *Clays and Clay Minerals*, 35(1):68–73, ISSN 0009-8604, 1987.
- /SIM 99/ Simunek, J., van Genuchten, M. T., Sejna, M., Toride, N., Leij, F. J.: *The STANMOD computer software for evaluating solute transport in porous media using analytical solutions of convection-dispersion equation*. Riverside, CA, USA, 1999.

- /SPA 95/ Spahui, K., Bruno, J.: A selected thermodynamical database for REE to be used in HLNW performance assessment exercise. SKB Technical Report, 95(35):91–, 1995.
- /SPO 98/ Sposito, G.: On points of zero charge. Environmental Science and Technology, 32(19):2815–2819, ISSN 0013-936X, 1998.
- /STE 00/ Stefánsson, A., Arnórsson, S.: Feldspar saturation state in natural waters. Geochimica et Cosmochimica Acta, 64:2567–2584, ISSN 0016-7037, 2000.
- /STE 11/ Steudtner, R., Sachs, S., Schmeide, K., Brendler, V., Bernhard, G.: Ternary uranium(VI) carbonate humate complex studied by cryo-TRLFS. Radiochimica Acta, 99:687–692, ISSN 0033-8230, 2011.
- /STE 17/ Steinbrecher, L.: Sorption von Cs an Orthoklas und Muskovit: Batchversuche und geochemische Modellierung. Technische Universität Braunschweig, Master thesis, available at GRS, Theodor-Heuss-Str. 4, 38122 Braunschweig, Germany, 2017.
- /STI 95/ Stillings, L. L., Brantley, S. L.: Feldspar dissolution at 25C and pH 3: Reaction stoichiometry and the effect of cations. Geochimica et Cosmochimica Acta, 59(8):1483–1496, ISSN 0016-7037, 1995.
- /STO 17/ Stockmann, M., Schikora, J., Becker, D.-A., Flügge, J., Noseck, U., Brendler, V.: Smart Kd-values, their uncertainties and sensitivities - Applying a new approach for realistic distribution coefficients in geochemical modeling of complex systems. Chemosphere, 187:277–285, ISSN 0045-6535, November 2017.
- /STU 06/ Stumpf, S., Stumpf, T., Walther, C., Bosbach, D., Fanghänel, T.: Sorption of Cm(III) onto different Feldspar surfaces: a TRLFS study. Radiochimica Acta, 94(5):243–248, ISSN (Print) 0033-8230, 2006.

- /STU 08a/ Stumpf, S., Stumpf, T., Lützenkirchen, J., Walther, C., Fanghänel, T.: Immobilization of trivalent actinides by sorption onto quartz and incorporation into siliceous bulk: Investigations by TRLFS. *Journal of Colloid and Interface Science*, 318(1):5–14, ISSN 00219797, 2008.
- /STU 08b/ Stumpf, S., Stumpf, T., Lützenkirchen, J., Walther, C., Fanghänel, T.: Immobilization of trivalent actinides by sorption onto quartz and incorporation into siliceous bulk: Investigations by TRLFS. *Journal of Colloid and Interface Science*, 318:5–14, ISSN 0021-9797, 2008.
- /SUT 98/ Suter, D., Biehler, D., Blaser, P., Hollmann, A.: Derivation of a sorption data set for the Gorleben overburden. In *International Conference on Radioactive Waste Disposal*, pages 581–584, 1998.
- /TAC 10/ Tachi, Y., Nakazawa, T., Ochs, M., Yotsuji, K., Suyama, T., Seida, Y., Yamada, N., Yui, M.: Diffusion and sorption of neptunium(V) in compacted montmorillonite: effects of carbonate and salinity. *Radiochimica Acta*, 98(9-11):711–718, ISSN 0033-8230, 2010.
- /TAH 93/ Taha, I. A., Morawetz, H.: Catalysis of Ionic Reactions by Polyelectrolytes .3. Quenching of Uranyl Ion Fluorescence by Iron(II) Ions in Poly(Vinylsulfonic Acid) Solution. *Journal of the American Chemical Society*, 4(93):829–833, ISSN 0002-7863, eISSN 1520-5126, 1993.
- /TER 06/ Tertre, E., Berger, G., Simoni, E., Castet, S., Giffaut, E., Loubet, M., Catalette, H.: Europium retention onto clay minerals from 25 to 150°C: Experimental measurements, spectroscopic features and sorption modelling. *Geochimica et Cosmochimica Acta*, 70(18):4563–4578, ISSN 00167037, September 2006.
- /THO 14/ Thoenen, T., Hummel, W., Berner, U., Curti, E.: *The PSI/Nagra Chemical Thermodynamic Database 12/07*, 2014.
- /TOR 98/ Toride, N., Leij, F. J., Genuchten, M. T. V.: *The CXTFIT code for estimating transport parameter from laboratory or field tracer experiments, Version 2.1*. U.S. Salinity Laboratory, Agricultural Research Service, U.S. Department of Agriculture, Riverside, CA, USA, 1998.

- /TOR 99/ Toride, N., Leij, F., van Genuchten, M.: The CXTFIT Code for Estimating Transport Parameters from Laboratory or Field Tracer Experiments, April 1999.
- /TUR 98/ Turner, D., Pabalan, R., Bertetti, F.: Neptunium(V) sorption on montmorillonite: an experimental and surface complexation modeling study. *Clays and Clay Minerals*, 46(3):256–269, ISSN 0009-8604, 1998.
- /MIL 11/ Vilks, P.: Sorption of Selected Radionuclides on Sedimentary Rocks in Saline Conditions Literature Review. Technical Report Report NWMO TR-2011-12, December 2011.
- /VOE 00/ Voegelin, A., Vulava, V. M., Kuhnen, F., Kretzschmar, R.: Multicomponent transport of major cations predicted from binary adsorption experiments. *Journal of Contaminant Hydrology*, 46(3-4):319–338, ISSN 0169-7722, December 2000.
- /WAL 05/ Walter, M., Arnold, T., Geipel, G., Scheinost, A., Bernhard, G.: An EXAFS and TRLFS investigation on uranium(VI) sorption to pristine and leached albite surfaces. *Journal of Colloid and Interface Science*, 282:293–305, 2005.
- /WAN 01a/ Wang, P., Anderko, A.: Thermodynamic modeling of the adsorption of radionuclides on selected minerals. II. Anions. *Industrial and Engineering Chemistry Research*, 40:4444–4455, 2001.
- /WAN 01b/ Wang, P., Anderko, A., Turner, D. R.: Thermodynamic modeling of the adsorption of radionuclides on selected minerals. I: Cations. *Industrial & Engineering Chemistry Research*, 40:4428–4443, 2001.
- /WAN 04/ Wang, Z., Zachara, J. M., Yantasee, W., Gassman, P. L., Liu, C., Joly, A. G.: Cryogenic Laser Induced Fluorescence Characterization of U(VI) in Hanford Vadose Zone Pore Waters. *Environmental Science & Technology*, 38(21):5591–5597, ISSN 0013-936X, 2004.

- /WAN 05a/ Wang, X.-D., Zhou, S.-M., Wang, H.-L., Fan, D.-F.: Biodegradation of imazapyr in typical soils in Zhejiang Province, China. *Journal of Environmental Sciences*, 17(4):593–597, February 2005.
- /WAN 05b/ Wang, Z., Zachara, J. M., Gassman, P. L., Liu, C., Qafoku, O., Yantasee, W., Catalano, J. G.: Fluorescence spectroscopy of U(VI)-silicates and U(VI)-contaminated Hanford sediment. *Geochimica et Cosmochimica Acta*, 69(6):1391–1403, ISSN 00167037, 2005.
- /WAR 90/ Ward, N. E.: Adsorption of Hexavalent Chromium on Kaolinite and Illite. Master of science with a major in hydrology, 1990.
- /WIL 98/ Wilson, W. E., Moore, J. E.: *Glossary of Hydrology*. American Geological Institute, Alexandria, Virginia, ISBN 0-922152-35-7, 1998.
- /WOL 12/ Wolf, J., Behlau, J., Beuth, T., Bracke, G., Bube, C., Buhmann, D., Dresbach, C., Hammer, J., Keller, S., Kienzler, B., Klinge, H., Krone, J., Lommerzheim, A., Metz, V., Mönig, J., Mrugalla, S., Popp, T., Rübél, A., Weber, J.-R.: FEP-Katalog für die VSG. Dokumentation. Bericht zum Arbeitspaket 7. Vorläufige Sicherheitsanalyse für den Standort Gorleben. Technical Report GRS-283, Köln, June 2012.
- /WOO 90/ Wood, S. A.: The aqueous geochemistry of the rare-earth elements and Yttrium: 1. Review of available low-temperature data for inorganic complexes and the inorganic REE speciation of natural waters. *Chemical Geology*, 82:159–186, ISSN 0009-2541, 1990.
- /WU 09/ Wu, T., Amayri, S., Reich, T.: Neptunium(V) sorption onto gibbsite. *Radiochimica Acta*, 97(2):99–103, ISSN 0033-8230, 2009.
- /ZAV 04/ Zavarin, M., Carle, S. F., Maxwell, R. M.: Upscaling Radionuclide Retardation: Linking the Surface Complexation and Ion Exchange Mechanistic Approach to a Linear K_d Approach. Technical Report LLNL-report UCRL-TR-204713, May 2004.

- /ZIR 03/ Zirngast, M., Zwirner, R., Bornemann, O., Fleig, S., Hoffmann, N., Köthe, A., Krull, P., Weiß, W.: Schichtenfolge und Strukturbau des Deck- und Nebengebirges. Technical Report BGR-Report 9G3411900000, Bundesanstalt für Geowissenschaften und Rohstoffe (BGR), Hannover, 2003.
- /ZOR 00/ Zorn, T.: Untersuchungen der Sorption von Uran (VI) an das Gestein Phyllit zur Bestimmung von Oberflächenkomplexbildungskonstanten. Dissertation, 2000.

Abbreviations

A

A	Cation A
AAS	Atom Adsorption Spectroscopy
Al-OH	Aluminol surface functional group
AT	Aquitard
ATR FT-IR	Attenuated total reflection Fourier transform – infrared spectroscopy

B

B	Cation B
BE	Background electrolyte
BET	Brunauer-Emmett-Teller theory for SSA determination after /BRU 38/
BGR	Federal Institute of Geosciences and Natural Resources
bi	Bidentate
BMWi	Bundesministerium für Wirtschaft und Energie (Federal Ministry for Economic Affairs and Energy)
BSM	Basic Stern model
BTC	Breakthrough curve

C

CCM	Constant capacitance model
CD-MUSIC	Charge distribution multi site complexation (model approach)
cip	Common intersection point
COMPO	SEM back-scattering measurement mode
CXTFIT	Transport code /TOR 99/ which is part of the free ware software package STAN-MOD (STudio of ANalytical MODels, Version 2.0, /SIM 99/)
Cr	crystalline

D, E

DDLm	Diffuse double layer model
DIC	Dissolved inorganic carbon
DNA	Deoxyribonucleic acid
EDH	Extended Debye Hückel
EDLM	Electric double layer model

EDX	Energy Dispersive X-ray spectroscopy
ESTRAL	Joint research project: Realitätsnahe Einbindung von Sorptionsprozessen in Transportprogramme für die Langzeitsicherheitsanalyse (Realistic implementation of sorption processes in transport codes for long-term safety analysis), grant numbers 02E10518, 02E11072A, funded by Federal Ministry of Economics and Energy (BMWi)
EXAFS	Extended X-ray absorption fine structure
F, G	
FeOX	Iron oxides, iron hydroxides
FEPs	Features, events and processes
FES	Frayed edge site
FS	Feldspar Orthoclase (Kali Norflot 600)
G20 EAS extra	Quartz sample used in the present study
gfw	Gram formula weight [g mol ⁻¹]
gof	Goodness of fit
GC	Generalized composite (approach)
gG	Generic gibbsite
GRS gGmbH	Gesellschaft für Anlagen- und Reaktorsicherheit gGmbH
H	
HF	Hydrofluoric acid
HYGOR	Hydrogeological database for Gorleben stite (BGR)
HZDR	Helmholtz-Zentrum Dresden-Rossendorf e.V.
I	
IAP	Ion activity product
iBMB	Institute of Building Material, Concrete Construction and Fire Protection of the Technical University of Braunschweig, Germany
ICP-MS	Inductively coupled plasma mass spectrometry
ICP-OES	Inductively coupled plasma optical emission spectrometry
ICSD	Inorganic Crystal Structure Database
ID	Identification
IEP	Isoelectric point
IR	infrared
IRE	Institute of Resource Ecology (HZDR)

K, L

Kali Norflot 600	Orthoclase sample used in the present study
LAF	Lower aquifer
LLNL	Lawrence Livermore National Laboratory
LSC	Liquid scintillation counting

M

M ³⁺	Trivalent metal cation
Max	Maximum
MCT	Mercury cadmium telluride
Me	Metal ion
Mica WG	Muscovite sample used in the present study
Min	Minimum
mod.	modified
Mono	Monodentate
MT	Mass titration
Musc	Muscovite (mica WG)

N, O

NAGRA	National Cooperative for the Disposal of Radioactive Waste
NB	Nutrient broth
NEA	Nuclear Energy Agency
No.	Number
nonEDLM	Non-electrostatic model
nphc	Net proton and hydroxide consumption
obs	Observations
OD	Optical density
OECD	Organization for Economic Cooperation and Development
ortho	Orthoclase (Kali Norflot 600)

P

p.a.	pro analysi
PARAFAC	Parallel factor analysis
PE	Polypropylene
PFA	Perfluoroalkoxy alkane polymer

PHREEQC	Geochemical speciation code /PAR 13/
pot	Potentiometric acid-base titration
ppzc	Pristine point of zero charge
PS	Planar sites
PSI	Paul Scherrer Institute
PTFE	Polytetrafluoroethylene
PV	Pore volume [V/V0]
pznpc	Point of zero net proton charge
pzc	Point of zero charge
pzse	Point of zero salt effect
Q, R	
Q	Quartz (G20 EAS extra)
R2A	Reasoner's 2A (culture medium)
Ref.	Literature reference
RES ³ T	Rosendorf Expert System for Surface and Sorption Thermodynamics /BRE 03/ (www.hzdr.de/res3t)
RN	Radionuclide
RTM	Reactive transport model (PHREEQC)
S	
s	Solid
S-	Surface
SA	Sensitivity analysis
SCM	Surface complexation model
SCP	Surface complexation parameter, SCPs comprise surface complexation constants, protolysis constants, SSD, SSA, co-/counter-ion associations, capacitances, and cation exchange selectivity coefficients
SCP M	ID for SCPs and SCM of muscovite
SCP O	ID for SCPs and SCM of orthoclase
SCP Q	ID for SCPs and SCM of quartz
SD	Spatial distribution
SEM	Scanning Electron Microscopy
SEM ²	Research project: Rare Earth Elements Metallurgy – Advanced methods for optimized extraction and beneficiation by ion-adsorption clays (project period June 2015 – March 2018)

Si-OH	Silanol surface functional group
SIT	Specific ion interaction theory
SynSed	Synthetic sediment
T	
TDB	Thermodynamic database
TDS	Total dissolved solids
tetra	Tetradentate
THEREDA	Thermodynamic Reference Database /MOO 15/ (www.thereda.de)
TLM	Triple layer model
TPM	Three plane model
tri	Tridentate
TRLFS	Time-resolved laser-induced fluorescence spectroscopy
TSM	Thermodynamic sorption model
U – Z	
UA	Uncertainty analysis
UAF	Upper aquifer
UCODE	Universal parameter estimation code /POE 08/
WD	Working distance
WEIMAR	Joint research project: Weiterentwicklung des Smart-K _d -Konzepts für Langzeitsicherheitsanalysen (Further development of the smart- K _d approach for long-term safety analysis), grant numbers 02E10528, 02E11072B, funded by Federal Ministry of Economics and Energy (BMWi)
WT	UCODE statistical means to describe weighing concept for LSOF optimization
X-	Surface
XRD	X-ray Diffraction
zeta	Zeta-potential measurement

Symbols

A, B, C

c	[-]	Index to identify conditional parameters
C	[mol L ⁻¹]	Concentration
CC	[-]	Correlation coefficient
C_0	[mol L ⁻¹]	Initial element concentration
C_1	[F m ⁻²]	Capacitance of the layer between the 0-plane and 1-plane (BSM)
C_x	[mol L ⁻¹]	Concentration of cation x in solution
C_{Br^-}	[mol L ⁻¹]	Br ⁻ concentration
CEC	[cmol(+) kg ⁻¹]	Cation exchange capacity
CEC_{pot}	[cmol(+) kg ⁻¹]	Potential cation exchange capacity
CEC_{WG}	[cmol(+) kg ⁻¹]	Cation exchange capacity of muscovite (mica WG sample) resulting from Na ⁺ , K ⁺ , Ca ²⁺ , and Mg ²⁺ exchange
CEV	[unit of measure]	Calculated error variance
C_{equil}	[μg L ⁻¹]	Equilibrium concentration
C_{Eu}	[mol L ⁻¹]	Eu concentration, also in [mol kg solid ⁻¹]
C_f	[mg L ⁻¹]	Flux-averaged concentration
C_{H^+, OH^-}	[mol L ⁻¹]	Proton and hydroxide ion concentration in solution
CI	[unit of measure]	Confidence interval
C_{max}	[mol L ⁻¹]	Maximum element concentration, also in [mol kgs ⁻¹]
CN	[-]	Coordination number
C_r	[mol L ⁻¹]	Volume averaged or resident concentration of the liquid phase
C_{sol}	[μg L ⁻¹]	Element concentration in solution
C_{immo}	[μg L ⁻¹]	Sorbed/immobilized element concentration
D		
d	[mm]	Diameter
d_{50}	[μm]	Mass-median diameter of cumulative particle size distribution $d_{50}[\mu\text{m}]$ 50 % quantile of cumulative particle size distribution

D	[cm ² h ⁻¹]	Dispersion coefficient
D	[-]	Debye Hückel term
E – J		
ϵ	[kg mol ⁻¹]	Specific ion interaction coefficient
γ	[-]	Molar activity coefficient
H ⁺	[mol L ⁻¹]	Proton(s)
H ₃ O ⁺	[mol L ⁻¹]	Hydronium ion (aq)
I_S	[mol L ⁻¹]	Ionic strength
K		
K_d	[L kg ⁻¹]	Linear distribution coefficient, also in [m ³ kg ⁻¹]
$\Delta \log K_d$	[L kg ⁻¹]	Error of K_d model predictions in comparison to experimental K_d based on /DAV 05a/
K^{int}	[unit of measure]	Intrinsic mass law constant
K_{sp}	[unit of measure]	Solubility constant
K_w	[unit of measure]	Dissociation constant of water at 298.15 K
$\log K$	[unit of measure]	Surface complexation constant / formation constant
$\log K_c$	[unit of measure]	Conditional selectivity coefficient
$\log K_c Na/H$	[unit of measure]	Conditional cation exchange selectivity coefficient of H ⁺ , index cation Na ⁺
$\log K_c Na/K$	[unit of measure]	Conditional cation exchange selectivity coefficient of K ⁺ , index cation Na ⁺
$\log K_c Na/Na$	[unit of measure]	Conditional cation exchange selectivity coefficient of Na ⁺ , index cation Na ⁺
$\log K_c Na/Eu$	[unit of measure]	Conditional cation exchange selectivity coefficient of Eu ³⁺ , index cation Na ⁺
$\log K_{prot}$	[unit of measure]	General notion for protolysis reactions regardless of the electrostatic model approach and/or considered site
$\log K_{ClO_4^-}$	[unit of measure]	Coion association coefficient for negatively charged mineral surfaces, here: perchlorate coion
$\log K_{Eu}$	[unit of measure]	General notion for intrinsic Eu surface complexation constants without identification of

		specific surface complex, e. g. monodenate, bi, tridentate, etc. – index Eu is independent of surface complex
$\log K_{Na+}$	[unit of measure]	Counterion association coefficient for negatively charged mineral surfaces, here: sodium counterion

L-N

L	[m]	Length
L_{cell}	[m]	Cell length
λ	[m]	Dispersivity
LOQ	[mol L ⁻¹]	Limit of quantification
$LSOF$	[unit of measure]	Least squares objective function
M	[g mol ⁻¹]	Molar mass
M	[g]	Solid mass
ME	[unit of measure]	Mean error
M/V	[g L ⁻¹]	Solid-liquid ratio
n	[-]	Number
N_A	[mol ⁻¹]	Avogadro constant (6.022140857 · 10 ²³ mol ⁻¹)
N_f	[-]	Nernstian slope
N_H	[-]	Average number of protons bound to DIC at given pH
$N_{H,0}$	[-]	Average number of protons bound to DIC at initial pH
N_{OH}	[-]	Average number of hydroxyl groups bound to Al-species at given pH
$N_{OH,0}$	[-]	Average number of hydroxyl groups bound to Al-species at initial pH
NP	[-]	Number of estimated parameters

P

p_0	[Pa]	Saturation vapour pressure
p	[Pa]	Partial pressure
PSD	[µm]	Particle size distribution
Pe	[-]	Péclet number
Pe_{grid}	[-]	Grid Péclet number

Δ_{pH}	[-]	Correction value of pH measurements in saline solutions /HAG 14/
pH_c	[-]	pH values that were corrected for electrolyte influences after /HAG 14/
psd	[-]	Parameter standard deviation
PV	[V/V ₀]	Pore volume: Amount of background electrolyte normalized to the pore space of the respective column ($PV = V / V_0$ with V [m ³] volume of background electrolyte, V_0 [m ³] pore space of each mineral-filled column)

Q, R

q	[cm h ⁻¹]	Darcy velocity
R	[J K ⁻¹ mol ⁻¹]	Universal gas constant (8.3144598 J K ⁻¹ mol ⁻¹)
R^2	[-]	Coefficient of determination
R_t	[-]	Retardation factor
ρ	[g cm ⁻³]	Specific mineral density
ρ	[bar]	Partial pressure at standard state
ρ_b	[g cm ⁻³]	Bulk density
RSD	[%]	Relative standard deviation
ΔRH	[J mol ⁻¹]	Reaction enthalpie

S

σ	[C m ⁻²]	Surface charge density
$\sigma_{0,1,d}$	[C m ⁻²]	Surface charge density at the 0-plane, 1-plane, d-plane
σ_o	[C m ⁻²]	Permanent structural surface charge density
SE	[unit of measure]	Standard error
SI	[-]	Saturation index ($\log_{10}(IAP/\log K)$)
$S - OH_2^x$	[-]	Protonated surface functional group, x = respective charge (x = +1 silanol sites, x = +0.5 aluminol sites)
$S - OH$	[-]	Neutral surface functional group

$S - O^x$	[-]	Deprotonated surface functional group, x - respective charge (x = -1 silanol sites, x = -0.5 aluminol sites)
sol	[-]	Index for species in solution
SSA	$[m^2 g^{-1}]$	Specific surface area
SSA_{BET}	$[m^2 g^{-1}]$	Specific surface area after /BRU 38/
SSD	$[sites nm^{-2}]$	Surface site density
T		
T	[K]	Absolute temperature
t	[h]	Time
θ	[-]	Porosity
V		
V	$[m^3]$	Volume
v	$[cm h^{-1}]$	Pore water velocity, water flow velocity
V_0	$[cm^3]$	Total pore space of a mineral-filled column
V_{tot}	$[cm^3]$	Empty column volume: 167.7 cm^3
W – Z		
x	$[mol l^{-1}]$	Correction term for proton and hydroxide concentration
z	[-]	Charge/valence

List of Figures

Fig. 2.1	Schematic picture of the different permafrost and talik types (after /MRU 11/, modified from /GAS 00/ and /KAR 79/)	7
Fig. 2.2	Calculated permafrost depth depending on the surface temperature for the past 50,000 a, modified from /DEL 98/	8
Fig. 2.3	Global sea level record of the past 500,000 a modified from /ROH 98/	10
Fig. 2.4	Schematic cross section of the hydrogeological system at the reference site Gorleben (modified from /KLI 02a/)	13
Fig. 2.5	Geometry of the groundwater flow and transport model, vertical exaggeration: factor 10	13
Fig. 2.6	Development of permafrost thickness and groundwater flow velocity (lateral inflow) for an assumed climatic cycle of 240,000 a (after /NOS 12b/)	16
Fig. 3.1	Aquifer subdivision in the overburden of Gorleben salt dome after /KLI 07/	18
Fig. 3.2	2D cross section for the new model geometry with a subdivision of the lower aquifer into two different hydrogeological units	18
Fig. 3.3	Al concentrations: Field data and data calculated with WEIMAR_PIT.dat and WEIMAR_EDH.dat, respectively, in equilibrium with generic gibbsite as function of pH value	25
Fig. 3.4	Al concentration in logarithmic scale calculated with WEIMAR_PIT.dat in equilibrium with gibbsite and measured Na-concentrations of the corresponding Gorleben field data as a function of pH value (left) and Al concentration as a function of Na concentration (right)	25
Fig. 3.5	Number of Al-bound hydroxyl ions as function of pH, calculated by PHREEQC (left) and fitted by a sigmoid function (right)	28
Fig. 3.6	Number of carbonate-bound protons as function of pH, calculated by PHREEQC and fitted by a step function	32
Fig. 5.1	Results of Fe acid leaching and extraction experiments using the quartz minerals G20 EAS extra and G20 EA	41
Fig. 5.2	Results of Al acid leaching and extraction experiments using the quartz minerals G20 EAS extra and G20 EA	41

Fig. 5.3	Analysis of quartz for amorphous SiO ₂	42
Fig. 5.4	Al released from quartz, orthoclase and muscovite equilibrated with 0.01 mol L ⁻¹ NaClO ₄ solution.....	43
Fig. 5.5	Experimental mass (A) and electrolyte (B) titration data of quartz after 24 h, 2 d, and 7 d.....	44
Fig. 5.6	Continuous potentiometric acid-base titration of quartz (solid symbols) in comparison to titration data of a silica sol at different electrolyte concentrations published by /BOL 57/ (open characters)	46
Fig. 5.7	EDX analyses (area scan) of orthoclase, PSF 30 μm - 400 μm.....	47
Fig. 5.8	XRD analysis of orthoclase, PSF 63 μm - 400 μm.....	48
Fig. 5.9	Dissolution of main elements and uranium from orthoclase obtained in batch leaching experiments (shown as red triangles) and in flow-through leaching experiments (shown as black squares).....	49
Fig. 5.10	Mass (A) and electrolyte (B) titration measurements of orthoclase after 5 h, 24 h, and 7 d.....	51
Fig. 5.11	Continuous potentiometric acid-base titration measurements of orthoclase	52
Fig. 5.12	SEM analysis of preconditioned (right) and pristine (left) muscovite, particle size fraction 20 – 400 μm.....	54
Fig. 5.13	Dissolution of main elements and uranium from muscovite obtained in batch leaching experiments (shown as red triangles) and in flow-through leaching experiments (shown as black squares).....	58
Fig. 5.14	Ni release from quartz, orthoclase and muscovite equilibrated with 0.01 mol L ⁻¹ NaClO ₄	60
Fig. 5.15	Ca released from orthoclase (A) and muscovite (B), equilibrated with 0.01 mol L ⁻¹ NaClO ₄	61
Fig. 5.16	Experimental mass (A) and electrolyte (B) titration results of muscovite after 5 h, 24 h, and 7 d.....	62
Fig. 6.1	Linear fitting of the logK values for the formation reaction of the EuF ²⁺ complex as a function of ionic strength	67
Fig. 7.1	Sorption kinetics of U(VI) in 0.01 mol L ⁻¹ NaClO ₄ onto muscovite	77
Fig. 7.2	Sorption of 10 ⁻⁶ mol L ⁻¹ U(VI) in 0.01 mol L ⁻¹ NaClO ₄ onto muscovite.....	77
Fig. 7.3	Sorption of 10 ⁻⁵ mol L ⁻¹ U(VI) in 0.01 mol L ⁻¹ NaClO ₄ onto muscovite.....	78

Fig. 7.4	Sorption kinetics of U(VI) in 0.01 mol L ⁻¹ NaClO ₄ onto orthoclase	79
Fig. 7.5	Sorption of 10 ⁻⁶ mol L ⁻¹ U(VI) in 0.01 mol L ⁻¹ NaClO ₄ onto orthoclase	79
Fig. 7.6	Sorption of 10 ⁻⁵ mol L ⁻¹ U(VI) in 0.01 mol L ⁻¹ NaClO ₄ onto orthoclase	80
Fig. 7.7	Sorption of 10 ⁻⁶ mol L ⁻¹ U(VI) in 1 mol L ⁻¹ NaClO ₄ onto muscovite.....	81
Fig. 7.8	Sorption of 10 ⁻⁶ mol L ⁻¹ U(VI) in 1 mol L ⁻¹ NaClO ₄ onto orthoclase	81
Fig. 7.9	Sorption of 10 ⁻⁶ mol L ⁻¹ U(VI) onto muscovite with 1.5·10 ⁻³ mol L ⁻¹ Ca as competing cation.....	82
Fig. 7.10	Sorption of 10 ⁻⁶ mol L ⁻¹ U(VI) onto orthoclase with 1.5·10 ⁻³ mol L ⁻¹ Ca as competing cation.....	83
Fig. 7.11	Sorption of 10 ⁻⁶ mol L ⁻¹ Np(V) onto orthoclase at varying M/V	84
Fig. 7.12	Sorption of 10 ⁻⁶ mol L ⁻¹ Np(V) onto muscovite at varying M/V.....	84
Fig. 7.13	pH-Eh diagram of 10 ⁻⁶ mol L ⁻¹ Np in 0.01 mol L ⁻¹ NaClO ₄ , under am- bient atmosphere. The grey square represents the area of interest for the performed experiments	86
Fig. 7.14	Sorption of 10 ⁻⁶ mol L ⁻¹ Np(V) under ambient atmosphere onto ortho- clase in 0.01 mol L ⁻¹ and 1 mol L ⁻¹ NaClO ₄	87
Fig. 7.15	Sorption of 10 ⁻⁶ mol L ⁻¹ Np(V) under ambient atmosphere onto mus- covite in 0.01 mol L ⁻¹ and 1 mol L ⁻¹ NaClO ₄	87
Fig. 7.16	Sorption onto orthoclase at 10 ⁻⁶ mol L ⁻¹ Nd(III) (left) and 10 ⁻⁵ mol L ⁻¹ Nd(III) (right) at M/V of 1/20 g mL ⁻¹ and 1/80 g mL ⁻¹	89
Fig. 7.17	Sorption onto muscovite at 10 ⁻⁶ mol L ⁻¹ Nd(III) (left) and 10 ⁻⁵ mol L ⁻¹ Nd(III) (right) at M/V of 1/20 g mL ⁻¹ and 1/80 g mL ⁻¹	89
Fig. 7.18	Sorption onto orthoclase (left) and muscovite (right) at two different ionic strengths, M/V 1/20 g mL ⁻¹ and 10 ⁻⁵ mol L ⁻¹ Nd(III)	90
Fig. 7.19	Results of Ca batch sorption experiments with orthoclase	91
Fig. 7.20	Results of Ca batch sorption experiments with muscovite.....	92
Fig. 7.21	Results of Eu batch experiments with quartz in 10 mM NaClO ₄ back- ground electrolyte	93
Fig. 7.22	Results of Eu batch experiments with orthoclase (10 mM NaClO ₄ background electrolyte).....	94

Fig. 7.23	Results of Eu batch experiments with orthoclase (blue), quartz (grey), and muscovite (green) (10 mM NaClO ₄ background electrolyte).....	95
Fig. 7.24	Results of Ni batch sorption experiments with 200 g L ⁻¹ quartz in 0.01 and 0.2 mol L ⁻¹ NaClO ₄ solutions	96
Fig. 7.25	Results of Ni batch sorption experiments with 50 g L ⁻¹ quartz in 0.01 and 0.2 mol L ⁻¹ NaClO ₄ solutions	97
Fig. 7.26	Comparison of Ni batch sorption results with quartz in 0.066 mol L ⁻¹ Na ₂ SO ₄ and 0.2 mol L ⁻¹ NaClO ₄ solutions	98
Fig. 7.27	Results of batch sorption experiments with Ni and 100 g L ⁻¹ orthoclase in 0.01 and 0.2 mol L ⁻¹ NaClO ₄ solution	99
Fig. 7.28	Results of Ni batch sorption experiments with 25 g L ⁻¹ orthoclase in 0.01 and 0.2 mol L ⁻¹ NaClO ₄ solutions	99
Fig. 7.29	Comparison of Ni batch sorption results with orthoclase in 0.066 mol L ⁻¹ Na ₂ SO ₄ and 0.2 mol L ⁻¹ NaClO ₄ solutions.....	100
Fig. 7.30	Results of Ni batch sorption experiments with 50 g L ⁻¹ muscovite in 0.01 and 0.1 mol L ⁻¹ NaClO ₄ solutions	101
Fig. 7.31	Results of Ni batch sorption experiments with 12.5 g L ⁻¹ muscovite in 0.01 and 0.1 mol L ⁻¹ NaClO ₄ solutions	101
Fig. 7.32	Comparison of Ni batch sorption results with orthoclase in 0.033 mol L ⁻¹ Na ₂ SO ₄ and 0.1 mol L ⁻¹ NaClO ₄ solutions.....	102
Fig. 7.33	Results of Al batch sorption experiments with 200 g L ⁻¹ MERCK quartz in 0.01 mol L ⁻¹ NaClO ₄ solutions	103
Fig. 7.34	Results of Cs batch sorption experiments with 50 g L ⁻¹ muscovite in 0.01 mol L ⁻¹ NaClO ₄	104
Fig. 7.35	Results of Cs batch sorption experiments with 50 g L ⁻¹ muscovite in 0.01 mol L ⁻¹ NaClO ₄	105
Fig. 8.1	Luminescence spectrum of aqueous U(VI) deconvoluted by PARAFAC analysis. ([U(VI)] = 10 ⁻⁵ mol L ⁻¹ , [Ca ²⁺] = 1.5 · 10 ⁻³ mol L ⁻¹ , [NaClO ₄] = 0.01 mol L ⁻¹ , T = 274 K).....	109
Fig. 8.2	Normalized intensity profiles of 10 ⁻⁵ mol L ⁻¹ U(VI) sorbed onto orthoclase in 0.01 mol L ⁻¹ NaClO ₄ in the absence of Ca ²⁺ referred to the amount of sorbed uranium (a) and in presence of 1.5 · 10 ⁻³ mol L ⁻¹ Ca ²⁺ (b). The capital letters in the plots indicate the species	

	determined with PARAFAC and the grey region represents the area with most differences	110
Fig. 8.3	<i>In situ</i> time-resolved ATR FT-IR spectra of U(VI) sorption on orthoclase (A) and muscovite (B) (20 $\mu\text{mol L}^{-1}$ U(VI), 0.01 mol L^{-1} NaCl, pH 6, air, 0.08 mg cm^{-2}). The spectra of the conditioning, sorption, and flushing processes are recorded at different times as given (from bottom to top). For more details, the reader is referred to the text. Indicated values are in cm^{-1}	114
Fig. 8.4	Comparison of ATR FT-IR spectra of U(VI) aqueous solution (20 $\mu\text{mol L}^{-1}$ U(VI), 0.1 mol L^{-1} NaCl, pH 5.6) and U(VI) surface complex on orthoclase and muscovite (20 $\mu\text{mol L}^{-1}$ U(VI), 0.01 mol L^{-1} NaCl, pH 6).....	114
Fig. 9.1	Experimental set-up of column experiments	119
Fig. 9.2	Eu transport through quartz (Q-iv, blue), orthoclase (FS-iii, green), and muscovite (mica-iii, red) with 50 mmol L^{-1} Na_2SO_4 background electrolyte, $\text{pH}_{\text{ini}} = 5.5$	122
Fig. 9.3	Eu transport through a synthetic sediment (SynSed, green) and natural sediment (NatSed, blue) with 10 mmol L^{-1} NaClO_4 , $\text{pH} \approx 3.5$	123
Fig. 9.4	Schematic overview of the developed method: Steps to be followed to identify U(VI) surface complexes via CLSM and TRLFS measurements.....	124
Fig. 9.5	U(VI) spatial distribution on quartz (G20 EAS extra), shaded rectangles indicate sample position for CLSM, TRLFS analysis	125
Fig. 9.6	TRLFS spectra of the top side of quartz column samples B, E, F (Fig. 9.5), measurements carried out in the center of each sample, inlet of the column sample F, outlet sample A. Geochemical conditions of column experiments: $\text{pH}_{\text{ini}} 4.9$, 10 mmol NaClO_4 , ambient conditions	125
Fig. 9.7	Br ⁻ tracer breakthrough curves of quartz columns: pH 5.0, 0.01 mol L^{-1} NaClO_4	127
Fig. 9.8	Br ⁻ tracer breakthrough curves of quartz columns: pH 7.3, 0.01 mol L^{-1} NaClO_4	128
Fig. 9.9	Ni breakthrough curve of quartz columns: pH 5.0, 0.01 mol L^{-1} NaClO_4	129
Fig. 9.10	Ni spatial distribution of quartz columns: pH 7.3, 0.01 mol L^{-1} NaClO_4 ...	129
Fig. 9.11	Br ⁻ tracer breakthrough curves of orthoclase columns: pH 5.8, 0.01 mol L^{-1} NaClO_4	130

Fig. 9.12	Br tracer breakthrough curves of orthoclase columns: pH 7.4, 0.01 mol L ⁻¹ NaClO ₄	131
Fig. 9.13	Ni spatial distribution of orthoclase columns: pH 5.8, 0.01 mol L ⁻¹ NaClO ₄	132
Fig. 9.14	Ni spatial distribution of orthoclase columns: pH 7.4, 0.01 mol L ⁻¹ NaClO ₄	132
Fig. 10.1	Flowchart of PHREEQC application in combination with UCODE for parameter estimation (after /BRI 18/ and /NOS 12b/).	136
Fig. 10.2	Fitted surface speciation for the U(VI) sorption onto orthoclase (10 ⁻⁵ mol L ⁻¹ and 10 ⁻⁶ mol L ⁻¹ U(VI), M/V 1/20 and 1/80 g mL ⁻¹)	139
Fig. 10.3	Fitted surface speciation for the U(VI) sorption onto muscovite (10 ⁻⁵ mol L ⁻¹ and 10 ⁻⁶ mol L ⁻¹ U(VI), M/V 1/20 and 1/80 g mL ⁻¹).....	140
Fig. 10.4	Aquatic and surface speciation of 10 ⁻⁶ mol L ⁻¹ U(VI) in 0.01 mol L ⁻¹ NaClO ₄ , under ambient air onto orthoclase (left) and muscovite (right)	140
Fig. 10.5	Prediction of sorption of U(VI) in presence of Ca ²⁺ for orthoclase (left) and muscovite (right) using the log <i>K</i> values obtained in this work.....	141
Fig. 10.6	Fitted surface speciation with ≡XO-NpO ₂ surface complex for Np(V) onto orthoclase (left) and muscovite (right) (10 ⁻⁶ mol L ⁻¹ Np(V), 0.01 mol L ⁻¹ NaClO ₄ , M/V 1/20).....	142
Fig. 10.7	Fitted surface speciation for the Nd(III) sorption onto orthoclase (10 ⁻⁵ mol L ⁻¹ and 10 ⁻⁶ mol L ⁻¹ Nd(III), M/V 1/20 and 1/80 g mL ⁻¹)	143
Fig. 10.8	Fitted surface speciation for the Nd(III) sorption onto muscovite (10 ⁻⁵ mol L ⁻¹ and 10 ⁻⁶ mol L ⁻¹ Nd(III), M/V 1/20 and 1/80 g mL ⁻¹). Legend given in Fig. 10.7	143
Fig. 10.9	1-pK DDLM results: Model was calibrated with experimental quartz batch data [%Eu(III) immobilized] (10 mM NaClO ₄ background electrolyte, laboratory conditions: pCO ₂ 10 ^{-3.4} bar, T = 296.0 K ± 2 K)	146
Fig. 10.10	Results of Eu batch experiments with quartz and fitted noEDLM results (10 mM NaClO ₄ background electrolyte, laboratory conditions: pCO ₂ 10 ^{-3.4} bar, T = 296.0 K ± 2 K).....	148
Fig. 10.11	Experimental batch data of quartz with Eu and 1-pK BSM results using mono-, bi-, and mono- combined with bidentate surface complexes (10 mM NaClO ₄ background electrolyte, laboratory conditions: pCO ₂ 10 ^{-3.4} bar, T = 296.0 K ± 2 K)	149

Fig. 10.12	Calibrated surface complexation models for orthoclase and Cs.....	152
Fig. 11.1	A: Experimental Br BTCs (black, grey symbols) of Q-iii and Q-vi. B: Experimental and fitted BTCs of Q-iii (red line = fit with $q = 84 \text{ cm d}^{-1}$) and Q-vi (blue line = fit with $q = 32 \text{ cm d}^{-1}$)	165
Fig. 11.2	Reactive transport simulations of Eu through quartz columns, $\text{pH}_{\text{ini}} \approx 5.5$ (Q-ii - Q-v)	171
Fig. 12.1	Flowchart of the coupled codes PHREEQC, UCODE and SIMLAB for calculating smart K_d -values and their sensitivity and uncertainty analysis.	179
Fig. 12.2	Histogram of 10,000 pre-calculated smart K_d -values for U(VI) sorption in the upper aquifer based on Random sampling (K_d in $\text{m}^3 \text{ kg}^{-1}$, logarithmic scale).....	188
Fig. 12.3	Smart K_d -values for UAF compared to respective published values	189
Fig. 12.4	Smart K_d -values for AT compared to respective published values	189
Fig. 12.5	3-D subsets from 5-D smart K_d -matrix for U(VI) sorption in the UAF as a function of pH, [DIC], and [Ca] (K_d in $\text{m}^3 \text{ kg}^{-1}$)	190
Fig. 13.1	Comparison of the procedures in PHAST and d ^{3f++} The superscript “T” stands for temporal.....	195
Fig. 13.2	Schema of the workflow in d ^{3f++} and the generation of the K_d -matrix	197
Fig. 13.3	Model domain with boundary conditions	197
Fig. 13.4	Spatial distribution of the tracer after 100,000 s simulation time.....	199
Fig. 13.5	Spatial distributions of DIC, Ca, IS, and pH after 100,000 s	200
Fig. 13.6	Spatial distribution of the radionuclides after 500,000 s model time	201
Fig. 13.7	Spatial distribution of the radionuclides after 500,000 s model time calculated with the new smart K_d -matrix.....	202
Fig. 13.8	K_d -values for Uranium as functions of pH, DIC, and Ca	203
Fig. A. 1	Mn concentration in groundwater samples from sedimentary overburden at Gorleben site derived from field database (top) and /BAU 89/ (bottom)	277
Fig. A. 2	Concentration of sulfate in groundwater samples from sedimentary overburden at Gorleben site	278

Fig. A. 3	Stability ranges and solubility of anhydrite and gypsum (top) and Ca concentration calculated in equilibrium with anhydrite (bottom) as function of ionic strength.....	279
Fig. A. 4	Saturation indices calculated with respect to the sulphate containing minerals gypsum, celestine and Na ₂ SO ₄ as function of the Cl concentration in water. /BAU 89/.....	280
Fig. A. 5	Concentration of phosphate in groundwater samples from sedimentary overburden at Gorleben site.....	281
Fig. A. 6	Ionic strength dependence of calcite solubility in NaCl solution at pH 8.36 calculated with Extended Debye-Hückel and Pitzer approach, respectively.....	282
Fig. A. 7	pH-dependence of calcite solubility in 5 M NaCl solution calculated with Extended Debye-Hückel and Pitzer approach, respectively.....	283
Fig. A. 8	Ionic strength dependence of gibbsite (amorphous) solubility in NaCl solution calculated with Extended Debye-Hückel and Pitzer approach, respectively.....	284
Fig. A. 9	pH-dependence of calcite (amorphous) solubility in NaCl solution calculated with Extended Debye-Hückel and Pitzer approach, respectively.....	284
Fig. A. 10	Concentration of Ca, DIC and Al in NaCl solution in equilibrium with gibbsite (amorphous) and calcite as a function of ionic strength calculated with Extended Debye-Hückel and Pitzer approach, respectively.....	285
Fig. A. 11	Concentration of Ca, DIC and Al in NaCl solution in equilibrium with gibbsite (amorphous) and calcite as a function of pH calculated with Extended Debye-Hückel and Pitzer approach, respectively.....	286
Fig. A. 12	Eh values in groundwater samples from sedimentary overburden at Gorleben site.....	287
Fig. A. 13	Eh value vs. concentration of O ₂ in groundwater samples from sedimentary overburden at Gorleben site.....	288
Fig. A. 14	Fe concentration in groundwater samples from sedimentary overburden at Gorleben site.....	288
Fig. A. 15	SO ₄ concentration in groundwater samples from sedimentary overburden at Gorleben site.....	289
Fig. A. 16	Ratio of Ca vs. Na concentration in groundwater samples from sedimentary overburden at Gorleben site.....	289

Fig. A. 17	Cl/Na-ratio as function of Cl concentration of Gorleben water, /BAU 89/	290
Fig. A. 18	Dependence of the Ca content from the Cl concentration in the Gorleben waters, /BAU 89/	291
Fig. A. 19	Experimental setup of flow-through leaching experiments	298
Fig. A. 20	Blank drift occurring during analysis of Si with ICP-MS	301
Fig. A. 21	Zeta-potential measurements of muscovite and orthoclase. Data from /RIC 15/	304
Fig. A. 22	Shift of relative muscovite titration data (relative meas. this study) in relation to pH_{IEP} with $\Delta\sigma = 0.005 \text{ C m}^{-2}$	308
Fig. A. 23	ΔpH vs. NaClO_4 concentration [mol kgw^{-1}] after /SCH 67/	309
Fig. A. 24	Comparison between batch experimental data of Eu, Am, Cm on quartz from literature and data collected in this study (after /FRI 14/),.....	312
Fig. A. 25	Al speciation diagram in $0.01 \text{ mol L}^{-1} \text{ NaClO}_4$	313
Fig. A. 26	Ni speciation diagrams with and without SO_4^{2-} in solution	313
Fig. A. 27	Batch experiments: sorption kinetics of Ni with quartz	316
Fig. A. 28	Batch experiments: sorption kinetics of Ni with orthoclase	316
Fig. A. 29	Batch experiments: sorption kinetics of Ni with muscovite	317
Fig. A. 30	Kinetics of Ca sorption with orthoclase and muscovite.....	317
Fig. A. 31	Aquatic U(VI) speciation of orthoclase supernatant with $10^{-5} \text{ mol L}^{-1}$ U(VI) in $0.01 \text{ mol L}^{-1} \text{ NaClO}_4$ without addition of Ca^{2+} (top) and with $1.5 \times 10^{-3} \text{ mol L}^{-1} \text{ Ca}^{2+}$ (bottom) under ambient atmosphere and at room temperature	318
Fig. A. 32	Aquatic speciation of $10^{-5} \text{ mol L}^{-1} \text{ Np(V)}$ in $0.01 \text{ mol L}^{-1} \text{ NaClO}_4$ under ambient atmosphere and at room temperature	319
Fig. A. 33	Aquatic speciation of $10^{-5} \text{ mol L}^{-1} \text{ Nd(III)}$ in $0.01 \text{ mol L}^{-1} \text{ NaClO}_4$ under ambient atmosphere and at room temperature.	320
Fig. A. 34	Saturation indices of Nd(III) phases calculated with PhreeqC ($10^{-5} \text{ mol L}^{-1} \text{ Nd(III)}$, $0.01 \text{ mol L}^{-1} \text{ NaClO}_4$, ambient atmosphere, at room temperature). SI values > 0 indicate the formation of a precipitate.....	320
Fig. A. 35	Image of microscopy of orthoclase with live-dead stain.....	324
Fig. A. 36	Image of microscopy of muscovite with live-dead stain.....	324

Fig. A. 37	Image of microscopy of quartz with live-dead stain	325
Fig. A. 38	Bacterial distribution on muscovite, orthoclase and quartz.....	326
Fig. A. 39	U(VI) sorption onto quartz, orthoclase, and muscovite (0.5 g mineral in 10 mL 0.01 mol L ⁻¹ NaClO ₄) according to the influence of microor- ganisms at pH 7 and an initial U(VI) concentration of 10 ⁻⁶ mol L ⁻¹	328
Fig. A. 40	Quartz III: Development of pH, U(VI) and Br concentrations	333
Fig. A. 41	Quartz IV: Development of pH, U(VI) and Br concentrations.....	335
Fig. A. 42	TRLFS spectrum of the top of the second quartz V slice (11-10 cm), inlet of the column 0 cm, outlet 12.25 cm, pH _{ini} 4.9	336

List of Tables

Tab. 2.1	Assumed climate evolution during the future 240,000 years /NOS 12b/.....	14
Tab. 3.1	Solubility products and stability constants of relevant complexes for Al.....	26
Tab. 3.2	Fitted set of parameters for the sigmoid function.....	28
Tab. 3.3	Solubility products and stability constants of relevant complexes for Ca.....	31
Tab. 3.4	Fitted set of parameters for the step function.....	32
Tab. 4.1	Chemical data for the different groundwater types of the Gorleben overburden (concentrations in mol L ⁻¹).....	36
Tab. 4.2	Mean mineral composition of the four sedimentary units UAF, AT and LAF1/LAF2 of the Gorleben overburden (in wt%).....	37
Tab. 5.1	Summary of multipoint BET analyses of muscovite (mica), orthoclase (ortho), and quartz.....	56
Tab. 5.2	Cation exchange capacities (CECs [cmol(+) kg ⁻¹]) of muscovite and illite.....	57
Tab. 6.1	Summary of the aqueous inorganic Eu complexation data records.....	66
Tab. 6.2	Solubility constants for orthoclase and muscovite.....	71
Tab. 6.3	Number of available SCM data in RES ³ T (Query date: 02/2018).....	72
Tab. 7.1	Geochemical boundary conditions of batch sorption experiments with Eu, Ni, Cs, Ca, Al and quartz, orthoclase, muscovite.....	74
Tab. 8.1	Luminescence decay lifetimes τ and main emission bands (peak maxima positions, rounded to full nm) for the species obtained from a series of TRLFS data of U(VI) sorbed on orthoclase compared to literature values.....	112
Tab. 9.1	Summary of quartz (Q), orthoclase (FS), muscovite (mica), synthetic sediment (SynSed), and natural sediment (NatSed) column experiments including geochemical conditions.....	120
Tab. 9.2	Overview of experimental details concerning quartz columns with Ni.....	128
Tab. 9.3	Overview of experimental details concerning orthoclase columns with Ni.....	133

Tab. 10.1	Summary of final SCPs and goodness-of-fit values of calibrated SCMs for orthoclase and Cs	151
Tab. 10.2	Calculated number of sites at the used parameters of the surface complexation modeling (* U(VI) / Nd(III))	153
Tab. 10.3	Experimentally determined surface complexation parameters for U(VI), Np(V), and Nd(III) sorption onto orthoclase and muscovite. This work* refers to peer-reviewed values published in /RIC 16/.....	153
Tab. 11.1	Summary of transport parameters of quartz (Q-i – Q-vi), orthoclase (O-i – O-iii), muscovite (mica-i – mica-iv), and synthetic sediment (SynSed-i, SynSed-ii) column experiments	167
Tab. 11.2	Summary of K_d -values calculated from experimental data and reactive transport simulations of quartz column experiments (Q-i - Q-v)	168
Tab. 12.1	Recommended minimum and maximum values of environmental parameters (concentrations in mol L ⁻¹).....	182
Tab. 12.2	Comparison of K_d -values (in m ³ kg ⁻¹) for temperature 14 °C and 5 °C...	183
Tab. 12.3	Recommended surface complexation parameters for site-specific minerals at the Gorleben overburden.....	185
Tab. 12.4	Mean smart K_d -values for UAF, and AT (LAF under discussion) and their minimum, maximum and standard deviation 2σ (K_d in m ³ kg ⁻¹ , logarithmic).....	187
Tab. 12.5	Statistical characteristics of the distribution of the log K_d -values for U(VI) in the upper aquifer (K_d in m ³ kg ⁻¹ , logarithmic)	187
Tab. 12.6	Sensitivity indices first order for log K_d -values for radionuclides in UAF and AT calculated with eFAST (25 000 parameter samples)	191
Tab. 12.7	Sensitivity indices for log K_d -values for U(VI) in UAF calculated with eFAST (25 000 parameter samples) using SimLab2.....	191
Tab. 13.1	Surface composition for UAF used for smart K_d -calculations	196
Tab. 13.2	Hydraulic parameters.....	198
Tab. 13.3	Composition of Solution 0 and 1	198
Tab. 13.4	Values in equilibrium for PHAST and d ³ f ⁺⁺ after 500.000 s	201

Tab. A. 1	Features, Events and Processes (FEPs) for Northern Germany from /MRU 11/ and /WOL 12/, including probability of occurrence, impact on the overburden and adjoining rock, and relevance for this project.....	266
Tab. A. 2	Comparison of supplier's data and HF digestion analysis of this study of muscovite ^[1] , quartz ^[2] , and orthoclase ^[3]	297
Tab. A. 3	Measured elemental concentrations and detection limits ($\mu\text{mol L}^{-1}$) after the leaching experiments of orthoclase and muscovite (by ICP-MS if not specified otherwise)	299
Tab. A. 4	Definitions of reference pH values and experimental measurements (Exp. Method) used in this study.	305
Tab. A. 5	Scattered light intensity (SLI in kilo counts per second / kcps) of Nd(III) as a function of pH at two different concentrations in $0.01 \text{ mol L}^{-1} \text{ NaClO}_4$	321
Tab. A. 6	Optical Density (OD_{600}) of quartz, orthoclase and muscovite samples in a NB and R2A culture medium as well as in $0.01 \text{ mol L}^{-1} \text{ NaClO}_4$	323
Tab. A. 7	Summary of all parameters for batch experiments referring to an influence of microorganisms	327
Tab. A. 8	Composition /KLI 02b/, /NOS 12a/ and specification of chemicals used for the artificial groundwater.....	332

A Digital Appendix

This appendix summarizes additional data and detailed information on environmental parameters, site characterization, mineral properties, data post processing, equipment, techniques, experimental set-up, and models. Furthermore, a pseudocode for the description of the concept for geochemical changes is provided. Relevant supplementary information, detailed documentations, and figures on methods, calculations, and experimental background are provided. The appendix complements the report GRS-500 of the WEIMAR research project (BMW FKZ 02 E 11072).

A.1 Evaluation of possible Features, Events and Processes (FEPs) and climate scenarios to be considered for Northern Germany

Based on the geoscientific site characterization and the long-term prognosis for the development of the site for the future one million years /MRU 11/ and the FEP catalogue /WOL 12/, a comprehensive table of all FEP and their evaluation is given in the following. Tab. A. 1 gives the name of the FEP, probability of occurrence, impact on the overburden and adjoining rock, and relevance for this project. Based on additional considerations for the application in this project (column "remarks"), the decision for the implementation in the model is given in the last column.

Tab. A. 1 Features, Events and Processes (FEPs) for Northern Germany from /MRU 11/ and /WOL 12/, including probability of occurrence, impact on the overburden and adjoining rock, and relevance for this project

Black: Less probable or probable FEPs with no impact on overburden and adjoining rock and thus no relevance for this project; Orange: Probable FEPs with an impact on overburden and adjoining rock, that have no relevance for this project or cannot be regarded with the concept or model; Green: Probable FEPs with an impact on overburden and adjoining rock and relevance for this project (bold: regarded in this project, not bold: not regarded in this project)

Name	Probability	Impact on overburden and adjoining rock	Relevance for this project	Remarks	Implementation in modeling approach
Early failure of a shaft/drift seal	Less probable	No	No	Only relevant for shafts and seals	No
Piping in sealing elements	Less probable	No	No	Only relevant for shafts and seals	No
Cryogenic fractures	Probable	No	No	By definition only occurring in the host rock formation	No
Inventory	Probable	No	No	By definition only to be regarded in the near field	No
Waste matrix	Probable	No	No	By definition only to be regarded in the near field	No
Spent fuel containers	Probable	No	No	By definition only to be regarded in the near field	No
Other final storage containers	Probable	No	No	By definition only to be regarded in the near field	No
Failure of spent fuel containers	Probable	No	No	By definition only to be regarded in the near field	No
Failure of other final storage containers	Probable	No	No	By definition only to be regarded in the near field	No

Name	Probability	Impact on overburden and adjoining rock	Relevance for this project	Remarks	Implementation in modeling approach
Backfill	Probable	No	No	By definition only to be regarded in the near field	No
Sealing material	Probable	No	No	By definition only to be regarded in the near field	No
Shaft seals	Probable	No	No	By definition only to be regarded in the near field	No
Drift seals	Probable	No	No	By definition only to be regarded in the near field	No
Alteration of drift and shaft seals	Probable	No	No	By definition only to be regarded in the near field	No
Other sealing constructions	Probable	No	No	By definition only to be regarded in the near field	No
Technical equipment and their characteristics	Probable	No	No	By definition only to be regarded in the near field	No
Borehole casings	Probable	No	No	By definition only to be regarded in the near field	No
Failure of borehole casings	Probable	No	No	By definition only to be regarded in the near field	No
Convergence	Probable	No	No	By definition only to be regarded in the near field	No
Fluid pressure	Probable	No	No	By definition only to be regarded in the near field	No
Crushed salt compaction	Probable	No	No	By definition only to be regarded in the near field	No
Drift in position of shaft seals	Probable	No	No	By definition only to be regarded in the near field	No
Failure of a sealing plug	Probable	No	No	By definition only to be regarded in the near field	No
Solutions in mine openings	Probable	No	No	By definition only to be regarded in the near field	No

Name	Probability	Impact on overburden and adjoining rock	Relevance for this project	Remarks	Implementation in modeling approach
Channeling in crushed salt	Probable	No	No	By definition only to be regarded in the near field	No
Solution intrusion into mine openings	Probable	No	No	By definition only to be regarded in the near field	No
Flow processes in mine openings	Probable	No	No	By definition only to be regarded in the near field	No
Swelling of bentonite	Probable	No	No	By definition only to be regarded in the near field	No
Geochemical environment in mine openings	Probable	No	No	By definition only to be regarded in the near field	No
Metal corrosion	Probable	No	No	By definition only to be regarded in the near field	No
Corrosion of fuel matrix	Probable	No	No	By definition only to be regarded in the near field	No
Corrosion of glass	Probable	No	No	By definition only to be regarded in the near field	No
Corrosion of materials with cement or soret phases	Probable	No	No	By definition only to be regarded in the near field	No
Material embrittlement by water uptake	Probable	No	No	By definition only to be regarded in the near field	No
Behavior of graphite containing materials and uranium tails (?)	Probable	No	No	By definition only to be regarded in the near field	No
Decomposition of organic matter	Probable	No	No	By definition only to be regarded in the near field	No

Name	Probability	Impact on overburden and adjoining rock	Relevance for this project	Remarks	Implementation in modeling approach
Microbial processes in mine openings and in the salt dome	Probable	No	No	By definition only to be regarded in the near field	No
Thermal expansion or contraction	Probable	No	No	By definition only to be regarded in the near field	No
Evaporation of water	Probable	No	No	By definition only to be regarded in the near field	No
Gas production	Probable	No	No	By definition only to be regarded in the near field	No
Gas volume in mine openings	Probable	No	No	By definition only to be regarded in the near field	No
Gas intrusion pressure	Probable	No	No	By definition only to be regarded in the near field	No
Radiation induced activation	Probable	No	No	By definition only to be regarded in the near field	No
Material embrittlement by radiation	Probable	No	No	By definition only to be regarded in the near field	No
Decomposition of organic matter (?)	Probable	No	No	By definition only to be regarded in the near field	No
Radiolysis	Probable	No	No	By definition only to be regarded in the near field	No
Excavation damaged zone	Probable	No	No	By definition only to be regarded in the near field	No
Host rock	Probable	No	No	By definition only to be regarded in the near field	No
Störungen und Klüfte im Wirtsgestein	Probable	No	No	By definition only to be regarded in the near field	No

Name	Probability	Impact on overburden and adjoining rock	Relevance for this project	Remarks	Implementation in modeling approach
Stress change and stress redistribution	Probable	No	No	Only relevant for near field and host rock	No
Hydrocarbon deposits in host rock	Probable	No	No	By definition only to be regarded in the near field	No
Thermomigration	Probable	No	No	By definition only to be regarded in the near field	No
Thermal dissociation of carnallite	Probable	No	No	By definition only to be regarded in the near field	No
Thermochemical sulfate reduction	Probable	No	No	By definition only to be regarded in the near field	No
Pressure driven infiltration of fluids into the salt rock	Probable	No	No	By definition only to be regarded in the near field	No
Radionuclide mobilization	Probable	No	No	By definition only to be regarded in the near field	No
Uplift or lowering of waste containers	Probable	No	No	By definition only to be regarded in the near field	No
Neotectonic processes	Probable	Low	No	No extreme stress in the underground, no changes in stress field to be expected	No
Lowering of the earth's crust	Probable	Low	No	No major reconfiguration/impacts solely by lowering of the earth's crust	No
Crustal deformation	Probable	Low	No	No proof of crustal deformation at the site up to now	No

Name	Probability	Impact on overburden and adjoining rock	Relevance for this project	Remarks	Implementation in modeling approach
Diapirism	Probable	Low	No	Trend of reducing diapirism, with a new glaciation a short-term rise of the ascent rate during a time of < 10.000 a is possible; Changes in model geometry cannot be regarded in d ^{3f++}	No
Subrosion	Probable	Yes	No (Only groundwater salinity, no geometry changes)	Subrosion of water-soluble evaporites through a contact with groundwater; Changes in model geometry cannot be regarded in d ^{3f++} , the geochemical process of salt dissolution and it's impact on the groundwater flow is already included in d ^{3f++}	No
Earthquakes	Probable	Yes	No	Low probability of earthquakes, low impact on groundwater flow	No
Erosion	Probable	Yes	No	Morphologic alteration, reduction of the sedimentary overburden, formation of channels; Changes in model geometry cannot be regarded in d ^{3f++}	No
Sedimentation	Probable	Yes	No	Equalization of the relief, new lithological composition of overburden and adjoining rock; Changes in model geometry cannot be regarded in d ^{3f++}	No
Complete cover by an ice sheet	Probable	Yes	No	Changes in model geometry cannot be regarded in d ^{3f++}	No
Development of glacial melt water channels	Probable	Yes	No	Changes in model geometry cannot be regarded in d ^{3f++}	No

Name	Probability	Impact on overburden and adjoining rock	Relevance for this project	Remarks	Implementation in modeling approach
Pathways in exploration boreholes	Probable	Yes	No	Radionuclide transport through boreholes is negligible in comparison with transport through highly permeable aquifers	No
Gas migration in overburden and adjoining rock	Probable	Yes	No	Two-phase flow cannot be described with the current code	No
Heat induced uplift or lowering of overburden	Probable	Yes	No	Changes in model geometry cannot be regarded in d ^{3f++}	No
Topography	Probable	Yes	No	Changes in model geometry cannot be regarded in d ^{3f++}	No
Radionuclide transport in the gas phase	Probable	Yes	No	Cannot be described with the current code	No
Colloids	Probable	Yes	No	Cannot be described with the current concept	No
Diagenesis	Probable	Yes	Yes	Insignificant diagenetic alteration of the uppermost Quarternary sediments, alteration of the porosity and permeability of the Quarternary sediments; Changes in model geometry cannot be regarded in d ^{3f++}	No
Global climatic change	Probable	Yes	Yes	Compilation of several FEP, will be explained in detail for the specific FEP (e. g. FEP Permafrost, near-by inland ice-sheet, complete ice cover)	Yes
Transgression/Regression	Probable	Yes	Yes	Sea level rise and decrease, groundwater flow and geochemical environment	Yes

Name	Probability	Impact on overburden and adjoining rock	Relevance for this project	Remarks	Implementation in modeling approach
Permafrost	Probable	Yes	Yes	Impact on groundwater flow and geochemical environment, described in project ESTRAL	Yes
Near-by inland ice sheet	Probable	Yes	Yes	Only possible to be regarded with a regional model	No
Porosity	Probable	Yes	Yes	Alteration of groundwater flow and sorption, e. g. during permafrost conditions or diagenesis	No
Permeability	Probable	Yes	Yes	Alteration of groundwater flow, e. g. during permafrost conditions or diagenesis	No
Dissolution and precipitation	Probable	Yes	Yes	Already part of the current concept	Yes
Overburden and adjoining rock	Probable	Yes	Yes	Compilation of several FEP, will be explained in detail for the specific FEP (e. g. FEP Subrosion and FEP Hydrochemical environment in overburden and adjoining rock)	Yes
Groundwater flow in overburden and adjoining rock	Probable	Yes	Yes	Compilation of several FEP, will be explained in detail for the specific FEP	Yes
Hydrochemical environment in overburden and adjoining rock	Probable	Yes	Yes	Compilation of several FEP, will be explained in detail for the specific FEP	Yes
Microbial processes in overburden and adjoining rock	Probable	Yes	Yes	Nitrate and sulfate reduction	Yes
Surface water bodies	Probable	Yes	Yes	Altered position of surface water bodies, leading to altered boundary conditions	Yes

Name	Probability	Impact on overburden and adjoining rock	Relevance for this project	Remarks	Implementation in modeling approach
Radioactive decay	Probable	Yes	Yes	Already part of the current concept	Yes
Sorption and Desorption	Probable	Yes	Yes	Already part of the current concept	Yes
Complexation	Probable	Yes	Yes	Already part of the current concept	Yes
Radionuclide transport in the fluid phase	Probable	Yes	Yes	Already part of the current concept	Yes
Advection	Probable	Yes	Yes	Already part of the current concept	Yes
Mechanical dispersion	Probable	Yes	Yes	Already part of the current concept	Yes
Diffusion	Probable	Yes	Yes	Already part of the current concept	Yes
Matrix diffusion	Probable	Yes	Yes	Already part of the current concept	Yes
Heat production	Probable	Yes	Yes	Influence on groundwater flow and geochemical environment	No
Faults and fractures in overburden and adjoining rock	Probable	Yes	Yes	Altered groundwater flow; very speculative; changes in model geometry cannot be regarded in d3f++	No
Other transport processes	Probable	Yes	Yes	Some are regarded in current concept/model	No

A.2 Supplementary information on environmental parameters

The geochemical concept has been further developed. One important aspect was the evaluation of the environmental parameters, namely the components competing cations and ligands as well as redox and ion exchange processes and high ionic strength conditions. It was checked, in which way these components, processes and effects might influence the chemical conditions. Therefore, a detailed analysis of existing geochemical data from groundwater wells measured during the hydrogeological investigation program at Gorleben site, was performed.

A.2.1 Competing cations

In addition to the existing concept the relevance of several cations has been investigated. It was decided to consider Al as an additional environmental parameter and its implementation is described in detail in Section 3.3.2. Mg as a divalent cation is of potential relevance. Analysis of site data shows that precipitations of mineral phases of Mg do not need to be considered. Dolomite $\text{CaMg}(\text{CO}_3)_2$ and magnesite MgCO_3 , which occur in the tertiary and quaternary sediments, do not precipitate under the geochemical conditions prevailing in the three hydrogeological units. Brucite $\text{Mg}(\text{OH})_2$ is rarely found in the overburden of Gorleben salt dome /GRI 82 – 94/ and is also strongly undersaturated according to PHREEQC /PAR 13/ calculations for the typical hydrochemical conditions in these units (saturation index < -6). However, a literature survey showed that SCM data only exist for sorption on the minerals goethite and quartz. Therefore, and due to the fact that the divalent cation Ca is already considered and generally occurs in higher concentrations (a higher competition effect for Ca is expected), Mg is neglected as an additional environmental parameter at the current stage of the project.

The trivalent lanthanides occur only in very low concentrations and will not be considered. The relevance of the trivalent forms of the elements V, Cr, Mn and Co was also checked. Therefore, the existing values of these elements in a comprehensive dataset from the Gorleben overburden were analyzed /KLI 04/. For V no data are available. The concentrations of Cr and Co were determined but with exception of one value all data are below the detection limit. The detection limit for both elements is $5 \mu\text{g L}^{-1}$, i. e. the concentration of both elements is typically lower than $5 \mu\text{g L}^{-1}$. It is not expected that elements in such low concentration ranges will act as competitive cations. Therefore, V,

Cr and Co are excluded from further considerations in the concept. The concentration distribution of Mn vs depth is illustrated in Fig. A. 1. The values scatter in the range from 0.01 to 8 mg L⁻¹ with four exceptional high values between 10 and 16 mg L⁻¹ (not shown) and an average value of 0.88 mg L⁻¹.

Consequently, Mn will be regarded as a potential competing cation with respect to sorption. Mn may occur in nature in the oxidation states +II, +III and +IV. As the redox state in the Gorleben groundwater samples is not well established, the project team decided to focus on +II to reflect the most reducing conditions. Thermodynamic data for complexation and potential relevant solid phases have been compiled consequently. In addition, data for surface complexation models were determined and transferred into the project-specific database WEIMAR_EDH.dat. Speciation calculations will be performed to determine the expected species in the groundwater of the overburden at Gorleben site. Incorporation into the analogue Pitzer-based database WEIMAR_PIT.dat is currently not possible due to the lack of respective reliable thermodynamic data and ion-ion interaction coefficients.

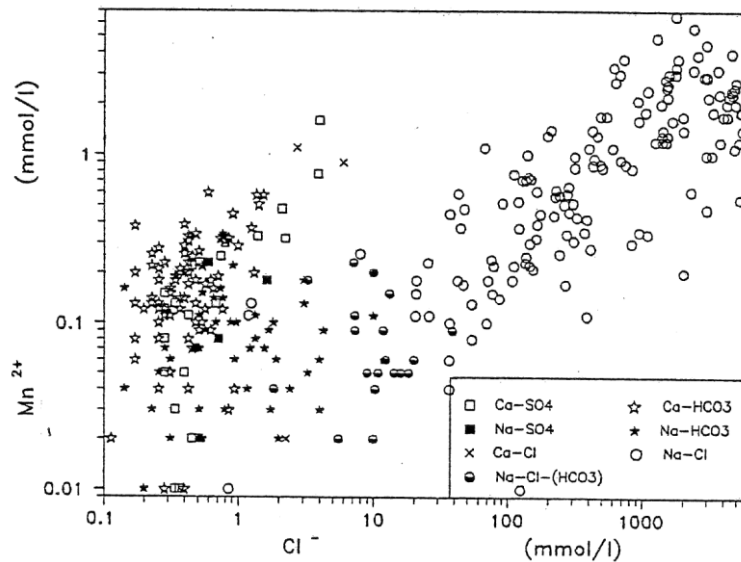
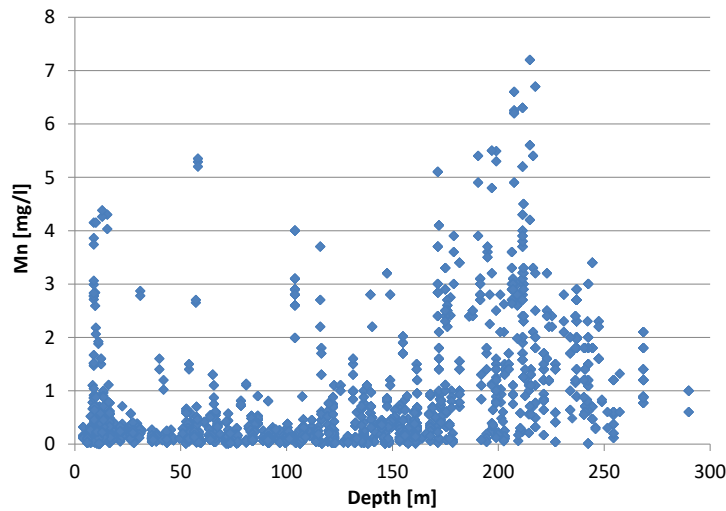


Fig. A. 1 Mn concentration in groundwater samples from sedimentary overburden at Gorleben site derived from field database (top) and /BAU 89/ (bottom)

A.2.2 Ligands

Further, potentially relevant anionic ligands will be regarded. Sulfate occurs in the cap rock as gypsum $\text{Ca}(\text{SO}_4) \cdot 2\text{H}_2\text{O}$ and anhydrite $\text{Ca}(\text{SO}_4)$. But due to its relatively high solubility these minerals are not found in the overlying sediments /GRI 82 - 94/. Other sulfate minerals as baryte BaSO_4 , kieserite $\text{MgSO}_4 \cdot \text{H}_2\text{O}$ und jarosite FeSO_4 are also not of relevance in these systems.

The cap rock (anhydrite) acts as a continuous source for sulfate /KLI 14/. Its concentration then decreases with decreasing depth due to dilution and microbial reduction

processes, particularly in the aquitard and the upper aquifer. The sulfate concentration as a function of depth in groundwater from the Gorleben area is shown in Fig. A. 2.

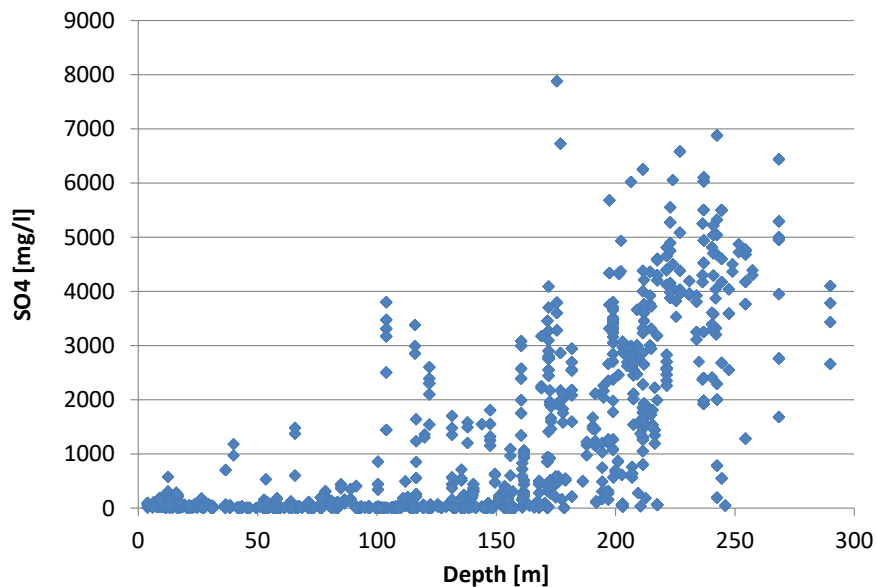


Fig. A. 2 Concentration of sulfate in groundwater samples from sedimentary overburden at Gorleben site

As mentioned the sources for calcium and sulfate are the sulfate-bearing minerals in the cap rock of the salt dome. This is indicated by data from /BAU 89/ compared to the saturation indices of sulfate bearing minerals. Updated thermodynamic calculations based on Pitzer interaction coefficients show that at high ionic strengths above app. 4 mol/l for a halite brine anhydrite is the concentration determining mineral (gypsum for ionic strengths below 4 mol/l), see Fig. A. 3 (top). In the cap rock area saturated salt brines will occur. Saturated NaCl brines are 6.147 molar. The Ca and SO₄ concentration in equilibrium with anhydrite is shown as function of ionic strength in Fig. A. 3 (bottom). Their concentration in saturated NaCl brine amounts to 0.0375 mol/l, which will be used as boundary conditions in the transport calculations for both components.

For the sulfate anion transport without sorption will be implemented in the conceptual model. Sulfate will become an additional environmental parameter E_i in our concept.

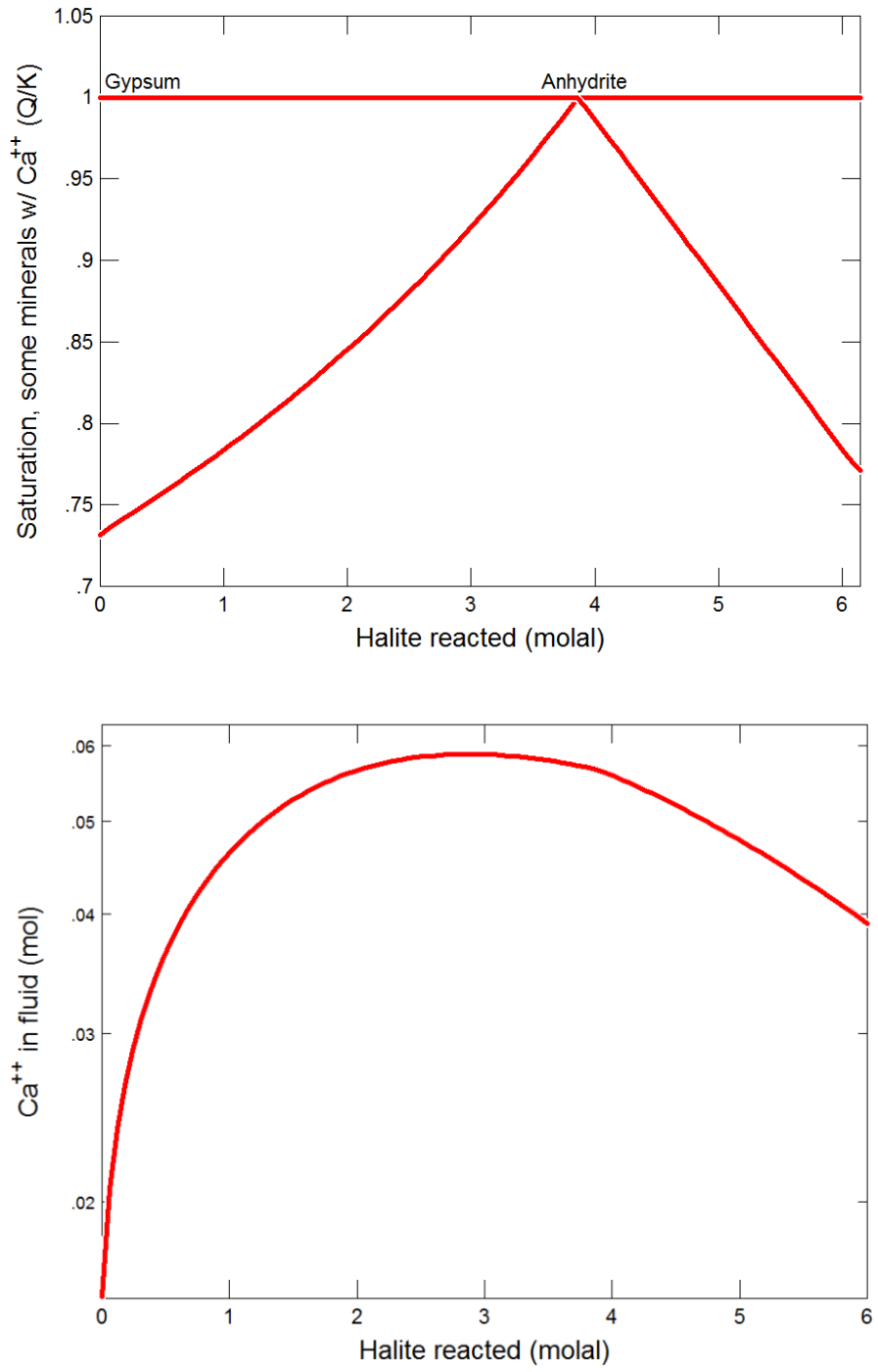


Fig. A. 3 Stability ranges and solubility of anhydrite and gypsum (top) and Ca concentration calculated in equilibrium with anhydrite (bottom) as function of ionic strength

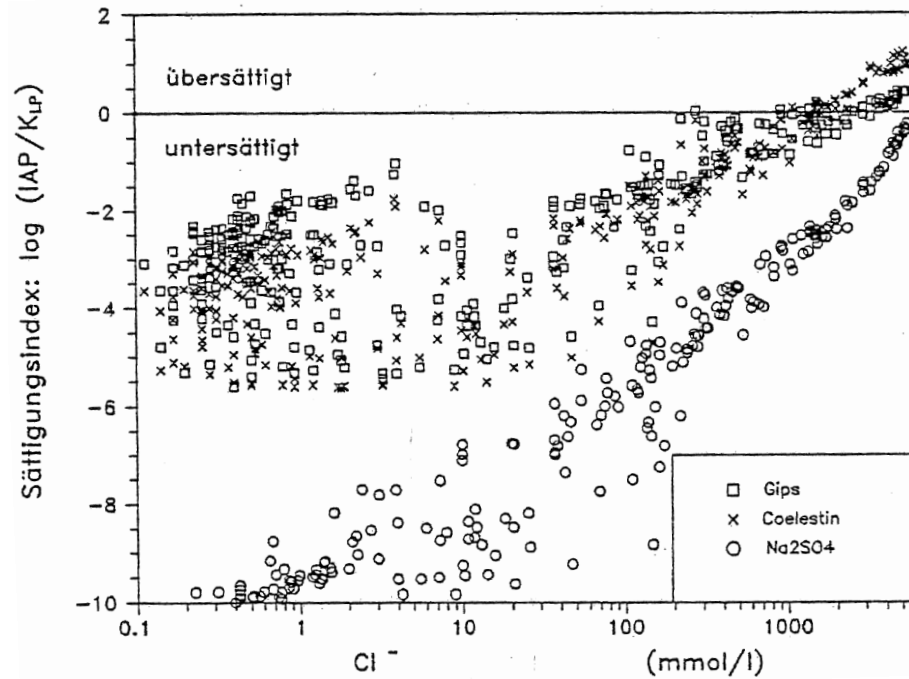


Fig. A. 4 Saturation indices calculated with respect to the sulfate containing minerals gypsum, celestine and Na₂SO₄ as function of the Cl concentration in water. /BAU 89/

Phosphate might be introduced by agricultural activity into the upper horizons. However, there is no indication for that from the groundwater data. Further, the P₂O₅-content in all three hydrogeological units is generally low and apatite Ca₅((F,Cl,OH)|(PO₄)₃) is rarely found /GRI 82 – 94/. Concentration profiles from sedimentary overburden at Gorleben site for PO₄ are illustrated in Fig. A. 5.

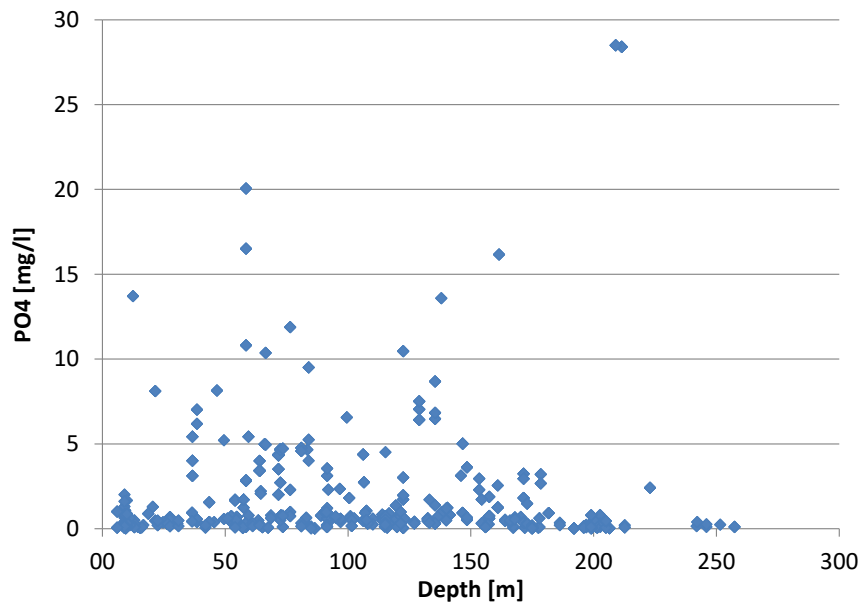


Fig. A. 5 Concentration of phosphate in groundwater samples from sedimentary overburden at Gorleben site

A.2.3 Ionic Strength

Two alternative approaches are available for speciation calculations of radionuclides in high saline solutions. The SIT (Specific Ion Interaction Theory, see /GRE 13/) model is less complex and a database in PHREEQC format is available, mostly building on the respective data collection from the OECD/NEA TDB, see /LEM 13/ for the most recent version. However, the data quality is quite heterogeneous and high effort is necessary for a systematic evaluation of all data needed. Data for the more complex Pitzer model /PIT 91/ can be derived with less effort from the THEREDA project. A limitation here is that not all ion-ion interaction coefficients are available so far. Therefore, it is decided to continue the concept development using the Pitzer model but to keep the SIT model as an alternative.

In a first step the effect of different models for ion-ion interactions for the systems relevant in WEIMAR project need to be checked. Although the Pitzer approach is recommended for activity correction in high mineralized solutions, the extent of the deviations to the extended Debye-Hückel (EDH) model (according to /DAV 62/) should be quantified. Thus, calculations with the PITZER model and the EDH model are applied and the extent of the differences in the results is analyzed. Three different test cases considering solubility calculations for calcite and amorphous gibbsite in dependence of ionic strength and pH-value are considered (see Appendix A.4.5).

All test case calculations demonstrate that the Extended Debye-Hückel approach is not adequate to treat the highly mineralized solutions at least occurring in the lower aquifer of our model area. Highest deviations of several orders of magnitude occur in the treatment of Al. It therefore confirms our approach to apply the Pitzer theory for ionic strength corrections to highly mineralized solutions. Therefore, a database with the available Pitzer interaction coefficients for the systems considered here had to be established.

A.2.4 Test case calculations related to ionic strength

Test case 1: Calcite solubility

In test case 1 the solubility of calcite in a sodium chloride solution is investigated. In the first set of calculations the pH value is kept constant at pH 8.36. The ionic strength dependence is shown in Fig. A. 6. At ionic strengths below 0.5 mol L⁻¹ the curves for Ca and DIC concentration agree well for both approaches, a significant difference can be observed making up more than one order of magnitude for Ca concentration at ionic strength of 5 mol L⁻¹.

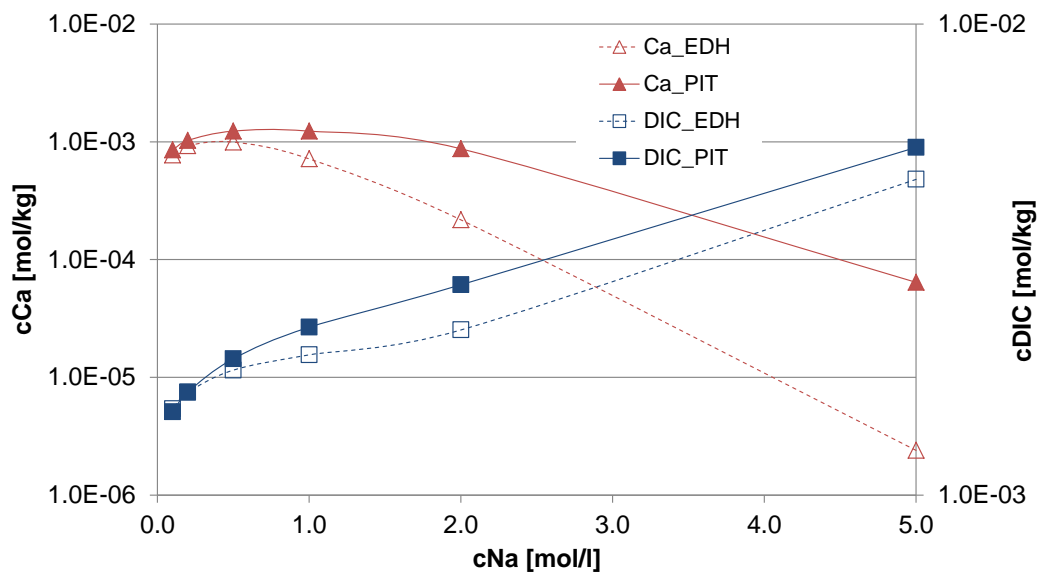


Fig. A. 6 Ionic strength dependence of calcite solubility in NaCl solution at pH 8.36 calculated with Extended Debye-Hückel and Pitzer approach, respectively

In the second set of calculations the ionic strength is kept constant at a value of 5 mol L⁻¹ and the pH is varied in the range between 6 and 8, shown in Fig. A. 7. For the DIC concentration a difference of less than a factor 2 is observed in the pH range 6.7 to 8

increasing up to nearly 2 orders of magnitude at a pH value of 6. For the Ca concentration the difference is more than one order of magnitude over the whole pH range investigated.

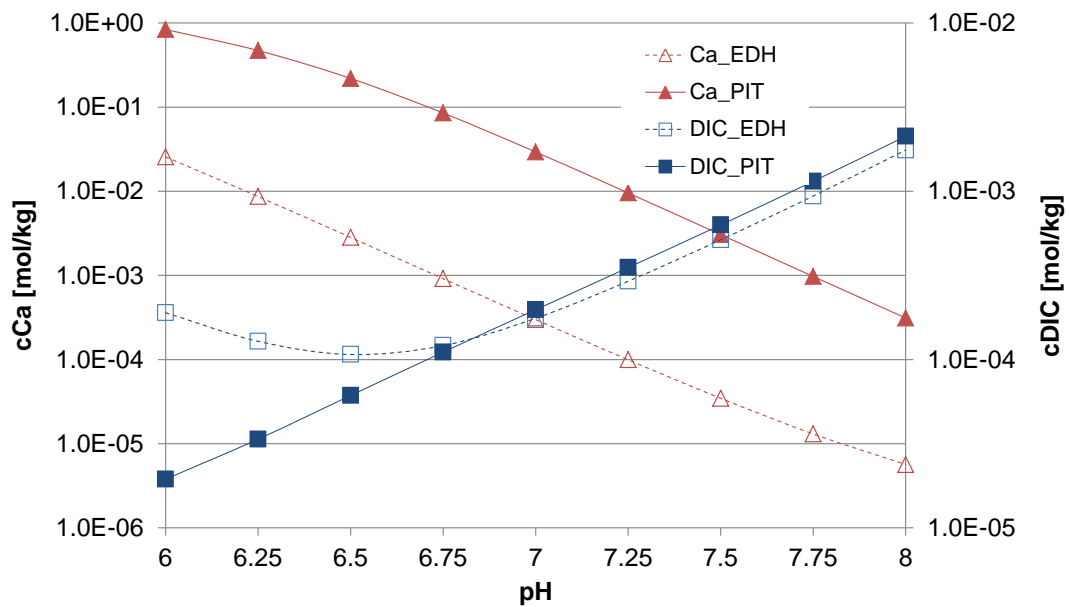


Fig. A. 7 pH-dependence of calcite solubility in 5 M NaCl solution calculated with Extended Debye-Hückel and Pitzer approach, respectively

Test case 2: Solubility of amorphous gibbsite

Similarly, in test case 2 the solubility of amorphous gibbsite in a sodium chloride solution is investigated. In the first set of calculations the pH value is kept constant at pH 6.3. The ionic strength dependence is shown in Fig. A. 8. At ionic strengths below 0.5 mol L⁻¹ the curve for the DIC concentration agrees well for both approaches. At higher ionic strengths differences appear with a maximum of app. a factor of 6 at ionic strength of 3 mol L⁻¹. For the Al concentrations differences are already visible at ionic strength >0.2 increasing to a difference of more than four orders of magnitude at ionic strengths of 5 mol/l.

The pH dependence of the concentration curves is shown in Fig. A. 9 for an ionic strength of 5 mol L⁻¹. The difference for DIC is only a factor of 2 for the whole pH range investigated. For Al the lowest difference is observed at pH 8 with already more than one order of magnitude increasing to a difference of more than five orders of magnitude at pH 6.

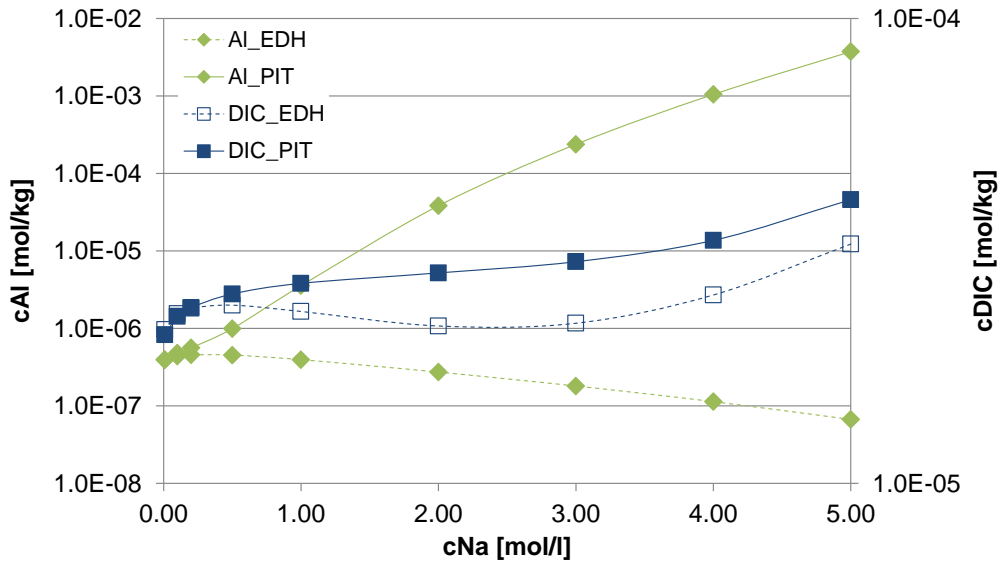


Fig. A. 8 Ionic strength dependence of gibbsite (amorphous) solubility in NaCl solution calculated with Extended Debye-Hückel and Pitzer approach, respectively

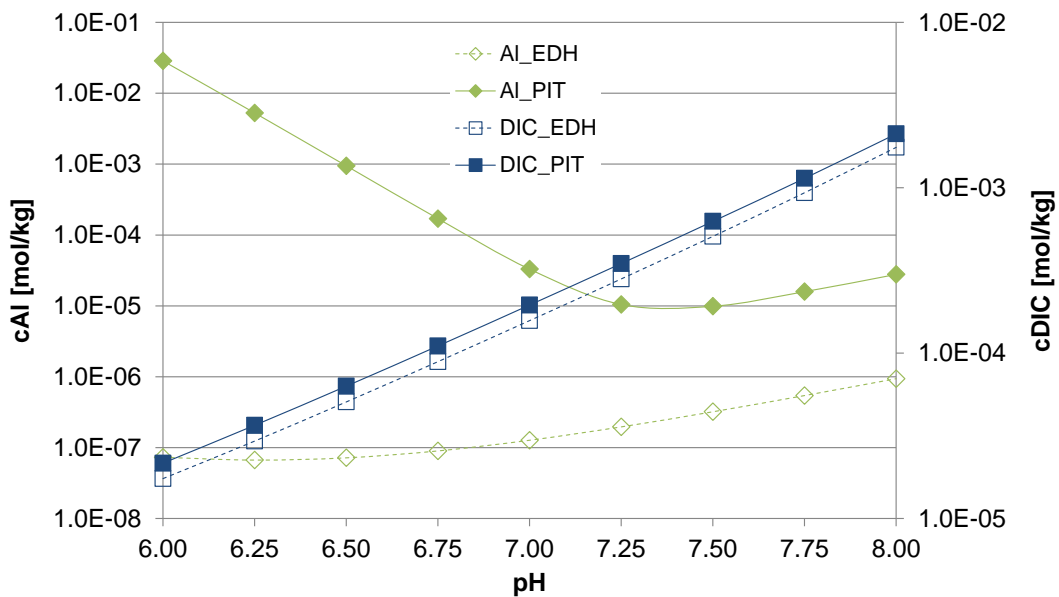


Fig. A. 9 pH-dependence of calcite (amorphous) solubility in NaCl solution calculated with Extended Debye-Hückel and Pitzer approach, respectively

Test case 3: Equilibrium with calcite and amorphous gibbsite

In test case 3 a system in equilibrium with calcite and amorphous gibbsite is considered. Calculations are again performed in dependence of ionic strength and pH value. The ionic strength dependence (at constant pH of 6.5) is shown in Fig. A. 10. The results

somehow reflect the results from test cases 1 and 2, confirming similar concentrations for both approaches at ionic strength below 0.5 for Ca and DIC and below 0.2 for Al. The difference increases to app. 2 orders of magnitude at ionic strength of 5 mol L⁻¹ for all three elements

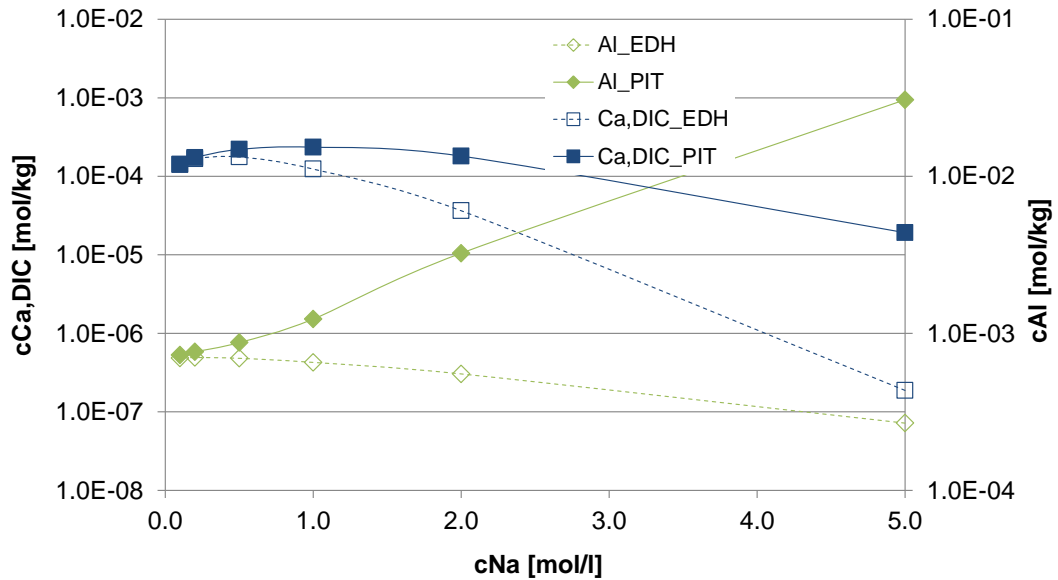


Fig. A. 10 Concentration of Ca, DIC and Al in NaCl solution in equilibrium with gibbsite (amorphous) and calcite as a function of ionic strength calculated with Extended Debye-Hückel and Pitzer approach, respectively

The pH dependence is shown in Fig. A. 11. Again, the characteristics of test case 1 and 2 are visible. The difference of about one order of magnitude in concentration of Ca and DIC for both approaches is nearly independent from pH, whereas differences for Al increase with decreasing p with a maximum at pH 6.

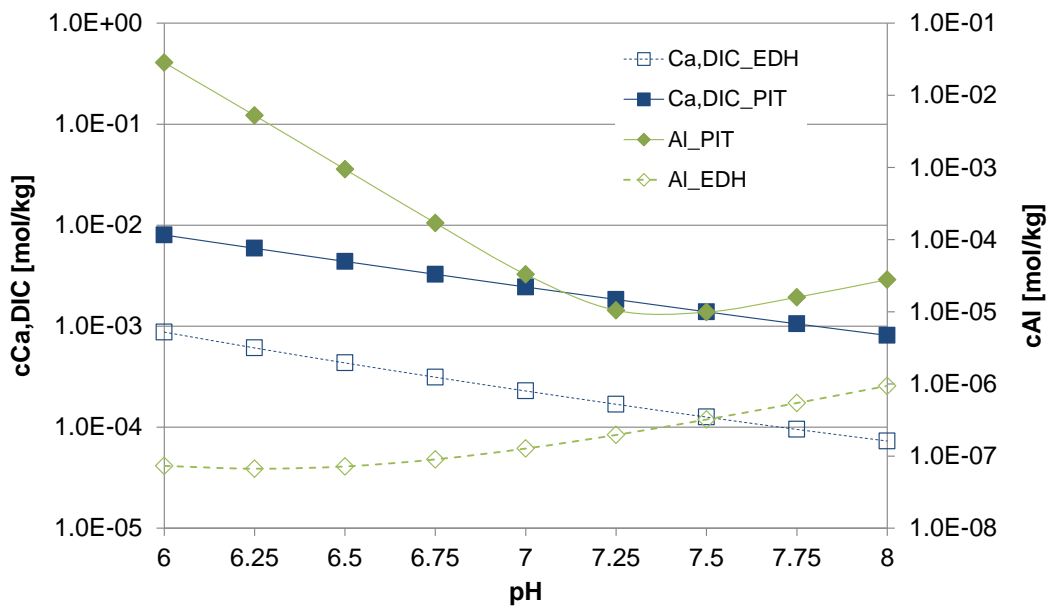


Fig. A. 11 Concentration of Ca, DIC and Al in NaCl solution in equilibrium with gibbsite (amorphous) and calcite as a function of pH calculated with Extended Debye-Hückel and Pitzer approach, respectively

A.2.5 Redox conditions

Relevant redox pairs in such sedimentary systems are amongst others $\text{NO}_2^-/\text{NO}_3^-$, $\text{Fe(II)}/\text{Fe(III)}$ and $\text{S}^{2-}/\text{SO}_4^{2-}$. Investigations in the area of the Elbe wetlands show that a complete degradation of nitrate occurs in the first 2-3 meters below the surface. In lower depths nitrate is not detectable. Therefore, the redox pair $\text{NO}_2^-/\text{NO}_3^-$ is not considered. In many water samples Fe(III) is not detectable. Values for Fe then correspond to the values for total Fe.

Analyses of sulfate concentrations and $\delta^{34}\text{S}$ values show that sulfate reduction in depths below 30 m. By $\delta^{34}\text{S}$ signatures the process can be identified in waters with sulfate concentrations of up to 200 mg/l. Although positive Eh values have been measured at depths below 30 m, H_2S smell indicates occurrence of sulfate reduction. However, analysis of sulfide in groundwater and no information about the existence of sulfide minerals are available. Data of methane analysis are not available; therefore, the redox pair CH_4/CO_2 is not considered.

In discussion with experts from BGR involved in the investigation program of Gorleben site /KLI 14/ a concept for treatment of the redox conditions in the model area was proposed. A surface near oxidizing area of few meters need not to be considered since it

has nearly no relevance for the overall radionuclide transport. A subsequent depth range of few tens of meters, determined by the Fe(II)/Fe(III) equilibrium is likely. A following depth range below 30 m might be determined by the redox pair S^{2-} / SO_4^{2-} due to sulfate reduction.

However, such a profile cannot be supported by any of the measured redox related field data. Depth profiles of parameters connected to the redox conditions are illustrated in this appendix Fig. A. 12 to Fig. A. 15. The Eh values are generally relatively high and do not represent conditions determined by the redox pair S^{2-} / SO_4^{2-} , cf. Fig. A. 12. Further, there is no plausible correlation between the Eh values and the content of O_2 in the groundwater, see Fig. A. 13.

In consequence, the critical evaluation of the redox measurements at Gorleben site in /KLI 94/ is supported by this detailed analysis of the field data. In the most recent discussion with experts from the BGR it was agreed, that these data are not suitable for the development of a simplified conceptual model for redox processes to be implemented in our approach. It is rather necessary to investigate a site with more sound and available redox data.

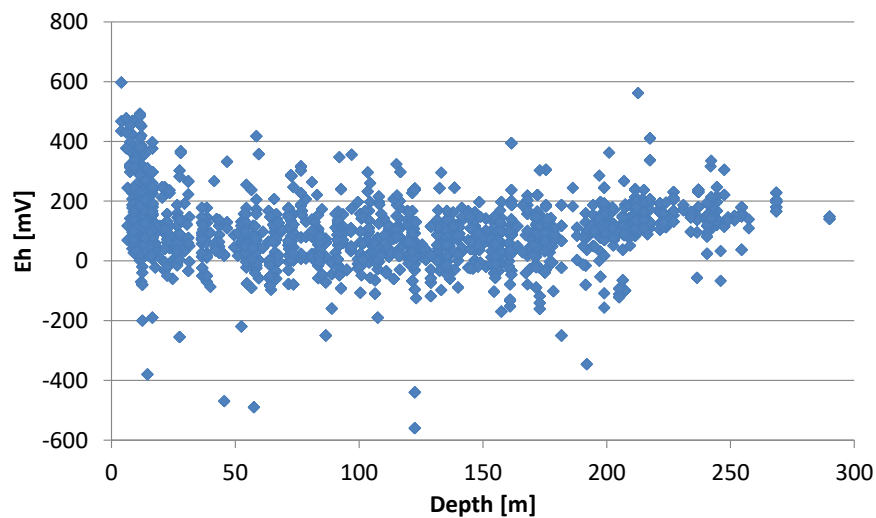


Fig. A. 12 Eh values in groundwater samples from sedimentary overburden at Gorleben site

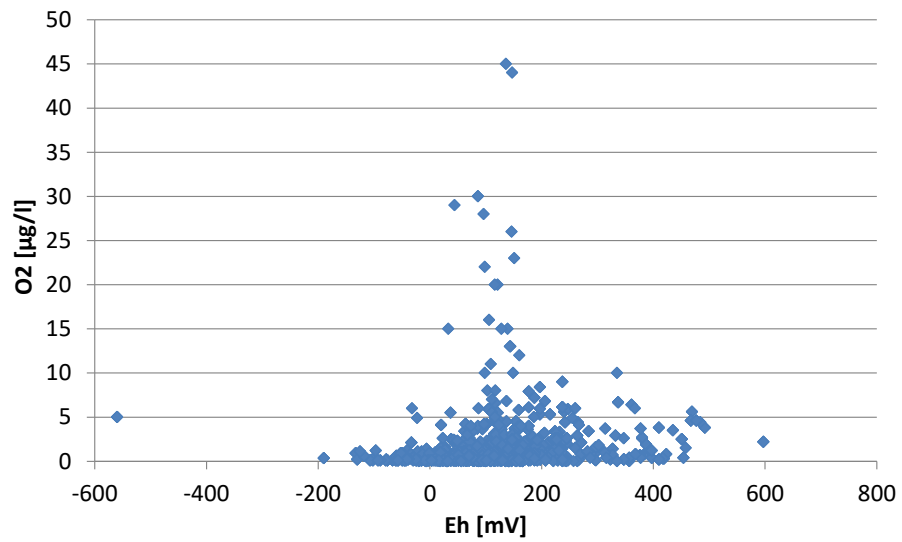


Fig. A. 13 Eh value vs. concentration of O₂ in groundwater samples from sedimentary overburden at Gorleben site

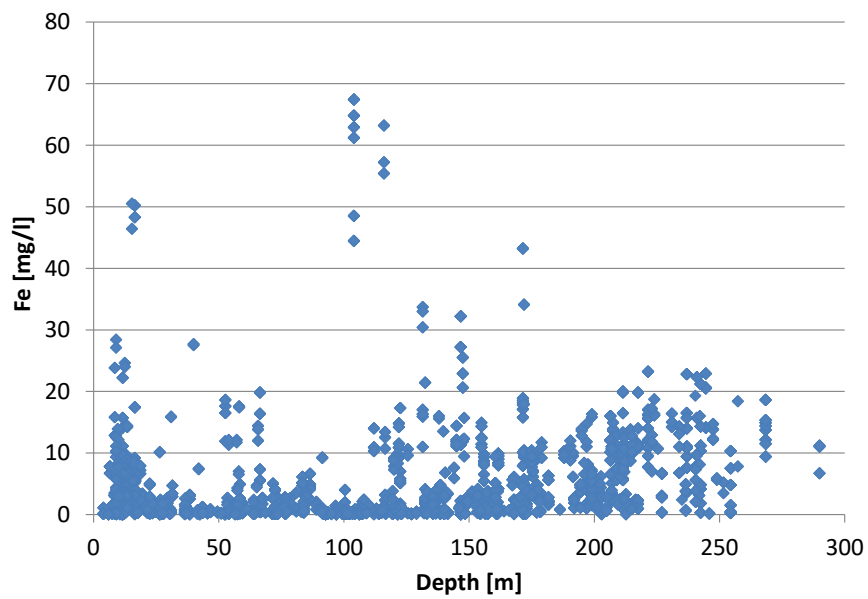


Fig. A. 14 Fe concentration in groundwater samples from sedimentary overburden at Gorleben site

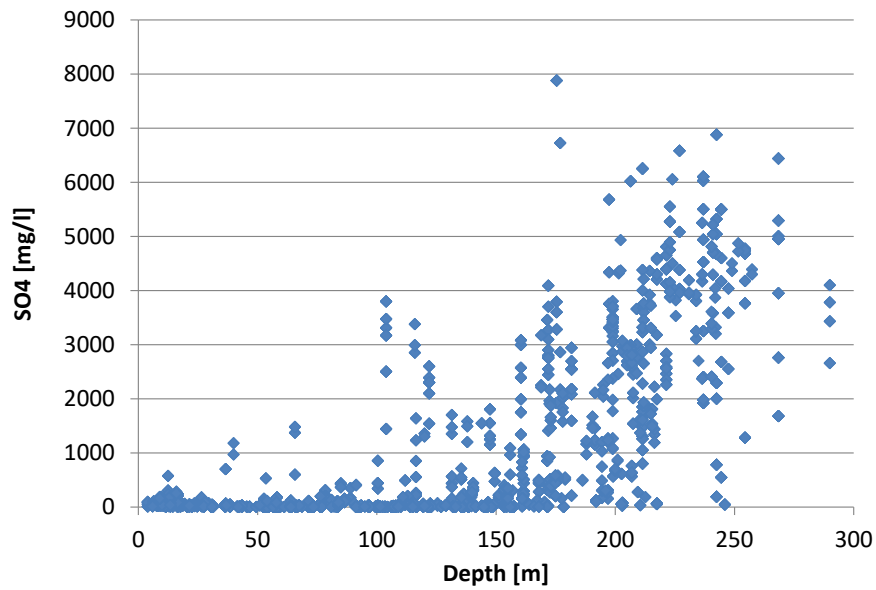


Fig. A. 15 SO_4 concentration in groundwater samples from sedimentary overburden at Gorleben site

A.2.6 Ion exchange

Ionic exchange processes might affect the concentration of cations in the groundwater. Its highest impact on the geochemical conditions was observed at the border of fresh water / salt water. To identify the location of ion exchange processes a profile of the ratio of Ca to Na concentration has been plotted, see Fig. A. 16.

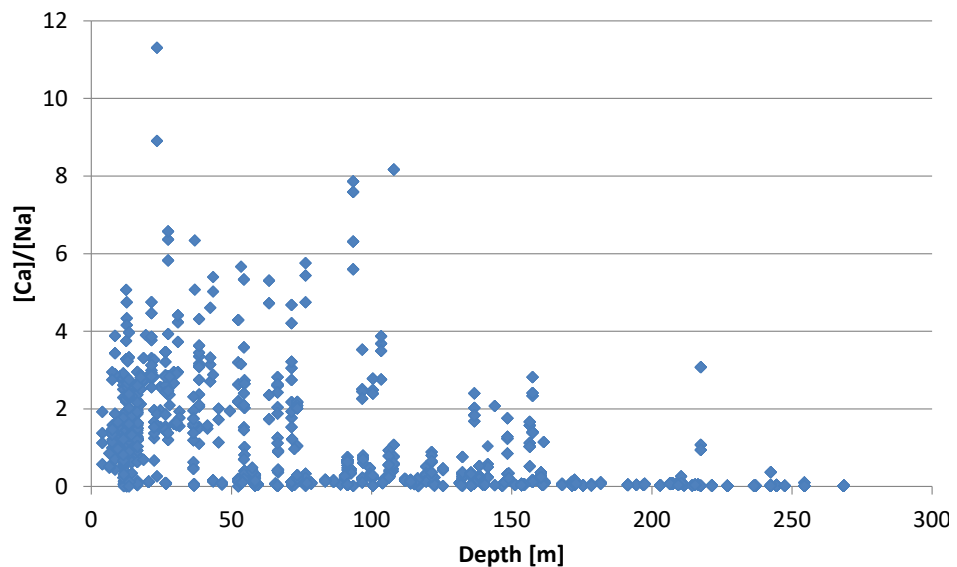


Fig. A. 16 Ratio of Ca vs. Na concentration in groundwater samples from sedimentary overburden at Gorleben site

As a first interpretation the features of high Ca/Na ratios seem to be correlated to the transition zone from LAF to AT and from AT to UAF. The high ratios in the UAF are due to the process of calcite dissolution.

A clearer picture is obtained from the figures in Fig. A. 17 and Fig. A. 18 in this Appendix taken from /BAU 89/, where Cl/Na ratio and Ca concentration are plotted against the Cl concentration. The figures show that two types of ionic exchange processes occur.

- Na exchange Ca(Mg) in high saline areas of the lower aquifer (LAF)
- Ca(Mg) exchange Na in lower parts of the UAF and upper part of the AT. CaHCO₃ waters change to NaHCO₃ and NaClHCO₃ waters

The first process is accompanied by a decrease of Na (increase of the Cl/Na-ratio to values above 1, Appendix Fig. A. 17) and an increase of Ca (Appendix Fig. A. 18) in solution at Cl concentrations above 70 mmol L⁻¹.

The second process is characterized by an increase of Na (Cl/Na ratio below 1, Appendix Fig. A. 17) and a decrease in Ca concentration (Fig. A. 18) Cl concentrations below 50 mmol L⁻¹.

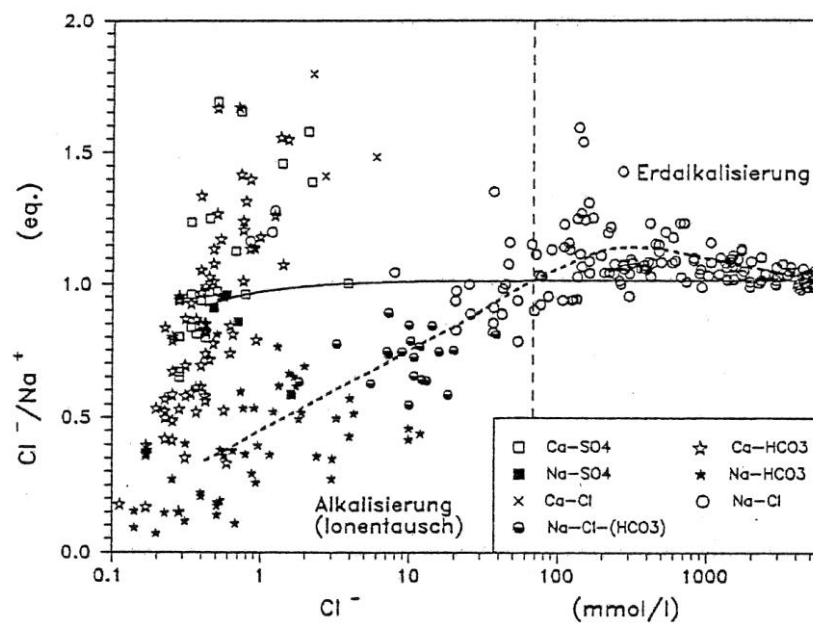


Fig. A. 17 Cl/Na-ratio as function of Cl concentration of Gorleben water, /BAU 89/

Sodium concentration is decreased compared to the mixing line (bold line) at low and increased at high Cl concentrations. This is shown by Cl/Na-values below 1 and above 1, respectively

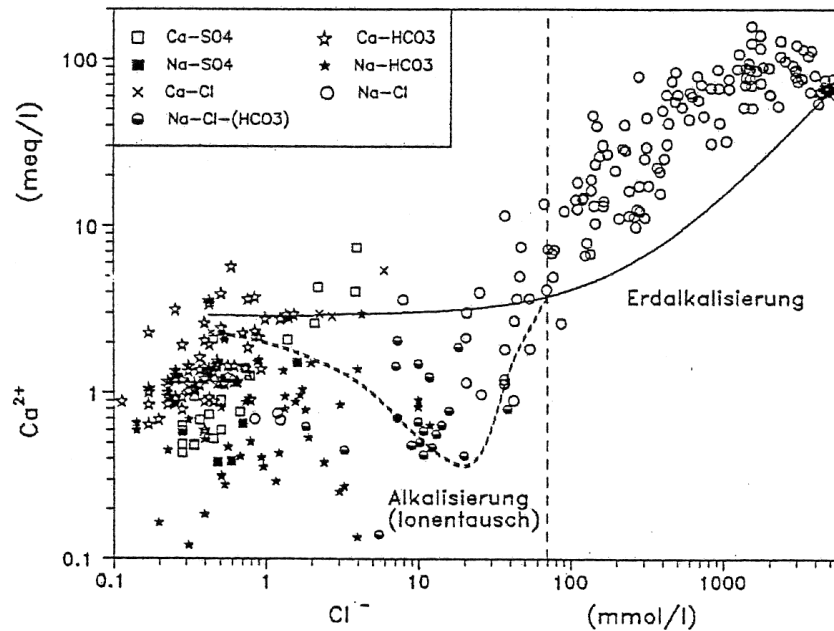


Fig. A. 18 Dependence of the Ca content from the Cl concentration in the Gorleben waters, /BAU 89/

An increase of Ca at high and a decrease of Ca at low Cl concentrations compared to the mixing line (bold line) is visible

A.3 Geochemical site characterization

New selection criteria have been applied to select groundwater data for the four different sedimentary units. As basis we used the well-documented HYGOR-BGR database /KLI 04/. However, data from the engineering office Pickel (IBP) as one of the executing company were unreliable and therefore not considered in our work. Main selection criteria are the groundwater type and the stratigraphic unit:

Upper aquifer (UAF): Groundwater type: Ca-HCO₃ and Na-HCO₃-SO₄
Stratigraphy: lqe

Aquitard (AT): Groundwater type: Na-HCO₃
Stratigraphy: lqe, lqs, ltBS, gtHT

Lower aquifer_1 (LAF1): Groundwater type: Na-Cl

Stratigraphy: lqe

Lower aquifer_2 (LAF2): Groundwater type: Na-Cl

Stratigraphy: ltBS

Legend of stratigraphic abbreviations: lqe: Aquifer, Quaternary, Elsterian

lqs: Aquifer, Quaternary, Saalian

ltBS: Aquifer, Tertiary, Brown coal sands

gtHT: Aquitard, Tertiary, Hamburg-Clay.

A.4 Mineral properties

Extensive mineral analyses have been conducted for muscovite, orthoclase, and quartz. Analyses offer valuable insight into intrinsic and extrinsic mineral traits necessary to interpret collected data correctly and to develop realistic surface complexation models (SCM) and hence surface complexation parameters (SCP). Used chemicals were of p.a. quality or of trace metal basis quality. In the following, tools, equipment, techniques, methods, and further background information used for the characterization of mineral properties are provided. Detailed information is given in /BRI 18/ and /RIC 15/.

- Particle size analysis (Institut für Partikeltechnik, iPAT, Technical University of Braunschweig (iBMB), Braunschweig, Germany; Institut für Mechanische Verfahrenstechnik und Aufbereitungstechnik, Prüflabor Partikelmesstechnik, TU BA Freiberg):
 - iPAT: Parallel beam laser diffraction HELOS (Helium-Neon Laser Optisches System, Sympatec GmbH, Clausthal-Zellerfeld, Germany)
 - TU BAF: Laser diffraction (diffraction spectrometer Helos H0735, Sympatec, wet dispersion QUIXEL) /RIC 15/
- Mineral analysis (Gesellschaft für Anlagen- und Reaktorsicherheit gGmbH, Braunschweig, Germany; Helmholtz-Zentrum Dresden-Rossendorf, Institute of Resource Ecology, Dresden, Germany):
 - Digestion of minerals with hydrofluoric acid (GRS): Inductively Coupled Plasma Mass Spectrometry (ICP-MS, Thermo Electron GmbH, X Series II, SN 1001 C)
 - Hydrofluoric acid digestion with Microwave oven (HZDR):

- mod. Multiwave, Anton Paar, Perkin Elmer
- ICP-MS (mod. ELAN 9000, Perkin Elmer, Boston, USA) for Si, Al, Fe, Ni, Nd, Eu, Gd, Dy, and U
- Optical Emission Spectrometry GRS (ICP-OES, Thermo Scientific, IRIS intrepid II XUV, 12262, Thermo Fisher Scientific Inc., Waltham, USA)
- Atomic Absorption Spectrometry (AAS)
 - Technical University Braunschweig, Germany: Hitachi Z-2000 Zeeman-Tandem-AAS, 1707-013, Hitachi High-Technologies Corporation, Tokyo, Japan.
 - HZDR: mod. AAS-4100, Perkin Elmer for K, Na, Ca, Fe, Mg, Sr, and Ba
- Liquid Scintillation Counting (LSC) (Tri-Carb 3100TR, Perkin Elmer) for Np(V) analysis
- SSA after Brunauer-Emmet-Teller theory /BRU 38/): Mod. Coulter SA3100, Beckman Coulter, AE16018, Software Version 2.13, Fullerton, USA (Helmholtz-Zentrum Dresden-Rossendorf, Institute of Resource Ecology, Dresden, Germany)
 - Quantachrome Autosorb Automated Gas Sorption System, Autosorb for Windows®, Version 1.19 (Karlsruhe Institute of Technology, Institute for Nuclear Water Disposal (INE), Karlsruhe, Germany)
- Scanning Electron Microscopy (SEM) in combination with Energy Dispersive X-ray (EDX) spectroscopy (Concrete Construction and Fire Protection (iBMB), Technical University of Braunschweig (TU BS), Braunschweig, Germany, Helmholtz-Zentrum Dresden-Rossendorf (HZDR), Institute of Resource Ecology, Dresden, Germany):
 - SEM (TU BS): JOEL Ltd, JSM-6700F, Tokyo, Japan (cold field emission gun)
 - EDX (TU BS): EDAX SUTW Sapphire detector, Ametek GmbH, EDAX Business Unit AMETEK GmbH, Wiesbaden, Germany
 - Software (TU BS): EDAX Genesis Sepctrum V5.21 (2007), Institute of Building Material
 - Scanning electron microscopy (HZDR): Hitachi S-4800 and X-ray diffraction (XRD) (D8 Advance, Bruker-AXS) analyses at HZDR /RIC 15/.
- X-ray Diffraction analysis (Gesellschaft für Anlagen- und Reaktorsicherheit gGmbH, Braunschweig, Germany):

- XRD, X'PertPRO, PANalytical
- Database: Inorganic Crystal Structure Database (ICSD) for powder diffraction analysis (PW3213/p2, PAN-ICSD Database HS Plus, version 1.5.0, released December 2009)
- Leaching experiments of the minerals with different concentrations of HCl and HNO₃ (Gesellschaft für Anlagen- und Reaktorsicherheit gGmbH, Braunschweig, Germany; Helmholtz-Zentrum Dresden-Rossendorf, Institute of Resource Ecology, Dresden, Germany):
 - Batch leaching experiments were performed with 20 g of the mineral suspended in 400 mL 0.01 mol L⁻¹ NaClO₄ (equals a solid-to-liquid ratio of 1/20) in a 500 mL polypropylene bottle. The samples were prepared as duplicates at pH 7 and stored in an overhead shaker for three months. Once a week a sample of 3 mL of the solution were taken, centrifuged at 4000×g for 30 minutes (Sigma 3K18, Laboratory Centrifuges) and the supernatant was analyzed by ICP-MS and AAS for Si, Al, K, Mg, Ca, Fe, Ni, Sr, Ba, Nd, Eu, Gd, Dy and U.
 - Flow-through leaching experiments were performed at pH 7 (muscovite) and pH 6 (orthoclase) in 0.01 mol L⁻¹ NaClO₄. In the reactor 0.5 g of the mineral was flown through by a fresh 0.01 mol L⁻¹ NaClO₄ solution continuously and mixed with a stirrer. At different time steps samples of the output solution were taken for analysis. Temperature, pH, and conductivity were measured continuously. The set-up for the experiment is shown in the appendix Fig. A. 19.
- Cation exchange capacity (Gesellschaft für Anlagen- und Reaktorsicherheit gGmbH, Braunschweig, Germany)
 - Inductively Coupled Plasma Mass Spectrometry (ICP-MS, Thermo Electron GmbH, X Series II, SN 1001 C)
 - Optical Emission Spectrometry (ICP-OES, Thermo Scientific, IRIS intrepid II XUV, 12262, Thermo Fisher Scientific Inc., Waltham, USA)
 - DIN ISO 13536:1997-04 (1997)
- Zeta-potential measurements (Helmholtz-Zentrum Dresden-Rossendorf, Institute of Resource Ecology, Dresden, Germany)
 - Laser Doppler velocimetry with a Zetasizer Nano ZS (Malvern Instruments, Malvern, U.K.) /RIC 15/. Zeta-potential was measured via electrophoreses

measurements using the Doppler shift in the laser beam (laser Doppler anemometry). Data was evaluated with the Smoluchowski approximation.

- Mineral titration experiments for surface charge characterization (Gesellschaft für Anlagen- und Reaktorsicherheit gGmbH, Braunschweig, Germany; Karlsruhe Institute of Technology, Institute for Nuclear Waste Disposal, Karlsruhe, Germany)
 - Ultrapure water
 - Sartorius arium® pro, H2OPRO-UV-D, 18.2 Mohm cm
 - Sodium perchlorate hydrate salt (NaClO₄)
 - 99.99 %, trace metal basis, 381225-500G, Aldrich, owned by Merck KGaA, Headquarter St. Louis, Missouri, U.S.A.
 - Nitric acid (HNO₃) for background electrolyte pH adjustment
 - Certified nitric acid, 65 % Suprapur®, Merck, Millipore, Merck KGaA, Headquarter St. Louis, Missouri, U.S.A.
 - Sodium hydroxide (NaOH) titrant solution
 - Titrisol®, Merck (Sodium hydroxide solution for 1000 ml, Titrisol®, 1 N), Merck KGaA, Headquarter St. Louis, Missouri, U.S.A.
 - pH measurements of mass and electrolyte titration
 - Electrode: glass microelectrode, 125 mm, Metrohm
 - Temperature sensor: ALMEMO MA 10302, Za 9030-FS7, calibrated Pt 100 (0.001°C), AHLBORN, Mess- und Regelungstechnik GmbH, Holzkirchen, Germany, calibration mark: DKD-K-06701
 - pH meter: 827 pH lab, 230 V, Metrohm
 - Calibration: linear multipoint calibration of electrical potential in solution [mV]
 - Merck standard buffer solutions pH 4, pH 7, pH 9, and pH 10: Merck, Certipur, NIST standard buffer solution (DIN 19266), Merck KGaA, Headquarter St. Louis, Missouri, U.S.A.
 - Sample preparation (scale): Mettler TOLEDO XP205, DeltaRange®

- Magnetic stirrer: Heidolph magnetic stirrer, MR 1000 (Heidolph Instruments GmbH & Co. KG, Schwabach, Germany)
- pH measurements of potentiometric acid-base titration (Karlsruhe Institute of Technology, Institute for Nuclear Waste Disposal, Karlsruhe, Germany)
 - Electrode: glass electrode "iTrode", Pt 1000, 854 iConnect, Metrohm
 - Automatic titrator: Titrand 907, Metrohm
 - Automatic dosing system: DOSINO 800: 0.1 ml 2 min⁻¹ (software MaJo)
 - Magnetic stirrer: 801 stirrer, Metrohm
 - Calibration: A blank titration (so solid) of background electrolytes with defined amounts of H⁺ was carried out. With the specialized evaluation tool MaJo the pH was calculated from measured electrical potential difference U [mV]. Blank titrations were conducted with the combined glass electrode 854 iConnect (Metrohm) and repeated at least once before and after each mineral titration procedure. Each titration of the mica, feldspar, and quartz mineral followed the same procedure.
- HZDR laboratory pH-Meter inoLab 7110 (WTW, Weilheim, Germany) with SenTix MIC electrodes (WTW, Weilheim, Germany) were used to determine the pH of the samples. Calibration was performed with standard buffers (WTW, Weilheim, Germany)
- Measurement of optical density at 600 nm (OD600) for monitoring of the growth of microorganisms with UV/Visible spectrophotometer (Ultrospe 1000, Pharmacia Biotech) (Helmholtz-Zentrum Dresden-Rossendorf, Institute of Resource Ecology, Dresden, Germany)
- Optical microscopy (Olympus BX61) with an excitation filter U-MSWB2 (420-480 nm) and U-MSWG2 (480-550 nm) (Helmholtz-Zentrum Dresden-Rossendorf, Institute of Resource Ecology, Dresden, Germany)

A.4.1 HF digestion of muscovite, orthoclase, and quartz

In the following, additional, detailed information on the mineral characterization of muscovite, orthoclase, and quartz are offered. Data on hydrofluoric acid digestion, EDX, XRD, as well as an example of BET analysis are provided. Error sources of BET measurements

are summarized; zeta-potential measurements of orthoclase, quartz, and muscovite are illustrated. Tab. A. 2 compares HF analysis carried out in this study with supplier data and the ideal geochemical composition of the respective minerals.

Tab. A. 2 Comparison of supplier's data and HF digestion analysis of this study of muscovite^[1], quartz^[2], and orthoclase^[3]

Values given in [wt%], – no data available, limit of quantification (LOQ) regarding MgO and Na₂O < 0.02 wt%. If not specified analyses carried out with ICP-MS and ICP-OES, * AAS measurement: Na 589.6 nm, K 766.5 nm.

	K₂O·3Al₂O₃·6SiO₂·(OH)₂^[1]	Normag GmbH	this study
SiO ₂	45.3	48.80 – 51.67	54.71
Al ₂ O ₃	38.5	29.37 – 31.05	28.42
K ₂ O*	11.8	-	9.40
Na ₂ O*		1.04 – 1.07	1.00
CaO		-	0.04
MgO		0.72 – 0.84	0.84
TiO ₂		0.77 – 0.81	0.65
Fe ₂ O ₃		2.00 – 4.16	4.93
	SiO₂^[2]	Schlingmeyer Quarzsand GmbH	this study
SiO ₂	100.0	>99.7	98.65
Al ₂ O ₃		0.09	0.20
K ₂ O		<0.01	0.05
Na ₂ O		<0.01	< 0.02
CaO		<0.01	0.05
MgO		<0.01	< 0.02
Fe ₂ O ₃		0.0068	0.04
TiO ₂		0.0084	0.01
	K₂O·Al₂O₃·6SiO₂^[3]	Sibelco GmbH	this study
SiO ₂	64.7	66.2	62.80
Al ₂ O ₃	18.3	18.8	18.57
K ₂ O*	16.9	10.5	12.80
Na ₂ O*		3.6	5.12
CaO		0.8	0.52
MgO		-	< 0.02
Fe ₂ O ₃		0.11	0.17
TiO ₂		-	0.02

A.4.2 Batch and flow-through leaching experiments of orthoclase and muscovite

Experimental set-up

For the batch leaching experiment 20 g of the minerals (orthoclase and muscovite) were weighted into 500 ml PE bottles and 400 ml of $0.01 \text{ mol L}^{-1} \text{ NaClO}_4$ was added (equals to M/V of $1/20 \text{ g mL}^{-1}$). The experiments were organized as twofold measurements. These experiments showed the dissolution of the minerals over the time and thus also the change of the composition of the background electrolyte. The duration of the experiment was set to three months because all other experiments need this time frame. The pH was adjusted to pH 7 and the samples were stored in an overhead shaker. Once a week an aliquot was taken from each sample, centrifuged with $4000 \times g$ for 30 min (Sigma 3K18 from Laboratory Centrifuges) and the supernatant was analyzed by ICP-MS and AAS for Si, Al, K, Mg, Ca, Fe, Ni, Sr, Ba, Nd, Eu, Gd, Dy and U.

Flow-through experiments were performed at pH 7 (muscovite) and pH 6 (orthoclase) with $0.01 \text{ mol L}^{-1} \text{ NaClO}_4$ as background electrolyte. The mineral 0.5 g (orthoclase or muscovite) was weighed in the flow-through reactor. Over a pump fresh $0.01 \text{ mol L}^{-1} \text{ NaClO}_4$ was continuously transported through the reactor (flow rate 0.3 mL min^{-1} , volume of 46 mL), where the suspension was mixed with a stirrer. These experiments were conducted for one week. At different time steps samples of the output solution were taken for analysis. The temperature, pH, and conductivity were measured continuously. The set-up for the experiment is shown in Fig. A. 19.

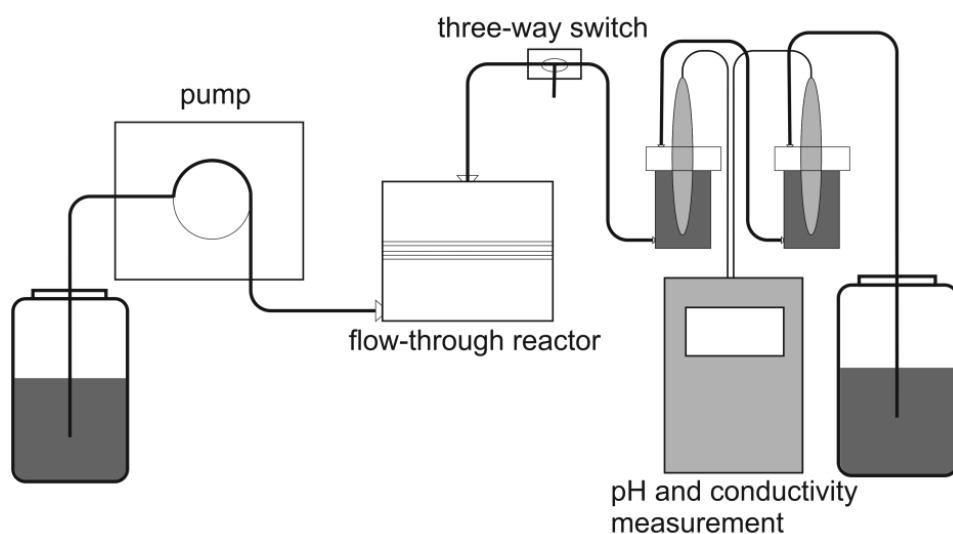


Fig. A. 19 Experimental setup of flow-through leaching experiments

The leached elements with their corresponding concentrations are given in Tab. A.2 for the final measurement of the batch and flow-through leaching experiments.

Tab. A. 3 Measured elemental concentrations and detection limits ($\mu\text{mol L}^{-1}$) after the leaching experiments of orthoclase and muscovite (by ICP-MS if not specified otherwise)

	Orthoclase		Muscovite		Detection limit
	Batch (after 91 d)	Flow-through (after 101 h)	Batch (after 91 d)	Flow-through (after 101 h)	
Mg*	20.5 ± 0.4	0.51 ± 0.01	38.2 ± 0.8	0.58 ± 0.01	0.0041
Al	2.2 ± 0.2	0.84 ± 0.08	4.91 ± 0.5	0.22 ± 0.02	0.037
Si	340 ± 30	6.8 ± 0.7	233 ± 20	4.3 ± 0.4	0.36
K*	118 ± 2	114 ± 2	269 ± 5	18.1 ± 0.4	0.26
Ca*	79 ± 2	2.7 ± 0.06	76 ± 2	n. d.	0.24
Fe	n.d.	n.d.	n.d.	n.d.	0.18
Ni	0.02 ± < 0.01	n. d.	0.02 ± < 0.01	n. d.	0.0017
Sr*	0.24 ± 0.02	0.007 ± < 0.01	0.08 ± < 0.01	0.003 ± < 0.01	0.0011
Ba*	0.19 ± 0.02	0.013 ± < 0.01	0.04 ± < 0.01	0.009 ± < 0.01	7.3E-04
U	0.01 ± < 0.01	0.003 ± < 0.01	n. d.	0.007 ± < 0.01	4.2E-05

In addition, the concentrations of four representative lanthanides (Eu, Gd, Nd, and Dy) were measured. The Nd and Dy contents were below the detection limit of $6.93\text{E}-05$ and $6.15\text{E}-05 \mu\text{mol L}^{-1}$, respectively. Furthermore, Gd as well as Eu was detected in such low concentrations (below $6.36\text{E}-05$ and $6.58\text{E}-05 \mu\text{mol L}^{-1}$, respectively) that no effect onto the sorption processes is expected.

A.4.3 Additional information on muscovite XRD measurements

Amongst others, XRD measurements offer information of swelling properties and the integrity of the mineral's structure that might change during preconditioning procedures. Sample preparation with diethylenglycol allows to study a clay mineral's swelling potential. Diethylenglycol preparation provided evidence for the presence of montmorillonite in the clay fraction of the muscovite sample. A shift of the {001} XRD reflection at 6.2° [2Theta] to 5.2° [2Theta] is characteristic for spreading of clay lattice structure where the spreading of montmorillonite interlayers is caused due to incorporation of

diethylenglycol into the lattice. This effect could be observed in this study and was more pronounced for the preconditioned muscovite sample in comparison to the untreated sample (data provided in /BRI 18/). Very briefly, X-ray reflection angles follow the Bragg formulation /BRA 13/. Thus, provided that the change of crystal lattice distance is the only variable, collected X-ray reflection angles/Bragg angles [2θ] decrease with increasing lattice distance. Diffraction angles are mineral specific. Montmorillonite swelling properties of lattice structure are attributed to changes in the range of $0^\circ - 10^\circ$ [2θ] depending on the degree of mineral layer distance alteration.

A.4.4 Experimental set-up for Al, Fe, and amorphous silica analyses of quartz minerals

The ammonium oxalate (0.2 mol L^{-1}) and oxalic acid (0.2 mol L^{-1}) were used with solid-liquid ratios (M/V) of $1/10 \text{ g ml}^{-1}$ and $1/20 \text{ g ml}^{-1}$ for amorphous silica extraction and Fe, Al leaching. Twofold measurements were carried out, equilibration times of 24 h and 48 h were realized. Acid leaching experiments for Fe and Al leaching was achieved with 0.01, 0.1 and 0.5 mol L^{-1} HCl and HNO₃, a solid-liquid ratio of $1/10 \text{ g ml}^{-1}$ was used.

The quartz minerals G20 EA and G20 EAS extra were investigated with a method that only affects amorphous SiO₂ leaving crystalline SiO₂ without any influences: 10 mg quartz of both quartz minerals (grain-size fraction: 200-250 μm) were leached in 50 ml 0.1 mol L^{-1} NaOH. Samples were temperature-controlled at 80°C and shaken head first. After 48 h samples are filtered with 0.2 μm cellulose-acetate-filters. Twofold and three-fold measurements were conducted.

ICP-MS analyses of relatively small Si concentrations in 0.1 mol L^{-1} NaOH are difficult to realize since high background noises are caused by concentration differences between analyte and background solution. Furthermore, Si signals are influenced and biased by silicate device components (torch, vaporizer chamber) of ICP-MS. To achieve a stable background noise the mass spectrometer was purged for 2.25 h with 1 % HNO₃. Since a drift in blanks still occurs in all series of measurements (Fig. A. 20) obtained data was corrected for this shift. Detected drift [counts s^{-1}] was subtracted from measured samples [counts s^{-1}] that were then converted into mg kg^{-1} . Hence, collected data should only be interpreted as semi-quantitative results.

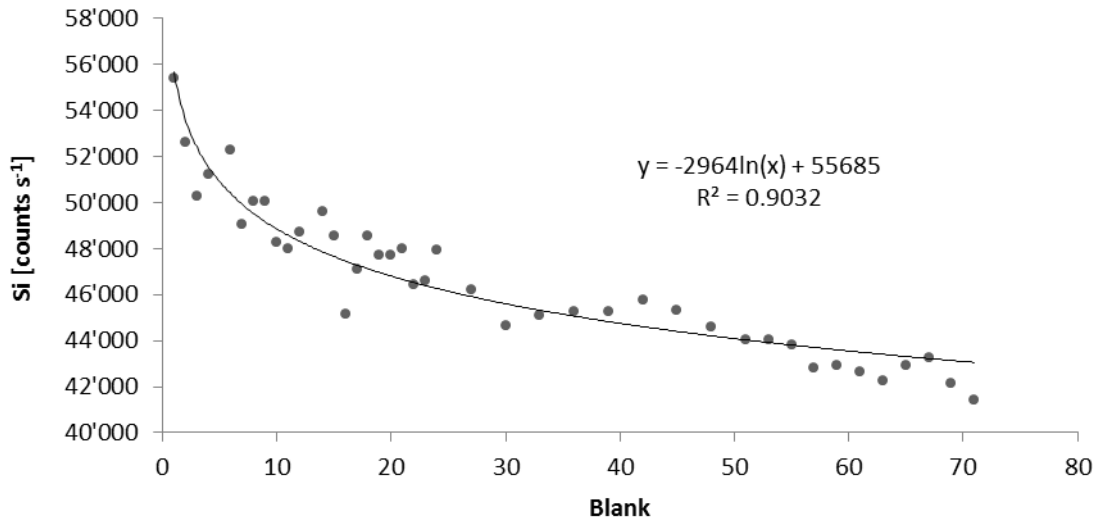


Fig. A. 20 Blank drift occurring during analysis of Si with ICP-MS

Detected drift [counts s⁻¹] is subtracted from measured samples [counts s⁻¹] that are subsequently converted into mg kg⁻¹

A.4.5 Methods for surface charge property characterization

This section offers an overview of experimental approaches of discontinuous mass, discontinuous electrolyte, and continuous potentiometric acid-base titration experiments. Data processing of relative titration data is presented in the digital Appendix Section A.4.6.

Experimental approach

Following /POL 10/, /PRE 06/ and /LÜT 12/ a complex combination of mass and electrolyte titrations as well as potentiometric continuous acid-base titration may identify a potential pH_{nphc} . Zeta-potential measurements can be conducted to obtain pH_{IEP} . With only one of the mentioned techniques the information in terms of pH_{nphc} or pH_{ppzc} remains incomplete while coupling all three experiments may provide information of acid-base impurities, potential dissolution processes, and charging behavior of a given mineral.

This study applied a combination of all three titration techniques, results involve pH measurements in suspensions. Titration experiments were conducted with pristine mineral phases (Tab. 5.1) An orthoclase sample with a particle size fraction (PSF) 30 – 400 μm was utilized, for quartz 150 – 800 μm and for muscovite 20 – 400 μm size

fractions were used, respectively (Tab. 5.1). All solutions were prepared with ultrapure water. Chemicals and tools used in experiments are summarized in Appendix A.2.1.

For discontinuous potentiometric mass and electrolyte titrations pH measurements were carried out with glass electrodes (digi. App. Sec. A.2.1). Discontinuous means that each measurement reflects an individual sample. For each M/V or ionic strength (IS) condition an individual sample was prepared. The experimental set-up was developed following /POL 10/ and /LÜT 12/. Mass and electrolyte titrations were conducted under Ar atmosphere at $295\text{ K} \pm 2\text{ K}$. Closed sample vials were stored under laboratory conditions at $296\text{ K} \pm 2\text{ K}$. Experiments were conducted in duplicate for both experimental set-ups.

Mass titration

Discontinuous mass titration experiments yielded pH_{mass} (cf. digi. App. Tab. A. 4): Samples with increasing M/Vs [g L^{-1}] in degassed $10^{-5}\text{ mol L}^{-1}$ NaClO_4 background electrolyte were prepared. Two different initial background electrolyte pH values (pH_{ini}) were chosen; $\text{pH}_{\text{ini}} = 3.0$ and $\text{pH}_{\text{ini}} = 4.5$ for quartz, for muscovite and orthoclase $\text{pH}_{\text{ini}} = 2.9$, $\text{pH}_{\text{ini}} = 4.7$. The pH_{ini} was adjusted by addition of appropriate amounts of HNO_3 and NaOH , respectively. Samples with 5, 12.5, 50, 100, 400, 800, and 1200 g L^{-1} of each mineral were prepared and suspended in $10^{-5}\text{ mol L}^{-1}$ NaClO_4 background electrolyte (with different pH_{ini}). Suspensions were stored in 125 ml, wide-mouth Nalgene LDPE screw cap bottles. Samples were bubbled with Ar and underwent a 15 min ultrasound treatment in a water bath to accelerate equilibration /LÜT 12/. The pH was measured after 5 h, 24 h, 2 d, and 7 d. Samples were shaken periodically. Before each pH measurement samples were stirred over approximately 1 min with a magnetic stirrer (digi. App. Sec. A.2.1). During the actual pH measurements stirring was discontinued.

Electrolyte titration

Following mass titration experiments, discontinuous electrolyte titrations were performed to determine pH_{pZSE} (cf. digi. App. Tab. A. 4): Electrolyte titrations were prepared with 400 g L^{-1} solid for orthoclase and muscovite, while 1200 g L^{-1} were used for quartz. For electrolyte titrations M/Vs equaled ratios at which a pH_{mass} had been reached (quartz = 1200 g L^{-1} , orthoclase = 400 g L^{-1} , muscovite = 400 g L^{-1}). Increasing amounts of NaClO_4 salt were then added to the suspensions, so that salt concentrations ranged from $10^{-6}\text{ mol L}^{-1}$ to 3 mol L^{-1} . Sample equilibration and sample treatment was the same as for mass titration experiments. For high IS NaClO_4 suspensions pH

measurements were corrected to exclude IS influence on the electrode's potential after /SCH 67/ and /HAG 14/ (digi. App. Sec. A.4.8).

Continuous potentiometric acid-base titration

Pristine minerals were used (orthoclase < 63 μm , muscovite 20 – 400 μm , quartz 150 – 800 μm). The experimental set-up was identical for all minerals. Titrations were conducted continuously, i. e. for each titration experiment one sample was prepared with a known M/V, suspension volume, and initially added volumes of acid or base; the titrant was continuously added. Suspensions were prepared with 10 mM NaClO_4 background electrolyte and equilibrated overnight. For orthoclase 3.595 g were suspended in 50.5 ml background electrolyte (71.2 g L^{-1}). The M/V of the mica titration experiment equaled 190 g L^{-1} . After equilibration, defined volumes of NaOH were added to the samples to increase the pH. Titrations proceeded then from high to low pH values. Every two minutes 0.1 ml titrant (5 mM L^{-1} HClO_4) was added to the suspensions. After each titrant addition the samples were mixed with a magnetic stirrer. All chemicals were of p.a. quality. The calibration technique of the pH meter and applied tools are summarized in Appendix A.2.1.

Zeta-potential measurements and the isoelectric point

The zeta-potential is the electrical potential at the shear plane (digi. App. Sec. A.4.5, /DAV 90/) and was determined via electrophoresis measurements. The pH value where the electrophoretic mobility is zero equals pH_{IEP} . Zeta potential measurements were conducted for mica and orthoclase. The particle size < 63 μm was used for both minerals. About ten samples were prepared and the resulting suspensions (0.1 g ml^{-1} in 10 mM NaClO_4) were equilibrated until the pH values remained constant over at least 48 h. Equilibrium pH values ranged between pH 2.4 and pH 7.8. Measurements were repeated at least three times at 298.2 K \pm 0.1 K.

As a consequence of e. g. permanent negative surface charge of e. g. phyllosilicates like muscovite, zeta-potential measurements result in very low isoelectric points (pH_{IEP}) due to very low electrokinetic potential over a wide pH range /LÜT 12/. Hence, pH_{IEP} does not coincide with pH_{mass} , pH_{pzse} , or pH_{pznpc} and, hence, $\text{pH}_{\text{ppzc}} \neq \text{pH}_{\text{IEP}}$.

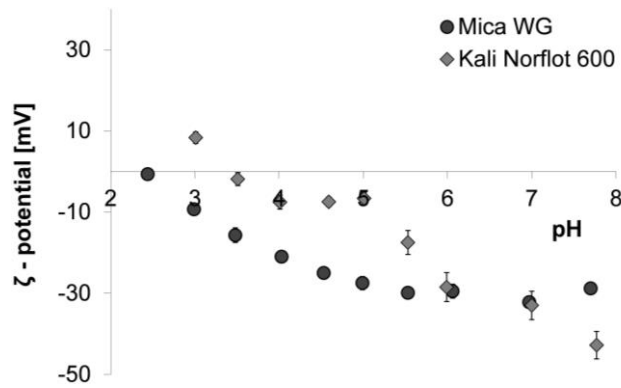


Fig. A. 21 Zeta-potential measurements of muscovite and orthoclase. Data from /RIC 15/

Mica WG refers to the muscovite sample, Kali Norflot 600 to the orthoclase sample of this study.

A.4.6 Points of zero charge

There are various points of zero charge or reference pH values, respectively, that characterize electrostatic properties of a mineral or a solid sample. Since no standardized nomenclature has been accepted so far and to ensure consistency, definitions and notations as suggested by /SPO 98/ are used in the present study.

All points of zero charge are defined as pH values at which one of the following surface charge categories (a) – c)) equals zero at defined geochemical conditions (temperature, pressure, IS) /SPO 98/ In this study, the surface charge is scaled in relation to the mineral surface area and is referred to as surface charge density σ [C m^{-2}] which can be classified into three categories /SPO 98/, /DAV 90/:

- permanent structural surface charge from isomorphic substitution of e. g. Al^{3+} for Si^{4+} in the crystal lattice for, e. g. phyllosilicates, referred to as σ_o ,
- coordinative surface charge resulting from proton (H^+) and/or hydroxide (OH^-) adsorption, denoted σ_H , and
- adsorbed ions with $\Delta q = q_+ - q_-$, where q_+ , q_- represent the adsorption of cations, anions, respectively. Δq includes all adsorption processes, i. e. innersphere and outer-sphere surface complexation, and the diffuse layer σ_d , but excludes H^+ and OH^- contributions, $\Delta q = \sigma_{is} + \sigma_{os} + \sigma_d$ with $\sigma_{is,os}$ being the net charge of inner-sphere, outer-sphere surface complexes, respectively.

Surface charge classifications are related following Equation Eq. A. 1

$$\sigma_o + \sigma_H + \Delta q = 0 \quad \text{Eq. A. 1}$$

which describes electroneutrality of any sample equilibrated in an aqueous background electrolyte /SPO 98/ The intrinsic surface charge density σ_{int} of a particle is defined as /SPO 98/, /DAV 90/

$$\sigma_{int} = \sigma_o + \sigma_H \quad \text{Eq. A. 2}$$

The total particle surface charge density σ_p is defined with

$$\sigma_p = \sigma_{int} + \sigma_{Stern} \quad \text{Eq. A. 3}$$

where σ_{Stern} denotes the Stern layer surface charge density ($\sigma_{Stern} = \Delta q - \sigma_d$).

In this study, the pH was chosen to present the different points of zero charge, reference pH values, respectively (Tab. A. 4). Tab. A. 4 provides an overview of notions, definitions, and experimental methods of common points of zero charge.

Tab. A. 4 Definitions of reference pH values and experimental measurements (Exp. Method) used in this study.

σ – absolute surface charge values [$C\ m^{-2}$], M/V – solid-liquid ratio, T – absolute temperature [K], p [Pa] – pressure, ET – electrolyte titration, MT – mass titration, IS – ionic strength, zeta – zeta-potential measurements, pot – potentiometric titrations. ^[1] utilized for natural and clay minerals as equivalent to pH_{pznpc} . Details on titration methods provides Appendix A.4.5.

Symbol	Name	Expression	Exp. Method
pzc	point of zero charge	$\sigma_p = 0$	ET, MT, zeta, pot
pznpc	point of zero net proton charge	$\sigma_H = 0$	pot
nphc	point of zero net proton and hydroxide consumption ^[1]	$\sigma_H = 0$	pot
IEP	isoelectric point	$\sigma_d = 0$	zeta
pzse	point of zero salt effect	$(\delta pH / \delta IS)_{T,p} = 0$	ET
cip	common intersection point	$(\delta \sigma_H / \delta IS)_{T,p} = 0$	ET
mass	end point of mass titration	$(\delta pH / \delta M/V)_{T,p} = 0$	MT
ppzc	pristine point of zero charge	$\sigma_p = \sigma_H = \sigma_d = \sigma_o = 0$	ET, MT, zeta, pot

Protonation and deprotonation takes place on silanol (Si-OH) and aluminol (Al-OH) surface functional groups. Assuming that the initial H^+ and/or OH^- concentrations of the suspension and of the solid (particles) are known, that the mineral sample is free of acidic or basic impurities, that only negligible mineral dissolution processes occur, and that enough surface is provided for protonation and deprotonation reactions with respect to titrant concentration, data obtained from potentiometric acid-base titration coincides with absolute surface charges ($pH_{pznpc} = pH_{pzc} = pH_{ppzc}$). Any deviation from the pristine, ideal surfaces as described above and without the knowledge of the initial H^+ and/or OH^- concentration of the solid results in relative surface charge densities that may include biasing influences from e. g. surface impurities, mineral dissolution processes, or lattice structure. With the knowledge of the pH_{ppzc} or pH_{nphc} it is possible to transform relative surface charge data into absolute values /LÜT 12/, /PRE 06/ which is illustrated in Appendix A.4.7.

The pH_{ppzc} is a material property, does not depend on the method, and can only be sufficiently determined if results of e. g. potentiometric (pH_{pznpc}), electrolyte (pH_{pzse}), and mass (pH_{mass}) titrations, as well as zeta-potential measurements (pH_{IEP}) agree. Potentiometric titrations that are carried out at different /Ss should exhibit a pH_{cip} for pristine metal oxide surfaces which can in return coincidence with pH_{IEP} , pH_{mass} , pH_{pzse} , and pH_{pznpc} to describe the pH_{ppzc} where $pH_{IEP} = pH_{mass} = pH_{pzse} = pH_{cip} = pH_{pznpc} = pH_{ppzc}$ is valid. For natural minerals or clays often pH_{cip} and pH_{ppzc} do not exist due to e. g. isomorphic substitutions of inter alia Si^{4+} for Al^{3+} ; hence, $\sigma_o \neq 0$ applies (e. g. /LÜT 12/). In addition, pH_{pznpc} may change as a function of /S, solid-liquid ratio (M/V), and as a function of mineral acidic or basic impurities resulting in $pH_{pznpc} \neq pH_{ppzc} \neq pH_{pzse} \neq pH_{IEP} \neq pH_{mass}$ (e. g. non-ideal surfaces). To distinguish between pH_{pznpc} of pure metal oxide surfaces ($pH_{pznpc} \neq pH_{ppzc}$) and natural minerals ($pH_{pznpc} \neq pH_{ppzc}$) the term zero net proton and hydroxide consumption pH_{nphc} is used /LÜT 12/.

The pH_{IEP} denotes the pH where the electrophoretic mobility is zero, hence, zero counterion charge occurs in the system /DAV 90/, /LÜT 12/. Ideally, the particle is electrokinetically uncharged /SPO 98/, and $\psi = 0$ is valid for pristine metal oxides (ψ – surface potential [V]). However, pH_{IEP} can be influenced by surface impurities but also by lattice structure such as e. g. permanent negative surface charge: Phyllosilicates, for example, exhibit negative electrokinetic potentials over a wide pH range due to isomorphic substitution which results in low pH_{IEP} /LÜT 12/. Hence, for most natural mineral surfaces and e. g. phyllosilicates $pH_{IEP} \neq pH_{ppzc} \neq pH_{pznpc} \neq pH_{pzse} \neq pH_{mass}$ is valid.

A.4.7 Data processing of relative titration data

As illustrated in Appendix A.4.6 pristine metal oxide surfaces can exhibit a pH_{cip} and pH_{ppzc} ; natural minerals on the other hand rarely have a pH_{cip} or only one specific reference pH value (e. g. pH_{nphc}). Since natural minerals were used in this study potentiometric titration data rather represented relative surface charge densities. To transform relative measurements (σ [C m^{-1}]) into absolute values, raw data (measurements) was referenced to the independently determined pH_{IEP} and/or pH_{mass} of the respective mineral, which unfortunately differed. Experimental surface charge was shifted such that $\sigma = 0 \text{ C m}^{-2}$ at the respective reference pH, i. e. pH_{IEP} , pH_{mass} (digi. App. Sec. A.4.6). The resulting charge difference is referred to as $\Delta\sigma$. The final, processed surface charge densities were treated as absolute values and used to determine protolysis constants for muscovite, orthoclase, and quartz /BRI 18/.

Orthoclase data processing

Two different approaches were followed to determine absolute surface charge data for orthoclase:

- First, measurements were set into relation with $\text{pH}_{\text{IEP}} = 3.5$ with a shift of $\Delta\sigma = 0.047 \text{ C m}^{-2}$. A linear relationship with respect to pH_{IEP} had to be assumed in the absence of more detailed data sets. Unfortunately, the lower the pH, the more prone to experimental error the measurements become, in particular with low surface area.
- Second, under the assumption of $\text{K}^+ - \text{H}^+$ exchange processes /STI 95/ the orthoclase surface was treated like a clay mineral with permanent negative surface charges due to isomorphous substitution. Hence, potentiometric data was shifted in relation to $\text{pH}_{\text{mass}} \approx 8.0$ ($\Delta\sigma = 0.3 \text{ C m}^{-2}$) to transform relative raw data to absolute values.

Shifting measurements relative to $\text{pH}_{\text{mass}} \approx 8.0$ resulted in positive surface charge data for $\text{pH} < \text{pH}_{\text{mass}} \approx 8.0$ and negative surface charge for $\text{pH}_{\text{mass}} > 8.0$. Applying pH_{mass} as pH_{nphc} resulted in the hypothetical charge representation of surface functional edge sites of orthoclase.

Muscovite data processing

Since $\text{pH}_{\text{pzse}} \neq \text{pH}_{\text{IEP}} \neq \text{pH}_{\text{mass}}$ for muscovite, acid-base titration delivered relative surface charge measurements. To transform relative data into absolute values a third order polynomial relationship between pH_{IEP} and relative experimental data had to be assumed in the absence of more precise data. Fig. A. 22 in this appendix depicts the third order polynomial illustrating a possible theoretical relationship between pH_{IEP} and relative titration measurements (grey symbols in Fig. A. 22). The polynomial was used to derive absolute surface charge data (Fig. A. 22 green symbols).

The application of the third order polynomial was related to a shift of relative raw data (measurements) equaling $\Delta\sigma = 0.005 \text{ C m}^{-2}$ and yielded a correlation coefficient (CC) of 0.998.

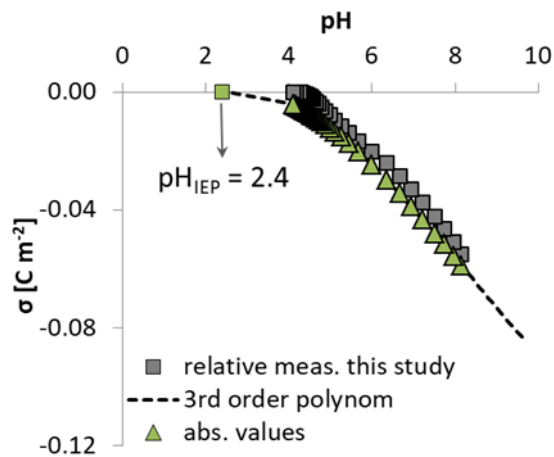


Fig. A. 22 Shift of relative muscovite titration data (relative meas. this study) in relation to pH_{IEP} with $\Delta\sigma = 0.005 \text{ C m}^{-2}$

Third order polynomial regression yielded $\Delta\sigma = 0.005 \text{ C m}^{-2}$.

A.4.8 Correction of pH measurements in high *IS* conditions

For electrolyte titration experiments the pH was measured with electrodes that determined the electrical potential [mV] in a solution or suspension, which was then recalculated to the pH (Eq. A. 4).

$$E_{\text{obs}} = E_c + Nf \log a_{\text{H}^+}$$

Eq. A. 4

where E_{obs} corresponds to the measured electrical potential [mV], E_c to the reference electrode potential [mV], $\log a_{H^+}$ to the hydrogen ion activity (pH), and Nf to the Nernstian slope (≈ 59 mV/Ph unit).

The measurement of the electrical potential of an electrolyte is dependent on the IS /SCH 67/. To account for IS influences a correction (ΔpH) as proposed by /HAG 14/ was determined where necessary (only for electrolyte titration experiments). Therefore, measurements once carried out by /SCH 67/ were repeated; it was found that experimental data of both studies agreed well (digi. App. Fig. A. 23). Experimental data of both studies presented the basis to determine ΔpH which was used to correct the IS influence for each pH measurement at elevated $NaClO_4$ concentrations (electrolyte titration experiments, Sec. 5.1.1.3, 5.1.2.2, 5.1.3.3). Corrected pH values are referred to as pH_c .

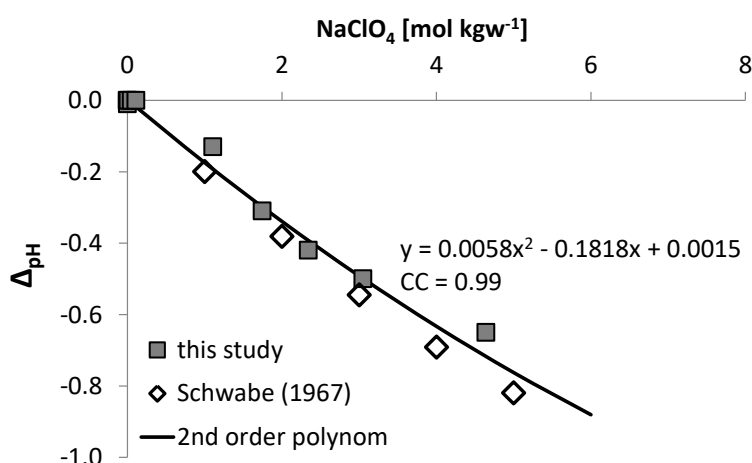


Fig. A. 23 ΔpH vs. $NaClO_4$ concentration [mol kgw⁻¹] after /SCH 67/

ΔpH – correction term for pH measurements in high IS $NaClO_4$ environments (also pH_c), CC – correlation coefficient.

pH measurements of electrolyte titration experiments (Sec. 5.1.1.3, 5.1.2.2, 5.1.3.3) were corrected with according ΔpH values: For example, ΔpH for 1 mol L⁻¹ $NaClO_4$ electrolyte concentration corresponded to a decrease in pH of 0.2 pH units. A second order polynomial was used for regression analysis of measurements of this study in combination with data from /SCH 67/ (Fig. A. 23), individual ΔpH values were calculated using this polynom. Additional information may be obtained from /HAG 14/ and /SCH 67/.

A.5 Eu(III), Ni(II), Ca(II), Cs(I), and Al(III) batch sorption experiments

A.5.1 Tools, equipment, and techniques

The following tools and equipment were used for the experimental set-up of batch experiments. Techniques and supporting institutions are summarized; if the institution is not mentioned measurements were performed at GRS gGmbH Braunschweig (Germany):

- Batch experiments
 - Sieve: Retsch Analysesieb, DIN 4188/DIN-ISO 3310-1, D-42759 Haan, Germany
 - Electrolyte: NaClO₄ hydrate salt, 99.99 %, trace metal basis, Aldrich, owned by Merck KGaA, Headquarter St. Louis, Missouri, U.S.A.; Sodium sulfate anhydrous, suprapur, Merck KGaA, Headquarter St. Louis, Missouri, U.S.A
 - Electrode: combined glass electrode, 6.0233.100 (Pt 1000), Metrohm; LL-Aquatrode plus with PT1000, 6.0257.600, Metrohm; Unitrode with Pt 1000, 6.0258.600, Metrohm
 - Bottles: 125 ml wide-mouth bottles, LDPE, NALGENE
 - Scale: AT261 Delta Range and Excellence plus XP 205, Delta Range®, METTLER TOLEDO, Gießen, Germany
 - Pipette: Eppendorf Research® plus, Eppendorf Research® pro
 - Magnetic stirrer: Heidolph magnetic stirrer, MR 1000 (Heidolph Instruments GmbH & Co. KG, Schwabach, Germany)
 - Europium ICP Standard, 1000 mg L⁻¹, Merck KGaA, Headquarter St. Louis, Missouri, U.S.A.
 - Nickel ICP Standard, 1000 mg L⁻¹, Merck KGaA, Headquarter St. Louis, Missouri, U.S.A.
 - Calcium ICP Standard, 1000 mg L⁻¹, Merck KGaA, Headquarter St. Louis, Missouri, U.S.A.
 - Aluminium ICP Standard, 1000 mg L⁻¹, Merck KGaA, Headquarter St. Louis, Missouri, U.S.A.

- Cesium ICP Standard, 1000 mg L⁻¹, Merck KGaA, Headquarter St. Louis, Missouri, U.S.A.
- Quartz fine granular, washed and calcined for analysis (order no.: 107536), Merck KGaA, Headquarter St. Louis, Missouri, U.S.A.
- Anotop syringe filter
- Acidification: Certified nitric acid, 65 % Suprapur®, Merck, Millipore, Merck KGaA, Headquarter St. Louis, Missouri, U.S.A.
- ICP-MS: Thermo Electron GmbH, X Series II, SN 1001 C
- Ultrapure water: Sartorius arium® pro, H2OPRO-UV-D, 18.2 mΩ
- Eu, Ni ICP-MS analysis uncertainty estimation (long-term precision measurements)
 - ICP-MS: Thermo Electron GmbH, X Series II, SN 1001 C
 - Europium ICP Standard, 1000 mg L⁻¹, Merck KGaA, Headquarter St. Louis, Missouri, U.S.A.
 - Nickel ICP Standard, 1000 mg L⁻¹, Merck KGaA, Headquarter St. Louis, Missouri, U.S.A.
 - Acidification: Certified nitric acid, 65 % Suprapur®, Merck, Millipore, Merck KGaA, Headquarter St. Louis, Missouri, U.S.A.
 - Ultrapure water: Sartorius arium® pro, H2OPRO-UV-D, 18.2 mΩ

A.5.2 Supplementary data of Eu batch experiments

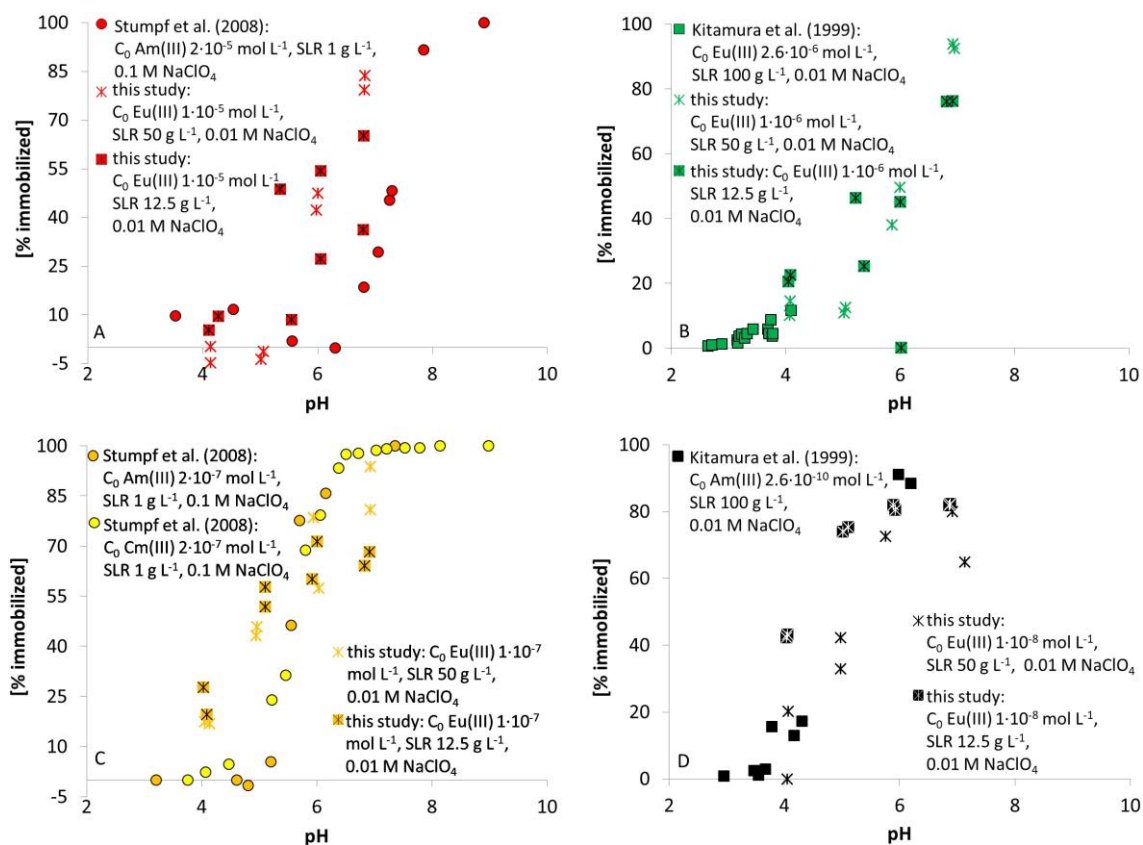


Fig. A. 24 Comparison between batch experimental data of Eu, Am, Cm on quartz from literature and data collected in this study (after /FRI 14/)

A: C_0 10^{-5} mol L⁻¹, M/V 1 – 50 g L⁻¹, 0.01 – 0.1 mol L⁻¹ NaClO₄.

B: C_0 10^{-6} mol L⁻¹, M/V 12.5 – 100 g L⁻¹, 0.01 mol L⁻¹ NaClO₄.

C: C_0 10^{-7} mol L⁻¹, M/V 1 – 50 g L⁻¹, 0.01 – 0.1 mol L⁻¹ NaClO₄.

D: C_0 10^{-10} mol L⁻¹ – 10^{-8} mol L⁻¹, M/V 12.5 – 100 g L⁻¹, 0.01 mol L⁻¹ NaClO₄.

A.5.3 Supplementary data of Al batch experiments

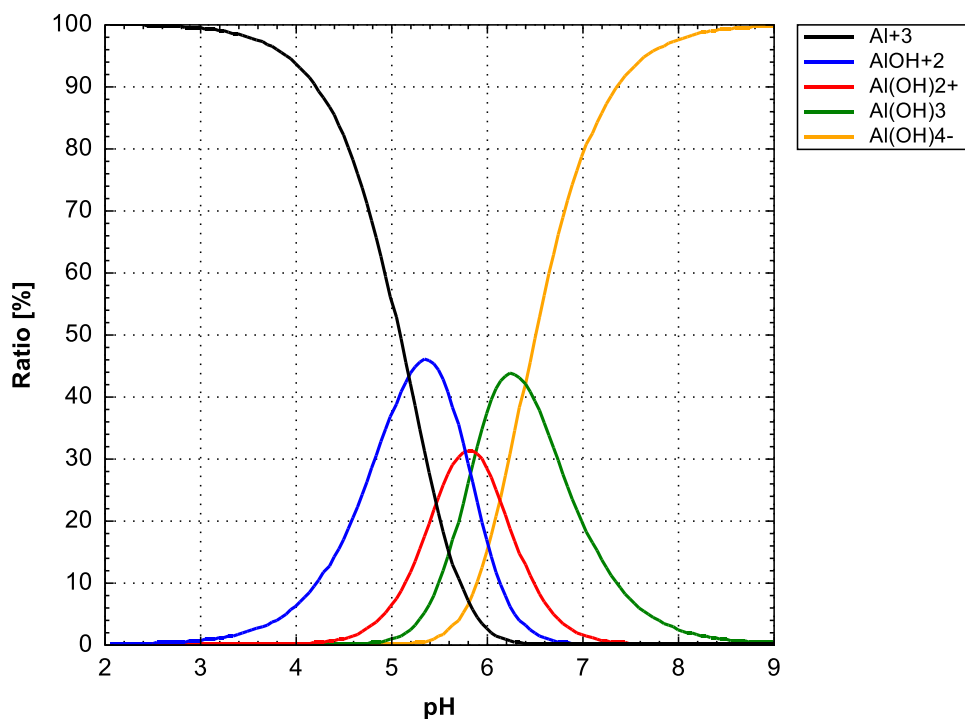


Fig. A. 25 Al speciation diagram in 0.01 mol L⁻¹ NaClO₄

Atmospheric conditions, 10⁻⁴ mol L⁻¹ Al.

A.5.4 Ni speciation

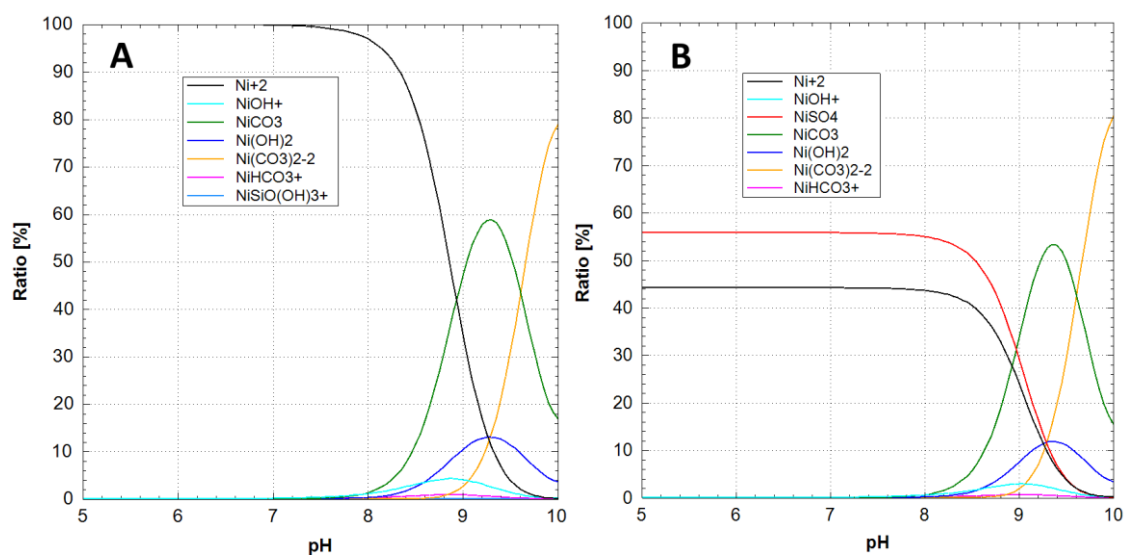


Fig. A. 26 Ni speciation diagrams with and without SO₄²⁻ in solution

A: 0.2 mol L⁻¹ NaClO₄, B: 0.066 mol L⁻¹ Na₂SO₄. Atmospheric conditions, 10⁻⁵ mol L⁻¹ Ni.

A.5.5 Estimation of Eu and Ni measurements uncertainties

Long-term precision measurements were carried out to assess Eu ICP-MS analyses uncertainties. Therefore, Eu and Ni samples were prepared with concentrations ranging between 10^{-5} – 10^{-8} mol L⁻¹ in 5 % HNO₃ background electrolyte. Samples were stored in chemically inert PFA vessels. ICP-MS measurements of samples were conducted over eight months: Twice a week for the first four months, the last four months samples were analyzed once a week.

From long-term precision measurements of Eu and Ni samples the relative standard deviation was calculated for each concentration. A logarithmic function was fitted to the relative standard deviation as a function of Eu concentration in solution and was used for the estimation of the ICP-MS measuring error for each batch sample. The double relative standard deviation was used to calculate Eu and Ni uptake uncertainties given in [%Eu immobilized]. Errors were used to illustrate measurement uncertainties (error bars), error estimations were not used for parameter optimization procedures with UCODE.

A.5.6 Preliminary tests for Ni batch sorption experiments

Pretests were conducted to design a proper experimental set-up of batch sorption experiments (Sec. 7.1) and to study Ni precipitation, formation of intrinsic Ni colloids, impact of syringe filters, sorption on vessel walls, and Ni sorption kinetics with quartz, orthoclase and muscovite under the given geochemical boundary conditions.

Investigation of Ni precipitation, formation of intrinsic Ni colloids

Since only sorption processes were supposed to be investigated precipitation and formation of intrinsic Ni colloids had to be avoided. Ni solutions were prepared in PFA bottles in the same way as they were used as stock solutions (dilutions of acidified Ni standard solution) for batch sorption experiments. In batch sorption experiments a definite amount of the stock solutions was added to batch sorption samples to adjust their initial concentrations. Stock solutions were fixed to higher pH values to avoid a shift in pH of batch samples after addition.

Stock solution A (first dilution step of the Ni standard) contained $4.26 \cdot 10^{-4}$ mol L⁻¹ Ni in a 0.01 M NaClO₄ background solution was adjusted to pH ~ 6 through NaOH. At this pH

PHREEQC calculations showed no precipitation of nickel hydroxides and carbonates. Stock solution B, prepared through dilution of solution A, had a concentration of $4.26 \cdot 10^{-5}$ mol L⁻¹ Ni. This solution was analyzed with ICP-MS in the beginning ($t = 0$) and after 7 days. During this time the solution was not moved. Samples were analyzed after following treatments: unfiltered, filtered with 0.2 μ m cellulose acetate, 0.1 μ m PTFE and 0.02 μ m alumina syringe filters. At $t = 0$ target concentration of $4.26 \cdot 10^{-5}$ mol L⁻¹ Ni was observed for all filter types (data not shown here). After 7 days no differences in concentrations between the filtration treatments were observed. Thus, no precipitation or formation of intrinsic Ni colloids $> 0.02 \mu$ m was observed to any significant amounts.

Impact of syringe filters

Another pretest was conducted to reveal whether filtration had an impact on low Ni concentrations. It was assumed that the lower the concentration, the higher a potential filtration impact. Therefore, a solution was prepared in a PFA bottle containing 10^{-7} mol L⁻¹ Ni in 0.01 M NaClO₄ background solution and adjusted to pH ~ 6 through NaOH. Again, samples were analyzed after following treatments: unfiltered, filtered with 0.2 μ m cellulose acetate, 0.1 μ m PTFE and 0.02 μ m alumina syringe filters. Samples were taken immediately after pH adjustment. The applied syringe filters showed no significant influence on Ni concentration (data not shown here).

Ni sorption on LDPE and PFA vessel walls

Former conducted batch experiments showed a remarkable chemical affinity of Eu³⁺ for LDPE and PFA vessel walls (data not shown). LDPE bottles were also used in batch sorption experiments with Ni. Therefore, a pretest should assess the affinity of Ni. As an alternative PFA vessels were investigated as well.

LDPE and PFA vessels were filled with 0.01 M NaClO₄ background solution. Experiments were conducted between pH 5-8. An initial concentration of $5 \cdot 10^{-7}$ mol L⁻¹ Ni was applied. Samples were taken after 0, 1, 2 and 7 days. As a result, Ni sorption on vessel walls could not be observed. Detailed information may be obtained from /HAL 15/.

Sorption kinetics of Ni(II) with orthoclase, muscovite and quartz

Batch experiments were conducted as described in Section 7.1. Different equilibration times (contact time between sorbate and sorbent) were applied to investigate the

sorption kinetics of Ni with orthoclase, muscovite and quartz. Results indicate that equilibration of Ni with quartz is reached within 3 d (digi. App. Fig. A. 27), orthoclase within 7 d (digi. App. Fig. A. 28) and muscovite within 14 d (digi. App. Fig. A. 29, cf. /HAL 15/). Error bars in Fig. A. 27 – Fig. A. 29 in the digital appendix represent the double standard deviation of the Ni measurement uncertainty of the ICP-MS which was calculated by 10^{-7} mol L⁻¹ Ni long term precision measurements of the ICP-MS (digi. App. Sec. A.5.4).

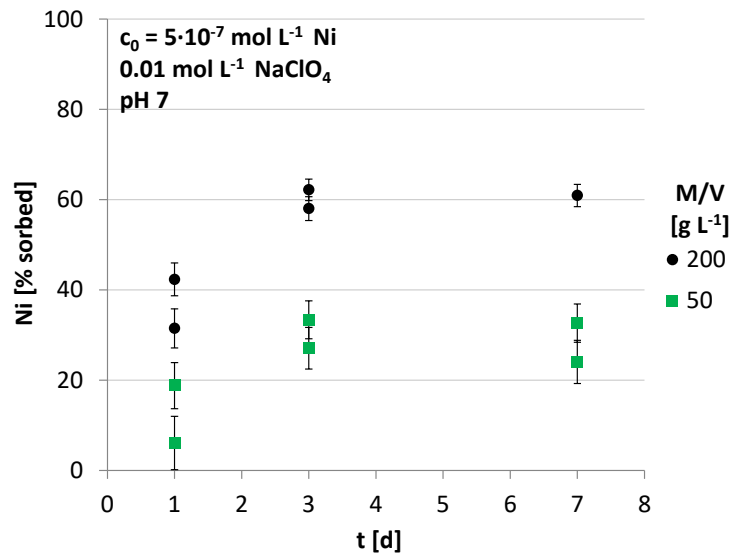


Fig. A. 27 Batch experiments: sorption kinetics of Ni with quartz

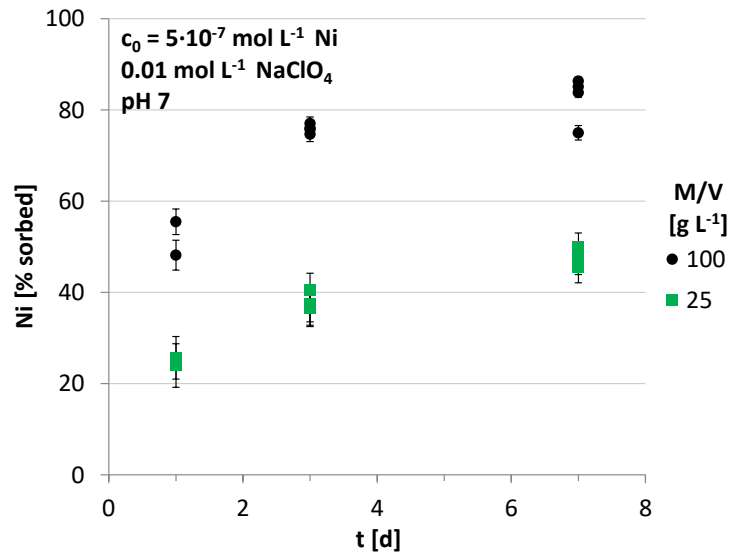


Fig. A. 28 Batch experiments: sorption kinetics of Ni with orthoclase

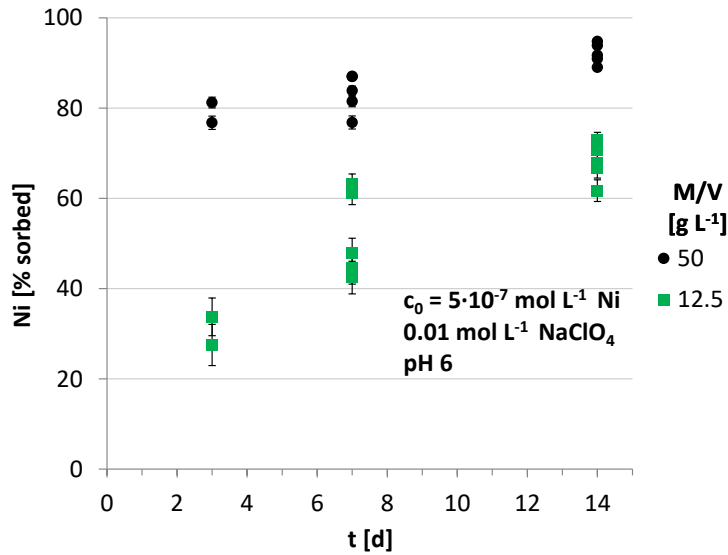


Fig. A. 29 Batch experiments: sorption kinetics of Ni with muscovite

A.5.7 Preliminary tests for Ca batch sorption experiments

Pretests were conducted to design a proper experimental set-up of batch sorption experiments (Sec. 7.1) concerning Ca sorption kinetics with orthoclase and muscovite.

Kinetic sorption results indicate that sorption equilibrium was reached within 7 d for orthoclase and muscovite (digi. App. Fig. A. 30).

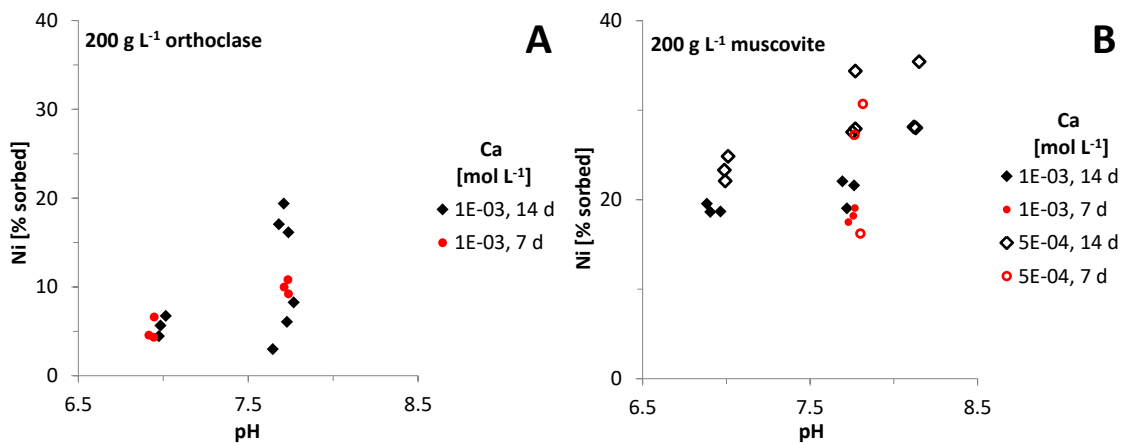


Fig. A. 30 Kinetics of Ca sorption with orthoclase and muscovite

A: orthoclase, B: muscovite. 0.01 M NaClO₄ background solution. Samples were taken after 7 d (red data) or 14 d (black data) equilibration time.

A.6 U(VI), Np(V), and Nd(III) batch experiments

Batch experiments with U, Np, and Nd were performed as described in Section 7.2. To understand the mobilization and immobilization of these elements some pre-calculations were conducted to design a proper experimental set-up of the batch sorption experiments.

A.6.1 Aqueous speciation and complex formation

The aqueous speciation of 10^{-5} mol L⁻¹ U(VI), Np(V), and Nd(III) in 0.01 mol L⁻¹ NaClO₄ was calculated with PHREEQC /PAR 13/ using the project-specific database WEIMAR_EDH.dat (Sec. 6.1) taking into account also the elements leached from the minerals. For U(VI) it was calculated in the absence and presence of 1.5×10^{-3} mol L⁻¹ Ca²⁺.

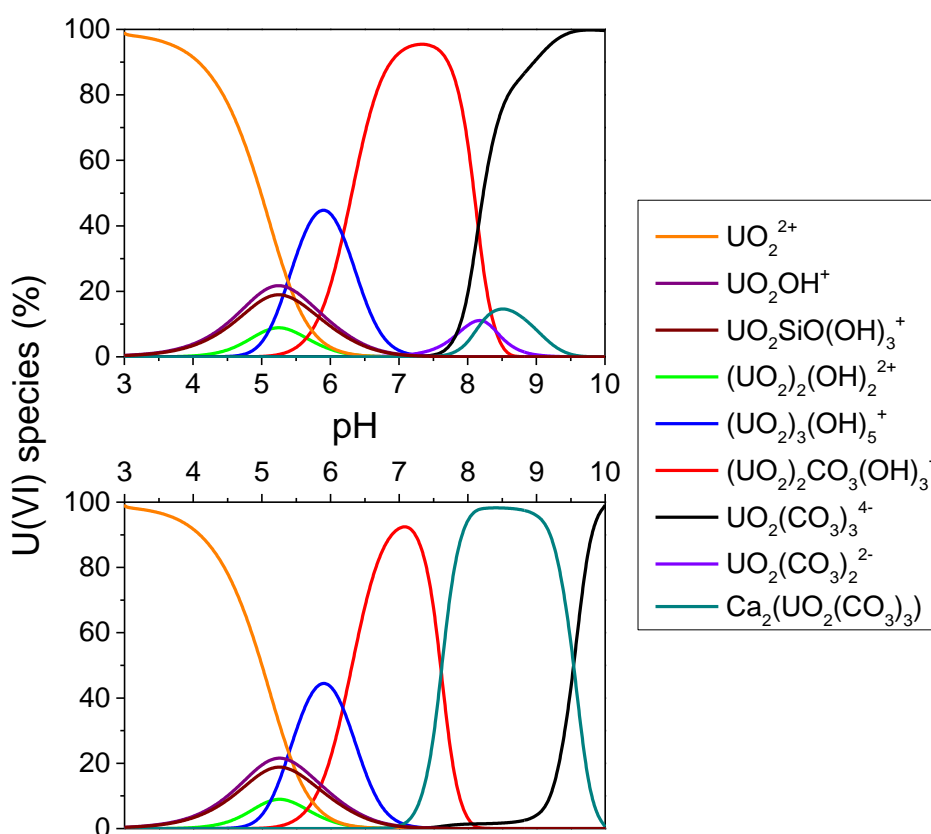


Fig. A. 31 Aquatic U(VI) speciation of orthoclase supernatant with 10^{-5} mol L⁻¹ U(VI) in 0.01 mol L⁻¹ NaClO₄ without addition of Ca²⁺ (top) and with 1.5×10^{-3} mol L⁻¹ Ca²⁺ (bottom) under ambient atmosphere and at room temperature

When the leached elements of the minerals were neglected, the only noted change was that the $\text{UO}_2\text{SiO}(\text{OH})_3^+$ complex, occurring between pH 4 and 6, was not present. This influences the U(VI) speciation from pH 4 to 7. At acidic pH values, the free uranyl(VI) ion dominates the speciation in all calculations. From pH ≥ 4 onwards the concentration of the complex UO_2OH^+ (and to a lesser degree $(\text{UO}_2)_2(\text{OH})_2^{2+}$) increases. In the pH range from pH 5 to 7 the species $(\text{UO}_2)_3(\text{OH})_5^+$ is predominant. At higher pH values the carbonate complexes $(\text{UO}_2)_2\text{CO}_3(\text{OH})_3^-$; $\text{UO}_2(\text{CO}_3)_2^{2-}$; $\text{Ca}_2\text{UO}_2(\text{CO}_3)_3$, and $\text{UO}_2(\text{CO}_3)_3^{4-}$ are present. With $1.5 \times 10^{-3} \text{ mol L}^{-1} \text{ Ca}^{2+}$, $\text{UO}_2(\text{CO}_3)_2^{2-}$ is suppressed and $\text{Ca}_2\text{UO}_2(\text{CO}_3)_3$ dominates the speciation between pH 8 and 10.

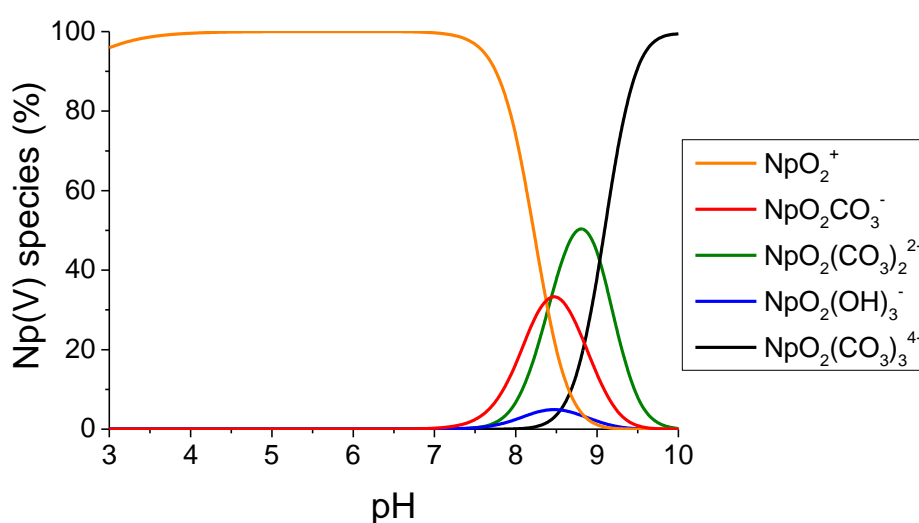


Fig. A. 32 Aquatic speciation of $10^{-5} \text{ mol L}^{-1} \text{ Np(V)}$ in $0.01 \text{ mol L}^{-1} \text{ NaClO}_4$ under ambient atmosphere and at room temperature

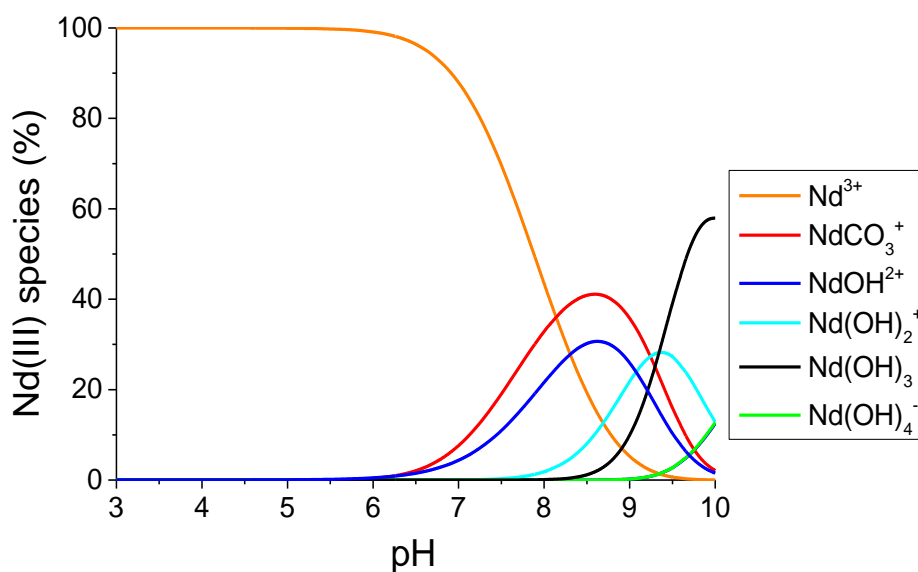


Fig. A. 33 Aquatic speciation of 10^{-5} mol L⁻¹ Nd(III) in 0.01 mol L⁻¹ NaClO₄ under ambient atmosphere and at room temperature.

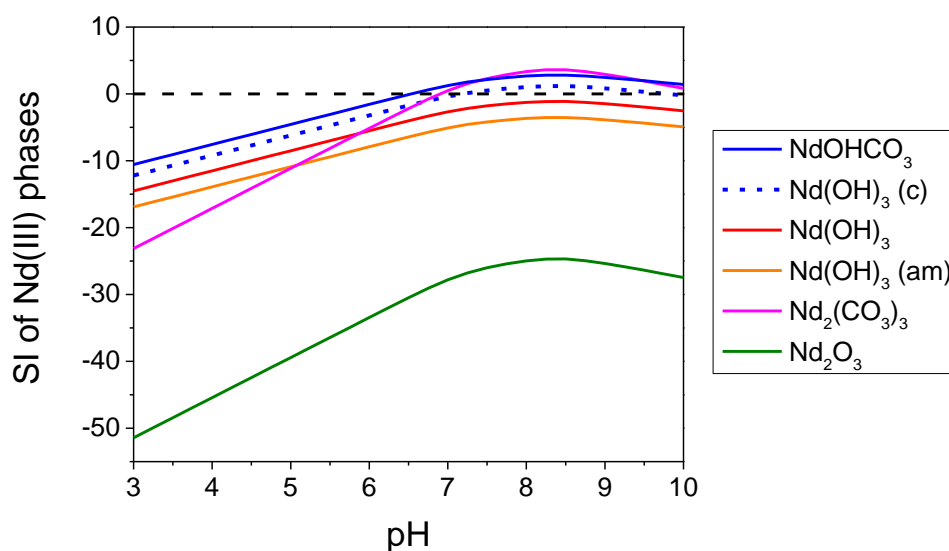


Fig. A. 34 Saturation indices of Nd(III) phases calculated with PhreeqC (10^{-5} mol L⁻¹ Nd(III), 0.01 mol L⁻¹ NaClO₄, ambient atmosphere, at room temperature). SI values > 0 indicate the formation of a precipitate

A.6.2 Nd(III) batch experiments

To be sure that no precipitation of Nd(III) in solution takes place, the scattered light intensity (using a Zetasizer Nano ZS, Malvern Instruments) of Nd(III) solutions in different concentrations was measured (Tab. A. 5).

Tab. A. 5 Scattered light intensity (SLI in kilo counts per second / kcps) of Nd(III) as a function of pH at two different concentrations in 0.01 mol L⁻¹ NaClO₄

pH (10 ⁻⁵ mol L ⁻¹ Nd)	SLI in kcps	pH (10 ⁻⁴ mol L ⁻¹ Nd)	SLI in kcps
3	42	3	70.4
3.5	43.6		
4	31.9	4	47.2
4.5	107.1		
5	39.6	5	59
5.5	53.5		
6	50.7	6	57.2
6.5	51.2		
7	40.2	7	540
7.5	50.4		
8	110.2	8	1116

The background values for pure water and 0.01 mol L⁻¹ NaClO₄ without Nd were between 40 and 60 kcps. Whereas for concentrations of 10⁻⁵ mol L⁻¹ Nd there was no significant increase due to a precipitation at all pH values, at 10⁻⁴ mol L⁻¹ Nd the scattered light increased at pH 7 and higher. Therefore, the sorption experiments were performed in lower concentrations and the stock solution was prepared at acidic pH values to avoid a precipitation of Nd phases such as Nd(OH)₃(am), Nd₂(CO₃)₃, or NdCO₃OH.

A.7 Microbial effects on sorption processes

Microorganisms (i. e., bacteria, archea, fungi, etc.) are ubiquitous in nature and are also present at actinide-contaminated sites /KRA 11/. They are often attached in large communities (so called biofilms) to mineral surfaces linked by extracellular polymeric substances /ALA 06/. Single individual bacteria as well as biofilms can impact the actinide speciation in many ways /NEW 14/. At neutral pH bacterial cell walls are typically negatively charged leading to a high affinity for metal cations like actinides. This can result in an accumulation and transformation of actinides into different species. For example, reducing conditions of cell surface regions can lead to reduced forms of redox-sensitive actinides /GRO 07/. In contrast, some bacteria can oxidize actinides, and thus produce more soluble species. Consequently, the interaction of actinides with microorganisms in the form of bioreduction, biosorption, biomineralization, bioaccumulation, or biotransformation can cause mobilization as well as immobilization /NEW 14/.

Sorption experiments were performed with commercially available natural minerals. Thus, the question arose if there are microorganisms associated with the minerals, and if so, how they affect the sorption process. Consequently, different experiments have been performed that shall provide some insight into such microbial effects.

A.7.1 Microbial growth monitoring

To stimulate the bacterial growth 0.2 g of quartz, orthoclase and muscovite were taken into 15 mL tubes. The samples were incubated in 10 mL of two different culture media a) the standard Nutrient broth (NB) (SIFIN GmbH, Berlin, 5 g L⁻¹ meat peptone, 5 g L⁻¹ meat extract, pH 7) for the growth of unambitious microorganisms and b) the Reasoner's 2A (R2A) culture medium (0.5 g L⁻¹ yeast extract, 0.5 g L⁻¹ bacto™ peptone, 0.5 g L⁻¹ bacto™ casitone, 0.5 g L⁻¹ glucose, 0.5 g L⁻¹ soluble starch, 0.3 g L⁻¹ K₂HPO₄, 0.05 g L⁻¹ MgSO₄·7 H₂O, 0.3 g L⁻¹ sodium pyruvate, pH 7.2) for bacteria which normally inhabit potable water under laminar flow conditions as well as in 0.01 mol L⁻¹ NaClO₄ as control. For each culture media one sample without mineral was prepared as reference. All experiments were triplicates.

The measurement of the optical density at 600 nm (OD₆₀₀) over time allowed monitoring of the growth of microorganisms, and was performed with a UV/Visible spectrophotometer (Ultrospe 1000, Pharmacia Biotech). For measurements, the samples were shaken, and following sedimentation for 30 s 1 mL of the supernatant was transferred to a cuvette. The OD₆₀₀ was measured directly after adding the culture media to the mineral, after three weeks of incubation, and once more after three months. In the meantime the samples with culture media were shaken at 30°C to promote the growth of microorganisms. Control samples containing 0.01 mol L⁻¹ NaClO₄ were shaken at room temperature to simulate conditions similar to batch experiments. Samples containing culture media and no mineral were set as references.

Additionally, optical microscopy was used to visualize the microbial cultures present on the minerals. Therefore, after a live-dead staining with LIVE/DEAD® Bac Light™ Bacterial Viability Kit L7012, Molecular Probes was used on the minerals incubated for three days in autoclaved ultrapure water, and optical microscopy (Olympus BX61) with an excitation filter U-MSWB2 (420-480 nm) and U-MSWG2 (480-550 nm) was performed.

The difference after three weeks and after three months for the mineral suspensions in both, culture media and in 0.01 mol L⁻¹ NaClO₄, is shown in Tab. A. 6.

Tab. A. 6 Optical Density (OD₆₀₀) of quartz, orthoclase and muscovite samples in a NB and R2A culture medium as well as in 0.01 mol L⁻¹ NaClO₄

mineral	medium	ΔOD*(3 weeks)	ΔOD**(3 month)
	NB	0.68 ± 0.13	0.59 ± 0.20
quartz	R2A	0.41 ± 0.24	0.47 ± 0.10
	0.01 M NaClO ₄	0.01 ± 0.01	0.00 ± 0.01
	NB	0.12 ± 0.13	0.74 ± 0.55
orthoclase	R2A	0.36 ± 0.25	0.42 ± 0.17
	0.01 M NaClO ₄	0.05 ± 0.01	0.03 ± 0.01
	NB	0.43 ± 0.16	0.67 ± 0.25
muscovite	R2A	0.76 ± 0.26	0.66 ± 0.19
	0.01 M NaClO ₄	0.22 ± 0.06	0.10 ± 0.16

* OD (t = 3 weeks) – OD (t = 0)

** OD (t = 3 months) – OD (t = 0)

For all minerals an increase in OD with time was observed. These results indicated that both nutrient conditions favored the growth of microorganisms attached to the mineral samples. Not surprisingly the samples in 0.01 mol L⁻¹ NaClO₄ showed a much smaller increase than the samples in culture media. Additionally, there may even be a contribution to the observed OD increase by abiotic effects, e. g., through the presence of small (colloidal) mineral particles. For orthoclase the increase in OD was lower than for quartz or muscovite. Probably, the microorganisms on orthoclase were less cultivable at these conditions than on the other minerals. Both culture media delivered different nutrients, thus promoting the growth of different microbial species. This may explain the differences between the OD values for the same mineral in both culture media.

A.7.2 Electron and optical microscopy

Scanning electron microscopy (SEM) images (Hitachi S-4800) were taken of the mineral samples before and after autoclaving to see if the increased heat and pressure due to autoclaving affect the surface of the minerals. The images showed no significant change of the surface, thus autoclaving don not show large effect on the mineral surface and affects only the microorganisms.

Furthermore, optical microscopy was performed after live-dead staining with LIVE/DEAD® Bac Light™ Bacterial Viability Kit L7012, Molecular Probes on the mineral samples. The presence of microorganisms on the minerals was proven by these microscopic investigations. Microbes are marked in the images with red arrows (digi. App. Fig. A. 35 – Fig. A. 37).

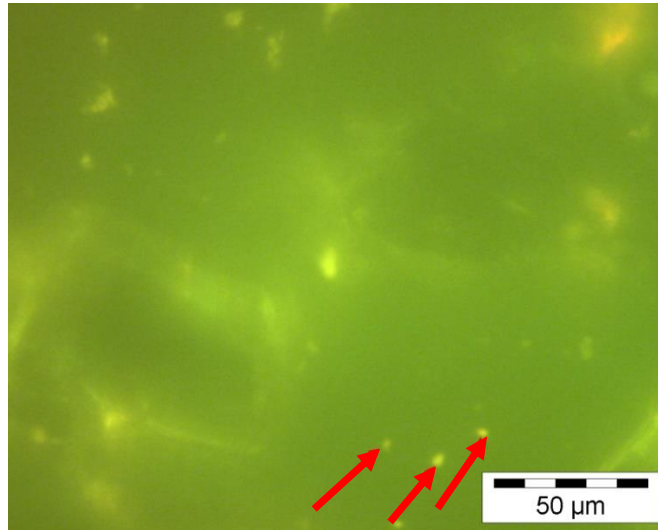


Fig. A. 35 Image of microscopy of orthoclase with live-dead stain

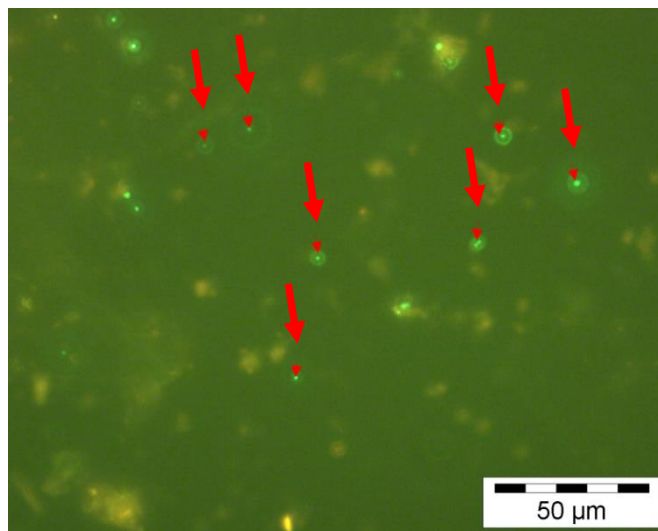


Fig. A. 36 Image of microscopy of muscovite with live-dead stain

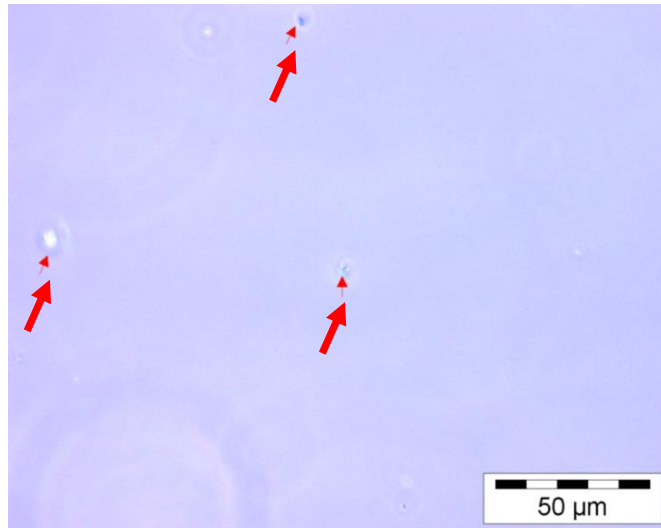


Fig. A. 37 Image of microscopy of quartz with live-dead stain

These results showed that typically microorganisms were present during experiments with the natural minerals used in this work. Thus, it was necessary to know what kinds of microorganisms were present and how they affected the sorption processes.

A.7.3 Sequencing

To clarify which kind of microbes were contained in the samples and where they originate from, the DNA of the microbes were isolated from the minerals (PowerWater DNA isolation kit) and cloned. After a restriction fragment length polymorphism analysis has been done, clones that are different were sent to the gene sequence analysis. The results showed that each mineral contains different kinds of microorganisms representing the different origin of the minerals (Fig. A. 38).

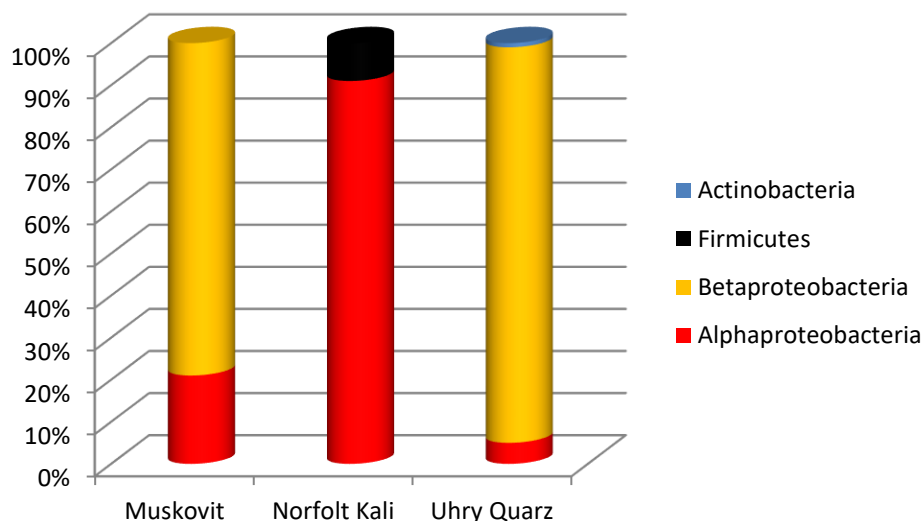


Fig. A. 38 Bacterial distribution on muscovite, orthoclase and quartz

There were no microbes contained in the minerals that originate from human skin (e. g. hand surfaces) but some soil microbes were present. Thus, the microbes were not in the samples because of the work in the lab, but they were rather bound to the pristine minerals from the area where they were mined and processed. A detailed look on the species of microbes can be found in /RIC 15/.

A.7.4 Microbial effects on U(VI) sorption

To investigate if there is an influence of this microorganisms in the utilized minerals on the U(VI) sorption, batch experiments were done under different conditions as summarized in Tab. A. 7. The experiment was conducted as a threefold measurement.

Autoclaving was used to avoid contaminations e. g., in growth media by external organisms. In the case of this work, the samples (mineral and background solution) were autoclaved to kill the contained microorganisms. A laminar flow box was also used to avoid the intake of microorganisms in the samples via air. Furthermore, some samples were treated in darkness to see if there are some microbes favoring growth under light or dark conditions. The last treatment to mention is the use of sodium azide (NaN_3) as an inhibitor, which acts in the way that it effectively suppresses microbial respiration and the activity of the relevant enzymes. This essentially inhibits the growth of microorganisms, but it does not kill them /WAN 05a/.

Tab. A. 7 Summary of all parameters for batch experiments referring to an influence of microorganisms

U(VI) (orthoclase, muscovite, quartz)					
ionic strength	0.01 M NaClO ₄				
solid-to-liquid ratio	1/20 (0.5 g mineral in 10 ml NaClO ₄)				
pH	7				
c(U)	10 ⁻⁶ M				
treatment	Not autoclaved	autoclaved	autoclaved, under a laminar flow box		not autoclaved with sodium azide
	without light	without light	with daylight	without light	with daylight

The results of these batch experiments are shown in Fig. A. 39. In the case of orthoclase and muscovite, the highest sorption of U(VI) was observed after treatment with sodium azide (NaN₃) as an inhibitor, which acts in the way that it effectively suppresses microbial respiration and the activity of the relevant enzymes. All other treatments showed only a slight sorption increase compared to the non-autoclaved sample at daylight. In case of quartz, the use of laminar boxes leads to the highest sorption. For muscovite, the combination of laminar flow box, autoclaving, and darkness, affects sorption the most. Here, the microbes obviously enhance sorption (dead or alive). This can be because from the fact that dead biomass sorbs better than live one /KUR 82/. Not all observed changes were significant. However, variations in sorption of U(VI) observed at different conditions cannot be attributed as a significant influence of the microorganisms.

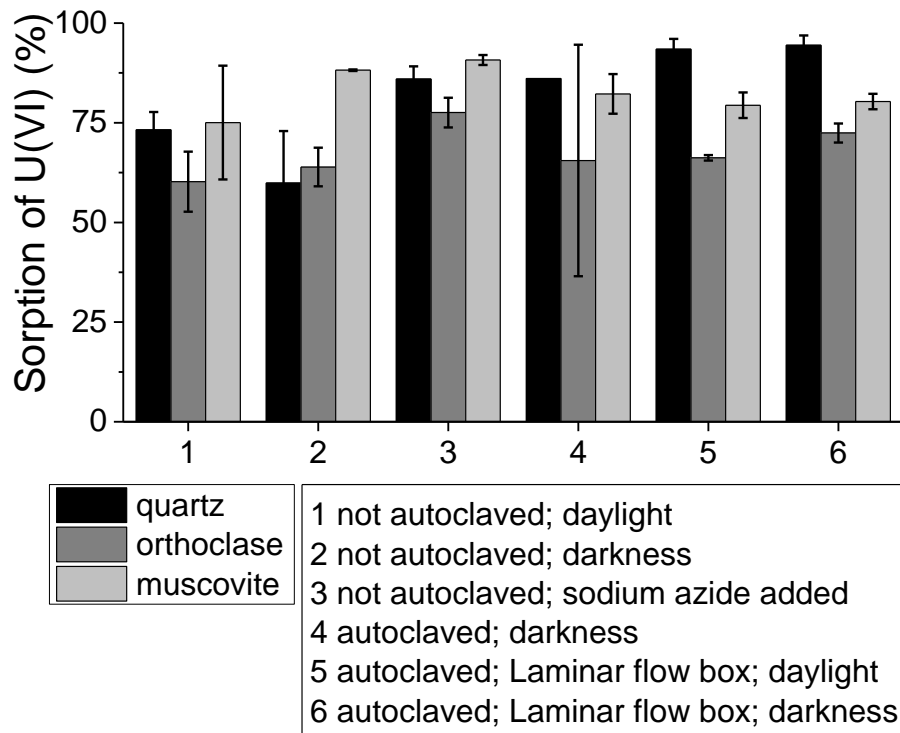


Fig. A. 39 U(VI) sorption onto quartz, orthoclase, and muscovite (0.5 g mineral in 10 mL 0.01 mol L⁻¹ NaClO₄) according to the influence of microorganisms at pH 7 and an initial U(VI) concentration of 10⁻⁶ mol L⁻¹

Spectroscopic investigations of the U(VI) surface species for orthoclase showed that in all samples the same species were dominating. Thus, no changes of surface species due to microorganisms occur. For quartz a variation of the dominant species was observed. This might be due to different binding forms affected by the treatment. Detailed information is given in /RIC 15/.

A.8 Transport experiments with europium and nickel

In the following, tools, equipment, chemicals, and techniques used for the experimental set-up of column experiments are summarized:

- Preconditioning (cf. digi. App. Sec. A.8.1 in the appendix)
 - Temperature: ALMEMO MA 10302, Pt 100, Ahlborn, Holzkirchen, Deutschland (ZA 9030-FS7, Norm E4) calibrated thermometer (German Calibration Service, DKD-K-06701)

- Electrolyte: NaClO₄ hydrate salt, 99.99 %, trace metal basis, Aldrich, owned by Merck KGaA, Headquarter St. Louis, Missouri, U.S.A.
- pH meter and electrode: Metrohm 827 pH lab, 6.0234.100 and Metrohm glass microelectrode (178 mm) (Metrohm AG, Herisau, Switzerland)
- Syringe filter: Minisart, syringe filter, 0.2 µm, cellulose acetate membrane, Sartorius, Göttingen, Germany
- ICP-MS, ICP-OES: Specifications given in Appendix A.2.1
- pH adjustment: Certified nitric acid, 65 % Suprapur®, Millipore, Merck KGaA, Headquarter St. Louis, Missouri, U.S.A.
- N₂-atmosphere: N₂, nitrogen 4.8, ISO 14175-N1-N, 99.998 Vol% N₂
- Glove box: Plas Labs, model 815-PGB/EXP, no 22105, Lansing, MI 48606, USA
- Sterile pipettes: TPP, Tissue culture and laboratory inventory, 2 ml, sterile serological pipettes
- Drying chamber: Binder FED 115, 283.15 – 573.15 K, 60 Hz, No 990580, Binder GmbH, 78532 Tullingen, Germany
- Autoclave treatment of mineral samples and equipment for preconditioning of minerals were performed at the Helmholtz-Zentrum Dresden-Rossendorf e.V.
- Column experiments
 - Background electrolytes:
 - NaClO₄: NaClO₄·xH₂O, trace metal basis, 99.99 %, Aldrich, owned by Merck KGaA, Headquarter St. Louis, Missouri, U.S.A.
 - Na₂SO₄: Sodium sulfate decahydrate, p.a., EMSURE®, Merck KGaA, Headquarter St. Louis, Missouri, U.S.A.; Sodium sulfate anhydrous, suprapur, Merck KGaA, Headquarter St. Louis, Missouri, U.S.A.
 - Artificial groundwater: See Tab. A. 8 in the appendix.
 - pH adjustment:
 - 65 % HNO₃: certified nitric acid, 65 % Suprapur®, Merck Millipore, Merck KGaA, Headquarters St. Louis, Missouri, U.S.A.

- NaOH: Titrisol, NaOH for 1000 ml, 1 mol L⁻¹, Merck KGaA, Headquarters St. Louis, Missouri, U.S.A.
- pH meter and electrode: Metrohm 827 pH lab, 6.0234.100 and Metrohm glass microelectrode (178 mm) (Metrohm AG, Herisau, Switzerland); LL-Aquatrode plus with PT1000, 6.0257.600, Metrohm
- Pipette: Eppendorf Research® plus, Eppendorf Research® pro
- Eu: Europium ICP Standard, 1000 mg L⁻¹, Merck KGaA, Headquarters St. Louis, Missouri, U.S.A.
- Nickel ICP Standard, 1000 mg L⁻¹, Merck KGaA, Headquarter St. Louis, Missouri, U.S.A.
- NaBr: NaBr suprapure®, 99.995 %, Merck KGaA, Headquarters St. Louis, Missouri, U.S.A.
- Peristaltic pump: IPC High Precision Multichannel Dispenser, ISM932D, ISMATEC, Cole-Parmer GmbH, Wertheim, Germany
- Peristaltic pump tubing: Fluran®Tubing, F5500-a (ISMATEC, IDEX Health & Science, Cole-Parmer GmbH, Wertheim, Germany).
- Fraction collector: Retriever 500 TELEDYNE ISCO, Lincoln, Nebraska, U.S.A.
- 65 % HNO₃: Specifications given above (v.s.)
- Syringe filter: Specifications given above (v.s.)
- Scale: AT261 Delta Range and Excellence plus XP 205, Delta Range®, METTLER TOLEDO, Gießen, Germany

A.8.1 Preconditioning of minerals for Eu and Ni column experiments

All mineral samples except for quartz underwent preconditioning procedures before transport experiments were initiated; quartz was used as provided by the supplier (Sec. 5.1.1). Muscovite and orthoclase underwent two different preconditioning treatments: In a first step (i), the muscovite and freshly milled orthoclase were suspended in NaClO₄, pH 7 to equilibrate the mineral surfaces with NaClO₄ background electrolyte. In a second step (ii), equilibrated minerals were preconditioned with NaClO₄ to the

according pH_{ini} of each column experiment to reduce the equilibration time between the solids and the background electrolyte during column experiments.

- **(i) Equilibration with NaClO_4 electrolyte, pH 7**

Milling of orthoclase resulted in freshly cleaved grains and potentially highly reactive surfaces which are not typical for naturally equilibrated systems. Muscovite on the other hand was provided by the supplier without information of mining conditions and pretreatment of the mineral. To create a sound basis for comparability 5 kg of each mineral were preconditioned in 20 L 0.05 mol L^{-1} NaClO_4 background electrolyte over approximately three months. Equilibration took place under ambient conditions in lightproof containers at $294.7 \text{ K} \pm 0.6 \text{ K}$ (\pm single standard deviation). On an everyday basis samples were stirred and the pH was measured. In regular time intervals samples from the supernatant solution were taken, filtered, and analyzed for Ti, Mn, Sr, Ba, Co, Cu, Zn, Cd, Eu, Pb, U (ICP-MS) and Al, Ca, Fe, K, Mg, Si (ICP-OES). The systems were assumed to be equilibrated after element concentrations and pH reached a constant level.

- **(ii) Preconditioning of mineral surfaces with NaClO_4 , pH adjustment to pH_{ini}**

A prerequisite for column experiments was a chemical equilibrium between the minerals and the background electrolytes: Equilibration was attained after the effluent pH of the column (pH_{equil}) equaled pH_{ini} of the background electrolyte (Sec. 9.1). This second preconditioning procedure was necessary to decrease equilibration times of column experiments to feasible time frames since pretests had shown that equilibration of column systems exceeded six months when mineral samples from preconditioning step (i) (v.s.) were used.

For the second preconditioning procedure, mineral samples and equipment (glass bottles, NaClO_4 electrolytes, screw caps, etc.) were autoclaved at 394 K over 20 minutes. The autoclaved orthoclase and muscovite samples were subsequently suspended in 10 mmol L^{-1} NaClO_4 with respective pH_{ini} values under N_2 atmosphere in a glove. The glove box itself and all equipment that was transferred into the glove box were sterilized with 70 % alcohol. The autoclaving and sterilization approach was necessary to minimize the possibility of algae growth during the second preconditioning step. Furthermore, influences caused by organic remains on the mineral surfaces were also eliminated. The adjustment of the suspension pH was achieved via the addition of appropriate amounts of 65 % HNO_3 on a daily basis during the first weeks; time intervals were extended as buffer capacities of the minerals reduced

over time. Samples were shaken on a daily basis. For pH measuring purposes sterile disposable pipettes were used to obtain approximately 2 ml aliquots from the suspensions. pH measurements were carried out outside the glove box under ambient conditions. After $pH_{\text{equil}} = \text{const.}$, suspensions were decanted and solids dried at 303 K in a drying chamber.

Orthoclase and muscovite samples used for column experiments underwent preconditioning procedure (i) and (ii) and are referred to as "preconditioned mineral(s)".

A.8.2 Composition of the artificial groundwater after /KLI 02b/

The artificial groundwater composition was used as suggested by /KLI 02b/ and /NOS 12a/ and represented a groundwater composition present at the Gorleben reference site. The NaHCO_3 concentration was decreased in relation to the /KLI 02b/ composition which was necessary to prevent degassing of CO_2 at pH 3.5. The geochemical speciation calculations with PHREEQC provided the maximum possible HCO_3^- concentration without degassing of CO_2 at pH 3.5 (PHREEQC calculation not provided here). Ion balance was reached with adaptations of Na^+ concentrations. The exact composition of the artificial groundwater as used in this study is provided in Appendix Tab. A. 8.

Tab. A. 8 Composition /KLI 02b/, /NOS 12a/ and specification of chemicals used for the artificial groundwater

NaHCO_3 concentration was decreased to prevent degassing of CO_2 at pH 3.5, ion balance was reached with adaptations of Na^+ . Salts and ICP standard from Merck KGaA, Darmstadt, Germany (Headquarters St. Louis, Missouri, U.S.A.).

Salt	Specification	Concentration [mol L ⁻¹]
$\text{CaSO}_4 \cdot 2\text{H}_2\text{O}$	2161.0500, p.a.	$2.84 \cdot 10^{-4}$
$\text{Ca}(\text{Cl})_2 \cdot \text{H}_2\text{O}$	1.42000.5000, p.a., EMPROVE®	$9.21 \cdot 10^{-4}$
NaHCO_3	1.6329.0500, p.a.	$1.50 \cdot 10^{-5}$
NaCl	1.06404.100, p.a., EMSURE®	$4.24 \cdot 10^{-4}$
KCl	1.04936.1000, p.a., EMSURE®	$5.40 \cdot 10^{-5}$
$\text{Mg}(\text{Cl})_2 \cdot 6\text{H}_2\text{O}$	1.05833.1000, p.a., EMSURE®	$1.67 \cdot 10^{-4}$
$\text{Al}(\text{NO}_3)_3$	Aluminium ICP Standard, 1000 mg L ⁻¹	$1.85 \cdot 10^{-6}$

A.9 Pretests of uranium(VI) column experiments

To begin with, breakthrough curves (BTCs) and spatial distributions (SDs) of U(VI) in quartz columns were collected to get a detailed overview of transport and sorption characteristics under the given geochemical conditions. After this first experiments, a new set of column experiments was conducted and terminated before U(VI) was detected in the effluent of the column. Based on this data, a feasible time to stop U(VI) column experiments was determined to identify U(VI) surface complexes as described in Section 9.3. Experiments were carried out in doublets to check for reproducibility.

Three column experiments (quartz III – quartz V) were conducted. The experimental set up of quartz III – quartz V followed the approach described in Section 9.1. All column experiments were filled with quartz (Sec. 5.1.1).

The aim of the first column experiment (quartz III) was the measurement of a U(VI) breakthrough curve. The bulk density of this first column equaled 1.64 g cm^3 with a pore volume of 38 %. As a background electrolyte $0.01 \text{ mol L}^{-1} \text{ NaClO}_4$ ($\text{pH}_{\text{ini}} = 4.9$) was applied with a flow rate of 0.28 ml min^{-1} . After equilibration (3 d), a pulse input of 2 PV (PV [V/V_0]) peak solution ($8.99 \cdot 10^{-6} \text{ mol L}^{-1} \text{ U(VI)}$, $\text{NaBr } 1.32 \cdot 10^{-5} \text{ mol L}^{-1}$) was injected into the column. The development of pH, U(VI) and Br concentrations were measured in the effluent of the column and are illustrated in Fig. 7.3 for quartz III.

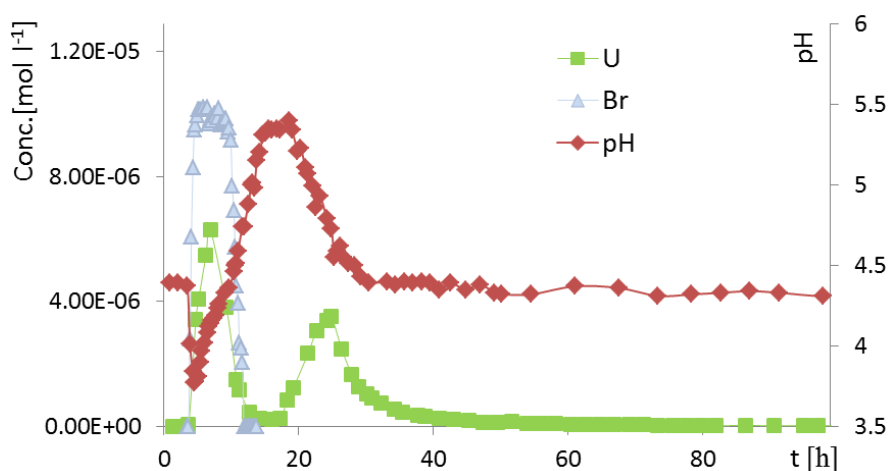


Fig. A. 40 Quartz III: Development of pH, U(VI) and Br concentrations

NaBr tracer – blue characters, pH development – red symbols, U(VI) development – green symbols. $\text{pH}_{\text{ini}} 4.3$.

As shown in Fig. A. 40, at $t = 0$ h U(VI) and Br were injected into the column. The experiment was finished after 130 h after the U(VI) concentration exceeded the limit of determination ($3.4 \cdot 10^{-11}$ mol L⁻¹ U(VI)). The first Br concentration was detected at $t = 3.4$ h, which corresponded to approximately one pore volume. As expected, the concentration of the tracer rose very fast to its maximum concentration, which appeared as a plateau (average concentration 10^5 mol L⁻¹). Due to U(VI) surface complexation Eq. A. 5 /PRI 01/ the pH decreased rapidly from pH_{ini} 4.3 to pH 3.8. As U(VI) sorbed to the surface protons were released and the pH dropped. As the pH decreased, sorbed U(VI) fractions were in return immobilized and travel through the column forming the first peak at $t = 6.9$ h.



As expected, surface complexation reactions of U(VI) were closely correlated to the system's pH-value. As U(VI) was remobilized, protons sorbed to the surface, the pH rose and the remaining U(VI) in the column was retarded. As the pH returned to its initial value, a second U(VI) peak was observed triggered by decreasing pH conditions in the column (Fig. A. 40). Comparable observations were made with Eu column experiments /BRI 18/. The recovery rate of U(VI) equaled 99 %, for Br 100 %, respectively.

For column experiment quartz IV pH_{ini} equaled 4.9 to increase surface complexation and, hence, to induce a lower first U(VI) peak in comparison to quartz III (cf. Fig. A. 40, Fig. A. 41). For quartz IV, the bulk density reached 1.69 g cm⁻³, the relative pore volume equaled 36.3 %, and the flow rate was set to 0.28 ml min⁻¹. Equilibration of the system was reached within 5 d. The initial concentrations of the peak solution equaled $1.19 \cdot 10^{-5}$ mol L⁻¹ Br and $1.01 \cdot 10^{-5}$ mol L⁻¹ U(VI). The recovery rate of U(VI) reached 90.4 % and 100 % for Br. The experiment was stopped after $t = 120$ h. As expected, the first peak was reduced in comparison to column experiment quartz III (cf. Fig. A. 40 and Fig. A. 41).

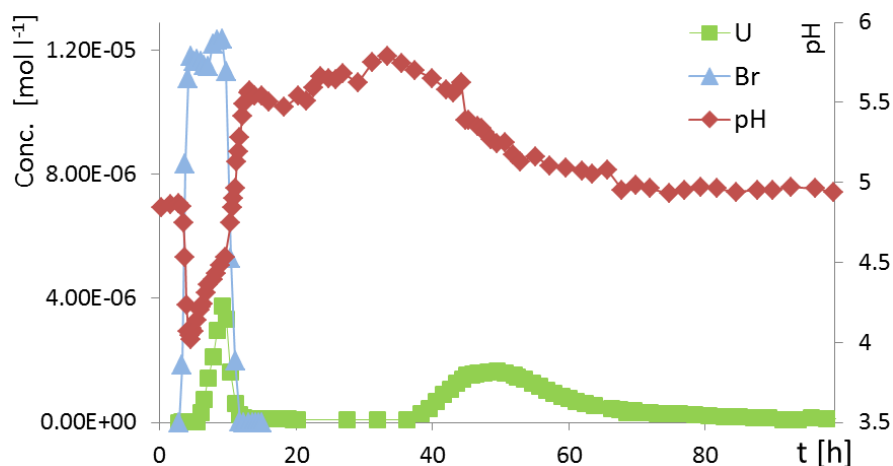


Fig. A. 41 Quartz IV: Development of pH, U(VI) and Br concentrations

NaBr tracer – blue characters, pH development – red symbols, U(VI) development – green symbols, pH_{ini} 4.9.

For a second set of pretests (quartz V), experimental conditions of quartz IV were used. However, instead of collecting U(VI) BTCs, column experiment quartz V was stopped after 30 h ($0.01 \text{ mol L}^{-1} \text{ NaClO}_4$, U(VI) $C_0 = 9.26 \cdot 10^{-6} \text{ mol L}^{-1}$, Br $C_0 = 1.33 \cdot 10^{-5} \text{ mol L}^{-1}$, flow rate 0.26 ml min^{-1}) and the column was fixed with liquid nitrogen to preserve the U(VI) SD in the column. In the next step the column was cut into 12 samples.

Three samples of quartz V were analyzed via CLSM and TRLFS. Both methods provided evidence of the surface complex $\equiv\text{SiO}_2\text{UO}_2^0$ which was identified by comparing collected data with literature spectra of U(VI) complexes on quartz surfaces /GAB 01/, /ILT 12/. A TRLFS spectrum of the second sample is illustrated in Fig. A. 42 (11 – 10 cm: inlet of the column 0 cm, outlet 12 cm). A major peak was detected between 400 and 480 nm which was not typical for U(VI) fluorescence. This peak was probably induced by abrasions or potential organic substances. However, two more peaks with lower intensities were found between 490 and 550 nm (Fig. A. 42). The decay time of the small peak at 515.8 nm was $168 \pm 25 \mu\text{s}$ which was typical for the mentioned $\equiv\text{SiO}_2\text{UO}_2^0$ U(VI) surface complex for the given geochemical conditions of quartz V.

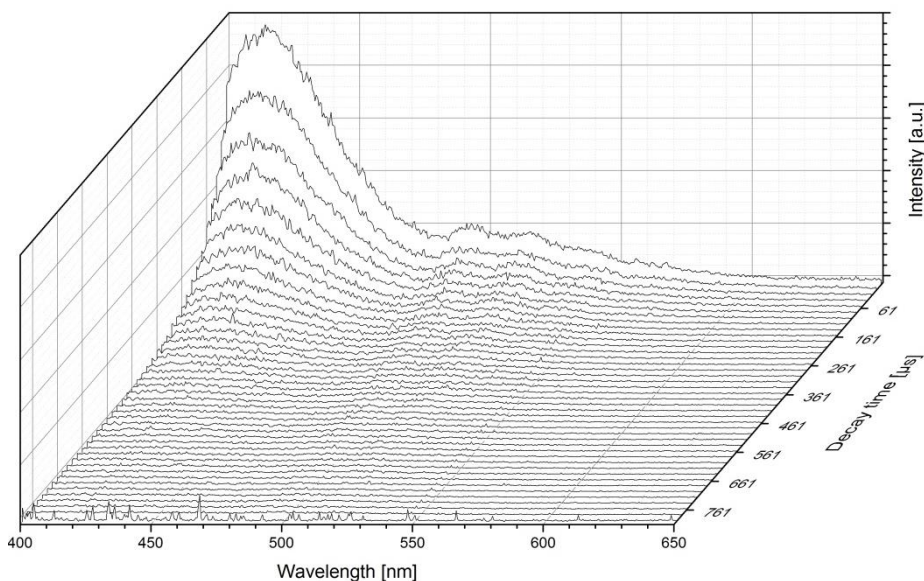


Fig. A. 42 TRLFS spectrum of the top of the second quartz V slice (11-10 cm), inlet of the column 0 cm, outlet 12.25 cm, pH_{ini} 4.9

Typical U(VI) surface complex peaks are found between 490 and 550 nm ($\equiv\text{SiO}_2\text{UO}_2$). Peak between 400 and 480 nm is an interfering signal and may originate from organic matter or abrasion of PFA column walls

To conclude, preliminary trials showed that identification of U(VI) surface complexes was possible with the developed method (Fig. A. 42). Further experiments were conducted to verify these first results (Section 9.3.1.2).

A.10 Formal (pseudocode) description of the concept for consideration of chemical changes in d^{3f++2}

A.10.1 “Calcite”

// Parameter for Calcite (Cc)

$\log K_{\text{spCc}} = 1.85;$
 $\log K_{\text{HCO}_3} = -6.35;$
 $\log K_{\text{CO}_3} = -10.329;$

// Parameter for generic Gibbsite (gG)

$\log K_{\text{spgG}} = 10.35;$
 $\log K_{\text{AlOH}} = -4.9573;$
 $\log K_{\text{AlOH}_2} = -10.5943;$

² The colour marks indicate the following aspects: general comments (purple); the main loops (yellow); abort criteria (grey) and call of the routine calculating gibbsite under- or oversaturation, respectively (green).

```
logKAlOH3 = -16.4328;
logKAlOH4 = -22.8797;
```

```
// Conversion of mass fraction in concentration
// Calculation of ionic strength
// Calculation of Debye-Hückel parameter
```

```
Compute_IS_D(*s, *IS, *D)
{
  *s = 5428.78*(*s);
  *IS = MAX(0, 2*(Ca_T+SO4_T+0.25*DIC_T)+1.13e-3*(*s));
  *D = 0.5114*sqrt(*I)/(1 + 1.5*sqrt(*I));
}
```

```
// Calculation of pH from H & OH with correction after transport
Compute_pH(H, OH, s, D)
```

```
{
  t = 0.5e-3*(H + OH);
  x = t - sqrt(t*t - 1e-6*H*OH + 1e-14/(exp10(-2*D + 0.00012*s)));
  H_korr = 1e-3*H - x;
  return -(log10(H_korr) - D + 0.00012*s);
}
```

```
// Calculation of log(Ion activity product) of calcite
```

```
logIAP_Cc(Ca, DIC, pH, s, D)
{
  return log10(1e-3*DIC) + pH + log10(1e-3*Ca) - log10(1 + exp10(6.35-pH-D) + exp10(pH-10.329+D)) - 5*D + 0.14e-3*s;
}
```

```
// Calculation of H & OH from new pH value
```

```
Update_H_OH(pH, s, D, *H, *OH)
{
  *H = 1e3*exp10(-pH)/exp10(-D + 0.00012*s);
  *OH = 1e3*exp10(-14+pH)/exp10(-D);
}
```

```
// Calculation of total concentration of Al
```

```
Al_tot(D, pH)
{
  return exp10(logKspgG + 9 * D - 3 * pH) + exp10(logKspgG+ logAlOH + 4 * D - 2 * pH) +
  exp10(logKspgG+ logAlOH2 + D - pH) + exp10(logKspgG+ logAlOH3) + exp10(logKspgG+
  logAlOH4 + D + pH);
}
```

```
////////////////////////////////////
//
// Main loop
//
// Input: H_T, OH_T, s, Ca_T, DIC_T; Cc_T from transport step
// d1, e1, d2, e2: damping parameter & Error bounds
//
```



```
Compute_IS_D(&s, &l, &D);
```

```
// Iteration for equilibration //
```

```
pH_T = Compute_pH(H_T, OH_T, s, D);  
H_T = 1e3*exp10(-pH_T + D - 0.00012*s);
```

```
// Saturation index for calcite
```

```
Si_Cc = exp10(logIAP_Cc(Ca_T, DIC_T, pH_T, s, D) - logKspCc);
```

```
if (Si_Cc > 1) // oversaturated
```

```
{  
  FD = d1;  
  do {  
    Fkorr = sqrt(Si_Cc);  
    if (Fkorr-1.0 < e1)  
    {  
      Al_T = Al_tot(D, pH_T)  
      break; // Below error bound => ready  
    }  
    // Precipitate some calcite  
    Ca_korr = Ca_T/Fkorr;  
    DIC_korr = DIC_T/Fkorr;
```

```
retry1:
```

```
  Delta_Ca = MIN(Ca_T - Ca_korr, DIC_T - DIC_korr)*FD;  
  Ca_star = Ca_T - Delta_Ca;  
  DIC_star = DIC_T - Delta_Ca;  
  // Calculate new temporary equilibrium (parameters with '*')  
  F_DIC = (DIC_T - DIC_star)/DIC_T;  
  H_star = H_T;  
  pH_star = pH_T;  
  do {  
    pH_old = pH_star;  
    HCO3 = DIC_star/(4.689e-8/H_star + 1.0);  
    H_star = H_T + F_DIC*(DIC_star - HCO3);  
    pH_star = -(log10(H_star) - 3.0 - D + 0.00012*s);  
  } while (fabs(pH_old - pH_star) > 1e-3);
```

```
// New temporary saturation index
```

```
Si_new = exp10(logIAP(Ca_star, DIC_star, pH_star, s, D) - 1.85);
```

```
if (Si_new >= 1.0) // Still oversaturated?
```

```
{  
  // Yes: take intermediary results and further precipitate calcite  
  Cc_T = Cc_T + (Ca_T - Ca_star) ;  
  Ca_T = Ca_star;  
  DIC_T = DIC_star;  
  pH_T = pH_star;  
  H_T = 1e3*exp10(-pH_T + D - 0.00012*s);
```

```

    Si_Cc = Si_new;
}
else {
    // No: precipitated too much calcite, try with less calcite
    FD *= 0.5;
    goto retry1;
}
} while (1);

} // End loop oversaturation
else // undersaturated
{
    if (Cc_T = 0)
        // Calculate Al_T and pH_T and break → separate file "Gibbsite"

    Kb = 2.133e-4; // =KCO3*I_H2O (Ion product of water)
    FD = d2;
    Cc_T = Cc_0
    do {
        Fkorr = sqrt(Si_Cc);
        if (1.0-Fkorr < e2)
            if (Cc_T < 0)
                {
                    //Dissolve all available calcite and update Ca and DIC
                    Ca_T = Ca_T + Cc_0; DIC_T = DIC_T + Cc_0; Cc_T = 0;
                    // Calculate Al_T and pH_T and break → separate file "Gibbsite"
                } else {
                    Al_T = Al_tot(D, pH_T)
                    break; // Below error bound => ready
                }
            // Attempt to dissolve some calcite
            Ca_korr = Ca_T/Fkorr;
            DIC_korr = DIC_T/Fkorr;
retry2:
            Delta_Ca = MIN(Ca_korr - Ca_T, DIC_korr - DIC_T)*FD;
            Ca_star = Ca_T + Delta_Ca;
            DIC_star = DIC_T + Delta_Ca;
            OH_star = 1e3 * exp10(pH_T-14.0+D) - Kb/2 + sqrt(Kb*Kb/4+0.001*Kb*Delta_Ca);
            pH_star = Compute_pH(H_T, OH_star, s, D);

            // New temporary saturation index
            Si_new = exp10(logIAP(Ca_star, DIC_star, pH_star, s, D) - logKspCc);

            if (Si_new <= 1.0) // still undersaturated?
            {
                // Yes: Adopt interim results and dissolve more calcite
                Cc_T = Cc_T - Delta_Ca ;
                Ca_T = Ca_star;
                DIC_T = DIC_star;
                pH_T = pH_star;
                H_T = 1e3*exp10(-pH_T + D - 0.00012*s);

```

```

    Si_Cc = Si_new;
  } else {
    // No: already too much calcite dissolved,
    // Try to dissolve less calcite
    FD *= 0.5;
    goto retry2;
  }
} while (1);
} // End loop undersaturation

// Calculate H & OH from new pH
Update_H_OH(pH_T, s, D, &H_T, &OH_T);

```

```

////////////////////////////////////
//
// Output: H_T, OH_T, Ca_T, DIC_T, Al_T in equilibrium
//
////////////////////////////////////

```

A.10.2 “Calcite” update

```

// Parameter for calcite and carbonate equilibria (Cc)
logKspCc = -8.481; //Comment: Ca2+ +CO32- = CaCO3
logKHCO3 = 16.6808;
logKCO3 = 10.329;
KHCO3 = exp10(logKHCO3);
KCO3 = exp10(logKCO3);

// Conversion of mass fraction in concentration
// Calculation of ionic strength
// Calculation Debye-Hückel parameters
Compute_IS_D(*s, *IS, *D)
{
  *s = 5428.78>(*s);
  *IS = MAX(0, 2*(Ca_T+SO4_T+0.5*DIC_T)+1.13e-3>(*s));
  *D = 0.5012*sqrt(*I)/(1 + 1.5*sqrt(*I));
}

//Calculation of activity coefficients
//  $\gamma_{\text{CO}_2(\text{aq})} = 1$ ;
 $\gamma_{\text{CO}_3} = \exp10(-4*D - 0.08*s)$ ;
 $\gamma_{\text{HCO}_3} = \exp10(-D)$ ;
 $\gamma_{\text{Ca}} = \exp10(-4*D + 0.14*s)$ ;

// Correction of pH, H, OH & Delta_H
pH_korr (H, OH, Delta_H, s, D)
{

```

```

t = 0.5e-3*(H + OH + Delta_H);
x = t - sqrt(t*t - 1e-6 *OH*(H + Delta_H) + 1e-14/(exp10(-2*D + 0.00012*s)));
H_korr = 1e-3*H - x;
return -(log10(H_korr) - D + 0.00012*s);
}

```

```

// Calculation of ion activity product for calcite

```

```

IAP_Cc(DIC, Ca, pH)

```

```

{

```

```

return  $\gamma_{\text{CO}_3} \cdot (1e-3 \cdot \text{DIC}) / (1 + \text{KCO}_3 / \gamma_{\text{HCO}_3} \cdot \gamma_{\text{CO}_3} \cdot \exp10(-\text{pH}) + \text{KHCO}_3 \cdot \gamma_{\text{CO}_3} \cdot (\exp10(-\text{pH}))^2) \cdot \gamma_{\text{Ca}} \cdot 1e-3 \cdot \text{Ca}$ ;

```

```

}

```

```

// Calculation of H & OH from new pH-value

```

```

Update_H_OH(pH, s, D, *H, *OH)

```

```

{

```

```

*H = 1e3*exp10(-pH)/exp10(-D + 0.00012*s);

```

```

*OH = 1e3*exp10(-14+pH)/exp10(-D);

```

```

}

```

```

//Calculation of sigmoid function (average number of carbonate bound protons)

```

```

Sig_T(pH)

```

```

{

```

```

return = -3.0/(3-0+1.98433*exp(-2.37406*(pH-6.42219))) - 3.0/(3.0+1.0747*exp(-2.22078*(pH-10.4078))) + 2;

```

```

}

```

```

// Initialization of valid DIC concentration range

```

```

DIC_low = 1.0e-5;

```

```

DIC_high = 1.0e-1;

```

```

// Definition of error range

```

```

e1 = 1.0e-4; // saturation index

```

```

e2 = 1.0e-3; // pH

```

```

////////////////////////////////////////////////////////////////////////////////////////////////////////////////////////////////

```

```

//

```

```

// WEIMAR-Calcit-case-main loop

```

```

//

```

```

// Input: H_T, OH_T, s, DIC_T, Ca_T from transport step

```

```

// e1, e2: error bounds

```

```

//

```

```

////////////////////////////////////////////////////////////////////////////////////////////////////////////////////////////////

```

```

Compute_IS_D(&s, &IS, &D);

```

```

pH_T = pH_korr(H_T, OH_T, 0, s, D);

```

```

Si_Cc = log(IAP_Cc(DIC_T, Ca_T, pH_T)) - logKsp_Cc;

```

```

Ca_korr = Ca_T;

```

```

/** Iteration for equilibration */

//Outer loop
Do
{
// Check saturation index of calcite
if (fabs((Si_Cc) < e1)
    break; // Fehlerschranke unterboten? => fertig!!

// Calculate new temporary equilibrium
if (fabs(Si_Cc) > 0) // oversaturated
    DIC_high = DIC_T;
else // undersaturate
    DIC_low = DIC_T;

// Initialization of inner loop
DIC_korr = 0.5*(DIC_high + DIC_low);
Delta_DIC = DIC_korr - DIC_T;
Delta_NH0 = Sig_T(pH_T);
Delta_H = Delta_NH0*Delta_DIC;
// Correction of pH from H, OH & Delta_H
pH_star = pH_korr(H_T, OH_T, Delta_H, s, D);
pH_low = Min(pH_T, pH_star);
pH_up = Max(pH_T, pH_star);
// New temporary saturation index for calcite
SI_new = log(IAP_Cc(DIC_korr, Ca_korr, pH_star)) - logKsp_Cc;

// Inner loop
Do until (fabs(pH_up - pH_low) < e2)
{
    pH_star = 0.5*(pH_up + pH_low);
    pH_ini = pH_star;
    Delta_NH = Sig_T(pH_star) - Delta_NH0;
    Delta_H = Delta_NH*Delta_DIC - Delta_NH0* DIC_korr;

// Correction of pH from H, OH & Delta_H
    pH_star = pH_korr (H_T, OH_T, Delta_H);
    if(pH_star > pH_ini)
    {
        pH_low = Max(pH_low, pH_ini);
        pH_up = Min(pH_up, pH_star);
    }

// Update of Ca-concentration
    Ca_korr = Ca_T + Delta_DIC;

// New temporary saturation index
    If Ca_korr < 0 //not enough Ca available
        SI_new = -1
    else

```

```

        Si_new = log(IAP_Cc(DIC_korr, Ca_korr, pH_star)) - logKsp_Cc;
    } // End inner loop

    // Take intermediate results
    DIC_T = DIC_korr;
    Si_Cc = Si_new;
    pH_Cc = pH_star;
}
While (1); // End outer loop
    Ca_T = Ca_korr;

// New calculation of H & OH from new pH value
Update_H_OH(pH_Cc, s, D, &H_T, &OH_T);

```

```

////////////////////////////////////
//
// Output: H_T, OH_T, Ca_T, DIC_T, in equilibrium
//
////////////////////////////////////

```

A.10.3 “Gibbsite”

```

// Parameter for generic gibbsite (gG)

```

```

logKspgG = 10.35;
logKAlOH = -4.9573;
logKAlOH2 = -10.5943;
logKAlOH3 = -16.4328;
logKAlOH4 = -22.8797;
KAlOH = exp10(logKAlOH)
KAlOH2 = exp10(logKAlOH2);
KAlOH3 = exp10(logKAlOH3);
KAlOH4 = exp10(logKAlOH4);

```

```

//Calculation of activity coefficients

```

```

γAl3 = exp10(-9*D + 0.00033* s;
γAlOH = exp10(-4*D + 0.00009* s;
γAlOH2 = exp10(-D + 0.00027* s;
γAlOH4 = exp10(-D + 0.00007* s;

```

```

// Calculation of pH from H & OH with correction after Al precipitation/dissolution

```

```

pH_korr (H, OH, Delta_OH, s, D)
{
    t = 0.5e-3*(H + OH+Delta_OH);
    x = t - sqrt(t*t - 1e-6*H*(OH + Delta_OH) + 1e-14/(exp10(-2*D + 0.00012*s)));
    H_korr = 1e-3*H - x;
    return -(log10(H_korr) - D + 0.00012*s);
}

```

```

// Calculation of log(ion activity product) of generic gibbsite

```

```

logIAP_gG(Al, pH, s, D)
{

```

```

return log(Al_T*1e-3 / exp10(-pH) / (1/  $\gamma_{Al_3}$  + KAlOH / ( $\gamma_{AlOH}$ *exp10(-pH))
+ KAlOH2 / ( $\gamma_{AlOH_2}$ *( exp10(-pH))2) + KAlOH3 / exp10(-pH))3
+ KAlOH4 / ( $\gamma_{AlOH_4}$ *(exp10(-pH)4)));
}

```

```

// Calculation of H & OH from new pH value

```

```

Update_H_OH(pH, s, D, *H, *OH)
{
*H = 1e3*exp10(-pH)/exp10(-D + 0.00012*s);
*OH = 1e3*exp10(-14+pH)/exp10(-D);
}

```

```

// Calculation of total concentration of Al

```

```

Al_tot(D, pH)
{
return exp10(logKspgG + 9 * D - 3 * pH) + exp10(logKspgG+ logKAlOH + 4 * D - 2 * pH) +
exp10(logKspgG+ logKAlOH2 + D - pH) + exp10(logKspgG+ logKAlOH3) + exp10(logKspgG+
logKAlOH4 + D + pH);
}

```

```

//Calculation of sigmoid function (average number of Al bound OH-ions)

```

```

Sig_T(pH)
{
return = 3.97949/(0.99836+3.14996*exp(-2.25661*(pH-5.25813))+ 0.01171;
}

```

```

// Initialisation of the valid Al concentration range

```

```

Al_low = 1.0e-6;
Al_high = 1.0e-4;

```

```

// Definition of error bounds

```

```

e1 = 1.0e-4; // saturation index
e2 = 1.0e-3; // pH

```

```

////////////////////////////////////////////////////////////////////////////////////////////////////////////////////////////////
//
// WEIMAR Al-case main loop
//
// Input: H_T, OH_T, s, Al_T from transport step
// e1, e2: error bounds
//
////////////////////////////////////////////////////////////////////////////////////////////////////////////////////////////////

```

```

Compute_I_D(&s, &l, &D);
pH_T = pH_korr(H_T, OH_T,0, s, D);
Si_gG = logIAP_gG(Al_T, pH_T, s, D) / logKspgG;
Al_T_ini = Al_T

```

```

/* Iteration for equilibration */

```

```

//Outer loop
Do
{
// Check saturation index of generic gibbsite
If fabs((Si_gG - 1.0) < e1)
    break; // Below error bound => ready

// Calculate temporary equilibrium
if (Si_gG > 1) // Oversaturated
    Al_high = Al_T;
else
    Al_low = Al_T;

// Initialisation inner loop
Al_korr = 0.5*(Al_high + Al_low);
Delta_Al = Al_korr - Al_T_ini;
Delta_NOH_0 = Sig_T(pH_T) - 3;
Delta_OH = -Delta_NOH_0*Delta_Al;
// Calculate corrected pH from H, OH & Delta_OH
pH_star = pH_korr(H_T, OH_T, Delta_OH, s, D);
pH_low = Min(pH_T, pH_star);
pH_up = Max(pH_T, pH_star);
// New temporary saturation index of generic gibbsite
SI_new = logIAP_gG(Al_korr, pH_star, s, D) - logKsp_gG;

// Inner loop
Do until (pH_up - pH_low < e2)
{
    pH_star = 0.5*(pH_up + pH_low);
    pH_ini = pH_star;
    Delta_NOH = Sig_T(pH_star) - 3 - Delta_NOH_0;
    Delta_OH = -Delta_NOH_0*Delta_Al - Delta_NOH*Al_korr;

.....// Correction of pH value from H, OH & Delta_OH
    pH_star = pH_korr (H_T, OH_T, Delta_OH, s, D);
    if(pH_star > pH_ini)
        pH_low = Max(pH_low, pH_ini);
    if(pH_star < pH_ini)
        pH_up = Min(pH_up, pH_star);

// New temporary saturation index
    SI_gG = logIAP_gG(Al_korr, pH_star, s, D) / logKsp_gG;
} // End inner loop

// Adopt interim results
Al_T = Al_korr;
}
While (1); // End outer loop

// Calculate H & OH from new pH
Update_H_OH(pH_star, s, D, &H_T, &OH_T);

```

```
////////////////////////////////////  
//  
// Output: H_T, OH_T, Ca_T, DIC_T, Al_T in equilibrium  
//  
////////////////////////////////////
```

**Gesellschaft für Anlagen-
und Reaktorsicherheit
(GRS) gGmbH**

Schwertnergasse 1
50667 Köln
Telefon +49 221 2068-0
Telefax +49 221 2068-888

Boltzmannstraße 14
85748 Garching b. München
Telefon +49 89 32004-0
Telefax +49 89 32004-300

Kurfürstendamm 200
10719 Berlin
Telefon +49 30 88589-0
Telefax +49 30 88589-111

Theodor-Heuss-Straße 4
38122 Braunschweig
Telefon +49 531 8012-0
Telefax +49 531 8012-200

www.grs.de